

WL-TR-96-4094

**PROCEEDINGS OF THE 1995
USAF STRUCTURAL INTEGRITY
PROGRAM CONFERENCE**



ASIP

VOLUME II

EDITORS:

Gary K. Waggoner
WL/Materials Directorate
Wright-Patterson AFB OH

John W. Lincoln
ASC/Deputy for Engineering
Wright-Patterson AFB OH

James L. Rudd
WL/Flight Dynamics Directorate
Wright-Patterson AFB OH

USAF Structural Integrity Program Conference
Hilton Palacio del Rio
San Antonio TX

AUGUST 1996

19961025 032

FINAL REPORT FOR 28-30 NOVEMBER 1995

Approved for public release; distribution unlimited

**MATERIALS DIRECTORATE
WRIGHT LABORATORY
AIR FORCE MATERIEL COMMAND
WRIGHT-PATTERSON AIR FORCE BASE, OH 45433-7718**

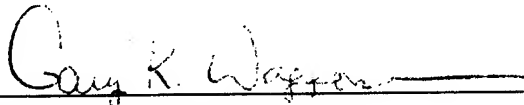
DTIC QUALITY INSPECTED 3

NOTICE

When government drawings, specifications, or other data are used for any purpose other than in connection with a definitely related government procurement operation, the United States Government thereby incurs no responsibility or any obligation whatsoever; and the fact that the government may have formulated, furnished, or in any way supplied the said drawings, specifications, or other data, is not to be regarded by implication or otherwise as in any manner licensing the holder or any other person or corporation, or conveying any rights or permission to manufacture use, or sell any patented invention that may in any way be related thereto.

This report has been reviewed by the Office of Public Affairs (ASC/PA) and is releasable to the National Technical Information Service (NTIS). At NTIS, it will be available to the general public, including foreign nationals.

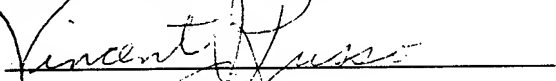
This technical report has been reviewed and is approved for publication.



GARY K. WAGGONER

Chief

Systems Support Division



VINCENT J. RUSSO

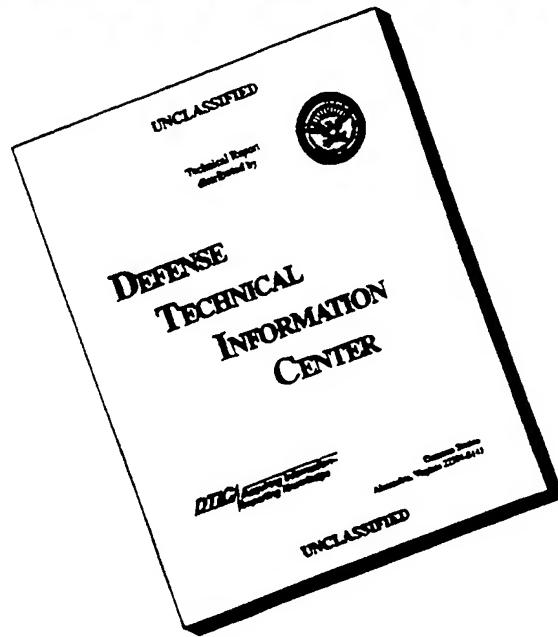
Director

Materials Directorate

If your address has changed, if you wish to be removed from our mailing list, or if the addressee is no longer employed by your organization, please notify WL/MLS Bldg 652, 2179 Twelfth St Ste 1, Wright-Patterson AFB, Ohio 45433-7718 to help us maintain a current mailing list.

Copies of this report should not be returned unless return is required by security considerations, contractual obligations, or notice on a specific document.

DISCLAIMER NOTICE



**THIS DOCUMENT IS BEST
QUALITY AVAILABLE. THE
COPY FURNISHED TO DTIC
CONTAINED A SIGNIFICANT
NUMBER OF PAGES WHICH DO
NOT REPRODUCE LEGIBLY.**

REPORT DOCUMENTATION PAGE			Form Approved OMB No. 0704-0188	
Public reporting burden for this collection of information is estimated to average 1 hour per response, including the time for reviewing instructions, searching existing data sources, gathering and maintaining the data needed, and completing and reviewing the collection of information. Send comments regarding this burden estimate or any other aspect of this collection of information, including suggestions for reducing this burden, to Washington Headquarters Services, Directorate for Information Operations and Reports, 1215 Jefferson Davis Highway, Suite 1204, Arlington, VA 22202-4302, and to the Office of Management and Budget, Paperwork Reduction Project (0704-0188), Washington, DC 20503.				
1. AGENCY USE ONLY (Leave blank)		2. REPORT DATE August 1996		3. REPORT TYPE AND DATES COVERED Final, 28-30 November 1995
4. TITLE AND SUBTITLE Proceedings of the 1995 USAF Structural Integrity Program Conference, Volume: II			5. FUNDING NUMBERS PE 62102F PR 2418 TA 07 WU 04	
6. AUTHOR(S) 1-Thomas D. Cooper, Compiler & Editor; 2-John W. Lincoln, ASC/ENF; and 3-James L. Rudd, WL/FIB, Editors				
7. PERFORMING ORGANIZATION NAME(S) AND ADDRESS(ES) 1-Materials Directorate and 3-Flight Dynamics Directorate, Wright Laboratory; 2-Aeronautical Systems Center, Deputy for Engineering, all three of the Air Force Materiel Command Wright-Patterson AFB OH 45433			8. PERFORMING ORGANIZATION REPORT NUMBER WL-TR-96-4094	
9. SPONSORING / MONITORING AGENCY NAME(S) AND ADDRESS(ES) POC: Gary Waggoner, WL/MLS, 513-255-4651 Materials Directorate Wright Laboratory Air Force Materiel Command Wright-Patterson AFB OH 45433 -7718			10. SPONSORING / MONITORING AGENCY REPORT NUMBER WL-TR-96-4094	
11. SUPPLEMENTARY NOTES				
12a. DISTRIBUTION / AVAILABILITY STATEMENT Approved for public release; distribution is unlimited.			12b. DISTRIBUTION CODE	
13. ABSTRACT (Maximum 200 words) This report contains the proceedings of the 1995 USAF Structural Integrity Program Conference held at the Hilton Palacio del Rio Hotel in San Antonio, Texas, from 28-30 November 1995. The conference, which was sponsored by the Aeronautical Systems Center's Engineering Directorate and the Wright Laboratory's Flight Dynamics and Materials Directorates, was hosted by the San Antonio Air Logistics Center Aircraft Directorate, Aircraft Structural Integrity Branch (SA-ALC/LADD). This conference, as in previous years, was held to permit experts in the field of structural integrity to communicate with each other and to exchange views on how to improve the structural integrity of military weapon systems. Sessions were primarily focused on analysis and testing, engine structural integrity, structural materials and inspections, structural repair, and force management. This year, as in previous years, our friends from outside the U.S. borders provided the audience with outstanding presentations on activities within their countries. It is anticipated this conference will include their contributions in the agenda of future meetings. This year, 16 countries were represented in the audience.				
14. SUBJECT TERMS			15. NUMBER OF PAGES 1225	
			16. PRICE CODE	
17. SECURITY CLASSIFICATION OF REPORT UNCLASSIFIED		18. SECURITY CLASSIFICATION OF THIS PAGE UNCLASSIFIED		19. SECURITY CLASSIFICATION OF ABSTRACT UNCLASSIFIED
				20. LIMITATION OF ABSTRACT SAR

GENERAL INSTRUCTIONS FOR COMPLETING SF 298

The Report Documentation Page (RDP) is used in announcing and cataloging reports. It is important that this information be consistent with the rest of the report, particularly the cover and title page. Instructions for filling in each block of the form follow. It is important to ***stay within the lines*** to meet ***optical scanning requirements***.

Block 1. Agency Use Only (Leave Blank).

Block 2. Report Date. Full publication date including day, month, and year, if available (e.g. 1 Jan 88). Must cite at least the year.

Block 3. Type of Report and Dates Covered. State whether report is interim, final, etc. If applicable, enter inclusive report dates (e.g. 10 Jun 87 - 30 Jun 88).

Block 4. Title and Subtitle. A title is taken from the part of the report that provides the most meaningful and complete information. When a report is prepared in more than one volume, repeat the primary title, add volume number, and include subtitle for the specific volume. On classified documents enter the title classification in parentheses.

Block 5. Funding Numbers. To include contract and grant numbers; may include program element number(s), project number(s), task number(s), and work unit number(s). Use the following labels:

C - Contract	PR - Project
G - Grant	TA - Task
PE - Program Element	WU - Work Unit Accession No.

Block 6. Author(s). Name(s) of person(s) responsible for writing the report, performing the research, or credited with the content of the report. If editor or compiler, this should follow the name(s).

Block 7. Performing Organization Name(s) and Address(es). Self-explanatory.

Block 8. Performing Organization Report Number. Enter the unique alphanumeric report number(s) assigned by the organization performing the report.

Block 9. Sponsoring/Monitoring Agency Name(s) and Address(es). Self-explanatory.

Block 10. Sponsoring/Monitoring Agency Report Number. (If known)

Block 11. Supplementary Notes. Enter information not included elsewhere such as: Prepared in cooperation with...; Trans. of...; To be published in.... When a report is revised, include a statement whether the new report supersedes or supplements the older report.

Block 12a. Distribution/Availability Statement. Denotes public availability or limitations. Cite any availability to the public. Enter additional limitations or special markings in all capitals (e.g. NOFORN, REL, ITAR).

DOD - See DoDD 5230.24, "Distribution Statements on Technical Documents."

DOE - See authorities.

NASA - See Handbook NHB 2200.2.

NTIS - Leave blank.

Block 12b. Distribution Code.

DOD - Leave blank.

DOE - Enter DOE distribution categories from the Standard Distribution for Unclassified Scientific and Technical Reports.

NASA - Leave blank.

NTIS - Leave blank.

Block 13. Abstract. Include a brief (*Maximum 200 words*) factual summary of the most significant information contained in the report.

Block 14. Subject Terms. Keywords or phrases identifying major subjects in the report.

Block 15. Number of Pages. Enter the total number of pages.

Block 16. Price Code. Enter appropriate price code (*NTIS only*).

Block 17 - 19. Security Classifications. Self-explanatory. Enter U.S. Security Classification in accordance with U.S. Security Regulations (i.e., UNCLASSIFIED). If form contains classified information, stamp classification on the top and bottom of the page.

Block 20. Limitation of Abstract. This block must be completed to assign a limitation to the abstract. Enter either UL (unlimited) or SAR (same as report). An entry in this block is necessary if the abstract is to be limited. If blank, the abstract is assumed to be unlimited.

Volume II

SESSION VII - ADVANCED MATERIALS AND PROCESSES

Damage Progression in Bolted Composite Structures	663
<i>C. Chamis, P. Gotsis and L. Minnetyan</i>	
High-Strength Aluminum Forged Product Durability and Damage Tolerance Capabilities for Weight and Total Life Cycle Cost Saving	681
<i>R. Bucci, R. Bush, A. Hinkle, H. Konish, M. Kulak, R. Wygonik & G. Kuhlman</i>	
The Impact of Fastener Hole Quality on Structural Life; A History of Success	703
<i>C. Radcliffe and W.H. Sproat</i>	
A Probabilistic Model for Predicting Fatigue Life for Crack Formation at Inclusions Using FASTRAN	727
<i>P. Laz, S. Rohrbaugh and B. Hillberry</i>	
The Application of the R-Curve Concept for the Prediction of the Residual Strength of Fiber Metal Laminates	751
<i>T. de Vries & M. Pacchione</i>	
Laser Shock Peening - An Analysis in Nearly Closed Form	777
<i>H. Swift</i>	

SESSION VIII - NDE/I

Nondestructive Electrochemical Corrosion Measurement: Electrochemical Impedance Pattern Recognition for Detection of Hidden Chemical Corrosion on Aircraft Components	791
<i>J. Bowers, M. Vreeke and A. Sammells</i>	
Detecting Weepole Cracks Using Ultrasonic Creeping Waves	821
<i>M. Golis</i>	
An Advanced ACPD System for Aircraft Structural Integrity Assessment	827
<i>S. Tiku, N. Marchand and R. Finlayson</i>	

SESSION IX - REPAIRS

C-141 Repair Tracking	845
<i>R. Alford and R. Sykes</i>	
The ForceTec® Rivetless Nut Plate System and Its Application to Military Aircraft Production and Repair	869
<i>L. Reid and E. Esterbrook</i>	
Design Development of a Bonded Fuselage Repair for the C-5A	887
<i>Major R. Fredell, C. Guijt, Lt D. Conley and Lt S. Knighton</i>	
An FEAM Based Methodology for Analyzing Composite Patch Repairs of Metallic Structures	903
<i>V. Nagaswamy, D.S. Pipkins and S.N. Atluri</i>	
The 1973-1974 F/RF-4C/D Damage Tolerance and Life Assessment Study Revisited	931
<i>R. Bader and R. Howell</i>	

SESSION X - CORROSION/FATIGUE

Aircraft Corrosion and Fatigue Damage Assessment	983
<i>R. Wanhill</i>	
Fuselage Lap Splice Joint Corrosion	1029
<i>R. Piascik, R. Kelly and S. Williard</i>	
The Effect of Corrosion on the Structural Integrity of Fuselage Lap Joints	1063
<i>N. Bellinger and J. Komorowski</i>	
Effects of Cyclic Immersion in 3.5% NaCl Solution on Fatigue Crack Propagation Rates in Aluminum 2024-T351	1089
<i>J. Kramer and D. Hoepfner</i>	
Corrosion Fatigue Interaction	1113
<i>P. Tong, D. Jeong and G. Neat</i>	

SESSION XI - FORCE MANAGEMENT

Automated Readiness Integrated Engineering System (ARIES)	1131
<i>J. Cochran and C. Burke</i>	
AMRL Support for RAAF F-111 ASIMP	1139
<i>K. Watters and J. Paul</i>	
RNZAF Project KESTREL	1159
<i>Squadron Leader J. ten Have</i>	
Application of Object Oriented Technology to an Aircraft Structural Integrity Program - FAA Flight Inspection Learjet Model 60 and Canadair Challenger 601-3R Aircraft	1167
<i>T. Kelley</i>	
ATTENDEES LIST	1195

SESSION VII

**ADVANCED MATERIALS
AND PROCESSES**

Chairman: *R. Meeker*, WL/MLS

Damage Progression in Bolted Composite Structures

Christos C. Chamis* and Pascal K Gotsis†

National Aeronautics and Space Administration
Lewis Research Center, Cleveland, Ohio 44135-3191

Levon Minnetyan‡

Clarkson University, Potsdam, New York 13699-5710

ABSTRACT

Structural durability, damage tolerance, and progressive fracture characteristics of bolted graphite/epoxy composite laminates are evaluated via computational simulation. The objective of this paper is to demonstrate a new methodology that scales up constituent material properties, stress and strain limits to the structure level to evaluate the overall damage and fracture propagation for bolted composites. An integrated computer code is used for the simulation of structural degradation under loading. Damage initiation, growth, accumulation, and propagation to fracture are included in the simulation. Results show the damage progression sequence and structural fracture resistance during different degradation stages. The effect of fastener spacing is investigated with regard to the structural durability of a bolted joint.

*Senior Aerospace Scientist, Structures Division.

†Aerospace Research Engineer, Structures Division.

‡Associate Professor, Dept Civil and Environmental Engineering.

INTRODUCTION

Modern applications of fiber composite structures require highly reliable structural joints that must remain safe under high tensile, compressive, shear, bending, and fatigue loads such as in aircraft wing and tail assemblies. In many cases critical composite structural components are assembled by mechanical fasteners such as bolts and rivets. The durability of a bolted graphite/epoxy laminated composite is evaluated via computational simulation. Damage and fracture propagation are considered due to tensile loading. An integrated computer code is used for the simulation of structural degradation. Damage initiation, growth, accumulation, and propagation to structural fracture are included in the simulation. The present approach by-passes traditional fracture mechanics to provide an alternative evaluation method, conveying to the design engineer a detailed description of damage initiation, accumulation, and propagation that would take place in the process of ultimate fracture of a mechanically fastened joint. Results show the damage progression sequence and structural fracture resistance during different degradation stages. This paper demonstrates that computational simulation, with the use of established material modelling and finite element modules, adequately tracks the damage growth and subsequent propagation to fracture for mechanically fastened fiber composite structures.

The behavior of a laminated composite structure under loading is rather complex, especially when possible degradation is to be taken into account. Under tensile loading, internal damage in composites is often initiated as transverse cracking in one or more plies. At the presence of stress concentrations, defects, or under longitudinal compressive loading, initial damage may also include fiber fracture. Further degradation is in the form of additional fiber fractures that usually lead to structural fracture by the coalescing of damage zones.

Because of the numerous possibilities with material combinations, composite geometry, ply orientations, and loading conditions, it is essential to have an effective computational capability to predict the behavior of composite structures for any loading, geometry, material combinations, and boundary conditions. The predictions of damage initiation, growth, accumulation, and propagation to fracture are important in evaluating the load carrying capacity and reliability of composite structures. Quantification of the structural fracture resistance is also required to evaluate the durability/life of composite structures.

The CODSTRAN (COMposite Durability STRuctural ANalysis) computer code [1] has been developed for this purpose. CODSTRAN is able to sim-

ulate damage initiation, damage growth, and fracture in composites under various loading, considering also the effects of residual stresses and environmental conditions. The simulation of progressive fracture by CODSTRAN has been verified to be in reasonable agreement with experimental data from tensile tests [2]. Recent additions to CODSTRAN have enabled investigation of the effects of composite degradation on structural response [3], composite damage induced by dynamic loading [4], composite structures global fracture toughness [5], effect of the hygrothermal environment on durability [6], damage progression in composite shells subjected to internal pressure [7], an overall evaluation of the progressive fracture in polymer matrix composite structures [8], the durability of stiffened composite shells under load combinations [9], design considerations for progressive fracture in composite shell structures and the simulation of damage propagation in thick composite shells under external pressure [10]. The purpose of this paper is to examine damage progression in bolted composites. Due to the tendency of bolted structural elements to deform independently and to pull apart, bolted joints present potential nucleation points for damage initiation and fracture. Damage progression in a bolted composite panel is examined.

For the purpose of the present discussion, the following terminology is used to describe the various stages of degradation in the composite structure: (1) *damage initiation* refers to the start of damage induced by applied loading; (2) *damage growth* is the progression of damage from the location of damage initiation to adjacent regions; (3) *damage propagation* is the rapid progression of damage to other regions of the structure. At any stage of damage progression, if there is a high level of structural resistance to damage progression, the structure is stable with regard to fracture. The corresponding state of structural damage is referred to as *stable damage*. On the other hand, if damage progression does not encounter significant structural resistance, it corresponds to an *unstable damage* state. Unstable damage progression is characterized by very large increases in the amount of damage due to very small increases in loading.

BRIEF DESCRIPTION OF CODSTRAN

CODSTRAN is an integrated, open-ended, stand alone computer code consisting of three modules: composite mechanics, finite element analysis, and damage progression modelling. The overall evaluation of composite structural durability is carried out in the damage progression module [1] that keeps track of composite degradation for the entire structure. The damage progression

module relies on ICAN [11] for composite micromechanics, macromechanics and laminate analysis, and calls a finite element analysis module that uses anisotropic thick shell elements to model laminated composites [12].

A computational simulation cycle in CODSTRAN begins with the definition of constituent properties from a materials databank. Composite ply properties are computed by the ICAN composite mechanics module [11]. Figure 1 shows a schematic of the computational simulation cycle in CODSTRAN. The ICAN composite mechanics module is called before and after each finite element analysis. Prior to each finite element analysis, the ICAN module computes the finite element nodal properties from material characteristics and the degradation history. The composite ply properties may be different at each node. The finite element analysis module [12] accepts the generalized properties that are computed by the ICAN module at each node and performs the analysis at each load increment. After an incremental finite element analysis, the computed generalized nodal force resultants and deformations are supplied to the ICAN module that evaluates the nature and amount of local damage, if any, in the plies of the composite laminate. Individual ply failure modes are determined by ICAN using failure criteria associated with the negative and positive limits of the six stress components in the directions of the material axes, interply delamination due to relative rotation of the plies, and a combined stress failure criterion based on modified distortion energy theory [11].

The generalized stress-strain relationships for each node are revised according to the composite damage evaluated by the ICAN module after each finite element analysis. The model is automatically updated with a new finite element mesh/properties and the structure is reanalyzed for further deformation and damage. If ply failure criteria indicate new or additional damage during a load increment, CODSTRAN degrades the composite properties affected by the damage and reanalyzes the structure under the same load. When there is no indication of further damage under a load, the structure is considered to be in equilibrium. Subsequently, another load increment is applied leading to possible damage growth, accumulation, or propagation. Analysis is stopped when global structural fracture is predicted.

Figure 2 shows a schematic of CODSTRAN damage tracking, expressed in terms of a load-displacement relationship. Point 1 represents the last equilibrium state before initial damage. When the structure is loaded by an additional load increment to point 2, ply failure criteria indicate damage initiation. At this stage CODSTRAN degrades the composite properties affected by the

damage, reconstitutes a new computational model with updated finite element mesh and material properties, and reanalyzes the structure under the same load increment to reach point 3. However, at point 3, composite ply failure criteria indicate additional damage. Accordingly, structural properties are further degraded and analysis is repeated under the same load increment to reach point 4. There is no further damage at point 4 because the structure is now in equilibrium with the external loads. Subsequently, another load increment is applied leading to point 5 with possible damage growth and propagation.

In general, overall structural damage may include individual ply damage and also through-the-thickness fracture of the composite laminate. CODSTRAN is able to simulate varied and complex composite damage mechanisms via evaluation of the individual ply failure modes and associated degradation of laminate properties. The type of damage growth and the sequence of damage progression depend on the composite structure, loading, material properties, and hygrothermal conditions. A scalar damage variable, derived from the total volume of the structure affected by various damage mechanisms is also computed as an indicator of the level of overall damage induced by loading. This damage variable is useful for assessing the overall degradation of a given structure under a prescribed loading condition. The rate of overall damage growth during damage progression may be used to evaluate the propensity of structural fracture with increasing loading. Computation of the overall damage variable has no interactive feedback on the detailed simulation of structural degradation. The procedure by which the overall damage variable is computed is given in reference [5]. In this paper, the structure is defined to be 100 percent damaged when all layers at all nodes develop some damage. Computational simulation is carried out up to global fracture.

BOLTED COMPOSITE JOINT

A graphite/epoxy laminate fastened by a single bolt as shown in Figure 3 is considered first. The laminate consists of 48 plies that are configured as $[0/\pm 45/90]_{16}$ with a total thickness of 6.35 mm (0.25 in). The 0° plies are oriented in the load direction and the 90° plies are oriented transverse to the load direction. The specimen has a width of 102 mm (4.0 in) and a length of 204 mm (8.0 in).

In order to track the interactive behavior of the bolt and the composite structure, the bolt is represented separately from the laminated composite structure. The bolt has a diameter of 25.4 mm (1.0 in) and is made of high-strength steel. Independent finite elements for laminate and fastener with master/slave

duplicate nodes at the bolt/laminate boundary are used to enforce the continuity of displacements between contacting elements. When generalized in-plane stresses become tensile at a boundary node of the bolt, the duplicate node relationship is terminated to allow the separation of the laminate from the fastener. Elastic deformations of the fastener are considered in the computational model. However, failure criteria are not imposed on the fastener elements.

The composite system is made of AS-4 graphite fibers in a high-modulus, high strength (HMHS) epoxy matrix. The fiber and matrix properties are obtained from a databank of composite constituent material properties resident in CODSTRAN [11]. The fiber and matrix properties corresponding to this case are as follows:

AS-4 Fiber Properties:

Number of fibers per end = 10000
Fiber diameter = 0.00762 mm (0.300E-3 in)
Fiber Density = 4.04E-7 Kg/m³ (0.063 lb/in³)
Longitudinal normal modulus = 227 GPa (32.90E+6 psi)
Transverse normal modulus = 13.7 GPa (1.99E+6 psi)
Poisson's ratio (ν_{12}) = 0.20
Poisson's ratio (ν_{23}) = 0.25
Shear modulus (G_{12}) = 13.8 GPa (2.00E+6 psi)
Shear modulus (G_{23}) = 6.90 GPa (1.00E+6 psi)
Longitudinal thermal expansion coefficient = 1.0E-6/°C (-0.55E-6 /°F)
Transverse thermal expansion coefficient = 1.0E-6/°C (-0.56E-6 /°F)
Longitudinal heat conductivity = 43.4 J-m/hr/m²/°C (580 BTU-in/hr/in²/°F)
Transverse heat conductivity = 4.34 J-m/hr/m²/°C (58 BTU-in/hr/in²/°F)
Heat capacity = 712 J/Kg/°C (0.17 BTU/lb/°F)
Tensile strength = 3,723 MPa (540 ksi)
Compressive strength = 3,351 MPa (486 ksi)

HMHS Matrix Properties:

Matrix density = 3.40E-7 Kg/m³ (0.0457 lb/in³)
Normal modulus = 4.27 GPa (620 ksi)
Poisson's ratio = 0.34
Coefficient of thermal expansion = 0.72/°C (0.4E-4 /°F)
Heat conductivity = 1.25 BTU-in/hr/in²/°F
Heat capacity = 0.25 BTU/lb/°F
Tensile strength = 84.8 MPa (12.3 ksi)

Compressive strength = 423 MPa (61.3 ksi)

Shear strength = 148 MPa (21.4 ksi)

Allowable tensile strain = 0.02

Allowable compressive strain = 0.05

Allowable shear strain = 0.04

Allowable torsional strain = 0.04

Void conductivity = 16.8 J-m/hr/m²/°C (0.225 BTU-in/hr/in²/°F)

Glass transition temperature = 216°C (420°F)

The HMHS matrix properties are representative of the 3501-6 resin. The fiber volume ratio is 0.60 and the void volume ratio is 2 percent. The laminate cure temperature is 177°C (350°F) and the use temperature is 21°C (70°F).

The bolted laminate is investigated under uniaxial tensile loading. The specimen is loaded by restraining the center node of the bolt and imposing a uniformly distributed tensile load at the far end of the laminate. Damage progression is computationally simulated as the loading is increased.

Figure 4 shows the damage progression with increasing tensile loading on the bolted joint as the progressive damage response of the laminate is evaluated. During the first load increment of 3559 N (800 lbs), finite element connectivities between the bolt and the composite are released where generalized membrane stresses N_x and N_y are both tensile. Under a 30.25 KN (6.8 kip) loading damage is initiated adjacent to the bolt by matrix cracking in the 90° plies. After damage initiation by σ_{22T} transverse tensile failures, the damaged plies also undergo σ_{11C} longitudinal compressive failures during the next iteration. Subsequently, damage grows to the -45° and +45° plies under the same load. When the load is increased to 44.48 KN (10 kips) damage grows to adjacent nodes. Gradual damage accumulation in selective plies continues until a 145.9 KN (32.8 kip) load is reached when fracture begins at the same nodes where damage initiation had occurred. Fracture is rapidly propagated to cause the ultimate break of the connection due to the fracture line that started from the side of the bolt transverse to the loading direction. Figure 5 shows the primary, secondary, and ultimate fracture lines, as well as remote damage locations.

The global Damage Energy Release Rate (DERR) is defined as the work done by external forces per unit damage produced during structural degradation. DERR can be used to evaluate structural resistance against damage propagation at different stages of loading. Figure 6 shows the DERR that is minimum under a 56.94 KN (12.8 kip) loading but recovers to higher levels as damage progression continues. Figure 7 shows the end displacement with applied

loading, indicating that initial damage stages will not be apparent from the observation of a test.

The second investigated structure is a composite panel fastened by two bolts. The composite system is made of the same high strength AS-4 graphite fibers in a high-modulus, high-strength epoxy matrix (AS-4/HMHS) as in the single bolt joint. The finite element model, shown in Figure 8, uses 72 thick shell elements with 99 nodes to represent the laminate and the two bolts. Figure 9 shows the damage initiation stage for laminate widths of $w=63.5, 76.2, 101.6,$ and 203.2 mm (2.5, 3.0, 4.0, and 8.0 in) as functions of the applied load per unit width of the laminate. In all four cases the laminate is fastened by two 25.4 mm (1.0 in) diameter bolts and the center to center bolt spacing is equal to the half width of the laminate. In all four cases damage initiation occurs after a tensile line load of approximately 175 KN/m (1000 lbs/in) is exceeded. The damage initiation mode is matrix cracking in the 90° plies of the laminate adjacent to the bolt. After damage initiation, the primary damage growth stage is influenced by the bolt spacing. Closer bolt spacing corresponds to a quicker initial growth of the damage. Figure 10 shows the cumulative DERR for bolt spacings of 31.75 mm (1.25 in) and 50.8 mm (2.0 in). Figure 10 indicates that the closer bolt spacing initiates damage at a higher energy release rate. Additionally, closer bolt spacing experiences lower energy release levels during the primary damage growth stage, indicating lower damage tolerance compared to the wider bolt spacing. Figure 11 shows computational simulation results of the overall damage progression for laminate widths of $w=76.2, 101.6,$ and 203.2 mm (3.0, 4.0, and 8.0 in) as functions of the applied load per unit width of the laminate. In all three cases the laminate is fastened by two 25.4 mm (1.0 in) diameter bolts and the center to center bolt spacing is equal to the half width of the laminate. In all three cases an extensive damage accumulation by matrix cracking in all plies occurs under a tensile line load of approximately 526 KN/m (3,000 lbs/in). After the matrix cracking stage is completed, the bolted laminate is able to sustain significantly higher loading prior to entering a final damage propagation stage that culminates in structural fracture. The ultimate fracture loading ranges in the range of 2.1 to 2.3 MN/m (12 to 13 Kips/in).

These results indicate that damage progression characteristics are not very sensitive to the laminate width or to the bolt spacing in the investigated range. Nevertheless, an optimal value of the bolt spacing-to-diameter ratio of 2.0 gives the best ultimate fracture load of approximately 2.3 MN/m (13 kips/in).

CONCLUSIONS

In the light of the durability investigation of the example bolted composite, and from the general perspective of the available CODSTRAN (COMposite Durability STRuctural ANalysis) computer code, the following conclusions are drawn:

1. CODSTRAN adequately tracks damage initiation, growth, and subsequent propagation to fracture for bolted composite structures.
2. For the examples considered, damage progression characteristics are not sensitive to bolt spacing under tensile loading.
3. Computational simulation, with the use of established composite mechanics and finite element modules, can be used to predict the influence of a bolted joint as well as loading and composite properties on the durability of mechanically fastened composite structures.
4. The demonstrated procedure is flexible and applicable to all types of constituent materials, structural geometry, and loading. Hybrid composites and homogeneous materials, as well as binary composites can be simulated.
5. CODSTRAN provides a new general methodology to investigate damage propagation, and progressive fracture for any structure.

USES OF COMPUTATIONAL SIMULATION

The presented computational simulation method is suitable for use in design and continued in-service evaluation of pressurized composite structures. The basic procedure is to simulate a computational model of the composite structure subjected to the expected loading environments. Various fabrication defects and accidental damage may be represented at the ply and constituent levels, as well as at the laminate level. Computational simulation may be used in the following ways:

1. Evaluation of damage tolerance: There are two distinct modes of structural damage. These are: a) accidental damage produced by inadvertent loading that is not an expected service load, and b) damage caused by the type of load the structure is designed to carry. Accidental damage may be specified in the computational model prior to the application of

loading. On the other hand, computational simulation will generate the damage that would be caused due to overloading.

2. Determination of design allowables based on damage tolerance requirements is an inherent use of the computational simulation results.
3. Identification of damage initiation/progression mechanisms and the sequence of progressive fracture modes convey servicable information to help with critical decisions in the structural design process.
4. Determination of the important parameters that significantly affect structural performance for each design case allows optimization for best structural performance. Sensitive parameters affecting structural fracture may be constituent strength, stiffness, laminate configuration, fabrication process, and environmental factors.
5. Computational simulation allows interactive experimental-numerical assessment of composite structural performance. Simulation can be used prior to testing to identify locations and modes of composite damage that need be monitored by proper instrumentation and inspection of the composite structure. Interpretation of experimental data can be significantly facilitated by detailed information from computational simulation. Sub-scale experimental results may be extended to full prototype structures without concern for scale effects since computational simulation of progressive fracture does not presume any global parameters but is based on constituent level damage tracking.
6. Simulation of progressive fracture from defects allows setting of quality acceptance criteria for composite structures as appropriate for each functional requirement.
7. Detailed information on specific damage tolerance characteristics help establish criteria for the retirement of a composite structure from service for due cause.

REFERENCES

1. C. C. Chamis and G. T. Smith, "Composite Durability Structural Analysis," NASA TM-79070, 1978.
2. T. B. Irvine and C. A. Ginty, "Progressive Fracture of Fiber Composites," *Journal of Composite Materials*, Vol. 20, Mar. 1986, pp. 166-184.
3. L. Minnetyan, C. C. Chamis, and P. L. N. Murthy, "Structural Behavior of Composites with Progressive Fracture," *Journal of Reinforced Plastics and Composites*, Vol. 11, No. 4, April 1992, pp. 413-442
4. L. Minnetyan, P. L. N. Murthy, and C. C. Chamis, "Progression of Damage and Fracture in Composites under Dynamic Loading," NASA TM-103118, April 1990, 16 pp.
5. L. Minnetyan, P. L. N. Murthy, and C. C. Chamis, "Composite Structure Global Fracture Toughness via Computational Simulation," *Computers & Structures*, Vol. 37, No. 2, pp.175-180, 1990
6. L. Minnetyan, P. L. N. Murthy, and C. C. Chamis, "Progressive Fracture in Composites Subjected to Hygrothermal Environment," *International Journal of Damage Mechanics*, Vol. 1, No. 1, January 1992, pp. 60-79
7. L. Minnetyan, C. C. Chamis, and P. L. N. Murthy, "Structural Durability of a Composite Pressure Vessel," *Journal of Reinforced Plastics and Composites*, Vol. 11, No. 11, November 1992, pp. 1251-1269
8. C. C. Chamis, P. L. N. Murthy, and L. Minnetyan, "Progressive Fracture of Polymer Matrix Composite Structures: A New Approach," NASA TM-105574, January 1992, 22 pp.
9. L. Minnetyan, J. M. Rivers, P. L. N. Murthy, and C. C. Chamis, "Structural Durability of Stiffened Composite Shells," Proceedings of the 33rd SDM Conference, Dallas, Texas, April 13-15, 1992, Vol. 5, pp. 2879-2886
10. L. Minnetyan and P. L. N. Murthy, "Design for Progressive Fracture in Composite Shell Structures," Proceedings of the 24th International SAMPE Technical Conference, Toronto, Canada, October 20-22, 1992, pp. T227-T240
11. P. L. N. Murthy and C. C. Chamis, *Integrated Composite Analyzer (ICAN): Users and Programmers Manual*, NASA Technical Paper 2515, March 1986.
12. S. Nakazawa, J. B. Dias, and M. S. Spiegel, *MHOST Users' Manual*, Prepared for NASA Lewis Research Center by MARC Analysis Research Corp., April 1987.

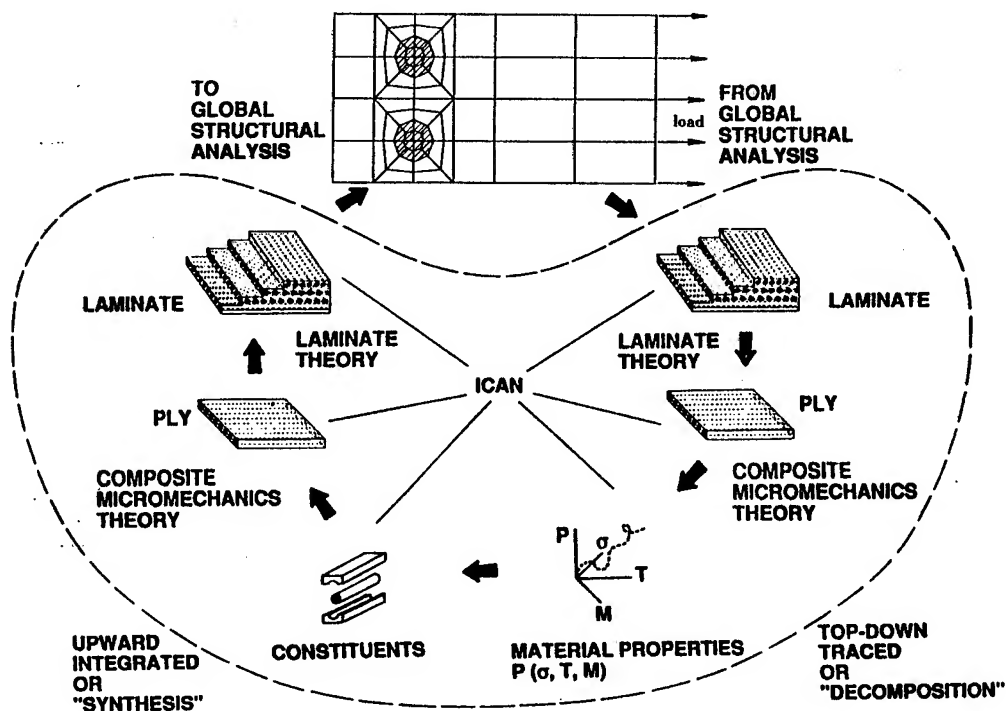


Fig. 1 Computational Simulation Cycle

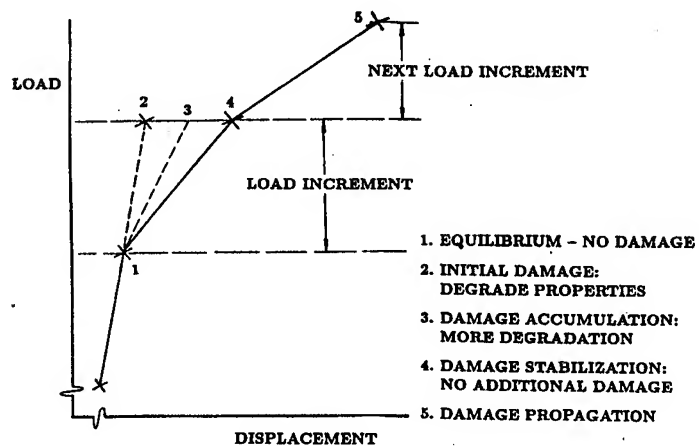


Fig. 2 CODSTRAN Damage Tracking

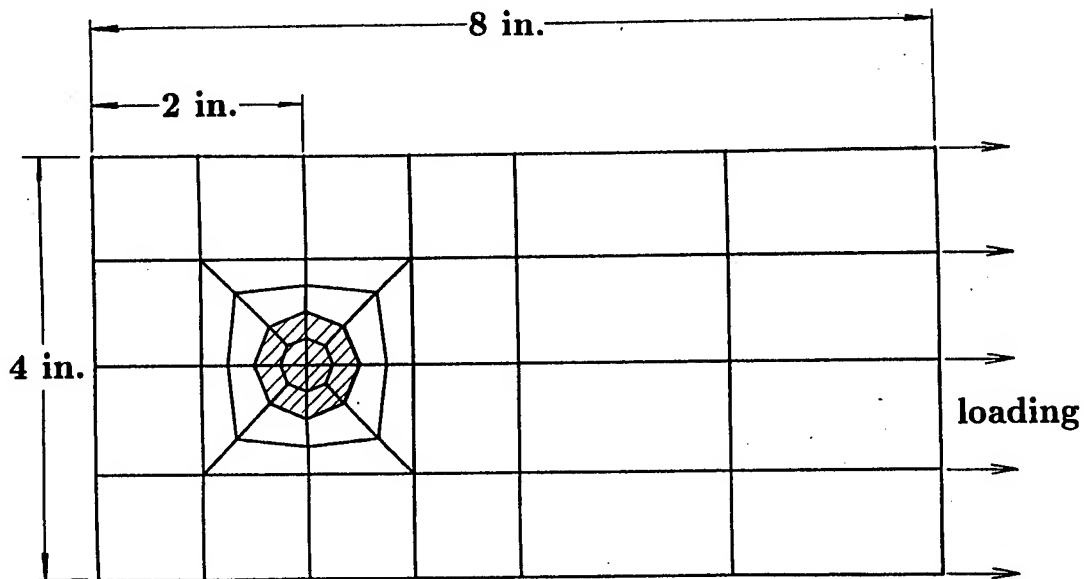


Fig. 3 Bolted Laminate Finite Element Model

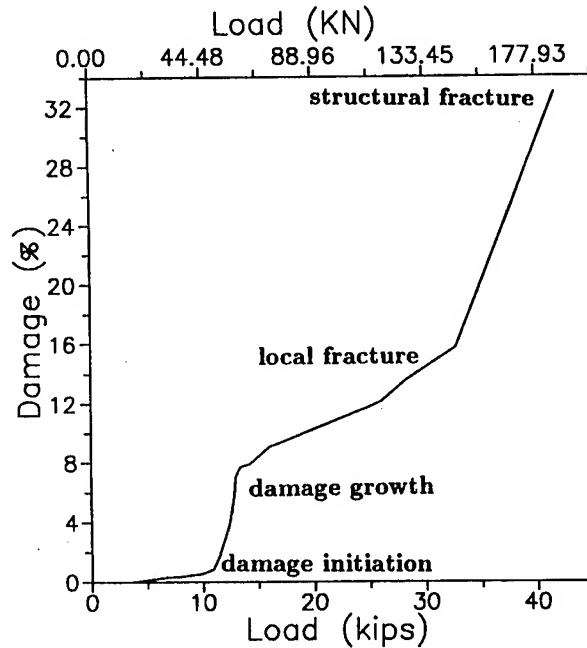


Fig. 4 Damage Progression for Bolted Laminate
AS-4/HMHS: 48 Plies $[0/90/\pm 45]_{12}$

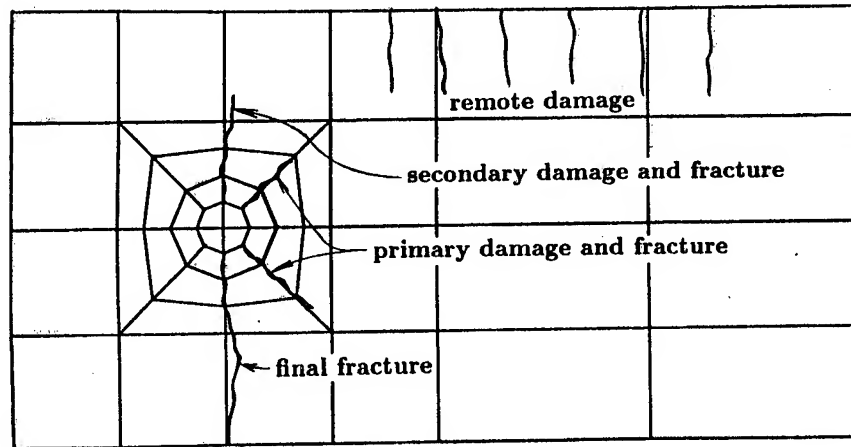


Fig. 5 Laminate Damage and Fracture Lines
AS-4/HMHS: 48 Plies $[0/90/\pm 45]_{12}$

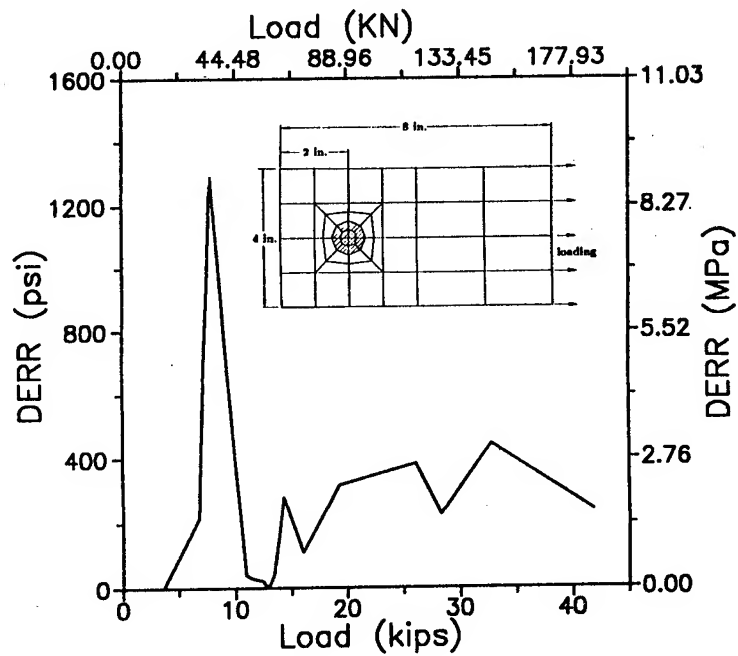


Fig. 6 Energy Release Rates for Bolted Laminate
AS-4/HMHS: 48 Plies $[0/90/\pm 45]_{12}$

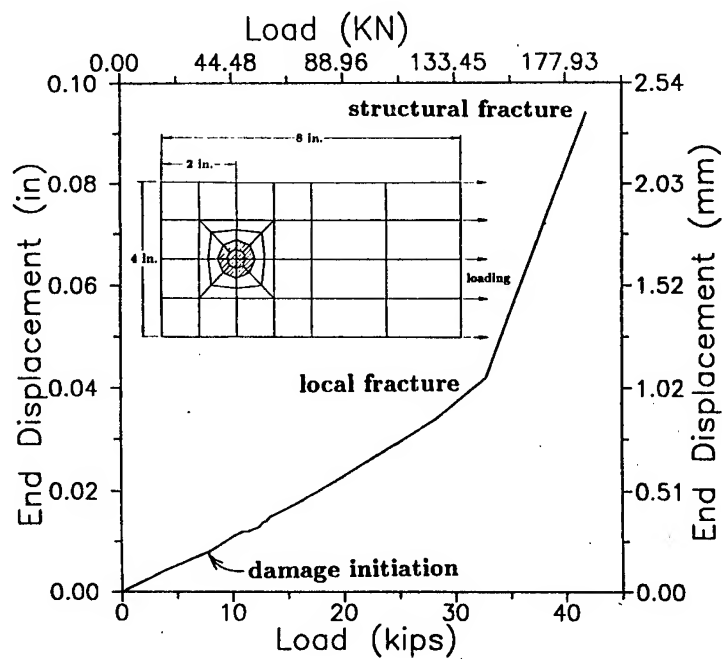


Fig. 7 End Displacement for Bolted Laminate
AS-4/HMHS: 48 Plies $[0/90/\pm 45]_{12}$

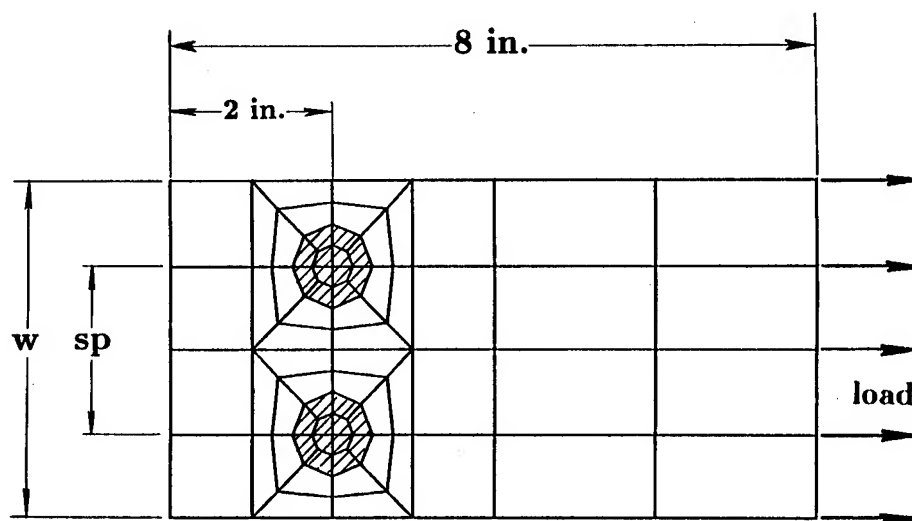


Fig. 8 Double Bolted Laminate Model

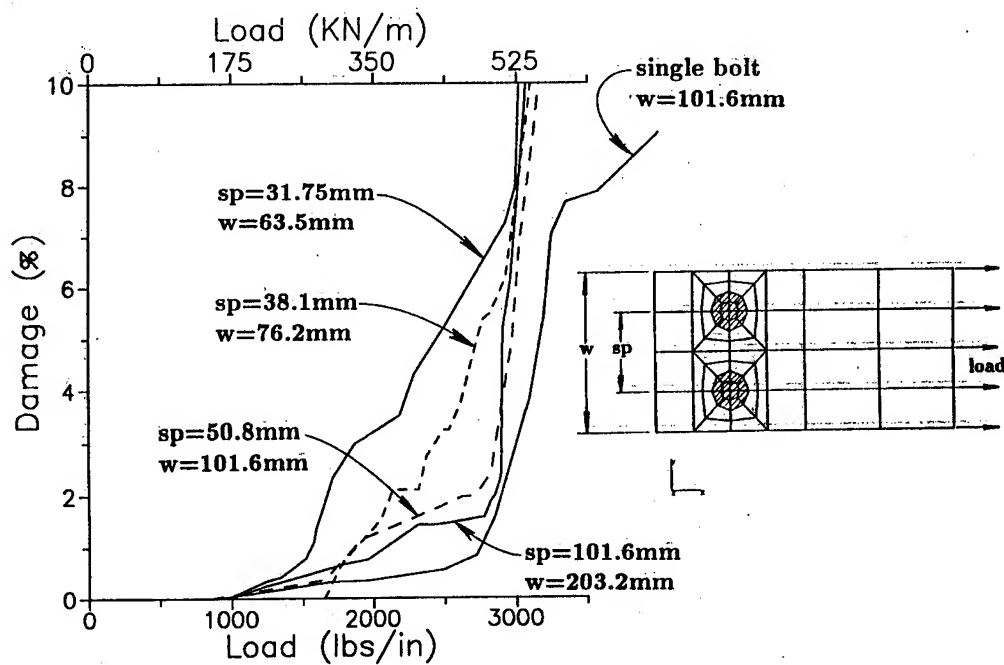


Fig. 9 Damage Initiation Stages for Double Bolted Laminate: AS-4/HMHS[0/90/±45]₁₂

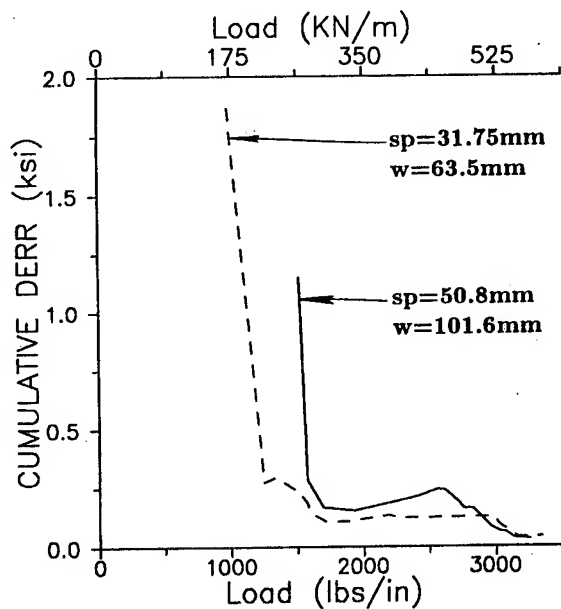


Fig. 10 Energy Release Rates for Double Bolted Laminate: AS-4/HMHS: 48 Plies [0/90/±45]₁₂

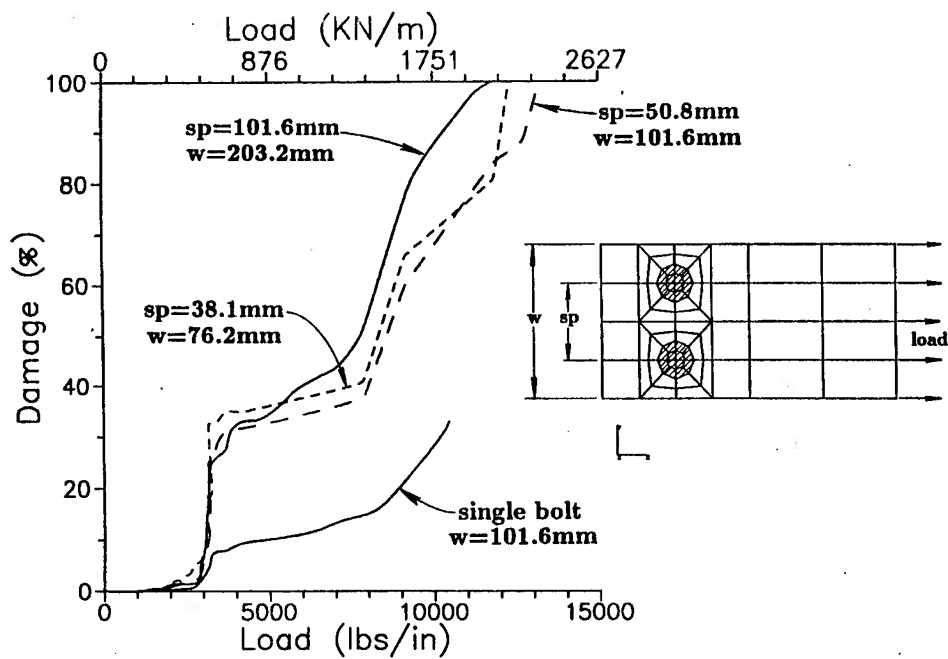


Fig. 11 Damage Progression for Double Bolted
Laminate: AS-4/HMHS[0/90/ ± 45]₁₂



High-Strength Aluminum Forged Product Durability and Damage Tolerance Capabilities for Weight and Total Life Cycle Cost Saving

by

R. J. Bucci, R. W. Bush, A. J. Hinkle, H. J. Konish, M. Kulak, and R. H. Wygonik
Alcoa Technical Center, Alcoa Center, PA 15069

&

G. W. Kuhlman
Alcoa Forging Division, Cleveland, OH 44105

at

1995 USAF Aircraft Structural Integrity Program (ASIP) Conference
San Antonio
November 28-30, 1995

Abstract

Forged and thick plate product forms in high strength aluminum alloys (e.g., 7050 and others) often compete for application in durability and damage tolerant critical airframe components such as bulkheads and attachment fittings. Because of mounting pressures to reduce airframe build costs, manufacturers are converting parts traditionally made from forgings to thick plate "hogouts." The historical preference toward forgings in many of these applications is being abandoned to achieve manufacturing cost saving through avoidance of lead time and machining distortion problems sometimes encountered with forgings.

While forged products are coming under increased scrutiny in terms of industry drives to reduce airplane manufacturing costs, examinations of high-strength aluminum process-microstructure-property relationships reveal that in some applications forged products offer distinct opportunity for end-product cost/performance advantages over machined plate. This presentation shows that excellent durability and damage tolerance capabilities of forgings emerge directly from aspects of product microstructure and fabrication (working) history, and new data are provided to convey the merits of forgings in terms of industry drives for longer life, lower weight and reduced maintenance costs. Progress being made to overcome the historical criticisms of forgings is reviewed, and actions to realize the full potential of forgings are defined.



Airframer interest is shifting from forgings to competing product forms.

- Forgings have historically been a preferred product form for certain heavy-sectioned aircraft components.
- Growing airframer interest in hogouts is being driven by considerations of manufacturing cost.
- Conventional design and selection processes may not capture all of the performance differences between competing product alternatives.

... The coupling of forging performance advantages with recent advances in residual stress control, analytic design tools and concurrent engineering practices begs for more rigorous evaluation of the shift away from forgings.



The historical preference for forgings was based on several factors.

- Forgings enjoy the advantages of net-shape parts.
 - Minimal machining
 - Favorable buy to fly ratios
 - Part count reduction
- Certain performance attributes of forgings were perceived superior to those of competing product forms.
- Thick section capability unattainable in other products.



The historical advantages of forgings are being challenged.

- Widespread availability of sophisticated machine tools.
- Improved quality and consistency of competing product forms.
- Machining distortion of forgings due to residual stress problems.
- Initial tooling costs and relatively long delivery schedules for forgings.
- Focus on aircraft production cost.



The forging process imparts some unique attributes to forged products.

- High levels of mechanical work
- Multi-directional mechanical work
- Contour-following grain flow
- Residual stresses



Explicit differentiation of forgings is difficult.

- Consistent testing and interpretation of data for many product variations is difficult.
 - Testing of forgings is expensive.
 - Different product form phenomena can obscure performance differences.
 - Data for different process histories exhibit differing degrees of scatter.
 - Forging design allowables generalized from pooled product data can be unduly conservative.
 - Design allowables should be compared on the basis of starting stock dimensions.
 - Few good examples exist to compare competing product forms on an equal component performance basis.
-
- Plate is a material product form, while forgings are a near net-shape component.
 - While testing directions with respect to product grain flow are well defined for plate, the ambiguous definition of the transverse test direction in forgings combines LT, ST and ± 45 data into one group.
 - When contrasting mechanical properties of die-forgings and plate hogouts, the plate product base-line should correspond to the thickness of starting stock required to machine the final part.
 - The lack of valid comparisons penalizes forgings unduly in conventional allowable/factor-based design scenarios.

The performance implications of forging attributes are more inferred than measured.

- Microstructural attributes of forgings are defined by the forging process.
 - The properties of the forgings are prescribed by the microstructural features.
 - The process/microstructure/properties/performance link has been shown to be independent of product form.
-
- The advantages of forgings are more clearly conveyed when the linkage between process, microstructure and performance is understood.
 - Alcoa's applicable knowledge base draws on more than four decades of R&D experience on process/microstructure/property/performance relationships.

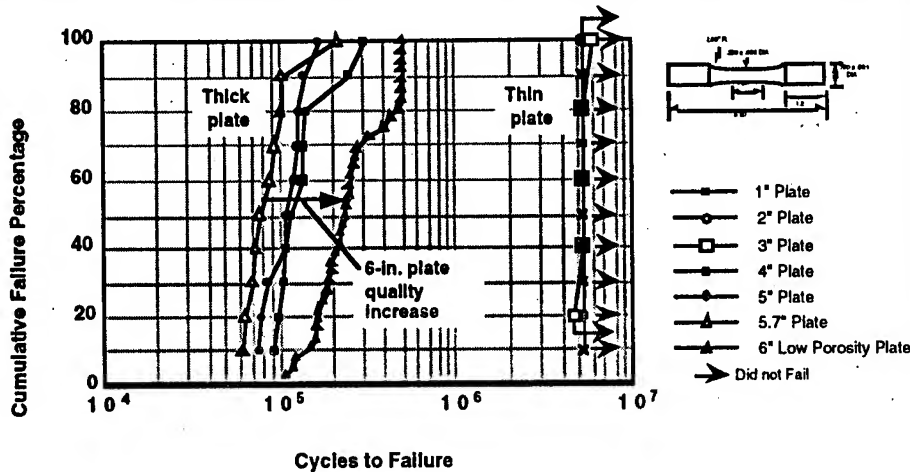
The unique attributes of forgings are reflected in their performance characteristics.

- Fatigue strength
- Fracture toughness
- Fatigue crack growth
- Tolerance to corrosion damage
- Short-transverse ductility

... The above attributes make forgings well suited for use in heavy-sectioned, durability and damage tolerance critical parts.

- Forgings are expected to exhibit good static and fatigue strength properties.
 - Mechanical working heals and/or breaks up deleterious remnants of original cast microstructure; reduces the size and frequency of potential life-limiting microfeatures.
 - The strength margins of forgings are not overridden by structural configuration and manufacturing features.
 - Good short transverse ductility.
- Mechanical work imparts good toughness and crack growth resistance.
 - Principle grain flows can be aligned to grow cracks across grains.
 - Part benefits can be tailored to more than one loading direction.
- Forgings are expected to resist corrosion penetration as a result of contour-following grain flow; they will also exhibit superior resistance to fatigue strength degradation with corrosion damage present.

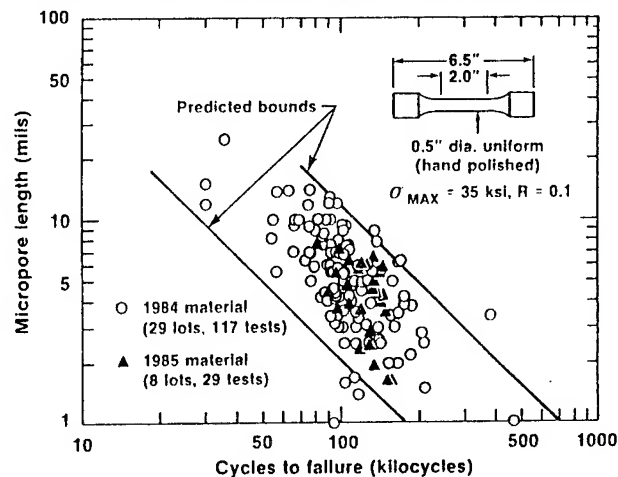
Plate fatigue performance is affected by product thickness and manufacturing pedigree.



Cumulative Fatigue Failure Distributions
7050-T7451 Plate (1 - 6 in. thk.)
 (Max. stress = 40 ksi, R = 0.1, kt = 1, long-transverse, T/2 test location)

- Engineers have known for some time that microporosity can shorten life of cyclically loaded components by accelerating the initiation of fatigue cracks.
- In thick plate, microporosity persists through to the final product where deformation during rolling is often insufficient to effectively break-up and/or heal porosity present in the starting ingot.
- Increased mechanical work in rolling to thinner plate gages decreases both the microporosity size and volume fraction, and hence fatigue resistance is improved over that of thick plate.
- Thick plate fatigue improvement potential has been demonstrated through control of manufacturing processes to curb microporosity.
- Because of the loss of inherent crack stoppers in consolidated parts, new cost reduction initiatives seeking to replace conventional assemblies with fewer, thick parts must consider control of microporosity as a fatigue crack preventive measure.

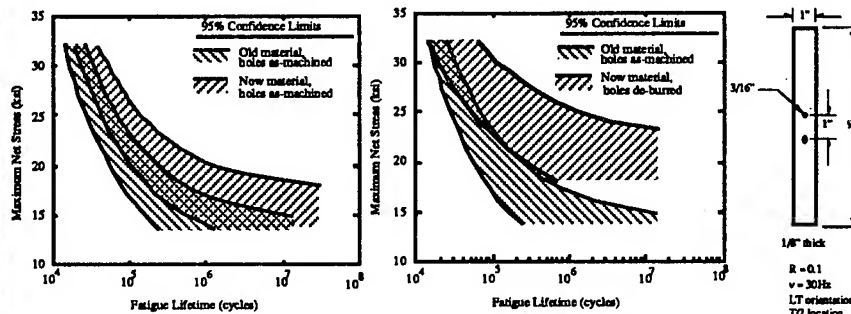
Alcoa historical data shows that smooth specimen cyclic lifetime depends on scale of the life-limiting microfeatures.



Micropore length vs. cyclic lifetime
7050-T7451 thick (5.7 - 5.9 in.) plate
(Long-transverse, T/2 test location)

- The smooth fatigue test is an ideal test for metal quality screening as the fatigue process will seek out the largest micropore (weakest link) within the specimen test section. Results such as those shown have led to adaptation of smooth fatigue testing in commercial thick plate material specifications.
- The micropore dimension plotted represents the largest pore dimension in any one direction determined from an SEM photo of the failed specimen fracture surface.
- When contrasted on a statistical basis, the 1985 material of higher pedigree has generally smaller failure initiating micropores, and thus generally longer fatigue lifetimes than the lower pedigree 1984 material.
- Conventional NDI methods are not sensitive enough to detect life-limiting microporosity on a reliable basis. The data does show, however, that life-limiting micropores in excess of 0.01 in. are possible.

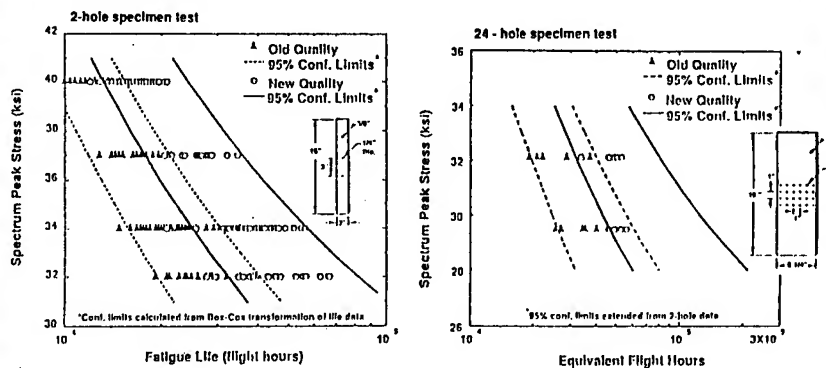
Microstructural effects on the fatigue performance of thick product are not masked by those of geometric features or machining.



Open hole fatigue performance of 7050-T7451 thick plate increases with metal pedigree (*hole deburring doubles the improvement*).

old material: 1980 commercial production practice
now material: 1990 commercial production practice

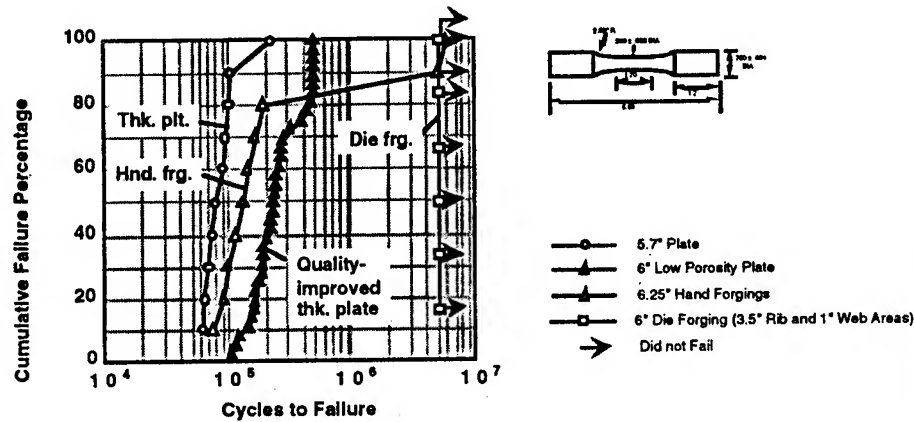
The metal quality effect was confirmed in USAF tests employing production machining practices and representative loadings.



Effect of metal quality on open hole specimen fatigue performance
7050-T7451 thick plate (5.7 in.), long transverse, T/2 test location
F-16 400 hr. lower wing spectrum (8000 hrs. = 1 service lifetime)

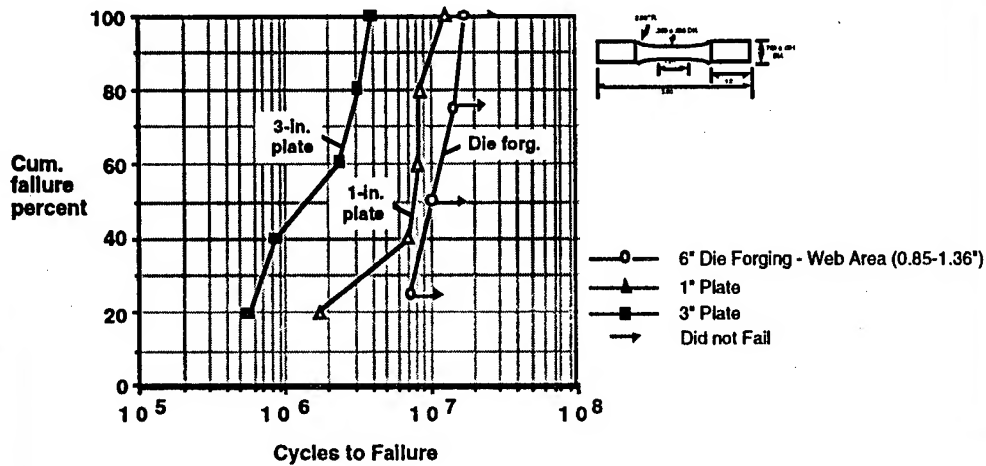
Product form (forging or plate) affects material fatigue performance.

Die forging fatigue resistance is superior to that of thick plate product needed to machine the same part.



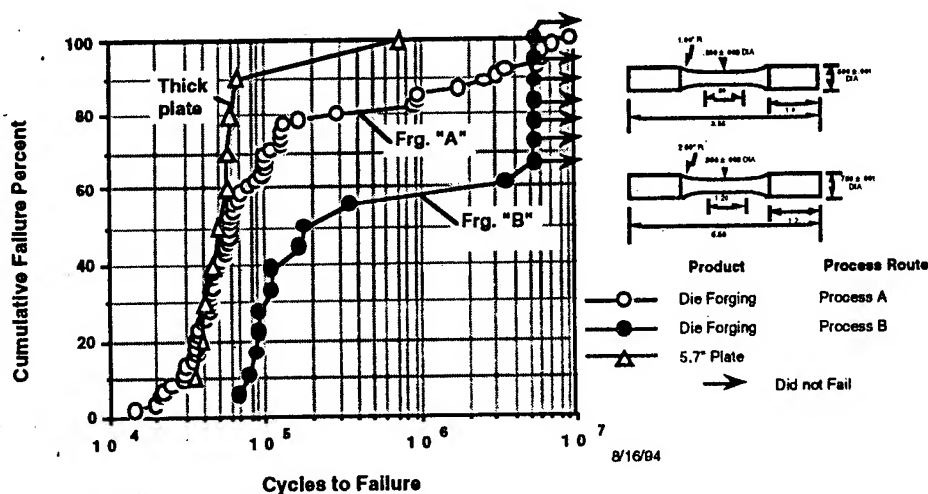
- The fatigue resistance of heavy section die-forgings is typically much greater than that of thick plate product needed to machine the same part.
- Hand forging fatigue resistance is generally equal to or better than that of standard thick plate, but somewhat inferior to that of the process improved low porosity plate.
- Hand forging fatigue performance is also limited by microporosity, and like plate, enhancement should also be possible through implementation of improved processing methods for control of microporosity.
- In the > 6" product thickness range hand forging fatigue resistance generally remains stable, whereas plate fatigue resistance generally degrades with thickness increase.

Cyclic lifetimes of specimens from heavy-worked die-forgings exceed those of specimens from thin plate.



Process route affects forged part performance.

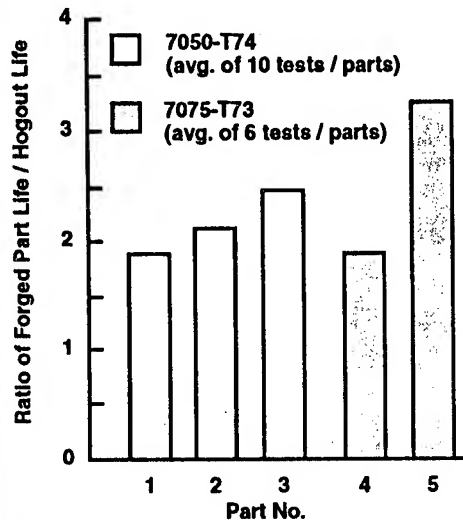
More sophisticated process route B increases fatigue performance.

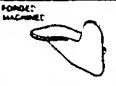


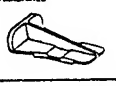



Effect of process route on cumulative fatigue failure distributions of 7050-T745X thick products
(Max. stress = 40 ksi, R = 0.1, kt = 1, short-transverse, T/2 test location)

- Forging process "B" employs a greater number of manufacturing steps to control microstructure (viz., microporosity), and thereby allow higher fatigue resistance to be attained.
- Die-forgings, and to lesser degree hand forgings, offer a variety of alternative paths to arrive at the same shape part shape. Optimal use of the forgings will result when user and vendor blend expertise and tune their respective manufacturing processes to requirements of the end-part. Such relationships may be necessary to offset the negative implications of forgings higher initial cost.
- Much recent progress has been made in developing modeling linkages among processing, microstructure and performance. These models are being used to challenge conventional airframer material selection processes to consider the benefit potential of quality-improved materials to gain an overall end component cost/performance advantage.

The fatigue advantage of forgings has been shown in tests of prototypical parts.

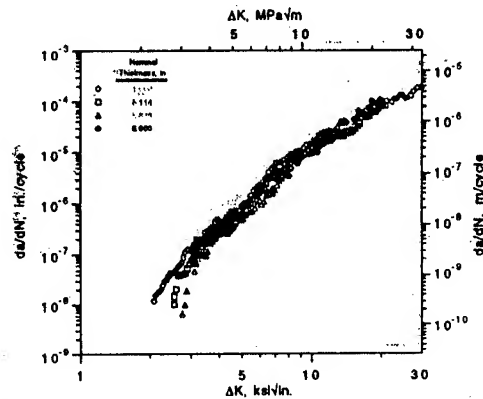


PRODUCT FATIGUE LIFE TEST PROGRAM		
PART	TEST SKETCH	TEST
AS FORGED AS MACHINED		Test Type: High Cycle Fatigue Maximum Load: 4,000 lbs Minimum Load: 400 lbs Frequency: 30 Hz
AS FORGED AS MACHINED		Test Type: Low Cycle Fatigue Maximum Load: 2,500 lbs Minimum Load: 250 lbs Frequency: 30 Hz
AS FORGED AS MACHINED		Test Type: Low Cycle Fatigue Maximum Load: 1,500 lbs Minimum Load: 150 lbs Frequency: 30 Hz
AS FORGED AS MACHINED		Test Type: High Cycle Fatigue Maximum Load: 2,000 lbs Minimum Load: 200 lbs Frequency: 40 Hz
AS FORGED AS MACHINED		Test Type: Low Cycle Fatigue Maximum Load: 1,000 lbs Minimum Load: 100 lbs Frequency: 33 Hz

- An independent laboratory study was conducted to determine the relative resistance to fatigue resulting from forging and hogout technologies. The program tested fatigue life of complete products instead of test specimens "cut" from the parts themselves. Precision forgings were manufactured and heat-treated to blueprint specifications, while hogout parts were machined to forging dimensions from certified and heat treated plate or extruded bar. When subjected to equivalent cyclic loading conditions, the precision forging on average doubled the life of its equivalently tested hogout counterpart. [Ref., *Special Report on Product Fatigue Life; Precision Forgings vs. Hogouts*, Precision Forging Association of Southern California, 1991.]

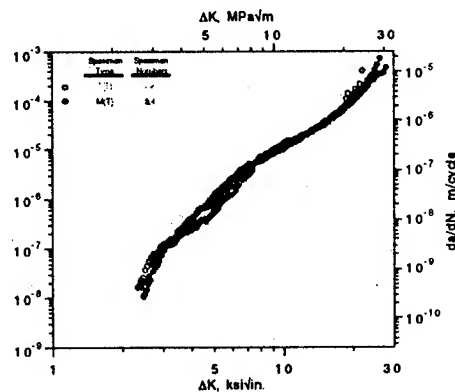
Plate fatigue crack growth rate properties are independent of product thickness.

No effect of product thickness holds in all three major test orientations (L-T, T-L & S-T).



Const.-load-amplitude FCG data for various thicknesses of 7050-T7451 plate
(L-T orientation, $R = 0.33$, high humidity air)

Fatigue crack growth rate properties of 7050 forging and plate are similar.

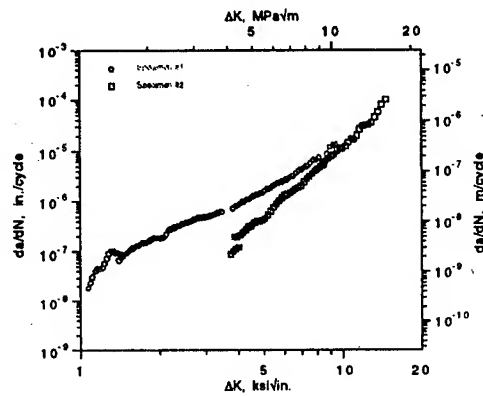


Const.-load-amplitude FCG data for thick 7050-T74 closed die forgings
(L-T orientation, $R = 0.33$, high humidity air)



The industry's forging FCGR data base is tainted by residual stress induced artifacts.

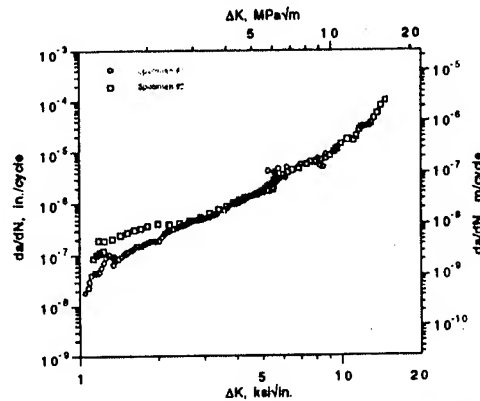
The forging residual stress effect is magnified in coupon tests.



FCGR data from thick, incompletely stress relieved 7050-T74X hand forgings
(S-L orientation, R = 0.33, high humidity air)

Alcoa has devised a corrective practice to remove residual stress bias from FCGR data.

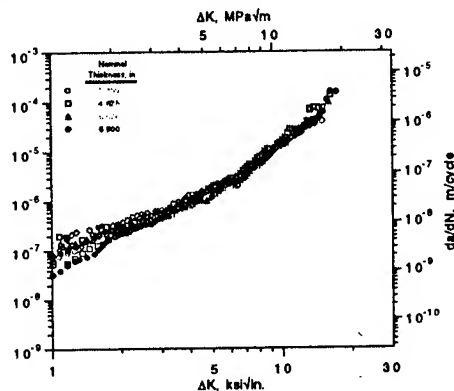
FCGR data from residual stress containing specimens are collapsed into a single curve when the crack closure based corrective practice is applied.



Closure corrected FCGR data from two incompletely stress relieved 7050-T7452 hand forging (6 in. thk.) (S-L orientation, R = 0.33, high humidity air)

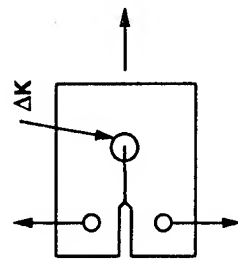
Closure corrected FCGR data from 7050 plate and non-stress relieved forging are similar.

Thus, intrinsic FCG resistances of plate and forgings can be considered equivalent, and plate and forging data can be used interchangeably for purpose of FCG life estimation.

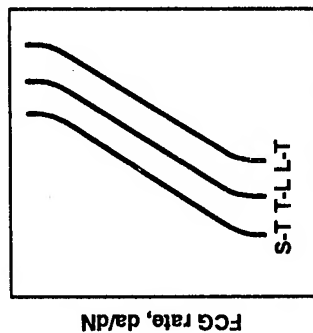
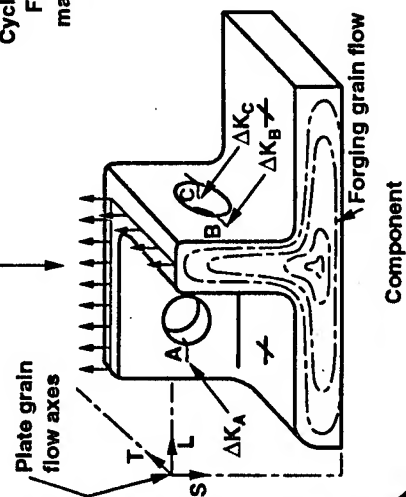


Closure based FCGR data for various thicknesses of 7050-T7451 plate (S-L orientation, R = 0.33, high humidity air)

The benefit of contour-following grain flow on forged part life can be estimated from plate data.



Coupon test

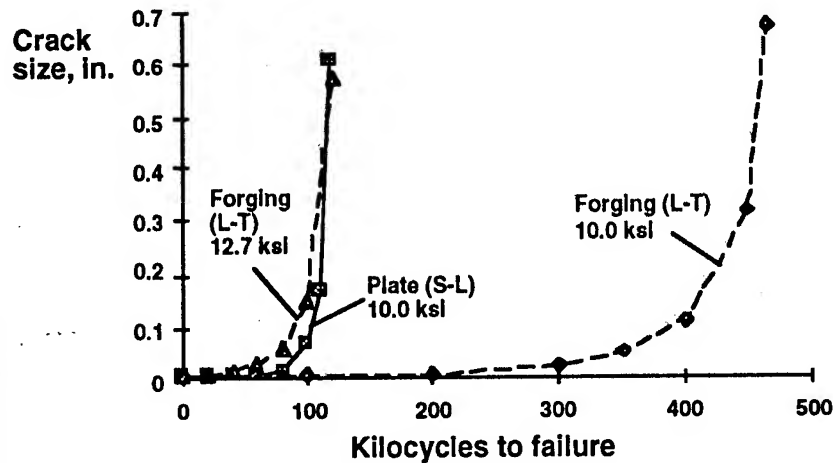
Cyclic stress intensity, ΔK
FCGR properties for
major plate grain flows

Component

Crack location	Plate equivalent FCG orientation		
	Plate	Forging	
A	S-L	L-T	
B	S-T	L-T	
C	S-L	L-S	

- End-product attributes are influenced by grain flow of the metal starting stock.
- Machining interrupts the grain flow in parts made from plate, while for many forgings the original grain flow is preserved, even after finish machining.
- In the example at the left, the corner flaw at location B would grow more slowly in forging (da/dN relationship is L-T) than in plate (da/dN relationship is S-T).
- The ideal die-forging would require minimal finish machining so not to disrupt the contour following grain flow in the final part. This is best done when the final part shape is known. Premature specification of an oversized forging to bracket uncertainties in part design may entail heavier machining than necessary, and thereby increase risk of exposing end-grains in the final part.

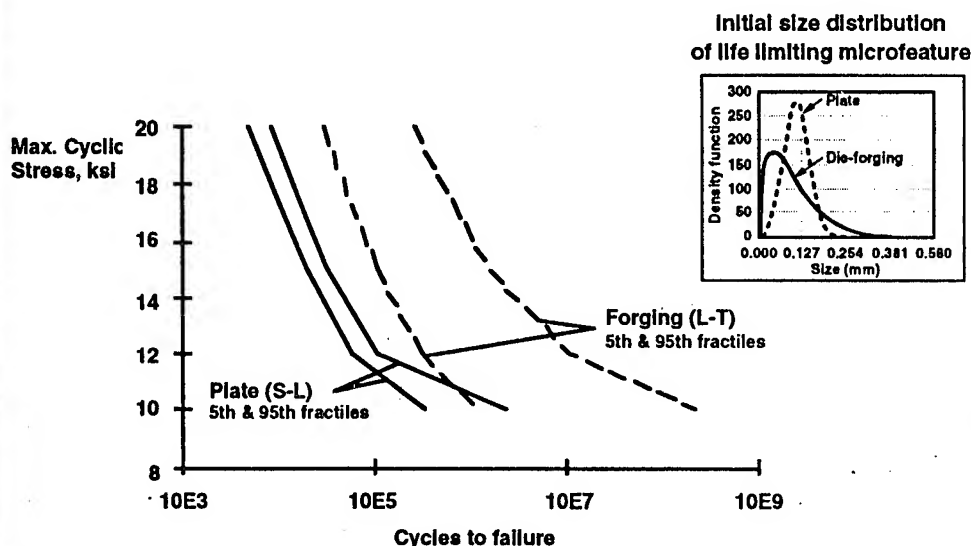
A favorable forging grain flow can be exploited to save weight and/or increase inspection interval.



Projected plate and die-forging crack growth lifetimes, initial 0.010 in. corner crack from open hole

- The above hypothetical example contrasts fatigue performance of a part machined from plate against that of the same part designed as an optimal forging. The calculation employs a deterministic crack growth model assuming a power law FCGR relationship (extended to the short crack regime). Crack growth is presumed to start from a mechanical, 0.010 inch corner flaw located at the corner of an open hole.
- Under the above best possible scenario, the forging accommodates 27% higher max. cyclic stress (from 10 to 12.7 ksi) at equivalent plate life, or an almost 4 times life increase over plate for the same 10 ksi max. cyclic operating stress.

An optimally designed die-forging can offer substantial total life advantage.



Predicted open hole S-N response of forging vs. plate

- The above plot contrasts the hypothetical open hole S-N fatigue response of a part machined from plate versus the same part designed as an optimal die-forging. The calculated result portrays the maximum possible difference between a forging and plate hogout for the modeling inputs used.
- The calculation employed a generalized probabilistic crack growth model with power law FCGR relationship (extended to the short crack regime). Cracks were assumed to initiate from the respective product life-limiting microfeature populations (inset), and the possibility that cracks could occur anywhere along the bore of the hole was considered by the model. The input FCGR behavior for the model was derived from plate $da/dN-\Delta K$ data, and crack growth presumed to be in the L-T and S-L orientation for forging and plate, respectively.



7050 die-forging mean fracture toughness is higher than plate in all test directions.

- Forging toughness standard deviations almost double those of plate; grouping forging capabilities from fewer shapes should help correct overly conservative property guarantees.
- Higher forging L-T toughness adds safety margin in parts designed to take advantage of contour-following grain flow.

Thick 7050-T74XX Product Fracture Toughness* (Kic, ksi√in.)

Product	Location	L-T	L-S	T-L	S-L
7050-T7451 thick plate (5.0 - 6.0 in.)	T/2	mean = 29.2 n = 675 std. dev. = 1.3 guar. = 24	-- -- -- --	mean = 25.6 n = 12 std. dev. = 1.6 guar. = 22	mean = 24.9 n = 1145 std. dev. = 1.1 guar. = 21
7050-T74 die-forging	T/2	mean = 34.3 n = 23 std. dev. = 5.6 guar. = 25	mean = 37.8 n = 20 std. dev. = 3.6 --	mean = 26.5 n = 12 std. dev. = 2.7 guar. = 19	mean = 25.5 n = 8 std. dev. = 2.1 guar. = 19

* Source: Alcoa data base, valid test results only

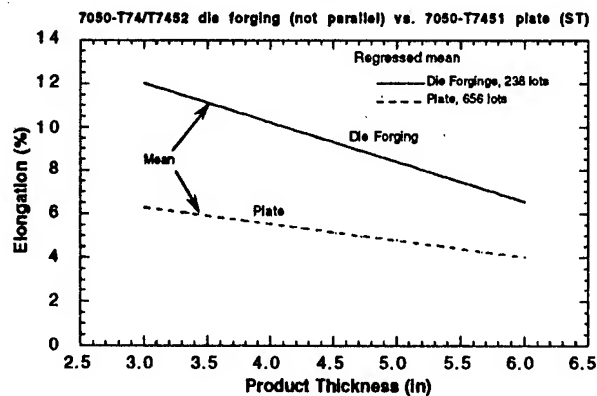
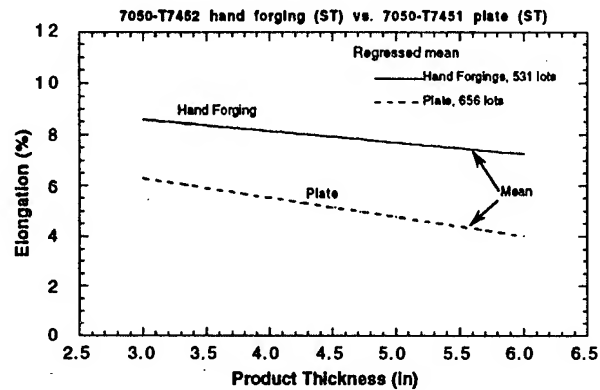


Forging strength properties

- Superior ST ductility at strength margins comparable to plate.
Recommendation: Forged section property comparisons with plate should be made on the basis of plate starting stock dimensions.
- Test/reporting practices employed by handbooks are not wholly consistent with those of plate.
 - Data base that consolidates many shapes and process histories accounts in part for greater statistical scatter displayed by forgings.
Recommendation: base specification values on fewer shapes.
 - Forging transverse (not parallel) properties integrate LT, ST and 45 degree plate property equivalents.
Recommendation: base allowables on grain orientation relative to the part.
 - When contrasted to plate Mil-5 bearing strength tables penalize forgings by as much as 15% because of difference in test specimen orientation (edgewise vs. flatwise).
Recommendation: add note to Mil-5 tables that references conversion factors for contrast of plate and forging properties on similar basis.



Forging ST ductility on average
is superior to that of plate.



7050 plate and forging ST elongation vs. product thickness



Corrosion

- Hundreds of Alcoa tests performed over many years show no difference in the corrosion resistance of 7050-T74 forged and plate products when tested in equivalent grain orientations.
- SCC resistance is sensitive to grain orientation with the ST orientation having the least resistance.
- Properly designed components fabricated as die-forgings will have part conforming grain flow and less exposed end grain than the same component made from plate.
 - Adds protection against SCC
 - Impedes corrosion damage penetration (*mechanical significance of corrosion has been shown to correlate with depth of attack*).
 - Favorable grain flow provides higher tolerance to corrosion damage as airplanes age (*i.e., fatigue with corrosion damage present*).



Summary

- Aluminum aerospace forgings can be differentiated as a high quality product, with performance benefits that in some applications can make forgings the preferred option.
- The superior fatigue and durability performance attributes of forgings are:
 - Correlatable to reduced size and frequency of life-limiting microfeatures and favorable grain flows in forged products.
 - Linked to working histories employed in fabrication.
 - Exploitable to save weight, increase safety margins, and/or reduce in-service support costs.
- The degree to which forgings can compete will depend on:
 - Ability to resolve the machining distortion problem.
 - Ability to select optimal working histories and material inputs to assure property/performance consistency.
 - Ability to shorten lead times.
 - Uniformity of the bases for comparison against competing product forms.
 - Ability to be judged cost-effective in the end-product.
 - Confidence built through a series of successful technical demonstrations.
 - A supplier/customer relationship that allows forging advantages to be worked into design and manufacturing processes.

The Impact of Fastener Hole Quality on Structural Life; A history of Success

Mr. C. T. Ratcliffe

*Mr. W. H. Sproat

Measurement Systems Incorporated

2262 Northwest Parkway, Suite B

Marietta, Georgia 30067

INTRODUCTION

Design and fabrication of airframes is based on widespread use of mechanical fasteners. This is because fasteners have a history of proven application and afford reliable load transfer in both shear and tension. However, fastener holes are inherent stress risers which, if out of tolerance or flawed, can significantly reduce fatigue life. Consequently, many variations of "fatigue life enhancement" fastener systems have been developed. A majority of these fastener systems involve interference fit installations which compression preload the material around the hole. Tensile stress on joints must exceed the static preload around the fastener hole before local stresses transition into a tensile range, therefore reducing cyclic stress maxima.

However, specified interference fit and fastener hole quality must be assured to rely on the fatigue life enhancement provided by the fastener system. Experience has shown that joint fatigue performance with interference fit fasteners is highly dependent on fastener hole preparation. A large body of evidence is available from airframe teardown data that supports this fact, but such assessments are qualitative. Structural teardown inspections have historically shown fatigue damage originating from fastener sites with poor fastener fit or poor fastener fill and fastener hole wall flaws, as well as design deficiencies. Test data, however, is the only means available for a quantitative assessment of fastener fit and hole quality on fatigue life.

FATIGUE LIFE AND FASTENER INTERFERENCE

A recent series of tests has been conducted by Douglas Aircraft Company (Materials and Processes Engineering Lab Report No. LR-15503, dated 11-28-94, Reference 1) to compare the durability of Hi-Shear pull pin and Taper-Lok interference bolts. Tests simulated MD-11 lower wing spar cap-to-panel joints. The objective was to determine whether the straight shank Hi-Shear system can provide equivalent (or better) joint durability compared with the more costly and time consuming installation of Taper-Loks. The test specimen design (Figure 1) represents a total joint thickness of 2.0 inches; 0.750 inch thick 2024-T351 aluminum and 1.250 inch thick 7075-T651 aluminum, with 0.375 inch diameter 6Al-4V Titanium fasteners. This corresponds to the wing panel- to-spar cap joint in a critical region.

Fastener interference and fastener type (straight shank compared to taper) were the controlled variables (Figure 2) in the test; given the test conditions of 22 Ksi gross stress, R factor of +0.2, and a cyclic rate of 3 Hz. Interferences were targeted in the range of 0.0020 inch to 0.0075 inch for straight shank fasteners and 0.0031 inch to 0.0054 inch for tapered fasteners. Actual fit of straight shank fasteners, as determined by the Measurement Systems Incorporated Capacitance Measurement System described later in this presentation, ranged from an 0.0008 inch average diameter oversize hole to 0.0086 inch interference. The specimen design called for three interference dimensions with the straight shank fasteners; 0.0020 inch, 0.0045 inch, and 0.0075 inch. Target interference and capacitance measured actual dimensions are different. Interference calculated from measured protrusion of the comparison set of tapered fasteners ranged from 0.0031 inch to 0.0054 inch.

Test results (Figure 3) showed that interference fit straight shank fasteners are capable of providing fatigue life comparable to the more costly tapered interference fasteners, provided their interference is in the range of 0.0040 inch to 0.0075 inch. Cycles to failure for the full complement of specimens ranged from 95,900 for the low (and negative) interference specimens to 947,300 for the high interference specimens; nearly one order of magnitude. Specimen failures showed no bias to either the simulated spar cap or panel.

If straight shank fastener interference is to be a proven major factor in durability, then fatigue cycles should especially correlate well with fastener interference at failure sites. Fastener interferences plotted for the straight shank primary failure sites range from 0.0000 inch to 0.0050 inch (Figure 4). Overall,

the specimen fatigue life trends upward with increasing fastener interference. Specimen numbers 6 and 19, two in an experimental group of 10 Hi-Shear types, did not exhibit the expected results. However, Specimen No. 6 showed the fatigue damage origin at the faying surface but no evidence of pre-existing damage. Specimen No. 19 showed hole surface fretting, grooves in one fastener hole, and evidence of lack of hole fill; non-uniform interference. Non-uniform interference may be significant in reducing durability but there is no quantity of data to support this.

FATIGUE LIFE AND FASTENER HOLE QUALITY

As discussed briefly above, structural teardown inspections have qualitatively evidenced fatigue damage at fastener sites where 1) fit was inadequate (non-uniform load transfer), 2) flaws were present in hole surfaces, or 3) design features imposed excessive stress levels. Quantitative evidence has been best presented with laboratory data from a 1977 report by Metcut Research Associates (Reference 2).

This Metcut project, "Verification of Production Hole Quality" conducted for the Air Force Materials Laboratory in conjunction with the Lockheed C-5 Project, had objectives as follows, with the first two of specific interest to the subject of this paper:

1. To establish quantitative hole quality data for an extruded aluminum alloy.
2. To identify the ranking or order of hole quality characteristics as a function of the effect on the life of fatigue critical interference fit fastener systems and joints.
3. To evaluate the performance of a tapered blade cutter in producing tapered holes suitable for fastener installation in a single operation.
4. To develop, fabricate and test specimens for an ongoing AGARD program.

This project used a variety of dogbone and strap specimens with tapered fasteners to evaluate both hole geometry and surface condition variables on fatigue life. The material was 5/16 inch thick 7175-T73511 shot peened, anodized

and coated aluminum alloy extrusion. Fasteners were 5/16 inch diameter 8740 alloy steel Taper-Loks. Fatigue loading was applied a 900 to 1800 cycles/minute with gross maximum stress in the 22 Ksi to 25 Ksi range and R ratios of +0.1 and -0.33. Fastener interferences ranged from 0.0005 to 0.0060 inches. Hole quality influence on fatigue life was as follows (Figure 5):

- Specimens with hole wall surface roughness of 125 microinches or better yielded similar fatigue behavior.
- Burrs on the nut side of the hole do not have a detrimental effect.
- Hole axis perpendicularity within 3 degrees is tolerable.
- Hole ovality is a serious concern.
- Bellmouthing and barreling are of concern, but less than ovality.
- Rifling, axial scratches, chatter, plastic deformation, tears, and laps (within the range of severity explored in this project) have minimal effect with fasteners installed, but are detrimental with open holes.

Holes were qualitatively checked for bearing, ovality, bellmouthing, barreling, rifling, and roughness with a bluing pin. Hole contour was checked with a multiple orifice tapered air gage probe. Bearing was also measured with an emerging capacitance gaging technology. Tapered fastener interference effects on fatigue life observed in the 1970s Metcut study was similar to the contemporary findings with four Taper-Lok comparison specimens used by Douglas Aircraft last year. Twenty Metcut tapered fastener specimens had interference in the range of 0.0005 inch to 0.0060 inch and resulting fatigue life over an order of magnitude from 100,000 cycles to 1,000,000 cycles (Figure 6). The Metcut report noted the following fastener interference effect:

“Specimens in which the fastener interference was 0.0035 inch or 0.0048 inch demonstrated maximum fatigue life. The 0.0060 inch level of interference, which is excessive of the (Lockheed) specification, showed a small but statistically insignificant drop in fatigue strength.”

GENERAL OBSERVATIONS

Evidence derived from both the Douglas and Metcut tests provide the following general observations: (Figure 7)

1. Durability of airframe joints is markedly influenced by degree of fastener interference and dimensional uniformity of holes.

2. The practical and effective interference range for fasteners is 0.0035 to 0.0050 inch.
3. Production flaws such as rifling, gouges and roughness are mitigated with appropriate fastener interference.

These observations emphasize the necessity for efficient, precise and thorough fastener hole dimensional measurement to assure desired fatigue properties. Little or no attention, however, has been given to the precise dimensional characteristics of the fasteners themselves. It must be emphasized that total joint fatigue life endurance is dependent on the fit between the fastener and the fastener hole, which makes the fastener dimensional characteristics as equally as important as the fastener hole quality characteristics. Several studies have shown that aircraft interference fasteners have a wide variance in dimensional quality within a specified size (References 3,4 and 5) which can dramatically affect the resulting interference fit.

The technology to provide a practical means for measuring and assuring the required fastened joint quality levels was originated by the U.S. Air Force Materials Laboratory in the 1970s. Fastener hole measurement technology has matured since then into the present day Capacitance Measurement System II (CMS-II). When the CMS-II is used with the complementing Fastener Measurement System (FMS), they can provide extremely fast, accurate and practical assurance of precise interference fastener hole fit and quality.

CAPACITANCE MEASUREMENT SYSTEM OVERVIEW

This technology uses electrical capacitance as a transducer function to measure distance. Two basic physical principles are employed by the CMS-II. The first principle is the behavior of a parallel plate capacitor, where the capacitance is proportional to plate separation. The second principle involves a capacitor discharge rate dependence on the resistance - capacitance time constant (Figure 8). The CMS-II transducer has a fixed capacitance plate area and circuit resistance, leaving the plate separation as the time dependent variable. A cylindrical probe capacitor plate placed into a hole which is the opposing electrically grounded "capacitor plate", provides for space measurement related to discharge time. Extending this concept to a precise multi-capacitor probe (Figure 9) enables detailed characterization of fastener hole features. The CMS-II (Figure 10) consists of four major components which are:

1. The capacitor probe which is inserted into the hole.
2. An electronics unit with circuitry to measure capacitance.
3. A microcomputer for capacitance data processing, storage, and display.
4. A hand held device for operator control of system operation.

System accuracy for a typical 5/16 inch diameter probe is to within less than 0.00015 inch measurement uncertainty. Calibration provides resolution to within +/-20 microinches, traceable to NIST (Figure 11). Data acquisition time is approximately 1 second per hole, in contrast with up to 5 minutes per hole for conventional inspection. The microcomputer affords convenient diskette data storage and graphical readout for statistical process control purposes. User information options include both axial profiles and section views at selected depths, and tabulated numerical records (Figures 12 and 13). Precise interference fit between fastener and fastener hole is dependent upon the dimensional characteristics of the fastener as well as the fastener hole. The same technology used in the CMS-II probe which measures the fastener hole has been transferred to a ring which now measures the fastener (Figure 14). This allows fasteners to be rapidly presorted into specific dimensional groupings within their acceptable size tolerance range and used to exactly match the CMS-II measured fastener holes with the proper fastener for an extremely precise interference fit.

CONCLUDING REMARKS

Fastener joint quality requirements for ever increasing structural endurance demands continue to challenge both new aircraft production as well as service life extension and rework operations. Demonstrated options for replacement of costly tapered interference fasteners and tedious close tolerance hole quality measurement have been discussed. Required levels of durability have been demonstrated with straight shank Hi-Shear interference fasteners. The fastener installation process has been complemented with precise and efficient fastener and fastener hole quality determinations employing the Capacitance Measurement System and including methods for matching fasteners with fastener holes to provide the precise interference fit required for maximum structural joint life. Increasing numbers of CMS users in both military and commercial

environments are applying this cost effective interference fastener hole quality tool (Figure 15).

REFERENCES

1. LR-15503, MD-11 Wing Box Fatigue Tests - Taperloks and Hi-Shear Pull-Stem Pins, R. C. Lewis, et. al., Douglas Aircraft Materials & Processes Engineering Report, November 1994.
2. AFML-TR-77-185, Verification of Production Hole Quality, William P. Koster, John B. Kohls, and John T. Cammett, Metcut Research Associates, Inc., Cincinnati, Ohio, and B.L. Cornell, Lockheed - Georgia Company, Marietta, Georgia, November 1977.
3. Engineering Report 03/002/0001, Measuring Results of the 6AL-4V Titanium Alloy "2NSA5092V07" - Pins Manufactured by Voi-Shan/Diessel GMBH, Voi-Shan/Diessel GMBH Aerospace Fasteners, 31113 Hildesheim, 13 August 1993.
4. Project No. 95-5577, Robins Laboratories Metallurgical Analysis Team, Warner Robins Air Logistics Center, Robins AFB, GA, 16 June 1995.
5. F-16 Tapered Fastener Installation Process, presentation by G.J. Melven, Lockheed Fort Worth Company, 27 April 1993.
6. LG81WP7254-002, Capacitance Technique for Quantitative Inspection of Fastener Holes - A New NDE Technology, H.S. Gibson and W. H. Lewis, Lockheed - Georgia Company, Marietta, Georgia, September 1981.
7. AFWAL-TR-82-4041, Fastener Hole Inspection for New Aircraft: Capacitance Hole Probe System, H. S. Gibson, Jr., P. E. Goodman, S. R. Glidewell and W. H. Lewis, Lockheed - Georgia Company, Marietta, Georgia, May 1982.
8. Capacitance - A Better and Cheaper Hole Inspection Method, W. H. Lewis, 14th Symposium on Nondestructive Evaluation, April 19-21, 1983, Nondestructive Testing Information Analysis Center, Southwest Research Institute, San Antonio, Texas.
9. IEEE Transactions, Vol. IM-32, No. 2, Design of Algorithms to Extract Data from Capacitance Sensors to Measure Fastener Hole Profiles, J. L. Hammond, Jr. And S. R. Glidewell, June 1983.

10. MR84-900, Society of Manufacturing Engineers 1984 Aerospace Engineering Conference, Anaheim, California, Capacitance - A Better and Cheaper Hole Inspection Method, W. H. Lewis and C. T. Ratcliffe, Lockheed - GETEX, Atlanta, Georgia, January, 1984.

11. Hole Probe System Inspects Northrop Jet Fighter Assemblies Fast at Less Cost, Nat Wood, CNC/West, October 1986.

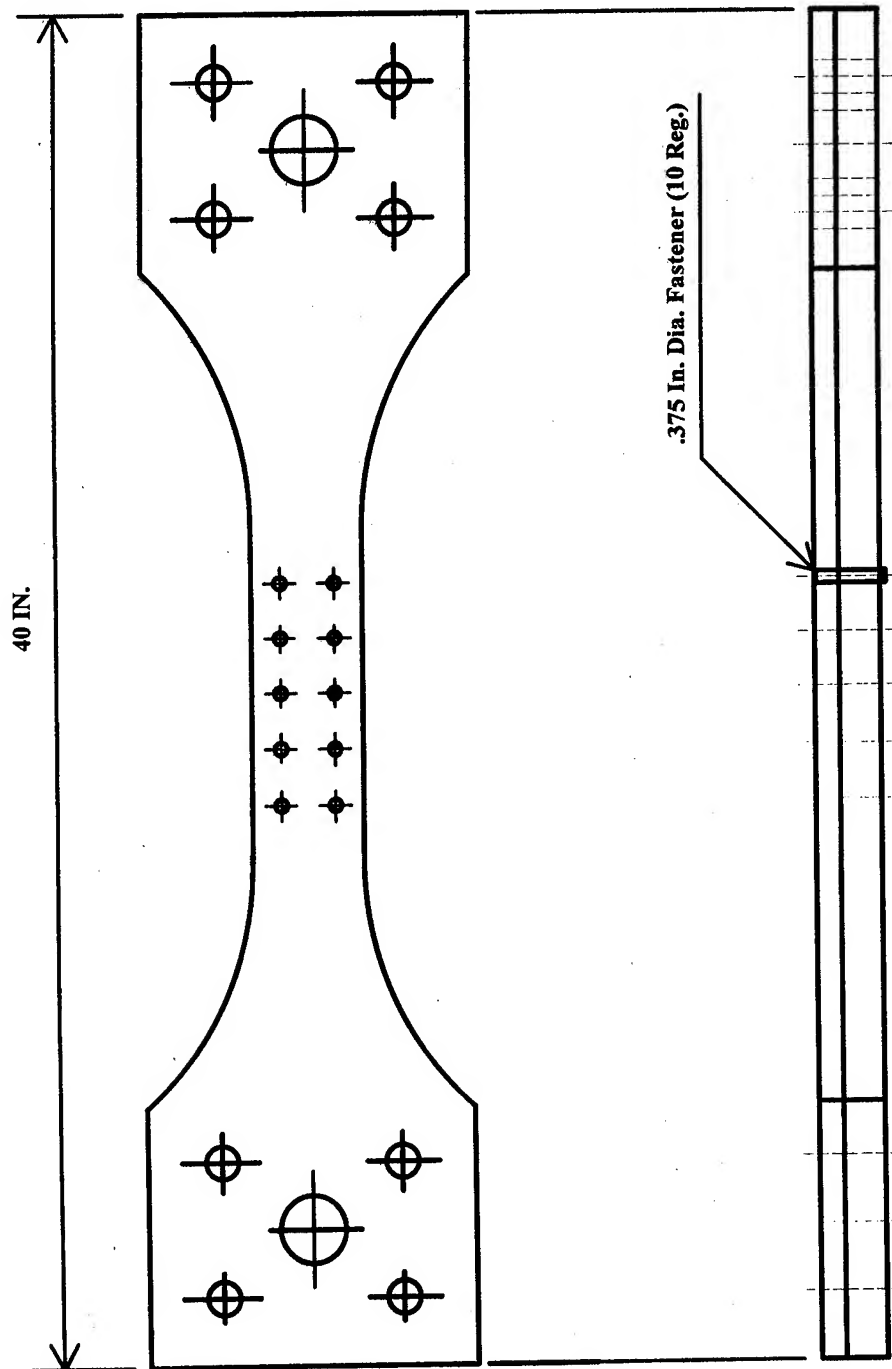


Figure 1. McDonnell Aircraft Company specimen design for fatigue life comparison of Taper-Lok and Hi-Shear interference fasteners.

- **Fastener Interference Range,
0.0020" - 0.0075"**
- **Gross Stress, 22 Ksi**
- **R Factor, 0.2**
- **Cyclic Rate, 3 Hz**

Figure 2. McDonnell Aircraft straight and tapered interference fastener comparison test parameters.

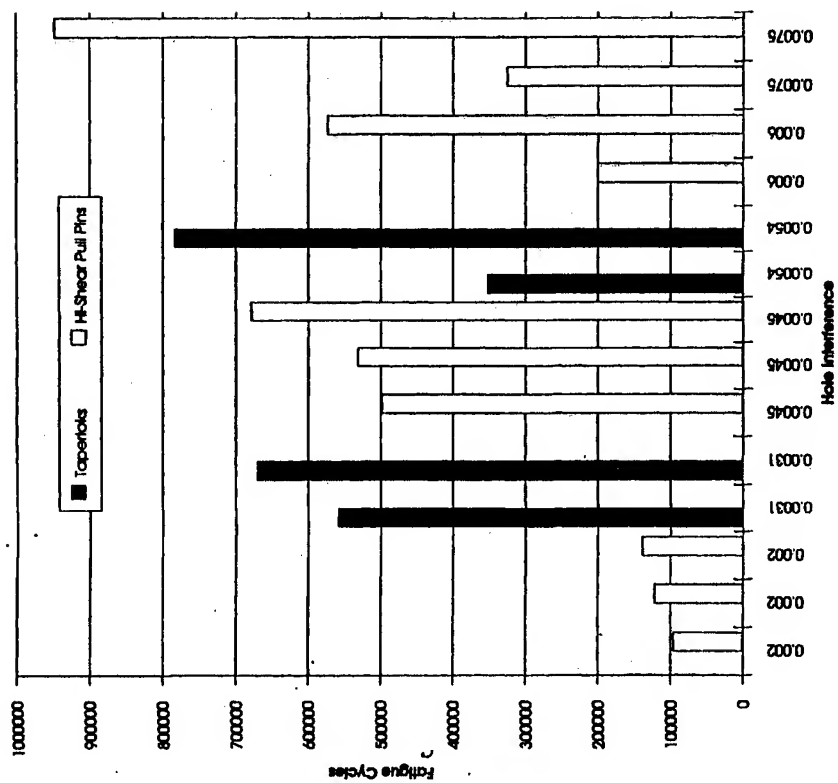
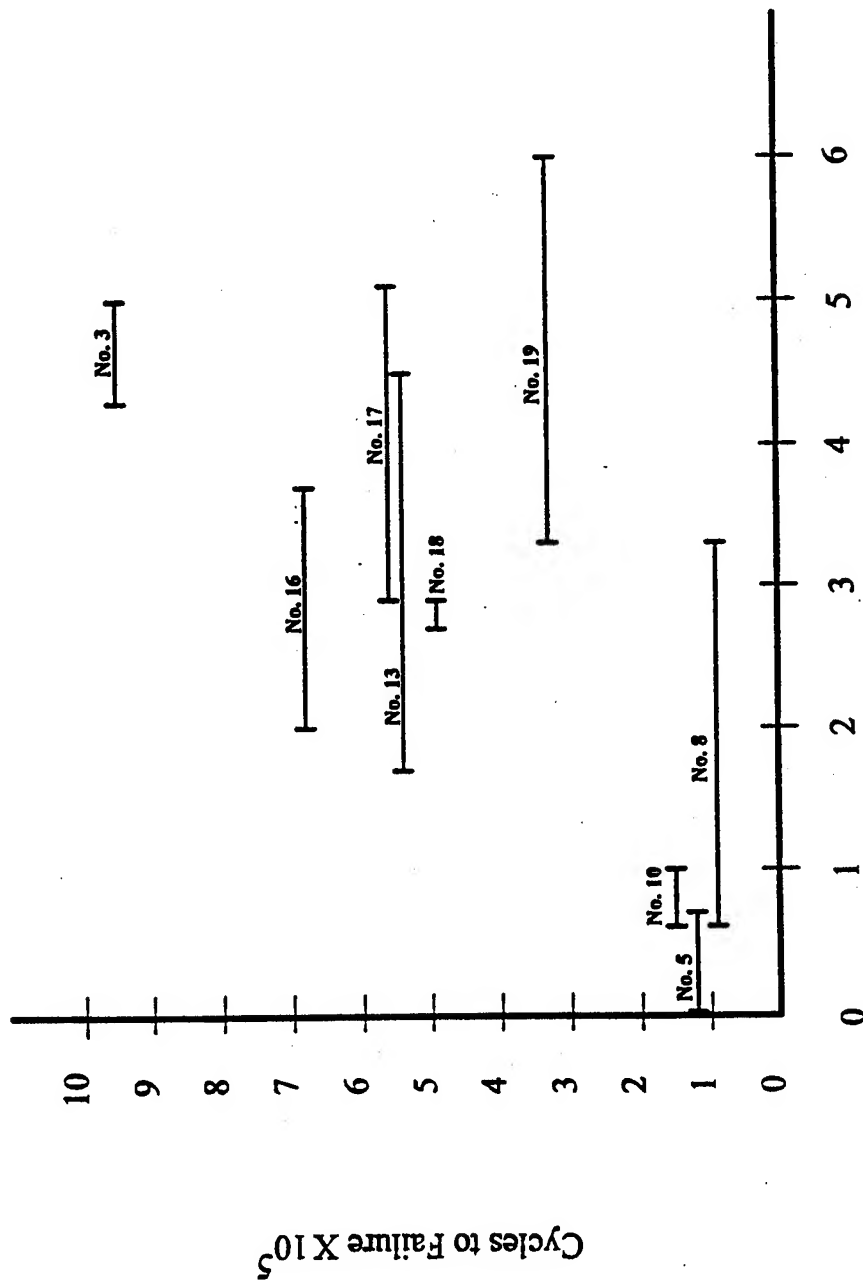


Figure 3. Graphic comparison of fatigue life related to tapered and straight shank fastener interference; McDonnell Aircraft lab tests.



Fastener Interference (Inch X 10⁻³)

Figure 4. Measured pre-installation fastener interference at specimen failure sites identified by specimen number; McDonnell Aircraft lab tests.

- **Roughness Tolerance to 125 Microinches**
- **Burrs on Nut Side Not Detrimental**
- **Perpendicularity to 3 Degrees Tolerable**
- **Ovality is a Serious Problem**
- **Bellmouthing and Barreling of Concern**
- **Minor Rifling, Scratches, Tears & Laps Tolerable**

Figure 5. Metcut lab findings relating tapered fastener hole quality with fatigue life.

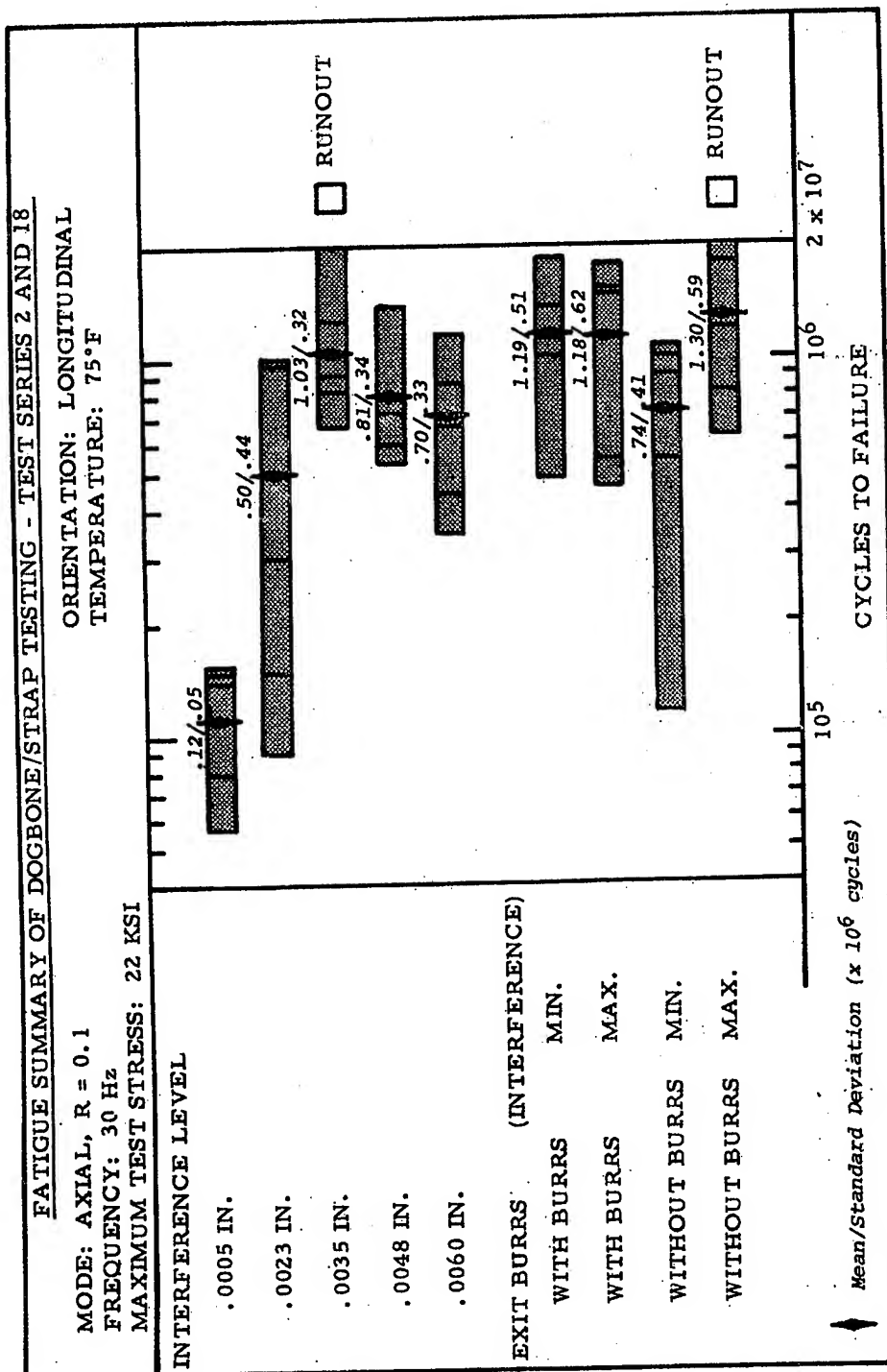


Figure 6. Fatigue life relative to Taper-Lok fastener interference level; Metcut lab tests.

- 1. Durability Correlates With Fastener Interference**
- 2. Practical Interference Range: 0.0035" to 0.0050"**
- 3. Minor Hole Surface Flaws are Tolerable**

Figure 7. McDonnell Aircraft Company specimen design for fatigue life comparison of Taper-Lok and Hi-Shear interference fasteners.

CAPACITANCE MEASUREMENT SYSTEM OVERVIEW

- Capacitance Principle

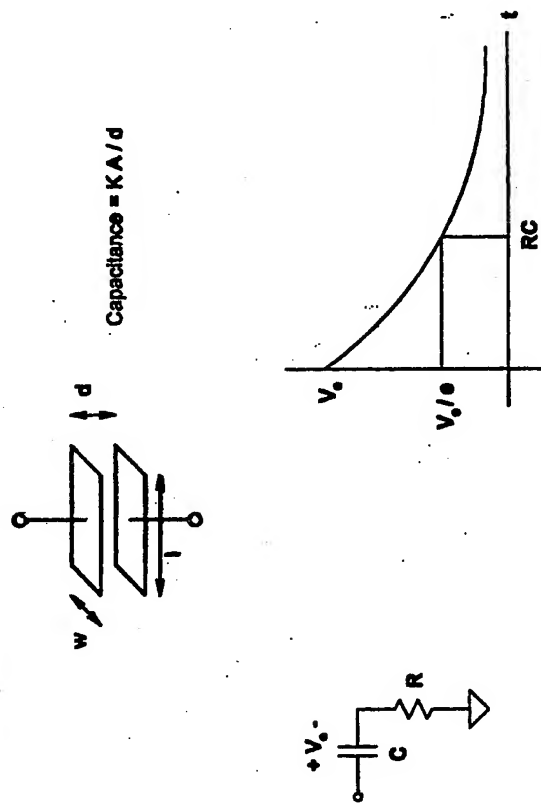
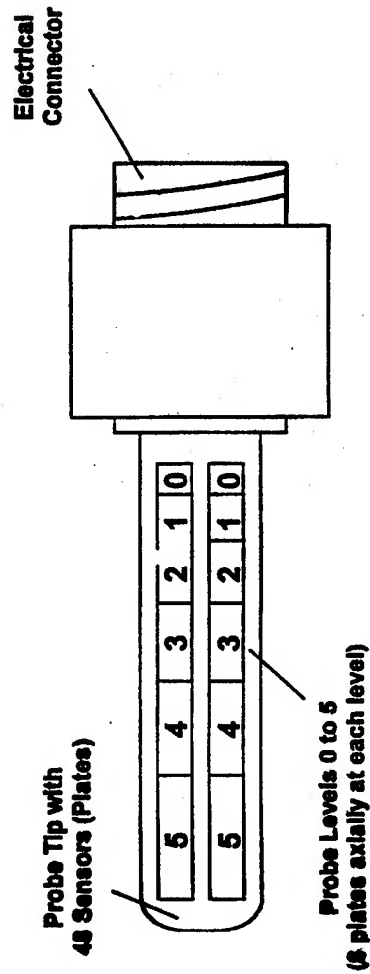


Figure 8. Physical principals of capacitance measurement use electrical discharge rate as a measure of space between plates.

CAPACITANCE MEASUREMENT SYSTEM OVERVIEW

- Probe Layout and Construction



- System Calibration

Measure the Capacitance of 2 ring gauge standards. The diameters of the standards are traceable to NIST to within ± 20 microinches

Figure 9. The Capacitance Measurement System (CMS) hole probe uses multiple capacitor plates to characterize hole quality.

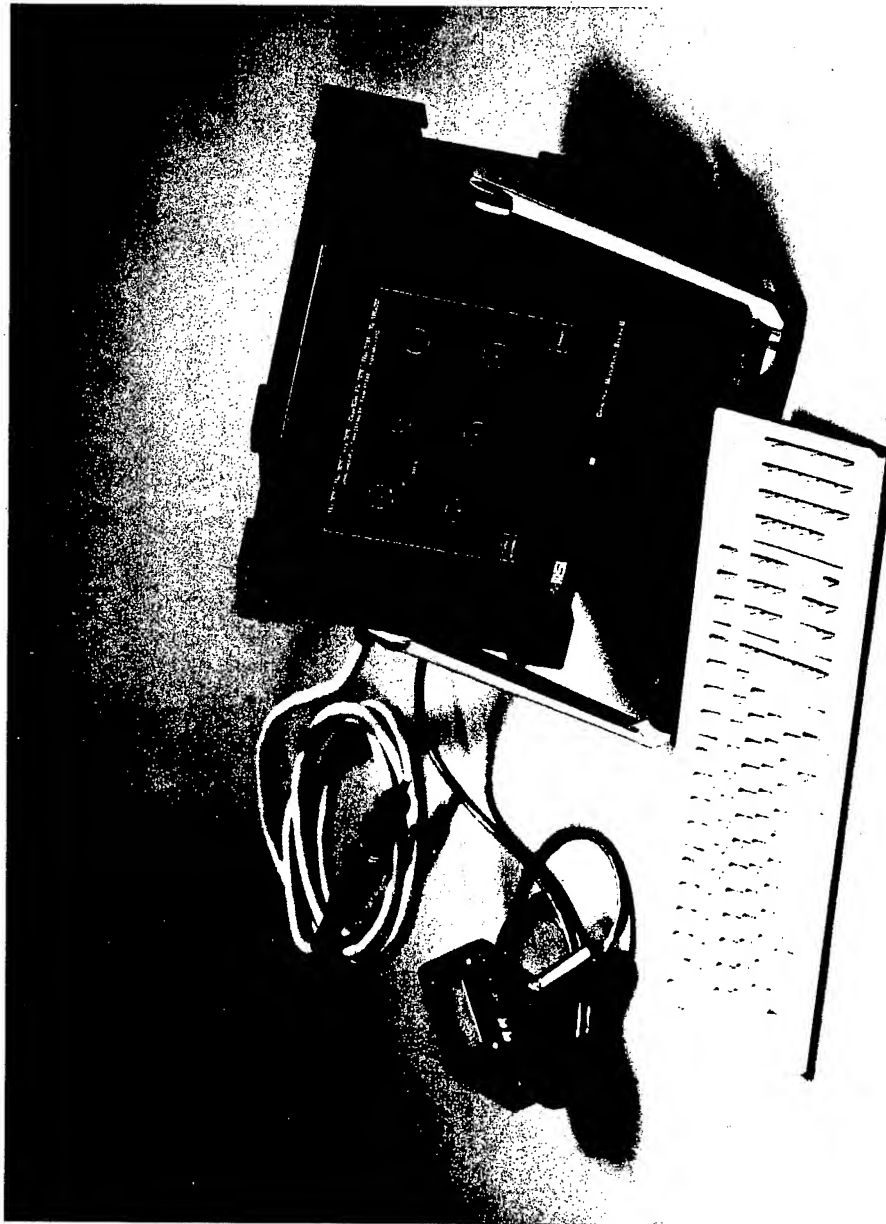


Figure 10. The four major components of the Capacitance Measurement System

CAPACITANCE MEASUREMENT SYSTEM OVERVIEW

- Accuracy Analysis - Measurement Uncertainty
 - Total Uncertainty = Calibration Error + Measurement Uncertainty
 - Worst Case Calibration Error is typically bounded by $\pm .0001"$
 - Total Uncertainty = $\pm (.0001" + \text{Measurement Uncertainty})$
 - For a .1" by .1" Plate (Typical 5/16" probe) the Total Uncertainty Over a .003" Specification Range is $\leq .00015"$

Figure 11. The Capacitance Measurement System calibration provides resolution to within ± 20 microinches.

CAPACITANCE MEASUREMENT SYSTEM OVERVIEW

- Graphical Analysis Tools

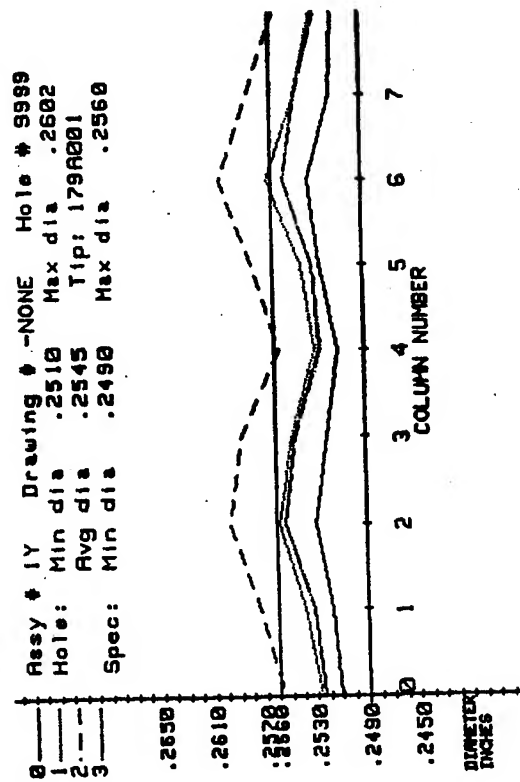


Figure 12. The Capacitance Measurement System axial profiles of a fastener hole surface.

CAPACITANCE MEASUREMENT SYSTEM OVERVIEW

Graphical Analysis Tools

Assy # 1 Drawing # GEMCOR Hole # 1
Hole: Min dia .297 Max dia .2972
Avg dia .297 Tip: 271A001
Spec: Min dia .2944 Max dia .2975

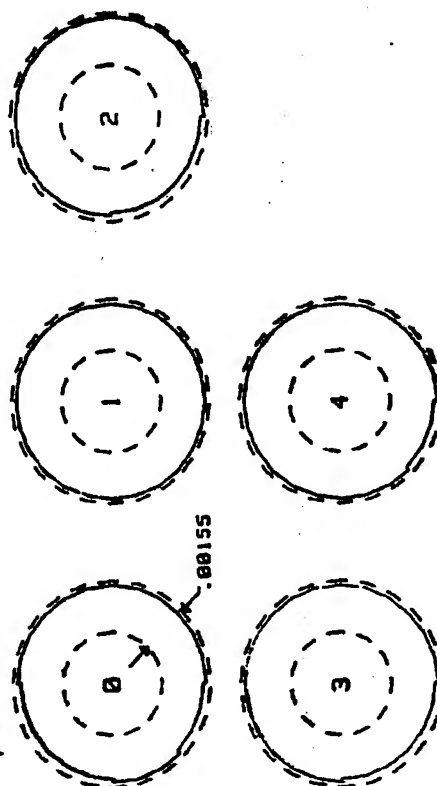


Figure 13. Capacitance Measurement System section profiles of a fastener hole surface.

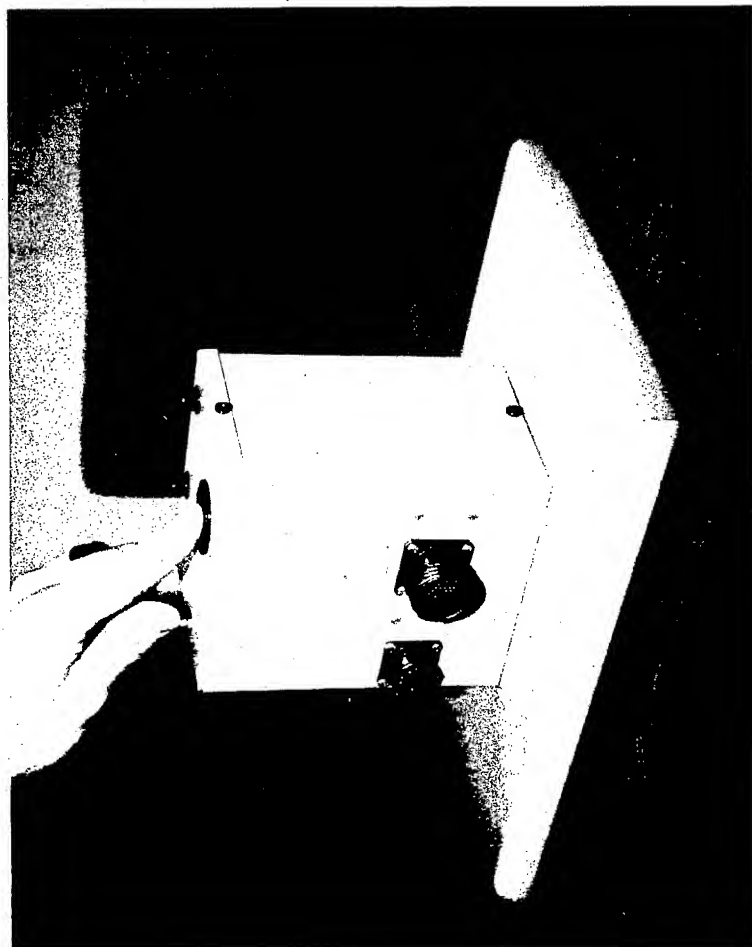


Figure 14. The Fastener Measurement System

- Aerospatiale
- McDonnell Aerospace
- Boeing Defense & Space Group
- Warner Robins Air Logistics Center
- Lockheed Martin - Georgia Division
- Naval Aviation Depot - San Diego and Jacksonville
- Boeing Commercial Airplane Group
- Deutsche Aerospace Airbus
- Pratt & Whitney - Canada
- McDonnell Douglas
- British Aerospace

Figure 15. Capacitance Measurement System II section profiles of a fastener hole surface.

A Probabilistic Model for Predicting Fatigue Life for Crack Formation at Inclusions Using FASTRAN II

P.J. Laz, S.M. Rohrbaugh, and B.M. Hillberry

School of Mechanical Engineering
Purdue University, West Lafayette, IN



USAF Structural Integrity Program Conference

November 28-30, 1995



Purdue University

Objectives

- Refine our probabilistic life prediction model for crack formation at inclusions
- Compare two deterministic crack growth models with experimental results
- Experimentally characterize fatigue crack formation mechanisms



Outline

- Background
- Probabilistic life prediction model
- Experimental program
- Results
 - Compare predicted and experimental cumulative distribution functions (CDF) for fatigue lives
 - Describe experimental observations
- Conclusions



Purdue University

Background

(Newman)

- Fatigue cracks observed to form at inclusions early in life
- Total fatigue life approach
 - Fatigue life entirely crack propagation
- Short crack effect
 - Short cracks grow at faster rates than long cracks
 - Short cracks can grow at ΔK values below the threshold
- Initial crack sizes can be approximated by the inclusion size



Purdue University

Probabilistic Life Prediction Model

- Assumptions
 - Fatigue cracks form at inclusions
 - Initial crack size equals the inclusion size
 - Initial crack size distribution can be represented by the inclusion size distribution
 - Cycles to crack formation is very small compared to total life
 - Specimen geometry: single edge notch tension (similar to AGARD specimen)



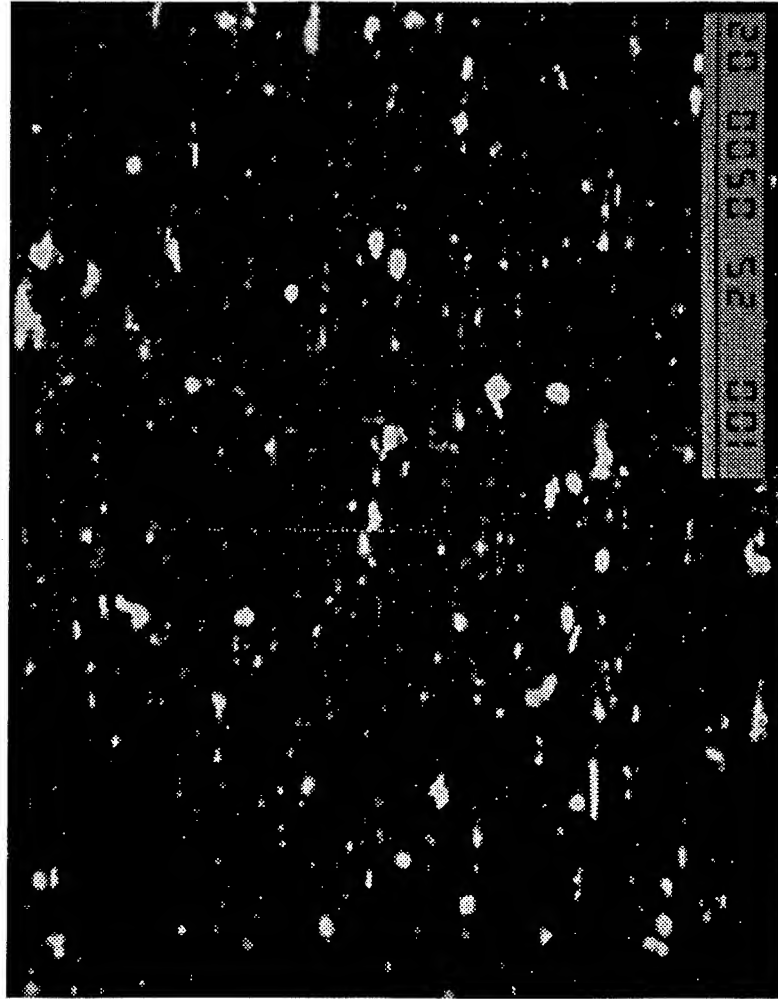
Probabilistic Life Prediction Model

- Assumptions (continued)
 - Crack forms at the center of the notch thickness
 - Crack growth is deterministic
 - ΔK solution for a semi-elliptical crack located at a notch
 - Life defined as number of cycles to through - thickness crack (breakthrough)



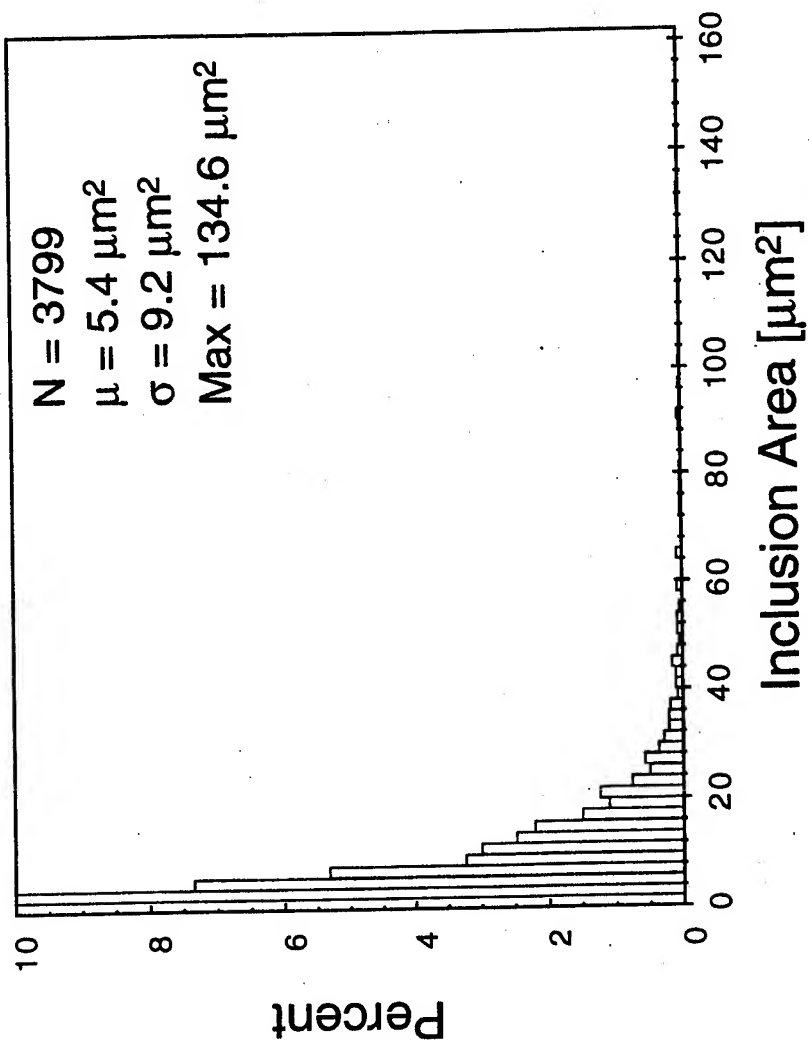
Aluminum 2024-T3 (Virkler)

ST Plane - 500X



Purdue University

Inclusion Size Distribution



Purdue University

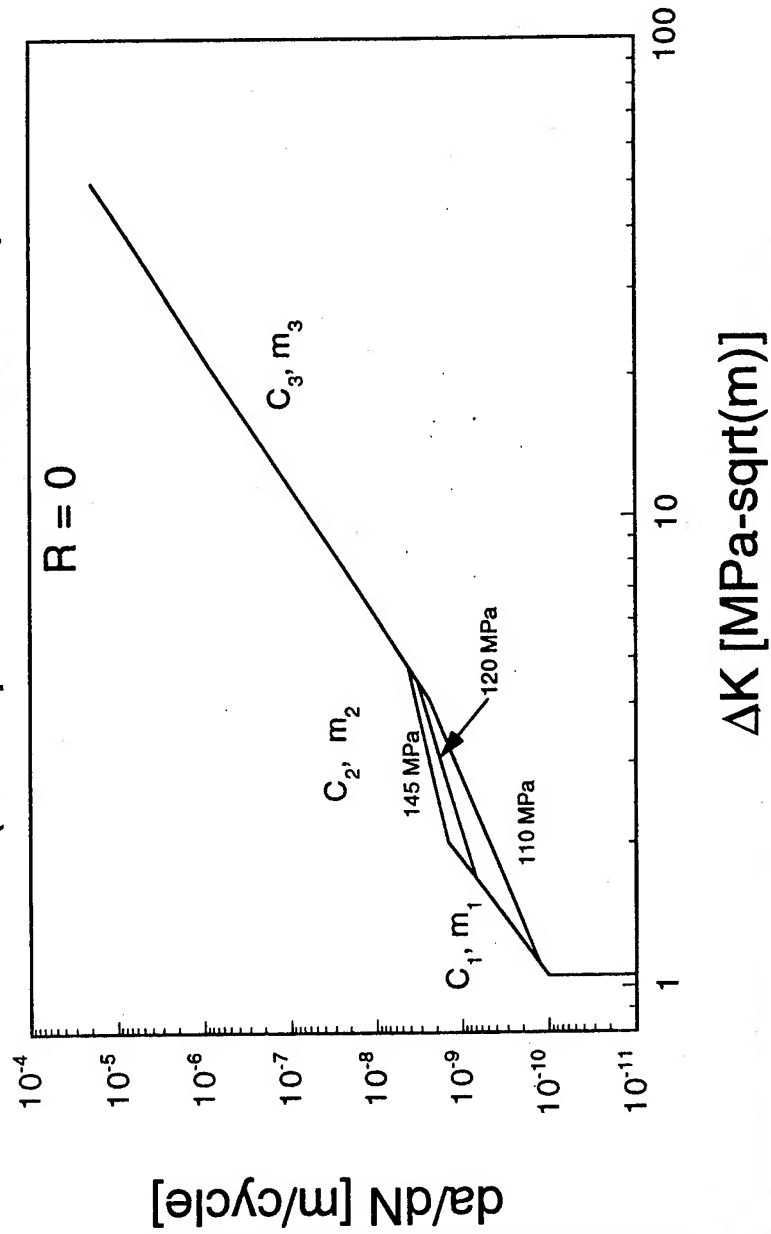
Probabilistic Life Prediction Model

- Monte Carlo method (1000 trials)
 - Select particle area randomly from distribution for each trial
 - Assume initial crack size is a semi-circular crack of area equal to that of the inclusion
- Grow crack with deterministic model
 - Segmented Paris Law for ΔK effective, short and long crack growth (Phillips and Newman)
 - FASTRAN II crack closure model (Newman)
- Cumulative distribution function for fatigue lives



Crack Growth Model

Segmented Paris Law (Phillips and Newman)



Purdue University

Crack Growth Model

FASTRAN II

(Newman)

- Incorporates analytical crack closure model
- Uses da/dN vs. ΔK_{eff} growth law and effective ΔK_{th}
- Includes plastic-zone corrected stress intensity factor
- Includes constraint variation for flat to slant crack growth
- Applied loading may be constant-amplitude, variable-amplitude or spectrum



Purdue University

Experimental Objectives

- Investigate fatigue crack nucleation and the dominant mechanisms of crack formation
- Compare results with life prediction model
- Determine the influence of inclusions and their size on crack formation

Experimental Program

- SENT specimen geometry
- Constant amplitude loading
 - $R = 0.01$
 - $\Delta S = 120 \text{ MPa}$



Purdue University

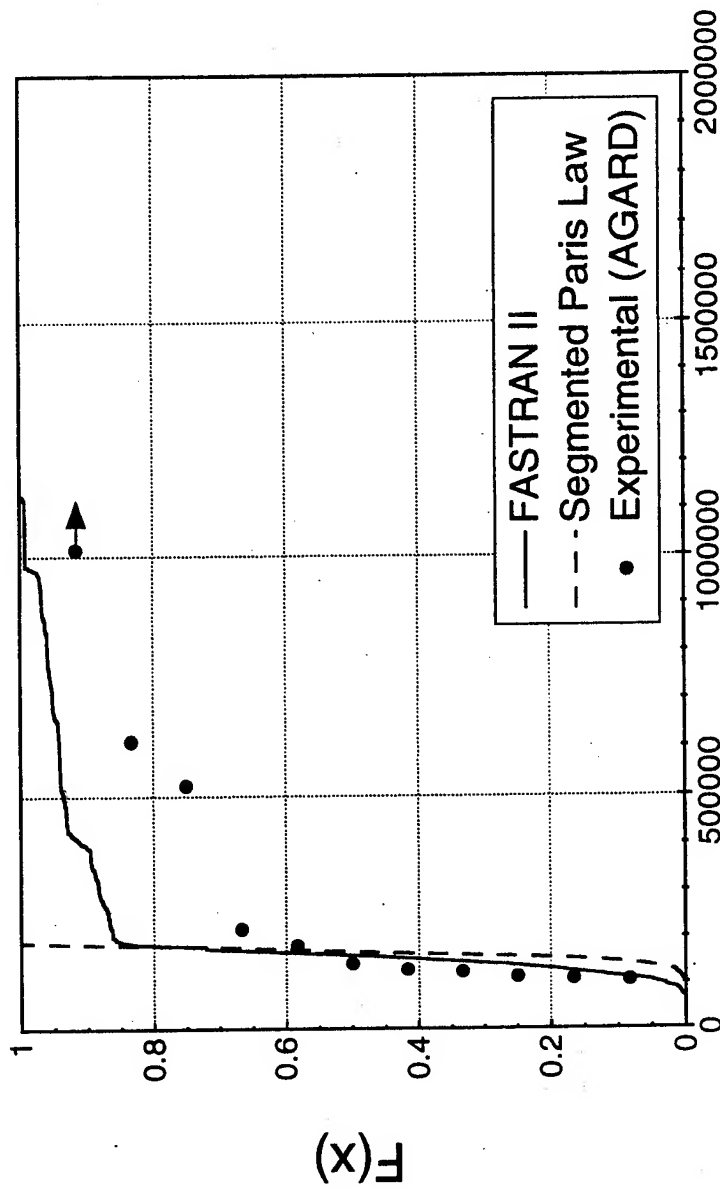
Results

- Cumulative distribution function of fatigue lives to breakthrough ($R=0$, $S_{\max} = 110, 120, 145 \text{ MPa}$)
 - Predicted results
 - Experimental results
 - Newman's AGARD data
- Evaluation of crack nucleation sites
 - Compare inclusion sizes that nucleated fatigue cracks with the initial distribution
 - SEM examination of fracture surfaces and replicas



Life to Breakthrough CDF

$R=0$ $S_{max}=110$ MPa



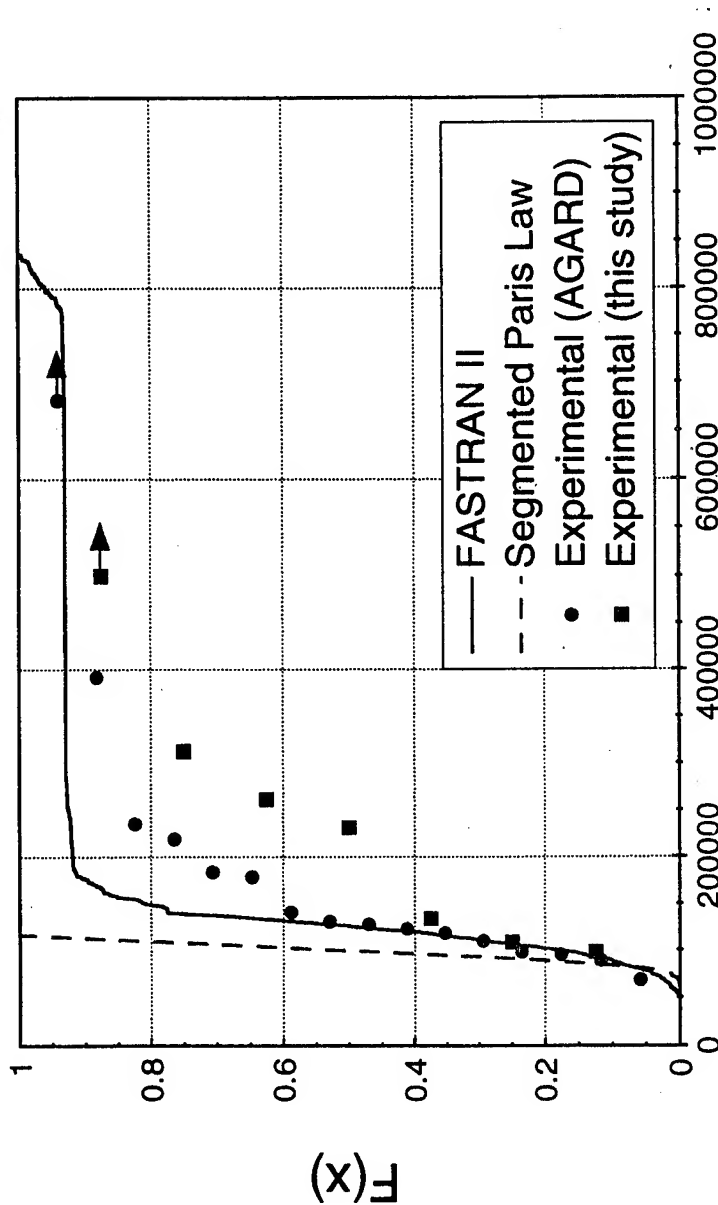
Life to Breakthrough [cycles]



Purdue University

Life to Breakthrough CDF

$R=0$ $S_{max}=120$ MPa



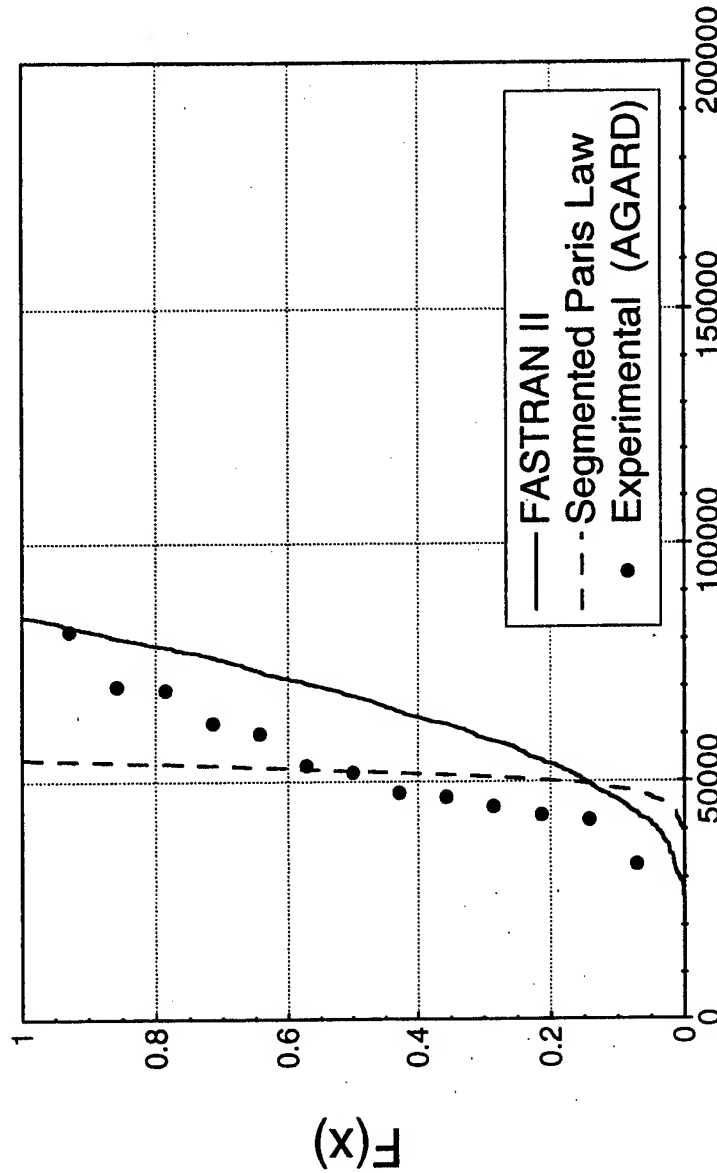
Life to Breakthrough [cycles]



Purdue University

Life to Breakthrough CDF

$R=0$ $S_{max}=145$ MPa



Life to Breakthrough [cycles]



Purdue University

Predicted Results

- FASTRAN II results
 - Predicts both the mean and variability of experimental fatigue lives
- Model closely predicts the shorter fatigue lives (most critical)
 - Correspond to the larger, more damaging inclusions
- Particle (crack) size threshold
 - Cracks below threshold - assumed not to grow
- Model does not account for multiple cracks forming along the notch bore



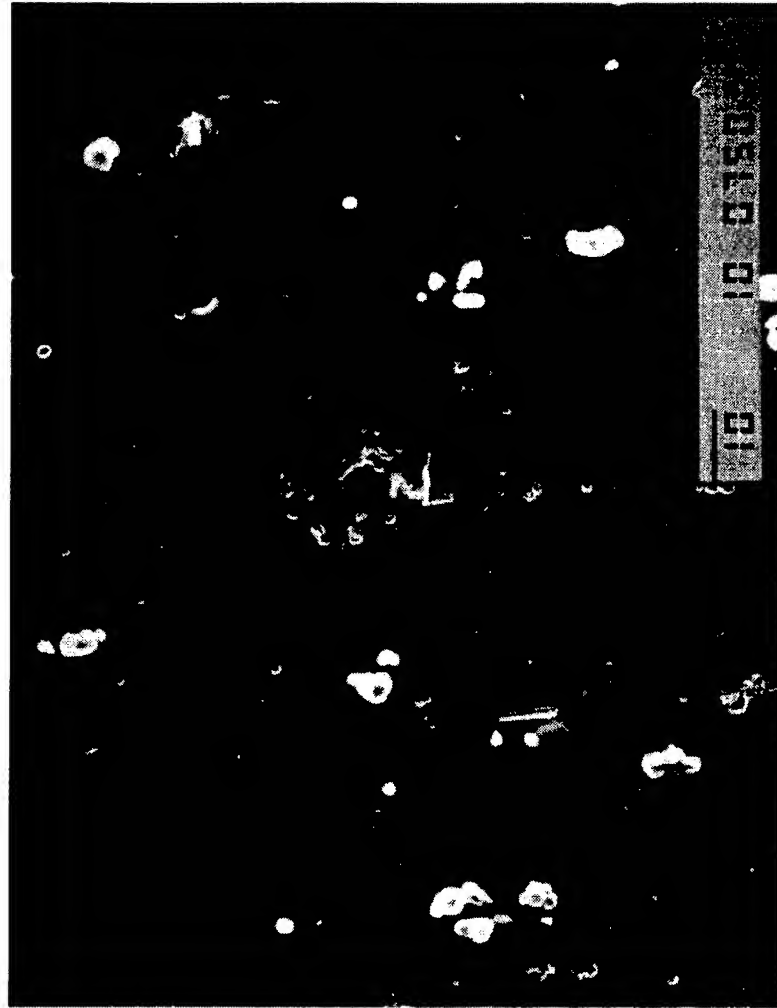
Experimental Observations

- Every fatigue crack started either at an inclusion or a void where an inclusion had pulled out
- Multiple fatigue cracks formed along the notch (1 to 3 cracks)
- Crack nucleating inclusion size range
 - $2a$ - 5 to 15 μm c - 7 to 25 μm
- Nucleating inclusion - tail of distribution
- Composition analysis of nucleation sites
 - Al, Cu, Fe, Mn
 - Al, Cu, Si



Crack Nucleation Site

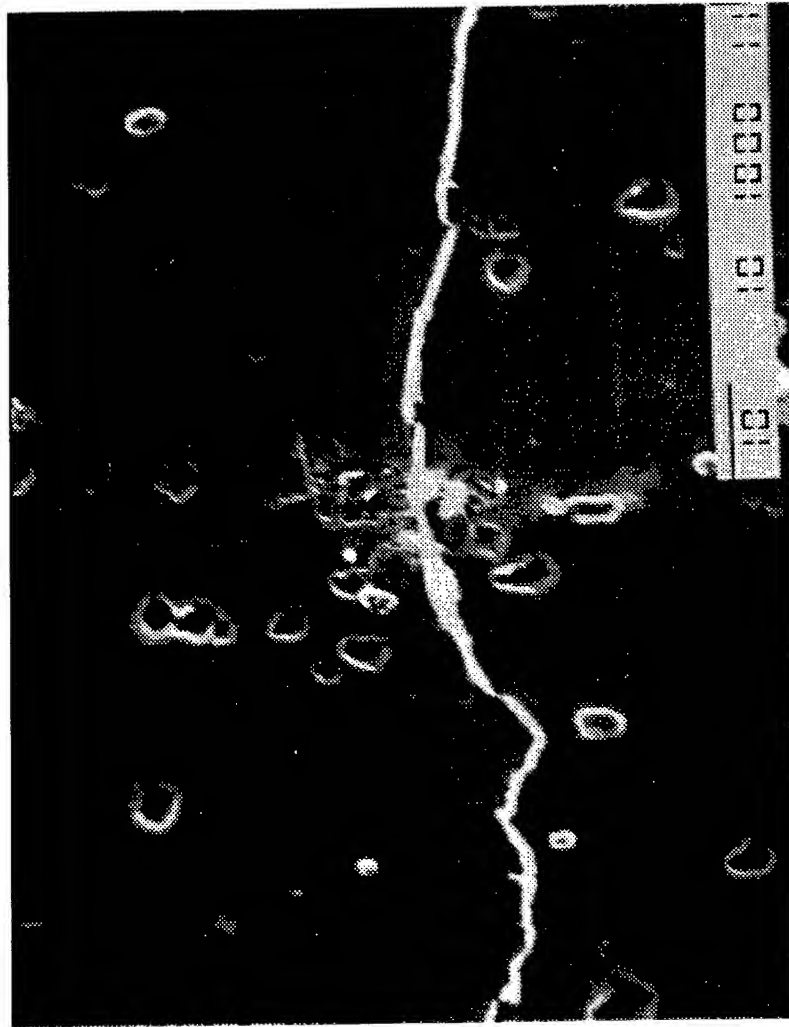
Acetate Replica (5,000 cycles - 750X)



Purdue University

Crack Nucleation Site

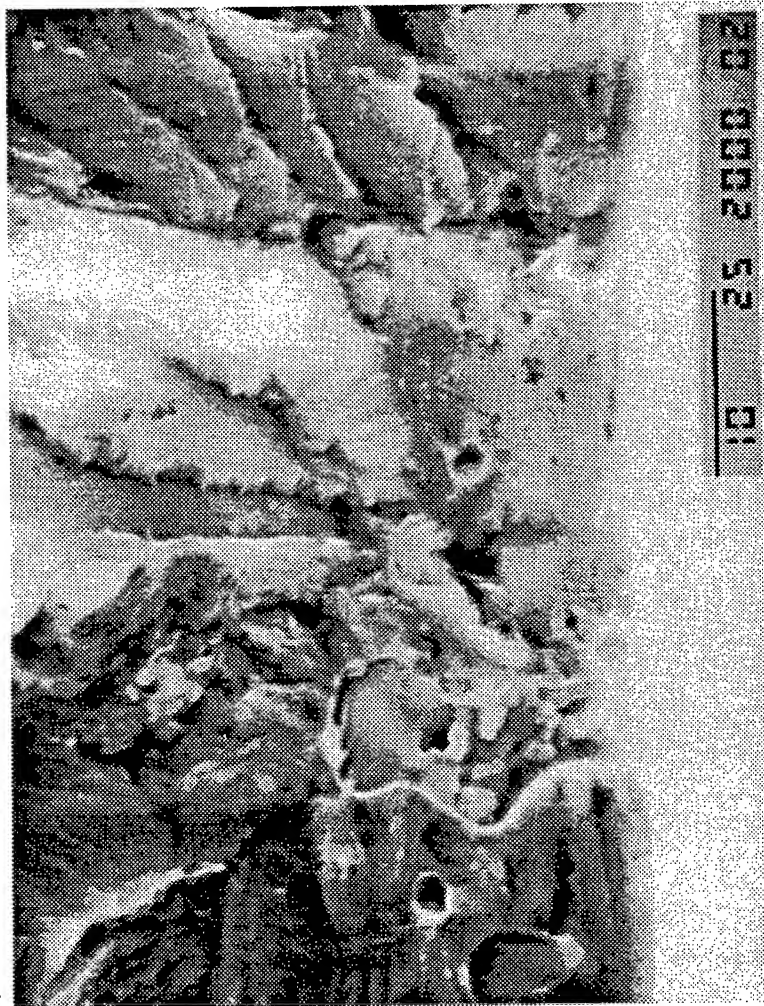
Acetate Replica (200,000 cycles - 1000X)



Purdue University

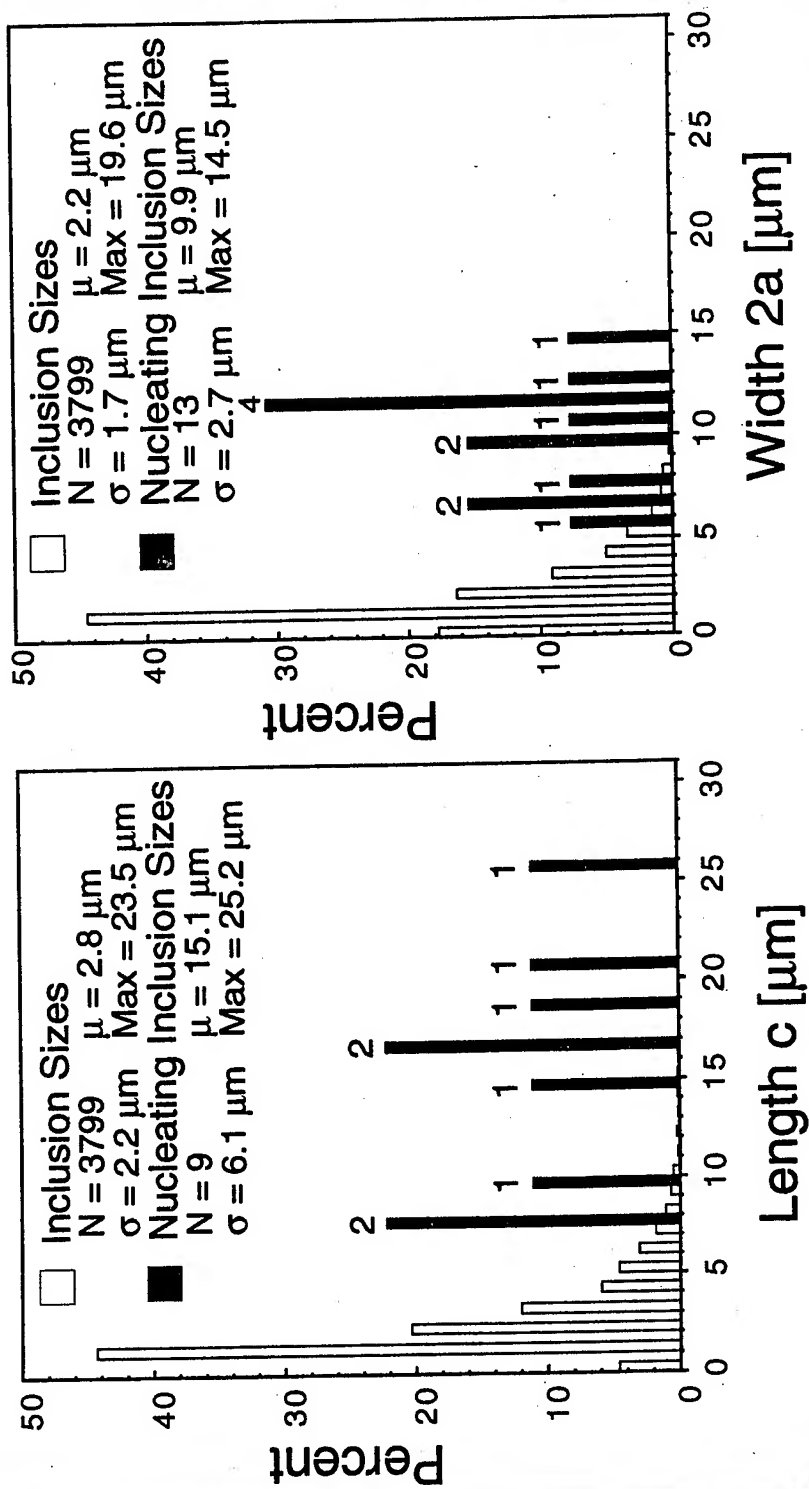
Crack Nucleation Site

Fracture Surface (2000X)



Purdue University

Crack Nucleating Inclusion Sizes



Purdue University

Summary

- Probabilistic model predicts fatigue lives from inclusion area distribution
- Inclusions are primary fatigue crack nucleation site in 2024-T3 aluminum sheet
- Life entirely due to crack propagation
- Inclusions that nucleated fatigue cracks are from the tail of the inclusion size distribution
- Probabilistic life prediction model predicts experimental fatigue lives



Summary

- Improved results obtained with FASTRAN II
- Variability in fatigue life values characterized with FASTRAN II
- Critical lowest lifetimes - correspond to largest particles

Acknowledgment

- This research was sponsored by the Air Force Office of Scientific Research under grant F49620-93-1-0377



Purdue University

The Application of the R-curve Concept for the Prediction of the Residual Strength of Fiber Metal Laminates

***Tjerk J. de Vries, MSc**

Marco Pacchione, MSc

Delft University of Technology, Faculty of Aerospace Engineering

P.O. Box 5058, 2600 GB Delft, The Netherlands

E-mail: tjerk@dutlbc1.lr.tudelft.nl

Abstract An experimental program is conducted to investigate the fracture toughness of Fiber Metal Laminates with glass fibers. This new family of aerospace materials is composed of thin aluminum layers bonded together with plies of glass fiber reinforced epoxy adhesive and offers outstanding fatigue resistance and high static strength. Because these materials exhibit stable tearing prior to final failure, the validity of the R-curve approach for residual strength predictions has been investigated. The necessary Irwin and compliance correction for plasticity, as proposed by the ASTM standard, both yield results, independent of the panel width and the initial crack length. Interchanging the results of both plasticity correction methods for residual strength predictions is not possible. Irwin's correction yields early plastic yielding but neglects the significant strain hardening capacity of the materials. The Compliance method is sensitive to local buckling and anisotropy of the material must be considered. The use of an effective yield stress for the Irwin method is proposed for materials with significant strain hardening. The R-curve approach for FML's is valid from an experimental point of view but needs an extended theoretical development.

1. INTRODUCTION

Fiber Metal Laminates (FML's) are a family of advanced hybrid aerospace sheet materials, made of thin metal layers and alternating plies of high strength fibers embedded in epoxy (preprep). These materials combine the traditional durability, formability and machinability characteristics of metals with the high specific strength and excellent fatigue resistance of composites [1]. Additional advantages are a high fire resistance and a high impact resistance. An illustration of the concept is shown in Figure 1.

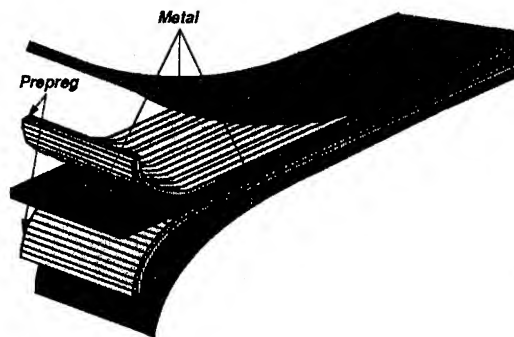


Figure 1, Build up of an FML

The occurrence of cracks due to fatigue is generally limited to the metal layers. The fibers are to a large extent insensitive to fatigue, remain intact and bridge the crack in the metal layers. Load is transferred from the metal layers in the vicinity of the crack to the undamaged fibers, reducing the stress intensity factor at the crack tip. Moreover the crack bridging fibers restrain in crack opening, which gives an additional reduction of K . For this reason, FML's have the potential to replace aluminum, used in fatigue sensitive aircraft structures.

As the intact fiber layers have a significant effect on the fatigue resistance of FML's, the question arises how the material behaves when the fibers are broken, e.g. in the case of an uncontained engine disintegration. The purpose of the present study is to focus on the fracture mechanism of GLARE, an FML with S2-glass fibers and aluminum metal layers [2]. The usefulness of fracture criteria derived for metals for the prediction of the residual strength of FML's is discussed. The research program is confined to center cracked tension specimens (CCT) with through cracks, both the fibers and the aluminum layers are broken at the crack. Because FML's show stable tearing before failure, attention is focused on the crack resistance approach or R-curve, based on the stress intensity factor, K . The experimental work was carried out at Delft University of Technology, The Netherlands and Pisa University, Italy.

The R-curve approach is part of Linear Elastic Fracture Mechanics (LEFM) and requires linear-elastic material behavior with a crack tip plastic zone size that is small compared to the K dominated region. To correct for plasticity, the fracture toughness is described as a function of a modified crack length, the effective crack length, a_{eff} . Two correction methods proposed by the ASTM

standard [3] are discussed here. The R-curves thus obtained are compared and discussed.

2. MATERIALS AND SPECIMENS

The materials selected for the present research are GLARE 2 3/2 0.3, GLARE 3 3/2 0.3 and the aluminum alloys Alclad 2024-T3 and Al 7075-T6 clad. The aluminum alloys were chosen to function as a reference.

GLARE 2 contains unidirectional prepreg layers with the fibers in rolling direction of the aluminum sheets. The volume fraction of fibers in the prepreg is about 60%. The code 3/2 denotes a combination of three aluminum (2024-T3 bare) and two double prepreg layers of 0.125 mm thickness each:

$$[2024 / 0^\circ / 0^\circ / 2024 / 0^\circ / 0^\circ / 2024]$$

The number 0.3 in the code represents the thickness of the aluminum layers, in this situation 0.3 mm. The total thickness of the panels is about 1.4 mm. The orientation of the fibers makes the material behavior orthotropically, with different Young's moduli and yield stresses in the principal material directions. The linear elastic fibers in combination with the elasto-plastic metal layers cause extreme strain hardening capabilities as shown by the double linear stress-strain curves in Figure 2.

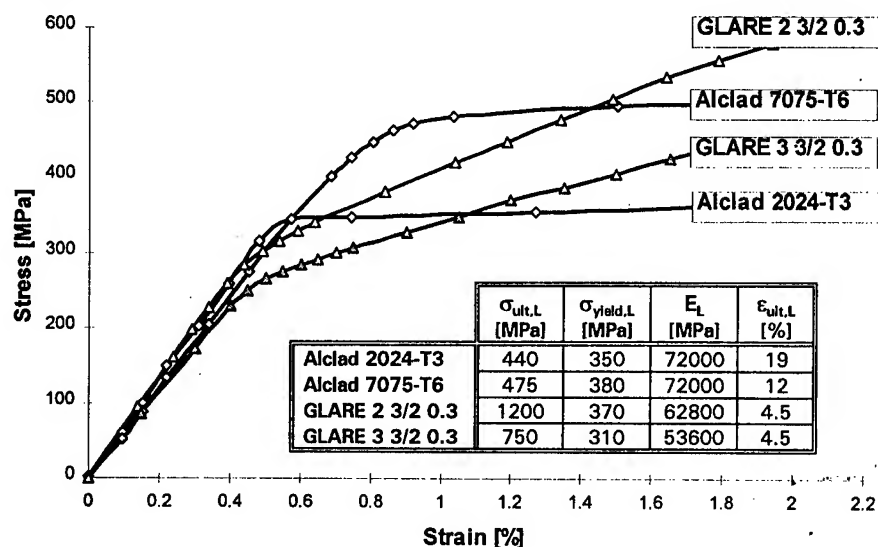


Figure 2, Experimental stress-strain curves of tested materials

The prepreg layers of GLARE 3 are positioned along both material principal directions (50/50 cross ply).

[2024 / 0° / 90° / 2024 / 90° / 0° / 2024]

Differences in material properties between the two directions are due to the different properties of the aluminum layers in Longitudinal, L, and Transverse, T, direction. Since these differences are small, the material is approximately quasi-isotropic in the plane of the sheet.

For all tests, CCT specimens are tested in L-T direction. Two different widths were used, $W=200$ mm and $W=400$ mm. The relative crack length $2a/W$ varied between 0.20 and 0.33. The crack was simulated by a saw cut. In addition, some were first fatigue loaded to sharpen the crack tip.

The tests were carried out under both displacement control and load control. The crack length was measured by the Potential Drop (PD) method and with a video camera, connected to a microscope. The PD apparatus applied a pulsed direct current over the specimen. For the application on GLARE panels, the crack length was measured in one of the outer aluminum layers, assuming equal crack growth in all separate aluminum layers. The layer used for measurements was electrically insulated from the other layers by a milling process and with the help of the fiber prepreg to avoid electric interference, see Figure 3. The Crack Opening Displacement (COD), defined as the distance between the upper and lower crack edges at the center of the crack, was measured with a clip gauge as described in the ASTM standard [3].

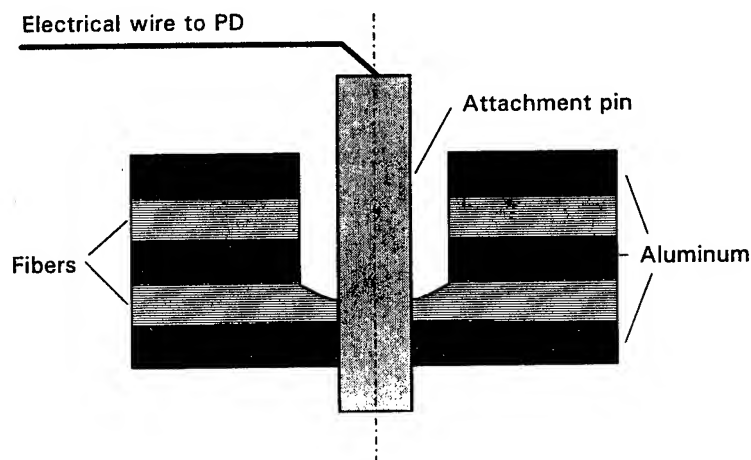


Figure 3, Insulation of the lower aluminum layer for PD measurement

The test program with all relevant parameters is presented in Table 1.

Table 1, Test program

Material	W [mm]	t ¹⁾ [mm]	2a/W	fatigue precrack	Control ²⁾
Alclad 2024-T3	400	1.0	1/4	No	Disp.
	400	1.0	1/3	No	Disp.
	400	1.6	1/4	No	Disp.
	400	1.6	1/3	No	Disp.
Alclad 7075-T6	400	1.0	1/4	No	Disp.
	400	1.0	1/3	No	Disp.
GLARE 2 3/2 0.3	200	1.4	1/4	Yes	Load
	400	1.4	1/5	No	Disp.
	400	1.4	1/4	Yes	Load
	400 ³⁾	1.4	1/4	No	Disp.
	400	1.4	1/3	Yes	Load
	400 ³⁾	1.4	1/3	No	Disp.
GLARE 3 3/2 0.3	200	1.4	1/4	Yes	Load
	200	1.4	1/4	Yes	Load
	400	1.4	1/5	No	Disp.
	400	1.4	1/4	Yes	Load
	400	1.4	1/4	No	Disp.
	400	1.4	1/3	Yes	Load
	400 ³⁾	1.4	1/3	No	Disp.

¹⁾ t is the nominal thickness of the specimen

²⁾ Disp. indicates displacement control and Load indicates load control

³⁾ Experiment carried out twice

3. FRACTURE MECHANISM

FML's, like metals, exhibit a capability for slow stable tearing before rapid failure. During the experiments, images of the crack tip zone were made with a high resolution video camera. The observations are discussed below.

Images of a GLARE 2 3/2 0.3 CCT specimen with blunting of the crack tip, crack initiation and crack propagation are shown in Figure 4. The specimen was first fatigue loaded until a crack growth of one millimeter had occurred, see Figure 4.1. During fatigue cycling, the fibers stay intact and bridge the crack in the aluminum layers resulting in a different physical crack length for both components of the material. Only the crack length in the outer aluminum layers could be visually recorded. To get an indication of the crack extension a millimeter grid was bonded to the specimen.

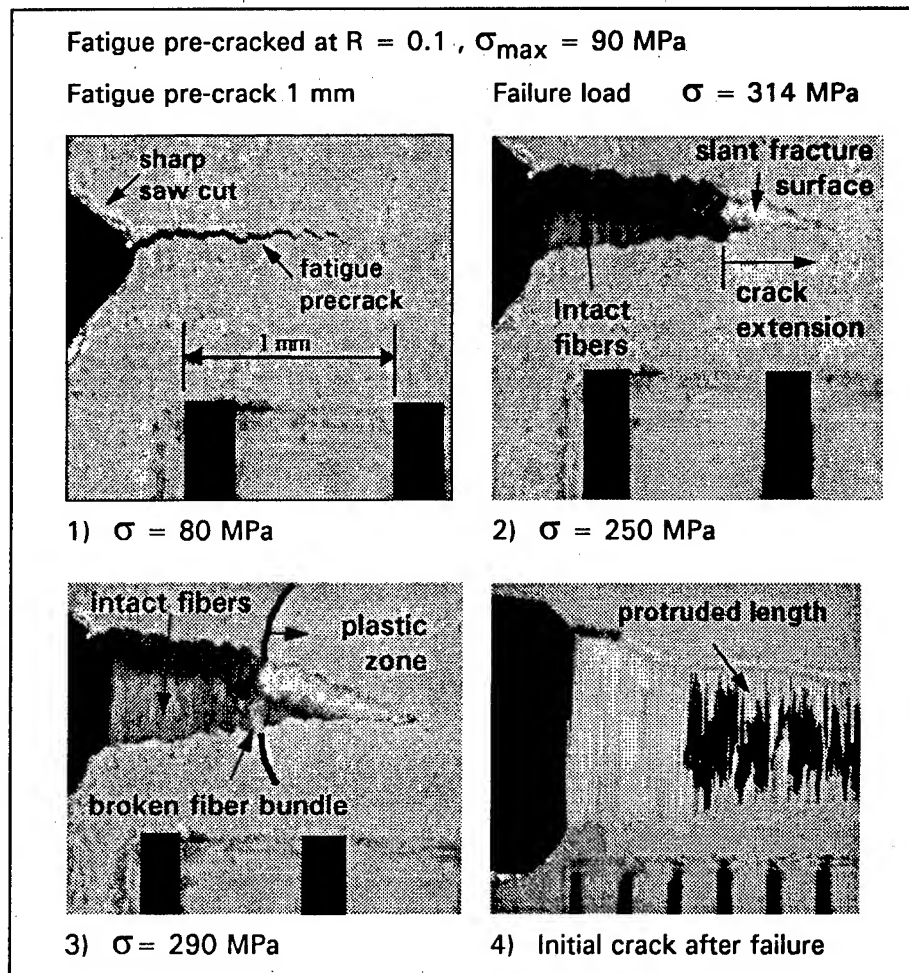


Figure 1, Crack growth sequence for a GLARE 2 3/2 0.3 specimen,
 $W = 400$ mm and $a_0 = 100$ mm

A load increase opens the fatigue crack in the aluminum. At a gross stress of 100 MPa crack growth in the aluminum layer is initiated. The fracture process generates slant crack faces, differing from the fatigue crack faces as the brighter crack surface, see Figure 1.2. Also the creation of plastic zones is slightly visible. Just before the gross stress reaches 290 MPa, the first fiber bundle fractures at the tip of the fatigue crack. This is shown in Figure 1.3 where this broken bundle is visible as a white zone. At this load, the other fibers are expected to remain until intact. By further increasing the load, random failure of the fibers is observed between the tip of the saw cut and the tip of the fatigue crack in the aluminum layer.

Due to the slant fracture surfaces, it can not be observed whether the fibers in front of the fatigue crack are already broken. In all likelihood, the crack extension is comparable for both the glass prepreg and aluminum layers. Because the ultimate strain of the glass fibers of 4.5% is significantly smaller than the 19% of 2024-T3, the glass fiber layer is expected to initiate and control crack extension. After fiber failure, the adjacent aluminum layer is unable to take over the high loads and will consequently crack. Delamination due to high strain gradients reduces the strain in the glass fibers and consequently delays fiber failure.

A further increase of load, pictures not shown in Figure 4, causes the crack to propagate up to 16 mm at a maximum load of 314 MPa. Figure 4.4 (notice different scale) which is taken after final failure, shows the protruded length of the broken fibers is significantly longer for the first two millimeter of crack extension. The first millimeter is caused by fatigue precracking of the starter notch, resulting in delamination between the prepreg and aluminum layers. The second millimeter is possibly due to the biaxial stress state in the aluminum in contradiction to the uniaxial stress state in the glass prepreg that can cause delamination. This effect is more severe at the initial crack tip where the crack bridging of the fibers is less effective and the crack tip in the aluminum layers can blunt more, but also for high loads present in GLARE 2 specimens before fracture. It is important to notice that the first observed fiber breakage started at a stress, higher than 90% of the residual strength. At fracture, the average stress in the net-section is 470 MPa, far above the yield stress of 370 MPa. For the GLARE 3 laminates, a comparable crack growth sequence as for GLARE 2 was observed.

After the residual strength tests, the outer aluminum layers were chemically removed to determine the extent of delamination, see Figure 5. Due to fatigue pre-cracking, a small semi-elliptical delamination is created at the crack tip, followed by delamination caused during the residual strength test. For the tested 3/2 lay-ups, this method can only detect delamination at or close to the interface between the fiber layers and the outer aluminum layers. The observed delamination occurred between the fibers and matrix located at the side of the outer aluminum layer. The delamination length does not show any correlation with the protruded length of the fibers. This suggests that most of the delamination is caused by a dynamic spring back of the elastically loaded fibers after fracture. In that case, the delamination can be divided into a static and

the more load carrying capacity of GLARE 2 with only fibers in 0° direction and the corresponding spring back after fracture.

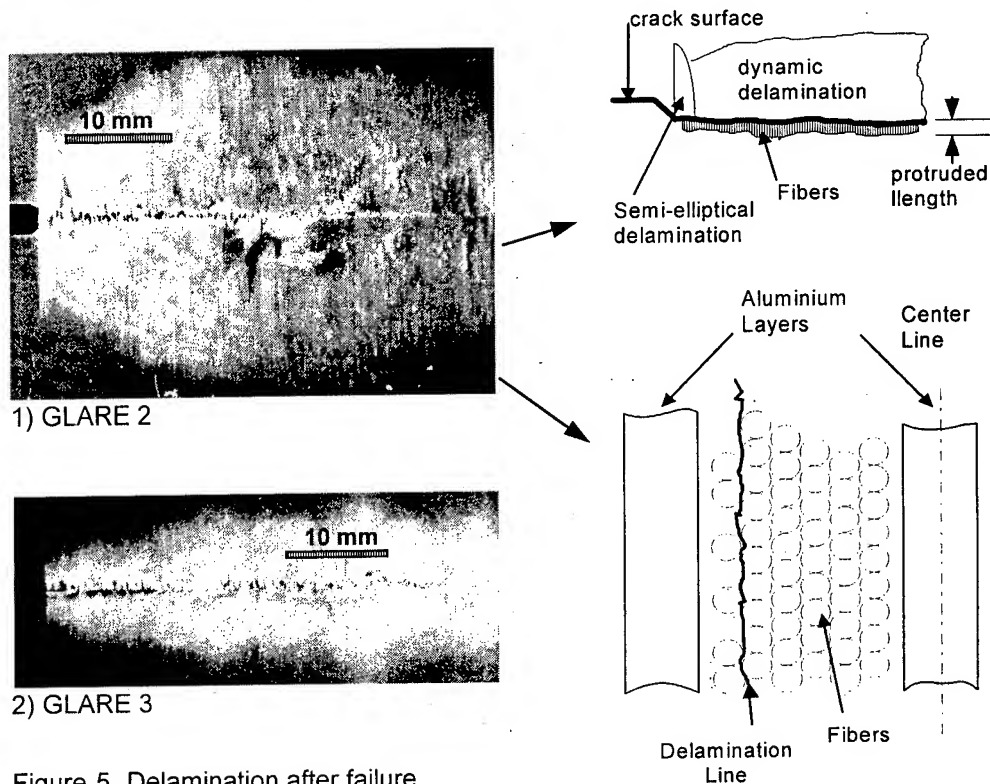


Figure 5, Delamination after failure

4. THE EFFECTIVE CRACK LENGTH

Linear elastic stress analysis yields infinite stresses at the crack tip which are prevented in practice by a finite crack tip radius and material plasticity. The plastic zone surrounding the crack results in larger displacements and a lower stiffness in comparison to the elastic situation. It makes the crack behave as an elastic crack that is longer than the actual physical crack.

As a result of plasticity, the K parameter no longer characterizes the stress field at the crack tip, but in front of the plastic zone a corrected K value may be used to describe the stress distribution. The K concept can still function as a fracture parameter as long as the plastic zone is small.

The ASTM standard [3] recommends two different methods to calculate a corrected K factor based on a newly defined effective crack length, a_{eff} : the Irwin correction and the Compliance correction respectively. According to the Irwin correction, the actual crack

behaves like a virtual elastic crack that theoretically extends till the center of the plastic zone, see Figure 6(a), whereas in the Compliance correction, the actual crack is assumed to have the COD of an elastic crack with a larger effective crack length, see Figure 6(b).

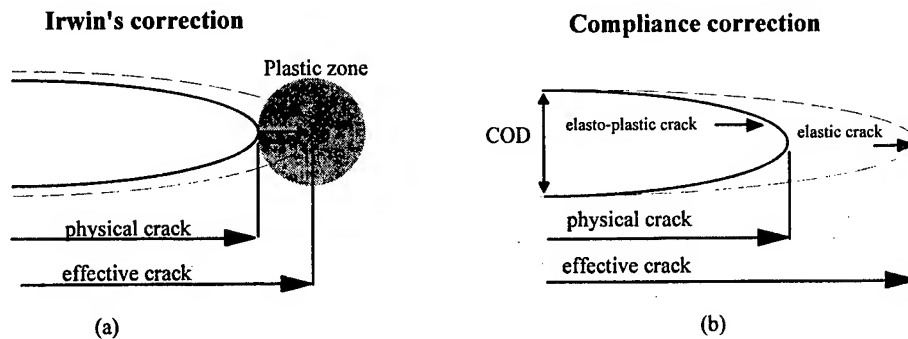


Figure 6, Different effective crack length definitions

The R-curve, being a material toughness property for a given thickness, should be independent of the initial crack length a_0 , and the panel width W . The plastic zone size varies only with the physical crack extension, Δa_{phys} . Whether this is valid for FML's will be discussed next for the Irwin- and followed by the Compliance correction.

4.1 The Irwin plastic zone correction

The Irwin correction for the physical crack length assumes no strain hardening of the material, i.e. the stresses can not exceed the yield stress. Stresses at the crack tip are confined to the uniaxial yield stress of the material and a stress redistribution must take place in the net-section to maintain equilibrium.

Figure 7 illustrates the plastic zone radius r_y , calculated for stable crack extension test results of Alclad 2024-T3 and clad 7075-T6 sheet specimens. It suggests that r_y is independent of the initial crack length for both alloys. Because 7075-T6 is more brittle, its plastic zone size is significantly smaller. The stiffness of both alloys reduces drastically during plastic deformation, illustrated earlier in Figure 2, making Irwin's assumption of ideal plastic material behavior plausible.

GLARE 2 and GLARE 3, however, exhibit significant strain hardening after yielding of the aluminum due to the presence of elastic glass fibers in loading direction. Irwin's correction underestimates the stress carrying capacities of the fibers and therefore the conventionally

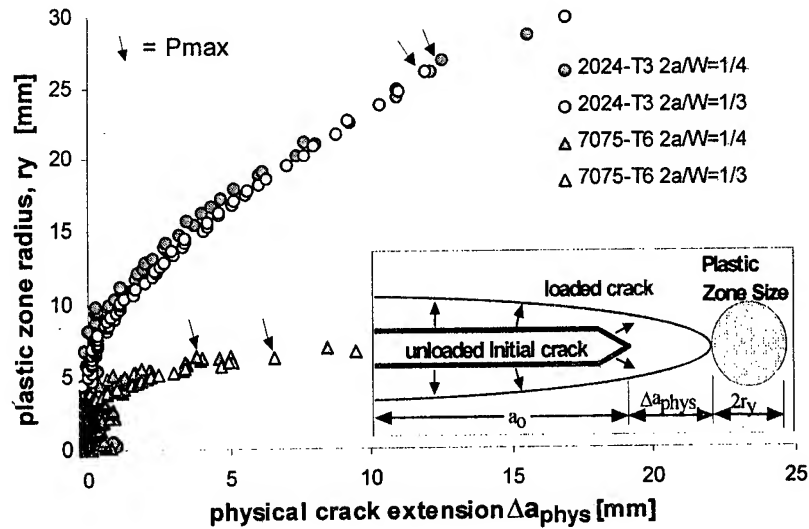


Figure 7, Irwin plastic zone size. CCT-specimen L-T; $W=400\text{mm}$ and $t=1.0\text{ mm}$

calculated r_y is too large. The calculated edge of the plastic zone can reach the edge before specimen failure in the test and the calculation has to be interrupted before final fracture. It implies that the applied load can exceed the load that can pass through the fully yielded ligament due to the strain hardening capability of the material. This is illustrated in Figure 8 and Table 2. The largest recorded crack extension during testing before the occurrence of net section yielding is denoted Δa_{nsy} .

The results and interrupted calculations for r_y before final fracture are illustrated in Figure 9 and Figure 10 for GLARE 2 and GLARE 3 respectively.

Table 2, Maximum net stress and critical crack length

Material	W [mm]	2a/W	$(\sigma_{net})_{max}$ [MPa]	σ_{yield} [MPa]	$\frac{(\sigma_{net})_{max}}{\sigma_{yield}}$	Δa_c ¹⁾ [mm]	Δa_{nsy} ²⁾ [mm]
2024-T3	400	1/4	345	350	0.98	12.55	12.55
	400	1/3	335	350	0.96	11.91	11.91
7075-T6	400	1/4	288	485	0.59	3.80	3.80
	400	1/3	275	485	0.57	6.60	6.60
GLARE 2	200	1/4	555	370	1.50	11.13	0.51
	400	1/4	469	370	1.27	14.95	1.12
	400	1/3	488	370	1.32	18.10	2.75
GLARE 3	200	1/4	361	310	1.17	7.09	1.05
	200	1/3	401	310	1.30	13.59	2.36
	400	1/5	325	310	1.05	12.09	0.04
	400	1/4	332	310	1.07	14.06	7.01
	400	1/3	334	310	1.08	14.28	7.30

¹⁾ crack length increment at failure, see Figure 8

²⁾ maximum recorded crack extension before "net section yielding", see Figure 8

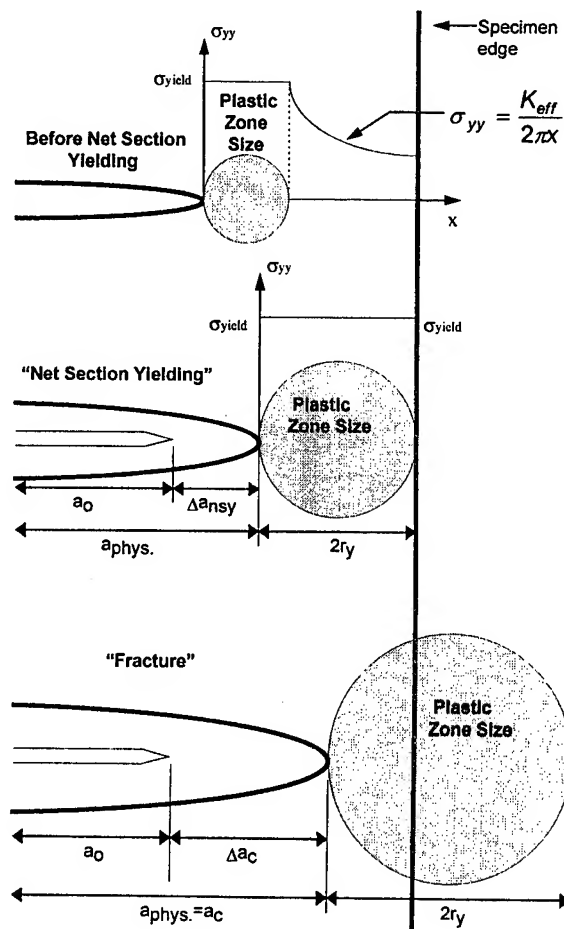


Figure 8, Plastic zone size during loading

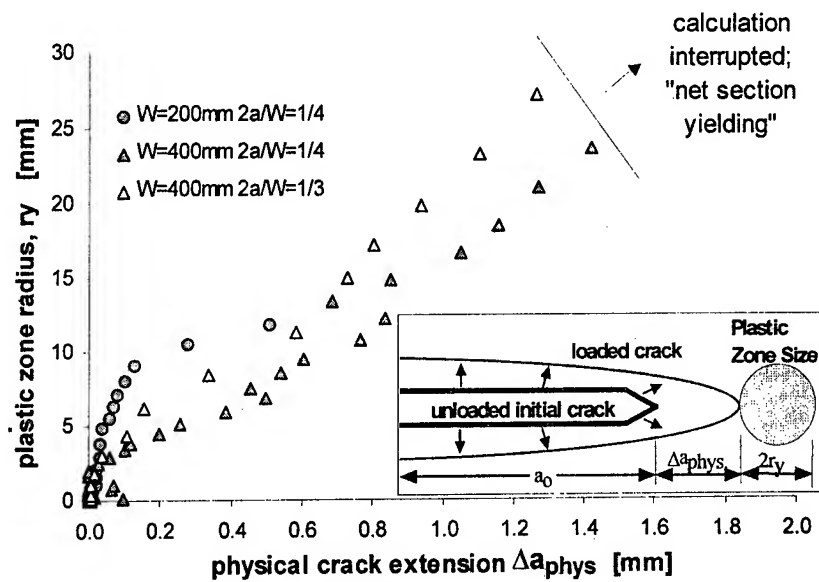


Figure 9, Irwin plastic zone size, GLARE 2 3/2 0.3

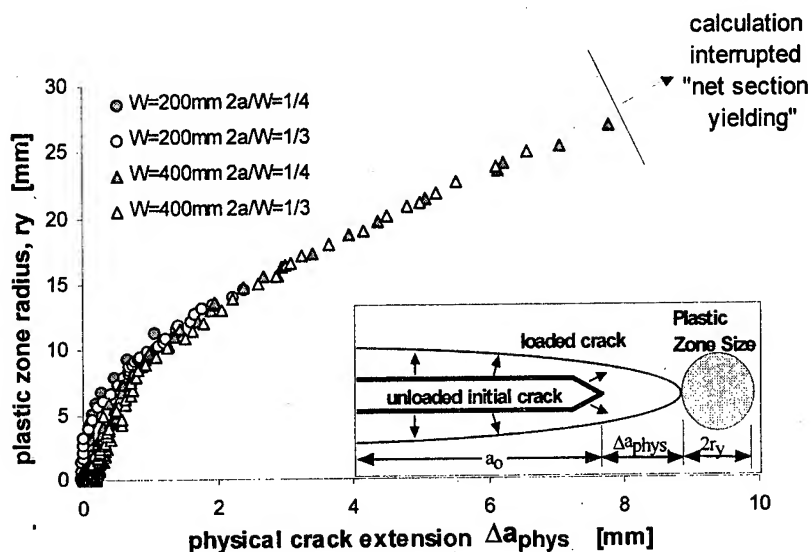


Figure 10, Irwin plastic zone size, GLARE 3 3/2 0.3

Although the strain hardening effect is neglected, Figure 10 for GLARE 3 shows r_y to be clearly independent of W and a_0 . This can not be observed for the GLARE 2 laminates in Figure 9. Because the prepreg layers of GLARE 3 are equally divided in 0° and 90° direction, only 50% of the prepreg contributes to the residual strength and strain hardening in the loading direction. Consequently, at the onset of fracture, the average stress in the GLARE 3 net section is not far above the yield stress. However, the

net stress in GLARE 2 is far above the yield stress, up to 50%. This is illustrated in Table 2. For example for the GLARE 2 specimens with $W=400\text{mm}$ and $2a/W = 1/4$, the average critical crack extension da_c , was 15 mm while the net section was fully yielding at a physical crack extension Δa_{phys} , of 1.5 mm. The calculated r_y for this $\Delta a_{\text{phys}} = 1.5$ mm, however, is 25mm. As a result, Δa_{eff} ($=\Delta a_{\text{phys}} + r_y$) is based for 94% on r_y when the calculation of the effective crack length is interrupted. Although r_y is in theory a function of the remote stress σ_{gross} and a_{phys} ($=a_o + \Delta a_{\text{phys}}$), the influence of Δa_{phys} can be neglected and r_y is in practice only a function of the initial crack length a_o , and σ_{gross} . Concluding, for GLARE 2 specimens $\Delta a_{\text{phys}} \ll a_o$ and $\Delta a_{\text{phys}} \ll r_y$ for the range until net section yielding. Therefore, the influence of Δa_{phys} on the calculation of Δa_{eff} and r_y can be neglected in this range.

To take into account strain hardening, an effective yield stress is introduced here for GLARE 2, equal to

$$\sigma_{\text{yield.eff}} = \sigma_{\text{yield}} + \frac{\sigma_{\text{ult}} - \sigma_{\text{yield}}}{4}$$

This effective yield stress is comparable with the one described in the ASTM standard for determination of J_{ic} [4] with the difference that here 25% of strain hardening is added to the yield stress instead of 50%. The reason for this is to balance the contribution of the physical crack extension and the plastic zone correction. In Figure 12 the results obtained with this higher yield stress are plotted. With this modification, "net section yielding" is delayed beyond the onset of unstable fracture. Furthermore, the modified plastic zone size is independent of the initial crack length. The same procedure followed for GLARE 3 laminates shows a remaining independence of a_o but a dependence of W , see Figure 11.

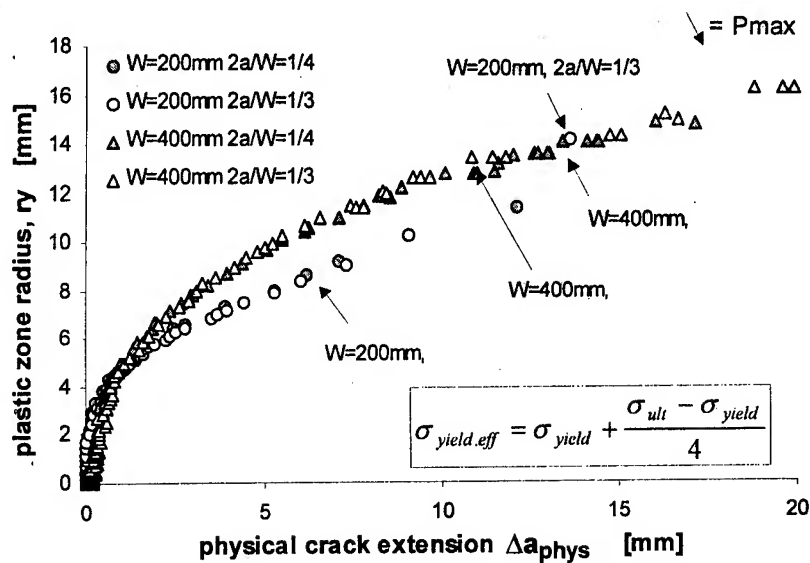


Figure 11, Irwin plastic zone based on effective yield stress, GLARE 3 3/2 0.3,

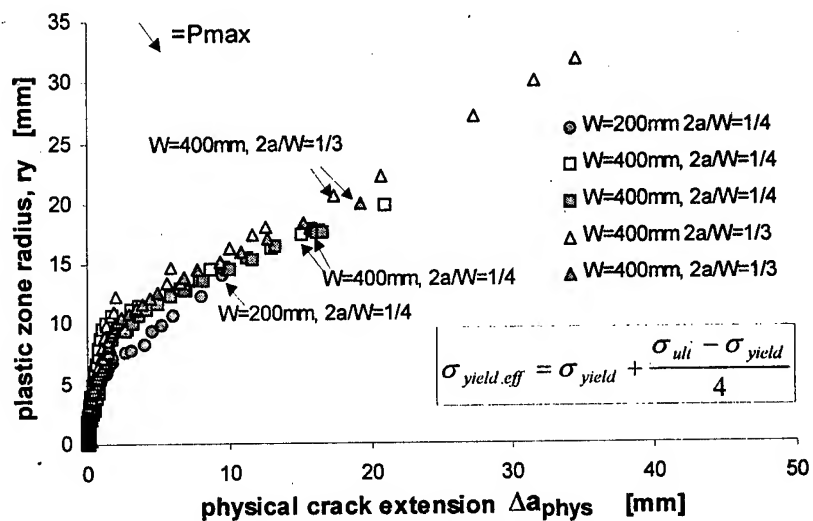


Figure 12, Irwin plastic zone based on effective yield stress, GLARE 2 3/2 0.3

4.2 The Compliance correction

Eftis and Liebowitz [5] derived an expression for the COD from a Westergaard-type stress function for a CCT specimen of finite width, loaded uniaxial in uniform tension. The material is elastic and

isotropic. The expression gives a direct relation between the opening of the crack at the center of the panel and the crack length. The elastic crack length can thus be calculated from the measured COD. It is used as the effective crack length.

To measure the COD, a clip gauge is attached between the crack edges in the center of the specimen. For the attachment, a very small slit was made in the anti buckling (AB) Guides. Despite the small size of the slit, local crack edge buckling as illustrated in Figure 13 could not be prevented. Although the residual strength is not influenced by this local buckling, the COD's measured were too large, resulting in an overestimation of a_{eff} . This discrepancy was especially important at low loads where the relative out of plane deformation is large compared to the COD.

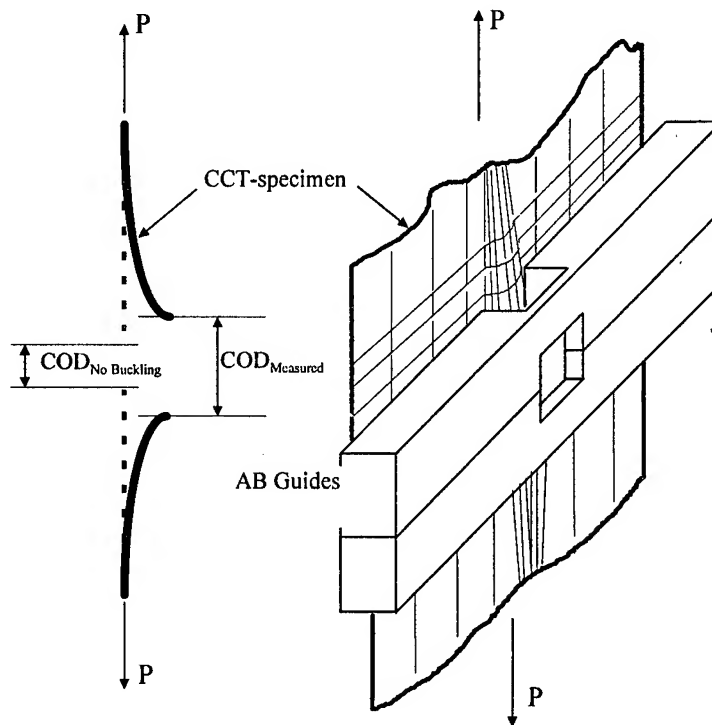


Figure 13, Local buckling under the AB Guides

Figure 14 shows the results for the r_y calculations for Alclad 2024-T3, derived with the compliance correction:

$$r_y = (a_{eff})_{COD} - a_{phys}$$

The test for $2a/W = 1/4$ and $t=1.0$ mm illustrates the effect of local buckling; the calculated r_y is overestimated. For the 1.6 mm

thickness, the influence of local buckling is less, due to the higher moment of inertia, and the experiments illustrate that r_y is independent of a_0 . Also for clad 7075-T6 the 1.0 mm thick specimens were sensitive for buckling and no independence of a_0 could be observed.

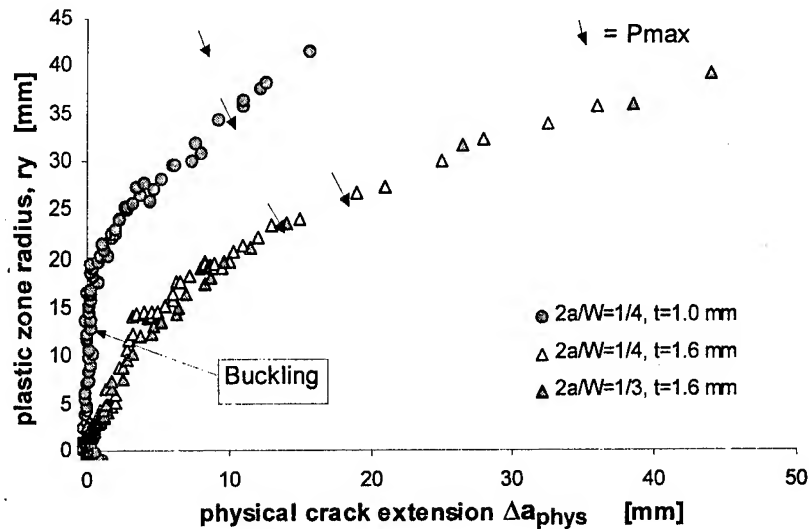


Figure 14, Plastic zone size based on compliance, Alclad 2024-T3, $W=400$ mm

Figure 15 shows a comparison between r_y obtained with both the Irwin plastic zone correction and COD measurements, for the Alclad 2024-T3 specimens with $t=1.6$ mm. Both methods result in the same plastic zone size for a certain crack extension and are thus comparable for the tested panel width of 400 mm.

For the FML's, tested in the present study, the compliance of the CCT specimens was always larger than for the aluminum alloys. This is due to the lower stiffness of the S2-glass fibers but also due to the anisotropy of the material. The reference [3] proposes to use a corrected E-modulus in these cases, but also requires that the correction value may not differ more than 10% from the material E-modulus. For the tested GLARE variants, the corrected E-modulus was always more than 10% different. However, a recent study [6] that takes into account the anisotropy of the material showed a perfect comparison between the theoretical and measured compliance, while the difference with the isotropic Eftis Liebowitz equation was always more than 10%. It shows that larger corrections are permitted to correct the Eftis Liebowitz equation for anisotropy.

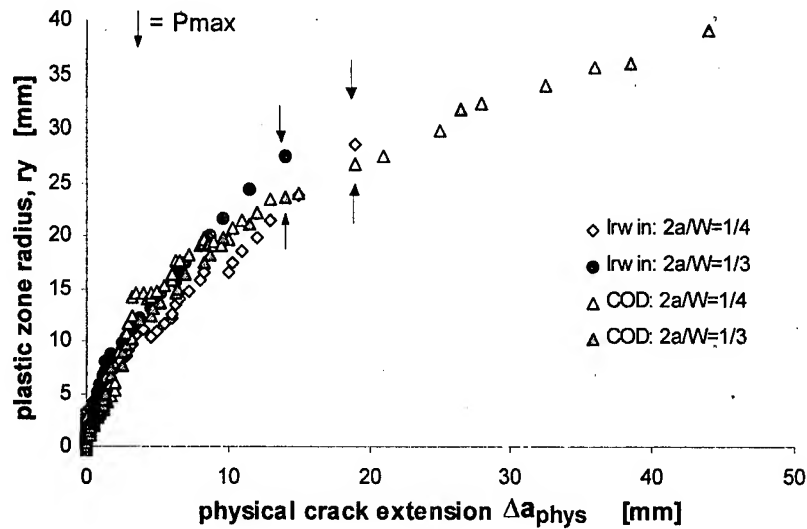


Figure 15, Comparison between r_y according to Irwin and to COD, Alclad 2024-T3 L-T, $W=400\text{mm}$, $t=1.6\text{mm}$

In Figure 16, the results of the r_y calculations for GLARE 2, with the COD measurements are plotted. When the scatter is ignored, the trend shows an independence of a_0 . Results are obtained for the two different initial crack tip shapes, see paragraph 2, but similar behavior is observed. Although a fatigue crack creates a sharp starter notch, it also creates delamination delaying fiber failure.

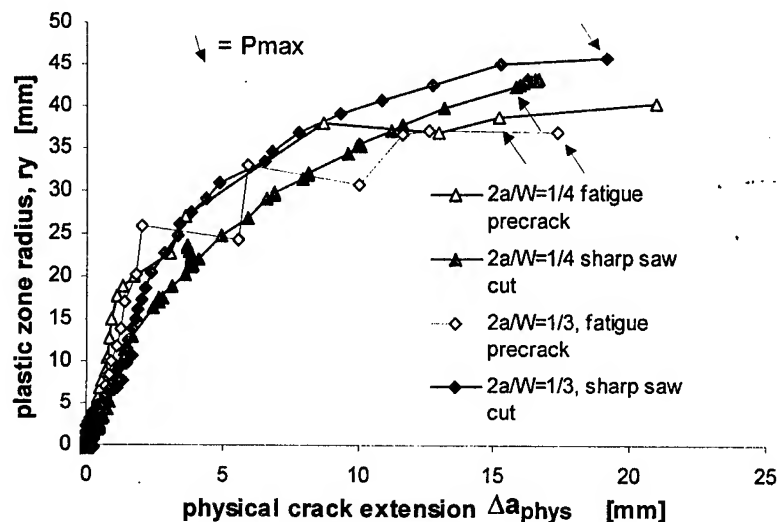


Figure 16, Plastic zone size based on compliance, GLARE 2 3/2 0.3, $W=400\text{mm}$

A comparison with the calculations of r_y according to the Irwin correction was not possible because of early net section yielding. However, for the first millimeter of crack extension the results are comparable.

The results for both r_y type calculations for the GLARE 3 laminates are plotted in Figure 17. Some scatter is present for the method based on the Compliance correction but the results show a similar trend. Again the conclusion of r_y -independence of a_0 and W can be drawn for this method. The results with the Irwin correction are not comparable with the COD results; the Irwin method calculates a larger plastic zone correction. Correction with $\sigma_{\text{yield,eff}}$ yields significant smaller plastic zone sizes but it is not a solution because of the dependency of W as described in section 4.1.

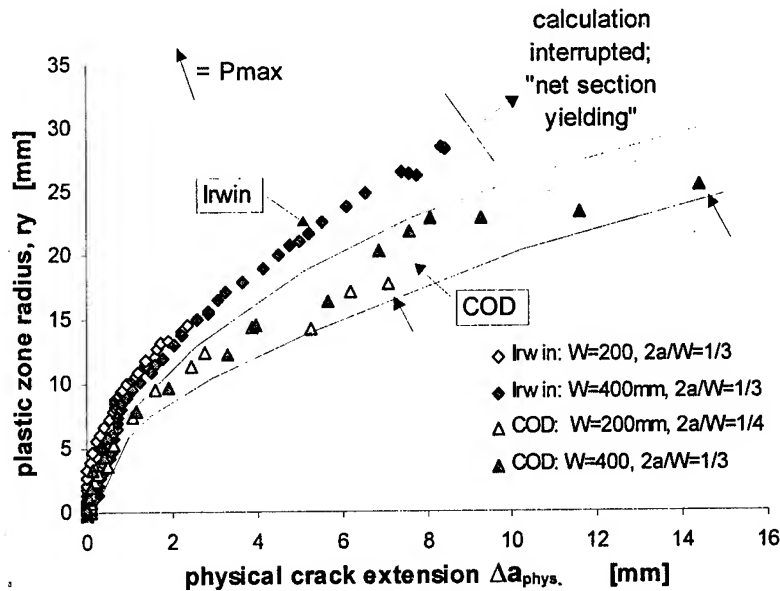


Figure 17, Plastic zone size based on compliance, GLARE 3, 3/2 0.2

5. Crack growth Resistance Curves

An R-Curve, as defined in the ASTM standard [3], is a continuous record of K_R or R plotted against the crack extension driven by a continuously increasing stress intensity factor K . For a CCT specimen of finite width, K is calculated with the secant formula:

$$K = \sigma_{gross} \sqrt{\pi a_{eff} \sec\left(\frac{\pi a_{eff}}{W}\right)}$$

The relation between the crack resistance R -equal to the energy release rate G during crack extension- and the stress intensity factor K is given by:

$$R(a_{eff}) = \frac{K^2(a_{eff})}{E}$$

The R -curve may be plotted in terms of either physical or effective crack extension, but according to the ASTM standard [3], residual strength predictions can be made only from effective crack extension plots.

Figure 18 shows the experimental K_R -curves for Alclad 2024-T3, obtained with the Irwin plastic zone correction for three curves and one curve based on COD. As expected, the curves are identical because of the similar plastic zone sizes for Δa_{phys} . In the presence of local buckling, the similarity disappears because of the sensitivity of the COD for this local non linear geometry behavior. This is illustrated in Figure 19. Local buckling increases the calculated a_{eff} for the σ_{gross} and shifts the curve to the right. The shape of the curve is typical for buckling. Clearly, this curve can not be used for residual strength predictions.

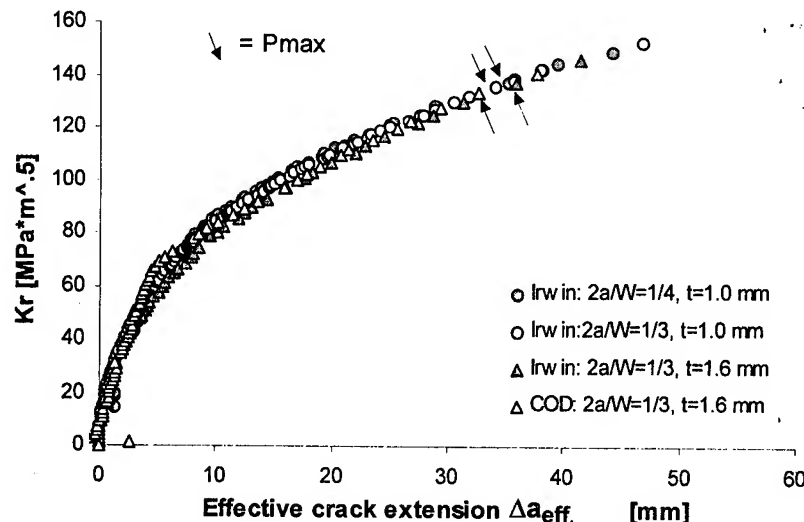


Figure 18, K_R - curve for Alclad 2024-T3, with COD- and Irwin correction, $W=400\text{mm}$

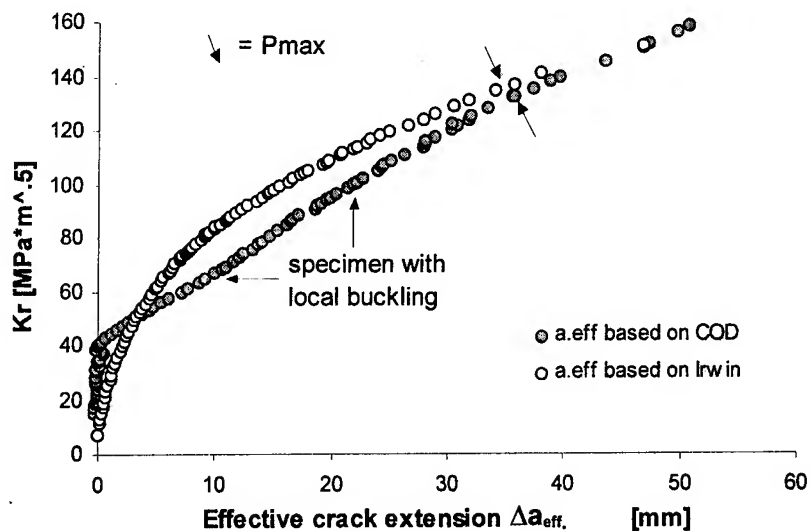


Figure 19, Example of the effect of buckling for Alclad 2024-T3, $t=1\text{mm}$

The K_R -curves for GLARE 2, based on the Irwin correction show an extremely good agreement. This is expected because the effective crack extension, Δa_{eff} , is based on r_y for 95% as was discussed in paragraph 4.1. The aluminum in the net section becomes fully yielded after only a small physical crack extension, while the critical crack extension was much larger, see Table 2.

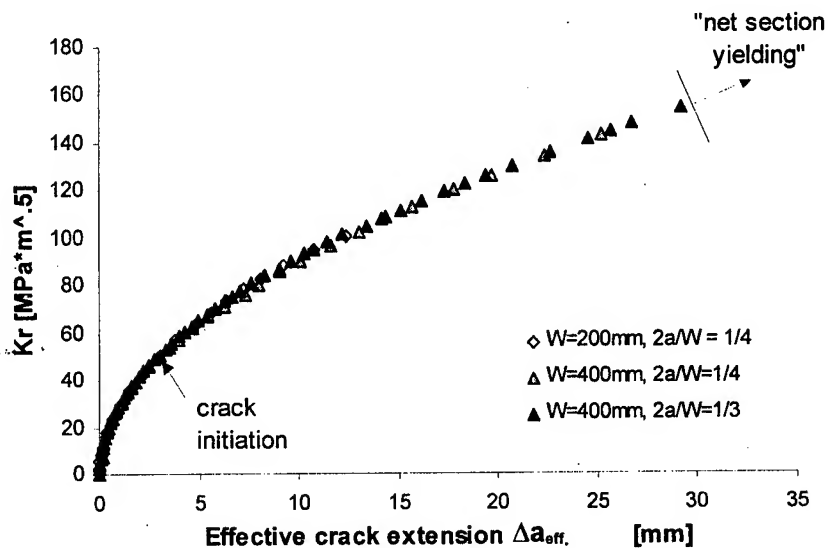


Figure 20, K_R -curve according to Irwin correction, GLARE 2 3/2 0.3

These curves must be interpreted carefully. For example, in [7] K_R -curves are illustrated for panels that were tested with and without AB Guides. Although the residual strength was lower due to testing without AB Guides, the K_R -curves were identical. The reason for this was the small crack extension before net section yielding occurred. Much wider panels should be tested for GLARE 2 to avoid interruption of the r_y calculation. For prediction purposes, this K_R -curve gives only valid results until the onset of net section yield. Curve fits lose their validity after this point and should not be used to predict the residual strength of wider panels or larger $2a/W$ ratio's.

A solution to avoid this problem is the use of $\sigma_{\text{yield,eff}}$ as proposed in paragraph 4.1. Figure 21 shows the K_R -curves based on the modified Δa_{eff} . Also, the points where the K_R -curves based on σ_{yield} were interrupted, are indicated in this figure. Until these points, the curves show little scatter, illustrating the independence of Δa_{phy} . Neglecting scatter, the modified K_R -curve is independent of a_0 and W .

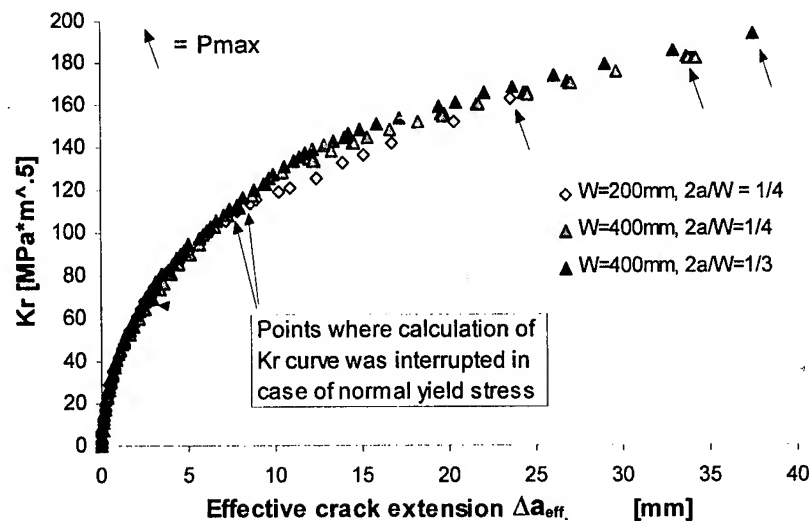


Figure 21, K_R -curve according to Irwin, based on an effective yield stress, GLARE 2 3/2 0.3

The K_R -curves for GLARE 2, obtained with the COD are plotted in Figure 22.

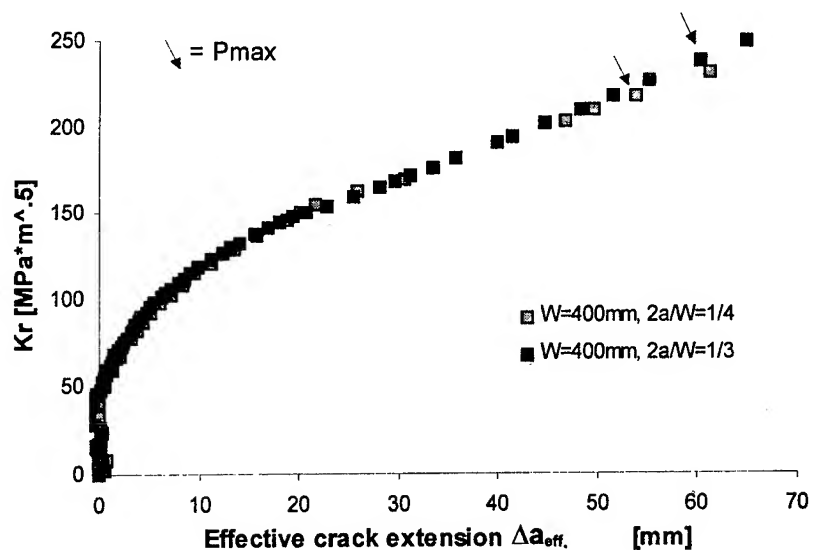


Figure 22, K_R -curve obtained with COD, GLARE 2 3/2 0.3

Figure 23 compares all three K_R -curves. The curves based on Irwin and COD show a clear difference; Irwin's curve is below the COD curve. Therefore, predictions must be based on the effective crack length, specific to the used method. The modified Irwin curve based on $\sigma_{\text{yield,eff}}$ is comparable with the COD curve and has the advantage to be valid up to failure. The critical Δa_{eff} is not the same for both methods.

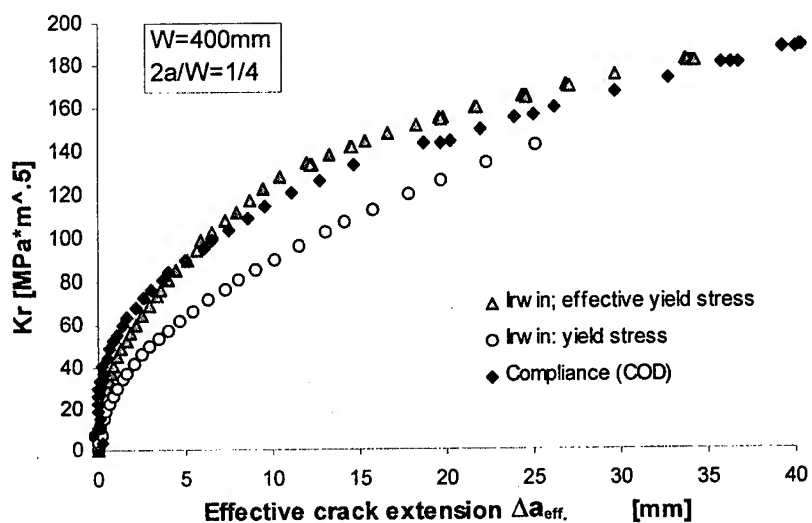


Figure 23, K_R -curve GLARE 2 3/2 0.3, Comparison between Irwin and COD

GLARE 3 shows comparable results as GLARE 2. A modified curve, based on $\sigma_{\text{yield,eff}}$, was advised against in paragraph 4.1 and therefore not used. Figure 24 and Figure 25 show the K_R -curve with the Irwin correction and Compliance correction respectively. Both methods yield a unique K_R -curve, invariant for a_o and W .

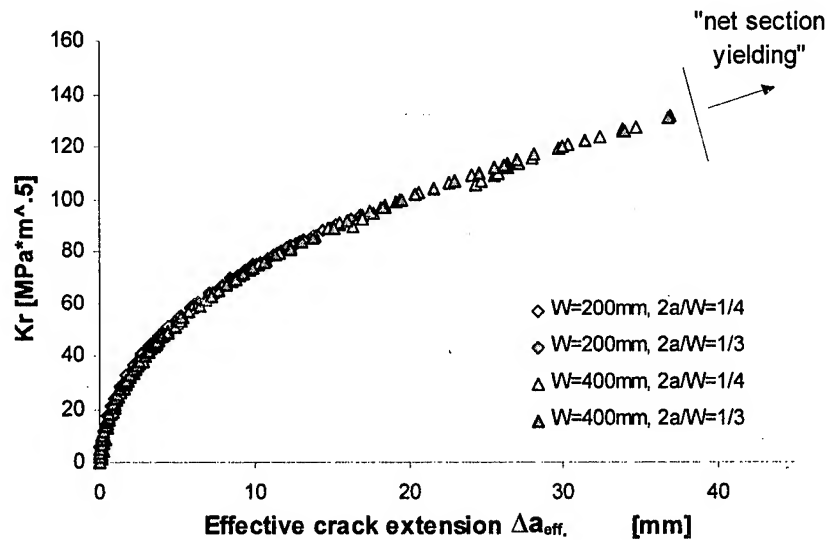


Figure 24 K_R -curve according to Irwin correction, GLARE 3 3/2 0.3

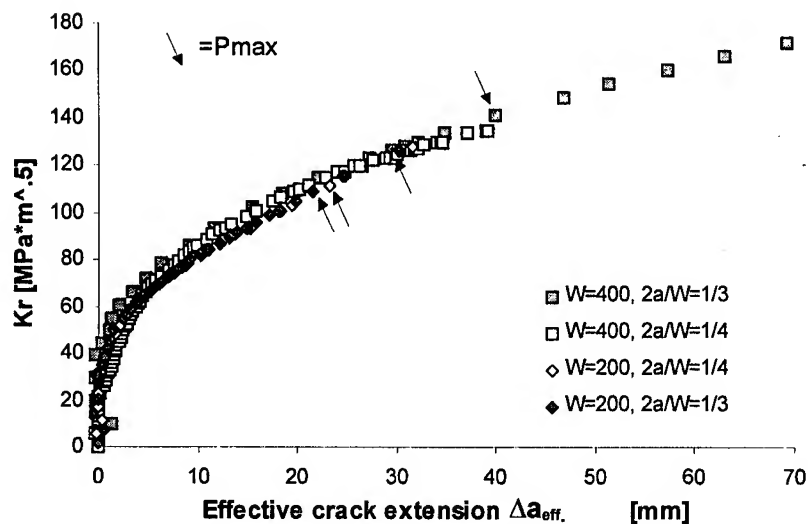


Figure 25, K_R -curve obtained with COD, GLARE 3 3/2 0.3

Figure 26 gives a comparison which clearly shows the difference between the two methods. This makes the curves not interchangeable.

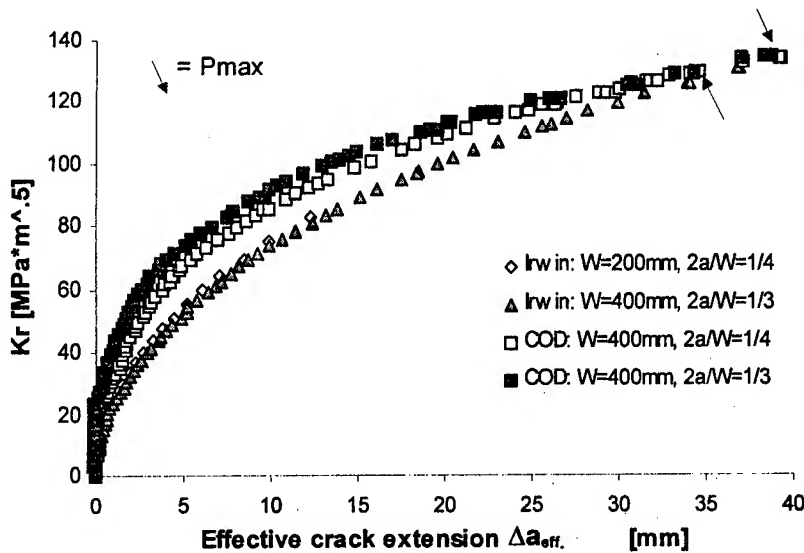


Figure 26, K_R -curve GLARE 3 3/2 0.3, Comparison between Irwin and COD

6. RESIDUAL STRENGTH RESULTS

The residual strength results of the various tests on 400 mm wide specimens are plotted as a function of $2a/W$ in Figure 27. The GLARE 2 specimens with UD glass-prepreg in loading direction show a remarkable high residual strength. Alclad 2024-T3 and GLARE 3 have a comparable residual strength while Clad 7075-T6 shows the lowest residual strength.

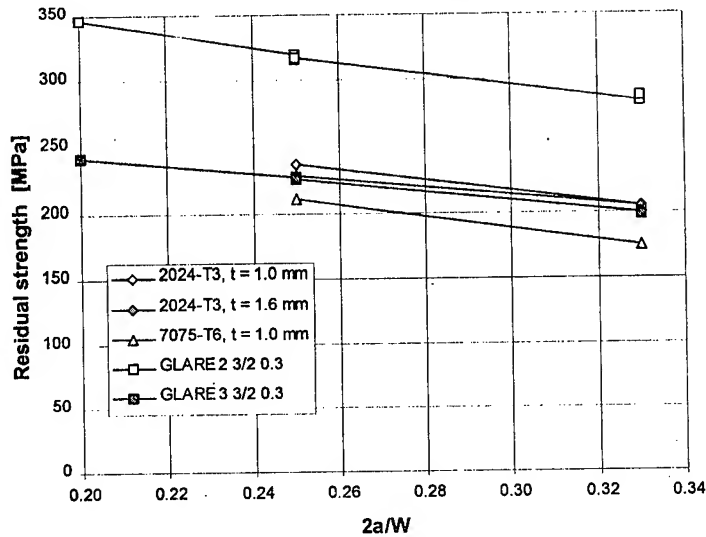


Figure 27, The residual strength as a function of $2a/W$, $W=400$ mm

7. CONCLUSIONS

1. GLARE 2 and GLARE 3 show stable crack growth before final failure. At high loads, the fibers in loading direction at the crack tip begin to break, directly followed by crack extension in the adjacent aluminum layers. After testing, static and dynamic delamination was observed. The static delamination before fiber failure is small.
2. The Irwin correction for effective crack length calculation, neglects the significant strain hardening that is present in FML's. As a result, the Irwin plastic zone size calculation is prematurely interrupted when the calculated edge of the plastic zone reaches the edge of the specimen, considerably before specimen failure.
3. For GLARE 3 material, the Irwin correction yields results close to failure and is independent of the initial crack length and width of the panel. For GLARE 2 with UD glass-prepreg, net section yielding occurred at a crack extension of only 10% of the critical crack extension. Therefore, an effective yield stress is proposed taking into account strain hardening. The results for the Irwin correction with the effective yield stress show an invariant behavior up to failure while the unmodified results showed large scatter before net section yielding.
4. The plastic zone sizes obtained with the Compliance correction shows an independence of the initial crack length and the width.

for all tested materials. However, the results obtained with this method are very sensitive to local buckling.

5. Invariant K_R -curves are obtained for both methods (Irwin and Compliance) but interchanging of the curves is not possible; the curves are specific for the used correction method. The K_R -curves for GLARE 2, based on the Irwin correction and effective yield stress are closer to the COD results than the results with the normal yield stress. These latter results can not be used for predictions.
6. Although the K_R curve with its correction methods is applicable for the purpose of residual strength predictions, an additional research is necessary for extending this method to FML's
7. The residual strength of GLARE 2 is superior to Alclad 2024-T3, Clad 7075-T6 and GLARE 3. Alclad 2024-T3 and GLARE 3 are comparable while Clad 7075-T6 has the lowest residual strength.

REFERENCES

- [1] R.J. Bucci, L.N. Mueller, L.B. Vogelesang and J.W. Gunnink, ARRALL Laminates, in *Aluminum Alloys - Contemporary Research and Applications*, Treatise on Material Sciences and Technology, Vol. 31, pp. 295-322, New York (1989)
- [2] G. Roebroeks, Towards GLARE, The Development of a Fatigue Insensitive and Damage Tolerant Aircraft Material, Ph.D. Thesis, Faculty of Aerospace Engineering, Delft University of Technology, Delft, The Netherlands, (1991)
- [3] Standard Practice for R-curve determination, ASTM-E561-86, *Annual Book of ASTM Standards, Metals Test Methods and Analytical Procedures*, Vol 03.01, pp 570-581 (1988)
- [4] Standard Test Method for J_{Ic} , A measure of Fracture Toughness, ASTM-E813-88, *Annual Book of ASTM Standards, Metals Test Methods and Analytical Procedures*, Vol 03.01, pp 698-712 (1988)
- [5] J. Eftis and H. Liebowitz, On the modified Westergaard equations for certain plane crack problems, In *International Journal of Fracture Mechanics*, Vol. 8, pp. 383-392 (1972)
- [6] S. Testi, A Study on the Compliance Calibration for GLARE, Master Thesis, Structures and Materials Laboratory, Delft University of Technology (1995)
- [7] T.J. de Vries, Various Parameters Concerning the Residual Strength of Aircraft Materials, Part II, Master Thesis, Structures and Materials Laboratory, Delft University of Technology (1994)

Laser Shock Peening An Analysis In Nearly Closed Form

**Mr. Hallock F. Swift
University of Dayton Research Institute
300 College Park Avenue
Dayton, Ohio 45469-0182**

ABSTRACT

Peening has been shown to increase wear and fatigue resistance of components made from high-strength metals. Shot peening is state-of-the-art but only affects thin surface layers of processed components. Using pulsed lasers to produce peening blows allows beneficial effects to be extended to depths of 1.0 mm and more. The laser peening process is multifaceted and complex but it can be modeled effectively by using principals from optics, plasma physics, shock physics, and materials response to high loading rates.

1.0 INTRODUCTION AND BACKGROUND

One of the most dominant thrusts in modern technology is development of new materials and processing technologies to provide materials with physical properties beyond current capabilities. One of the most important subcategories of this thrust is the emergence of anisotropic materials with local properties such as strength, rigidity, resistance to chemical attack, etc. that are tailored to meet requirements for specific components rather than volumetric properties of the material from which the components are fabricated. Examples of this approach abound ranging from elegantly tailored fiber composites with strengths, moduli and toughness levels tuned to a component's specific needs to chemical tempering of glass surfaces which makes an inherently brittle material functionally ductile.

One important application of this approach is peening of metal components to improve surface hardness (wearability) and resistance to fatigue loading. Surface peening is a relatively old technology that was practiced as early as the 17th Century where iron parts were pounded with a ball-shaped hammer to harden material adjacent to the surface and to introduce beneficial compressive stresses. The peening blows deformed the surface material slightly which caused hardening through cold working. It also tended toward increasing the surface area of the component without increasing component volume. The underlying material resists this tendency which produces biaxial compression stresses in material adjacent to the component surface. These compressive stresses, of course, must be balanced by tensile stresses within the underlying material. Peen-produced compressive stresses have been used for many years for straightening slender components such as shafts and gun tubes. Strangely enough, the surface on the concave side of a bend is peened which might appear to increase the severity of the bend. Instead, the near-surface compressive stresses produced cause the surface to expand slightly which reduces and even illuminates the bend.

More recently, peening has been found to increase significantly high cycle fatigue resistance of components made from strong metals such as titanium alloys. Spectacular results have been reported for increasing the high-cycle fatigue strength of 6Al4V titanium alloy used for aircraft engine fan and compressor blades. Peening benefits in this and related applications appear to develop rapidly as the depth of peening-induced stress fields is increased. Prevailing theory explains these substantial gains in terms of the surface compression stresses produced by peening. Microcracks which might otherwise grow catastrophically during fatigue loading are held closed by the compressive stresses and do not grow at all. This explanation may or may not ultimately explain the fatigue resistance phenomenon completely but the benefits of peening are unquestionable.

The current state-of-the-art for peening components made from high strength metals involves impacting component surfaces repeatedly with air-launched glass or metallic shot. The violence of individual impacts is controlled through choice of shot materials properties, average size, and impact velocities to

the point where benefits from peening are realized while out-of-plane surface distortion is almost eliminated. Up to thousands of impacts per square centimeter are employed to produce both surface hardening and lateral bi-axial compressive stress fields. The dual requirements for producing high impact stresses needed to achieve plastic deformation of strong metals and the equally important requirement that the shape and surface quality of peened components not be degraded significantly lead to the use of small-size peening shot. Small impacts produce highly divergent shockwaves in the processed material which produce the desired cold working and lateral compressive stress fields through only very limited material depths making shot peening a near-surface preparation process.

A recently invented technique, laser shock peening, (Refs. 1, 2, 3, 4) produces similar cold working and lateral compressive stress fields but the depths to which the effects penetrate can be varied over relatively wide ranges and controlled closely through suitable choices of operating parameters. The remainder of this paper describes the laser peening process. An quantitative analysis of laser peening processes in nearly closed form appears in the appendix.

2.0 THE LASER PEENING PROCESS

The heart of a laser peening system is a pulsed lasers which produce one or two radiation beams of extreme intensity. Radiation beam power densities may reach $2 \times 10^{10} \text{ w/cm}^2$. Although the pulse durations are relatively short (typical 0.5 to 20 n.sec), total energy delivered typically reach levels near 200 J/cm^2 . The laser systems used to date employ relatively low powered Q-spoiled lasers where crystals of yttrium activated garnet (YAG) are pumped optically with brilliant light flashes from Xenon flashlamps while mounted in optically inefficient cavities. Once pumping is complete, the cavities are switched to high optical efficiency which causes the stored energy to dump into infrared coherent radiation laser pulses ($\lambda = 1.05 \mu\text{m}$) each containing a Joule or so of energy and having durations near 20.0 n.sec. The pulses are routed through slabs of glass which are doped with neodymium ions. Each slab is pumped optically with flashlamps prior to being excited with low energy laser pulses. They amplify the YAG laser pulses

to energy contents near 50 J each without affecting their other characteristics such as, their wavelengths, phase structures, and durations. The coherent output for each glass slab amplifier is directed through mirrors and relay lenses to form a circular spot approximately 5 mm in diameter upon the face of the specimen to be peened (thus producing the typical power densities near 10 GW/cm² and energy densities near 200 J/cm²). As will be shown shortly, resulting mechanical pulses delivered to relatively thin specimens by such radiation pulses are sufficiently intense to perforate the specimen being processed. This problem has been solved by using the original YAG laser pulse to excite two glass slab amplifiers. The resulting intensified pulses are directed to strike opposite sides of the component being processed at the same time, thus eliminating gross momentum transfer to the component while simultaneously peening both sides.

The intense radiation pulses must be converted to mechanical pulses whose properties can be controlled precisely. The specimen to be peened is first coated with a thin layer of polymeric material (such as paint) and then a layer of water of controlled depth is flowed slowly over the polymer surface as sketched in Figures 1 and 2. Each incoming radiation pulse passes through the water layer nearly without attenuation and strikes the polymeric surface which is heated in less than 10.0 p.sec (10^{-11} sec) violently enough to produce a sheath of ionize plasma. The free electrons in the plasma sheath absorb essentially all of the remaining incoming radiation as it arrives. Pressure and temperature rise very rapidly in the plasma and its thickness expands due to retreating of both the polymeric and water surfaces. These retreats are caused both by action of shockwaves propagating into the solid and liquid materials and vaporization of the bubble walls as they absorb black-body radiation from the plasma sheaths.

The rate of plasma sheath (bubble) growth is controlled by the rate of energy injection from the laser beam, the thermal properties of the bubble wall materials, and the mechanics of shockwave production and propagation through the wall materials.

One overriding principle governs bubble growth. The available energy per unit of available volume within the bubble plasma remains proportional to

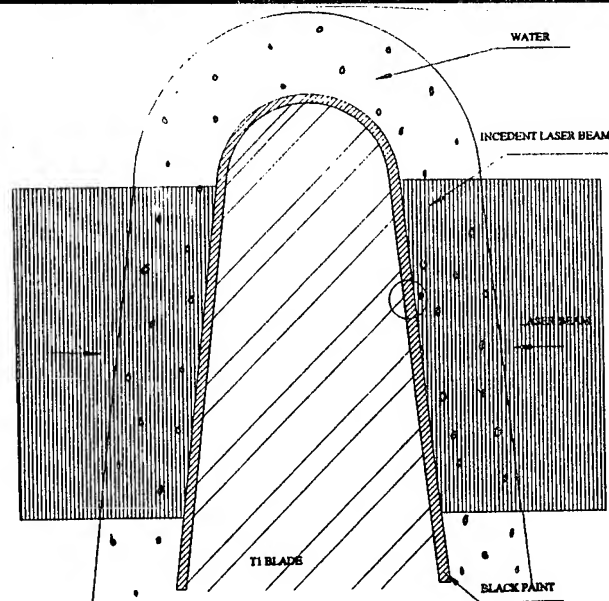


FIGURE 1

Sketch of laser peening process applied to a thin jet engine component made from titanium.

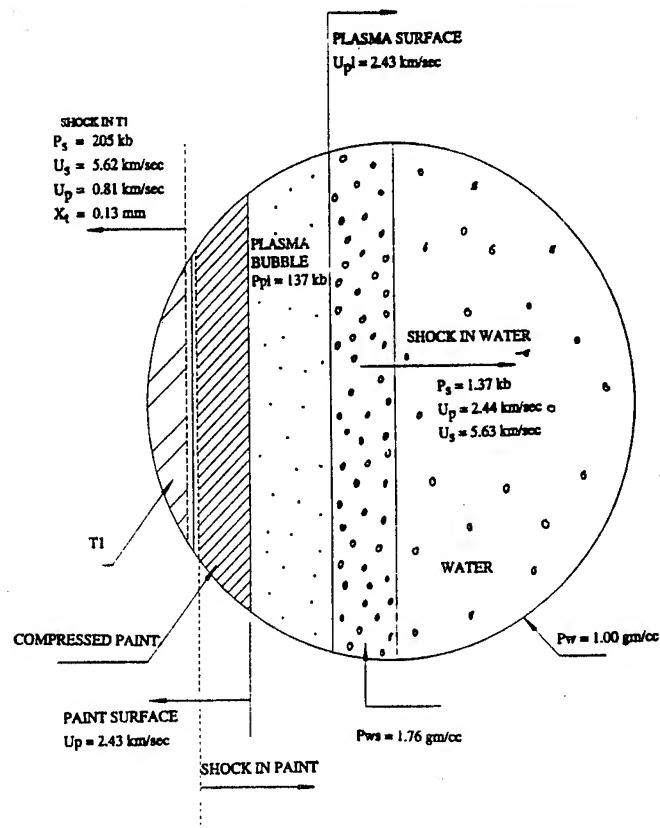


FIGURE 2

Magnified view of a portion of Figure 1 approximately 20.0 n.sec after laser beam turn-on.

pressure within the bubble at every instant of time. During the period when the laser is providing energy, pressure within the plasma bubble rises quickly to levels near 140 kbar and remains roughly constant. This pressure drives shockwaves forward through the polymer coat and rearward through the water. About the time the forward-running shockwave in the polymer reaches the metallic surface, the laser beam shuts down, thus ending power input to the system (see Figure 2). When the forward-running shockwave reaches the metallic boundary, it encounters a material of higher shock (acoustic) impedance than the polymer. The wave reflects from this boundary to produce an intensified wave in the metal which continues propagating forward plus a second compression wave that propagates rearward back into the polymer. Thus, the metallic surface experiences a compressive wave with an amplitude near 205 kb as does the polymer (caused by the forward-running primary wave superimposed upon the rearward-running reflected wave).

The volume of the bubble continues to enlarge after laser shutdown but pressure within the bubble falls since pressure remains proportional to the ratio of available energy to bubble volume available to particle motion throughout the process. Release characteristic waves emanate from the bubble/polymer surface as soon as bubble pressure begins its decline. They propagate through the shocked polymeric material and into the metallic substrate at velocities considerably above these of the primary shockwave. Therefore, the release characteristic waves overtake the ongoing shockwave and start its attenuation. Meanwhile, the shock wave propagating rearward through the water reaches the free surface either before or after it has been attenuated by release characteristic waves (caused by the declining bubble pressure) traveling through the shocked water. The shockwave reflects from the water/air surface as a tensile wave which propagates back through the compressed water thereby approximately doubling the rearward-directed speed of the shock-treated water. Arrival of this reflected shockwave at the bubble surface effectively terminates bubble growth by allowing the bubble to vent to atmosphere. A final large release characteristic wave then propagates forward across the expanded bubble plasma, through the remainder of

the polymeric film, and through the shocked metal until it overtakes the partially attenuated shockwave in the metal and brings its pressure to virtually zero, thereby completing the laser peening blow.

Analyses presented in the Appendix should be capable of predicting normal stress applied to the metallic substrate along the axis of the blow by the evaluating quantitatively processes described above.

An additional phenomenon occurs at points near the edge of the laser footprint which leads to production of the lateral compressive stresses produced by the peening process. Material in the metallic substrate adjacent to the edge of the laser-induced bubble is not shock compressed to the full level calculated by the preceding analysis because the shockwave responsible for compression must also propagate radially outward into substrate material beyond the bubble boundary where it is attenuated through radial expansion. Material movement behind this part of the shockwave possess an outward-directed component away from the event axis. This outward-directed motion continues during the entire substrate loading cycle and leads to finite material displacements in planes parallel to the substrate surface. The shockwave also produces finite material displacement in the axial direction. After loading is terminated, the substrate material reacts elastically to both of these deformations which causes most of the displacements to be reversed. The remaining residual plastic material displacements produce finite residual deformations and the bi-axial compressive stresses associated with them. The entire residual deformation field constitutes the cold working that the material receives from the laser peening process. The radial component of the deformation appears to produce the compressive stress fields whose presence improves the fatigue resistance of peened specimens.

The advantage of laser peening over its alternatives is that the intensities of the shockwaves propagated into the metallic material can be controlled readily by adjusting energy content of the laser pulses. The depths to which the peening shockwaves penetrate into the component material can be controlled independently by adjusting the shock impedance and thickness of the tamping

material (water in the cases considered) used to hold the plasma bubble temporarily in place.

We have applied the analysis presented in the Appendix to a specific example of laser peening the leading edge of a titanium fan blade from a jet engine. The blade material is thin enough to require simultaneous peening blows to opposite surfaces to avoid "punchout" as sketched in Figure 1. The specific parameters used for the analysis are as follows. Consider a 40-Joule infrared laser pulse ($\lambda = 1.06 \mu\text{m}$) whose duration is 20.0 n. sec. The pulsed beam is focused to a circle, 5.0 mm in diameter so that incident power density is approximately uniform across the beam cross section. The beam is directed to fall normally upon a component made from 6Al4V Titanium which is covered 0.1 mm deep with a polymeric coating (such as paint) and also a layer of slowly moving water 1.0 mm deep.

For one moment after laser turn-on in Figure 2 and results of the analysis are presented as a time line in Figure 3 which describes the situation near the laser impingement site at a variety of times after initial laser turn-on.

Future work on this effort involves developing progressively more sophisticated mathematical models for the several individual processes that make up laser peening. these models will be combined into a fast-running computer program that will allow the mechanical effects of individual or multiple shifts of input parameters to be determined. Once its reliability has been established, such a program is indispensable for optimizing laser peening processes to meet evolving and intensifying needs for protecting mechanical components from wave and fatigue.

T = 0 • Laser Turns On

- Shock Starts Into Paint

$P_s = 137 \text{ kb}$	$\rho_o = 1.00 \text{ gm/cc}$
$U_p = 2.44 \text{ km/sec}$	$\rho_s = 1.76 \text{ gm/cc}$
$U_s = 5.63 \text{ km/sec}$	

- Shock Starts Into Water

$P_s = 137 \text{ kb}$	$\rho_o = 1.00 \text{ gm/cc}$
$U_p = 2.44 \text{ km/sec}$	$\rho_s = 1.76 \text{ gm/cc}$
$U_s = 5.63 \text{ km/sec}$	

- Plasma Bubble Starts At Paint-Water Interface

T = 17.8 NS • Paint Shock Reaches Titanium

- Shock Propagates In Ti

$P_s = 205 \text{ kb}$	$\rho_o = 4.52 \text{ gm/cc}$
$U_p = 5.62 \text{ km/sec}$	$\rho_s = 5.28 \text{ gm/cc}$
$U_s = 6.81 \text{ km/sec}$	

- Shock In Water @ $X_s = 0.1 \text{ mm}$
- Bubble Thickness = 0.13 mm

T = 20 NS

- Laser Shutdown
- Shock Propagates 0.013 mm in Ti
- Reflected Shock Propagates 0.015 mm Into Compressed Paint

$P_{SR} = 205 \text{ kb}$
$U_p = 3.1 \text{ km/sec}$
$U_s = 6.61 \text{ km/sec}$

- Shock Propagates In Water To $X_s = 0.11 \text{ mm}$

T = 23.5 NS

- Reflected Shock Reaches Paint/Bubble Boundary
- Movement Of Paint Boundary Is Arrested

FIGURE 3

Timeline describing evolution of the laser peening process chosen for the example

T = 48.3 NS

- **On-Going Shockwave In Water Is Overtaken By**
- **First Release Characteristic From Bubble**

T = 50.8 NS

- **Shock Overpressure in Ti Produced By Paint Falls to Bubble Pressure**
- **(X_S) Ti = 225 μm**

T = 75.8 NS

- **Shock in Ti Overtaken By First Release Wave From Bubble**
- **(X_S) Ti = 395 μm**
- **Pressure "Rampdown" Begins**

T = 152 NS

- **Shock Stress in Ti Falls to Half Sustained Value**
- **(X_S) Ti = 928 μm**
- **Effective Depth of Peening Process**

FIGURE 3 (continued)

**Timeline describing evolution of the laser peening
process chosen for the example**

REFERENCES

1. Forget, P. "Laser Shock Surface Treatment of Ni-Based Superalloys." *Materials & Manufacturing Processes* 5(4) 501-528, 1990.
2. Claver, A.H., J.H. Holbrook, and B.P. Fairand. "Effects of Laser-Induced Shock Waves." *Shockwaves and High-Strain-Rate Phenomena in Metals*. Plenum Press, NYC, 1981.
3. Fairand, B.P., B.A. Wilcox, W.J. Galligar, and D.N. Williams. "Laser Shock-Induced Microstructural and Mechanical Property Changes in 7075 Aluminum." *JAP43*, 3893-3895; 1977.
4. Claver, A.H. and Fairand, B.P. "Interaction of Laser-Induced Stress Waves with Metals." *Application of Lasers in Materials Processing* ASM, Metal Park, OH.

APPENDIX

Available from the Author

Mr. H.F. Swift
University of Dayton Research Institute
300 College Park Drive
Dayton, Ohio 45469-0182

Voice (513) 229-3860
FAX (513) 229-3869

SESSION VIII

NDI/I

Chairman: *R. Paglia*, WL/MLS-OL

**Nondestructive Electrochemical Corrosion Measurement:
Electrochemical Impedance Pattern Recognition for
Detection of Hidden Chemical Corrosion on Aircraft
Components**

Mr. Jim S. Bowers
*Dr. Mark S. Vreeke
and
Dr. Anthony F. Sammells
Eltron Research, Inc.
2830 Wilderness Place
Boulder, CO 80301-5455

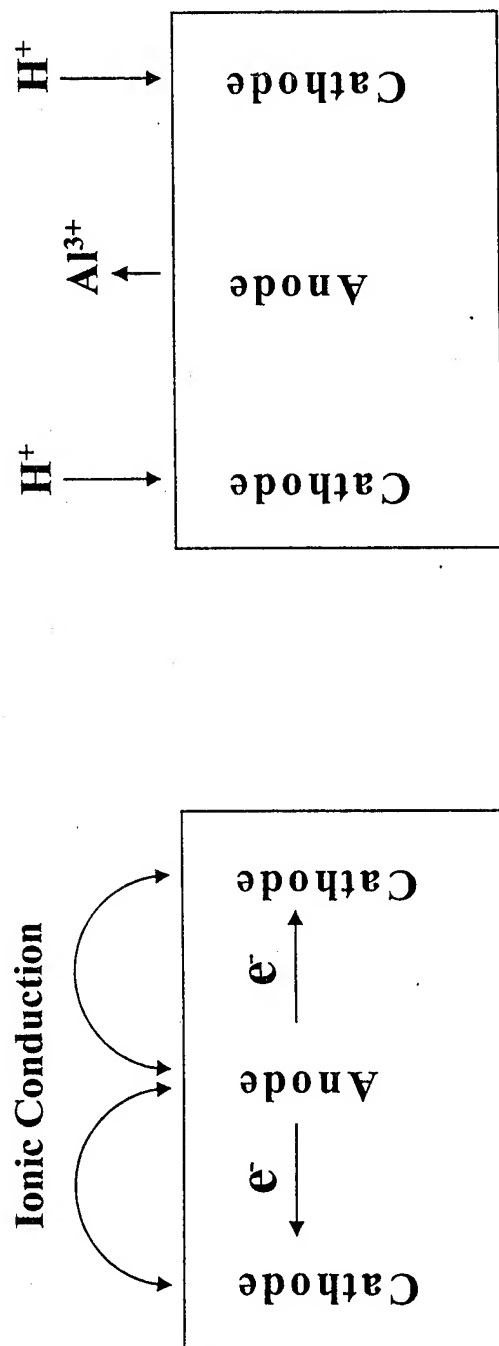
A non-destructive evaluation method for the detection and grading corrosion using fast Fourier transform electrochemical impedance spectroscopy (FFTEIS) and neural network analysis (NNA) is described. FFTEIS is used to rapidly acquire 0.01Hz to 10kHz impedance spectra. NNA of the complex impedance data is used to isolate and determine corrosion patterns. The neural network was trained using corrosion samples of known composition. The resulting analysis was able to identify the relative exposure duration for Al7075, Al2024 and Ti15-3 coupons in an accelerated corrosion environment.

OBJECTIVES OF ELECTROCHEMICAL IMPEDANCE PATTERN RECOGNITION PROGRAM

- **Diagnostic instrumentation compatible for nondestructive Evaluation (NDE) of Hidden Chemical Corrosion.**
- **Accuracy, sensitivity and versatility.**
- **Applied to titanium and aluminum alloys used in Aircraft components.**

ELTRON RESEARCH, INC.

Schematic of a Local Cell Showing Direction of Current Flow and Ion Migration



Direction of Positive ion Movement

Current Flow

ELTRON RESEARCH INC.

Electrochemical Reactions Occurring at the Cathode and Anode

Anode (oxidation)

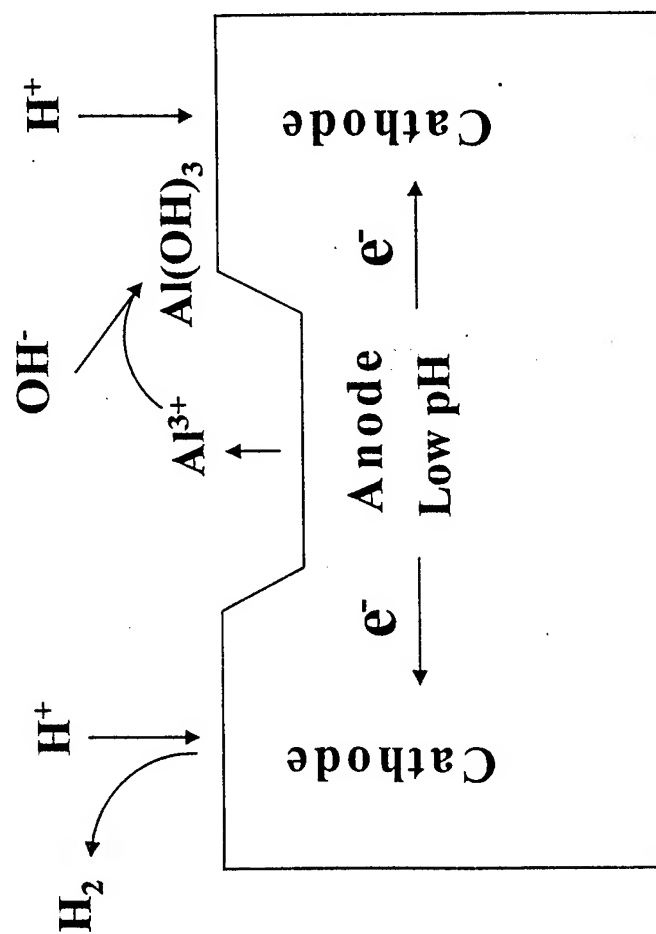


Cathode (reduction)



ELTRON RESEARCH INC.

Localized Corrosion: Pitting and Crevice



ELTRON RESEARCH INC.

Principle of Electrochemical Testing

Stress the Interface

Electrode

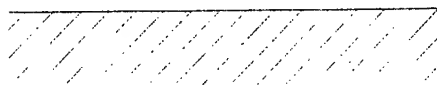
fix potential

potential function

force current

Electrolyte

introduce new
solution species



Current

Charge

Potential

Δ potential

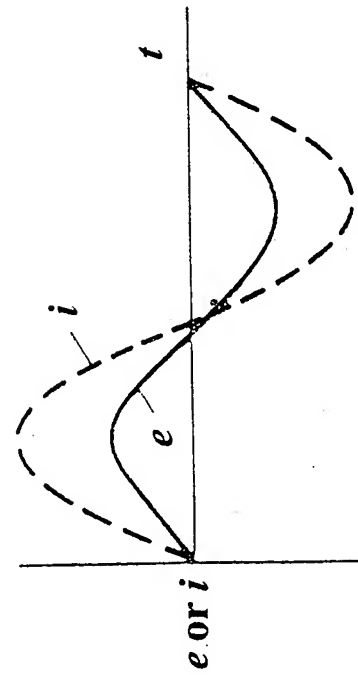
ELTRON RESEARCH INC.

ELECTROCHEMICAL IMPEDANCE SPECTROSCOPY

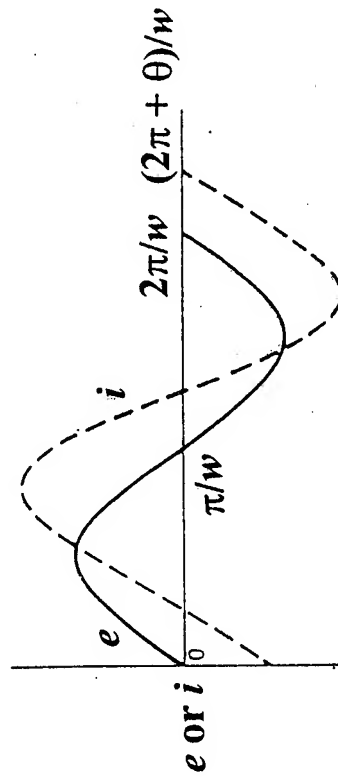
- Apply a voltage and measure resulting current and phase shift.
- Only introduces a small signal perturbation to the system.
- Measurements performed as a function of frequency.
- Gives information on the degree and kinetics of slow processes - Corrosion.
- Does not impose irreversible changes on corrosion site.

ELTRON RESEARCH, INC.

Impedance Response



Purely Resistive Element

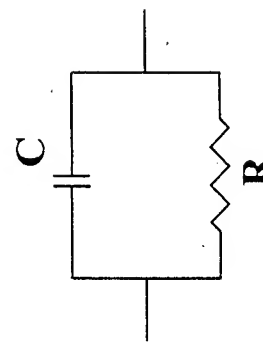
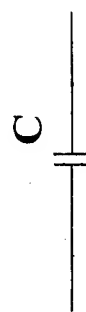
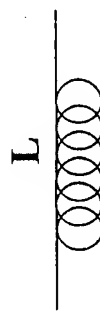


Resistive and Capacitive Elements

ELTRON RESEARCH INC.

Impedance Equations for Equivalent Circuit Elements

Circuit Element



Impedance Equation

$$Z = R + 0j \quad j = \sqrt{-1}$$

$$Z = 0 + j\omega L \quad \omega = 2\pi f$$

$$Z = 0 - \frac{j}{\omega C} \quad \omega = 2\pi f$$

$$Z = \frac{R - j\omega CR^2}{1 + \omega^2 C^2 R^2}$$

ELTRON RESEARCH INC.

EIS MEASUREMENTS POSSESS IMPEDANCE ELEMENTS ASSOCIATED WITH CORROSION

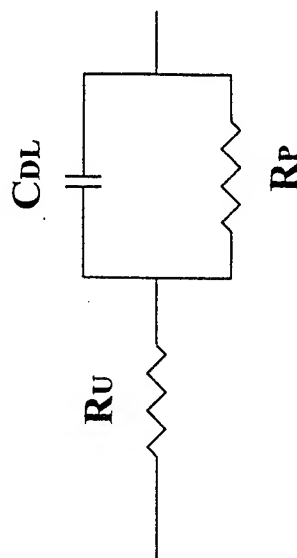
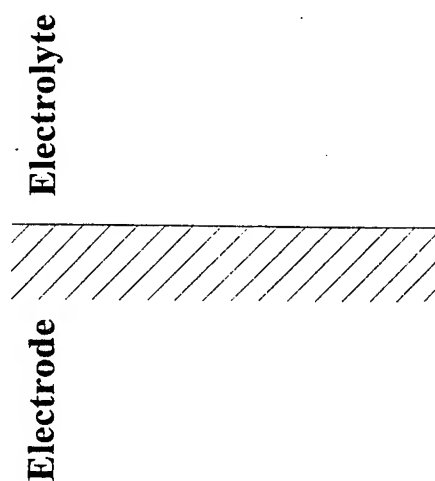
A series equivalent circuit can be generated by summation of individual impedance components, via for example:

$$\mathbf{Z(\text{total circuit}) = Z1 + Z2 + Z3 + Z4 + \dots}$$

ELTRON RESEARCH, INC.

Equivalent Circuit Analysis

Equivalent Electronic Circuit for
a Simple Electrochemical Cell



R_U : uncompensated resistance

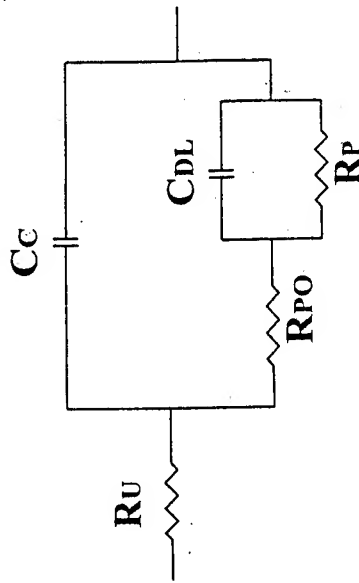
R_P : polarization resistance

C_{DL} : double layer capacitance

ELTRON RESEARCH INC.

Equivalent Circuit Analysis

Equivalent Electronic Circuit for
an Electrode with a Porous Coating



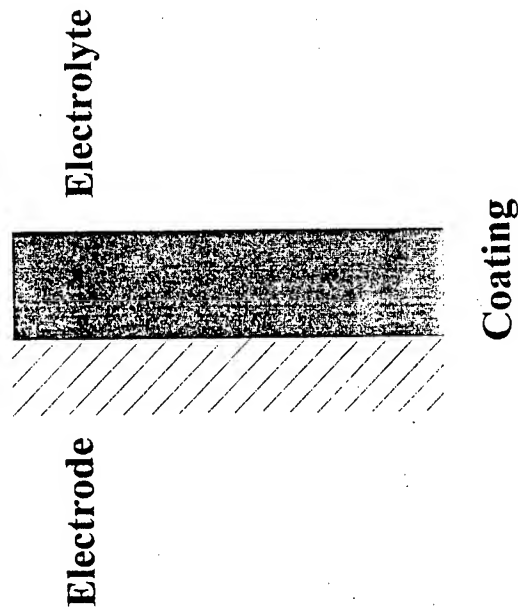
R_U : uncompensated resistance

R_P : polarization resistance

C_{DL} : double layer capacitance

R_{PO} : pore resistance

C_c : coating capacitance



ELTRON RESEARCH INC.

TECHNICAL INCENTIVES FOR APPROACH

- Corrosion is an electrochemical process.
- In Electrochemical Impedance Spectroscopy (EIS) a small sinusoidal potential is applied to the substrate under test over a defined frequency range and the resulting sinusoidal current phase shift measured.
- Impedance elements have distinct RC time constants associated with corrosion - the corrosion site does not become damaged during measurement.

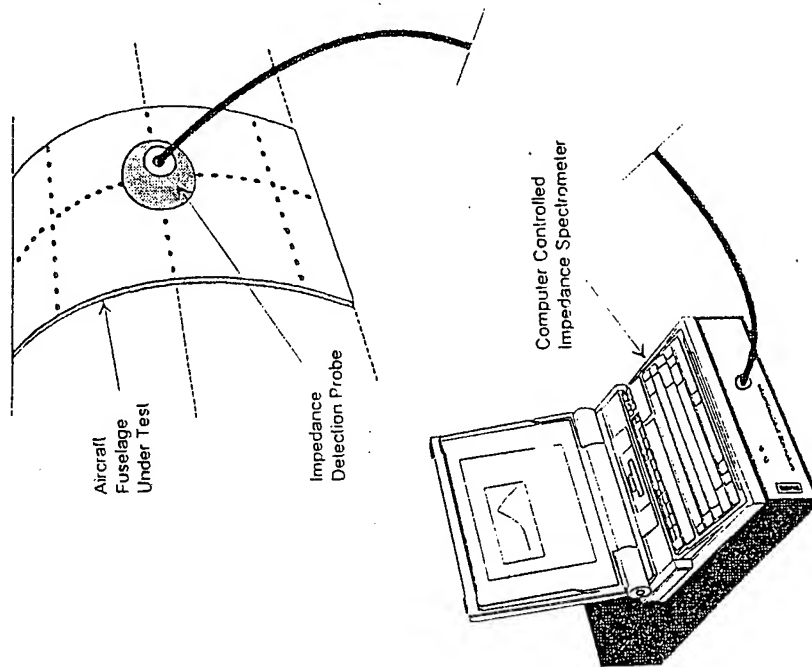
ELTRON RESEARCH, INC.

DATA COLLECTION AND ANALYSIS

- Obtain FFEIS data from suspect corrosion site.
- Application of NNA to impedance data.
- NNA transformed data used by software to classify hidden corrosion site.

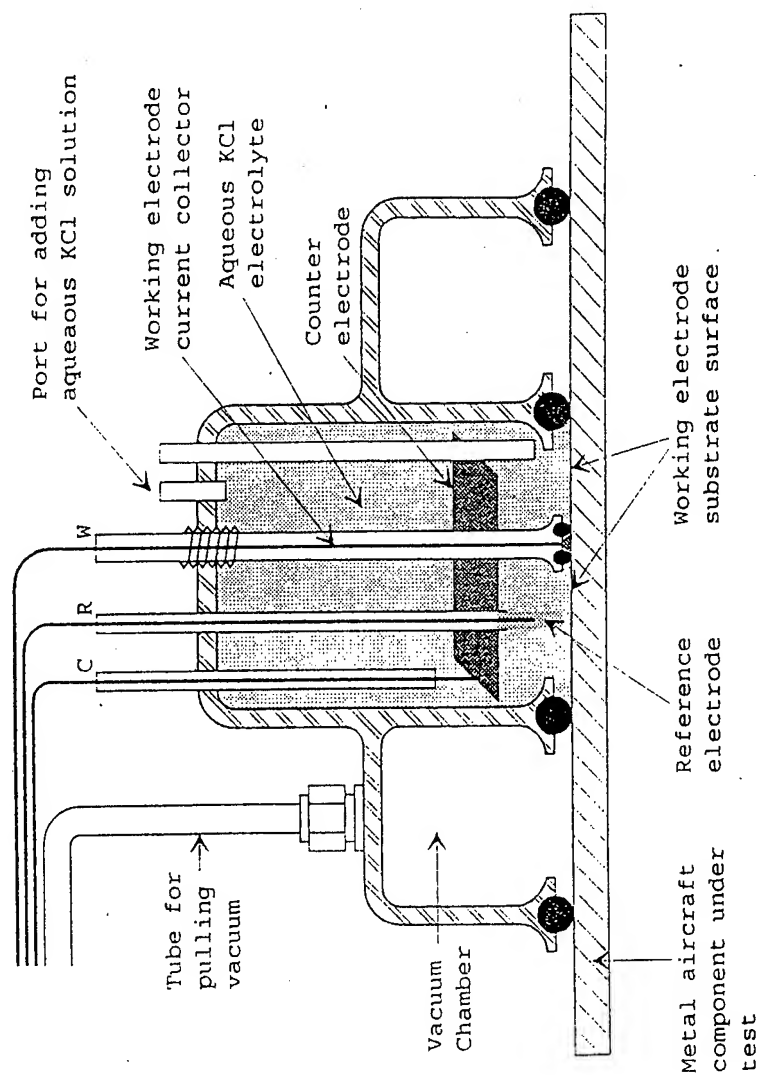
ELTRON RESEARCH, INC.

DETECTION OF HIDDEN CORROSION ON AIRCRAFT FUSELAGE COMPONENTS



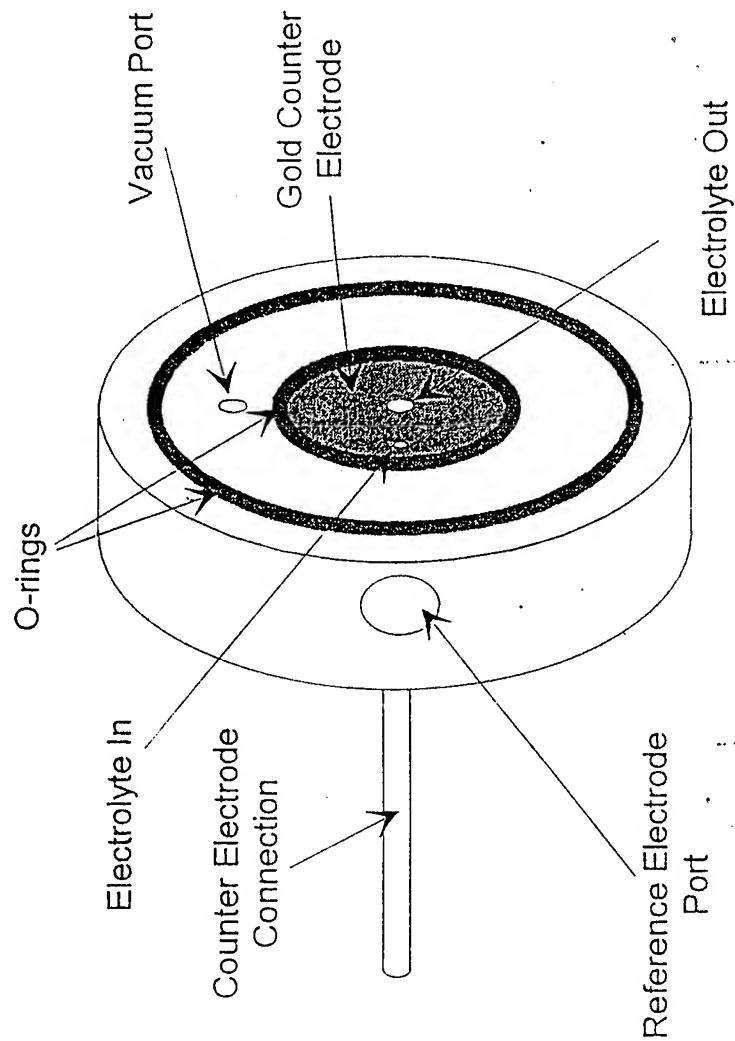
ELTRON RESEARCH, INC.

SCHEMATIC ELECTROCHEMICAL IMPEDANCE ELECTRODE ARRANGEMENT



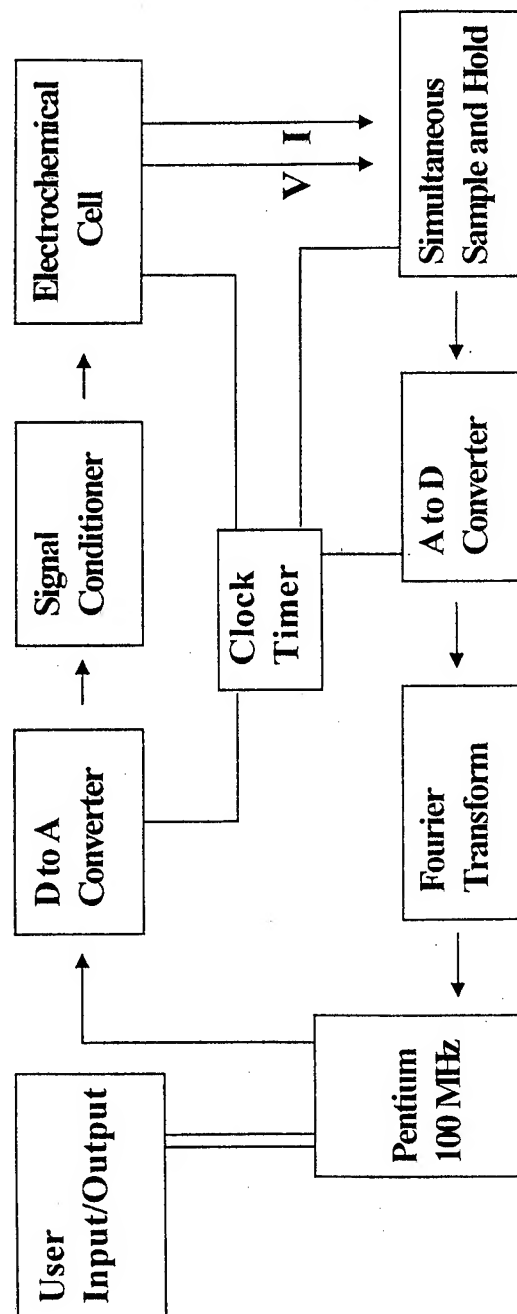
ELTRON RESEARCH, INC.

ELECTROCHEMICAL IMPEDANCE ELECTRODE ARRANGEMENT



ELTRON RESEARCH, INC.

Block Diagram of Components Incorporated into the Impedance Spectrometer



ELTRON RESEARCH INC.

EXPERIMENTAL PROTOCOL

- **Expose corrosion sites to aqueous corroding media.**
- **Perform EIS measurements as a function of time.**
- **Curve fit phase shift impedance data with log-normal peaks.**
- **Correlate data to directly observed corrosion by SEM.**

ELTRON RESEARCH, INC.

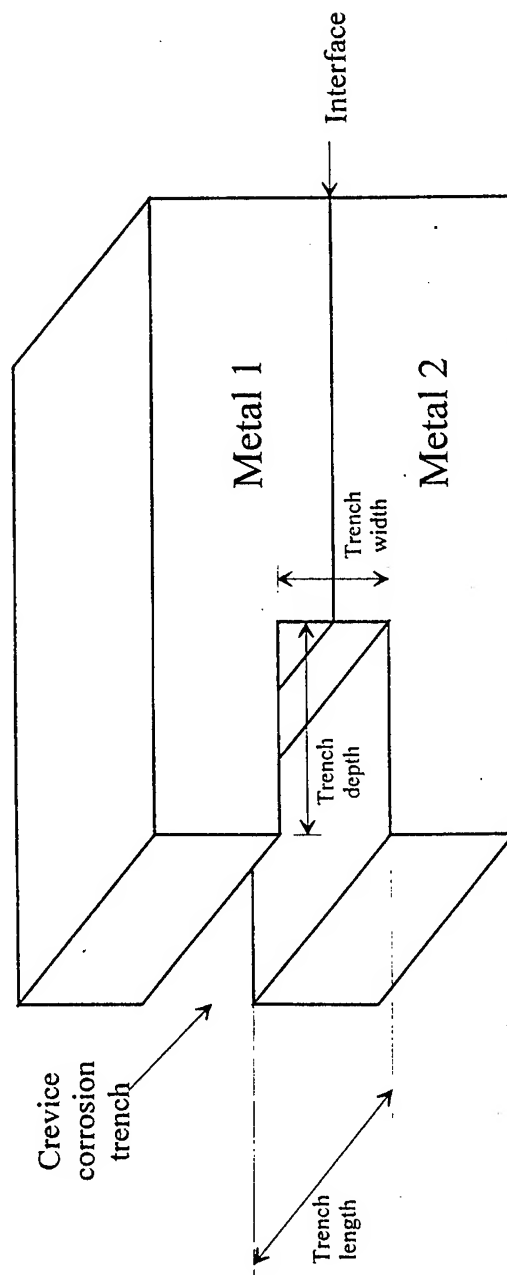
**SAMPLES SUBJECTED TO
HIDDEN CORROSION**

Al 2024/Al 2024, Al 7075/Al 7075, Ti 15-3/Ti 15-3

Al 2024/Al 7075, Al 2024/Ti 15-3, Al 7075/Ti 15-3

ELTRON RESEARCH, INC.

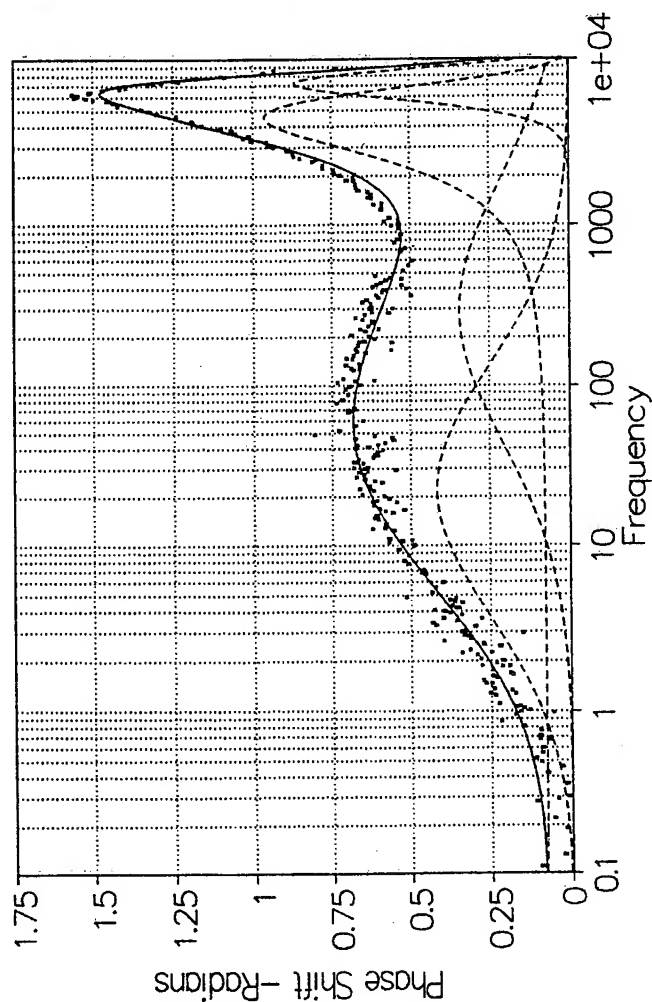
SCHEMATIC ILLUSTRATION OF CREVICE CORROSION AT METAL ALLOY INTERFACE



ELTRON RESEARCH, INC.

FFTEIS MEASURED PHASE ANGLE DEPENDENCY ON FREQUENCY

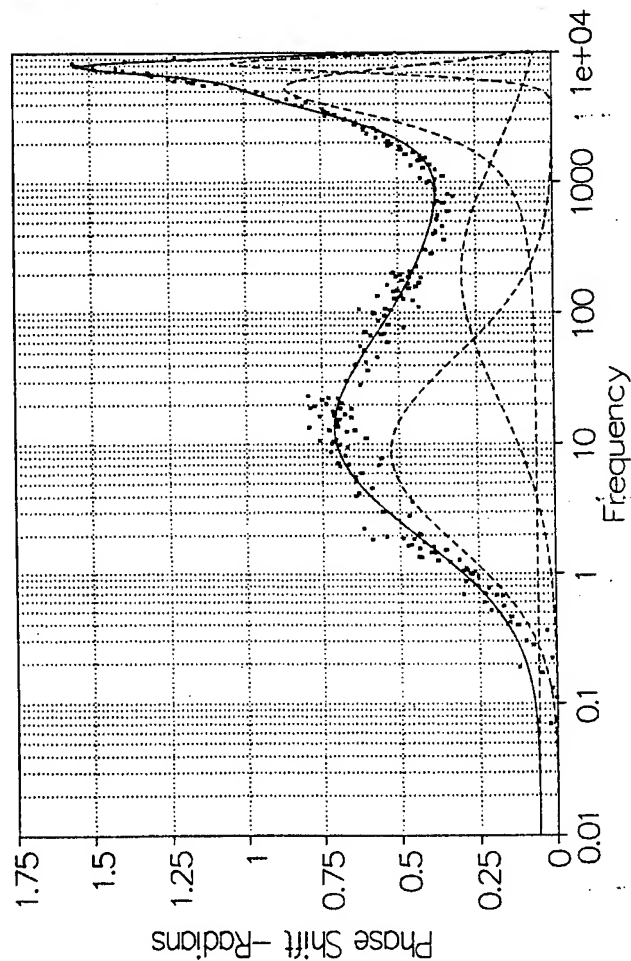
74 HOURS



Conditions
Coupons
Al/7075/Al2024
Corrosion bath
0.1M HNO₃
Cell Electrolyte
0.1M KNO₃
Operated at
0mV vs open
circuit potential

ELTRON RESEARCH, INC.

FFTEIS MEASURED PHASE ANGLE DEPENDENCY ON FREQUENCY 471.5 HOURS

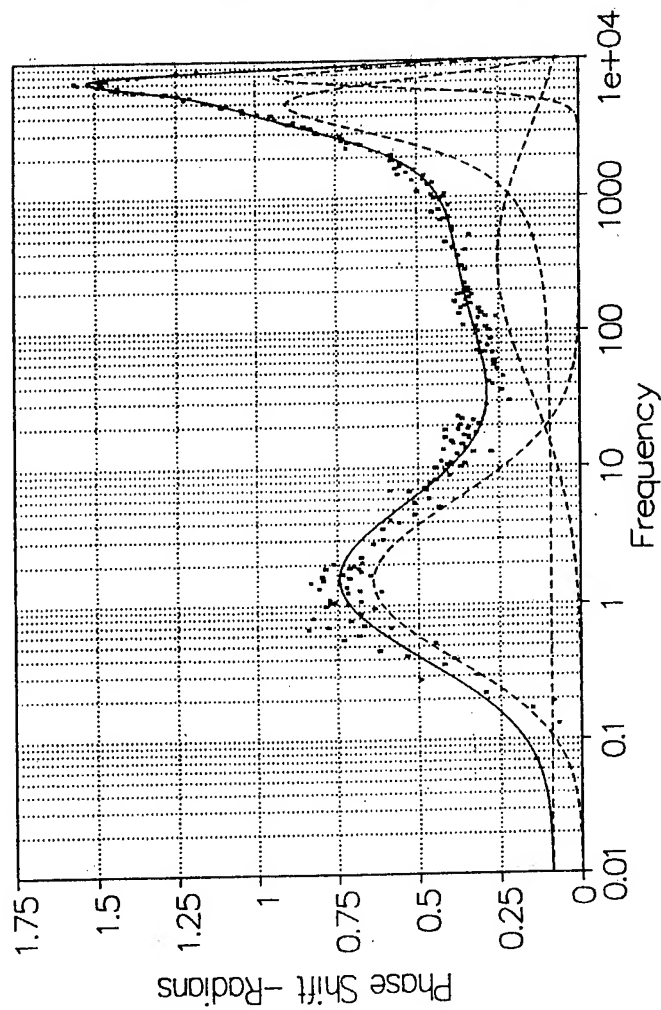


Conditions
Coupons
Al/7075/Al2024
Corrosion Bath
0.1M HNO₃
Cell Electrolyte
0.1M KNO₃
Operated at 0mV
vs open circuit
potential

ELTRON RESEARCH, INC.

FFTEIS MEASURED PHASE ANGLE DEPENDENCY ON FREQUENCY

1308 HOURS

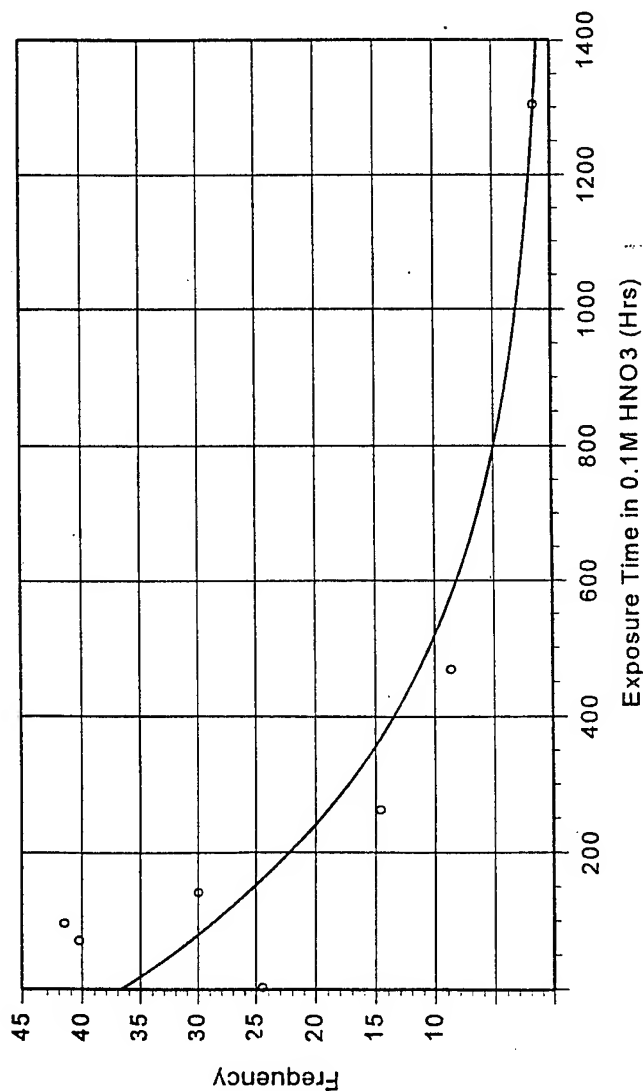


Conditions
Coupons
Al/7075/Al2024
Corrosion bath
0.1M HNO₃
Cell Electrolyte
0.1M KNO₃
Operated at
0mV vs open
circuit potential

ELTRON RESEARCH, INC.

POSITION OF FIRST LOG-NORMAL PEAK CENTROID

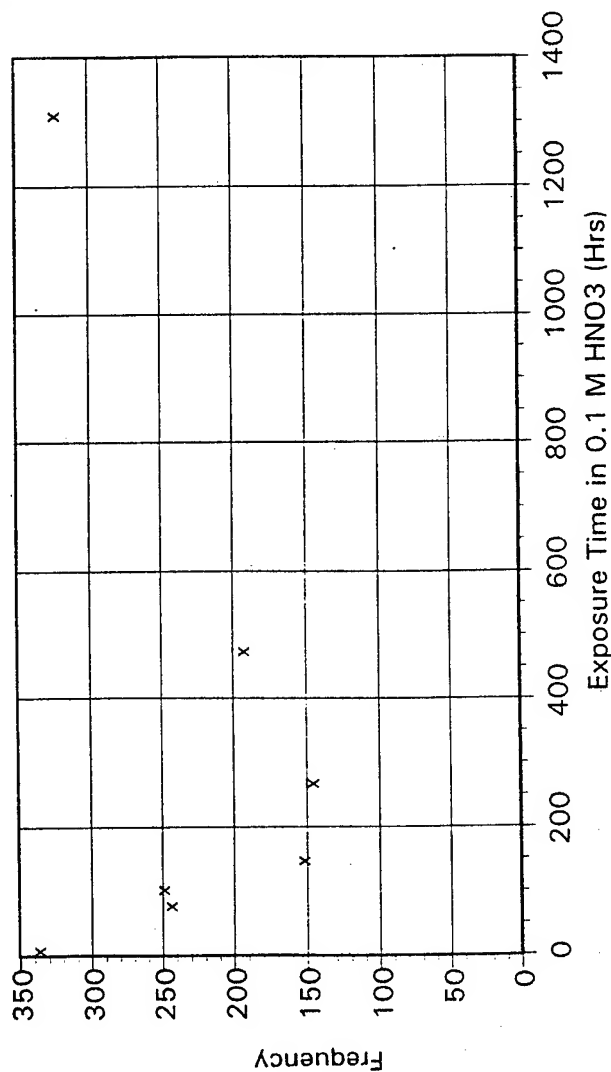
Conditions
Coupons
Al7075/Al2024
Corrosion bath
0.1M HNO₃
Cell
Electrolyte
0.1M KNO₃
Operated at
0mV vs open
circuit
potential



ELTRON RESEARCH, INC.

POSITION OF SECOND LOG-NORMAL PEAK CENTROID

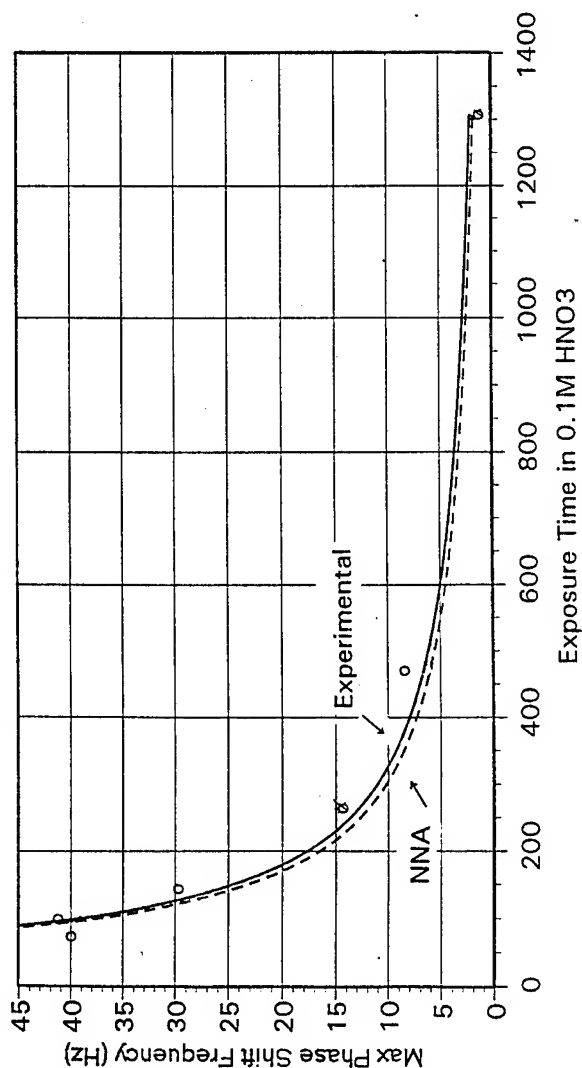
Conditions
Coupons
Al/7075/Al2024
Corrosion bath
0.1M HNO₃
Cell Electrolyte
0.1M KNO₃
Operated at
0mV vs open
circuit potential



ELTRON RESEARCH, INC.

COMPARISON OF EXPERIMENTAL AND NNA PREDICTED POSITION OF FIRST LOG- NORMAL PEAK CENTROID

Conditions
Coupons
Al/7075/Al2024
Corrosion bath
0.1M HNO₃
Cell
Electrolyte
0.1M KNO₃
FFTEIS run at
0mV vs open
circuit potential



ELTRON RESEARCH, INC.

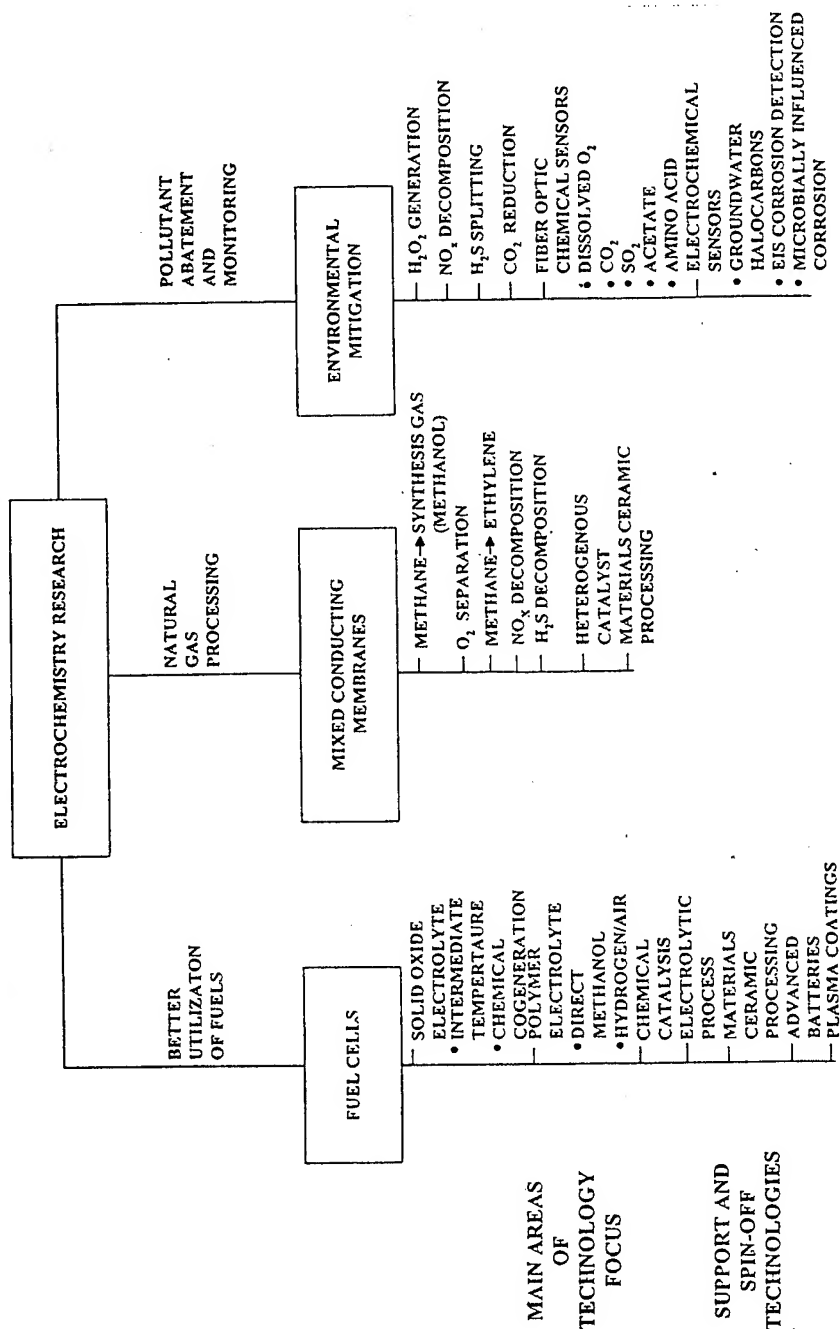
CONCLUSION

Electrochemical Impedance Pattern Instrumentation has been fabricated and shown effective for achieving the non-destructive quantitative detection of corrosion in simulated hidden corrosion sites.

ELTRON RESEARCH, INC.

ELTRON RESEARCH, INC.

TECHNOLOGY BASIS



ELTRON RESEARCH, INC.

ELTRON RESEARCH, INC.

an electrochemical, environmental and catalysis research company

Boulder, CO 80301

(303) 440-8008

Fax (303) 440-8007

E-mail: EltronCo@aol.com



ELTRON RESEARCH, INC.

Detecting Weepole Cracks Using Ultrasonic Creeping Waves

Dr. Matthew J. Golis
Advanced Quality Concepts
Columbus, Ohio 43214-6388

The technical staff from Wright Laboratory recently responded to the need for an improved way to detect cracking caused by the presence of weepoles in the risers of the lower wing planks of the C-141 fleet. As a result, an ultrasonic technique was demonstrated that reliably detects the presence of cracks that initiate from such weepholes. The inspection is done from the outside of the wing tanks and is capable of detecting cracks as small as 0.010 inches deep. Although weepole cracks can be found using Eddy Current (EC) techniques, such inspections must be done from within the tanks.

The ultrasonic technique is based on the creation of a quasi-surface (creeping) wave that follows the cylindrical inner contour of the 0.25 inch diameter weep holes. When the creeping wave encounters a crack as small as a few mils, a portion of the wave is reflected while the remainder of the wave's energy continues around the hole. The relative reflected and transmitted wave energies depend largely on the crack's depth. The effectiveness of the technique for measuring depth of cracks is limited to the depth of penetration of the creeping waves (about 0.050 inches for a frequency of 5 MHz). The waves are launched and detected using a dual-element ultrasonic transducer with its mode of operation (pulse-echo or through-transmission) controlled by a simple switching device.

The technique is superior to that of single element transducer pulse-echo approaches in that it avoids the common problem of a large specular reflection signal received from the cylindrical surface of the weepole which masks the slightly delayed pulses generated when cracks are present. The design of the dual element transducer tends to enhance the generation of creeping waves while selectively discriminating against the masking effects of specular reflection. The technique is simple to use, relies on conventional ultrasonic inspection equipment and involves very little specialized training. The technique has been used only in a manual mode to date.

THE PROBLEM

Weepholes were placed in the vertical risers of C-141 wing planks to permit fuel migration and to allow for the fullest utilization of the available fuel. Due to the stress concentration effects of such holes, fatigue cracking developed in both the upward (toward the fuel) and downward directions in some aircraft. Initial data indicated that the cracking was widespread, that uncracked holes could be cold-worked to extend fatigue lives, and that cracked holes could be repaired (patched) to extend their useful life. The urgency of the inspection requirement, plus the necessity to open and enter all C-141 wing fuel tanks to conduct cold work and repairs, resulted in the selection of a rotating probe eddy current method, described in T.O. 1C-141A-36, for the initial inspection of the C-141 fleet.

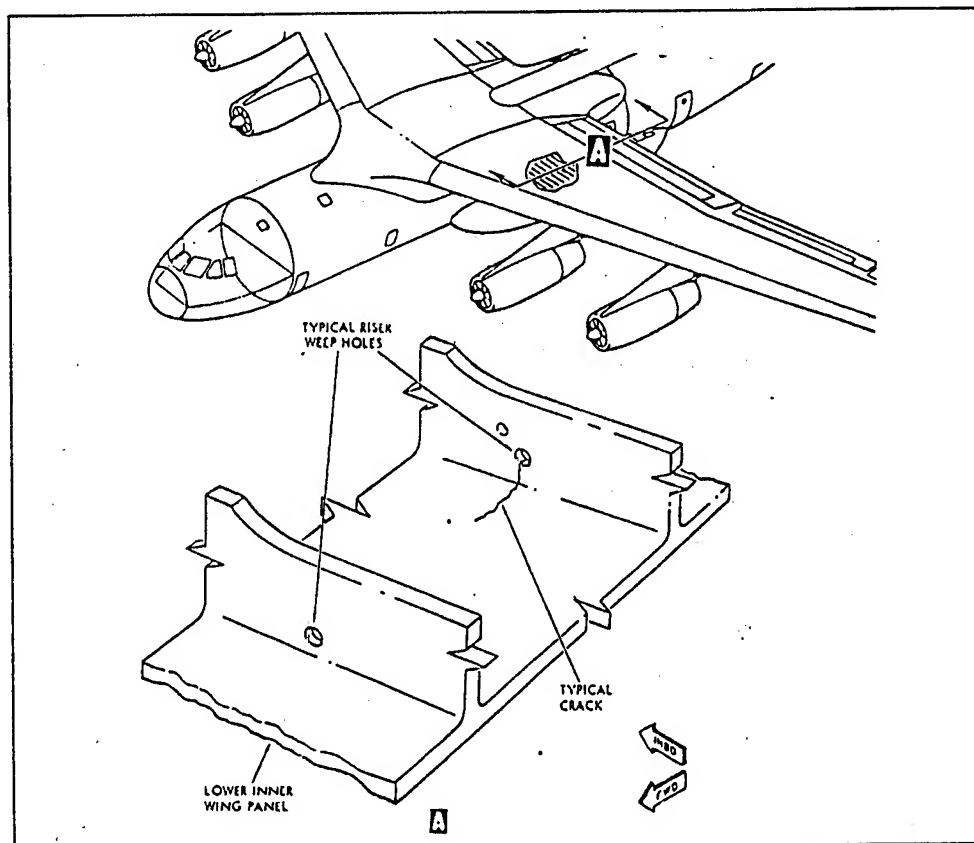


Figure 1 - Weep hole geometry and general location on the C-141 aircraft.

Future management of the C-141 fleet may require follow-up inspections to determine the effectiveness of the cold-work life extension efforts performed on uncracked weepholes. An inspection method that accurately detected the presence of very small cracks in any orientation from outside the fuel-filled tanks would be highly desirable. Other aircraft employ weepholes as part of their fuel management structure and thus could also benefit from a non-intrusive method of assessing weephole integrity early in their projected fatigue life.

A SOLUTION

The most promising approach was a creeping wave that encircles the hole and detects either reflected or attenuated pulses. The necessary conditions for launching weephole creeping waves can be satisfied using shear waves introduced from the wing skin. Creeping waves tend to follow the surface contour of hole, similar to surface waves. Some of the energy from the creep wave radiates (leaks) into the surrounding aluminum as a bulk compression wave. It is the leaky wave that is detected at the skin surface. Figure 2 shows the concept. The shear wave is generated by a 45 degree, 5 MHz transducer. The creep wave is induced when incidence is slightly off-set from specular reflection.

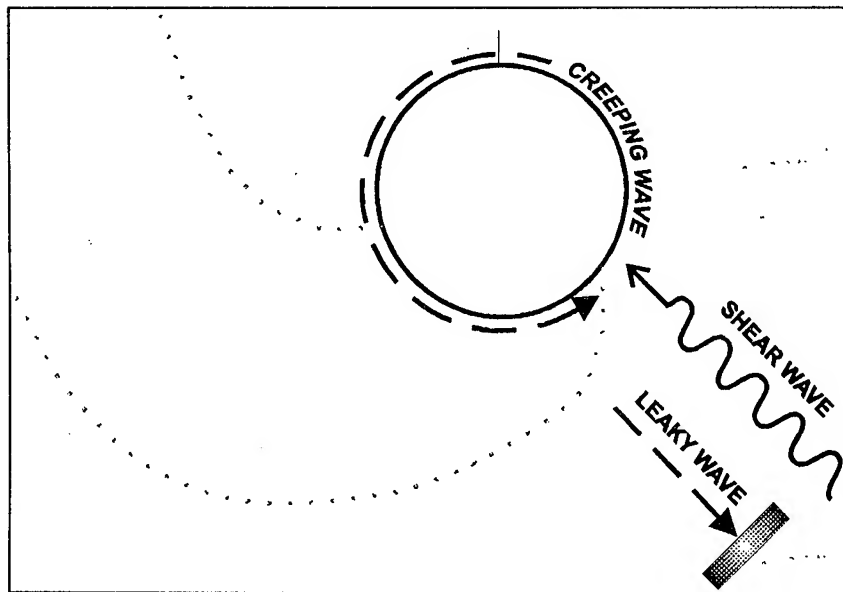


Figure 2 - The concept of a shear wave being mode converted into a creep wave that radiates (leaks) into the surrounding solid material.

HOW DOES THE TECHNIQUE WORK?

A dual element, 5MHz transducer is used to launch a 45 degree shear wave in the aluminum. The one element, acting as a conventional pulse-echo unit directs the sound beam slightly behind the position that yields the strongest specular reflection from the surface of the hole. At this position the shear wave is best aligned to be partially transformed into a creeping wave. If a crack exists emanating radially from the hole, a reflected pulse will be detected by this same transducer element. When the system is in the pulse-echo mode, displayed are the pulse signals received at this transducer element.

As the creeping wave encircles the hole, some of its energy leaks off into the aluminum as a pressure wave in a somewhat pinwheel fashion. A transducer positioned anywhere around the circumference could detect the presence of this leaking wave energy. For convenience, the receiver transducer is located on the same wedge used to introduce the shear wave. When the system is in the through-transmission mode, it is the pulse signals received at this transducer element that is displayed, indicative of the strength of the creeping wave that makes an entire trip around the weephole. Conceptually, this signal is equivalent to a through-transmission or back-reflection indication in pulse-echo testing. Figure 3 shows the configuration.

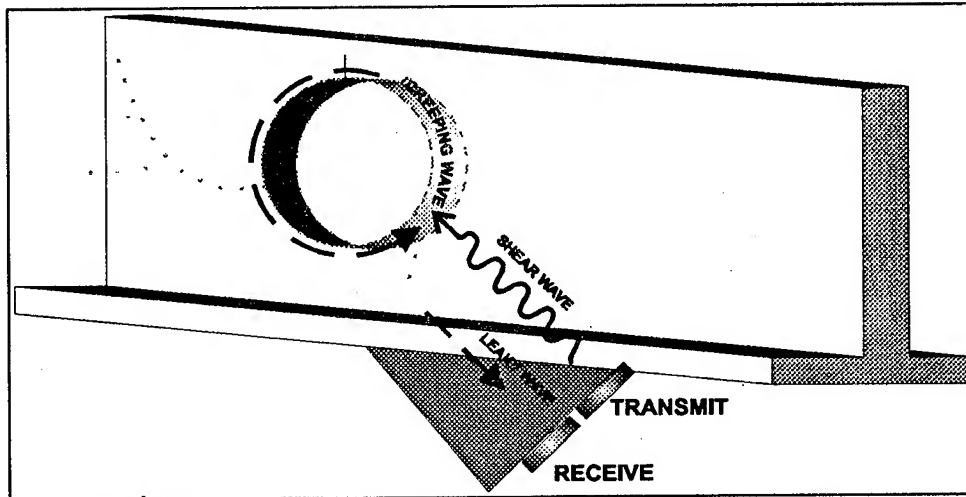


Figure 3 - Dual element transducer used to induce creeping waves in weepholes.

For holes with no cracks present, the through-transmission signal is strong while no significant echoes are seen in the pulse-echo mode. When a crack is present, the through-transmission signal drops off while the pulse-echo signal increases. By switching between the through-transmission and pulse-echo modes without moving the transducer, the changes displayed on the screen can be readily compared and easily interpreted. The response of these two modes is shown in Figure 4 for a collection of saw cuts placed in a set of simulated weepholes. The depth of the cuts ranged from zero to 60 mils.

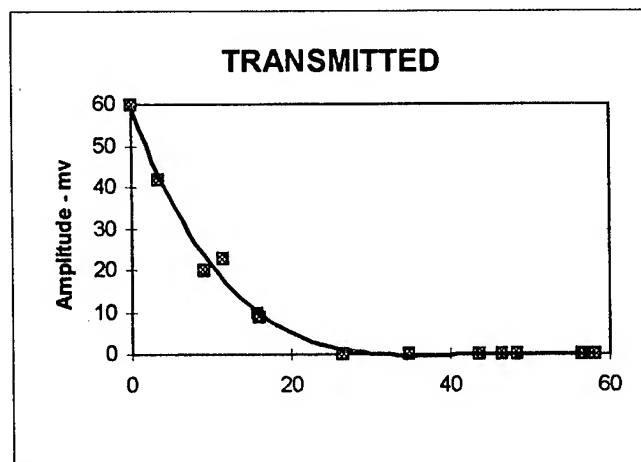


Figure 4a - Falloff in transmitted signal strength as a function of depth of saw cuts placed in simulated weepholes. Total loss of signal occurs at about 0.025-inches while a 6dB drop occurs at about 0.005-inches.

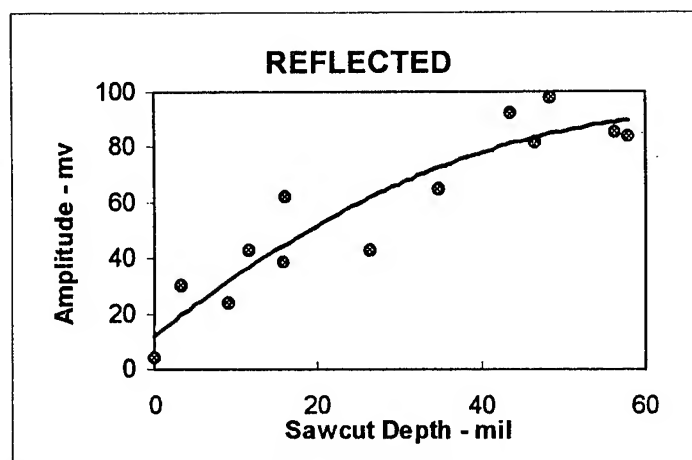


Figure 4b - Increase in reflected pulse amplitude as a function of sawcut depth. The scatter in data is ascribed primarily to inconsistencies in the manner by which the sawcuts were made.

DOES IT REALLY WORK ON WEEPHOLES?

The dual element transducer was tested on a set of samples taken from C-141 aircraft that exhibited fatigue cracks ranging from none to very severe, as identified by the Eddy Current method. The largest crack was estimated to be on the order of 0.5-inches deep. The surface conditions ranged from bare metal to tightly-adhering glossy to heavily-coated painted finishes. Ultrasonic scans taken of these samples correlated precisely with the crack conditions recorded for each weep hole.

Preliminary performance data have been gathered on fluid-filled weep holes in order to estimate the extent to which the creeping waves are attenuated as a result of the waves "leaking" off into the fluid. The attenuation using water was as little as 6 dB. An on-going study has developed a theoretical basis for predicting the attenuation to be expected for varying fluids. Although the signal levels with fuel present will be less than those experienced to date, it is expected that the attenuation will be of little significance in determining the early on-set of cracking in the weep holes.

CONCLUSIONS

The technical staff at Wright Laboratories was successful in translating the theoretical concepts of creeping waves into an ultrasonic inspection system capable of detecting cracks as small as 0.010-inches deep in weep holes. The technique is implemented from the outer surface of the wing, and thus all of the problems involved in gaining entry into the fuel tanks is removed. For other aircraft with similar holes placed in the risers of similar wing planks or equivalent geometries, the use of creeping waves for crack detection is a definite possible solution.

Further information on this subject can be found in the article, *Weep hole inspection by circumferential creeping waves*, NDT&E International 1994 V. 27, No.3 by Peter B. Nagy et.al., a visiting professor and technical developer of the concept. Mark Ruddell of UDRI assisted with transducer construction and field testing while Grover Hardy, MLSA and Matt Golis, a visiting scientist with MLLP coordinated many of the Wright Laboratory NDI efforts. The issue was brought to their attention by Bill Elliot and Norm Woodward, while field activities were made possible by Tom Mullis, all from WR/ALC.

An Advanced ACPD System for Aircraft Structural Integrity Assessment

Mr. Sanjay Tiku*

Graduate Student, Département de Métallurgie et Génie des Matériaux, Ecole Polytechnique, University of Montréal, P.O.Box 6079, Station "Centre Ville", Montreal, Canada, H3C 3A7.

Dr. N.J. Marchand

AMRA Technologies Inc., 4700 de la Savane, Montréal, Canada, H4P 1T7.

Major R.D. Finlayson

Department of National Defence, DTA 3-2, M.GEN. George R. Pearkes Bldg
Ottawa, Ontario, Canada, K1A 0K2.

ABSTRACT. In the current economic scenario the importance of non destructive inspection (NDI) and on - line monitoring has been growing in the aerospace field. There is an increasing demand for measurement of cracks with higher reliability and the need for crack growth rates to be predicted with higher accuracy. To meet the above objectives a novel on - line strain and damage measurement sensor, based on an advanced alternative current potential difference (ACPD) technique, has been designed and built. The sensor makes use of a new technology called current focusing and of advanced flat lock - in phase technology operating from 1 kHz up to 240 kHz (CGM6-3). The present article reports the strain measurements carried out on different specimen geometries of Al 7075 alloy and on the crack calibration measurements obtained. The reliability of the calibration curves is shown to be better than 98%. These sensors have been installed on the three critical locations (bulkheads) of CF-18 aircraft for monitoring strain and cracking during full scale testing (IFOST Program). The procedures to design and install these sensors on a CF-18 aircraft are described. Preliminary results pertaining to full scale testing of the CF-18 aircraft are presented. The system is shown to accurately measure (on-line) the strain changes associated with a flight loading spectrum.

1. Background

The International Follow-on Structural Test Project (IFOSTP) is a cooperative project between the Royal Australian Air Force (RAAF) and the Canadian Air Force (CF). The objective of this project is to certify the F/A-18 structural life under representative CF/RAAF usage. Out of the several critical locations, three critical areas, namely the Y488 bulkhead hydraulic hole, the Y470.5 bulkhead at the center line, and the Y497 bulkhead former segment flange radius have been identified and allocated for monitoring strain and cracking while the full scale testing is being carried out. The purpose of this work was to develop sensors which can be used on-line to measure strain, detect crack initiation and monitor crack growth while the aircraft is flying; thus providing information about the structural integrity at regular intervals.

This paper provides a brief summary of the work carried out to obtain calibration curves for strain and cracks, the installation of these sensors on the CF-18 and the preliminary results obtained pertaining to full scale testing.

2. AC-Field Technology

The potential drop technique makes use of an increase in electrical resistance in conducting materials due to strain and cracking. The skin effect resulting from the high frequency current passing through the specimen makes alternating current potential drop (ACPD) technique very sensitive to strain and cracking compared with direct current potential drop (DCPD) technique. A new technology named current focusing was recently developed which allows the current distribution to be confined in a narrow region rather than spreading in the whole area, akin to skin depth. [1]. This confinement of the current results in higher current density distribution in the area of our interest (i.e. high stress/strain gradient area). Thus, the use of AC currents, in conjunction with the current focusing technique, results in having a 3-dimensional control of the current distribution in the solid. Moreover, having the ability to steer the current makes this technique very flexible and useful for complex geometries found in real life structures (e.g. panels, bolt holes, notches, sharp bends, etc.). The details of AC field technology and the current focusing are explained elsewhere [2].

The electronics designed and developed within the scope of this work is an advanced two channel ACPD system named CGM 6-3. The crack growth monitor, CGM6-3 has capabilities of generating a current of continuously variable frequency up to 240 kHz with a high stability of 0.1% over a 5°C variation of the

ambient temperature. The voltage to current generator can generate up to 5 amperes of constant current with a stability better than 0.1 %. The switching waveform generator produces two square waves one in phase with the current passing through the specimen and the other at 90° with the current. The phase sensitive detection is done dynamically and the synchronization of these waveforms is better than 5 nano seconds. The signal can also be amplified in steps of 1000, 3000, 10,000 and 30,000X.

3. Strain Calibration

Three different specimen geometries namely four point bending, single edge notch (SEN) and hour glass specimens were selected to study the changes of ACPD due to load cycling. The four point bending specimen (6" radius), machined out of 7075 T651 aluminium plate, was designed to represent the flange fillet region of the bulkhead Y488 of CF-18 aircraft. The details pertaining to four point bending experiment and the verification of ACPD readings with strain gauge readings and finite element analysis have been reported elsewhere [2]. The calibration curve of strain versus ACPD obtained at 30 kHz, 1 Amp. and at a gain of 70 dB (3162 X) was found to be :

$$\text{ACPD (V)} = 0.141 (\text{strain}) + 0.17$$

with the reliability of the regression being better than 97%.

The single edge notch (SEN) specimen geometry as shown in figure.1. was selected because it reflected a complicated version of critical locations on the CF-18 aircraft which are being monitored by the ACPD technique. The experiments were carried out by measuring AC potentials at regular load intervals of 44, 439, 834, 1229, 1624 and 2019 lb. for the loading and unloading sequences. The experiment was fully computerized and procedure was repeated 276 times. The ACPD readings were obtained at 120 kHz, 5 Amp and 3000 gain. Figure 2 shows a plot of ACPD as a function of applied load. The potential is found to be directly proportional to the load. The plot of ACPD versus load at cycles 1-10, 90-100 and 265-275 cycles are shown in figure 3a-3c respectively. As can be seen, the hysteresis behavior (loop) decreases with increasing number of cycles indicating that the material has reached a saturation limit. Figure 4a-4c show the plot of ACPD versus time for 1-10, 40-50, and 90-100 cycles intervals respectively. These figures indicate that the potential is decreasing with time. This result can be explained by the fact that there were compressive residual stresses present at the notch at the beginning of the test. With load cycling the residual

stresses were slowly being relieved since the applied load was tensile in nature. The presence of compressive residual stresses was verified by X-ray diffraction. The detailed analyses associated with quantifying residual stresses will be reported elsewhere.

The Hourglass specimen geometry which is shown in figure 5 was provided by the Department of National Defence (DND) Canada. This testing geometry was used because it represents the flange fillet region of the bulkhead Y488 with a K_t of 1.03. Unlike the previous two types of experiments, this particular geometry was subjected to continuous cycling instead of stepped loading. The loading conditions for fatigue cycling were, stress ratio (R) equal to zero, a maximum stress of 45 ksi and a frequency of 1 Hz. Figure 6a shows a plot of ACPD measurements taken at 30 kHz, 1 Amp and 70 dB(3162 X) versus number of cycles. Figure 6b shows a zoom of first section of the figure 6a. Here a very stable ACPD curve, slowly increasing with the number of cycles can be seen. With continued cycling the saturation limit of the material is reached which is associated with no further change in the potential. In essence, a strain hardening curve is observed indicating that the ACPD is tracking the load cycling history and the microplastic deformation. Thus, the hardening/softening characteristics of a material behavior are also being resolved emphasizing the sensitivity of the ACPD system.

4. Crack Calibration

Fatigue tests were performed on SEN specimens for obtaining a crack calibration curve. Testing was carried out at $R = 0$ and 1 Hz frequency. The CGM6-3 was operated at 30 kHz, 5 Amp and 3000 Gain. Figure 7 shows an example of a typical ACPD curve versus number of cycles. As can be seen the potential is very stable in the beginning. As soon as a crack is detected by the ACP probes, the potential difference (PD) starts to increase continuously. In this particular case, the crack depth was found to be 300 μm for a PD of 2 mV. Several fatigue tests were carried out with the cycling stopped at a pre-determined changes of potential. After stopping the tests a high tensile overload was applied to pry open the cracks and the final crack depths were measured using a scanning electron microscope. The dominant crack depths versus the corresponding change in AC potential were measured and plotted. Figure 8 details the crack calibration curve, i.e. the crack depth as a function of change in AC potential (PD). The graph covers the range of crack depths from 200 μm to 6 mm. The relationship between crack depth and the corresponding change in potential was found to be :

$$a = 0.258 + 0.0231 PD - 2.2 \times 10^{-5} PD^2$$

where a = Crack Depth (mm)

PD = ACPD (mV)

The reliability of the regression is 99.5%.

Figure 9 shows a plot of ACPD versus time. In the case shown here, the ACPD is being used as an off-line measurement tool. At point A in the graph the cycling was stopped, the system brought down to zero load and the CGM6-3 disconnected from the specimen. Measurements were taken for some time and the readings had dropped as indicated in figure 9. The instrument was then connected back and the cycling resumed. The AC potential returned to its original value. This process was repeated three times (Location A, Band C). In all cases the ACPD signal was not affected by the interruptions. At locations D, E, F, G and H the cycling was again stopped and the system brought down to zero load but the ACPD readings were taken continuously. The potentials dropped all the times when the cycling was stopped but returned back to their original values as soon as the cycling was resumed. When the difference in the potential was around 2.5 mV the experiment was stopped and the system was brought down to zero load. The difference in potential at zero load during the cycling and after the cycling was also 2.5 mV. This experiment clearly proved that ACPD can be effectively used as an off-line measurement tool and that the specimen or the structure does not have to be under load for crack detection. Therefore, this technique can be used as an effective maintenance tool (periodic inspection) for assessing the status of a structure.

5. Installation and monitoring on CF-18 Aircraft

As mentioned earlier, three critical locations on three different bulkheads were assigned for installation of ACP probes. The procedure to design and install these sensors are described briefly in this section.

Bulkhead Y470 at the center line : There is a strain gauge installed in the center of this location where the crack is expected to initiate. On both sides of the strain gauge a current focusing device was installed is glued. Two active probes are attached across each current focusing device covering the critical area. Attachment of the probes was carried by an ultrasonic welding technique. The details of this technique are explained elsewhere[2]. One reference probe was attached away from the critical area across one of the current focusing device thus providing a reference. The current and potential cables are connected to scanners.

The schematic of this probe design is shown in the figure 10a.

Figure 10b shows a schematic of the probe design used for on-line monitoring of the bulkhead Y488 hydraulic hole. As can be seen the principle of this probe design is the simple. There is a current focusing device in the middle with five probes welded across it, thus covering about 180° of the hydraulic hole.

The schematic of the probe design installed on the bulkhead Y497 location is shown in figure 10c. It is similar to the probe design of the Y470 location. It has two current focusing devices, two active probes across the critical area and one reference probe.

In essence the probe design for the three sensors installed on three different locations is the same. Similar probe design has been used on different specimen geometries tested in the laboratory proving and assessing the flexibility and simplicity of this technique.

Figures 11 and 12 show the snap shots of the strain survey conducted on the CF-18 aircraft. Here the data pertains to the Y470 location. The current was switched between the two current focusing devices every 1.5 seconds. During these 1.5 seconds, 20 readings were taken of the active probes with the reference probe being read continuously. Figure 11a shows the reference signal and one of the active probe signal. The drift and the noise level is very low ($\sim .5\text{mV}$). During strain survey, a spike of 0-100-0% load was first applied. The aircraft was then reloaded in fifteen steps. Figure 11b shows four such loading sequences. Figure 12a is displaying one such stepped loading of the active probe. The active probe, figure, 12b is able to resolve the fifteen steps applied to the structure during the loading and unloading sequences. This demonstrates that this novel ACPD technology is capable of monitoring the loading exactly as it is applied to the structure. This also proves that the present ACPD technique is very sensitive and can be used effectively for on-line measurements of strain and damage in structures.

6. Conclusions

The major conclusions of the paper can be summarized as follow :

- A novel AC-field technology has been designed, developed and calibrated for on-line monitoring of strain accumulation and crack detection.
- Strain measurements have been carried out on different geometries. A strain

calibration curve has been obtained with the reliability of the regression being better than 97%.

- A crack calibration curve has been obtained for the range of 200 μm to 6 mm with the reliability of the regression being better than 99%.
- The sensors have been installed on the CF-18 aircraft and are monitoring accurately the loadings applied to the structure.
- This technique can also be used off-line for assessing the status of the structure and therefore be a reliable effective maintenance tool.

References

1. Unvala, B.A. and Marchand, N.J. - Method, test probe and apparatus for the measurement of alternating current potential drop by confining test current to a skin region of a test specimen, United States Patent, No. 5, 202,641, April 13, 1993.
2. Sanjay Tiku and N.J. Marchand - A novel technology for on-line strain measurement and crack detection, (in press) in the Proceedings of Third Aircraft Structural Integrity Symposium ASIP 94, Ottawa, Canada.

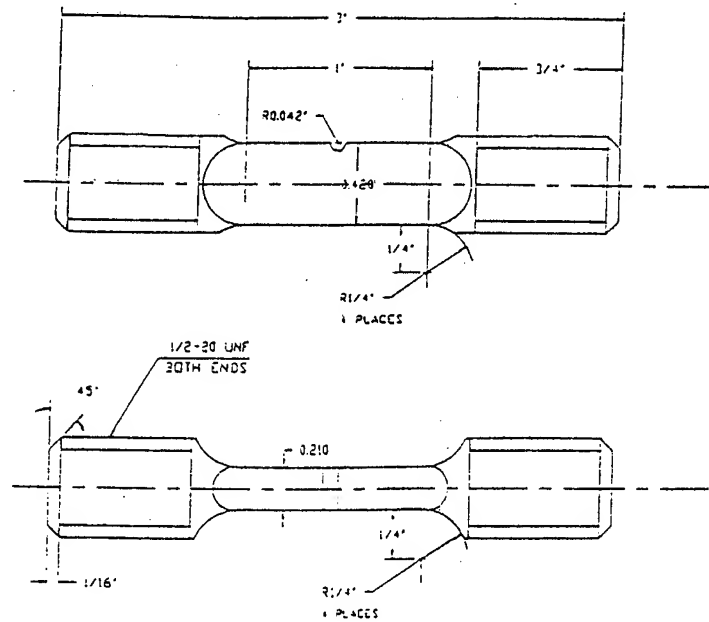


Figure 1. The detailed geometry of the SEN specimen used in the testing program.

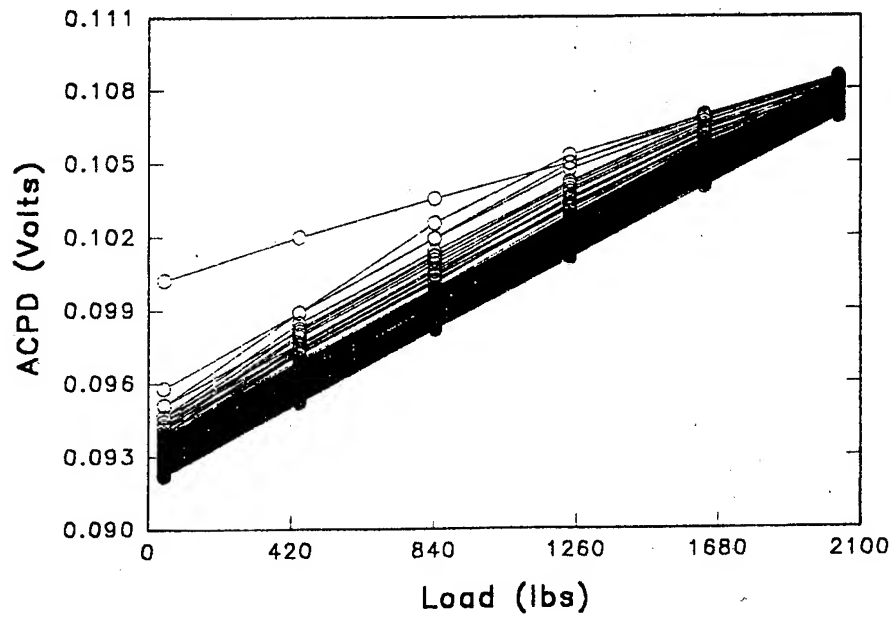


Figure 2. Plot of ACPD as a function of load, Cycle 1-276.

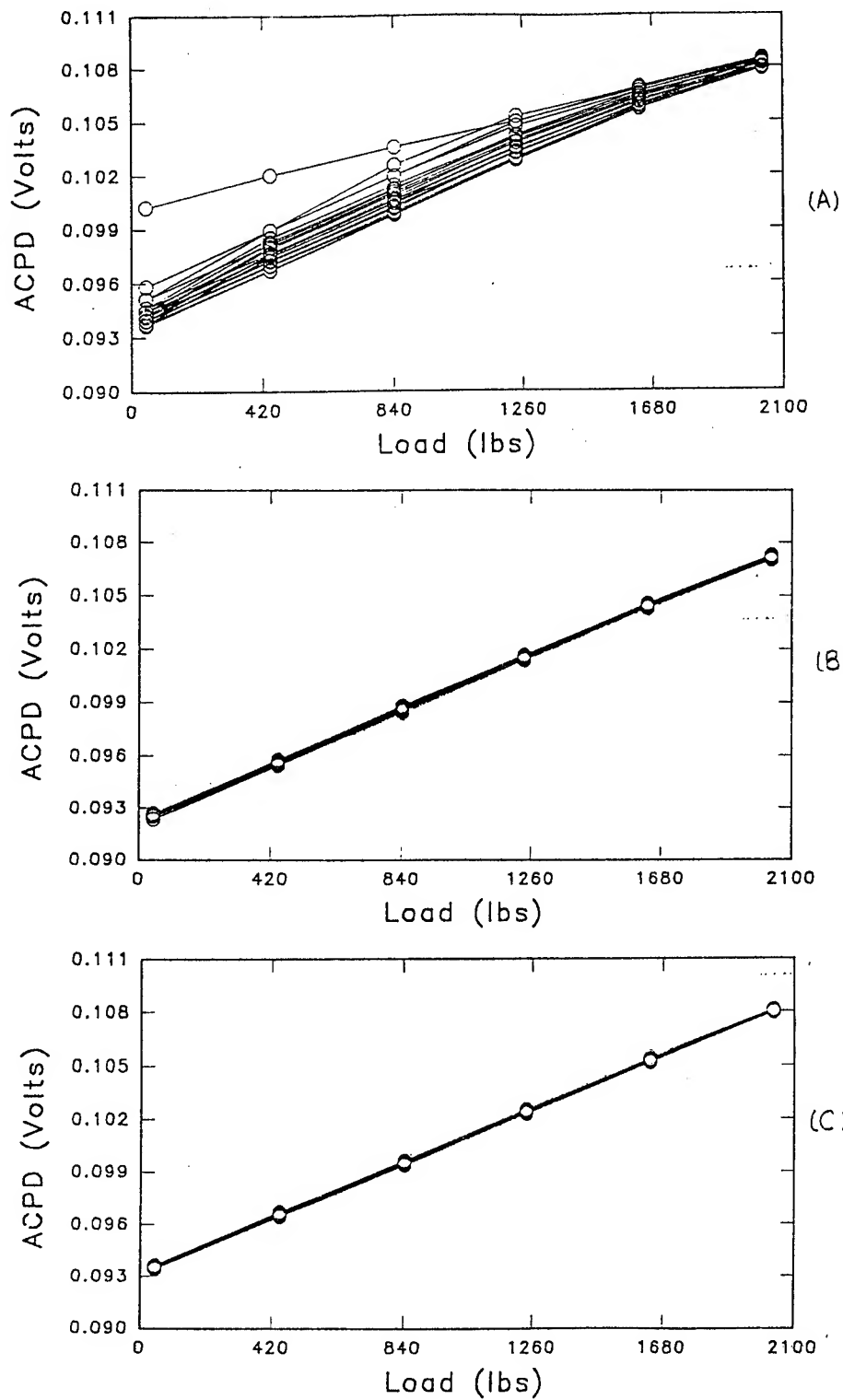


Figure 3. Plot of ACPD as a function of load (a) Cycle 1-10, (b) Cycle 90- 100, (c) Cycle 265-275.

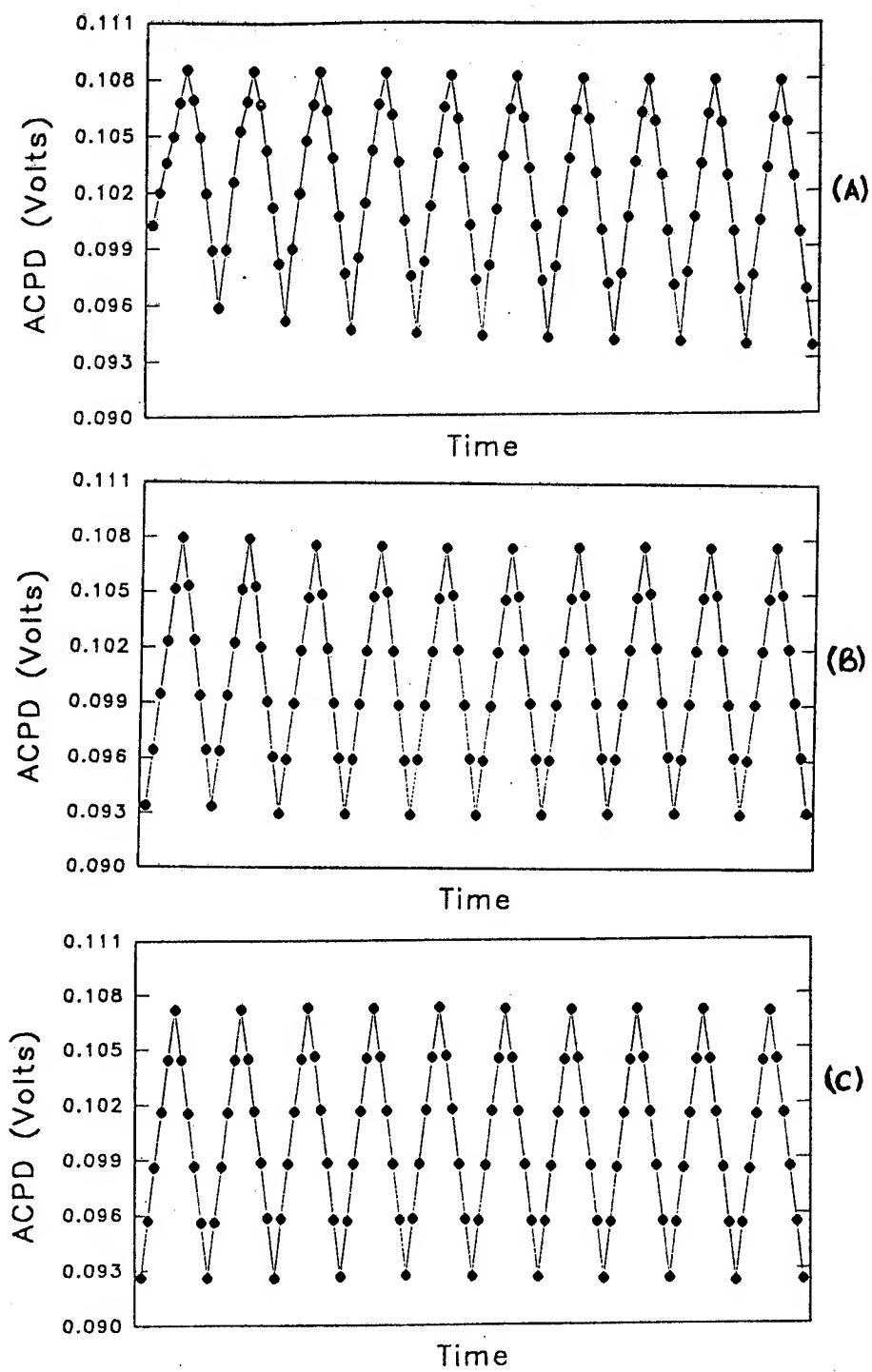


Figure 4. Plot of ACPD as a function of time (a) Cycle 1-10, (b) Cycle 40-50, (c) Cycle 90-100.

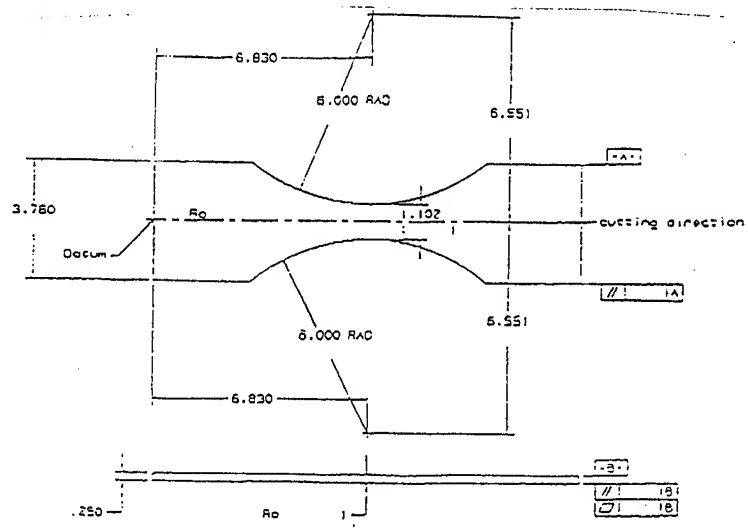


Figure 5. The detailed geometry of the Hourglass specimen used in the testing program.

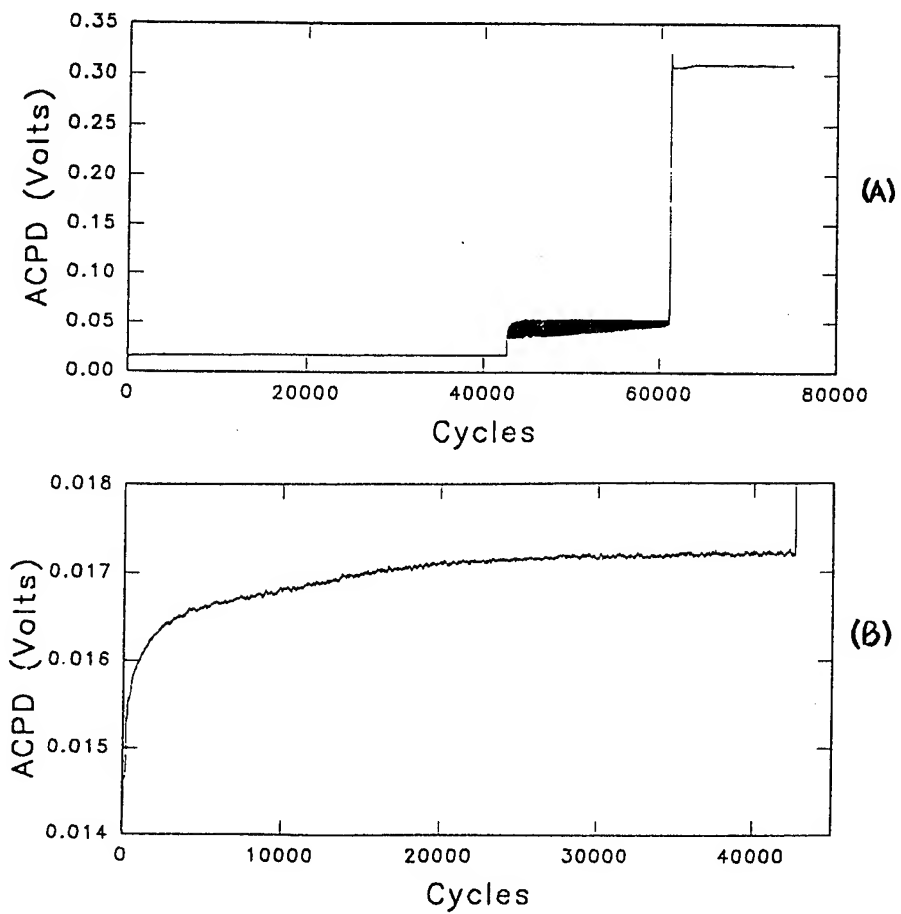


Figure 6. Plot of ACPD versus number of cycles (a) complete experiment, (b) Zoom of (a).

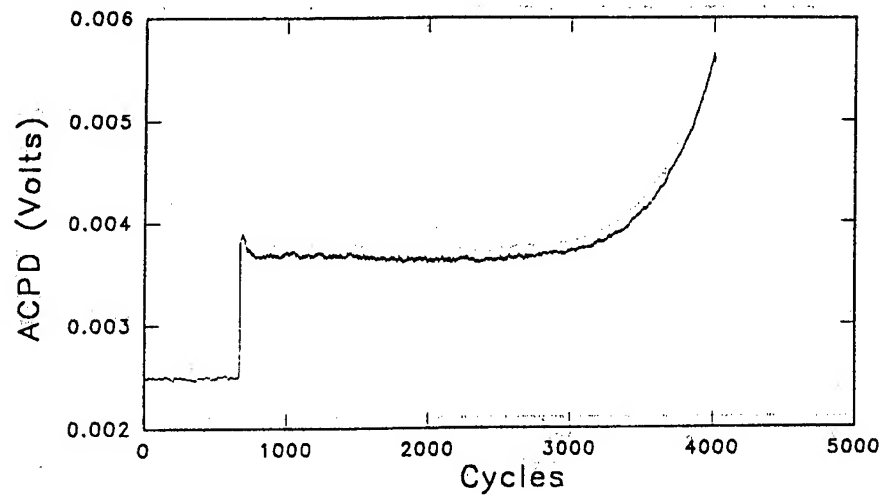


Figure 7. ACPD as a function of the number of cycles.

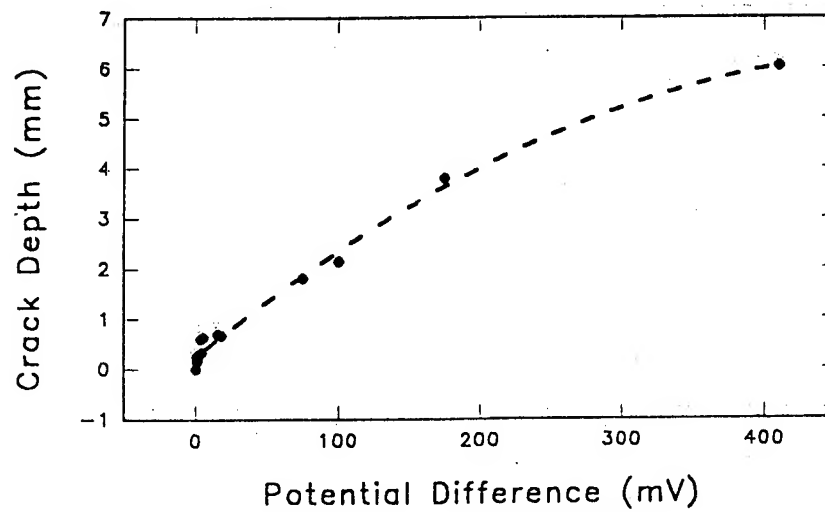


Figure 8. The calibration curve for ACPD as a function of the crack depth.

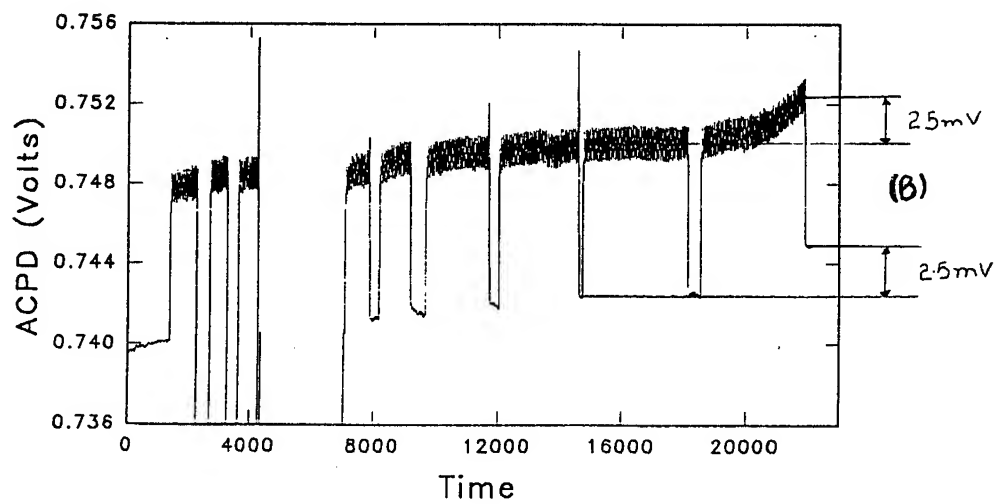
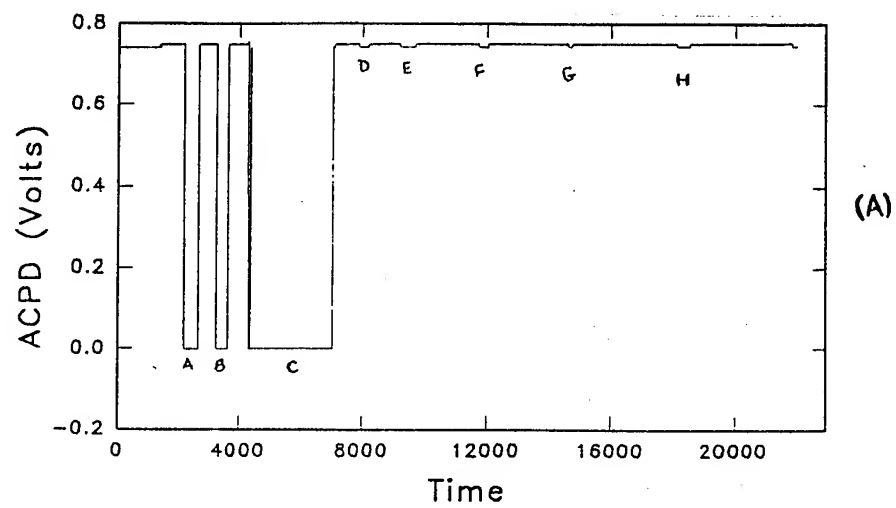


Figure 9a. Plot of ACPD versus time. (b) zoom of (a).

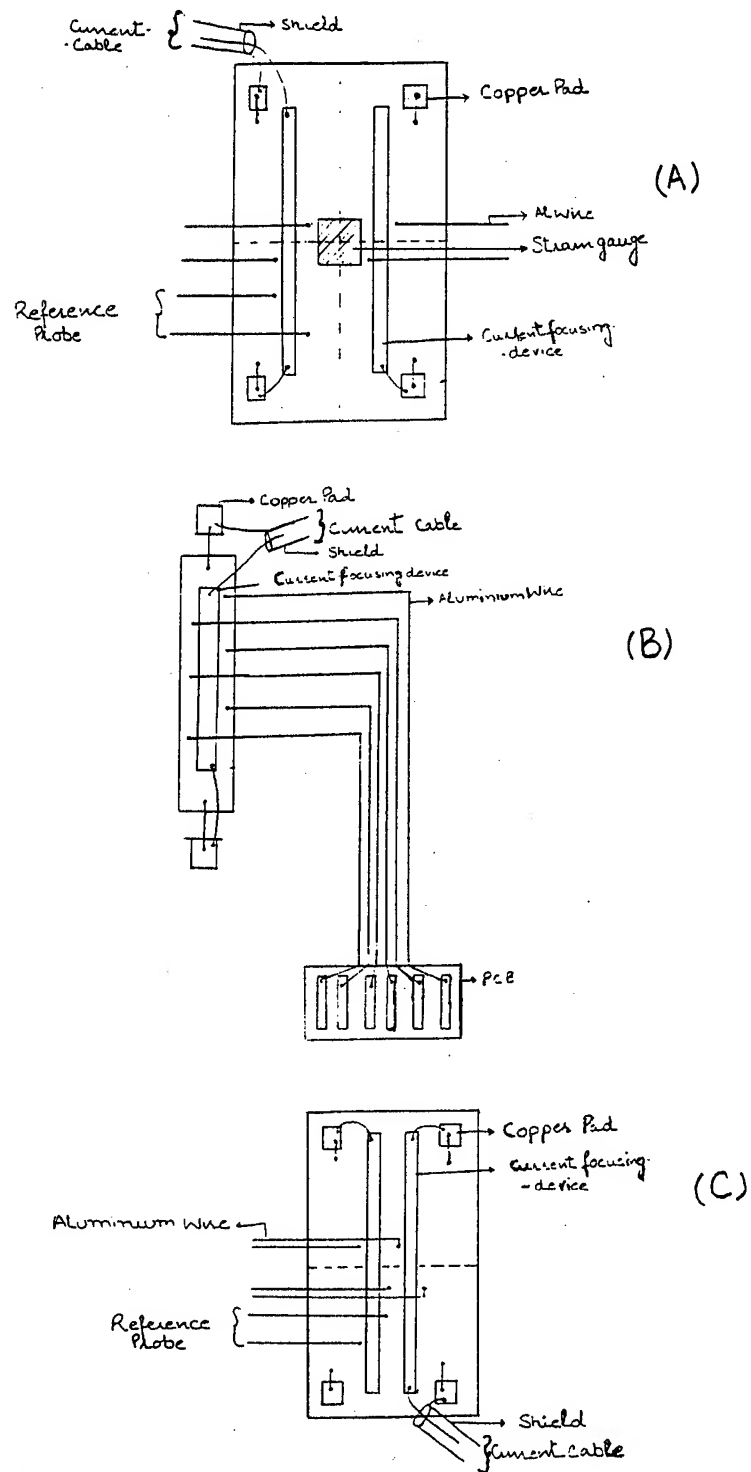
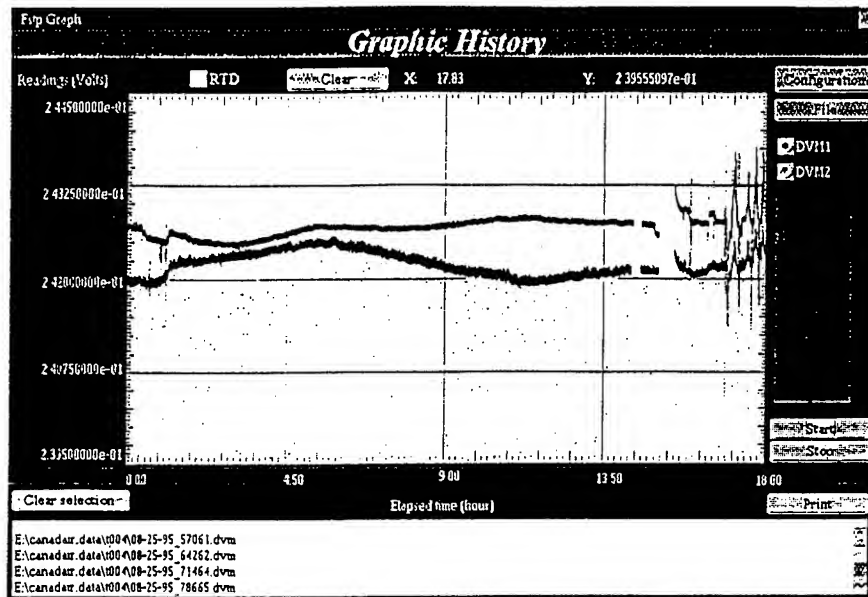
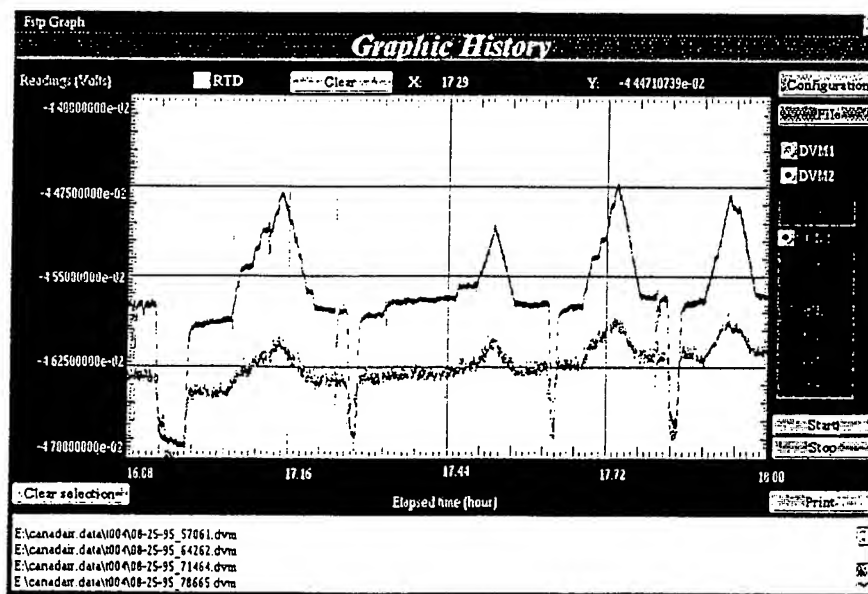


Figure 10. The schematics of probe design installed on CF-18 aircraft. (a) Bulkhead 470, (b) Bulkhead 488, (c) Bulkhead 497.

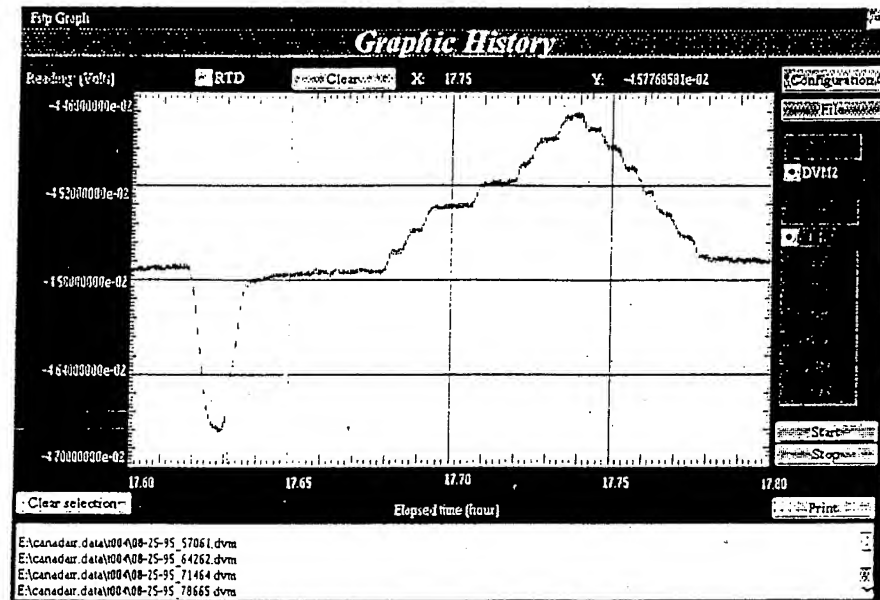


(A)

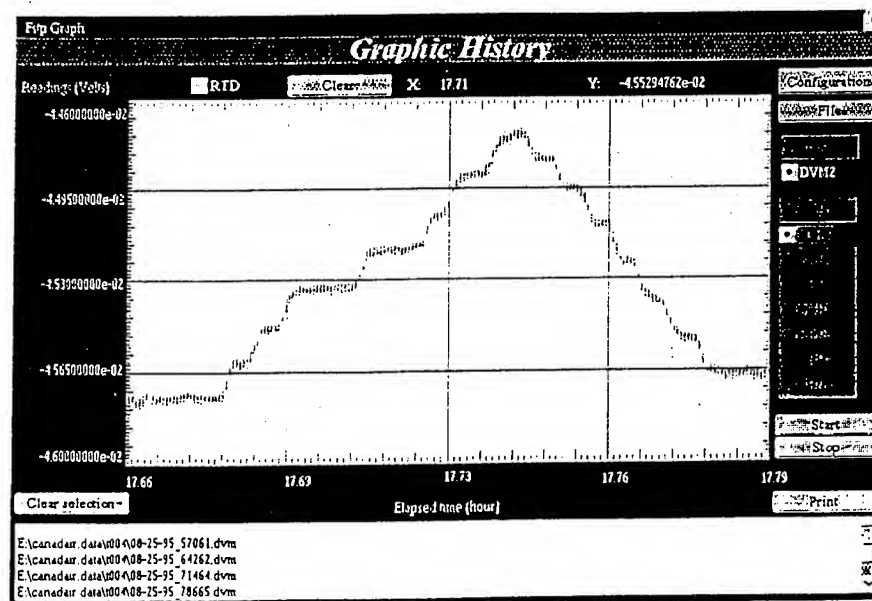


(B)

Figure 11a. Snapshot of ACPD signal acquired on-line on CF-18 aircraft, (b) Zoom of (a).



(A)



(B)

Figure 12. Active probe signal for one complete loading sequence, (b) zoom of (a).

SESSION IX

REPAIRS

Chairman: *J. Mazza*, WL/MLSE

C-141 REPAIR TRACKING

Presented To

1995 USAF Aircraft Structural Integrity Program Conference

28-30 November 1995

San Antonio, Texas

Russ Alford

WR-ALC/LJLEA

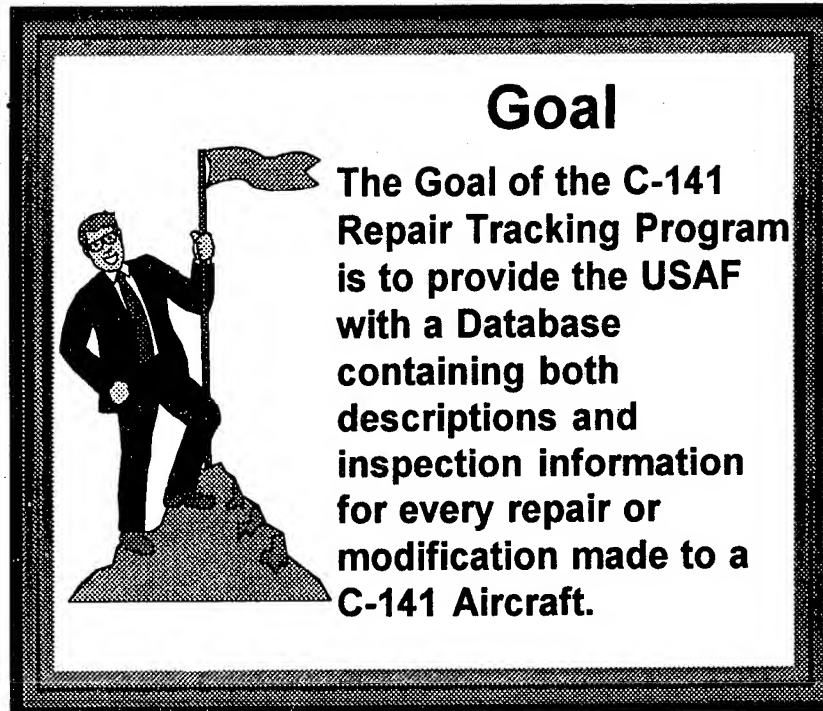
C-141 ASIP Manager

Ralph Sykes

Lockheed Martin

Aeronautical Systems

The aging of the C-141 Force brings Repair Tracking activities to the forefront of its force management program. As an aircraft ages, more and more repairs or modifications are made to each aircraft. No matter how well a repair was designed, it increases the stress level in the adjacent structure. Increasing the stress level can cause premature failures in the repair or in the adjacent structure. Therefore, every repair or modification made to an aircraft has to be documented and inspected periodically to protect the aircraft from catastrophic failure.



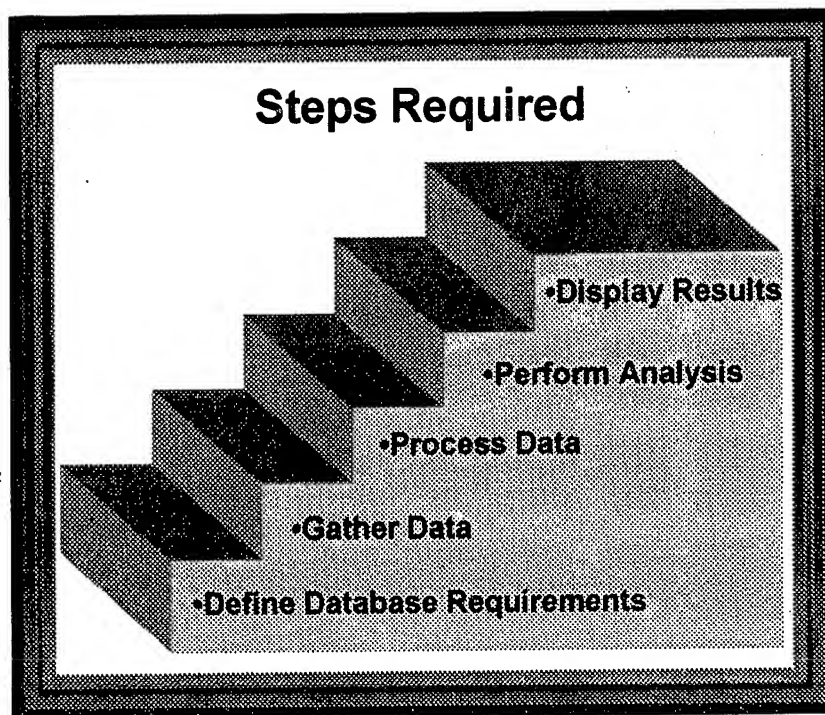
The goal of the C-141 Repair Tracking Program is to provide the USAF with a database containing both descriptions and inspection information for every repair or modification made to a C-141 aircraft. To accomplish this goal, C-141 engineers use a database where all pertinent information about a repair or modification is accessible through a variety of main frame and personal computer software. The information contained in this database allows the engineer to easily assess the purpose and inspection requirements of each repair or modification.

Results Required



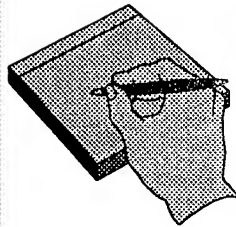
The Results required of the C-141 Repair Tracking Program are Inspection Intervals and Projected Inspection Dates for the Repairs contained in the Repair Tracking Database

The results required of the C-141 Repair Tracking Program are inspection intervals and projected inspection dates for the repairs contained in the Repair Tracking Database. Projecting the inspection dates would allow USAF planners to easily add inspections to ISO's or PDM's. If every repair/modification is inspected when required, the aircraft is protected from any failures resulting from cracks caused by the modifications. The rest of the presentation explains the steps required in setting up such a repair tracking program.



The steps required to create the C-141 Repair Tracking Program were defining the database requirements, gathering the data, processing the data, performing analysis to determine inspection intervals, and displaying the results in an user friendly manner.

Database Requirements



- Damage Found (Crack, Corrosion, Etc.)
- Damage Location
- Repair Configuration
- Inspection Date
- Flight Hours @ Inspection
- Inspection Intervals
- Pictures of Repairs

First, the information required for the database must be defined as completely as possible. The information contained in the database must both describe the repair and define the inspection requirements. The C-141 Repair Tracking database contains information such as damage found, damage location, repair configuration, inspection date, flight hours, inspection intervals, and digital pictures of the repairs. Defining the database is probably the most important step in the entire process. If the data required keeps changing, then the previously collected data is obsolete and could be rendered useless.

Data Gathering History



- **AFTO 58 Form**
- **Lack of Forms Being Returned**
- **Accuracy of Data on Forms**
- **Need for "On-Site" Recording**

The AFTO 58 form was created in the early 1980's to gather information on repairs made to the C-141 Force. The AFTO 58 form is an opscan form where the basic data required for the C-141 Repair Tracking Database is entered. It quickly became apparent that there were problems with the form. First, since filling out the form required additional work for the repair facility, forms for every repair were not being returned. Furthermore, the accuracy of data on the forms was questionable. The inspectors were not filling out all the required information.

The AFTO 58 Form

STRUCTURAL REPAIR/CORROSION TRACKING RECORD

Handwritten entries are visible in the form, including aircraft serial number 100, repair location 100, and a large area for handwritten remarks.

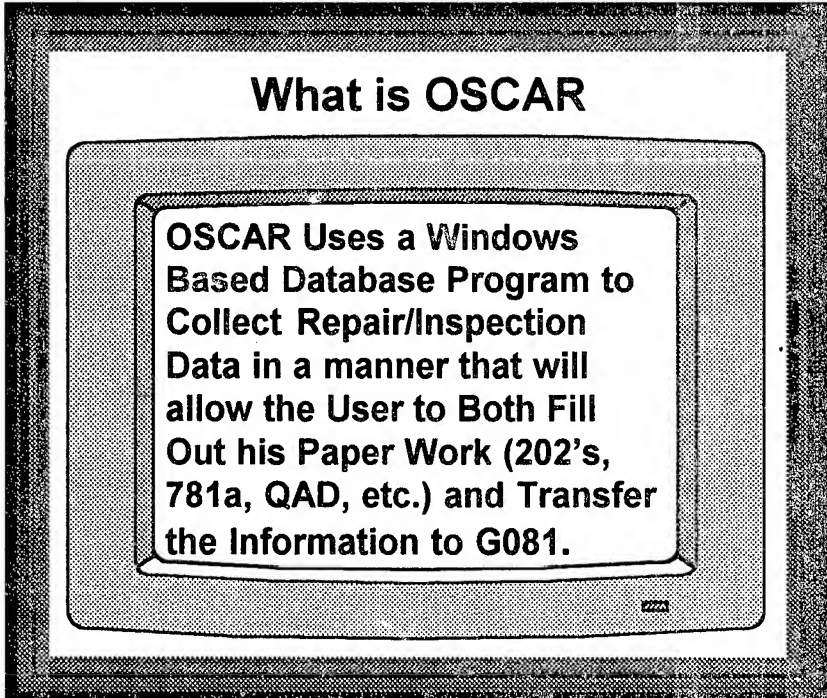
This is the AFTO 58 form. The inspectors simply filled it out and mailed it to WR-ALC for processing. On the form there is a hand written remarks area, this area could not be opscanned and therefore, any additional information placed in this area was lost forever. All these problems illustrate the need for "On-Site" recording of the repair information.

OSCAR **On-Site Collating And Recording**



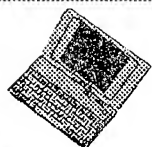
OSCAR stands for On-Site Collating And Recording. OSCAR is used to collect repair information at the C-141 bases and depot. As one can see from this picture, OSCAR can run on any PC platform anywhere.

What is OSCAR



OSCAR Uses a Windows Based Database Program to Collect Repair/Inspection Data in a manner that will allow the User to Both Fill Out his Paper Work (202's, 781a, QAD, etc.) and Transfer the Information to G081.

OSCAR uses a WINDOWS based database program to collect repair/inspection data in a manner that will allow the user to both fill out his standard paper work and transfer the information directly to G081. This means that filling out the information required for the Repair Tracking database is no longer an extra step. Furthermore, OSCAR should allow for a virtually paperless inspection reporting process.



OSCAR Goals

- **OSCAR Will be Used to Collect C-141 Structural and System Repair Data**
- **OSCAR Will Allow for Post Processing of Inspection Results**
- **OSCAR Will Allow Inspection Personnel to Electronically Fill Out Forms and Transfer Data to G081**
- **OSCAR Will Be Developed for Use at Bases, Depots, and Contractor Facilities**
- **Oscar Will First Be Used with the C-141 Major ISO Inspections**

These are the goals for OSCAR. First of all, Oscar will be used to collect C-141 structural and system repair data. It will allow for post processing of the inspection results. OSCAR will allow inspectors to electronically fill out their standard paper work and transfer the information to the G081 database. A version of the program will be developed for use at all C-141 facilities. The OSCAR prototype is being designed for use at the C-141 bases to collect Major ISO inspection data. The accomplishment of these goals will show that electronically filling out forms saves inspection time and will also provide the required data for the C-141 Repair Tracking Database.



What OSCAR Does

Makes the User Select From A List of Acceptable Answers

Lists Include:

Parts

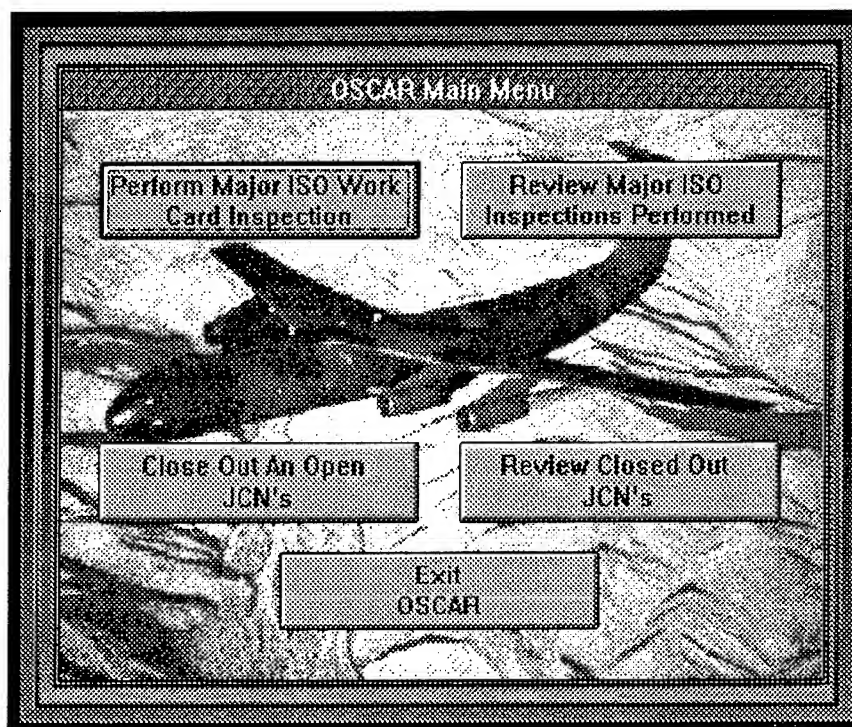
WUC (Work Unit Code)

Location

Displays Results on Required Paper Work

Management Can Track Results

OSCAR makes the user fill out inspection forms completely and accurately. The user must select from a list of acceptable answers. The answer lists include parts, WUC (Work Unit Codes), location, discrepancy, and corrective action. The user does not have to pick answers from long lists because OSCAR can limit each list to just answers pertinent to the local area. For example, when entering information about a fuselage part, there is no need to see wing information. OSCAR can display inspection results in the C-141 Bases or Depots standard paper work. Furthermore, once the information is entered into the computer, OSCAR can be used by the manager to track the progress of the inspections and any open paper work.



This is the OSCAR Main Menu. From the Main Menu, the user can perform new inspections, review inspections performed, close out open paper work, or review closed out paper work.

ISO Inspection Screen

The screenshot displays the ISO Inspection Screen with the following fields and data:

- WORK CARD NO:** M-060
- CHANGE NO.:** 0
- INSPECTION TIME (MINUTES):** 60
- WORK AREA:** RH MLG/RH WG
- TYPE MECH RUN:** NDI
- MECH NO.:** g500676
- ELECTRICAL POWER:** [Blank]
- SERVICE:** [Blank]
- FIGURE:** [Blank]
- MAJOR INSPECTION REQUIREMENTS:**
 - 2.1 INSPECT LOWER OUTER WING PANEL FOR CAT RISER RUN-OUT AREA PLACED TO ADANCE WITH TO 1C-141D-31
- VIEW PARTS** (button)
- VIEW T.O. PAGES** (button)
- IS INSPECTION OK?** (prompt) with **YES** and **NO** buttons.

This is the ISO inspection screen. Notice that this screen is linked to the T.O. pages which describe the inspection and to digital pictures of the inspection area. The inspector performs the inspection and answer the yes or no question: "Is Inspection OK." If the inspector answers "YES", he is done with the inspection and can do another inspection. If he answers "NO", he advances to the next screen and starts to fill out the discrepancy action paper work.

Building the G081 Entry

Selection and Entry Sub-Form

Part Description: Inner Wing Box Rear Beam Cap Done Cancel

Location: Wbff5 374 Pal B: 51 Riser # 51

Side: LH Surface: Upper Hole #: 1234

A/C Area	Sub Assy	Component	Part	Detail
Center Wing	Flaps	Access Door	Flaps	
Fuselage	Leading Edge	Beam Web		
Wing Slab	Spars	Chin		
Wing Slab	Trailing Edge	Fillet		
Wing		Panel		
Outer Wing		Hub		
Wing Slab		Stiffener		

Record 1 of 1

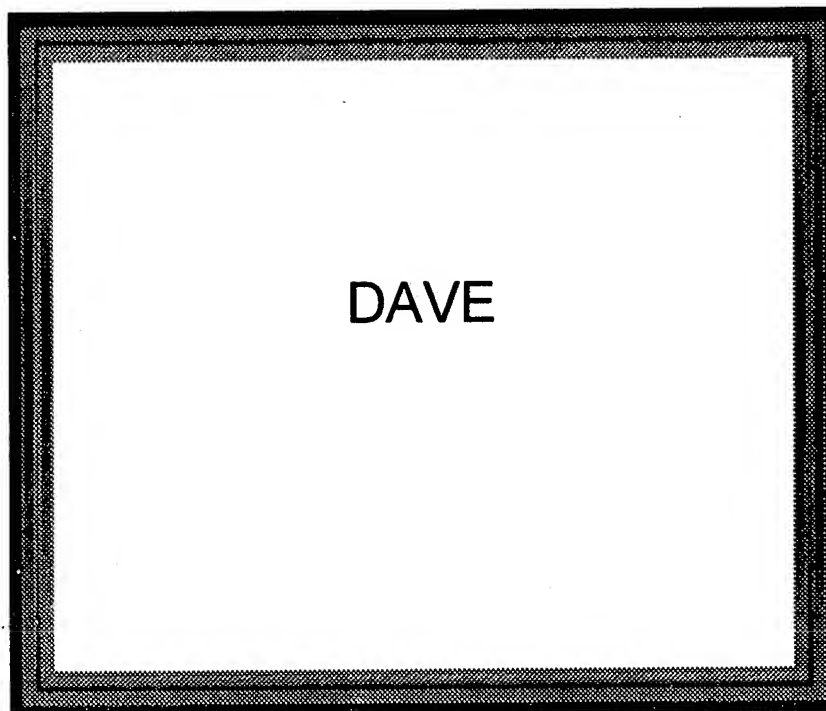
This is the screen where the inspector defines the discrepant part. Before he can advance from this screen, information such as location and part description must be filled in. The discrepancy (i.e. corrosion, crack, etc.) and the corrective action (remove and replace, SAI, etc.) are selected from similar screens. Selecting answers in this manner assures accurate information.

Transfer to G081

Print Current Record Print All Records Back Up									
SERIAL NUMBER 61-2775					CARD NUMBER: M-001 12.				
SYM:	ICN:	WDC:	DATE DISC:	INFO:	WUC/REFDES:	TAG:	DATE TRANS TO K:		
WE	14567	123	4/25/95		123	QA	03/13/95		
DISCREPANCY:					FAULT CODE:	DATE CAW:	STA CODE:		
Upper LH WS23, Pnl #2, Riser #4 Center Wing Box					A	03/15/95	CHAR		
Beam Cap 3/4 thru crack					CORRECTIVE ACTION:				
					REMOVE/REPLACE SEGMENT PER 3W2912H				
DISCOVERED BY:					GRADE EMP NO:		INSPECTED BY:		
Joseph Edward Tanner					NDI 6580676		Joseph Edward Tanner		
					NDI 6580676		GRADE EMP NO:		
							18 6467345		

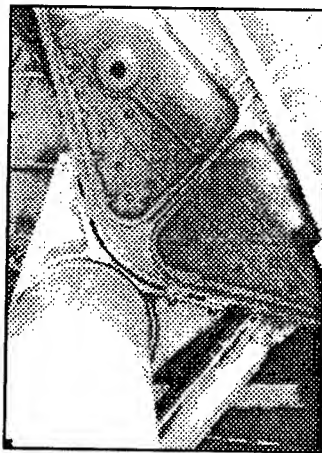
Record 1 of 1

This is an electronic copy of the 781A form. The 781A form is the C-141 Bases' discrepancy and corrective action paper work. On the form is the information, that prior to OSCAR, was manually typed into the F9050 and F8070 forms in G081. With OSCAR, the 781A form is filled out by the inspector himself. The data on the form is already in the G081 format and it also contains all the required information for the C-141 Repair Tracking Database. Using OSCAR will not only improve data completeness and accuracy, it will also save time at the C-141 Bases by eliminating paper work and by allowing managers to easily track problems and open paper work.

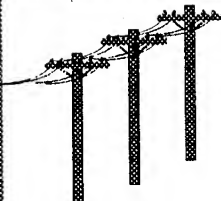


DAVE stands for Damage Assessment by Visual Enhancement. DAVE is digital pictures taken from a digital camera or a standard camcorder.

Digital Picture of Discrepancy



DAVE provides a digital picture of the discrepancy and/or the corrective action. The digital picture will help engineers at WR-ALC define inspection intervals for the repair. DAVE, when used in conjunction with OSCAR, will also help inspectors locate and inspect the repair.

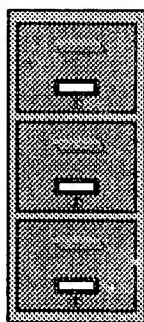


**Transfer Data
Using G081 and Assign
Inspection Requirements**

- **Upload Via Direct Data Link With G081**
- **Down Load From G081 to Depot**
- **Assign Inspection Intervals Using Tracking Zones and Other Programs**
- **Upload Completed Data to Repair Tracking Database**

The next step is to transfer the inspection results to the G081 and assign inspection intervals. The information can be transferred from the bases to the G081 and then down loaded at the Depot. Engineers assign inspection intervals by factoring the inspection intervals of adjacent tracking zones or by performing a damage tolerance analysis. Next, the data is up loaded to the Repair Tracking Database.

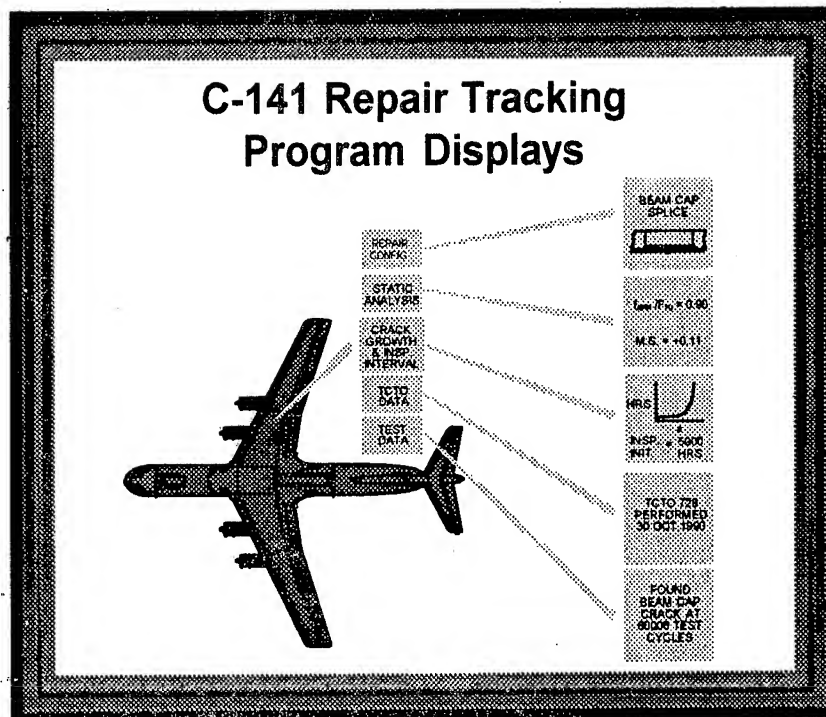
Repair Tracking Database



- Program Updates Projected inspection Data Monthly
- Can Be Sorted By Single Aircraft or Groups of Aircraft
- Can Be Sorted for General Location
- Can Be sorted For Over Due Inspections
- Can Be Sorted By Parts or Location
- Link to G081 - This Means REAL-TIME Data

Once the repair data is up loaded to the Repair Tracking Database, projected inspection dates are calculated. These dates are calculated using the flight hours since last inspection, inspection interval, and the repair location severity factor. The severity factor converts the flight hours flown to damage hours flown. The damage hours flown are subtracted from the flight hours remaining till inspection (inspection interval) and a date function is used to project the inspection date.

The information in the Repair Tracking Database can be sorted in many ways. The data can be sorted by single aircraft, groups of aircraft, location, over due inspections, etc. These sorts allow the engineer to not only add inspections for the aircraft during ISOs or PDMs but it also allows him to locate new hot spots on the aircraft or in the Force. Furthermore, linking the database to the G081 means real-time data.

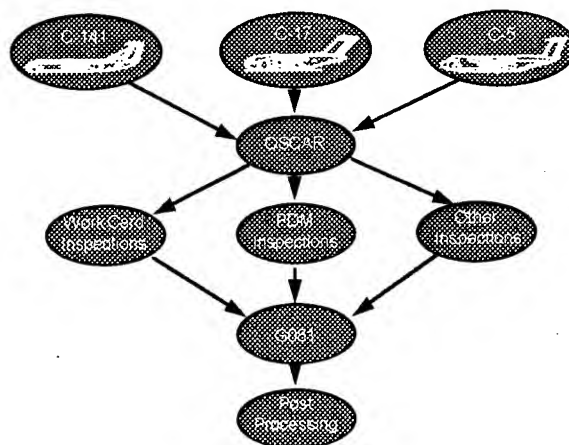


The sorted data is plotted on a picture of the C-141 and the user selects a repair location. The engineer can view a description and picture of the repair, check the static analysis, review the crack growth curve and inspection requirements, look over the TCTO data, and see any test data.

[illegible]

865

Cross Weapon System Repair Tracking Program



A similar Repair Tracking Program could easily be created for any aircraft. OSCAR collects the inspection/repair data. The data is transferred through G081. Finally, the data can be post processed and inspection dates projected.

The Future

- **Voice Activated Software**
- **Networked to G081**
- **Add inspections to the G081 -6 Work Cards**

The future looks busy for the C-141 Repair Tracking Program. Voice activated software will be investigated. The linked through G081 must be established. Finally, the inspection requirements generated by the program need to be available at ISOs and PDMs through G081's -6 Work Cards.

The ForceTec® Rivetless Nut Plate System and its Application to Military Aircraft Production and Repair

***Mr. Len Reid, Vice President of Engineering
Mr. Eric Easterbrook, Engineering Manager
Fatigue Technology Inc.
100 Andover Park West, Seattle, WA 98188-2868**

ABSTRACT

This paper discusses an advanced design rivetless nut plate which overcomes inherent problems associated with both typical riveted and rivetless nut plates used in blind assembly of aerospace structures. The ForceTec® (FtCx_m) rivetless nut plate system uses cold expansion technology to expand a nut plate (retainer) into the fastener hole. Torque and push-out resistance are achieved by the resulting high interference fit of the retainer. ForceTec meets MIL-N-25027 specifications in both aluminum and titanium structure and has been qualified and specified for F-22 production in typical blind nut areas as well as primary structural attachment. It is being evaluated for a number of other military production and repair applications. The design and system characteristics of ForceTec are presented, along with a brief description of military production and repair applications.

INTRODUCTION

Aerospace structures incorporate a wide variety of fastening methods to facilitate assembly of components and structural assemblies. Many of these applications require use of blind fastening systems, the most common of these being riveted nut plates. The attaching satellite rivet holes add to the complexity and cost of manufacture and assembly. They are also a major source of fatigue-induced structural cracks. Attempts to produce an effective "rivetless" nut plate have been marginally successful because these systems do not meet the necessary resistance to push-out and torque. Most have mechanical locking features that have a negative effect on fatigue.

An advanced design rivetless nut plate called ForceTec[®] (FtCx_m), which overcomes the inherent problems associated with both typical riveted and rivetless nut plate configurations, has been developed by Fatigue Technology Inc. to meet the requirements of MIL-N-25027 [1]. ForceTec is incorporated into the design of the F-22 in typical blind nut areas as well as primary structural attachment to facilitate aircraft assembly. It is also being evaluated for use on C-17 production as well as repair applications on F-16, F-5/T-38 and F-15. It is also being used in a C-130 modification. Commercial applications include Boeing 737 and Global Express production as well as Airbus A300 and Boeing 747 repairs.

CURRENT NUT PLATE CONFIGURATIONS

Current riveted nut plates have provided an effective means of captivating a blind nut to facilitate assembly. However, in highly loaded or fatigue-critical locations, riveted nut plates pose a problem for design and manufacturing engineers. Usually, three holes are required which increases the local stress concentration of the installation and requires specific orientation to the free edge. Typical fatigue cracks associated with riveted nut plates are shown in Figure 1.

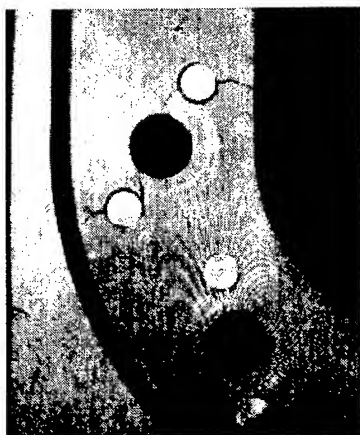


Figure 1
Typical Fatigue Crack
Originating at Riveted
Nut Plate

Other installation problems include drill bit breakage while drilling the small rivet holes, especially in high strength material, and the use of special gang channel assemblies to captivate a series of nuts for an access panel attachment which adds to the weight of the joint.

RIVETLESS STYLE NUT PLATES

Existing rivetless style nut plates either rely on adhesives, mechanical interference (splines or lobes), anti-torque pins or posts, swaging/flaring, or combination of these to meet torque and push-out requirements. Some other types do not provide a changeable or floating nut capability. The use of mechanical devices to prevent rotation often induce stress risers

that initiate fatigue problems. In general, these rivetless styles have not been fully successful although they have found some application. They are not used for primary structural attachment. Some examples of mechanically restrained rivetless nut plates are shown in Figure 2.

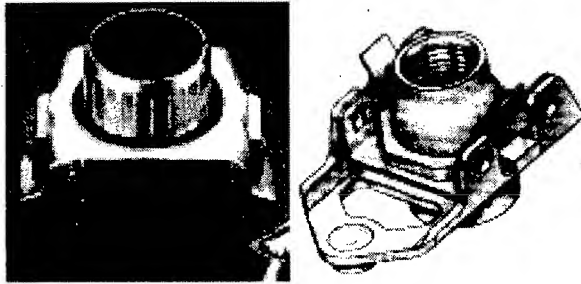


Figure 2
Examples of Mechanically
Restrained Rivetless Nut Plates

FORCETEC RIVETLESS NUT PLATE SYSTEM

Fatigue Technology Inc. (FTI) of Seattle, Washington, has developed and tested a patented rivetless nut plate system, ForceTec (FtCx), which provides a faster and more consistent installation compared to conventional riveted and rivetless nut plate installations. By the unique method of this installation, it also provides significant

fatigue life improvement of the basic structure. Unlike the riveted or swaged-in nut plates, the ForceTec system utilizes a combination of FTI's Split Sleeve Cold Expansion[™] (SsCx[™]) [2] and ForceMate (FmCx[™]) bushing cold expansion technologies [3] to expand a nut retainer into the actual fastener hole. The ForceTec concept is shown in Figure 3.

The single piece retainer fits into an oversize fastener hole. It is not restrained by rivets nor does it have any integral splines to resist torque and does not require swaging or flaring. Torque and push-out resistance is provided by the high interference fit of the retainer into the material. Furthermore, the hole is protected from fastener fretting and elongation by the bushing-like retainer. Alignment of the mating holes is also ensured by the installation concentricity of the retainer in the actual fastener hole.

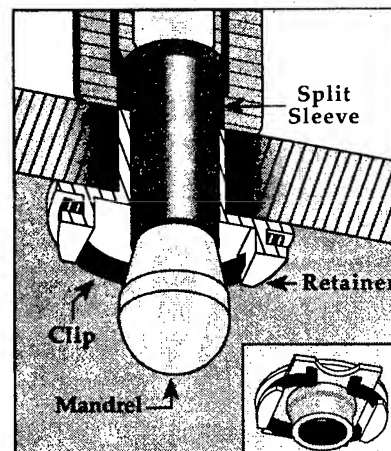


Figure 3
Schematic of ForceTec
Retainer Expansion

The retainer has an integral "basket" incorporating a flexible clip, that will accept and captivate a variety of NAS 1793 or 1794 standard floating locking nuts. A typical installation assembly used to attach a cover plate is shown in Figure 4.

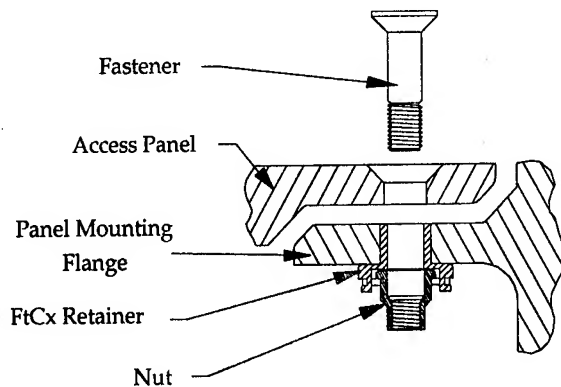


Figure 4
Typical ForceTec Nut Plate
Installation

PROCESS OVERVIEW

Installation of the ForceTec retainer is accomplished by using the method of Split Sleeve Cold Expansion (SsCx) used by industry to extend the fatigue and crack growth lives of typical fastener holes [4]. In a typical installation, an initially clearance fit retainer is placed into a prepared starting hole (fastener hole) in the structure. A pre-lubricated split sleeve is placed over a tapered expansion mandrel, which is attached to a hydraulically operated puller unit as shown in Figure 5.

The mandrel/sleeve combination is placed into the retainer assembly and the puller unit is activated. The nose cap of the puller unit holds the split sleeve in the retainer while the mandrel is pulled through it. As the major diameter of the mandrel passes through the sleeve and retainer, both the retainer and the surrounding base material are subjected to radial expansion forces. These forces yield the retainer and parent material, which results in a residual compressive stress around the hole. This stress effectively shields the hole from cyclic tensile stresses that propagate fatigue cracks. After installation, the disposable split sleeve is removed and discarded.

Retainer lengths are available in 0.010 inch increments; however, if the bushing end of the retainer is overflush after installation, it can be trimmed to flush. Finally, the nut is inserted into the basket end of the retainer. In service, fasteners can be installed and removed, and the nut element can be replaced as required, similar to conventional nut plate systems.

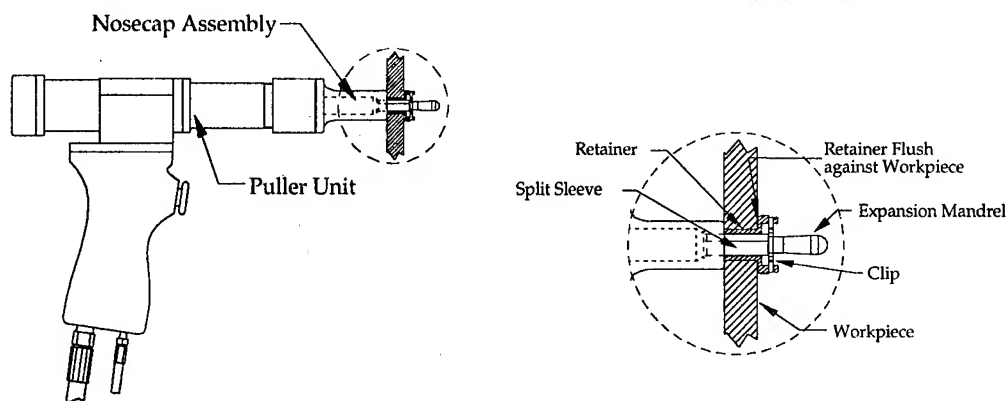


Figure 5
Tooling Associated with ForceTec Nut Plate Installation

The retainer assembly is held in place by the resultant high interference fit between the retainer and surrounding base material. The combined effect of high interference and the residual compressive stresses from cold expansion, prevent rotation of the retainer and also provide significant fatigue and crack growth life improvement of the structure.

Although the starting hole required for the ForceTec retainer is larger than the fastener hole for a conventional riveted nut plate, the effective stress concentration at the hole is reduced by the compressive residual stresses of cold expansion and by elimination of the satellite rivet holes. Fatigue testing has shown that no allowance is needed to compensate for the reduced effective edge margin resulting from the larger starting hole needed for the ForceTec system. In fact, all tests with ForceTec have shown considerable life improvement in this configuration over other nut plate systems. Results discussed later from tear-out tests have also shown no reduction in tear-out values compared to a nominal fastener at 2-D edge margin.

SYSTEM PARAMETERS

The FtCx system is designed for use in a wide range of aerospace materials such as aluminum, titanium, steel and high temperature alloys. An adaptation of the process, currently in development, will allow for its use in some composite materials.

The standard FtCx system covers a range of four sizes ranging from 3/16 inch to 3/8 inch. Sizes extending up to 9/16 inch have been developed for specific F-22 modular applications. Retainers are available in 17-4 H1025 passivated stainless steel and annealed Ti 6Al-4V. The stainless retainers have been designed for use in aluminum and steel applications. These retainers may be installed with wet sealants or may be covered with protective coatings prior to installation. The titanium retainers have been designed for titanium structure and other moderately high temperature applications. These retainers are typically installed without protective coatings because of the galvanic compatibility. These also may be wet installed to meet particular requirements. For those applications where there is a high operating temperature, retainers have been successfully made from Inconel 718.

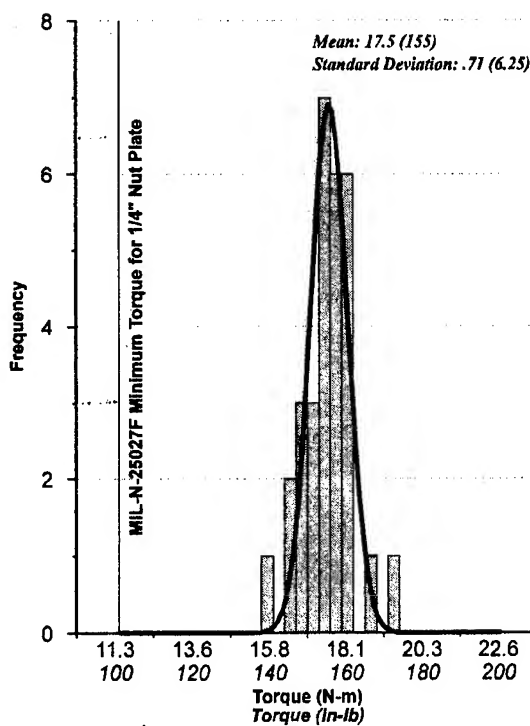


Figure 6
Distribution of Torque Values
for 2.5 mm Length 4-0-1 Titanium
Retainers Installed in
Ti-6Al-4V (30 Installations)

Retainers are available in three distinct classes of fit with the fastener. The Class I fit requires a final ream after installation and is for those areas requiring a 0.000 to 0.004 inch clearance fit. The Class II and III fits do not require a final ream after installation and provide clearance fit ranges of 0.000 inch to 0.007 inch and 0.029 inch to 0.041 inch, respectively.

There are a number of factors that determine the resistance of the retainer to torque and push-out force. These are identified as retainer and parent material properties, installed interference and surface finish. Because the installation parameters and material properties are tightly controlled, the retainer's resistance to removal forces is reduced primarily due to the thickness of the structure, i.e., frictional forces. Through statistical analysis of test results, the minimum thickness in which the retainer meets

the MIL-N-25027 torque and push-out requirements has been established for each size and class of fit. The limiting performance factor on the retainers is typically torque resistance. An example of the design torque values for a 1/4 inch titanium retainer installed in 0.100 inch (2.5 mm) thick materials is shown in Figure 6.

STRUCTURAL ADVANTAGES OF NEW SYSTEM

The key benefits of ForceTec over riveted and other types of blind nut plates are: 1) the reduction in stress concentration (K_t) by having only one hole, 2) lack of mechanical anti-torque splines on the barrel which can induce stress risers, and 3) a secure, single hole fastener attachment to provide a positive load transfer at the joint. The other important advantages for design and stress engineers are the greatly improved fatigue life of the ForceTec nut plate installation and the potential for reducing the weight of the surrounding structure because of this increased fatigue life.

FATIGUE LIFE BENEFITS - Cold expansion creates a zone of beneficial residual compressive stresses around a hole. These compressive stresses effectively reduce the

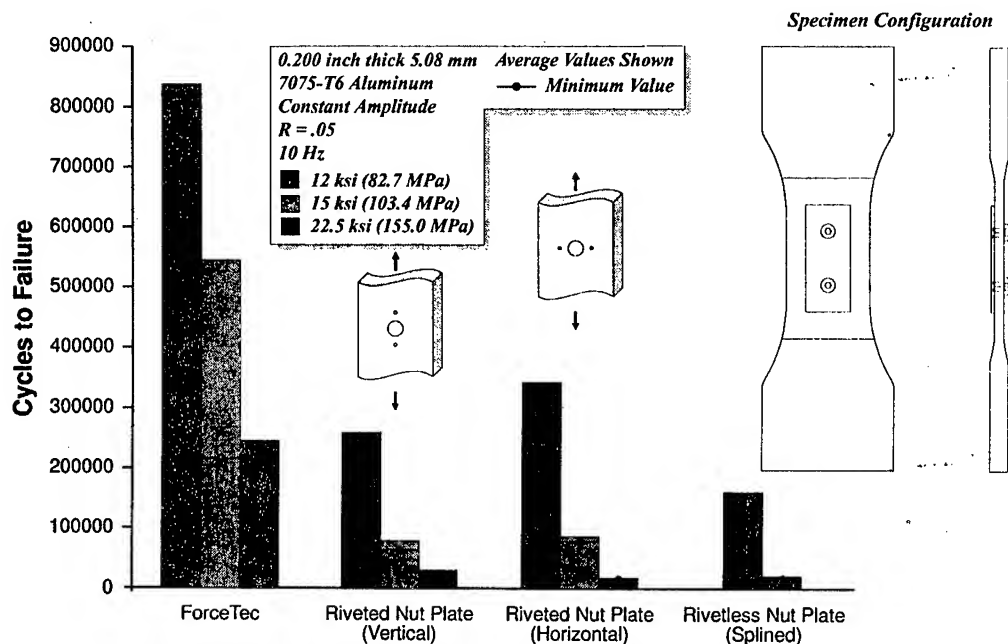


Figure 7
 Comparative Fatigue Test Results for Low Load - Transfer Specimen

magnitude of applied cyclic tensile stresses and thereby increase fatigue and crack growth life. Additionally, similar to interference fit pins; interference fit bushings have also been shown to provide fatigue life enhancement of a bushed hole through a reduction in applied cyclic stress range at a hole [3].

The ForceTec retainer is installed at typically 4% to 7.5% applied expansion, depending on fastener diameter size. This results in retainer to parent material interference fit levels of about 0.002 inch (0.05 mm) to 0.006 inch (0.15 mm). These interference levels will depend on the applied expansion level, manufacturing tolerances, the ratio of retainer modulus to the material modulus and the final diameter of the retainer. Comparative fatigue test results from a low load-transfer specimen are shown in Figure 7 for different stress levels [5].

ForceTec specimens show significant life improvement over all other methods tested. This improvement has also been shown when using ForceTec retainers to rework existing riveted nut plate installations where fatigue cracks have originated at either the satellite rivet holes or the fastener hole. Validation testing of such repairs in various commercial and military aircraft applications is continuing.

POTENTIAL WEIGHT SAVINGS - The weight savings associated with nut plate types is typically associated with the differences in weight of the nut plate elements (i.e. weight of retainer and nut assembly). However, due to the fatigue life

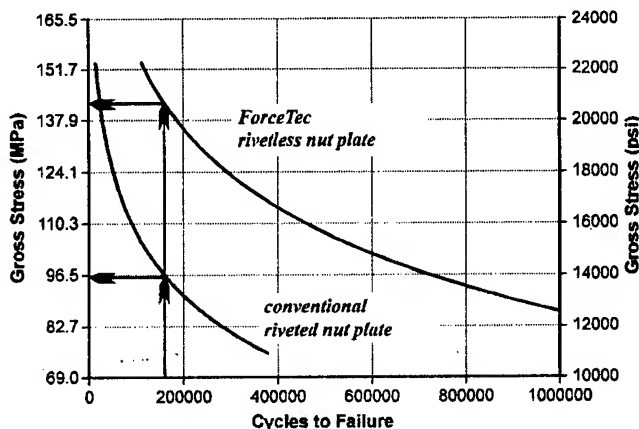


Figure 8
Comparison of Fatigue Life Improvement vs.
Stress Level as Potential for Weight Savings

benefits using the ForceTec system, additional weight savings may be obtained by reducing the structural thickness of material in the area of the nut plate. As shown in Figure 8, structural fatigue life may be extended for a given operating stress level compared to other nut plate installations.

Alternatively, by maintaining a constant fatigue life, the local stress level could be in-

creased. This increase in stress could be achieved by maintaining the same loads and reducing the thickness of the parent material. This would result in an actual reduction in structural weight without decreasing the fatigue life of the part. A combination of these two approaches could be used to optimize the benefits.

SEALED NUT VERSION

A sealed nut version of the ForceTec nut plate has been designed to accept a modified sealed or domed riveted nut plate, defined by NAS 1473 and 1474. Again, the sealed or domed nut element is replaceable. No allowance was made in the retainer basket design to accommodate float since the nut is allowed to float inside the sealing dome. The sealed nut plate assembly is also designed to meet the installed sealing requirement of the NAS sealed nut plate specification. Static and cyclic leak tests were conducted to ensure sealing was positive with and without the attaching bolt installed in a typical aviation fuel environment.

Sealed nut plate retainers made from titanium are specified for a number of locations on the F-22 wing. The small footprint of the titanium retainer and snap-on style domed nut was ideal for the F-22 wing structure.

COMPOSITE APPLICATIONS

The use of ForceTec retainers in composites is still in the experimental stage. Installation of ForceTec retainers in metals results in cold expansion of the hole in the structure in combination with a high interference fit. In composites, the amount of initial expansion is tailored to ensure insert retention while precluding the occurrence of delaminations or local fiber buckling. As a result, the final interference and hence retention force and resistance to rotation in a composite installation is somewhat less than in a standard metal installation.

Trial installations of ForceTec in composite samples have shown potential to meet the metallic material torque and push-out values as detailed in MIL-N-25027.

The single hole configuration is preferred to minimize composite delamination and secondary damage to the composite matrix. Although adhesively bonded nut plates

are used in some applications, in general, they do not meet durability requirements under repeated loads. ForceTec retainers in composites will generally be point designed for the specific application, composite material and structure.

OPEN-HOLE COMPRESSION IN COMPOSITES - A strength comparison test using composite open-hole compression specimens was performed to evaluate the potential beneficial effects of the ForceTec retainers to the strength of a composite laminate. The results of this test are summarized in FTI Technical Report #50542. Testing was performed on specimens made from graphite-epoxy composite material provided by McDonnell Douglas. The compressive strengths of specimens with no holes (baseline), open hole specimens and specimens with holes filled with FtCx retainers were compared. The open hole compressive strength was 65% of the baseline specimens; a reduction typical for composites. The compressive strength of specimens with FtCx retainers was 95% of the baseline specimens (no hole) strength. Results are shown in Figure 9. Putting it another way, with 23% of the net area

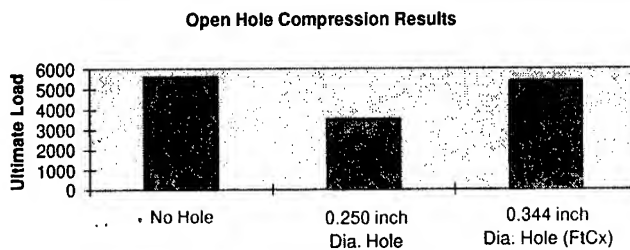


Figure 9
Open Hole Compression Results

removed by the hole the FtCx retainer was able to almost match the no-hole specimen strength. This test shows the tremendous potential for improving static strength of fastened composite structure.

In addition to the compression test discussed retention testing was performed on two FtCx retainers installed into a spare specimen from the open-hole compression portion of the test. The minimum torque and push-out requirements of MIL-N-25027G for 0.250 inch fastener nut plates are 100 inch-pounds and 125 pounds, respectively. The torque and push-out values recorded from the test were 144 in-lbs and 296 lbs, respectively. The data is even more impressive when one considers that the baseline thickness of the laminate was approximately 0.078 inches.

FORCETEC QUALIFICATION

The FtCx retainers have been qualified to a rigorous standard set by the F-22 partners. The retainers must meet prescribed break-away torque and push-out values at ambient conditions. Additional qualification efforts, using reusability torque and push-out requirements, were performed on retainers immersed in water, hydraulic fuel, jet fuel and exposure to temperatures up to 400°F. (Results of the F-22 partner tests were not available for release at presentation of this paper.)

A number of other tests not required for qualification have been completed to assure complete reliability of the system. These tests included:

- Fatigue
 - under zero load transfer
 - in a load transfer configuration
- Break-away torque and push-out after fatigue cycling
- Static shear out
- Weight Comparison
- Corrosion

A short summary of each of the tests follows.

FATIGUE USING ZERO LOAD TRANSFER

This simple test was one of the first test conducted on the FtCx system. Typical dogbones specimens made from 7075-T651 aluminum were tested under zero load transfer conditions. The specimens were fitted with a 1/4 inch FtCx retainer and compared with an open hole baseline. The test conditions were 30 ksi gross stress, R-ratio of 0.05 and 20 Hz. Under these fairly severe stress conditions the FtCx system provided a life improvement of 3.7:1.

FATIGUE IN A LOAD TRANSFER CONFIGURATION

Results of fatigue load transfer testing were previously discussed. Additional generic testing and some application-specific tests are being conducted at FTI and by other aircraft manufacturers.

BREAK-AWAY TORQUE AND PUSH-OUT AFTER FATIGUE CYCLING

Basic ForceTec torque and push-out specifications have been established on as-installed retainers. Recent testing at an airframe manufacturer showed that the FtCx retainers still met the MIL-N-25027 torque and push-out specifications even after being cycled for more than one million cycles.

STATIC SHEAR OUT

A concern expressed about the FtCx system is its impact on the edge margin of existing structure. As an example a -4 Class II (1/4 inch) retainer has an approximate outside diameter of 0.344 inches. When used as a direct replacement for a riveted nut plate with a center hole of 0.255 inches diameter and an edge margin (e/D) of 2.0, the installed FtCx edge margin reduces to about 1.5. This reduction of edge margin has raised concerns about static margins. A shear-out test was done using the ASTM E-238 specification as a guideline. The predicted reduction in

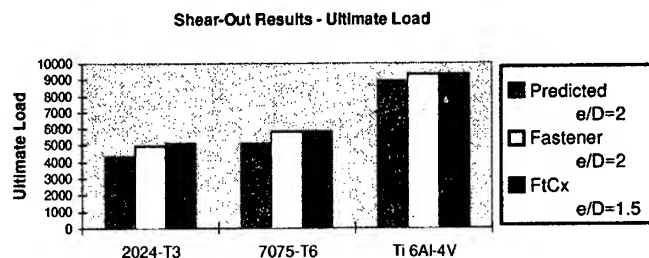


Figure 10

Shear-Out Results - Ultimate Load

shear-out capability did not match well to the test data. It turns out that the prediction was too low as the data shows the shear out strength of the reduced e/D of 1.5 (with FtCx) is equal to the baseline e/D of 2.0 as shown in Figure 10. It appears that the failure mode transitions from a shear failure for the riveted nut plate configuration to a bearing failure for the FtCx installation. This may explain the increase in static strength of the ForceTec installation.

WEIGHT COMPARISON

An installation test was conducted on NAS1791C3-2 riveted nut plates and an equivalent FtCx rivetless nut plate to determine the difference in installed weight.

Titanium FtCx retainers, installed in titanium parent material, resulted in an installed weight savings of approximately four percent when compared to installed NAS1791C3-2 riveted nut plates. For this example the installed weight savings is 0.075 kilograms (0.165 pounds) for every 100 installed parts (3% lighter). Stainless steel retainers installed in aluminum specimens were 0.82% heavier than conventional installed riveted nut plates.

CORROSION

A test conducted to the ASTM B117 standard has shown that shaved 17-4 stainless steel FtCx retainers can withstand the rigors of the 96-hour salt spray without evidence of corrosion when properly treated. The shaving process removes the surface passivation. Results of this test are summarized in FTI Technical Report #49742. Under the conditions tested, it appears that treatment of the surface of the installed retainer is more important than treating the bore of the hole prior to installation. It is essential that a surface protection compound be applied to the shaved retainer end to provide a barrier against the environment.

Results showed that retainers treated with rubberized sealant provided the best barrier between the retainer and plate to preclude galvanic corrosion. Shaved ends treated with MIL-C-5541 alodine and the MIL-P-85582 primer also provided excellent resistance to corrosion. Using MIL-C-5541 alodine solution alone as a corrosion barrier did not provide an acceptable level of galvanic corrosion resistance. Treating the shaved ends with a two-part epoxy was also not adequate in preventing corrosion.

Unshaved (as installed) retainers coated with IVD and phenolic resin showed good resistance to galvanic corrosion. Further testing of retainer coatings and surface treatments after shaving is planned to determine the best available level of galvanic corrosion protection without affecting the process specifications or qualification parameters. Retainers can also be wet installed with MIL-P85582 primer with only a slight reduction in torque resistance.

CURRENT MILITARY APPLICATIONS

F-22 Aircraft - The FtCx system is being used in a large number of locations on the F-22 wing, wing carry-through bulkheads (which are fracture-critical) and other areas. Approximately 6000 retainers, comprising sealed and non-sealed, stainless and titanium retainers, will be installed. The proven benefits for the F-22 include installation ease, fatigue life improvement and weight savings. The sizes of the retainers range from 3/16 inch to 1/2 inch. A 9/16 inch diameter retainer has been designed and built as an oversize contingency. ForceTec will also be used for primary structural attachment to facilitate final assembly.

Other areas on the F-22 where ForceTec is being tested or considered include:

- wing upper surface (compression dominated spectrum)
- metal composite stack-up areas
- composite structural locations

C-130 GUNSHIP MODIFICATION - Chrysler Technologies is designing an upgrade to aft fuselage electronics area in the C-130 Gunship. Part of the modification involves changing structure that contains 56 nut plates. The parent material is 7050-T7541 aluminum and has a configuration such that there is 20 degree angle to the front side of the hole. FtCx retainers, pre-angled to match the surface, will be installed as a repair/rework method. Because of the angled configuration of the retainer barrel it is important that the installation be done with an alignment fixture.

POTENTIAL MILITARY APPLICATIONS

The following potential military applications incorporating ForceTec are being reviewed:

- T-38 - Lower wing surface, "D" panel and aileron access panel
- F-5 - Cockpit longeron repair
- F-15 - Lower wing skin access panel, gang channel repair
- F-14 - Left sponson top deck access panel
- C-17 - Several locations on the C-17 which have reported fatigue cracking

associated with riveted nut plates are being considered for ForceTec, including nacelle redesign

- C-130J - Cargo rails
- F-16 - Rework of upper fuselage skin access panel (discussed under "Repair/Rework" section)

C-141 LAP SPLICE - A test is planned to determine the viability of a repair using either BushLoc or ForceTec. When detectable cracks around the fastener holes are relatively small the proposed repair method is to simply ream out the holes enough to remove the crack then install repair bushings/retainers using cold expansion technology. The bushing/retainer repair allows for fastener standardization.

The test will evaluate the effects of hole diameter, bushing/retainer expansion, and edge distance on the fatigue lives of the 7075-T6511 aluminum panels. Specimens will be tested under a C-141 flight-by-flight spectrum representative of the lower inner wing panel. Test specimens will be fabricated from an actual C-141 wing panel.

REPAIR/REWORK POTENTIAL

ForceTec has been considered for rework applications to repair and prevent cracking from installed riveted nut plate applications. An evaluation test program was conducted on an F-16 fuselage access panel area. Brief details of this rework evaluation follow. A similar repair is already being carried out on a commercial aircraft application on Airbus A330-600 lower wing access panel holes. ForceTec retainers are being installed to replace riveted nut plates. These are removed, the satellite rivet holes are plugged, and a sealed nut ForceTec retainer is installed in the enlarged fastener hole.

F-16 REWORK - FTI Manufactured and assembled zero load transfer specimens designed by Lockheed Fort Worth that simulated the upper fuselage skin of the F-16. The specimens included a fitting with twelve nut plate locations with rivets angled at either 30° or 45° to the load line. One of the configurations had FtCx retainers installed in the fastener holes and interference fit pins in cold expanded rivet holes.

The specimens were tested under variable amplitude F-16 spectrum loading using a spectrum file provided by Lockheed and cycled at an average frequency of 5 Hz. The

maximum peak spectrum load was 32,250 lbs that corresponded to a peak stress of 74.5 ksi. Specimens were reworked at 2000 equivalent flight hours. This was the expected time for rework to be performed on the aircraft. After rework, testing was continued on the specimens to failure or 16,000 equivalent flight hours. Failure was defined as a crack through the web from the edge of the hole to the radius.

Both of the specimen configurations fitted with FtCx rivetless nut plates and interference fit pins produced life improvement of at least 3:1 over baseline riveted specimens as shown in Figure 11.

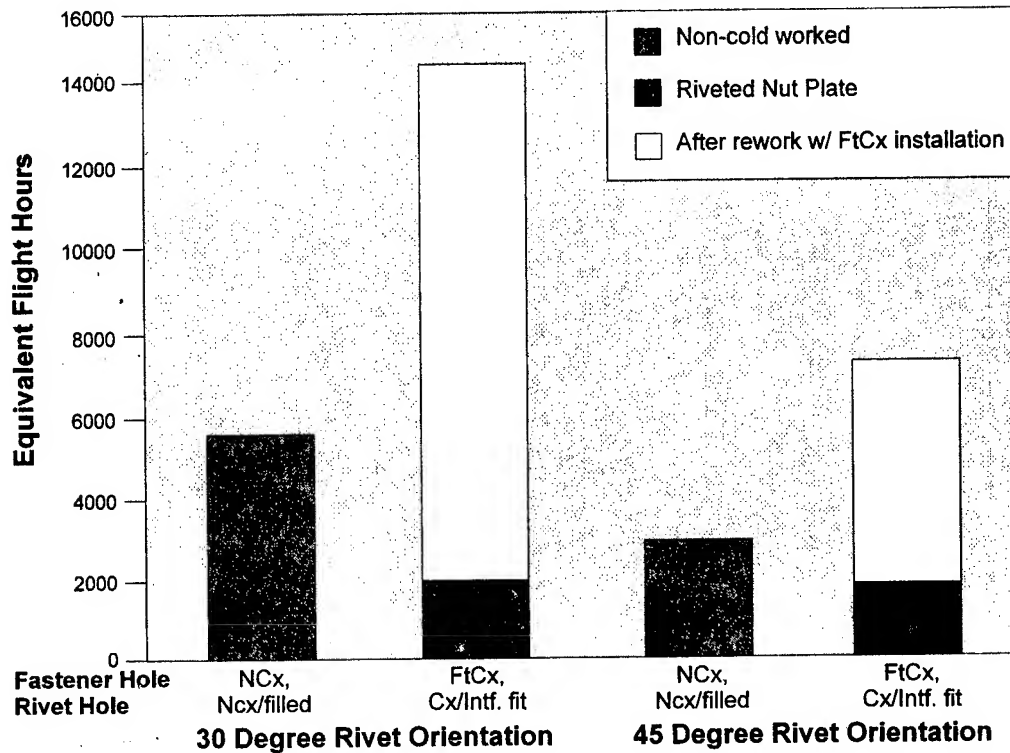


Figure 11: F-16 Rework Test Data Summary

SUMMARY

ForceTec is a fully qualified rivetless nut plate which accommodates a floating and easily changeable nut element to MIL-N-25027 specifications. The ForceTec system has been accepted for military and commercial aircraft production and repair. Military applications include:

- F-22 - wing, carry through bulkheads and fuselage
- C-130 - aft fuselage fitting modification

There are a number of potential military applications under consideration on the F-16, F-14, F-15, F-5, T-38, C-141 and C-130J.

Comparative fatigue/load transfer testing confirms the suitability of ForceTec in fatigue loaded structure and for primary structural attachment. Parts of the F-22 will utilize ForceTec to facilitate primary structural assembly.

A comprehensive test program on an F-16 repair showed the suitability of ForceTec to rework existing riveted nut plate configurations. A similar repair is already applied to a commercial aircraft.

Shear-out tests conducted on a reduced edge-margin ForceTec installation showed that ForceTec restored shear-out resistance to the equivalent e/D of the original fastener. The combination of this result and the fatigue life benefit attained from the cold expanded retainer confirm the suitability of ForceTec to directly replace existing design fastener or riveted nut plate configurations without re-designing the joint to increase the edge-margin.

The use of ForceTec in composite structure is also possible under controlled conditions. ForceTec filled holes in composite restored the compressive strength to 95% of the composite with no hole. MIL-N-25027 torque and push-out specifications for metals have been achieved on thin composite panels.

All tests have shown ForceTec to be a superior blind nut attachment for all structural applications on military aircraft.

REFERENCES

- [1] Military Specification MIL-N-25027F, "Nut, Self-Locking, 250 Deg. F, 450 Deg. F, and 800 Deg. F," February, 1994.
- [2] Fatigue Technology Inc. Engineering Process Specification FTI8101C, "Cold Expansion of Holes Using the Standard Split Sleeve System (SsCxÔ) and Countersink Cold ExpansionÔ (CsCxÔ)," July, 1994.
- [3] Champoux, R. L., Landy, M. A., "Fatigue Life Enhancement and High Interference Bushing Installation Using the ForceMate Bushing Installation Technique," Fatigue in Mechanically Fastened Composites and Metallic Joints, ASTM STP 927, John A. Potter, Ed., American Society for Testing and Materials, Philadelphia, 1986, pp. 39-52.
- [4] Reid, L., Easterbrook, E. T., Rufin, A. C., "Production and Repair of Fastened Joints Incorporating Cold Expansion," SAE Technical Paper Series 922400, Aerofast '92, October 1992.
- [5] Fatigue Technology Inc. Technical Report #92045-1, "Fatigue Performance Comparison Testing of the ForceTec Rivetless Nut Plate," February, 1992.

Design Development of a Bonded Fuselage Repair for the C-5A

**Major Robert Fredell
Mr. Cornelis Guijt*
HQ USAFA/DFEM
2354 Fairchild Drive, Suite 6H2
USAF Academy, CO 80840-6240**

**Lieutenant David Conley*
WL/FIBEC
Bldg 65
2130 Eighth Street, Suite 1
Wright Patterson AFB, OH 45433-7542**

**Lieutenant Shane Knighton
Mr. Elias Collas
SA-ALC LADD
Building 323
514 Shop Lane, Suite 2
Kelly AFB, TX 78209**

ABSTRACT

The aging of the world jet transport fleet has led researchers and maintenance engineers to seek advanced technology solutions to the problems of stress corrosion cracking and widespread fatigue damage. Adhesively bonded composite repairs give the maintenance engineer an additional tool to deal effectively with fatigue cracks in tension structures.

This paper describes the development of a bonded composite repair for cracks in the crown of the C-5A fuselage. Several composite patch materials were studied: Boron/epoxy, SP 500-2 carbon fiber/epoxy, and an S2 glass fiber/epoxy/aluminum laminate. Based on parametric analyses performed, boron/epoxy and the glass/epoxy/aluminum laminate) were continued into the experimentation phase. Fatigue tests were carried out on boron/epoxy and glass/epoxy/aluminum repairs to cracked new 2024-T3 and 7079-T6 aluminum panels taken from C-5A fuselages in service.

The experimental results matched the analytical studies in showing good to excellent crack retardation compared with unrepaired cracks. The better performance of the glass/epoxy/ aluminum patches was attributed to more closely matched thermal characteristics between the patch and the skin. Based on the analytical and experimental results, a prototype bonded repair was installed on an operational C-5A fuselage.

KEY WORDS: aging aircraft, bonded repair, composite materials, fatigue, thermal expansion.

Introduction

The challenge of aging aircraft grows more severe as the USAF transport fleet continues to age. For example, the average age of the KC-135 tanker fleet is now near 35 years, while the average age of a C-5A Galaxy is a relatively young 27 years. By contrast, the typical US airline operates a fleet that averages 10-15 years in age. Fatigue and corrosion of the geriatric transport fleet places constantly increasing burdens on the USAF maintenance organizations.

A typical sign of aging in the C-5A fleet is multiple small cracks in the upper (crown) section of the fuselage. The crown section experiences significant longitudinal tensile bending in addition to biaxial tension due to internal pressurization. Multiple short cracks (25 to 50 mm long) have been found in the crown of several aircraft. The cracks are believed to have nucleated in the rivet holes of the 7079-T6 aluminum skins due to high fit-up stresses induced in manufacturing. Riveted repairs have been attempted without success; new skin cracks nucleate quickly from the corner rivet holes attaching the patch. Thus, the remaining repair alternatives are a bonded repair or reskinning the affected area.

The following pages discuss the development and installation of bonded composite repairs to cracks in the C-5A fuselage crown. Analytical studies involved three composite patch materials, including SP 500-2 carbon fiber/epoxy, boron/epoxy, and the S2 glass fiber/ epoxy/aluminum laminate known as GLARE 2.

The parametric analyses performed confirmed earlier work indicating the dominant importance of patch coefficient of thermal expansion (CTE) in bonded repairs of cracks [1]. Moderate- to high-CTE patch materials were shown to be more effective in slowing or stopping crack growth than low-CTE patches.

As a result of the parametric studies, the two most promising patch materials were continued into the experimentation phase. Constant amplitude fatigue tests were carried out on bonded boron/epoxy and glass/epoxy/aluminum repairs to cracked 2024 T3 aluminum panels. The experimental results matched the analytical predictions. The glass/epoxy/aluminum patches stopped crack growth in the 2024 panels for over 200,000 cycles. At a 5% lower stress level, the boron/epoxy patches immediately re-initiated and grew at approximately twice the rate of the glass/epoxy/aluminum repairs. The better performance of the glass/epoxy/aluminum repairs was attributed to more closely matched thermal characteristics between the patch and the skin. Finally two glass/epoxy/aluminum repairs were tested on 7079-T6 panels taken from a C-5A in service.

The encouraging analytical and experimental results led to the installation of a prototype bonded repair on an operational C-5A fuselage. Successful service performance of the bonded repair promises to avoid the much more expensive re-skinning the fuselage crowns of the C-5A fleet.

Analysis of Candidate Bonded Repair Materials

Table 1 lists the key mechanical and physical properties of the candidate repair materials considered in this study.

Table 1. Properties of candidate repair materials.

<i>Material</i>	E_{11} , GPa	s_{ult} , MPa	α_{11} , $10^{-6}/^{\circ}\text{C}$	<i>Comments</i>
SP 500-2 carbon/epoxy	186	2190	-0.9	data for unidir. prepreg more drapable prepreg needs galvanic protection lowest CTE
fiber number boron/epoxy	210	1590	4.5	data for unidir. prepreg less drapable prepreg large experience base low CTE
S2 glass/epoxy/ 2024-T3 aluminum	68	1100	16	data for sheet material cold formable no shelf life limitation highest CTE

The material properties were input into a computer code used to perform a continuum analysis of the cracked C-5A fuselage crown structure. The computer code, known as CalcuRep for Windows, is a modified version of the Rose model. CalcuRep considers the bonded patch repair as a stiff inclusion in a sheet, and performs a two-step calculation to determine the following quantities:

- stress intensity factor (K) of the repaired crack,
- stress in the skin at the run-out of the patch, including thermal and bending effects,
- shear strain in the adhesive over the crack, and
- stress in the patch over the crack location.

All of the above include the complex effects of thermal expansion in the patch and skin, a detailed description of which may be found in [1,2]. Thermal effects in bonded repairs may be summarized as follows:

- *During the bonding operation*, typically carried out at 120 °C (250 °F), the patch expands freely, while the locally heat skin is constrained from free expansion by the surrounding cool structure. Thus, the *effective* expansion of the heated structure can be much less than the unconstrained coefficient of thermal expansion (CTE). When the adhesive cures, the bond line is stress free.
- *Upon cooling to room temperature*, the constraint of the surrounding stiffened structure disappears. Patches with a low CTE, which expanded approximately the same amount as the constrained locally heated structure, contract by the same amount, resulting in a relatively stress-free bond line at room temperature. Moderate and high CTE patches cause residual compression on the crack.
- When the aircraft is in service, the entire structure is cooled equally. Wing structures see their highest loads in takeoff and low altitude gust conditions, where air temperatures are relatively benign. Fuselages, on the other hand, are loaded primarily by internal pressurization, which reaches a maximum at high altitude, where outside air temperatures are -54 °C.

To further illustrate these effects, several parametric analyses were performed on the candidate materials. In all cases, a 1.0 mm thick fuselage skin of 2024-T3 aluminum was modeled. The applied skin stress level was 120 MPa. The modeling compared various patch materials and various *patch stiffness ratios* ($E_{11t \text{ patch}}/E_{11t \text{ skin}}$) at room temperature. A patch stiffness ratio of 1.0 means that the patch and skin have equal extensional stiffness. Most designers of boron patches aim for a patch stiffness ratio of approximately 1.4.

Figure 1 shows a plot of the repaired stress intensity factor versus the patch stiffness ratio ($E_{11t \text{ patch}}/E_{11t \text{ skin}}$) for a *room temperature cure* and a *sea level cruise altitude*. The lowest possible repaired K value is important in slowing crack re-initiation and producing the lowest achievable crack growth rate.

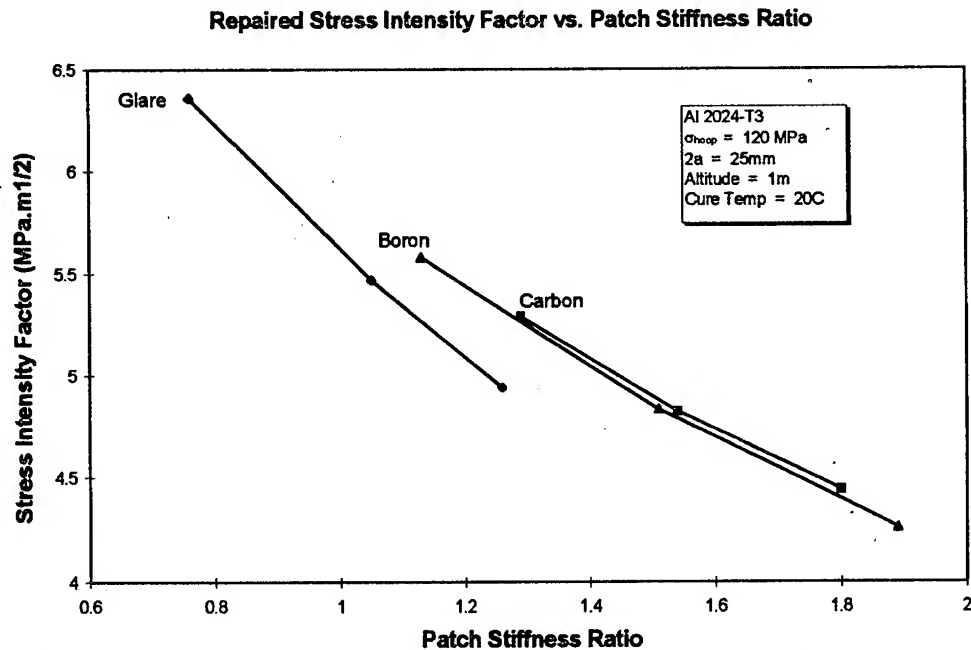


Figure 1. Stress intensity factor after bonded repair versus patch stiffness ratio.
Room temperature curing, sea level cruising altitude.

Because of the generally lower mechanical performance and poorer long-term durability of room temperature curing (paste) adhesives, most bonded repairs employ higher cure temperature epoxy film adhesives. Figure 2 shows a plot of the repaired stress intensity factor versus the patch stiffness ratio ($E_{11t \text{ patch}}/E_{11t \text{ skin}}$) for a more typical 120 °C (250 °F) cure and a sea level cruise altitude.

Figure 3 illustrates the influence of patch selection and stiffness ratio on the maximum shear strain in the adhesive. Maximum shear strain in the adhesive occurs at the crack flanks, and excessively high shear strains can lead to delaminations and poor patch durability. To reduce shear strain in the adhesive, some designers use thicker bond lines. The effect of a thicker bond line is also shown in Figure 3.

Repaired Stress Intensity Factor vs. Patch Stiffness Ratio

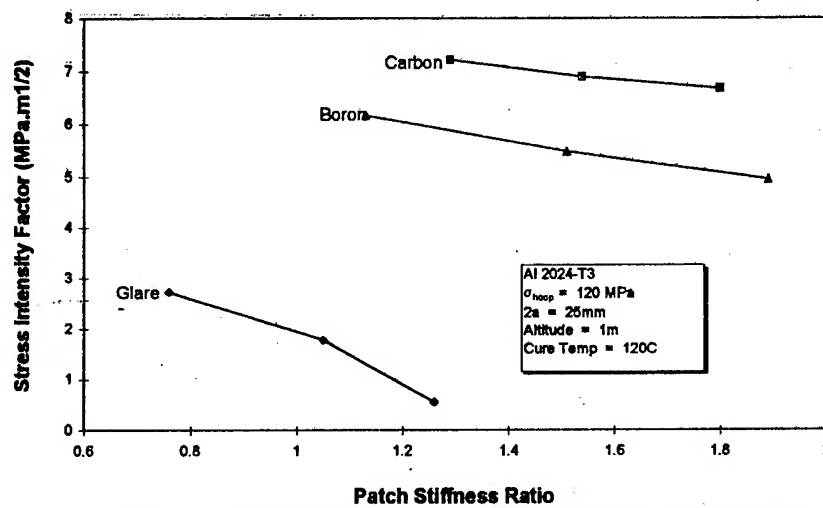


Figure 2. Repaired stress intensity factor versus patch stiffness ratio.

Max Adhesive Shear Strain vs. Patch Stiffness Ratio

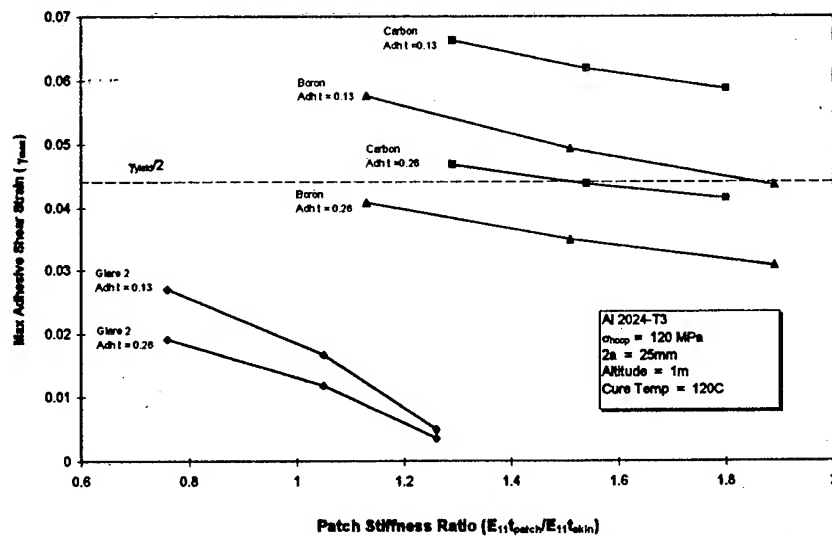


Figure 3. Maximum adhesive shear strain versus patch stiffness ratio.

Another key item in the design of a bonded repair the maximum stress in the skin adjacent to the repair. High stress concentrations may exist in the skin at the patch edge due to parasitic load attraction due to high local stiffness, thermal effects, and the bending that results from single-sided reinforcement. If skin stresses grow too high, new cracks may nucleate just outside the patched region in the skin. Figure 4 plots the maximum skin stress against patch stiffness ratio.

Max Skin Stress vs. Patch Stiffness Ratio

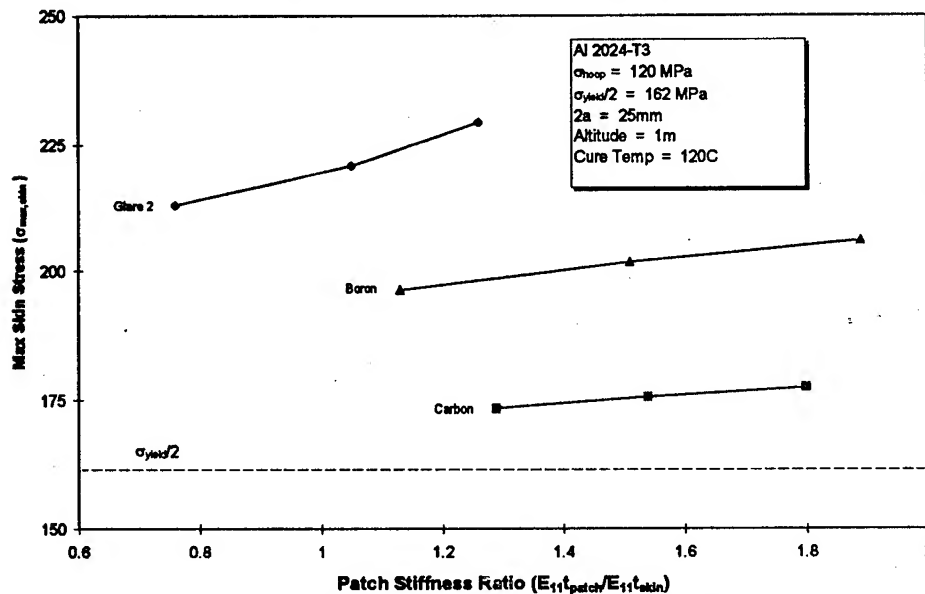


Figure 4. Maximum skin stress versus patch stiffness ratio. 120° C (250° F) curing, sea level cruising altitude, 0.13 mm bond line.

Experimental results

To verify the predictions of the CalcuRep code, several fatigue specimens matching the modeled configuration were built and tested. Coupon tests were performed on pre-cracked 2024-T3 aluminum panels. Based on the analysis, only two repair materials were continued into the experiments: boron/epoxy and glass/epoxy/aluminum. The configuration of the test panels was:

- Panel width 152 mm, length 400 mm
- Fatigue pre-crack length 25 mm
- Uniaxial loading, 6-120 MPa (Glare) and 12-120 MPa (Boron)
- Test frequency 5 Hz, room temperature
- Adhesive AF163-2, 0.13 mm thick and for some boron panels 0.26 mm thick
- Cure temperature 120° C (250° F)
- Patch size: 75 mm long x 50 mm wide (GLARE)
79 mm long x 50 mm wide (boron/epoxy)

The boron panels could not be tested down to as low a minimum stress because of residual bending caused by the CTE mismatch between the aluminum panel and the boron patch.

Figure 5 shows the results for an unpatched panel and both glass/epoxy/aluminum and boron/epoxy patched panels. Both patches extend the fatigue life of the panel considerably over the unpatched case. However, the glass/epoxy/aluminum patched panel gave by far the longest fatigue life, showing no crack growth for over 200,000 cycles. The better crack-stopping performance of the glass/epoxy/aluminum versus the boron patch was predicted by the CalcuRep analysis (lowest K, lowest adhesive shear strains) and can be attributed to the better CTE match between the glass/epoxy/aluminum laminate and the aluminum skin material. By contrast, the boron repair results in higher repaired K and higher adhesive shear strain values, allowing immediate crack growth, even at a 5% lower applied stress amplitude. A higher stiffness ratio hardly improved the performance of the Boron patches. A thicker adhesive bondline will result in lower adhesive shear strains but does not improve the fatigue life of the patched panel.

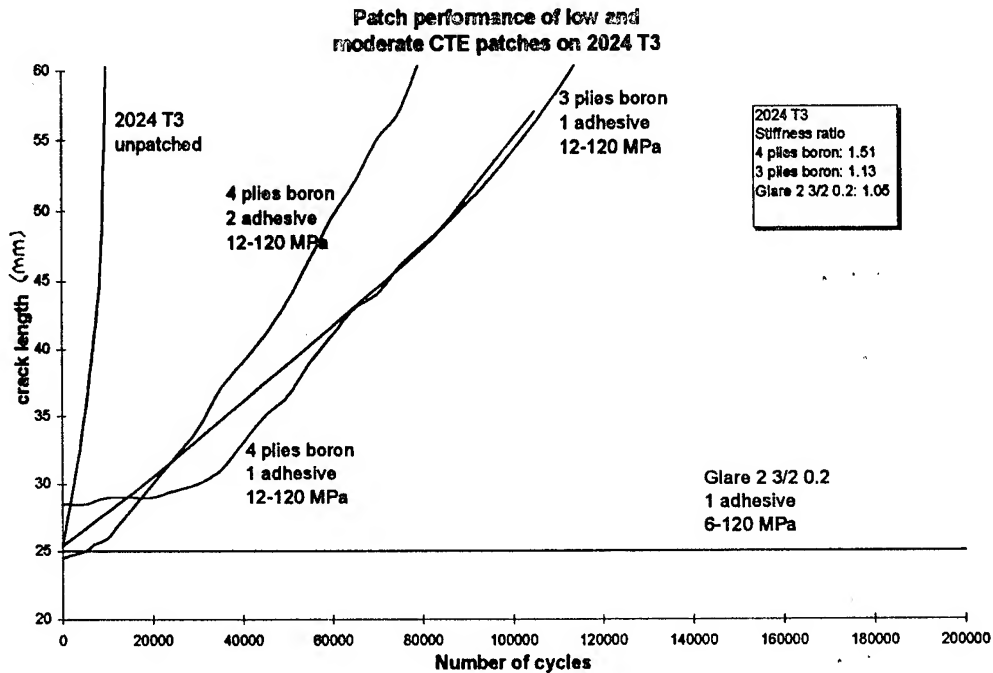


Figure 5. Constant amplitude fatigue test results, pre-cracked 2024-T3 panels.

Based on the analysis and the results of the fatigue tests performed on 2024-T3 panels, the glass/epoxy/aluminum patch was carried forward. Limited amounts of 7079-T6 sheet taken from an operational C-5A were available for testing; thus only two panels were tested. Panels were pre-cracked and repaired. The many existing rivet holes in the fuselage panels were filled with cold-expanded rivets to prevent crack nucleation in those holes (outside the patched test area).

Figure 6 shows the crack growth of the two patched 7079-T6 panels. It should be noted that 7079-T6 typically shows about four times faster crack growth rates (unrepaired) than 2024-T3. This makes achieving the lowest possible repaired stress intensity value even more necessary. The first 7079-T6 panel showed no crack growth up to 79,000 cycles, when the panel failed in the grip area away from the patched crack. The second repaired panel re-initiated crack growth at about 20,000 cycles. In 25,000 more cycles, the crack grew into the existing rivet holes under the patch. There was no further crack growth up to 175,000 cycles.

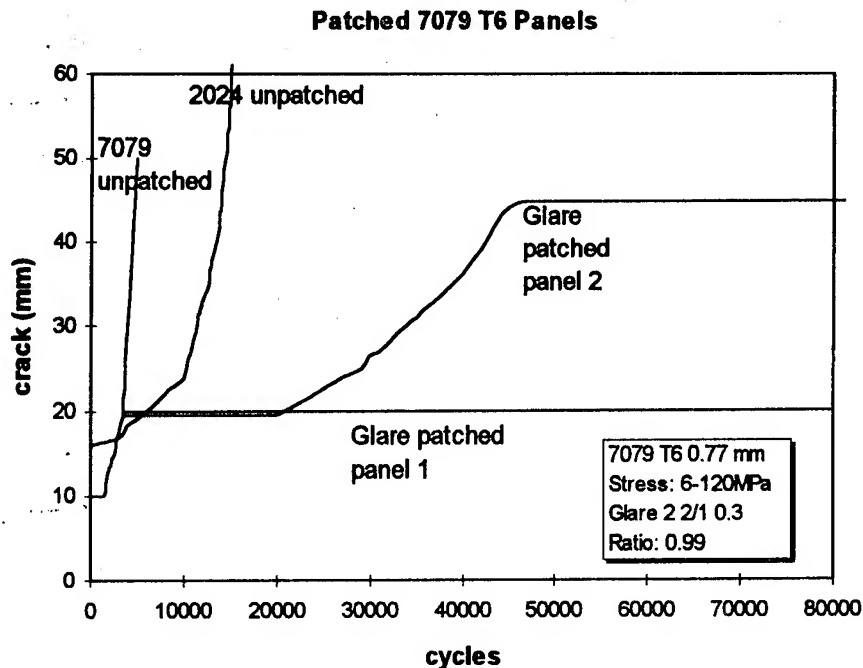


Figure 6. Crack growth in repaired and unrepaired 7079-T6 panels.

Design of the C-5A Repair Patches

With the results of the parametric analyses and the coupon tests, two prototype patch repairs were designed for installation on an operational C-5A undergoing Programmed Depot Maintenance at San Antonio Air Logistics Center.

A properly designed bonded repair patch must meet the guidelines for typical loads, limit load and ultimate load. At typical loads, the repair must show durable behavior, and greatly slow crack growth. At limit load, no yielding of any component of the repair system or parent structure is allowed. At ultimate design load (equal to 1.5 times the design limit load), the structure shall not fail, which means that all stresses should be less than the ultimate strength of the respective components.

Table 2 gives the design limits of the critical design variables for three different load cases (typical, limit, and ultimate).

Table 2. Design limits for bonded patches

	Typical loads	Limit load	Ultimate load
K, MPa√m	$da/dN < 10^{-4}$ mm/cyc	$K < K_c/2.25$	$K < K_c/1.5$
Patch stress, MPa	$< 0.5 \sigma_{yield}$	$< \sigma_{yield}$	$< \sigma_{ultimate}$
Skin stress, MPa	$< 0.5 \sigma_{yield}$	$< \sigma_{yield}$	$< \sigma_{ultimate}$
Adhesive shear strain	$< 0.5 \gamma_{yield}$	$< \gamma_{yield}$	$< 1.8 \gamma_{yield}$
Patch length/ adhesive load transfer length	40	40	40

For the typical repair configuration on a 7079-T6 crown panel, this results in the guidelines given in Table 3.

Table 3. Design limits for bonded GLARE 2 patches on 7079-T6 skins

	Typical loads	Limit load	Ultimate load
K, MPa√m	$< 4 \text{ MPa}\sqrt{\text{m}}$	$< 22 \text{ MPa}\sqrt{\text{m}}$	$< 33 \text{ MPa}\sqrt{\text{m}}$
Patch stress, MPa	< 180	< 360	< 1100
Skin stress, MPa	< 213	< 426	$< \text{ultimate}$
Adhesive shear strain	< 0.0446	< 0.1070	< 0.1606
Patch length/adhesive load transfer length	40	40	40

Installation of the Bonded Repairs

A team of engineers from San Antonio Air Logistics Center, Wright Laboratory, and the US Air Force Academy carried out the installation of two bonded repairs to a cracked C-5A fuselage in October of 1995. The details follow. Two fuselage cracks were repaired on the aft upper fuselage. The cracks are presumed to have nucleated at the rivet holes due to high fit-up stresses and stress corrosion cracking.

Thermal Survey. Before the surface pretreatment could begin, a thermal survey was conducted to locate any potential thermal problems (e.g., heat sinks) created by the substructure under the fuselage skin. Since frames and stringers will absorb more heat, good thermal control is needed to assure proper curing in all areas. Extra heat blankets or insulating the substructure can decrease the problem.

The thermal survey of the repair locations identified temperature fluctuations not greater than 10 °C, which was considered acceptable. Cure times were adjusted to match the lowest cure temperature. An ACR-6000A computer-controlled hot bonding unit monitored and adjusted the heating to keep the maximum temperature at or below 130 °C to avoid charring the adhesive. An even temperature distribution allows a higher maximum cure temperature and therefore a faster cure cycle in the complete section.

Surface preparation. The silane surface preparation used is described in detail in [3].

Patch manufacturing. The most efficient shape for a reinforcement is an ellipse, which was sketched with a commercial drafting program and printed on paper before being transferred to the Glare sheet material. A small sheet of Glare was then cold-rolled to match the diameter of the fuselage. A shear cutter was used to cut the patch to the rough dimensions, and a belt sander was used to trim the patch to the final outer dimensions.

To decrease secondary bending effects in the skin, the patch edges were tapered to a minimum thickness of 0.3 mm. Too thin a minimum taper thickness will reduce the ability to produce a good bond fillet and risks damaging the edge of the patch. The taper angle should be about 1:10. The taper angle was defined by drawing a smaller ellipse on the patch and filing the material by hand.

After manufacturing to the proper shape, the pre-primed patch was cleaned with MEK to clean the surface and to activate the primer and make the patch ready for bonding to the fuselage skin.

Bonding. After the surface preparation and patch manufacturing were complete, the area to be bonded was kept free of contamination by covering and sealing it with a plastic film. The patch was bonded to the pre-treated fuselage skin using AF 163-2M modified epoxy film adhesive using a cure cycle of 125 °C (250 °F) for one hour under 50 kPa (15 inches of mercury) vacuum.

Inspection. The crack under the glass/epoxy/aluminum patch will be monitored by using off-the-shelf low frequency eddy current techniques. Bond line quality assurance against voids or disbonds is best accomplished using pulse-echo ultrasonic methods. A simpler but rather effective inspection method is a visual inspection of the adhesive fillet and the bleeder. When the fillet looks smooth and the bleeder has a moderate amount of adhesive in it all the way along the bond line, good adhesive flow has occurred, indicating that the bond should be acceptable.

Discussion

Figures 1 and 2 show the repaired stress intensity factor at the crack tip after patching is as much dominated by thermal considerations as by patch extension stiffness. The higher coefficient of thermal expansion (CTE) patch materials resulted in lower repaired stress intensity factors and thus produce slower crack growth. The differences in repaired K are even more pronounced when more realistic cure temperatures are modeled, as shown in Figure 2.

The analysis showed that in addition to reducing repaired K at the crack tip, higher CTE patches also resulted in favorably lower adhesive shear strains (Figure 3). Lower adhesive shear strains should produce better patch durability and damage tolerance. As shown in Figure 3, a thicker bond line can somewhat reduce the adhesive shear strain, and this reduction is more pronounced when using low CTE patches. However, producing a thicker bond line in service can be difficult. The effect of a bond line thickness will be experimentally evaluated in the near future.

The thinner and stiffer patches result in a lower skin stress at the patch tips, as shown in Figure 4. With any patch material, lower skin stresses can be achieved by reducing the patch length/width ratio.

The analysis predicted that increasing the patch stiffness ratio only marginally improved patch performance in terms of K -reduction and adhesive shear strain, as shown in Figures 2 and 3. On the other hand, Figure 4 shows that increasing patch stiffness results in higher skin stresses at the patch tip.

Figure 5 shows the results of fatigue tests performed with boron and glass/epoxy/ aluminum laminate patch systems. The analytically predicted behavior is confirmed. Cracks repaired with the low CTE patches (boron/epoxy) re-initiated directly while the glass/epoxy/aluminum patch halted crack re-initiation for over 200,000 cycles, even though it was tested at a 5% higher stress amplitude. The lower K value achieved with the glass/epoxy/aluminum repair system stopped crack re-initiation despite the more severe stress level.

The glass/epoxy/aluminum patches applied to the 7079-T6 panels also increased the life of the panels significantly, as shown in Figure 6. The cracks showed varying amounts of time to re-initiation, from 20,000 to over 79,000 cycles. Cracks that re-initiated grew slowly. When crack tips reached pre-existing rivet holes under the patch, crack growth stopped for more than 175,000 cycles.

All specimens discussed here were modeled and tested at room temperature. However, a repaired fuselage operates at the low temperatures seen at a cruising altitude of over 10 km (31,000 feet). These lower operating temperatures should increase effect of the thermal mismatch between patch and skin. Cracks repaired with lower CTE patch materials will see higher stress intensity factors, and thus faster crack growth can be expected. Hence, high-strength, moderate-CTE materials should be the more effective patch system for pressurized fuselage repairs. For thicker structures in aerodynamically critical areas (e.g., wing skins), higher stiffness/low CTE patch materials may be the only option because of volume restrictions on the repair.

Summary and Conclusions

After extensive analytical and experimental development, two glass fiber/epoxy/aluminum composite patches were successfully bonded over fuselage skin cracks in a C-5A during Programmed Depot Maintenance at San Antonio Air Logistics Center in October 1995. The repairs represent a breakthrough cost-effective solution to the problem of widespread cracking in the aft fuselage crown and can extend the useful service life of the C-5As at a fraction of the cost of reskinning the fleet. These repairs will be monitored as the aircraft is returned to service in early 1996. Pending successful performance, the technique will be considered for fleet-wide implementation.

Extensive analysis and experimentation indicate that moderate-CTE, high-strength materials can be more effective for adhesively bonded crack repairs in pressurized fuselages. When aerodynamic drag is a critical concern (i.e., the repair of thick wing structures), higher stiffness/low CTE patch materials like boron/epoxy may be a better option because of volume (thickness) restrictions on the repair.

Acknowledgments

The authors wish to thank MSgt Bryan Cramer and Mr. James Mazza of the USAF Wright Laboratory's Materials Directorate for their tremendous support of the installation of the repairs on the C-5A. Further thanks are due to Warner Robins Air Logistics Center, especially to Mr. Bill Schweinberg, who designed the boron patches used in this development program. And finally, grateful appreciation goes to Delft University, the Netherlands, for the development of the glass fiber/epoxy/aluminum laminate and the support in the research program.

References

1. Fredell, R., W. van Barneveld and A. Vlot, "Analysis of Composite Crack Patching of Fuselage Structures: High Patch Elastic Modulus Isn't the Whole Story," *Proc. 39th International SAMPE Symposium and Exhibition*, Anaheim, California, USA, April 1994, pp. 610-623.
2. "Damage Tolerant Repair Techniques for Pressurized Aircraft Fuselages," Wright Laboratory Technical Report 94-3134, June 1994.
3. "Understanding the Australian Silane Surface Treatment," R.J. Kuhbander and J.J. Mazza, *Proc. 38th International SAMPE Symposium and Exhibition*, Anaheim, California, May 1993.

AN FEAM BASED METHODOLOGY FOR ANALYZING COMPOSITE PATCH REPAIRS OF METALLIC STRUCTURES

V. Nagaswamy

D.S. Pipkins

S.N. Atluri

Computational Modeling Center
Georgia Institute of Technology
Atlanta, GA

ABSTRACT

Repairs to pressurized fuselages have been done traditionally by using mechanical doublers. While bonding of metal structures and bonded repair techniques have existed for about 50 years now, bonded repairs have not gained as much acceptance as the mechanical doubler repairs. This is mainly due to the disappointing early experience with bonding and the lack of widespread understanding of bonded repairs among technicians. This provides the motivation for the development of effective analysis techniques that can be implemented on low end workstations. In this investigation, the mechanical doubler repairs have been compared with bonded repairs in the repair of cracks in the fuselage skin. To analyze the effect of global loading (viz. pressure loading in the fuselage shell), on the essentially local feature of repair, a hierarchical approach has been used. This allows the fuselage to be modeled with increasing detail over smaller regions. Using this approach the stress redistribution caused by mechanical doubler repair is compared with that caused by composite patch repairs. The residual strength and fatigue life of fuselages with composite patch repairs have been compared with those of the un-repaired case. The stress intensity factors have been evaluated by considering the adhesive

as elastic material and as an elastic perfectly plastic material. Parametric studies of composite repairs are conducted using this methodology

INTRODUCTION

This paper describes an efficient computational methodology for the analysis of structural repairs. It builds on the work of Atluri and Tong (1991), Park, Singh, Pyo, Atluri and Tan(1993), Pyo, Okada and Atluri (1994), Park and Atluri (1992) etc. As discussed in these works, the method is not only efficient but very accurate also. In general, stress intensity factors can be calculated within 2% of their exact values.

Most of the present day repairs to cracked aircraft fuselages are performed by using mechanical doublers. The cracked portion is cutout, a sheet is placed in the region thus created; and finally, another sheet is riveted to this cutout portion and the skin.

From the Second World War, successful applications of adhesive bonding have been made in aircraft structures. The Fokker F-27 aircraft is an example of successfully operating aircraft that has employed adhesive bonding for primary structure (Baker and Jones (1988)). While such success stories exist, doubts about

adhesive bonded repairs still exist. It is the objective of this paper to study such bonded repairs and to compare them with mechanical doubler repairs.

Many workers have estimated various crack-tip parameters in stiffened aircraft structures. Miller et. al. (1992) and Samavedam and Hoadley (1994) have estimated the stress intensity factors for such structures by a geometrically non-linear finite element analysis. Shenoy et. al. (1994) have estimated the nonlinear fracture parameter, T^* integral, for bulging cracks. See references therein for more on such work.

There are several methods for the analysis of patched cracks. They can be broadly divided as

1. Analytical
2. Finite Element Approach

The analytical approach of Rose (1981) is an elegant method based on Hart-Smith's (1974) theory of bonds, elastic inclusion analogy, and on some simplifying assumptions. Fredell (1994), in his exhaustive thesis, has extended this analysis to include thermal effects. He has also carried out an evaluation of mechanical doubler repairs. Erdogan and Arin (1972) have used integral equations approach to study the patched cracks. The assumptions of Erdogan and Arin were subsequently used by Ko (1978) and Hong and Jeng (1985) in the analysis of sandwich plates with part-through crack.

Jones and co-workers (1979, 1981, 1983), Mitchell et. al. (1975), Chiu and Ko (1989) have used finite element method to study patched cracks. Park et. al. (1992) have used an integral approach combined with FEAM to estimate the stress intensity factors for patched panels. Tarn and Shek (1991) have combined boundary element method approach (for the plate) and finite element method (for the patch) to estimate the stress intensity factors. Other work in this area includes Atluri and Kathiresan (1978), Sethuraman and Mathi (1989), and Kan and Ratwani (1981).

In most of these approaches, only patches of infinite size, or very narrow strip type patches, or infinite sheet cases are considered. All of these cases are valid only for flat sheets. The loading for all these analyzes are hoop stresses evaluated from basic thin shell theory. While, in most cases this is a good approximation, this does not take into account the stress re-distributions due to the curvature and due to the presence of stiffeners.

The present work addresses the problem of the study of patched cracks in actual commercial airliner fuselages. A hierarchical modeling strategy is used to study the repairs to fuselages. The methodology is as follows. The whole of the fuselage is studied in the first stage.

In the next stage, a portion of this is studied with an increase in complexity of the model. Finally a small portion around the crack and the repairs is studied to estimate the stress intensity factors. The procedure used to analyze the local zone is the finite element alternating method. The finite element alternating method is an efficient numerical-analytical method to evaluate the stress intensity factors of cracks.

In the following section, the methodology is described in detail. The analytical solution for the finite element alternating method is also presented. Later, this methodology to study repairs to fuselages. The stress re-distributions caused by mechanical doubler repairs is contrasted with those by patch repairs. The effect of various parameters such as the patch dimensions, patch material, patch thickness, adhesive material and adhesive thickness on patch efficiency is studied.

METHODOLOGY

The problem of cracks and their repairs is a localized phenomenon. The known loading conditions on the fuselage are essentially global - viz. the pressure loading. Therefore the analysis requirements are conflicting - a global loading and an essentially local phenomenon. This necessitates a hierarchical modeling strategy (Starnes and Britt 1991). Fig 1. This allows an increasing level of complexity and fidelity in the modeling without a prohibitively high computational effort.

The global model is a linear elastic shell finite element analysis. In this analysis the stiffeners are modeled as beams. The fuselage is modeled with shell elements. The fasteners are modeled as shear springs. In the analysis of the cracked unrepaired fuselage, the crack is modeled in the global analysis only crudely, i.e., via unconnected finite elements while ignoring the crack-tip singular fields. In the analysis of a composite patch-repaired fuselage, it is assumed that the bending caused by the patch dies down and at this global stage of analysis, it can be considered as an uncracked fuselage. Therefore, the repaired fuselage is considered as an intact fuselage in the global level of analysis. In both cases, symmetry conditions approximating a full fuselage are applied to the region analyzed. As the shell length considered is small when compared to the length of actual fuselages, the axial ends are restrained from motion in the axial direction.

A portion of the fuselage in the circumferential as well as longitudinal directions is now taken and analyzed in the intermediate model. In this model, the fidelity is increased by modeling the stiffeners with shell elements. The fasteners are modeled by short beams. The essen-

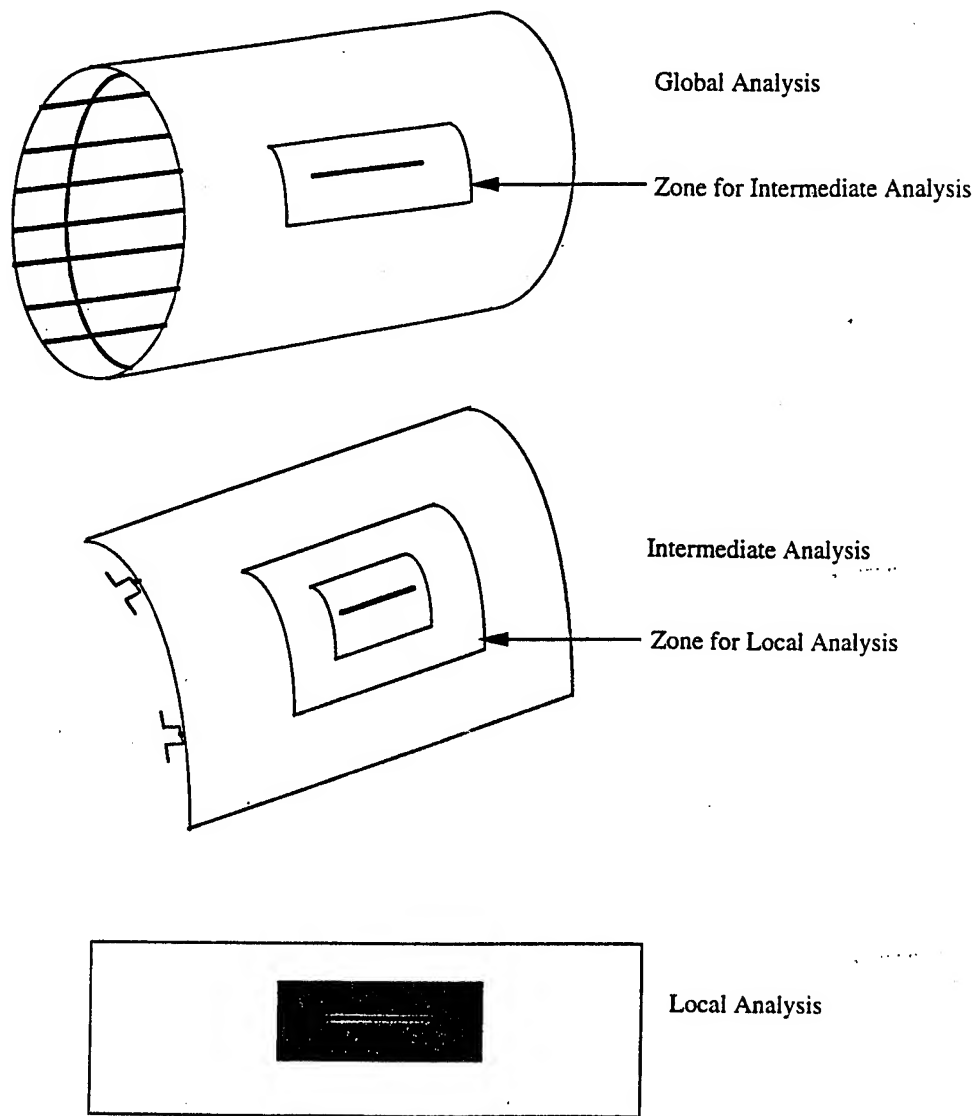


Figure 1: Schematic of the Hierarchical Modeling Strategy

tial boundary conditions for this model are obtained from the global analysis. In both of the above models the loading is internal pressure.

A smaller portion of the fuselage that contains the crack and repair is then analyzed in the local analysis. As the region is small, the pressure loading and the curvature are disregarded. The loading on this region are the tractions obtained from the intermediate model. The local analysis proceeds in two stages. In the first stage, the crack is explicitly modeled with ordinary finite elements, (i.e., without paying attention to the singular fields) and the stresses exerted by the composite patch on the metallic sheet are deduced. The mesh for this analysis is not detailed as the aim at this stage is to obtain the stresses exerted by the patch and adhesive on the sheet and not to model the crack tip singularity. Once the patch stresses are deduced, the finite element alternating method is used to obtain the stress intensity factors. The theoretical formulations of each model are now presented.

Global Analysis

The global analysis is conducted in the shell space. The principle of minimum potential energy is invoked to obtain the equilibrium equations.

$$\Pi(\mathbf{u}) = \int_V W(\epsilon) dV - \int_{\partial V^t} \mathbf{t} \cdot \mathbf{u} dS \quad (1)$$

$$(2)$$

$$\delta \Pi = 0$$

where Π is the potential energy, ∂V^t is the boundary that has specified tractions \mathbf{t} , on it. On making the usual Kirchhoff-Love assumptions, and specifying the in-plane strains as $\epsilon_{\alpha\beta}$, and the bending strains by $\kappa_{\alpha\beta}$, the strain energy function, W is specified by

$$W(\epsilon) = \frac{1}{2} \left[h C^{\alpha\beta\gamma\delta} \epsilon_{\alpha\beta} \epsilon_{\gamma\delta} + \frac{h^3}{12} C^{\alpha\beta\gamma\delta} \kappa_{\alpha\beta} \kappa_{\gamma\delta} \right]$$

where the elasticity tensor is given by

$$C^{\alpha\beta\gamma\delta} = \frac{E}{1-\nu^2} \left[\nu g^{\alpha\beta} g^{\gamma\delta} + \frac{1-\nu}{2} (g^{\alpha\delta} g^{\beta\gamma} + g^{\alpha\gamma} g^{\beta\delta}) \right]$$

E is the Young's Modulus, ν is the Poisson's ratio, $g^{\alpha\beta}$ is the metric tensor of the middle surface and h is the shell thickness.

This forms the basis for the finite element analysis. In this analysis a four-noded 5 degree of freedom element developed by Ashwell and Sabir (1972) is used. This element a quasi-conforming element wherein an independent variation of strains is assumed. By setting the

strains to zero, a general rigid body motion with six parameters is obtained upon solving the resultant differential equations. The strains are discretized by using fourteen other parameters. The discretized strains are forced to satisfy a simplified version of compatibility. These twenty parameters are used as generalized degree of freedom and are expressed in terms of the nodal degrees of freedom. Thus the strains are expressed in terms of nodal degrees of freedom and this is used to obtain the basic finite element equations.

The stiffeners at this stage are modeled as beams. The beam element is obtained by collapsing the shell element described above. As the fastener flexibility is crucial (Swift (1974), (1984)), the fasteners are modeled by flexible shear springs. The stiffness for this fastener element is given as in Swift (1974, 1984) by

$$K = \frac{E_s D}{A + C \left(\frac{D}{t_1} + \frac{D}{t_2} \right)} \quad (3)$$

where E_s is the sheet Young's Modulus, D is the rivet diameter, t_1 and t_2 thicknesses of joined sheets, $A = 5.0$ for Al rivets and 1.66 for steel fasteners, and $C = 0.8$ for Al rivets and 0.86 for steel fasteners. The rivet holes are not explicitly modeled.

The crack is modeled with split nodes. There is no explicit modeling of the crack tip singularity.

Intermediate Analysis

The intermediate analysis is also a linear finite element analysis and is also based on the aforementioned principles. The element used at this stage is a four-noded six degree of freedom per node element (Rankin and Brogan(1991)). In the analysis of shells a two parameter specification of the the director field about the mid-surface is sufficient if the mid-surface is smooth. In the presence of shell intersections, this is not sufficient. A standard way of handling such intersections is the usage of shell elements with drilling degrees of freedom (See Simo (1993) and Fox and Simo (1992) for example). The element used is one such element. Therefore, the facets that arise as a result of modeling the stiffeners with shells elements can be handled. This element uses an incompatible displacement field with a cubic variation of the bending field and a linear/cubic variation of the in-plane field.

In this model, the stiffeners are also modeled with the same shell elements. The fasteners are modeled as short beams. As in the global model the rivet holes are not explicitly modeled. Again the cracks are modeled with split nodes and there is no explicit modeling of the stress singularity.

Local Analysis

The local analysis is a two stage analysis. They are

1. Evaluation of the stresses exerted by the adhesive and patch on the sheet, using a coarse mesh.
2. The stresses obtained from stage 1 are applied as body forces on the base sheet, and the finite element alternating method (Atluri(1986)) is used to find the stress intensity factor.

In step 1, a traditional finite element methodology is used to deduce the stresses exerted by the patch. As the crack tip is not meshed for the singularity, a coarse mesh is sufficient for this purpose. The sheet and the patch are modeled with eight noded 2D elements. The adhesive is modeled by elements as in Jones and co-workers (1979, 1981, 1983) and Mitchell et. al. (1975). This element is obtained by assuming a constant shear stress in the adhesive. Under the present conditions the shear stress can be obtained from

$$\tau_{xz} = \frac{u_s - u_p}{\frac{t_a}{g_a} + \frac{3}{8} \left(\frac{t_s}{g_s} + \frac{t_p}{g_p} \right)} \quad (4)$$

$$\tau_{yz} = \frac{v_s - v_p}{\frac{t_a}{g_a} + \frac{3}{8} \left(\frac{t_s}{g_s} + \frac{t_p}{g_p} \right)} \quad (5)$$

where u and v are the displacements in the x direction and y direction respectively, t, g are the thickness and shear modulus respectively. The subscripts a, s and p refer to the adhesive, sheet and the patch respectively.

Large strains are induced in the adhesive when the difference between the patch stiffness and sheet stiffness is large. Therefore, this results in the yielding of the adhesive. This reduces the patched efficiency, and a linear elastic analysis would grossly overestimate the efficiency and would be anti-conservative. Therefore, the adhesive is modeled as an elastic perfectly plastic material. As there is no unloading (crack growth is not considered), a deformation theory of plasticity is considered sufficient. An initial stress algorithm (Nayak and Zienkiewicz (1972)) has been implemented. In view of the model as in Jones and co-workers (1979, 1981, 1983) and Mitchell et. al. (1975) the Von Mises yield criterion reduces to

$$\sqrt{\tau_{yz}^2 + \tau_{xz}^2} = \frac{\sigma_{yp}}{\sqrt{3}} = \tau_{yp} \quad (6)$$

The algorithm for this is as follows

1. A load step is taken and the displacements are found.
2. The stresses are computed at each Gauss Point and yielding is checked for.
3. The residual load is computed.
4. The displacements for this residual load are then computed.
5. Repeat steps 2, 3 and 4 for convergence. Convergence is reached when there is no yielding at any Gauss point.
6. Repeat the steps 1,2,3,4 and 5 for more load steps till the desired load is reached.

The stage 2 of the analysis is 2-D finite element alternating method (Atluri (1986), Atluri and Tong (1991), Park, Ogiso and Atluri (1992)). This is illustrated in Fig. 2. In finite element alternating method, the stresses in the uncracked body are first analyzed, by a traditional finite element method, for the given system of external loading. To model the crack, the tractions at the locations of the crack in an otherwise uncracked body must be erased.

To erase the crack face stresses, the tractions found by the finite element solution are reversed. As is often the case, analytical solutions exist for cracks subjected to arbitrary crack face stresses but for infinite bodies. Therefore, if these solutions are to be used for erasing crack face stresses, the residual stresses at the finite body extent in the infinite body have to be erased. This is done by reversing the residual stresses applied to the finite uncracked body. This results in residual traction at the crack location. To erase this, the analytical solution is used again. This is repeated for convergence. Convergence is achieved when the stress intensity factors for each analytical iteration become small. The final stress intensity factor is the sum of all the stress intensity factors. This procedure has been shown to converge and converge to the stress intensity factor of the cracked finite body. (See Liao (1990) and references therein). Calculated stress intensity factors can be expected to be within 2% of their exact values.

Here, the analytical solution needed for this work is outlined (Park Ogiso, and Atluri (1992), Muskhelishvili (1953) and England (1971))

Suppose there is a line crack on $y = 0, |x| \leq a$ in an infinite plate, and arbitrary tractions are applied to the crack face. The tractions are specified as

$$\sigma_y - i\tau_{xy} = -[p(t) + is(t)] \quad (7)$$

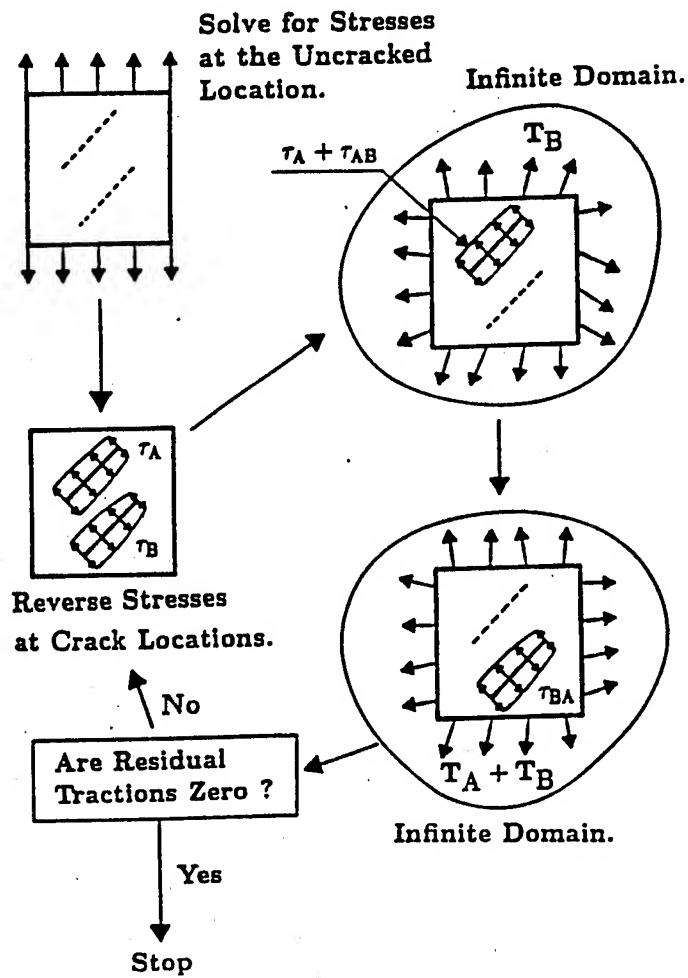


Figure 2: Schematic of the Finite Element Alternating Method

for the domain $|t| \leq a$. These are expressed by Chebyshev polynomials as

$$p(t) + is(t) = - \sum_{n=1}^N b_n U_{n-1}$$

for $|t| \leq a$, where

$$U_n(t) = \frac{\sin[(n+1)\theta]}{\sin \theta}$$

and

$$t = a \cos \theta$$

The complex stress function that provides the solution for this problem is expressed as (Gladwell and England(1977)).

$$2\Omega'(z) = \sum_{n=1}^N b_n G_{n-1}$$

$$2\Omega(z) = \sum_{n=1}^N b_n \frac{R_n(z)}{n}$$

where the prime denotes differentiation with respect to z and $z = x + iy$ and

$$R_n(z) = a[z_1 - (z_1^2 - 1)^{1/2}]^n$$

$$G_{n-1} = -(z^2 - a^2)^{-1/2} R_n(z)$$

$$z_1 = \frac{z}{a}$$

From the above, denoting the x and y displacements as u and v , as before, we have the following expressions for stresses and displacements.

$$\sigma_x + \sigma_y = 2\Omega'(z) + 2\overline{\Omega'(\bar{z})}$$

$$\sigma_y - i\tau_{xy} = \Omega'(z) + \overline{\Omega'(\bar{z})} + z\overline{\Omega''(\bar{z})} + \omega'(z)$$

$$2\mu(u + iv) = \kappa\Omega(z) - z\overline{\Omega'(\bar{z})} - \overline{\omega(z)}$$

where the overbar indicates complex conjugate and μ is shear modulus and $\kappa = 3 - 4\nu$ for plane strain or $\kappa = (3 - \nu)/(1 + \nu)$ for plane stress condition and ν is the Poisson's ratio,

$$\omega(z) = \overline{\Omega(\bar{z})} - z\Omega'(z)$$

The stress intensity factors are then given by

$$K_I - iK_{II} = -\sqrt{\pi a} \sum_{n=1}^N b_n \quad (8)$$

for $x = a$ and similary for $x = -a$ we have

$$K_I - iK_{II} = -\sqrt{\pi a} \sum_{n=1}^N (-1)^n b_n \quad (9)$$

Summarizing the steps in the finite element methodology,

1. Solve for the uncracked finite body under given loads by traditional finite element method.
2. Compute the stresses at the crack location from step 1.
3. To reverse the above found stresses, use least-squares approximation to fit the stresses to Chebyshev polynomials.
4. Use the above solution and find the stresses at the boundaries of the finite body.
5. Sum the Chebyshev coefficients to find the stress intensity factors for this iteration.
6. If the stress intensity factor for this iteration is small then convergence is obtained.
7. If convergence is not obtained, apply the reversed residual stresses on the finite body boundaries and use traditional finite element method to solve for the displacements and go to step 2.

To find the final solution add all the stress intensity factors for all iterations.

Software

The above methodology has been implemented in a software based on several in-house and commercial finite element codes. The global model has been implemented in an in-house software called SOFRAC (Singh, Park and Atluri (1994)). The results from this analysis are taken and applied to the intermediate analysis. At this point it is relevant to point out the methodology adopted to interpolate the displacements between the models. While the fuselage shell has been modeled with shell elements in both the models, the stiffeners in the global model was modeled as beams; but are modeled as shells in the intermediate analysis. Therefore, a direct application of the displacements at the relevant locations becomes impossible. Instead, using the rotations and displacements in the beams that constitute the stiffeners in the global analysis, the displacements at the nodes of the shell elements that constitute the stiffeners in the intermediate model are obtained by extrapolation. It is noted at this point this could lead to a stress mismatch in the boundary of the intermediate model as the idealization is different.

The intermediate model, with the kinematic boundary conditions obtained as illustrated above, is now solved by using STAGS (Almroth, Brogan and Stanley 1986). The pre-processor used to generate the input

files for STAGS analysis is an in-house pre-processor that carries out the aforementioned extrapolations.

The solution from the above is now used as the applied boundary condition for the local analysis wherein only a very small portion of the skin (with the patch) are modeled. As indicated above, the local analysis is based on 2-D finite element alternating method. Therefore, only the in-plane stresses are used. The out-of-plane stresses are neglected. As the substructure of the structure would restrict any severe bending this is believed to be a good approximation. The local zone is implemented in an in-house software PAN-MD. The input files for this analysis are generated by an in-house post-processor for STAGS. The entire analysis from the global to local has been automated in a PERL script.

ANALYSIS OF REPAIRED CRACKS

The fuselage as described by Table 1 is used for the various test cases studied. The stringers used are of hat cross section and the frames are of Zee cross section. The stiffener properties are given in Table 2. It is noted that the frame is attached to the sheet on the tearstraps. This is considered as an approximation to attaching the frame to the sheet with shear clips. In view of the unavailability of the exact stiffener dimensions this is considered sufficient. The crack is assumed to be a mid-bay crack. The rivets used are NAS1097DD6 rivets of 0.15625 in diameter.

The dimensions of the different models are given in Table 3. The finite element meshes used for various models are shown in Fig. 3, Fig. 4 and Fig. 5.

Patch Repairs

The above fuselage is repaired with a patch of dimensions 5 in X 3 in as shown in Fig. 6. The patch is 0.04 in thick and is made of Boron Epoxy. The adhesive is 0.004 in thick and has a shear modulus of 104.73 ksi with 5.250 ksi being the Yield Point in shear.

To analyze the effect of the patch, the crack length was varied from 1 in to 16 in. The variation of the stress intensity factor, K_I , with the crack length is shown in Fig. 7. (Unless otherwise noted all the stress intensity factors are in $ksi\sqrt{in}$ and the crack lengths are in in.) The efficiency of crack patching is plotted in Fig. 8. The efficiency is defined as

$$= \frac{SIF_{unpatched} - SIF_{patched}}{SIF_{unpatched}} \times 100$$

Internal Pressure	9.0 psi
Radius	78 in
Thickness	0.036 in
Material	Al 2024T3
Young's Modulus	10,500 ksi
Poisson's Ratio	0.33
Yield Point	47.0 ksi

Table 1: Properties of The Fuselage Shell

Rivet Specification	NAS1097DD6
Rivet Diameter	0.15625 in
Stringer Spacing	9.25 in
Stringer Area	0.0384 in ²
Stringer Moment of Inertia	0.162 in ⁴
Axis to skin distance	0.465 in
Frame Spacing	20.0 in
Frame Area	0.1248 in ²
Frame Moment of Inertia	0.3271 in ⁴
Axis to skin distance	1.148 in
Tear Strap Thickness	0.036 in
Tear Strap Width	2 in

Table 2: Stiffener Properties

Global Region Length	100 in
Global Region Arc Length	46.25 in
Intermediate Region Length	40 in
Intermediate Region Arc Length	18.5 in
Local Region Length	10 in
Local Region Width (Arc Length)	8 in

Table 3: Dimension of different fuselage models

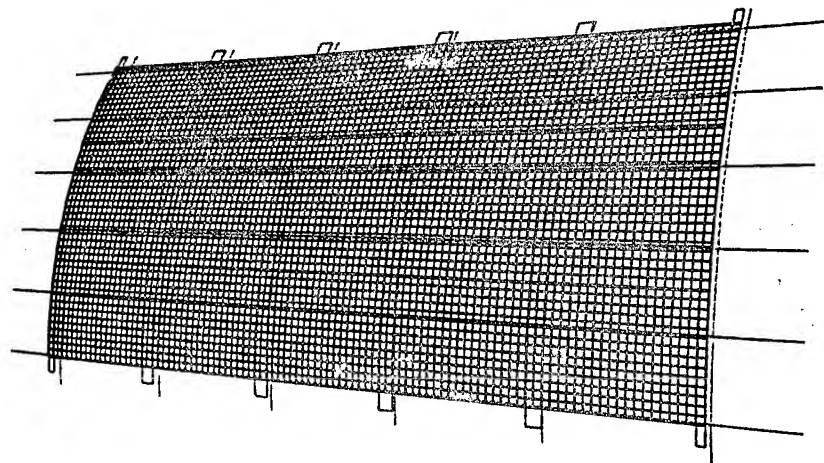


Figure 3: Mesh for Global Analysis

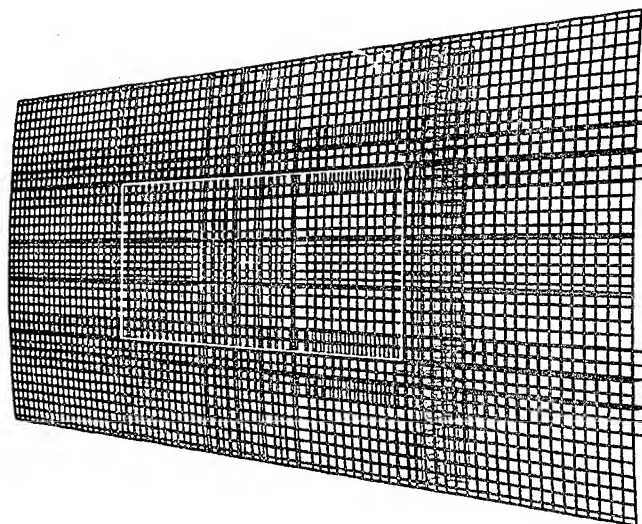


Figure 4: Mesh for Intermediate Analysis

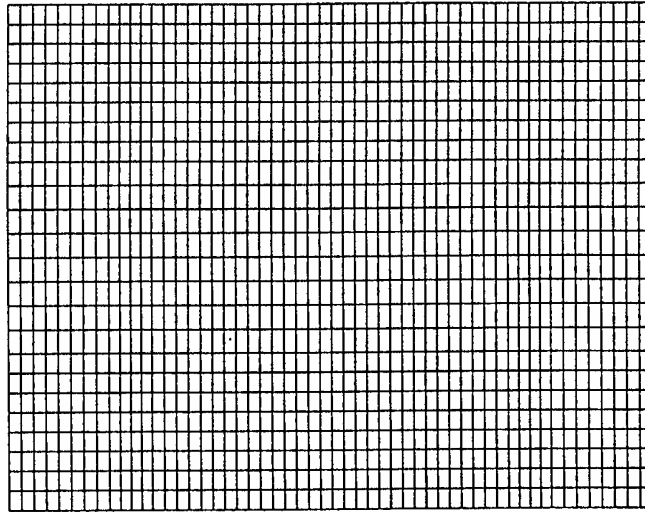


Figure 5: Mesh for Local Analysis

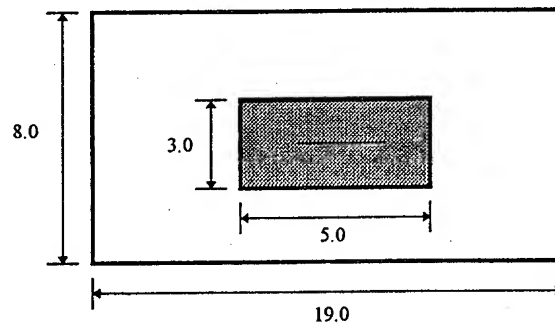


Figure 6: Geometry of the Local Zone showing the patch

The asymptotic nature of the stress intensity factor, as in Fredell (1994) and Baker and Jones (1988) is clearly observed. Unlike the methodology of Rose (1981) and Fredell (1994), the present methodology can analyze cracks longer than the width of the patch. It is seen that while the stress intensity factors show a significant increase as the crack emerges from the patch, it still demonstrates an asymptotic behavior. In these two situations, viz. crack shorter than the width of the patch and longer than the width of the patch, the patch transfers load in significantly different ways. When the crack is shorter than the width of the patch, most of the load is transferred by the edges of the patch parallel to the crack. This is seen from the Fig. 10, where the effective stress in the adhesive has been plotted. As the crack grows longer than the width of the patch, the regions near the crack tips also start to transfer the load and the patch transfers the load as in bonded overlap joints. This is shown in the effective stress in the adhesive contour plot Fig. 11. This increase in the effective stress lead to a final yielding of the adhesive. Once the adhesive yields, a very significant reduction in the effectiveness is seen. (Fig. 8 and Fig. 9).

Patch Repairs and Mechanical Doubler Repairs

A mechanical doubler repair, Fig. 12, for the above mid-bay cracked fuselage is also analyzed. The axial (Fig. 13) and hoop stress (Fig. 14) resultants for the doubler repaired fuselage has been compared with that of the composite patch (Fig. 15 and Fig. 16) repaired fuselage and the intact fuselage (Fig. 17 and Fig. 18).

As can be seen, a patch repair, despite the presence of the singularity involves a much lower value stress. In the doubler repair case, the cutout provides a site for stress concentration. Therefore, the maximum hoop stress in the doubler repair case increases from 19.1 ksi in the intact fuselage to 30 ksi. Whereas, in the fuselage repaired with a patch, the hoop stress went up marginally to 19.4 ksi. A similar pattern is also seen in the axial stresses where the stresses went up from 6.5 ksi to 11.7 ksi.

Effect of Patch Geometry

To study the effect of the patch overlap length of the patch (the length along the y direction), it was varied from 1.5 in to 3.5 in. The results are in Fig. 19. The patch is 5 in wide and 0.04 in thick and is made of Boron/Epoxy composite. The adhesive is 0.004 in thick and has a shear modulus of 104.73 ksi.

When the crack is longer than the width of the patch, the patch serves to transfer the load across the crack and reduce the ligament stress near the crack tip. Therefore, a longer patch, having a longer overlap length and therefore larger area transfers this stress better and therefore perform better than the shorter patches (Fig. 19 and Fig. 20). Whereas, when the crack is shorter than the width of the patch, the longer patches perform poorly (Fig. 21). The composite system of the patch, adhesive and the sheet attracts parasitic load from other regions in the sheet, (Fredell (1995) and Baker and Jones (1988)). When the crack is shorter than the width of the patch, this parasitic load attraction, increases the load near the crack tip. Larger patches attract larger parasitic loads, therefore they perform poorly when compared to shorter ones. When the crack is longer, this parasitic load attraction does not increase the load near the crack tip, therefore a similar behavior is not seen in those cases.

The patch width is varied from 4 in to 8 in. The results are shown in Fig. 22. The patch is 3 in long, and 0.04 in thick and is made of Boron/Epoxy. The adhesive properties remain the same as above. As was illustrated earlier, the stress intensity factors shows two asymptotic values, one obtained when the crack is shorter than the width of the patch and the other when the crack is longer than the width of the patch. When the crack is shorter than the width of the patch, the asymptotic value reached does not vary much with the patch width. While wider patches cause the second asymptotic value to be reached at a longer crack length (the cracks emerge from the patch later with wider patches), the asymptotic value reached does not appear to change. Therefore the narrower patches also seem to perform adequately. Wider patches, because of larger areas, have better damage tolerance.

The patch thickness was varied from 0.01 in thick to 0.04 in. The patch is 5 in wide and 3 in long and is made of Boron/Epoxy. As expected, thicker patches perform better (Fig. 23).

Effect of Patch Material

To evaluate different materials as possible candidates for patching materials several are investigated, following Fredell (1994) and Fredell (1995). The properties of the materials are given in Table 2. In each of the cases the patch is 5 in wide and 3 in long and 0.04 in thick. The adhesive shear modulus is 104.7 ksi and the thickness considered is 0.004 in. The Yield Strength of the adhesive is taken as 5254 psi. The results are depicted in Fig. 24.

The composite patches perform the best, followed by

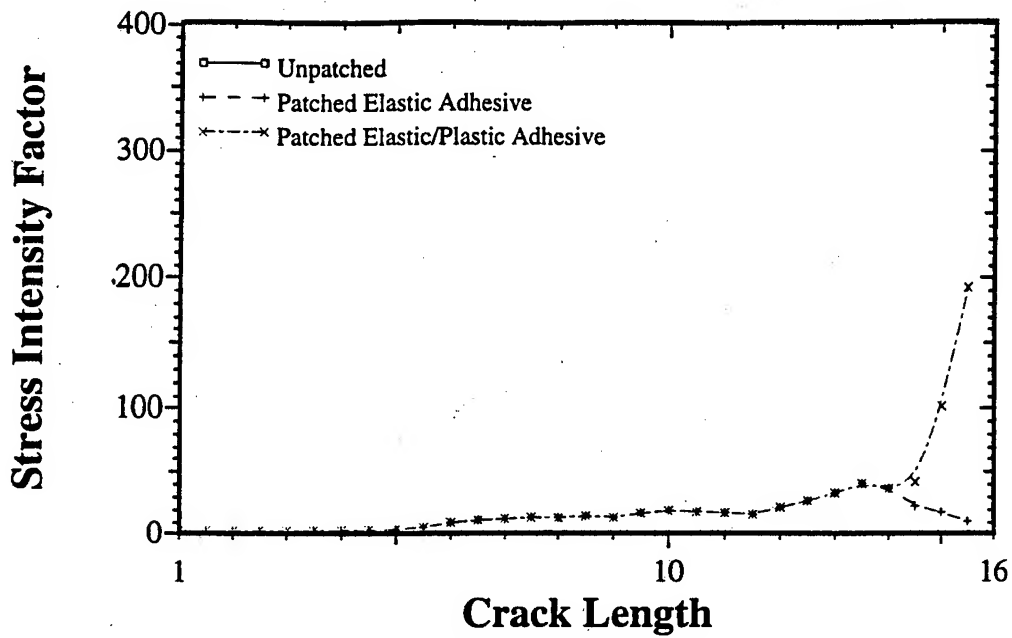


Figure 7: Stress Intensity factors Vs. Crack Length

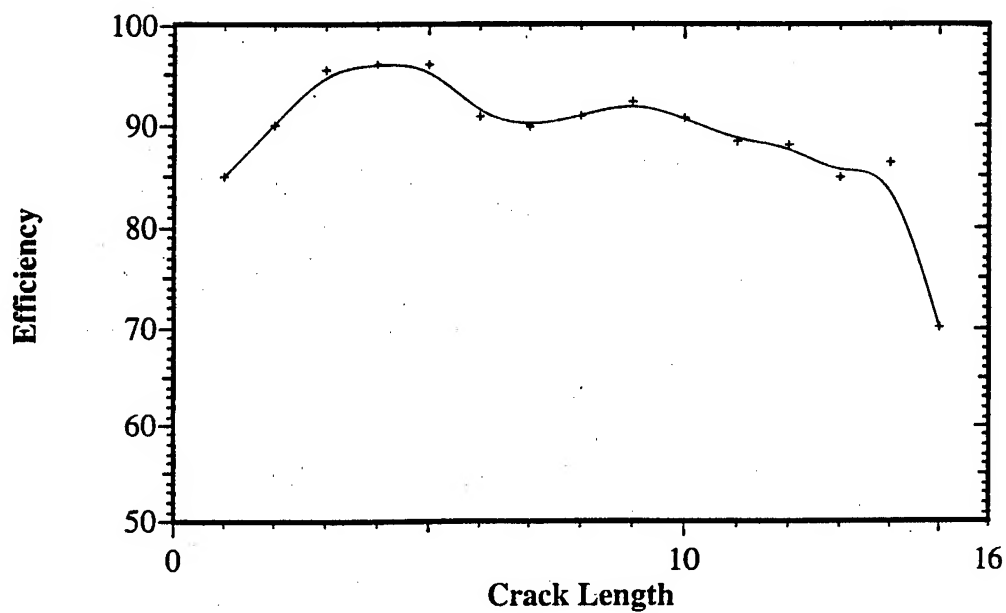


Figure 8: Efficiency of Crack Patching

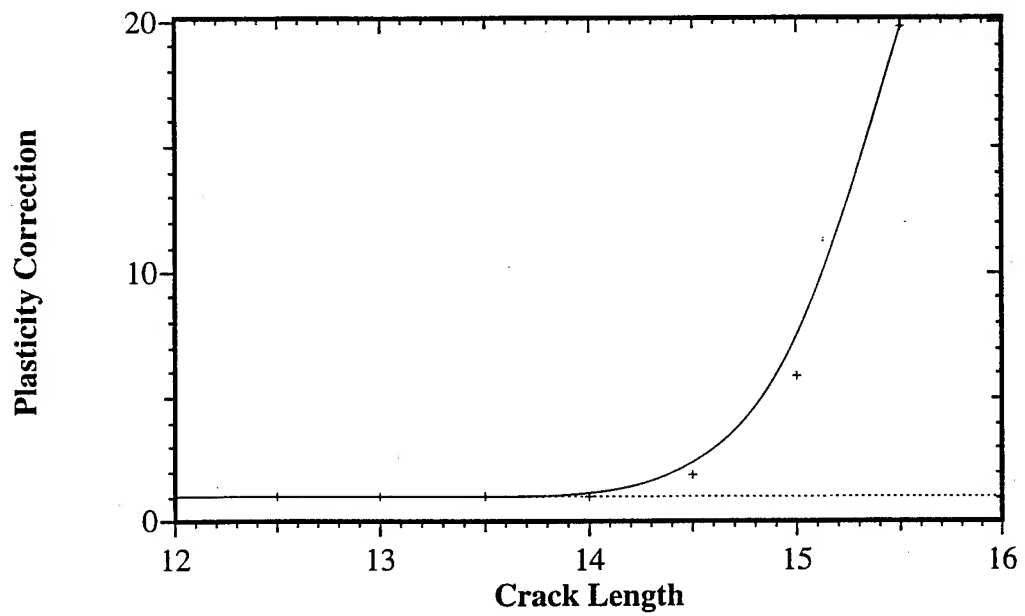


Figure 9: Effect of Plasticity



Figure 10: Effective Stress in the Adhesive for Crack Length 3 in

Material	E_1	E_2	ν_{12}	G_{12}
Boron/Epoxy	3.02×10^7 psi	3.69×10^6 psi	0.1677	1.05×10^6 psi
Carbon/Epoxy	1.97×10^7 psi	1.814×10^6 psi	0.30	1.015×10^6 psi
Al 2024-T3	1.05×10^7 psi	1.05×10^7 psi	0.32	3.977×10^6 psi
GLARE	9.565×10^6 psi	7.358×10^6 psi	0.33	2.685×10^6 psi

Table 4: Properties of Various Patching Materials Considered

Al 2024-T3, and finally the metal laminate GLARE. When the crack is under the patch, the difference is marked. But once the crack becomes longer than the width of the patch, the difference is marginal. When the crack is shorter than the width of the patch, the induced strains cause larger stress to be transferred in stiffer patches. Therefore, the load near the crack tip is reduced and the stress intensity factor reduction is more pronounced for stiffer patches. On the other hand when the crack is longer than the width, the patch transfers the load as in a bonded lap joint and the load transferred is the ligament stress and has little relationship with the stiffness. This is confirmed by the fact that when the crack is extremely long, the stress intensity factor for patched cracks, with patch of various materials is almost the same.

Effect of Adhesive Properties

With the effect of the patch material and geometry determined the effect of the adhesive is now examined. With the boron-epoxy patch of 5 in X 3 in X 0.04 in, the adhesive thickness is varied from 0.001 to 0.005 for a crack of length 8 in. The results are shown in Fig. 25. Thin adhesive layers perform better than thick adhesive layers because, a thick adhesive makes the composite system of the sheet, adhesive layer and patch softer. Often, a thick adhesive layer is needed for good durability as a thick adhesive will experience lesser strains. As can be seen from Fig. 26 the detrimental effect of having a thick adhesive is not severe.

The shear modulus of the adhesive is varied for the same patch dimensions and for 0.004 in thick adhesive. The result is shown in Fig. 26. As can be seen, stiffer adhesives were found to perform better. While, the conditions considered were insufficient for adhesive yield, a stiffer adhesive would result in the yield point being reached earlier. Thus, the material would yield and reduce the patch effectiveness as illustrated earlier. This being the case, it is also noted that the advantage in using a stiffer adhesive (in terms of stress intensity reduction) is not significant.

DEFICIENCIES OF THE METHODOLOGY

Cracks on fasteners rivet rows can be studied using a different local analysis (as in Park Atluri (1992)). As the methodology is based on a finite element alternating method, only straight cracks can be analyzed. In the present work, the pressure loading on the local zone is neglected. As this is a small region, it is good enough approximation. A better approach would be to use a different local zone that can take into account bending also.

In the intermediate model, the adhesive is discretized and modeled as beams. This results in lack of compatibility between the patch and the sheet. As the discretization at this level is not very dense for the adhesive, the error due to this lack of compatibility is thought to be small. A possible remedy for this is the usage of an element as the one used in the local model.

As the traction conditions are being transferred from intermediate to local, extra kinematic boundary conditions have to be applied. In the cases studied, the line of the crack is an axis of symmetry and therefore this line could be fixed. But such an approach might not be applicable in other cases. The effect of constraining other lines has not been studied. A possible remedy is to transfer kinematic conditions from intermediate to local and use a finite element alternating method as in Wang and Atluri (1995) which can handle mixed boundary conditions on the boundary of the local zone. Also, only in-plane stresses are transferred, as a 2-D local analysis is used, the out-of-plane stresses are neglected. Again this can be remedied if a bending finite element alternating method is used. The transfer of kinematic conditions from the global to intermediate between different models (beams - shells) could lead to stress mismatch at the boundary of the models. The error accumulation in such a procedure is not known.

This analysis does not account for the thermal stresses induced during manufacture and operation. These stresses will reduce the patch efficiency. Fredell (1994) has studied the influence of these stresses and

has demonstrated that the efficiency reduction due to these is severe and that it cannot be ignored. The analysis done here has to be modified to take into account the thermal effects. This analysis does not take into account the peel (normal) stresses.

CONCLUSION

In this work, the repairs to airplane fuselages have been analyzed. Mechanical doubler repairs have been compared with patch repairs. The stress intensity factors for patch repaired cracks in actual fuselages have been obtained. The stress intensity factors for the unrepaired fuselages have been obtained and efficiency of patch repairs has been demonstrated. The effect of considering the adhesive as an elastic perfectly plastic material has been analyzed. Using this methodology repairs to fuselages have been analyzed. The effect of various parameters on the performance of the repairs have also been analyzed.

REFERENCES

- Almroth, B. O.; Brogan, F. A.; Stanley, G. M., 1986: Structural analysis of general shells, User's Instruction for STAGSC-1, Lockheed Missiles and Space Company, LMSC D633873, Palo Alto, CA.
- Ashwell, D. G.; Sabir, A. B., 1972: A new cylindrical shell finite element based on simple independent strain functions. *Int. J. Mech. Sci.* 14: 171-183.
- Atluri, S. N.; Kathiresan, K., 1978: Stress Analysis of typical flaws in aerospace structural components using 3D hybrid displacement finite element method. 19th AIAA/ASME/SAE Structures, Structural Dynamics and Materials Conf., Bethesda, MD, 340-351.
- Atluri, S. N., 1986: Computational Methods in the Mechanics of Fracture. Elsevier Science Publishers B. V.
- Atluri, S. N.; Tong, P., 1991: Computational schemes for integrity analyzes of fuselage panels in aging airplanes. In: Atluri, S. N.; Sampath, S. G.; Tong, P. (eds) Structural integrity of aging airplanes, Springer series in Computational Mechanics. Springer-Verlag, Berlin.
- Baker, A. A.; Jones, R. (eds), 1988: Bonded Repair of Aircraft Structures. Martinus Nijhoff Publishers, Dordrecht.
- Chu, R. C.; Ko, T. C., 1989: Isoparametric shear spring element applied to crack patching and instability. *Theoretical and Applied Fracture Mechanics*, 11: 93-102.
- England, A. H., 1971: Complex Variable Methods In Elasticity. Wiley, London.
- Erdogan, F.; Arin, K., 1972: A sandwich plate with a part-through and a debonding crack. *Eng. Frac. Mech.* 4: 449-458.
- Fox, D. D.; Simo, J. C., 1992: A drill rotation formulation for geometrically exact shells. *Computer Methods in Applied Mechanics and Engineering*, 98:329-343.
- Fredell, R. S., 1994: Damage tolerant repair techniques for pressurized aircraft fuselages, Ph. D. Dissertation, Faculty of Aerospace Engineering, Delft University of Technology.
- Fredell, R. S., 1995: Personal Communication.
- Gladwell, G. M. L.; England, A. H., 1977: Orthogonal Polynomial solutions to some mixed boundary-value problems in elasticity theory. *Q. J. Mech. Appl. Math.* 30:175-185.
- Hart-Smith, L. J., 1974: Analysis and design of advanced composite bonded joints. NASA CR 2218.
- Hong, C. S.; Jeng, K. Y., 1985: Stress intensity factors in anisotropic sandwich plate with a part-through crack under mixed mode deformation. *Eng. Frac. Mech.* 21:285-292.
- Jones, R.; Callinan, R. J., 1979: Finite element analysis of patched cracks. *J. Structural Mech.* 7(2):107-130.
- Kan, H. P.; Ratwani, M. M., 1981: Nonlinear behavior effects in cracked metal-to-composite bonded structures. *Eng. Frac. Mech.* 15:123-130.
- Ko, W. L., 1978: An orthotropic sandwich plate containing a part-through crack under mixed mode deformation. *Eng. Frac. Mech.* 10:15-23.
- Liao, C-Y, 1990: Alternating method applied to 3-D part-through crack problems, with application to the weight function method. Ph. D. Dissertation, School of Civil Engineering, Georgia Institute of Technology.

- Miller, M.; Kaelber, K. N.; Vorden, R. E., 1992: Finite element analysis of pressure vessel panels. In: Atluri, S. N.; Harris, C. E.; Hoggard, A.; Miller, N. J.; Sampath, S. G.: Proceedings of International Workshop on Structural integrity of aging airplanes, Mr. 31 - April, 2 1992. pp 337-348.
- Mitchell, R. A.; Wooley, R. M.; Chivirut, D. J., 1975: Analysis of composite reinforced cutouts and cracks. AIAA J. 13: 774-749.
- Muskhelishvili, N. I., 1953: Some basic problems of the mathematical theory of elasticity. Noordhoff, Groningen.
- Nayak, G. C.; Zienkiewicz, O. C., 1972: Elasto-plastic stress-analysis. A generalization for various constitutive relations including strain softening. Int. J. for Num. Meth. in Eng. 5:113-135.
- Park, J. H.; Atluri, S. N., 1992: Fatigue Growth of Multiple-Cracks near a row of fastener-holes in a fuselage lap-joint, In: Atluri, S. N.; Harris, C. E.; Hoggard, A.; Miller, N. J.; Sampath, S. G.: Proceedings of International Workshop on Structural integrity of aging airplanes, Mr. 31 - April, 2 1992. pp 91-116. Also Computational Mechanics (1993) 13:189-203.
- Park, J. H.; Ogiso, T.; Atluri S. N., 1992: Analysis of Cracks in aging aircraft structures, with and without composite-patch repairs. Computational Mechanics, 10: 169-201.
- Park, J. H.; Singh, R.; Pyo, C. R.; Atluri, S. N.; Tan, P. W., 1993: Residual strength of fuselage panels with wide-spread fatigue damage, In: Bom, A. F. (ed): Durability and structural reliability of airframes, ICAF 1993, Stockholm.
- Pyo, C. R.; Okada, H.; Atluri, S. N., 1994: Analysis of MSD and its linkup in aircraft panels by using an elastic-plastic FE alternating method. FAA/NASA international symposium on advanced structural integrity methods for airframe durability and damage tolerance, NASA CP-3274.
- Rankin, C. C.; Brogan, F. A., 1991: The computational mechanics test bed structural element processor ES5: STAGS shell element, NASA CR 4358.
- Rose, L. R. F., 1981: An application of inclusion analogy, Int. J. Solids and Structures, 17: 827-838.
- Samavedam, G.; Hoadley, D., 1994: Fracture and fatigue strength evaluation of multiple site damaged aircraft fuselages - curved panel testing and analysis. DOT-VNTSC-FAA-93-8.
- Sethuraman, R.; Mathi, S. K., 1989: Determination of mixed mode stress intensity factors for a crack-stiffened panel. Eng. Frac. Mech. 33: 355-369.
- Shenoy, V. B.; Potyondy, D. O.; Atluri, S. N., 1994: A methodology for computing nonlinear fracture parameters for a bulging crack in a pressurized aircraft fuselage. Computational Mechanics, 14:529-548.
- Simo, J. C., 1993: On a stress resultant geometrically exact shell model. Part VII: Shell intersections with 5/6 -DOF finite element formulations. Computer Methods in Applied Mechanics and Engineering, 108:319-339.
- Singh, R.; Park, J. H.; Atluri, S. N., 1994: Growth of multiple cracks and their link-up in a fuselage lap joint. AIAA J.
- Starnes, J. H.; Britt, V. O., 1991: Damaged stiffened shell research at NASA Langley research center, Proc. of 1991 Intl. Conf. on Aging Aircraft and Structural Airworthiness, Washington DC, C. E. Harris, ed., NASA conference Publications 3160, pp 203-220.
- Swift, T., 1974: The effect of fastener flexibility and stiffener geometry on the stress intensity in stiffened cracked sheet. Prospect of fracture mechanics. Noordhoff, The Netherlands.
- Swift, T., 1984: Fracture analysis of stiffened structures. Damage tolerance of metallic structures. ASTM STP 842, 69-107.
- Tarn, J. Q.; Shek, K. L., 1991: Analysis of crack plates with a bonded patch. Eng. Frac. Mech. 40: 1055-1065.
- Wang, L.; Atluri, S. N., 1995: An implementation of the Schwartz-Neumann alternating method for collinear multiple crack problems with mixed type of boundary conditions. Submitted to Computational Mechanics.



Figure 11: Effective Stress in the Adhesive for Crack Length 15 in

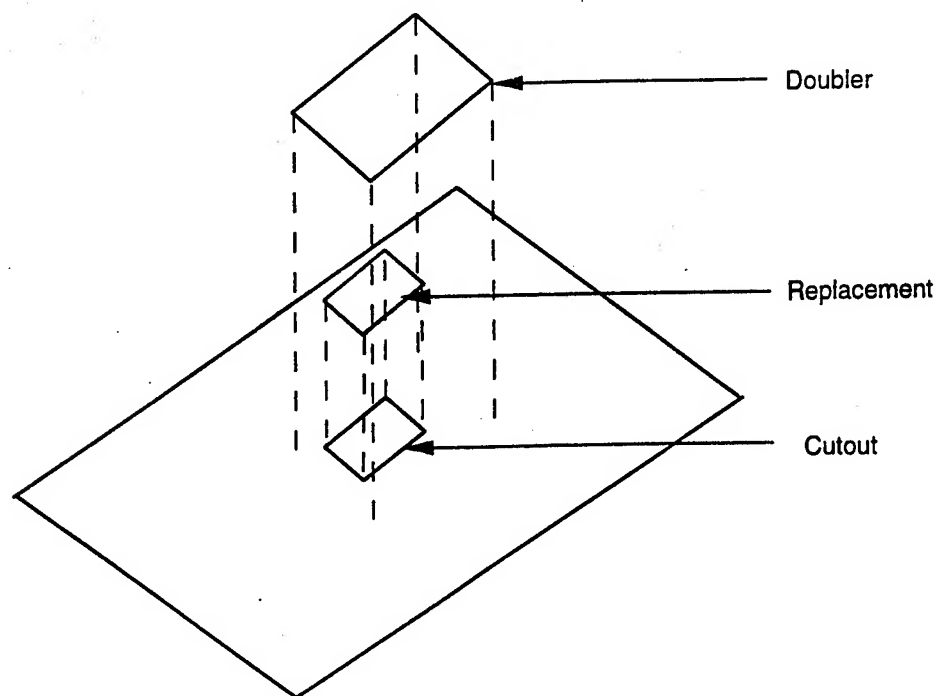


Figure 12: Geometry of the doubler repair

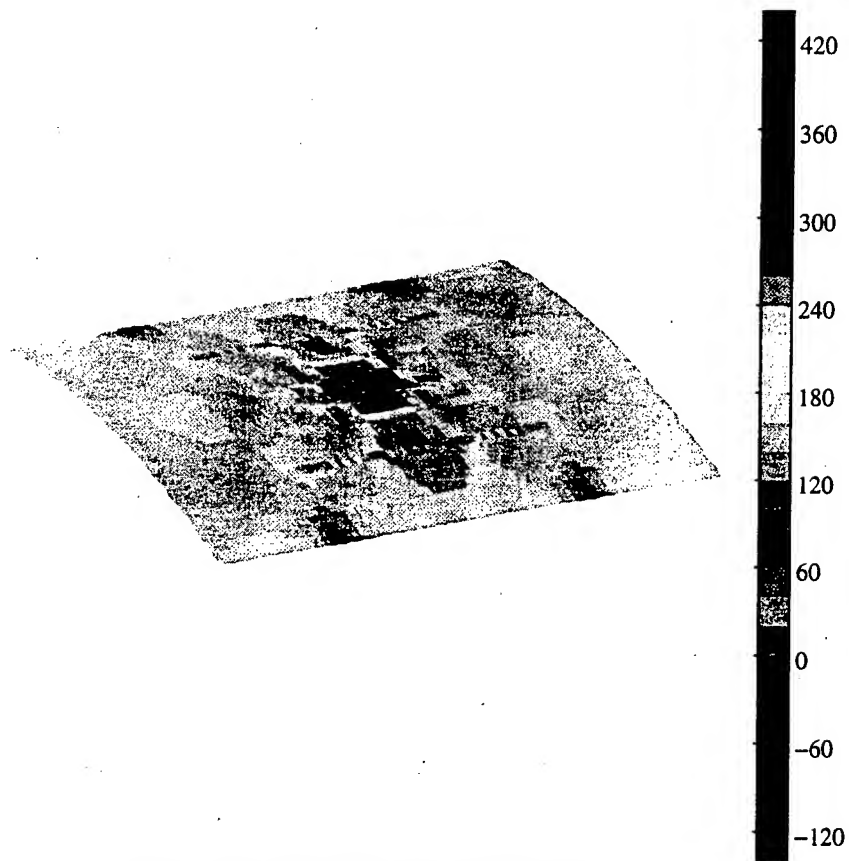


Figure 13: Axial Stress Resultant for Doubler Repair

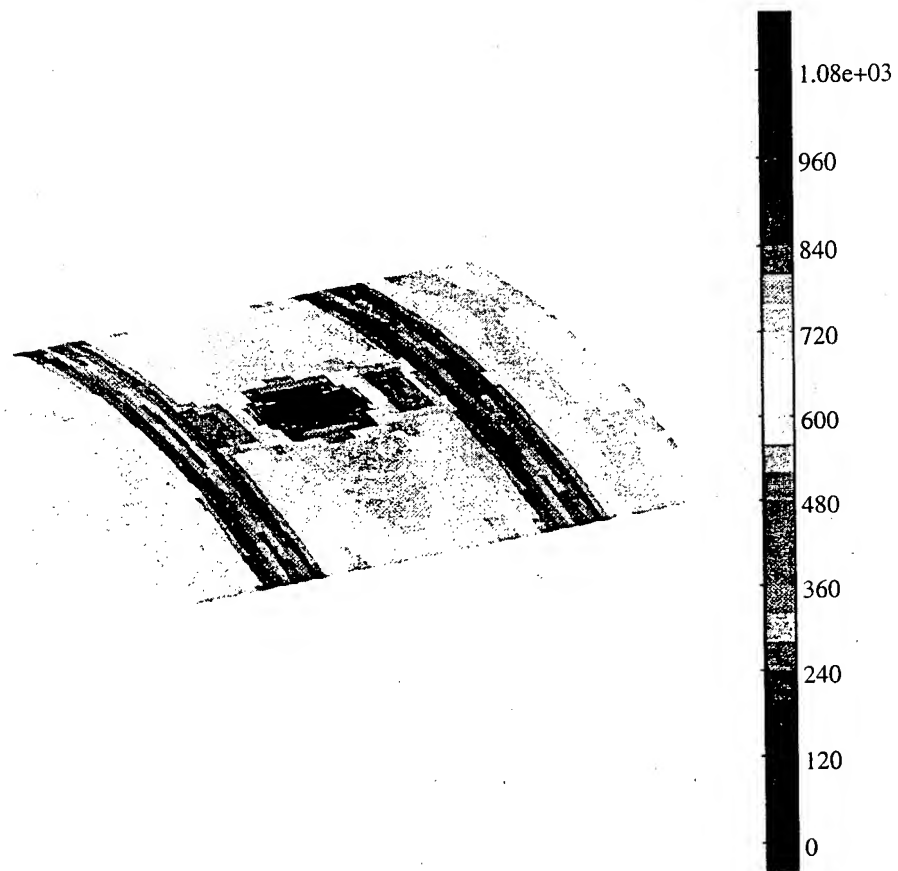


Figure 14: Hoop Stress Resultant for Doubler Repair

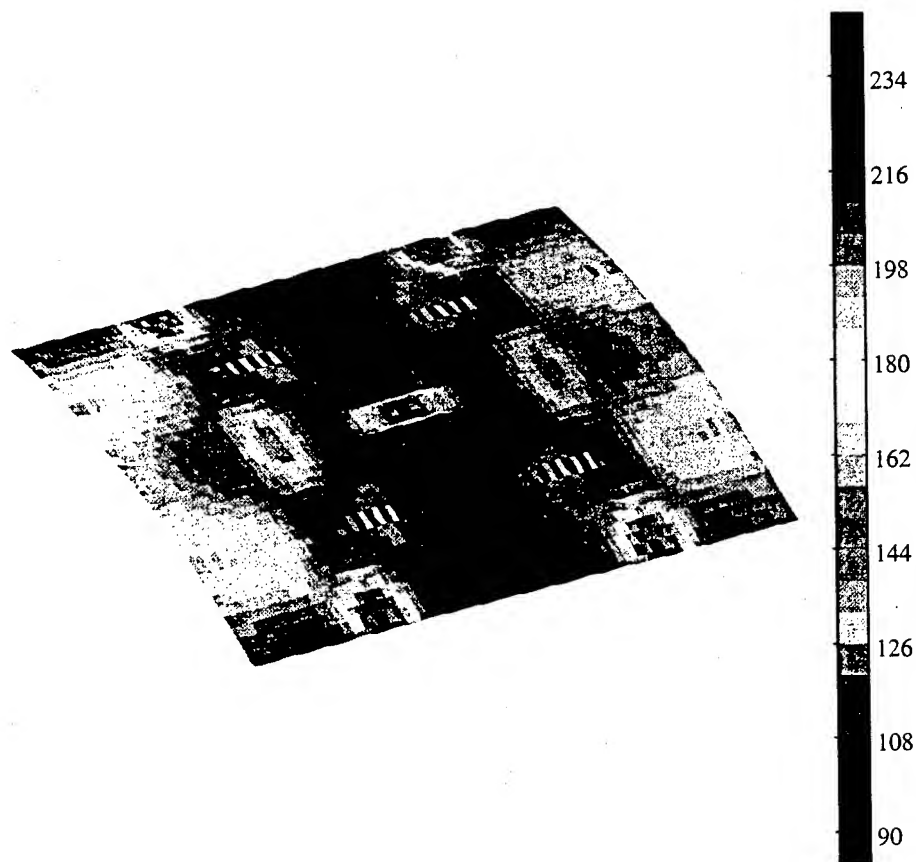


Figure 15: Axial Stress Resultant for Patch Repair

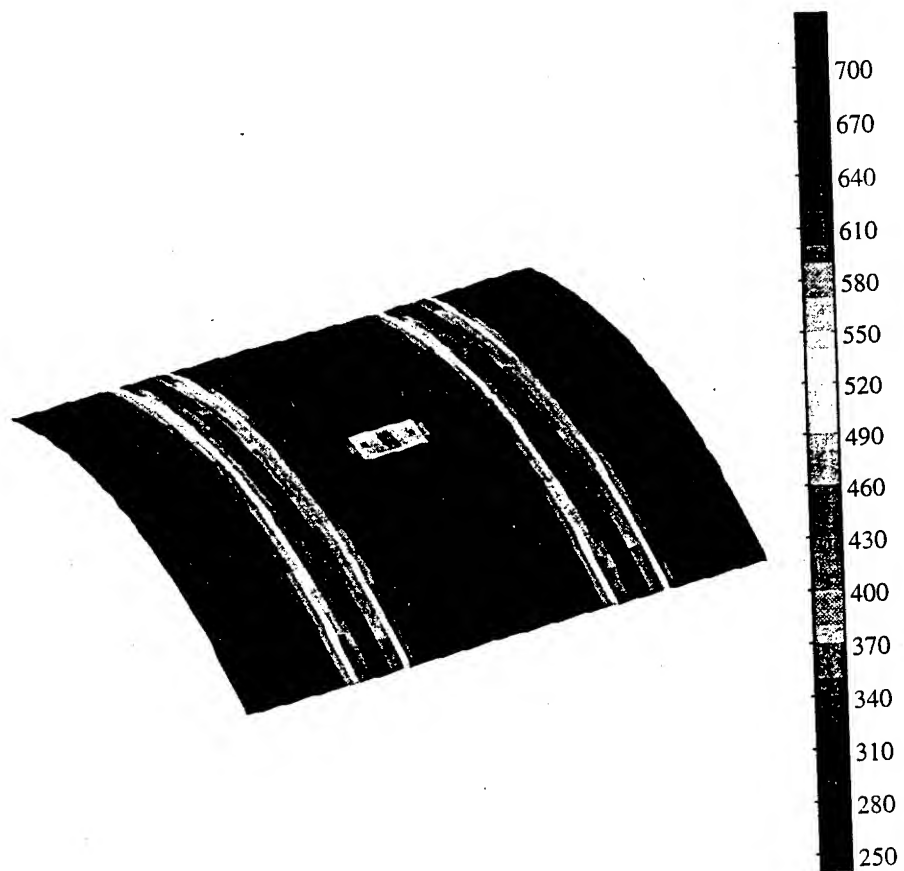


Figure 16: Hoop Stress Resultant for Patch Repair

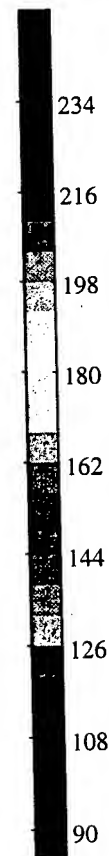
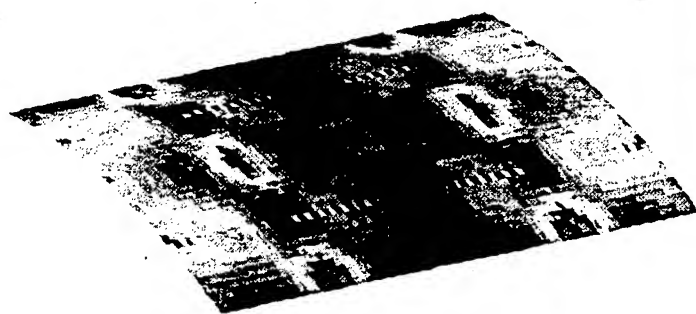


Figure 17: Axial Stress Resultant for Intact fuselage

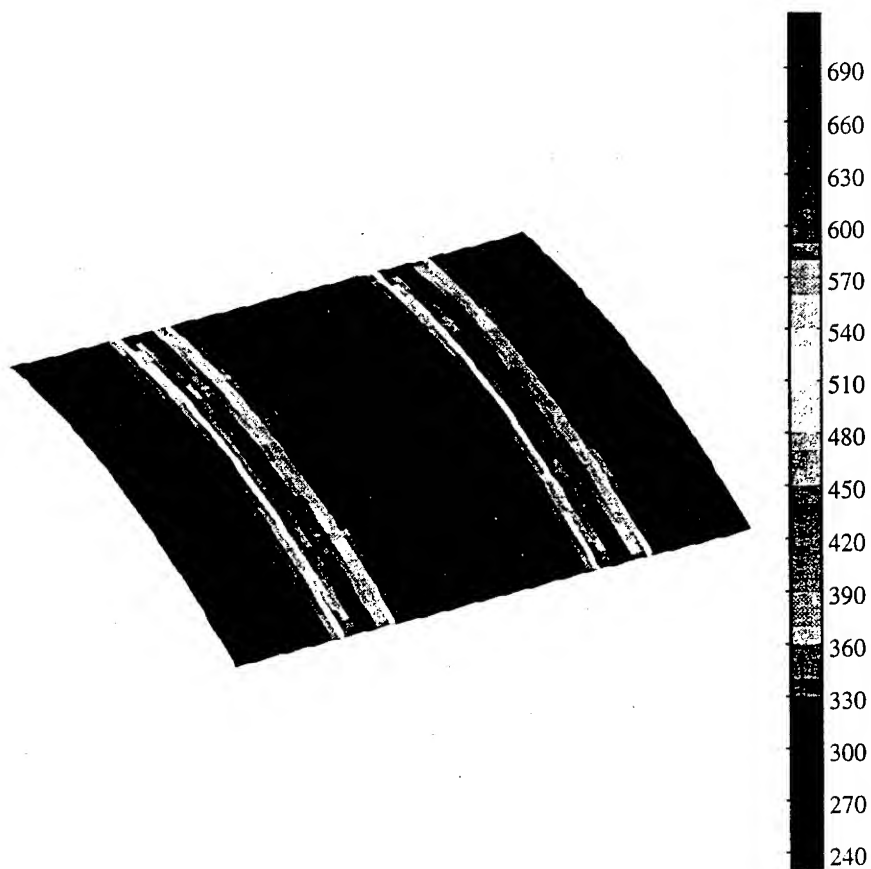


Figure 18: Hoop Stress Resultant for Intact Fuselage

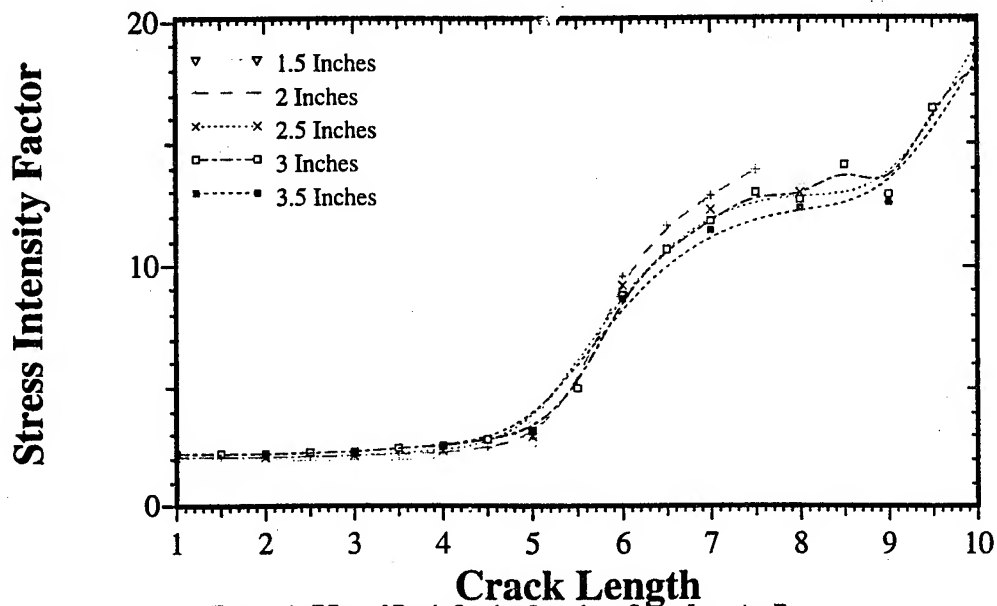


Figure 19: Effect of Patch Overlap Length on Stress Intensity Factor

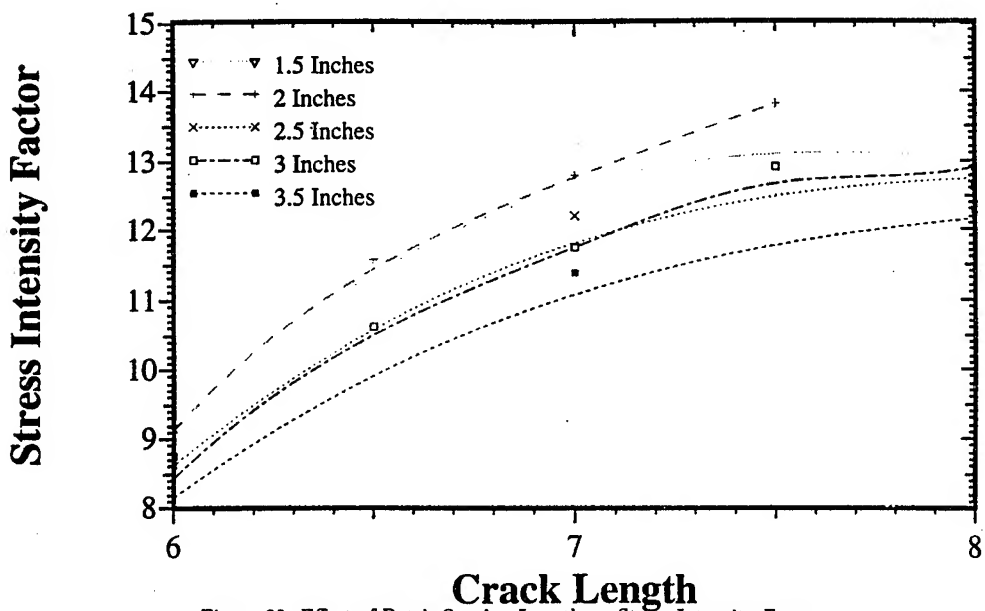


Figure 20: Effect of Patch Overlap Length on Stress Intensity Factor

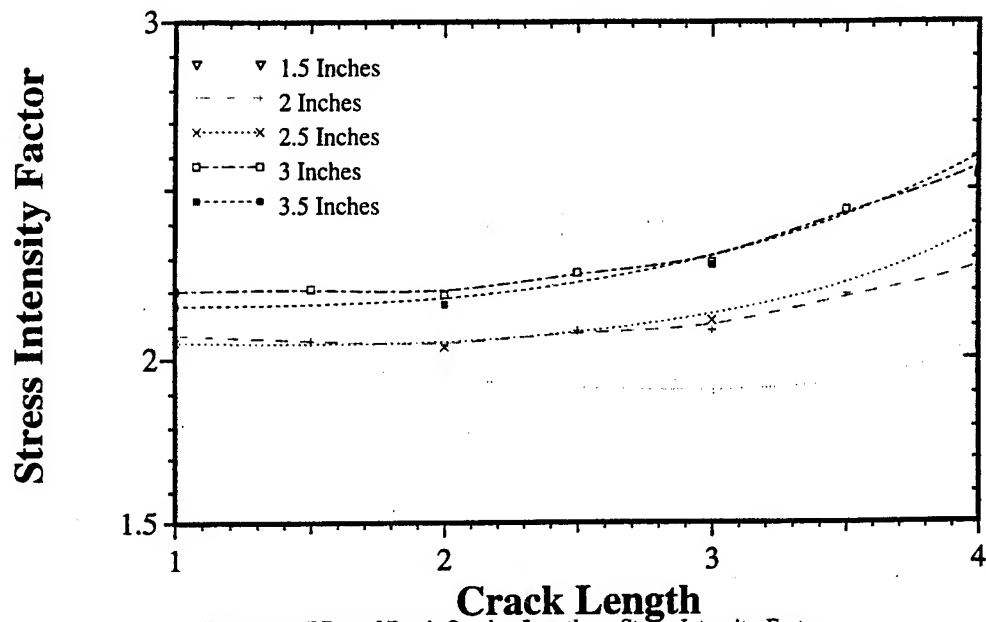


Figure 21: Effect of Patch Overlap Length on Stress Intensity Factor

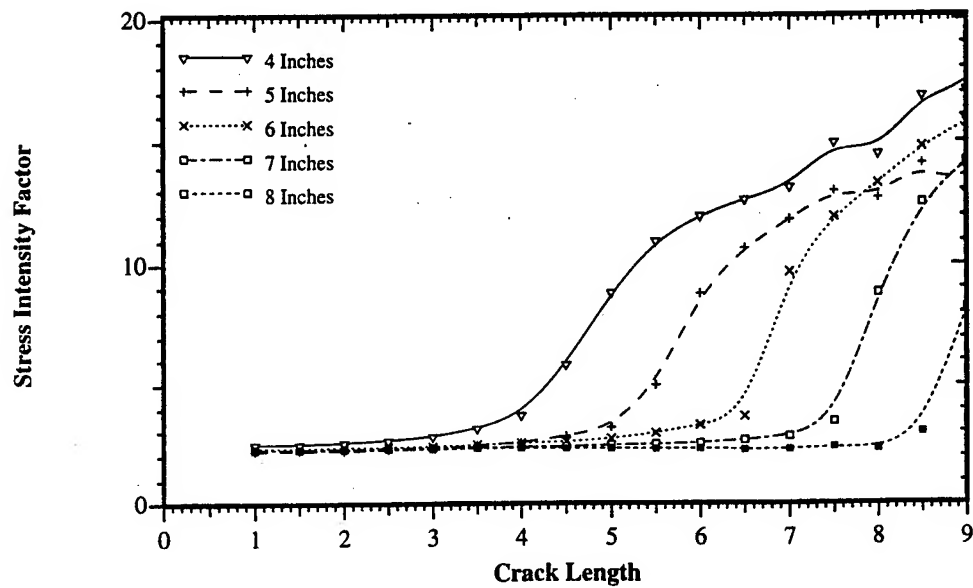


Figure 22: Effect of Patch Width on Stress Intensity Factor

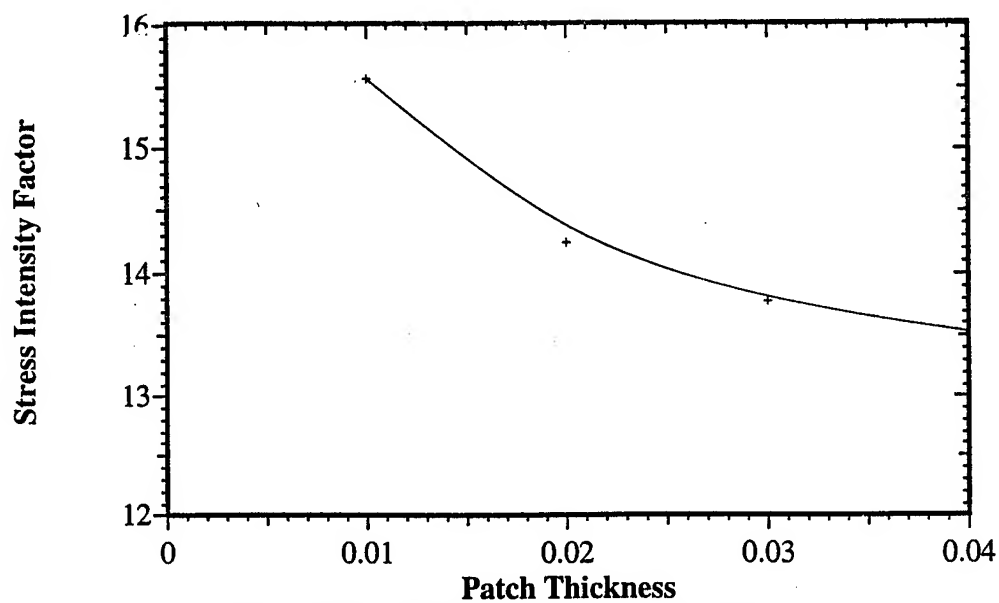


Figure 23: Effect of Patch Thickness on Stress Intensity Factor

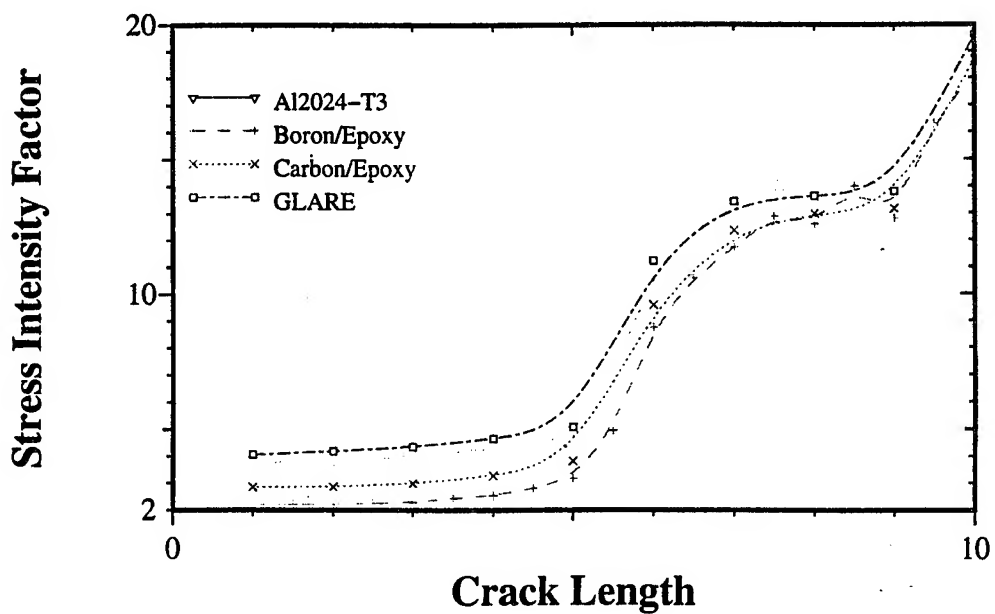


Figure 24: Comparison of Different Patching Materials

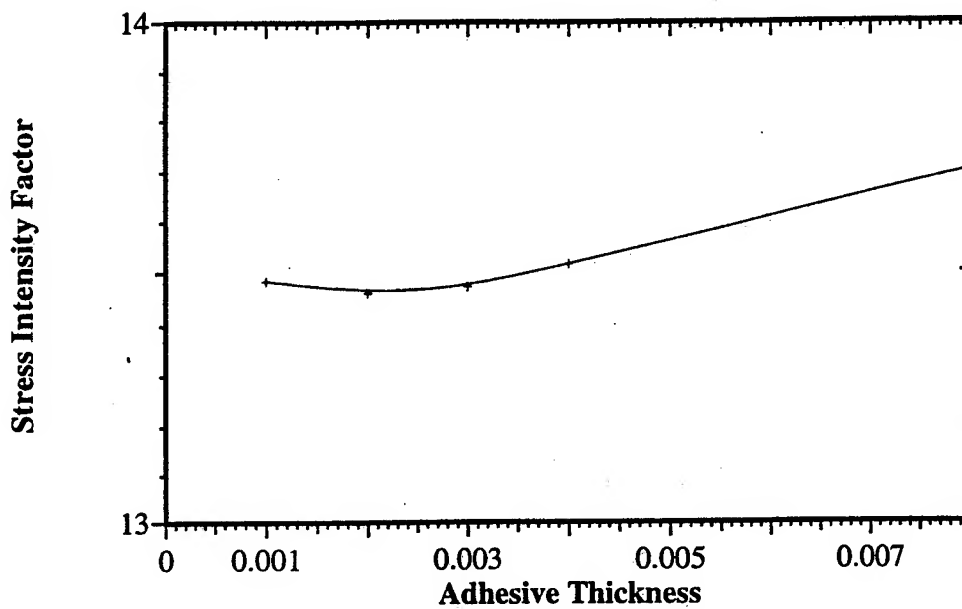


Figure 25: Effect of Adhesive Thickness on Patching Materials

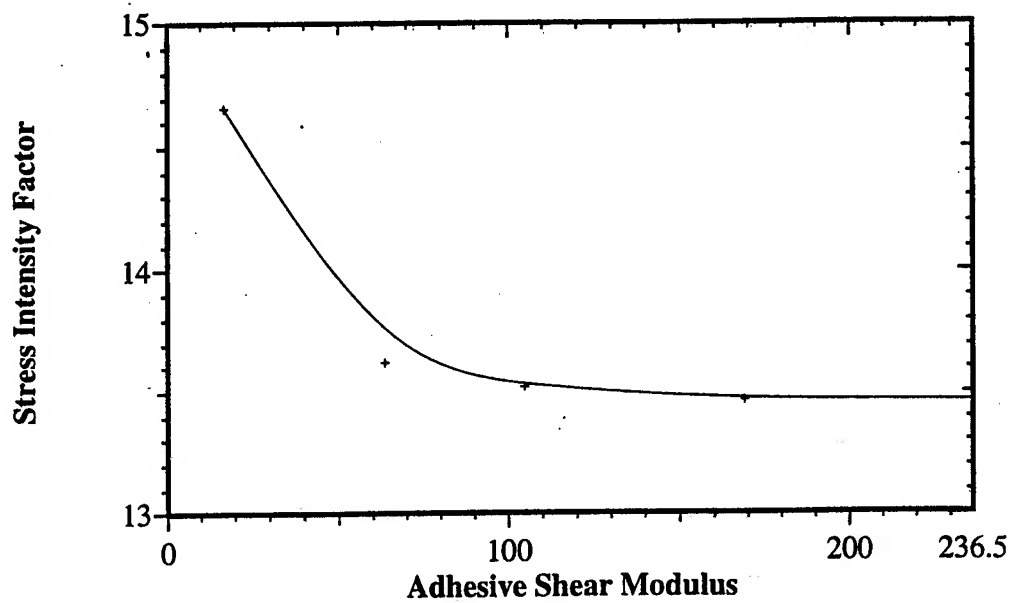


Figure 26: Effect of Adhesive Shear Modulus on Stress Intensity Factor

THE 1973-1974 F/RF-4C/D DAMAGE TOLERANCE AND LIFE ASSESSMENT STUDY REVISITED

Robert M. Bader
Consultant
1613 Kingsway Dr.
Xenia, OH 45385-9589

Roger D. Howell
Ogden Air Logistics Center/LACM
7278 4th Street
Hill AFB, UT 84056-5205

BACKGROUND

The outline for the presentation is shown in Figure 1.

The purpose of this presentation is to examine the Damage Tolerance and Life Extension Study that was accomplished on the F/RF-4C/D aircraft, the implementation of the results of the study by the Ogden Air Logistics Center and the impact that the study may have had on the fleet of F-4's since that time.

The F-4 is a two-place supersonic, long range, all-weather fighter bomber built by McDonnell Douglas Corporation. Mission capabilities include: long range, high altitude intercept utilizing air-to-air missiles; long range attack missions utilizing a wide range of bombs, rockets, dispenser units, gun pods, special weapons and air-to-ground missiles. The F-4C was the first USAF model procured and it was based on a minimum change from the F-4B - the USNavy model then in production. Subsequent USAF models, the F-4D/E and the RF-4C, have used the basic structural configuration of the F-4C. The only significant structural reconfiguration was that required to mount the internal gun in the forward fuselage of the F-4E and the addition of leading edge slats. The F-4E has a 20mm internal gun for air-to-air and air-to-ground use. A select number of F-4Es were modified to the F-4G configuration by removing the gun and developing the Wild Weasel capability. The F-4G Wild Weasel is an all weather hunter-killer used for SAM and AAA suppression. The RF-4C is a supersonic, long range, all weather, multiple-sensor reconnaissance version.

The F-4 was built in many models; illustrated in Figure 2 is an F-4 flying over downtown St. Louis. It was originally

designed in the 1950's for the US Navy. The US Air Force began procuring the F-4 in the 1960's. Over 5,000 F-4's have been procured and it has been operated by 11 foreign countries as well as the Air Force, Navy and the Marine Corp. The F/RF-4C/D Damage Tolerance and Life Extension Assessment was conducted in the 1973 - 1974 time period. The study was also applicable to the E models that were "unslatted", or those F-4Es without leading edge slats. The F-4Es, with leading edge slats, were the subject of a future damage tolerance assessment. Updates of the damage tolerance studies have been accomplished by the Ogden ALC periodically to assure the currency of these evaluations.

Figure 3 illustrates the F-4 structural arrangement. The F-4 primary structure was originally qualified for a 6.5G load factor under the F-4A and F-4B contracts. The evolution of the various F-4 models culminated in the F-4E airplane which is qualified for 8.5G load factor in subsonic flight. Static testing for the various design changes subsequent to the original model verified the design changes. There was no initial design fatigue life requirement for the F-4 although there were several major fatigue tests conducted on various models.

During that period - late 1960's/early 1970's - the USAF was experiencing structural problems with its aircraft. The F-4 was no exception. In addition, the USAF appeared to be in a reactive mode. As structural problems arose in the fleet aircraft a modification would be developed and implemented, and that would fix the aircraft until the next problem arose. However, in general, there was no overall life goal, plan or knowledge of how long the aircraft might, or could, last, nor how much it might cost to keep it in service. Thus, one of the goals of the F-4 assessment, as well as other assessments, was to "get out in front" of the aircraft with a look ahead, and develop a plan of action.

At the time of the assessment there were about 1800 F-4s in the USAF active inventory. Today, there are less than 100 and by the end of the calendar year all F-4s are scheduled to be removed from the active inventory. They probably fall into the category of aging aircraft, or maybe a better description - aged aircraft. The age distributions for the F-4Es, F-4Gs and RF-4Cs that are currently on active duty are shown in Figures 4, 5 and 6. The flight hour distributions for these models are shown in Figures 7, 8 and 9.

DAMAGE TOLERANCE AND LIFE ASSESSMENT STUDY

The goals of the F/RF-4C/D assessment were as illustrated in Figure 10. The purpose of the assessment was to identify the modifications and inspections required to extend the service life of the F-4 to 8,000 hours. Some of the F-4s already had

many flight hours on them so this assessment was faced with applying damage tolerance principles to an aircraft that was already built as opposed to applying the principles to a new design.

The overall program was divided into seven separate assessment tasks. The interrelationships of these tasks are shown in Figure 11. In Task 1, the structurally critical areas of the aircraft were identified. In Task 2, stress spectra were developed for each critical area. In Task 3, the initial "as manufactured" quality of the F-4 was established. These three tasks developed the necessary background information and methods required for the subsequent tasks. In Task 4, a baseline or "average" F-4 aircraft was evaluated. A baseline or average aircraft was defined as an aircraft flying standard missions with average usage. Economic limits, safety limits and the inspection intervals were developed for this baseline aircraft. In Task 5, these methods were applied to determine the economic limits, safety limits and the inspection intervals for each individual aircraft by tail number. The sixth Task included determining and evaluating the structural modifications required to extend the life of the F-4 force to 8,000 hours. Finally, in the seventh task the preliminary costs and implementation schedules were developed along with the actions necessary to implement the results of the study.

The primary considerations in identifying the structural critical areas are (a) the impact of failure, (b) type of structure, and (c) degree of criticality as depicted by Figure 12. The previously accomplished full scale fatigue tests and service experience, if available, along with analyses were used to determine those areas which were most critical on the F-4. For example, an area would be a most critical item if (1) failure would impair flight, (2) it was slow crack growth or monolithic structure, and (3) the critical flaw sizes were small and not inspectable. At the other extreme, if an area was of minor economic impact to repair, was fail safe or multiple load path structure, had a large critical flaw size and was inspectable, that item would be categorized as a non-critical area. Most items were not clearly either most critical or noncritical and would require engineering judgment for evaluation. In the study over one hundred areas were initially screened for their criticality. Fifty areas were investigated in detail. Eleven areas were classified as being noncritical, leaving thirty-nine areas identified as critical either from a safety or a durability (economic) aspect.

Counting accelerometer and multi-channel (VGH) data from force aircraft formed the basis for developing stress spectra (Figure 13) required for the F-4 evaluation. These data were used to determine mission usage and severity of usage. The Nz exceedances per thousand hours versus load factor for air-

to-air, air-to-ground and nontactical missions for the F-4 are schematically shown in Figure 13. From these data, a baseline exceedance curve was developed. VGH data, flight load survey data and strain survey data from full-scale fatigue tests were used to convert the load factor data into stress exceedance curves. From the stress exceedance data, the baseline stress exceedance curves were developed. These exceedance data were formatted into flight-by-flight stress spectra hours involving 730 unique flights per 1000 hours. These baseline flight-by-flight spectra were developed for 19 locations on the aircraft, then interpolated for the other 20 locations, in order to give stress spectra for the 39 critical areas.

In addition, spectra representing past usage were developed for (a) an air combat maneuvering (ACM) training spectrum, (b) a non-ACM training spectrum, (c) a Southeast Asia spectrum (SEA), (d) a reconnaissance (RF) Southeast Asia spectrum, and (e) an RF training spectrum (Figure 14). In addition, the sensitivity of the baseline spectra to usage variations was evaluated. Examples of variations included a substitution of air-to-air for air-to-ground, a look at the air base having most severe usage, and an evaluation of hard landing effects.

The next task was a determination of the initial "as-produced" quality of the F-4 aircraft as illustrated in Figure 15. A Navy full-scale fatigue test article formed the basis for the initial quality assessment. This structure was manufactured in the middle 1960's and was felt to be representative of the quality of the F-4 model production aircraft. In teardown inspections, crack locations were determined and the final flaw sizes were measured. These fracture surfaces were examined by optical and electron fractography and, knowing the test load spectrum, were "traced back" to assist in determining the equivalent flaw sizes at the beginning of the test. These cracks were tracked back as far as possible with fractography and then extrapolated by analysis to time zero to determine the equivalent initial flaw size for each location. An equivalent initial flaw size distribution was then determined. These data were then analyzed statistically to assist in determining the initial flaw sizes for use in the economic and safety limit analyses.

Figure 16 depicts considerations other than the equivalent initial flaw size necessary for the calculation of the safety limit, the economic limit and the inspection interval. Severe conditions were chosen for the calculation of the safety limit and the inspection interval. An initial flaw size of 0.03 inches was assumed. The flaw shape was assumed to be a through crack at a fastener hole. The environment selected was water and air or water and fuel dependent upon the location on the airframe. Flight-by-flight crack growth

analysis, including spectrum retardation effects, was used. For the economic limit calculations, average or normally expected conditions, were selected. An 0.01 inch initial flaw size and a corner or "thumbnail" shape crack typical of what are normally to be expected were chosen. The environment chosen was air or fuel dependent upon the location. Similarly, flight-by-flight flaw growth analysis, including spectrum retardation effects, was used.

Figure 17 shows the relative flaw growth life of the past usage spectra in relation to the baseline spectrum. The relative flaw growth life shown is the ratio of the flaw growth life for the past usage spectrum divided by the flaw growth life for the baseline spectrum. In particular, these lives are the crack growth life from an initial crack of 0.01 inches to 0.03 inches. The ACM base life is slightly less than the baseline life. The Southeast Asia life is also less than the baseline life even though the Southeast Asia load factor frequency curve was less severe than the baseline. This is because the average weights of the aircraft during the Southeast Asia missions were much higher and thus were more damaging. Both RF-4C spectra have longer life than the baseline spectra life.

Applying the techniques just discussed resulted in establishing the areas of concern. Figure 18 lists the resulting operational limits for the baseline aircraft for some of the critical areas. The economic limit, inspection interval and safety limit are given in terms of baseline flight hours. These baseline or average hours are not necessarily representative of any specific aircraft in the force, but represent the hours associated with average or nominal mission mix and severity of usage.

The individual aircraft assessment is discussed in Figure 19. The question arose, "Can the damage index computed at one location on the aircraft be used to predict flaw growth characteristics at other locations?" The study team determined that for the safety and economic limit calculations there was a small band of scatter for all critical locations when the results were normalized. Likewise, for the range of spectra examined, the scatter was small when the data was normalized. From these results, it was concluded that the flaw growth could be scaled from location to location and also among spectra.

This study finding was, of course, very significant in the reduction and interpretation of fleet tracking data. Since the flaw growth data could be scaled from location to location and from spectra to spectra, only one damage index calculation was needed per aircraft. The point selected called the control point, was the lower wing skin at butt line 44 (B.L.44). The allowable damage index was chosen equal to unity (Figure 20) to correspond to 3900 baseline flight

hours, which is the economic limit at that location. The allowable damage indices for all other critical locations in the structure are then the ratios of the baseline operating limits (hours), inspection intervals (hours) or safety limits (hours) to 3900 hours. The fraction of life (or inspection interval) used at any location at any point in time is the ratio of the aircraft damage index to the allowable index for the specification location.

The damage index for each individual aircraft was determined using available counting accelerometer data and the procedures discussed. The aircraft that exceeded the damage index allowables, for critical areas were identified by tail number. In general, problem areas predicted by the tracking program correlated with service experience.

At the time of the study, the survey established, for example, that several aircraft had exceeded the Class I safety limit for a specific location on the wing (the pylon hole). An inspection program for this area was immediately initiated for the specifically identified aircraft. A team from the Ogden ALC inspected the aircraft wherever they were located around the world to determine if cracks did exist in the location identified. Initially, two aircraft were determined to have crack-like defects and the aircraft were subsequently repaired or modified. The results of these and other inspections tended to verify predictions and corrective actions were made.

Those aircraft exceeding the safety limits for other structural locations were also identified by tail number. Those aircraft exceeding the economic limits and/or the inspection intervals were programmed for inspection, repair and/or modification at the earliest opportunity.

The baseline and individual aircraft assessments identified when and where the modifications were needed. The selection of the preferred modifications and the rationale leading to their selection are discussed. Some possible major alternatives to the preferred modifications are briefly discussed and then the operational limits of the modified aircraft are determined.

Modifications were grouped in three general categories: (a) the fastener system, (b) local reinforcement, and (c) part replacement. Three options were considered for the fastener system. The first, an oversize ream with a straight shank clearance fit fastener which is typical of the original manufacture on the F-4. The second option considered an oversize ream with a tapered interference fit fastener. The third option considered an oversize ream with a cold work life improvement process in the hole and a straight shank fastener. Local reinforcement depended upon the peculiar situation or local design options. For the part replacement

category, the options considered were identical design or a redesigned part within the geometric constraints of the subject part.

The cold work process was selected for fastener holes and is described briefly: The inspection of the hole is accomplished and then an oversize ream is used to clean up the hole. This process is repeated until there is no indication of any cracks in the hole. Then, an oversized mandrel is pulled through a thin wall split bushing in the fastener hole. This process introduces beneficial compressive residual stresses around the hole bore. After the hole expansion, a light ream is accomplished to clean up the hole. The principal application of the cold work process is on the wing. The reasons for selection of the cold work process are: (1) It is highly effective in retarding crack growth if any cracks should remain in the fastener holes, (2) it permits the use of straight shank fasteners, (3) it is tolerant to minor process errors and (4) it is considered to be cost effective.

Figures 21, 22, 23 & 24 list the preferred modifications for the critical areas. Most of the items on the lower wing skin are fastener hole critical areas and the preferred modification is identified as the cold work process. The pylon holes and the drain holes were recommended to be fixed by cutting out a local area and installing a steel press fit bushing. The B.L. 100 area had previously been modified with Taper Lok fasteners. This area has sufficient life provided that it is inspected for edge or corner cracking. The 29% stiffener area is a stiffener on the lower wing skin and this stiffener attaches to a span-wise shear web. This area was thought to be inspectable only with a major tear down of the wing and thus would be very expensive. However, feasibility inspections indicated that this internal area could be inspected through the lower surface of the lower wing skin to determine if cracks exist. Other modifications are as shown and consist of part replacement, fastener changes, fastener hole cold working and local reinforcement.

Two major modification alternatives were considered as possible candidates for the wing rather than the many local modifications required. The first was a complete new inner wing torque box. However, it was determined that the cost of the new inner wing greatly exceeds the cost of all the preferred modifications, therefore, that alternative was rejected. The other major alternative considered was the installation of a steel strap along the main spar. However, this modification, while it does fix the main spar area, does not fix seven other items on the wing or provide a life greater than the preferred modifications. Thus, an additional cost would be incurred without fixing all the areas, therefore, this approach was rejected. For the fuselage the only practical approach available, because of its construction, was to incorporate the preferred

modifications. Figures 25, 26, 27 and 28 illustrate four of the locations requiring modification.

IMPLEMENTATION OF STUDY RECOMMENDATIONS

Figures 21, 22, 23 & 24 also summarize the modifications chosen for implementation by the Ogden ALC. The implementation locations that include a strap are related to the unslatted E models that were later converted to E models with leading edge slats. The Ogden ALC opted to inspect the pylon hole and the drain hole and repair as necessary. It was necessary to replace the centerline rib as opposed to just inspecting the rib. This was identified by the full scale fatigue test teardown inspection and service experience revealed difficulties there, also. Other service revealed deficiencies included the outer wing lower torque box skin, the stabilator attach bulkhead and the stabilator lower outboard skin. It was also necessary to replace the wingfold rib two times instead of a one time replacement as suggested by the study team. Blank locations indicate no modification action was taken by the ALC unless inspection indicated the need. For the most part, though, the recommended modifications were accepted by the Ogden ALC.

FULL SCALE FATIGUE TEST

The full scale fatigue test, Figure 29, was conducted in the Structures Test Facility at Wright-Patterson AFB. The overall schedule in relationship to the other elements of the F-4 Aircraft Structural Integrity Program (ASIP) programs is as illustrated in Figure 30. The fatigue test program required about five years to complete. Figure 31 illustrates the time line for the full scale fatigue test. The shaded areas are the actual test times. Much time was spent waiting for the modifications to be provided. The fatigue test article was manufactured on the F-4 production line at McDonnell Aircraft without the structural modifications that were being incorporated into the production aircraft. It was desired to have an airframe as close as possible to an original F-4C/D airframe so that the structural modifications identified in the study could be incorporated during the full scale fatigue test as close as possible to the recommended fleet incorporation times.

All test conditions were derived from the three basic flight profiles: air-to-ground, air-to-air and non-tactical missions. The flight conditions were further defined with variations of airspeed, altitude and vertical accelerations within each flight. Aircraft weight was also a variable with a different value being assigned to each of the three missions. Loads were applied in a flight-by-flight sequence. The 1,000 hour flight segment consisted of 730 flights and

139 combinations of airspeed and altitude. The 139 airspeed/altitude combinations are distributed as 46 air-to-ground missions, 48 air-to-air missions and 45 non-tactical missions. Random load cycles were scattered through ten 1,000 hour segments making the sequence repetitive in 10,000 hour increments.

The modifications as described previously were installed in the fatigue test article at different baseline hours to simulate incorporation into the fleet aircraft as close as possible. The modifications were installed by crews from the Ogden ALC to simulate as much as possible the manner in which the modifications would be installed in the fleet aircraft. An additional modification not originally identified (for an engine mount and backup structure) was required due to a failure during the test. The test was completed at 24,000 simulated flight hours. The modifications performed well and thus were verified for the recommended life extension.

The fatigue test article was subsequently torn down for evaluation. Extensive cracking was found in the following areas: inboard wing fold rib, internal wing stiffeners and the centerline rib and splice suggesting that one or more of these areas might require reevaluation.

TRACKING PROGRAM

The topics from the individual aircraft tracking program that were originally printed out in a summary report are indicated in Figure 32. The Damage Index calculation, of course, was the item of most interest because with this information, those individual aircraft that required attention could be identified. Later, a projection of future damage indices per calendar time was instituted; this information would be valuable to project work load, estimate costs and help identify aircraft to stand down. Figure 32 also summarizes the revised heading topics.

Results from the individual airplane tracking program are illustrated in Figure 33. Shown is a plot of damage index vs. flying hours for the RF-4C aircraft for 1979. There is a wide dispersion of damage indices for a given flying hour total proving again that flying hours is not necessarily a measure of fatigue damage. Figure 34 shows the damage index rate for various models of the F-4 for several periods of time. The damage index rate is obviously influenced by length of the flights and severity of flying. Figures 35, 36 37 & 38 illustrate the damage index distributions for the F-4's that are currently in the inventory.

PRELIMINARY COST INFORMATION

Preliminary cost information was developed to provide rough order of magnitude estimates. Kit costs were estimated by McDonnell Aircraft and man hours required for inspections and for modification installations were estimated by the Ogden ALC. These estimated costs were rolled up to provide a total. Estimates per fiscal year were determined by assuming that all modifications would be installed during the next PDM cycle. Figures 21, 22, 23 & 24 indicate the man hours identified by the Ogden ALC required to accomplish the actual implementations. The original man-hour estimates were about one-half of those experienced in the actual implementation, although direct comparison is difficult because the estimates involved a different mix of models.

OBSERVATIONS

There has been one class A structural failure subsequent to the completion of the damage tolerance assessment that was conducted on the F/RF-4C/D aircraft. In 1979, an RF-4C was practicing dissimilar defensive maneuvering against an F-5E aggressor. The left outer wing assembly separated from the aircraft. The cause was determined to be a fatigue crack which had originated at a bolt hole in the lower skin.

However, the F-4 ASIP can be considered a success from the application of damage tolerance principles, life extension techniques, and individual airplane tracking program development and implementation. A plan was developed to manage the aircraft structural life. The success is due principally to the personnel at the Ogden Air Logistics Center who are responsible for the management of these USAF assets. The study team consisting of McDonnell Aircraft Company and Air Force personnel contributed greatly to the development of procedures that ultimately were used, not only for the F-4, but also for the many damage tolerance and life extension programs that followed. Figure 39 summarizes the observations of the F-4 ASIP program that were directly related to the elements discussed in this presentation.

- * The study provided insight for the future structural management of the F-4 aircraft.

- * The program was implemented and carried out extremely well by the Ogden ALC.

- * There has been one Class A structural mishap in the F-4 program since the study was completed.

BIBLIOGRAPHY

Evolution of the F-4 Phantom, H. D. Barkey, MCAIR Report 71-017, McDonnell Aircraft Company, April 1971

Final Technical Report on the F-4C/D and RF-4C Damage Tolerance and Life Assessment, C. F. Tiffany, John Axley and R. M. Bader, Wright-Patterson AFB, OH, June 1974

The F-4C/D and RF-4C Damage Tolerance and Life Assessment Study -- Modification Costs and Installation Schedule Estimates, R. M. Bader, AFFDL-TM-75-88-FBR, Air Force Flight Dynamics Laboratory, Wright-Patterson AFB, OH, June 1975

A Normalization Scheme for Describing Crack Growth Behavior, J. P. Gallagher and R. M. Bader, Air Force Flight Dynamics Laboratory, Wright-Patterson Air Force Base, OH. Proceedings of the Fourth Army Materials Technology Conference - Advances in Joining Technology, September 1975

Damage Tolerance and Durability Assessments of United States Air Force Aircraft, M. D. Coffin, C. F. Tiffany and R. M. Bader, AGARD Paper, Wright-Patterson AFB, OH, 1978

Damage Tolerance Assessment of F-4 Aircraft, R. E. Pinckert, McDonnell Aircraft Company, MCAIR Report 76-015 - Revision A, September 1976

F-4C/D Life Extension Program, Robert L. Schneider, AFWAL-TR-82-3047, Flight Dynamics Laboratory, Wright-Patterson AFB, OH, October 1982

Damage Tolerance - USAF Experience, J. W. Lincoln, Proceedings of the 13th Symposium of the International Committee on Aeronautical Fatigue, Pisa, Italy, May 1985

Maintaining Aircraft Structures at the Air Force's Ogden Air Logistics Center, Roger D. Howell, Alan Schliep and Tom Burkland, Ogden Air Logistics Center, Hill Air Force Base, Utah, AIAA Paper, March 1995

Figure 1 OUTLINE

BACKGROUND

DAMAGE TOLERANCE AND LIFE ASSESSMENT STUDY

IMPLEMENTATION OF STUDY RECOMMENDATIONS

FULL SCALE FATIGUE TEST

TRACKING PROGRAM

PRELIMINARY COST INFORMATION

OBSERVATIONS

BIBLIOGRAPHY

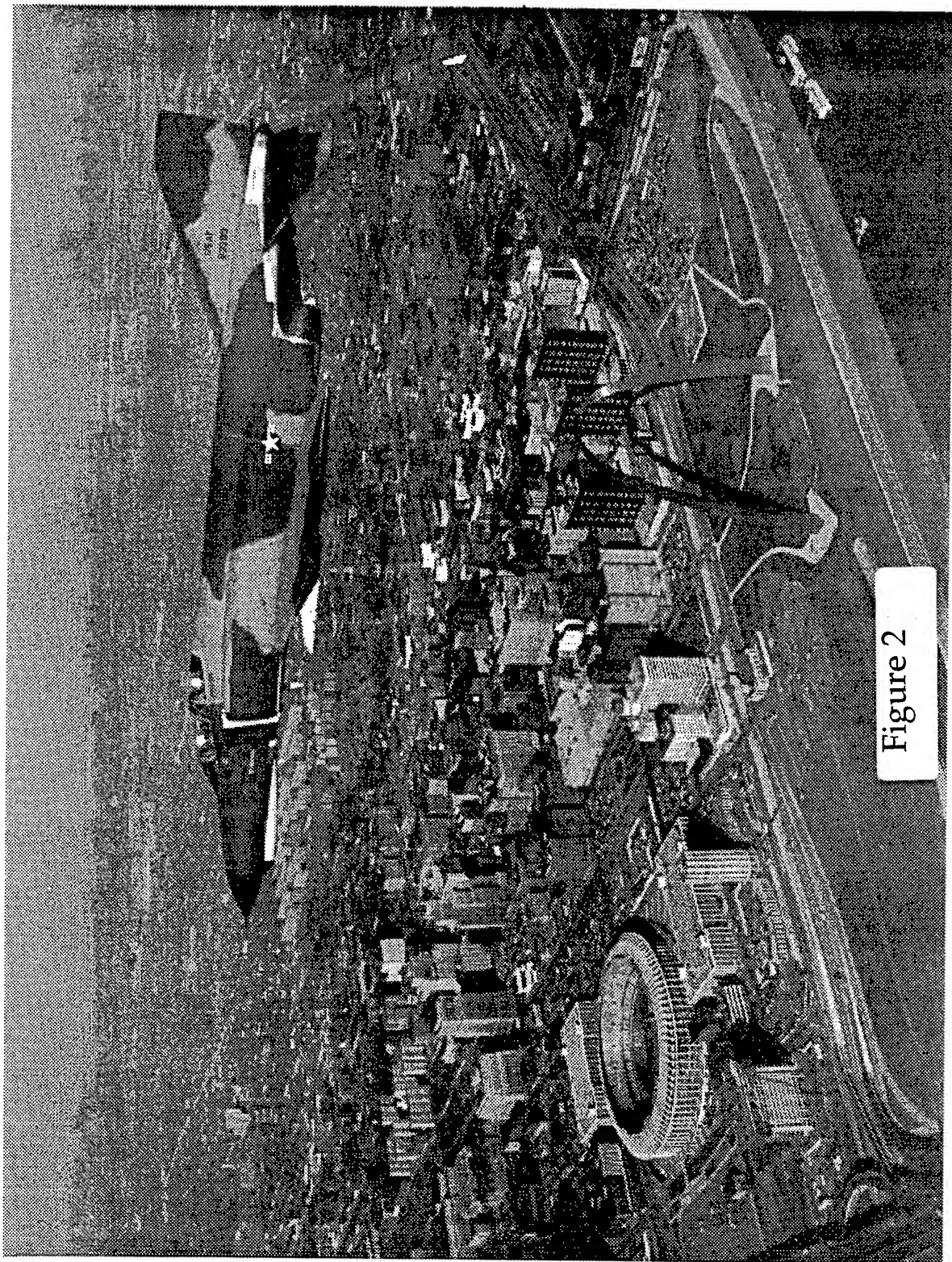


Figure 2

Figure 3
F-4 INTEGRAL STRUCTURE

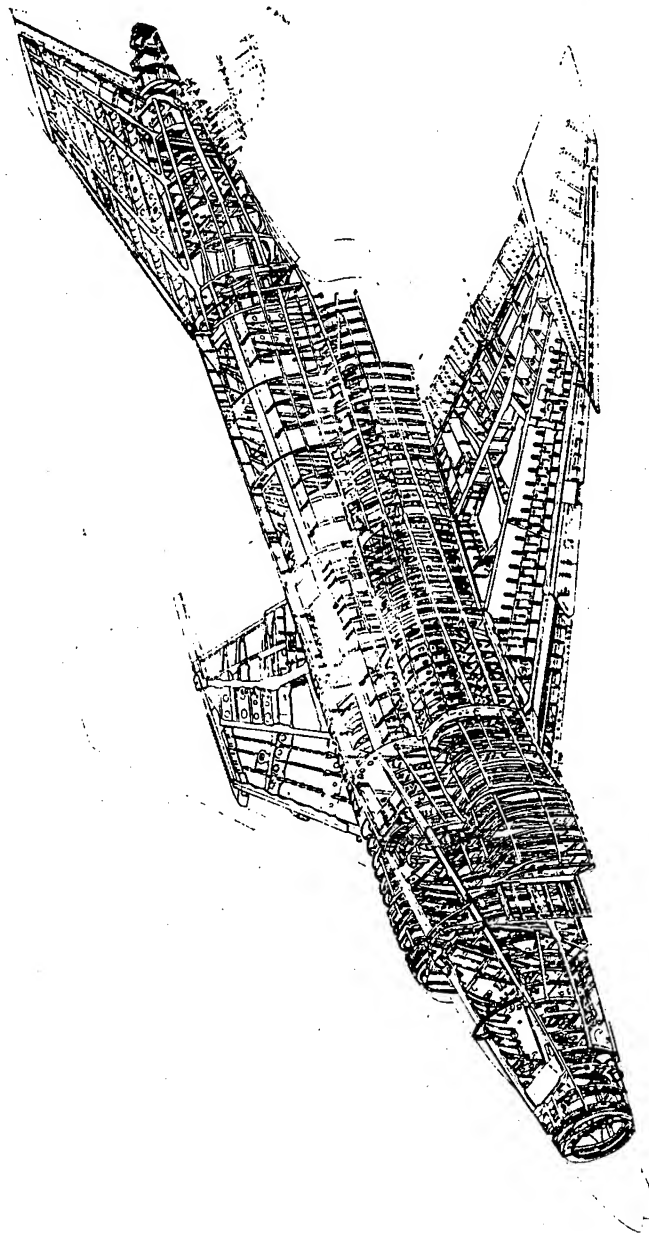
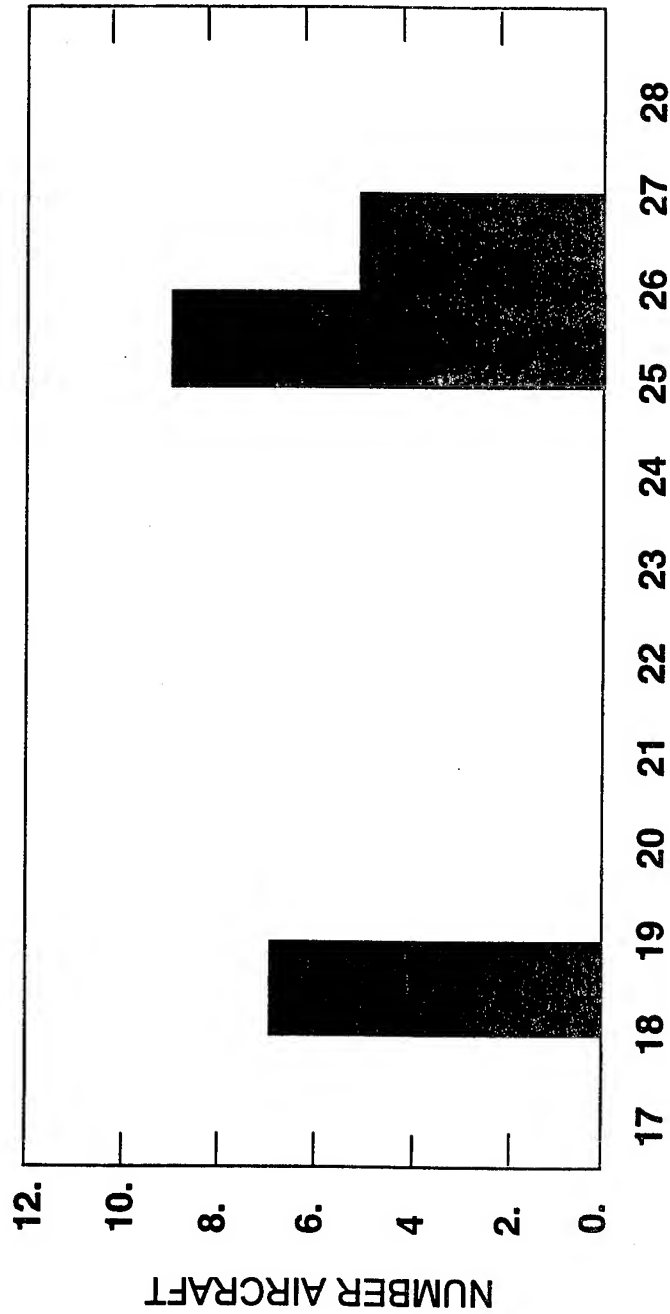


Figure 4

AIRCRAFT AGE DISTRIBUTION F4E



0	7	0	0	0	0	0	0	0	9	5	0	0
---	---	---	---	---	---	---	---	---	---	---	---	---

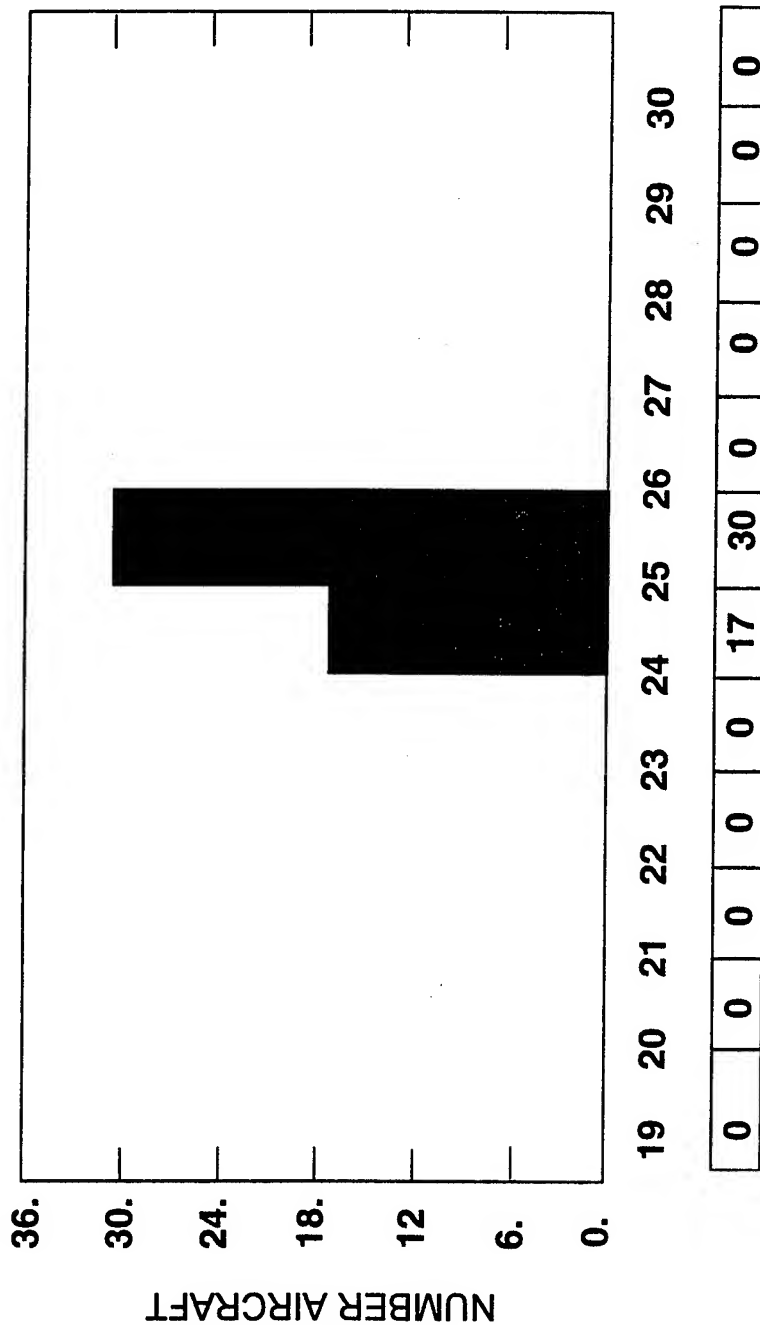
AGE IN YEARS

21 AIRCRAFT

AS OF: 6-SEP-95

Figure 5

AIRCRAFT AGE DISTRIBUTION F4G

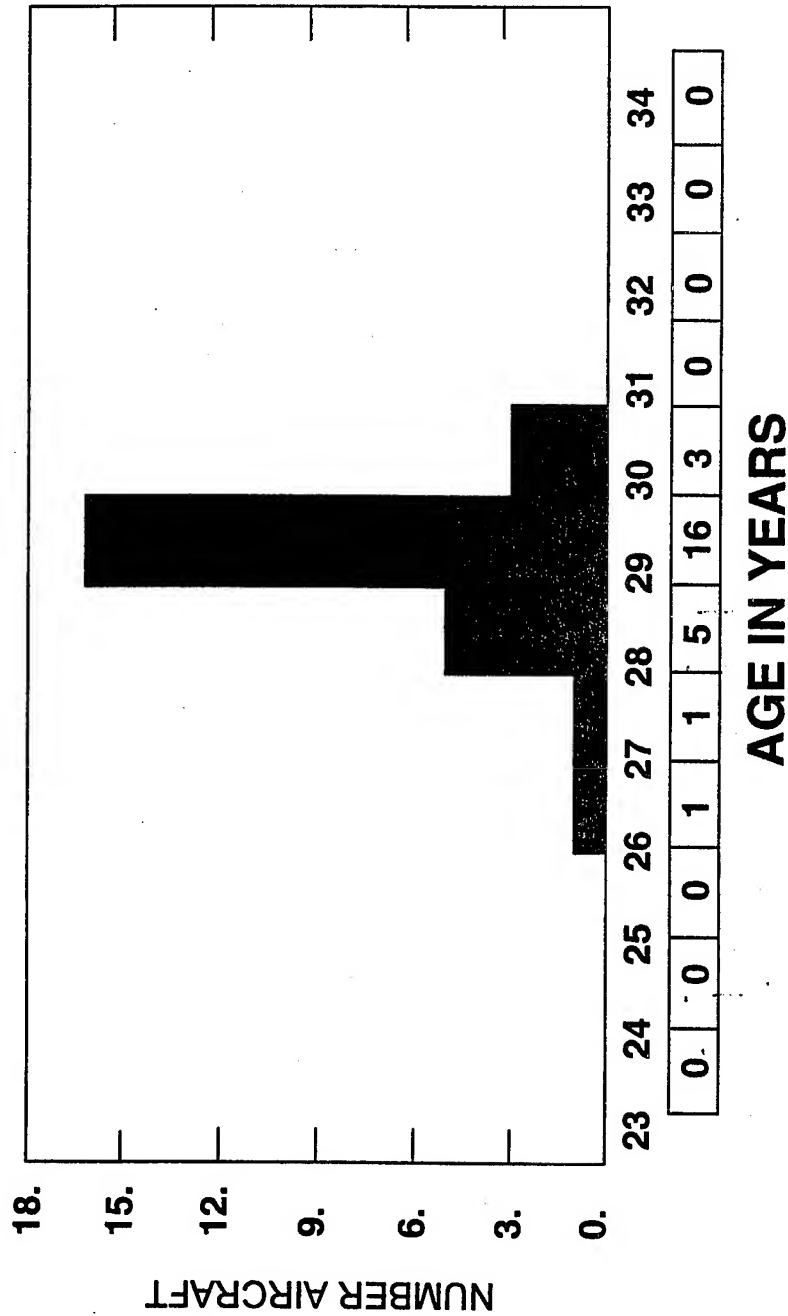


47 AIRCRAFT

AS OF: 6-SEP-95

Figure 6

AIRCRAFT AGE DISTRIBUTION RF4C



26 AIRCRAFT

AS OF: 6-SEP-95

Figure 7

FLYING HOUR DISTRIBUTION F4E

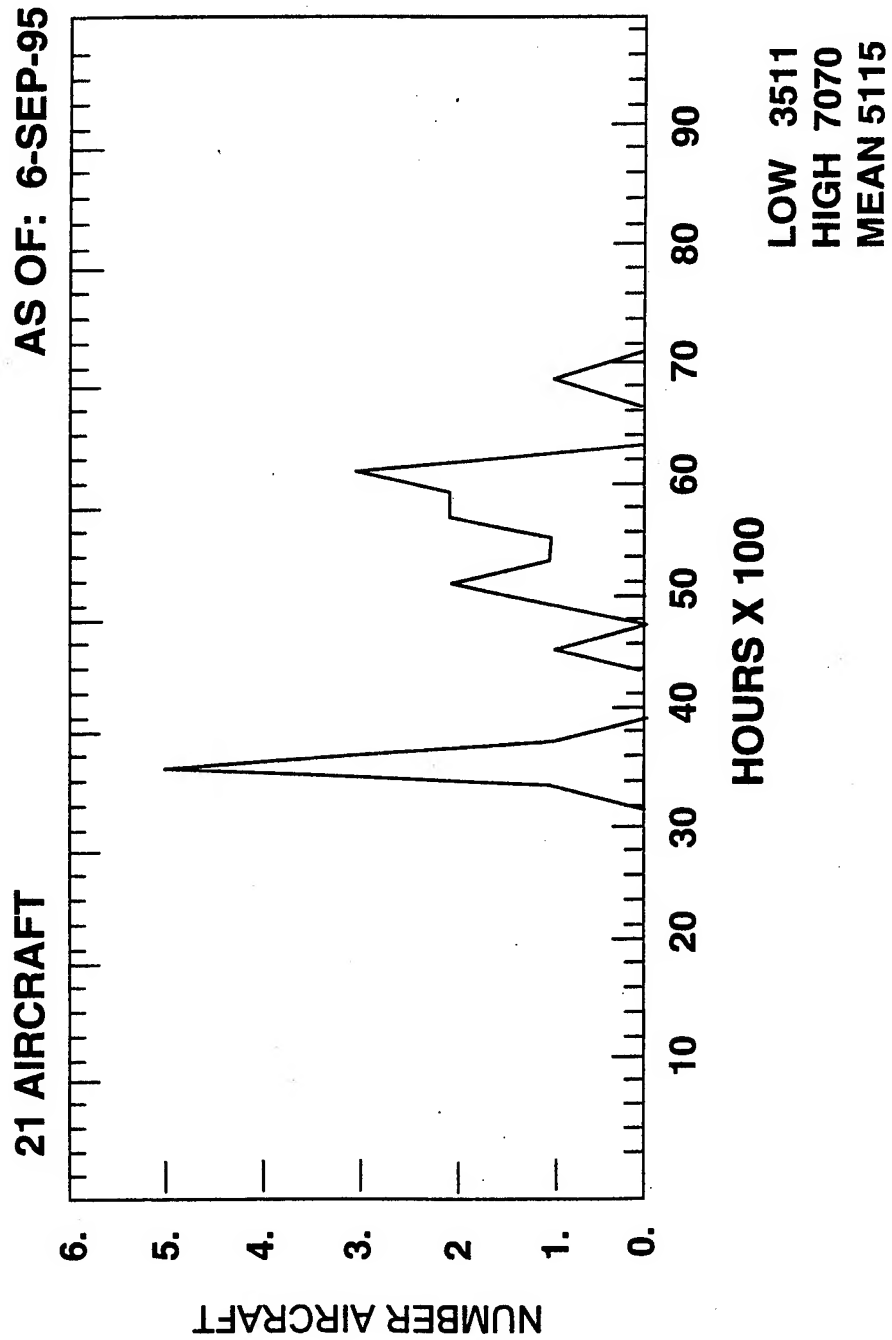


Figure 8

FLYING HOUR DISTRIBUTION F4G

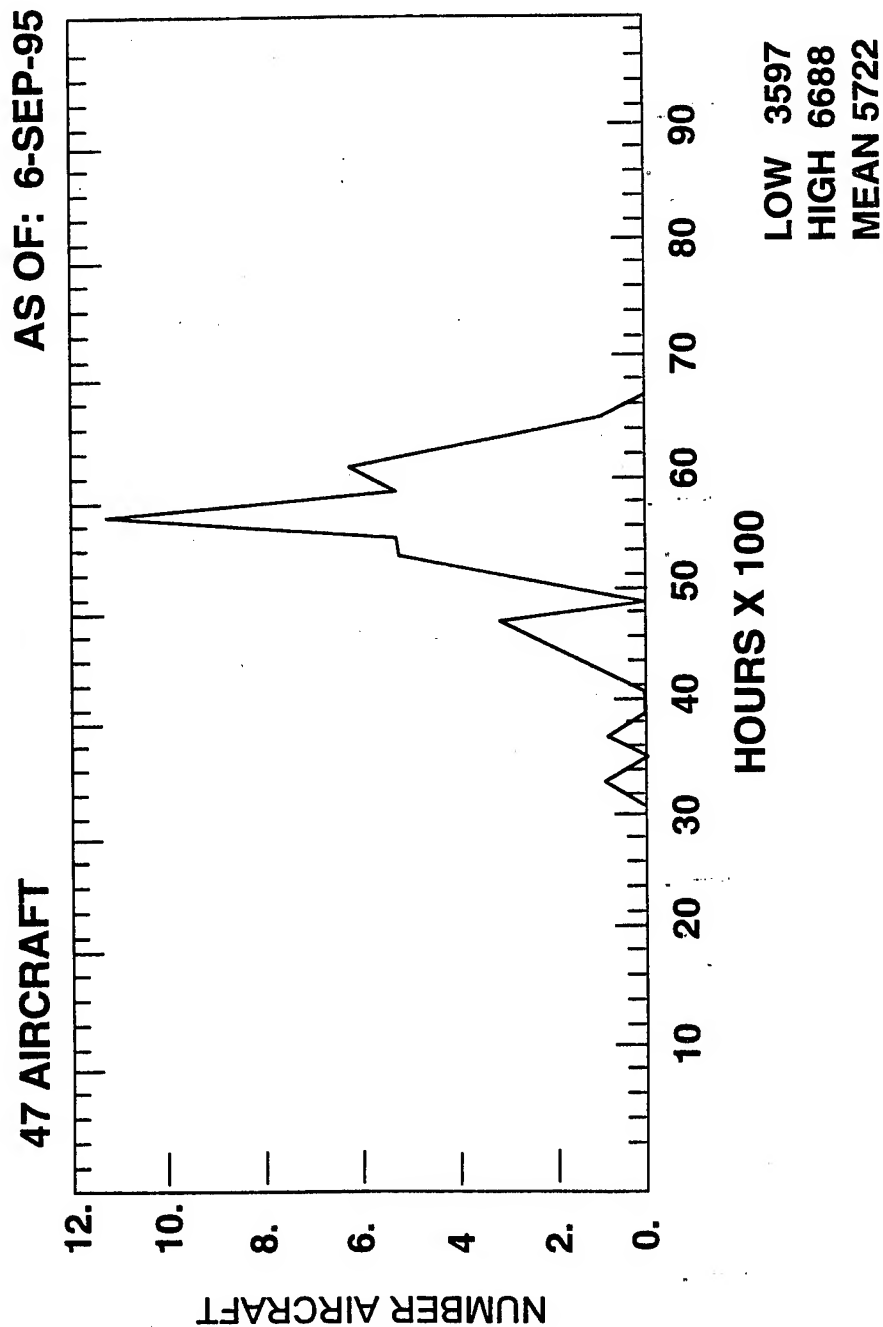


Figure 9

FLYING HOUR DISTRIBUTION RF4C

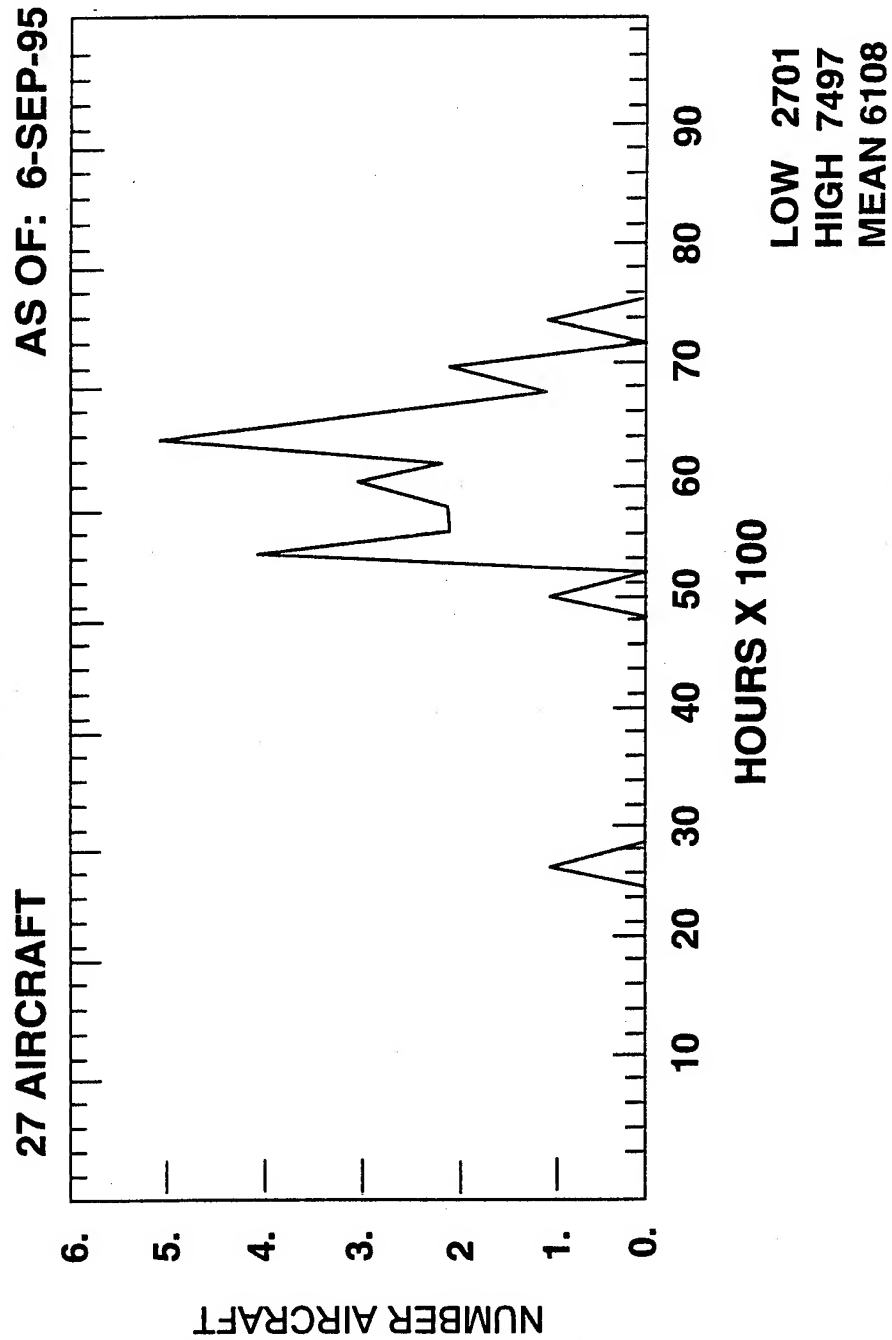


Figure 10

OBJECTIVES

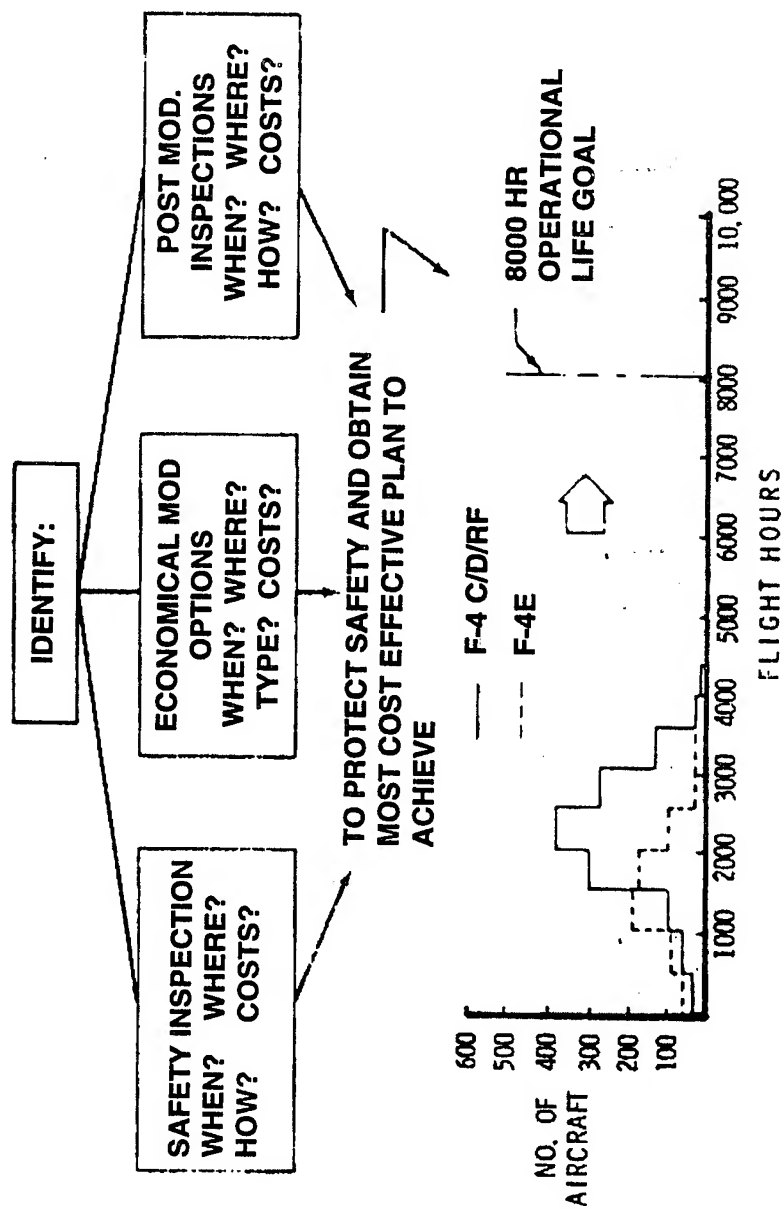


Figure 11

ASSESSMENT TASK

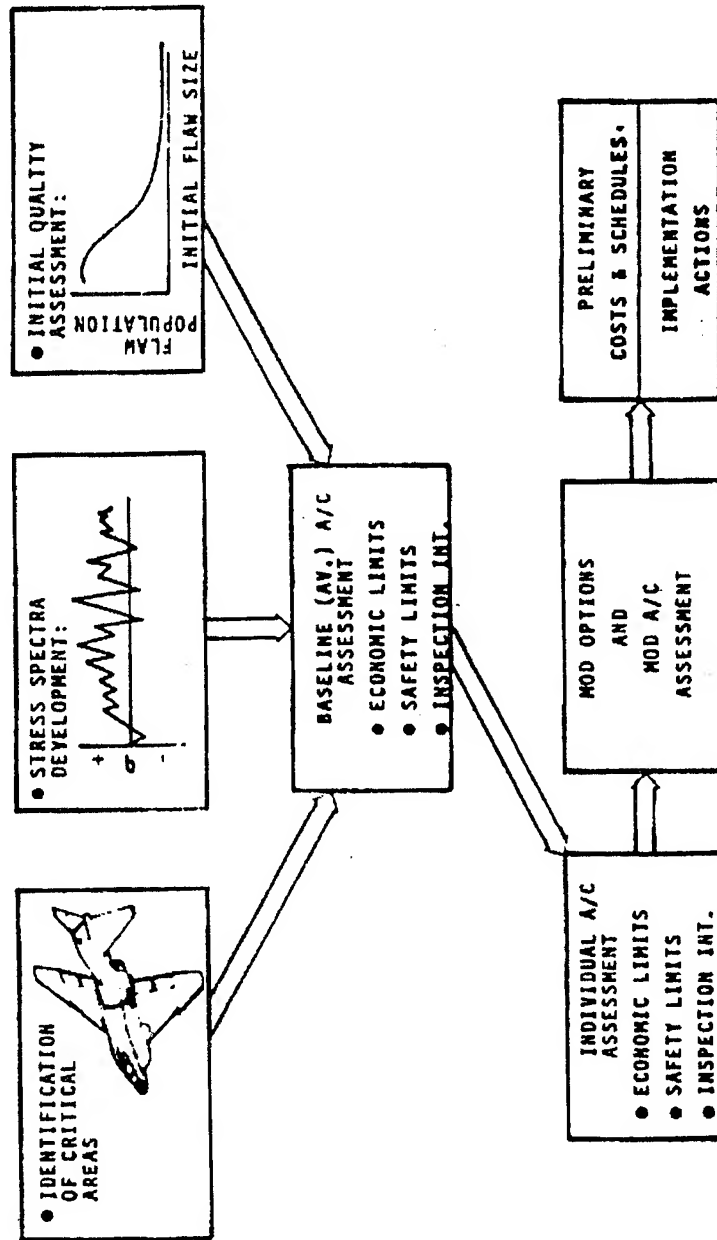


Figure 12

IDENTIFICATION OF CRITICAL AREAS

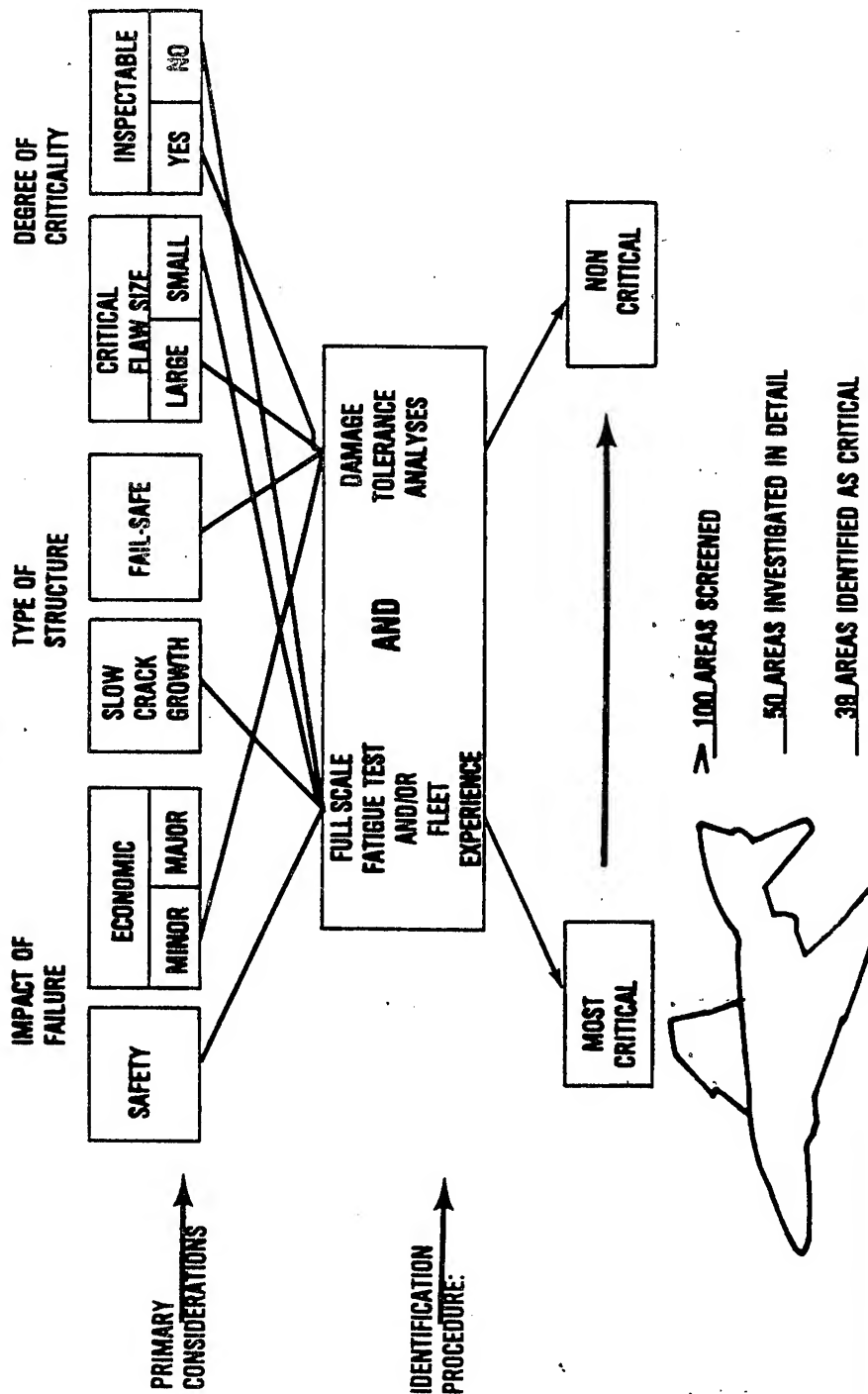
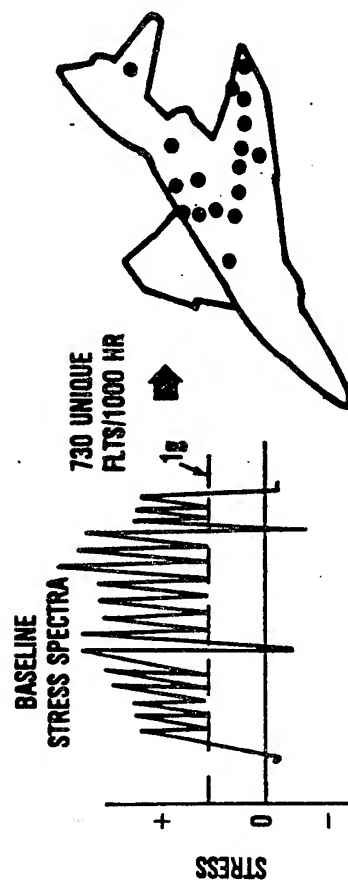
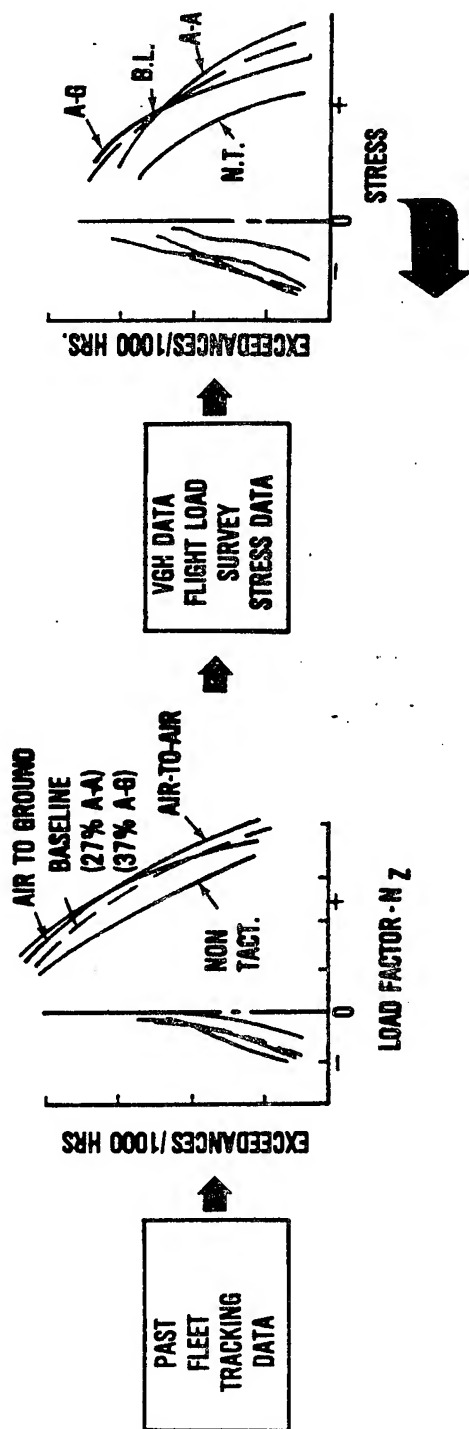


Figure 13

STRESS SPECTRA DEVELOPMENT



FLIGHT BY FLIGHT STRESS SPECTRA FOR:

- 18 LOCATIONS ON A/C
- BASELINE (AV.) USEAGE
- FIVE PAST USEAGES
 - ACM - NON ACM - S.E.A.
 - RF (S.E.A.) - RF (TRAIN.)
- 6 BASELINE VARIATIONS

Figure 14

LOAD FACTOR FREQUENCY DATA (PAST USAGES)

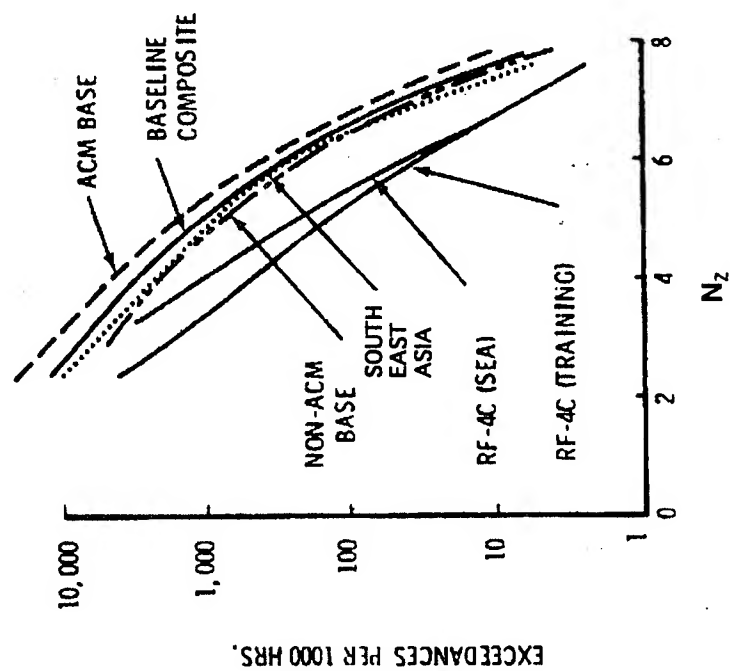


Figure 15

INITIAL QUALITY ASSESSMENT

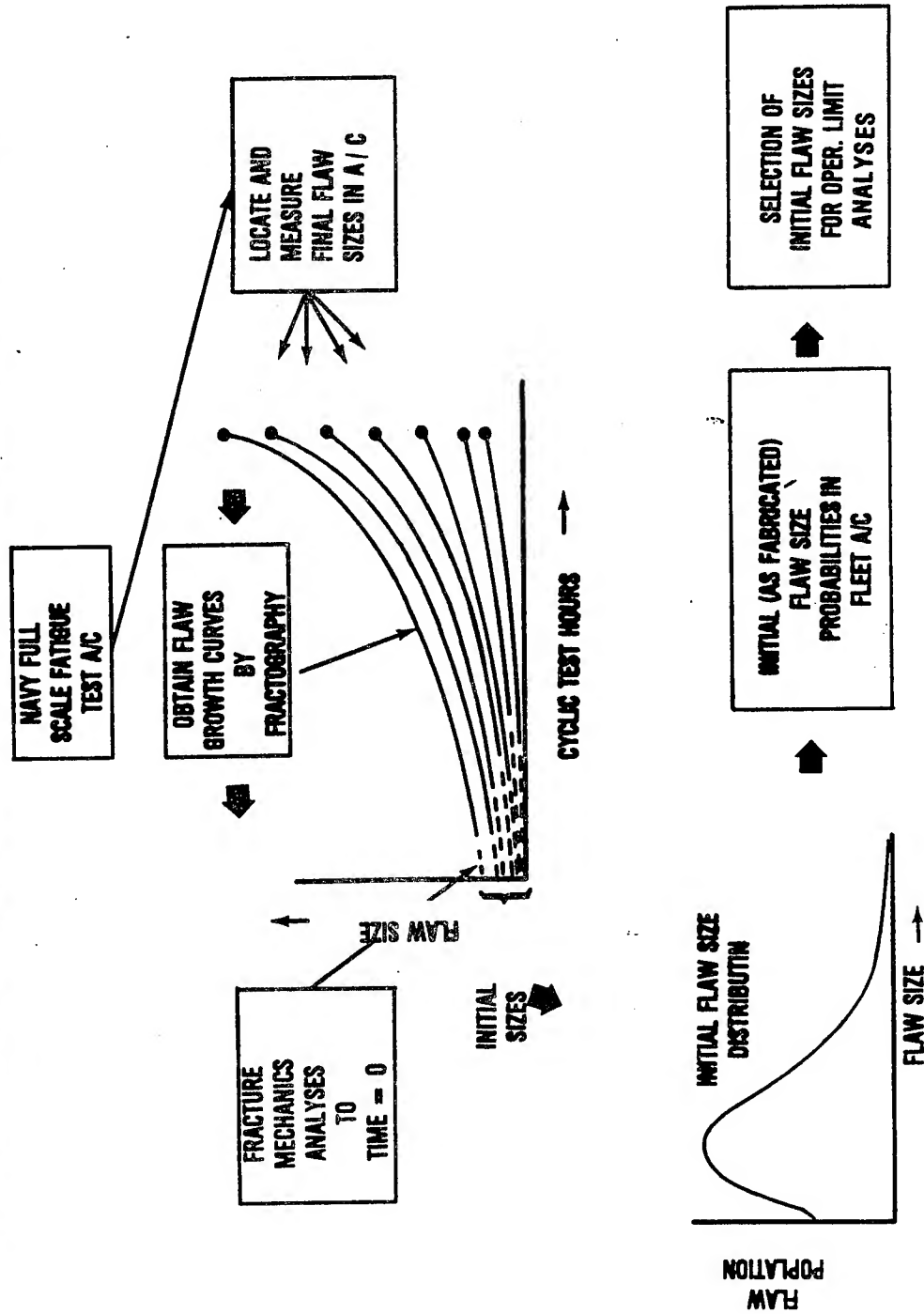
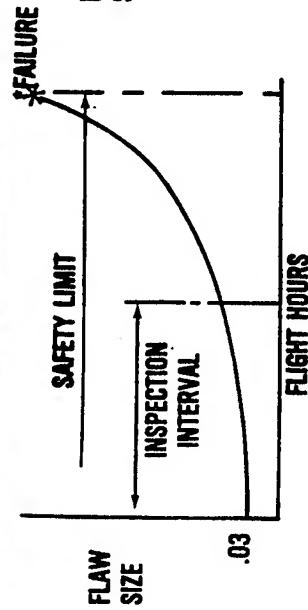


Figure 16

CRITERIA

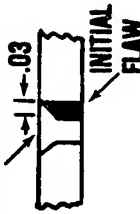
DAMAGE TOLERANCE CONSIDERATIONS

SAFETY LIMIT AND INSPECTION INTERVAL



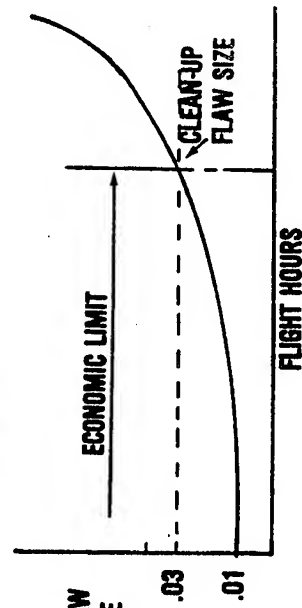
FASTENER HOLE

FLAW SHAPE AND
LOCATION:

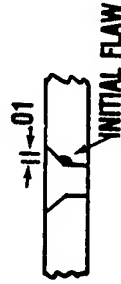


DURABILITY CONSIDERATIONS

ECONOMIC LIMIT



FLAW SHAPE AND
LOCATION:



ENVIRONMENT:

WATER AND AIR
OR
WATER AND FUEL

ENVIRONMENT:

AIR OR FUEL

FLAW GROWTH
ANALYSIS:

FLIGHT BY FLIGHT
INCLUDING RETARDATION
EFFECTS

FLAW GROWTH
ANALYSIS:

FLIGHT BY FLIGHT
INCLUDING
RETARDATION EFFECTS

Figure 17

RELATIVE USEAGE SEVERITY

<u>SPECTRUM</u>	<u>RELATIVE FLAW GROWTH LIFE</u>
BASELINE	1.0
ACM BASE	.85
NON-ACM BASE	1.10
SOUTH EAST ASIA (S.E.A.)	.94
RF-4C S.E.A.	1.33
RF-4C TRAINING	1.8

$$* \text{REL. FLAW GROWTH LIFE} = \frac{\text{SAFE FLAW GROWTH LIFE (PAST USEAGE SPECTRA)}}{\text{SAFE FLAW GROWTH LIFE (BASELINE SPECTRA)}}$$

Figure 18

OPERATIONAL LIMITS - BASELINE AIRCRAFT SLOW CRACK GROWTH STRUCTURES

<u>ITEM</u>	<u>ECONOMIC LIMIT</u>	<u>INSPECTION INTERVAL</u>	<u>CLASS I SAFETY LIMIT</u>
LOWER WING SKIN @ PYLON HOLE	N/A	2850	5700
@ BL 44	3900	4500	9000
@ MLG TRUNNION	5500	4550	9100
@ BL 70	5500	4850	9700
@ BL 132.50	4900	5600	11200
@ FWD MLG RIB	7000	5500	11000
@ CENTERLINE	5650	23200	40400
@ BL 100	SEE MODIFIED AIRCRAFT ASSESSMENT		
@ FWD SBA RIB	7000	7100	14200
@ TORQUE RIB	7450	7550	15100
@ 29% STIFFENER	N/A	7700	15400
@ FRONT SPAR	9400	12850	25700
@ DRAIN HOLE	N/A	10300	20600
@ WINGFOLD	11000	14200	28400
WINGFOLD RIB	6900	4000	8000

Figure 19

INDIVIDUAL AIRCRAFT ASSESSMENT

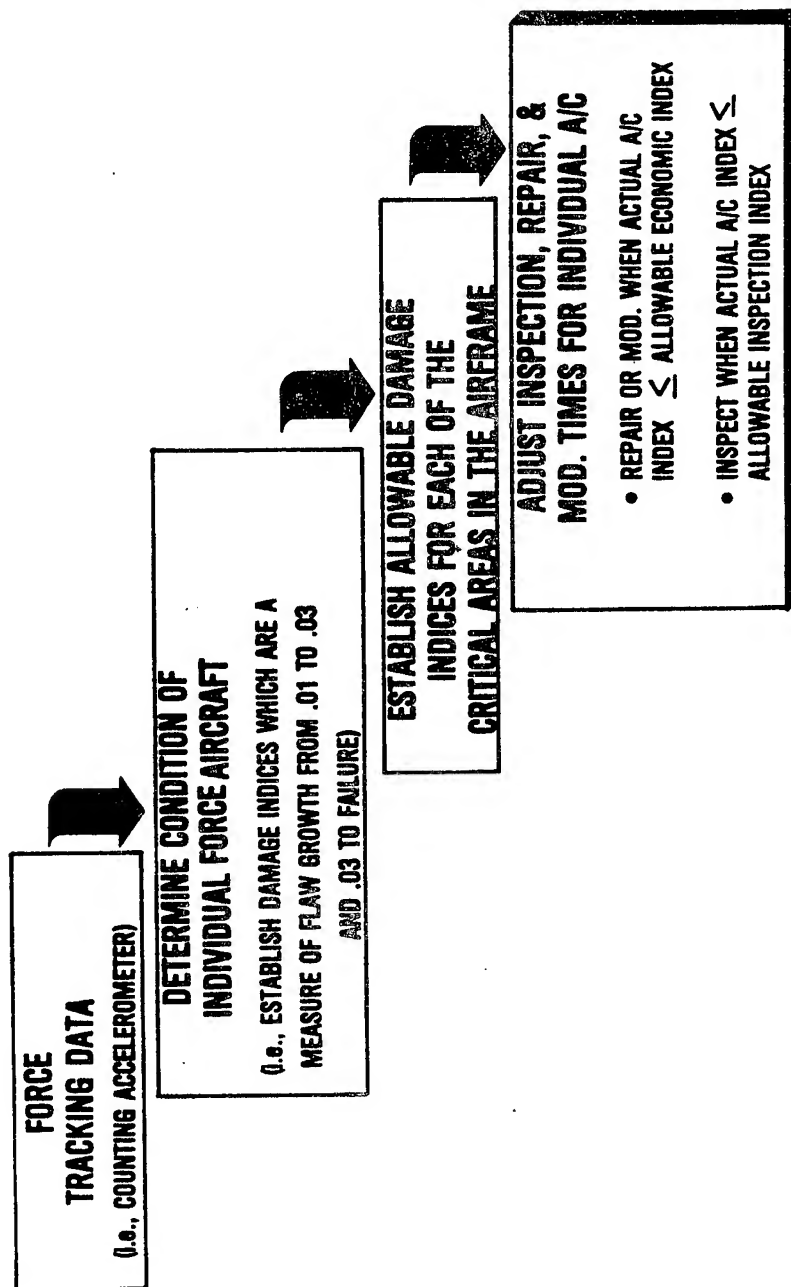


Figure 20

ALLOWABLE DAMAGE INDICES

<u>ITEM</u>	<u>ECONOMIC LIMIT</u>	<u>INSPECTION INTERVAL</u>	<u>CLASS I SAFETY LIMIT</u>
LOWER WING SKIN @ PYLON HOLE	N/A	0.73	1.46
@ BL 44	1.00	1.15	2.30
@ MILG TRUNNION	1.41	1.17	2.34
@ BL 70	1.41	1.25	2.50
@ BL 132.50	1.26	1.44	2.88
@ FWG MILG RIB	1.80	1.41	2.82
@ CENTERLINE	1.45	5.17	10.34
@ BL 100	SEE MODIFIED AIRCRAFT ASSESSMENT		
@ FWE SBA RIB	1.80	1.82	3.64
@ TORQUE RIB	1.91	1.94	3.86
@ 29% STIFFENER	N/A	1.96	3.90
@ FRONT SPAR	2.41	3.29	6.58
@ DRAIN HOLE	N/A	2.64	5.28
@ WINGFOLD	2.82	3.64	7.28
@ WINGFOLD RIB	1.77	1.03	2.06

Figure 21

RECOMMENDED VS ACTUAL MODIFICATIONS

<u>ITEM</u>	<u>RECOMMENDED MODIFICATION</u>	<u>OO-ALC IMPLEMENTATION</u>	<u>TC TO</u>	<u>MAN HOURS</u>
Lower Wing Skin At:				
Pylon Hole BL44	Press Fit Bushing Cold Work	Mod and Inspect Taper Loks Cold Work Strap	1302/1556 1179/566/710	19/5 3891/7971/ 1363
MLG Trunion	Cold Work	Cold Work Strap	1179/566/710	389/7971/1363
BL 70	Cold Work Cold Work	Cold Work Strap	1179/566/710	3891/7971/ 1363
BL 132.5				
FWD MLG RIB	Cold Work	Cold Work	1100	193
Centerline RIB	Cold Work	Taper Loks	566	7971
BL 100		Taper Loks	809	72
FWD SBA RIB	Cold Work	Taper Loks	1179/710	3891/1363
Torque RIB	Cold Work			
29% Stiffener	Inspect	Inspect	1229/1239/1339	1/10/04
Front SPAR				
Drain Hole	Press Fit Bushing	Inspect		
Wingfold	Cold Work	Cold Work	1123/1589	654/270

Figure 22

RECOMMENDED VS ACTUAL MODIFICATIONS

<u>ITEM</u>	<u>RECOMMENDED MODIFICATION</u>	<u>OO-ALC IMPLEMENTATION</u>	<u>TCIO</u>	<u>MAN HOURS</u>
Wingfold RIB	Replace, Cold Work	Replace, Cold Work	1123/1589	654/270
Upper Tangential Link	Replace, New Material			19/5
Turtle Back Door At FS 335	Taper Loks	Taper Loks	1179/633 On F- 4C/D/E/G	3891/169
FWD Upper Engine Mount (Tension)	New Compression Mount	New Compression Mount	1481 On E/G/RF 1179 on C/D	850/3891

Figure 23

RECOMMENDED VS ACTUAL MODIFICATIONS

<u>ITEM</u>	<u>RECOMMENDED MODIFICATION</u>	<u>OO-ALC IMPLEMENTATION</u>	<u>TCTO</u>	<u>MAN HOURS</u>
Turtle Back Door at FS 359	Rework Holes	Rework Holes	1179/633	3891/169
FWD Upper Engine Mount Back-up	Reinforce Structure	Reinforce Structure	1481 On E/G/RF 1179 on C/D	850/3891
Turtle Back Door at FS 303	Rework Holes	Rework Holes	1179/633 on F-4C/D/E/G	3891/169
Stringer No 1 at FS 359 (Early F-4C)	Add Straps	Add Straps	1179	3891
Stringer No 1 at FS 359 (F-4C, F-4D)	Add Straps	Add Straps	1179	3891
Main Spar at BL 132.5	Cold Work	Cold Work Strap	1179/566/710	3891/7971/ 1363
Fuselage Skin at FS 303 Stringer No 1 at FS 303	Rework Add Straps	Add Straps	1179	3891

Figure 24

RECOMMENDED VS ACTUAL MODIFICATIONS

<u>ITEM</u>	<u>RECOMMENDED MODIFICATION</u>	<u>OO-ALC IMPLEMENTATION</u>	<u>TCTO</u>	<u>MAN HOURS</u>
Centerline Rib	Inspect	Replace	1489	1690
Turtle Back Door at FS 351	Add Doublers	Add Doublers	1179/633 on F-4C/D/E/G	3891/169
Outer Wing, AFT Locklug	Replace With Steel	Replace with Steel	1024/1025	20/90
Stabilator	Install Strap	Install Straps	1348/969	42/72
Fuel Cell No 3, 4, 5, and 6 Floor	Corrugated Reinforcement	Corrugated Reinforcement	1071	1309
Fuel Cell No 4 Cover	Corrugated Reinforcement	Corrugated Reinforcement	951	21
FS 303 Bulkhead	Gapped Bolts, Taper Loks	Gapped Bolts, Taper Loks	1179 on F-4C/D 710 on RF-4C	3891 1363
FIN Finger Plates				
Skin at FS 493 Splice	Install Fitting, Cold Work			
Outer Wing Lower	Cold Work	Cold Work, Inspect, Mod, Replace	1342/1351/ 1274/1392/915	8/134/150/11/ 30

Figure 25

CENTER WING LOWER TORQUE BOX SKIN FASTENER HOLES @ BL 44.

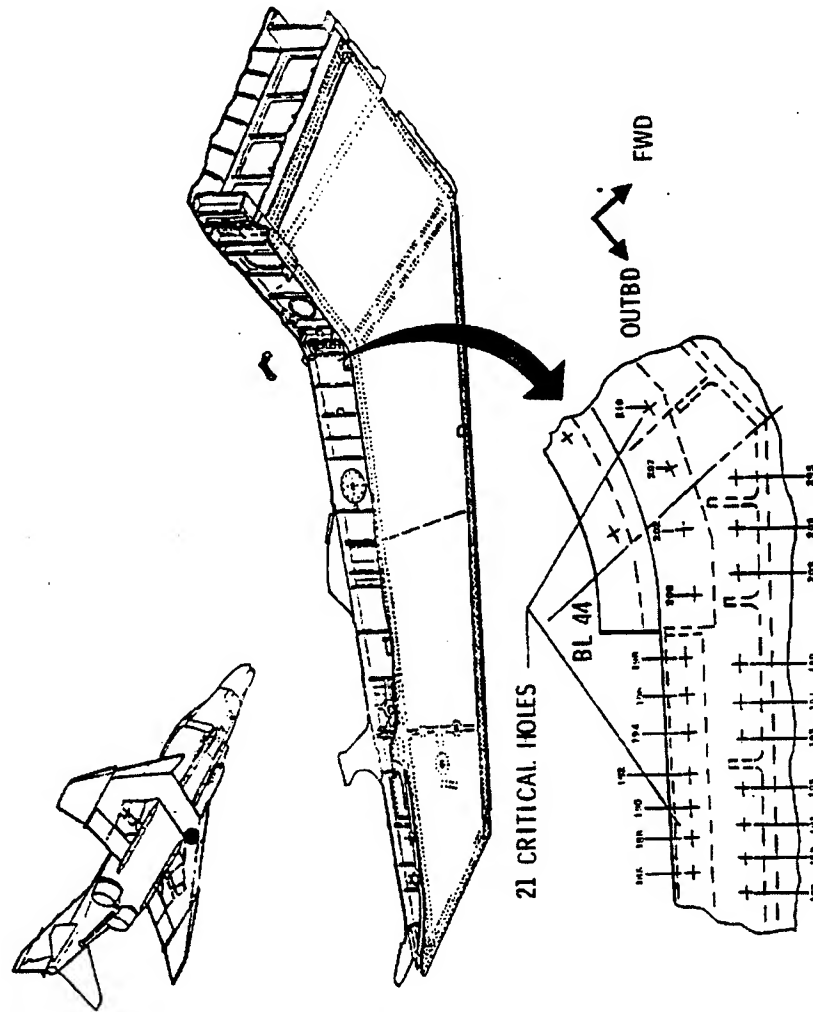


Figure 26

CENTER WING LOWER TORQUE BOX SKIN @ BL 100

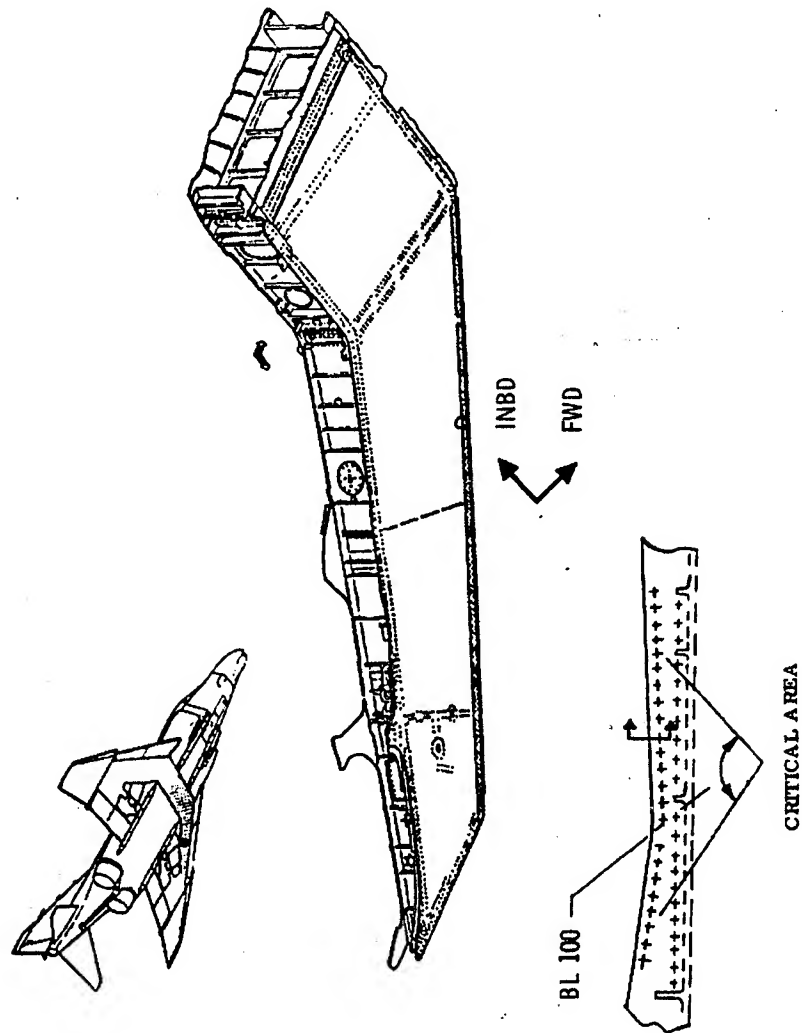


Figure 27

CENTER WING LOWER TORQUE BOX SKIN @ BL 4.5 @ FUEL DRAIN PLUG

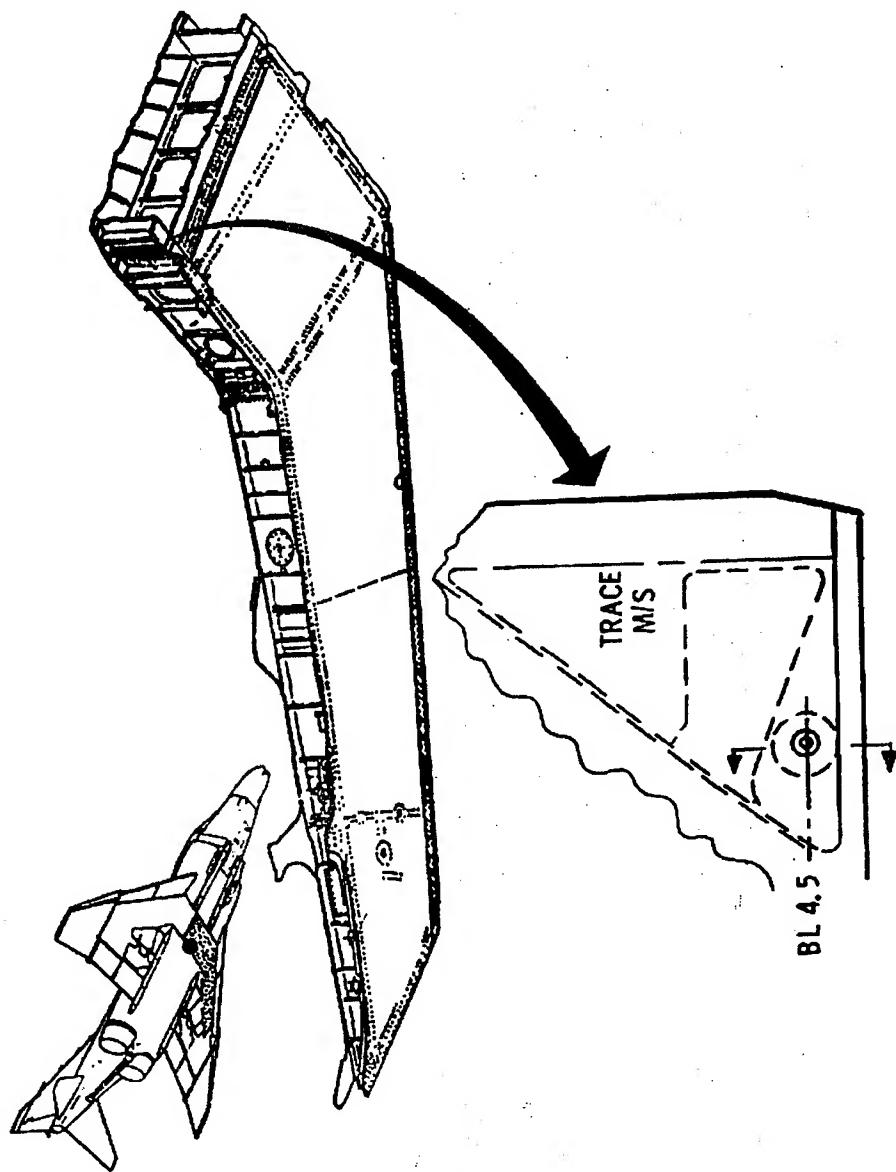


Figure 28

WING FOLD RIB ASSEMBLY

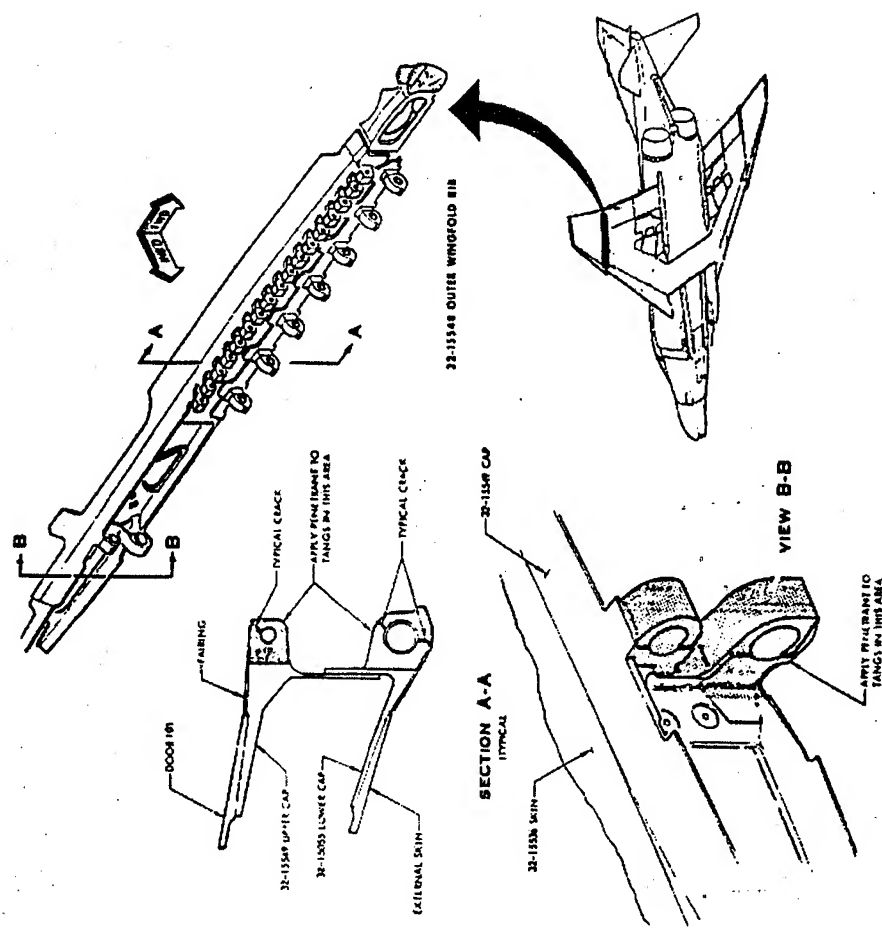


Figure 29

F-4 C/D FATIGUE TEST



Figure 30

F-4 ASIP SCHEDULE

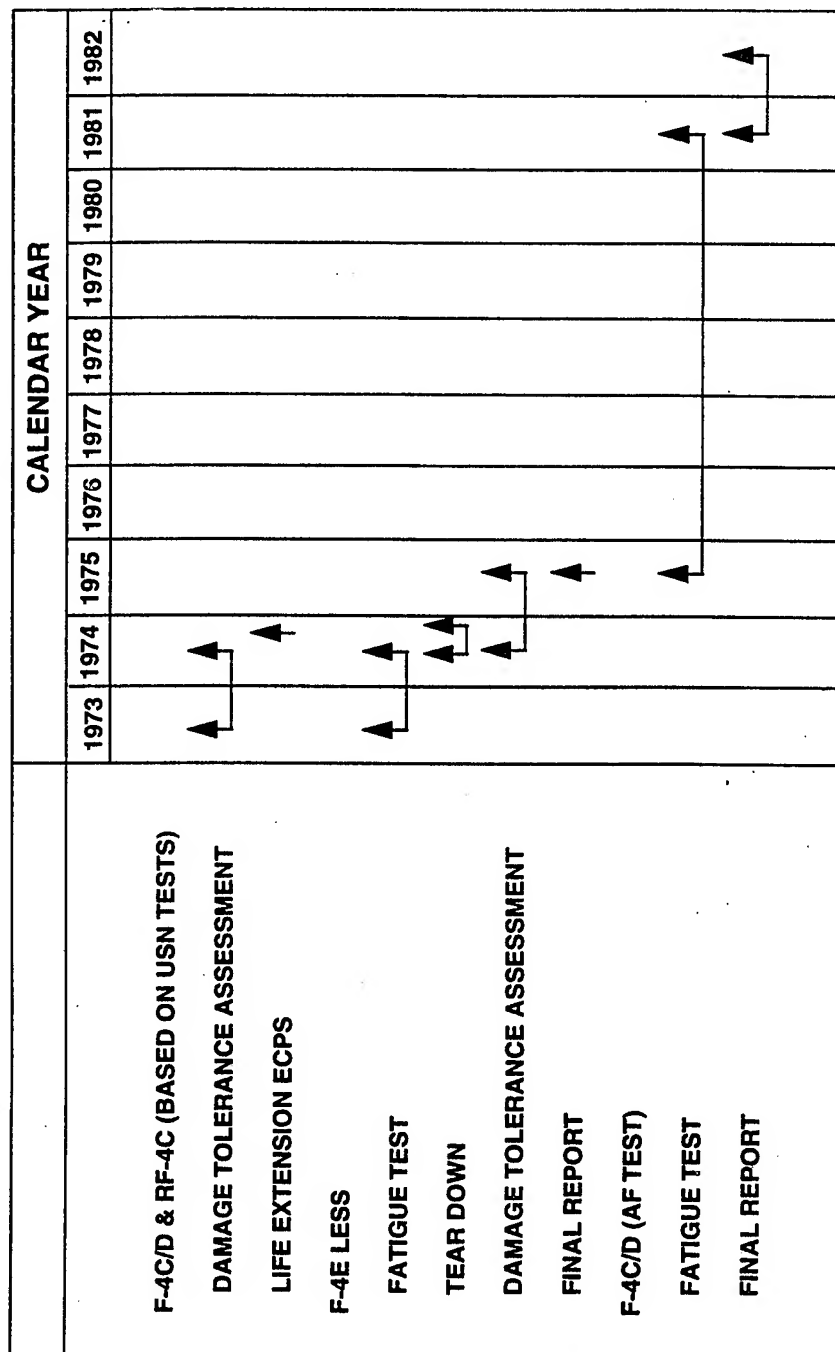


Figure 31

TEST SCHEDULE

YEAR	JAN	FEB	MAR	APR	MAY	JUN	JUL	AUG	SEP	OCT	NOV	DEC
1974												
1975												
1976												
1977												
1978												
1979												
1980												
1981												

Figure 32

FATIGUE DAMAGE INDEX REPORT

Individual Airplane Tracking Program

Original Report

A/C Serial Number

MDS

Last Report Date

Total Flight Hours

Combat Hours

ACM Hours

Hours Estimated

Estimated Exceedances

Total Exceedances

Damage Index

Damage Index per 1,000 Hrs

Revised Report

A/C Serial Number

MDS

Last Report Date

Base

Base ABV

Command

Aircraft Damage Index

Cum Base D.I. Rate

Cum A/C D.I. Rate

A/C Flight Hours

Projected D.I. Rate

Projected Date

PDM Date

Figure 33

DAMAGE INDEX - FLYING HOURS RF-4C

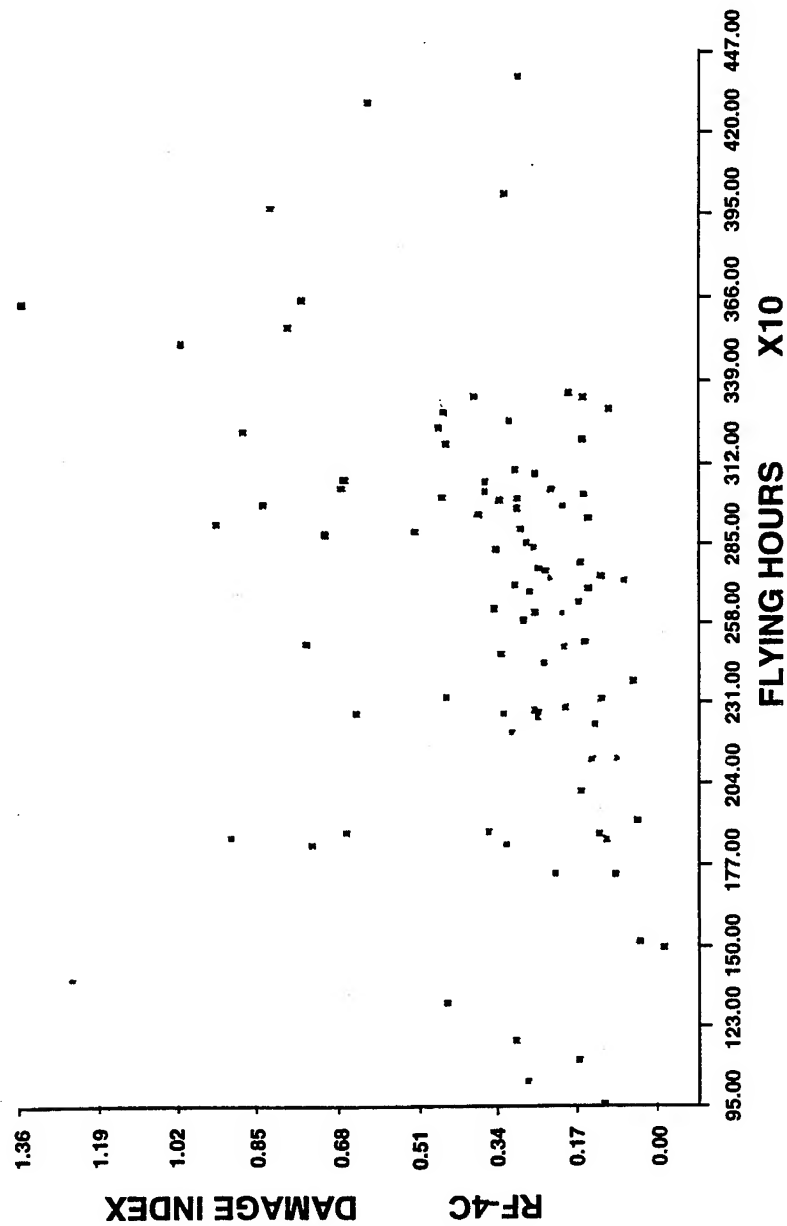


Figure 34

DAMAGE INDEX ACCUMULATION RATES

AIRCRAFT	PRE-1973	1973-1977	1977-1981	1981-1985
	D.I. RATE/1000 HRS	D.I. RATE/1000 HRS	D.I. RATE/1000 HRS	D.I. RATE/1000 HRS
USAF F-4C/D	.1531	.256	.390	.277
F-4E(s)	.1531	.309	.248	.241
USAF RF-4C	△1	.067	.0695	.0725/.233 △4
ANG F-4C/D	△1	△1	.272	.277
ANG RF-4C	△1	△1	.0691	.0725/.263 △4
F-4G	△2	△2	△3	.440

△1 NO D.I. RATE/1000 HR. WAS DETERMINED FOR THESE AIRCRAFT. ANG F-C/D AND RF-4C WERE IN USAF AT THIS TIME.

△2 NO D.I. RATE/1000 HR. WAS DETERMINED FOR THIS PERIOD. F-4G ACFR DID NOT EXIST PRIOR TO 1977.

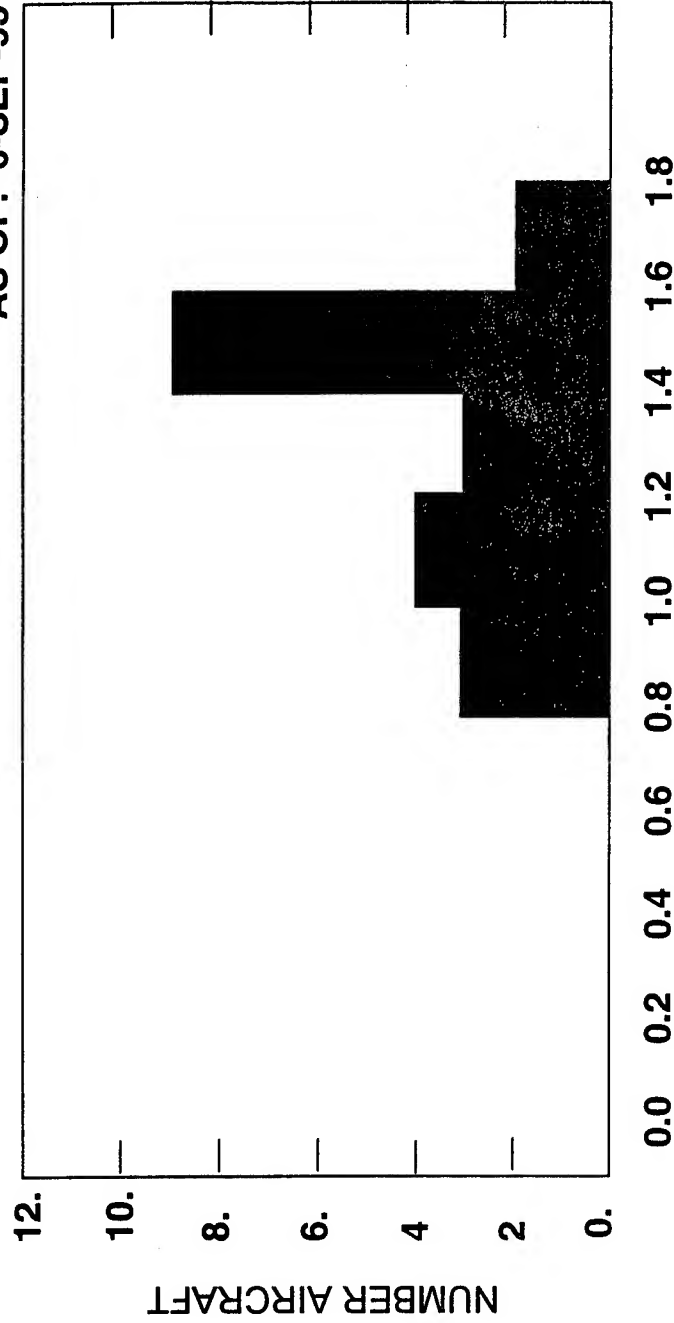
△3 F-4G AIRCRAFT WERE TRACKED AS F-4E(s) FROM 1977 THRU 1981.

△4 RF-4C RATE ESTIMATED FROM COUNTING ACCELEROMETER DATA

Figure 35

DAMAGE INDEX DISTRIBUTION F4E

AS OF: 6-SEP-95



0	0	0	0	0	3	4	3	9	2	0
---	---	---	---	---	---	---	---	---	---	---

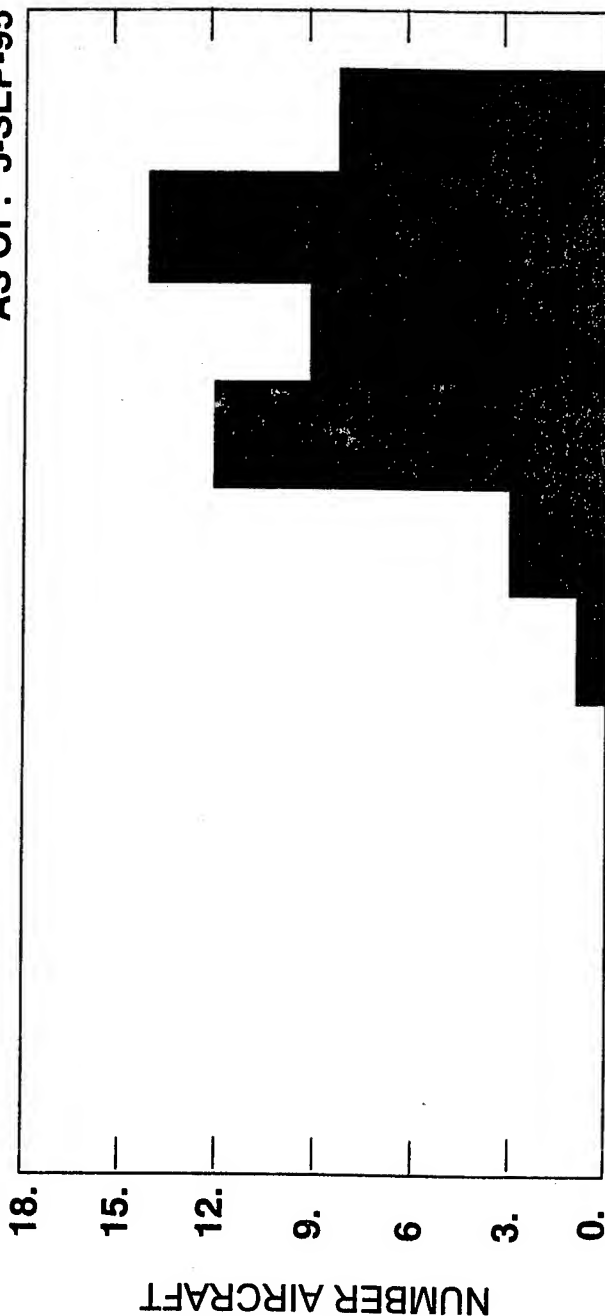
DAMAGE INDEX

21 AIRCRAFT

Figure 36

DAMAGE INDEX DISTRIBUTION **F4G**

AS OF: 5-SEP-95



0.0 0.2 0.4 0.6 0.8 1.0 1.2 1.4 1.6 1.8

0	0	0	0	0	1	3	12	9	14	8
---	---	---	---	---	---	---	----	---	----	---

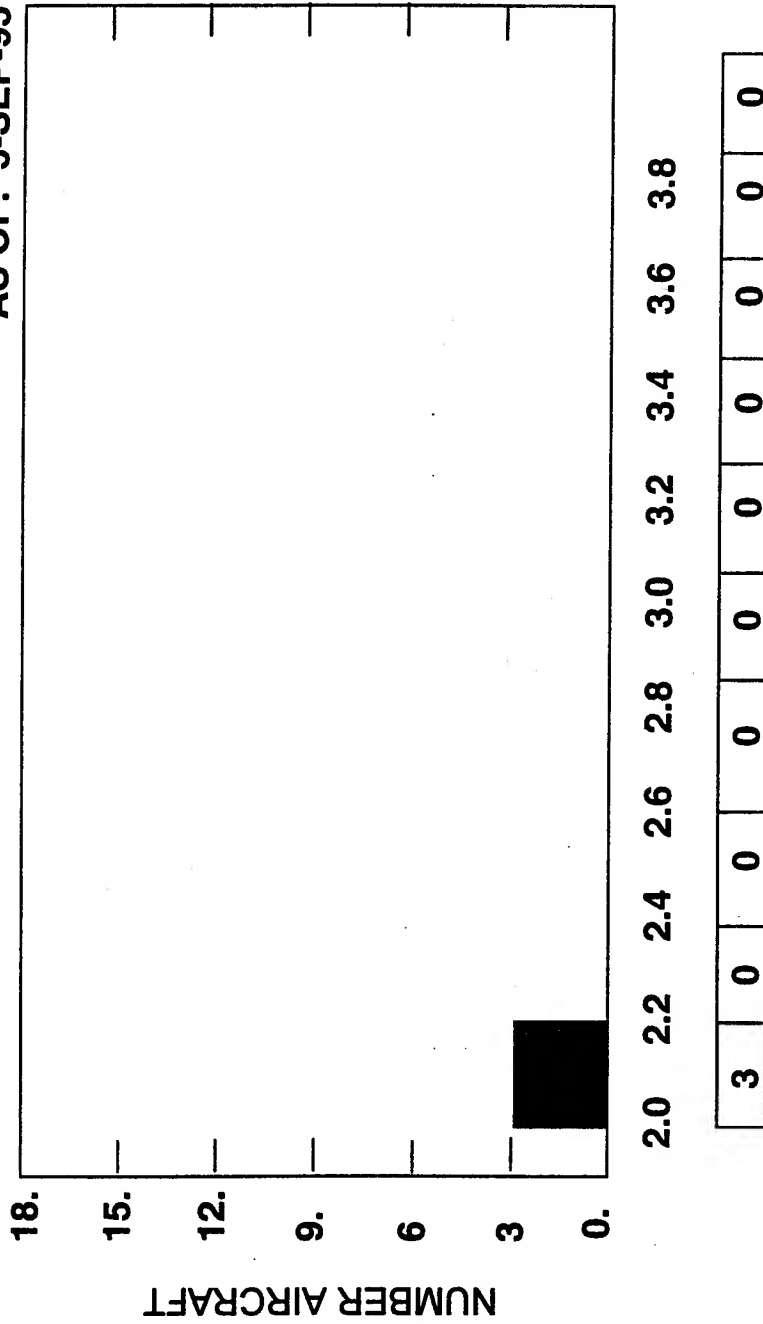
DAMAGE INDEX

50 AIRCRAFT

Figure 37

DAMAGE INDEX DISTRIBUTION **F4G**

AS OF: 5-SEP-95



DAMAGE INDEX

50 AIRCRAFT

Figure 38

DAMAGE INDEX DISTRIBUTION **RF4C**

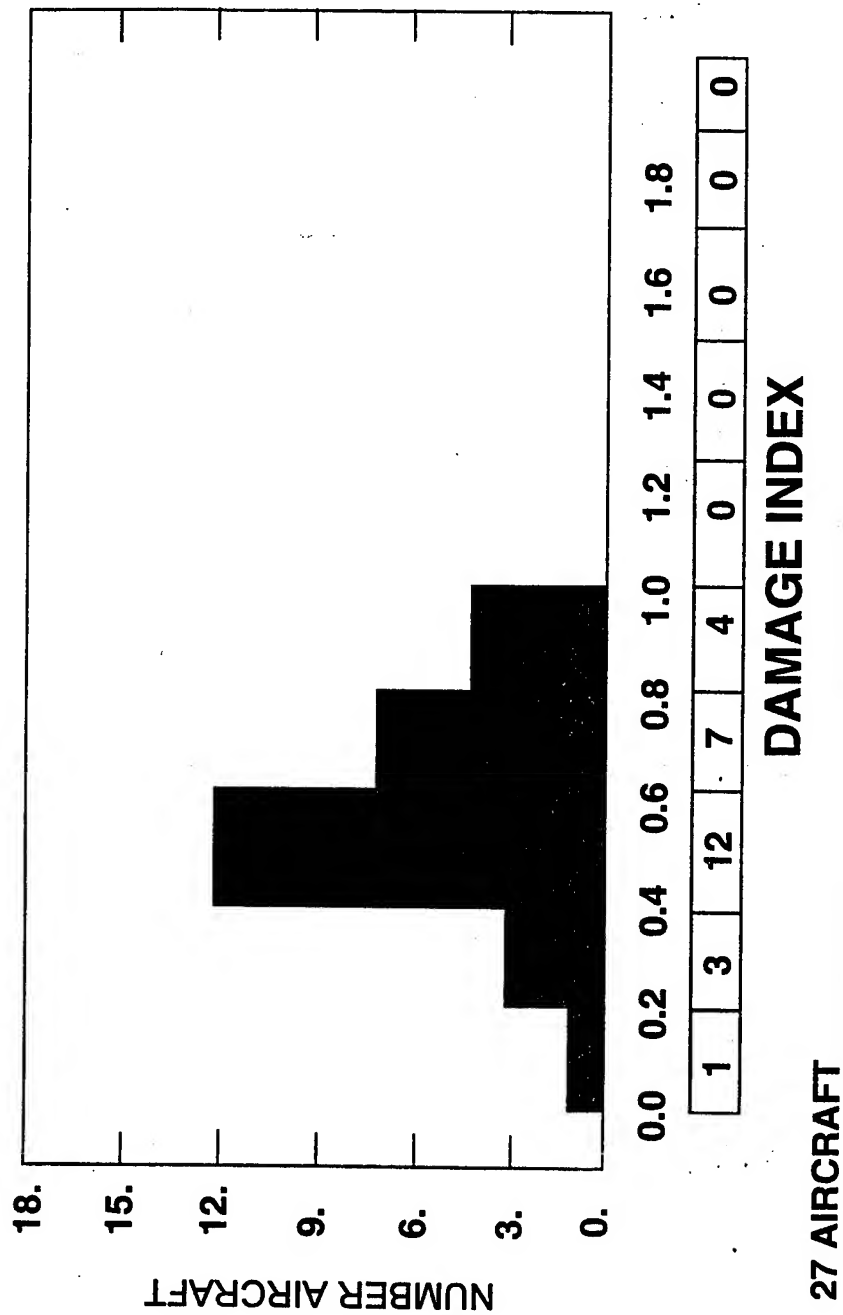


Figure 39

OBSERVATIONS

- The Study Provided Insight for the Future Structural Management of the F-4 Force.
- The Program Was Implemented and Carried Out Extremely Well by the OO-ALC.
- There Has Been One Class A Structural Mishap in the F-4 Program Since the Study Was Completed.

SESSION X

CORROSION/FATIGUE

Chairman: *C. Seher*, FAA Tech Center

AIRCRAFT CORROSION AND FATIGUE DAMAGE ASSESSMENT

Dr. Russell J.H. Wanhill
National Aerospace Laboratory NLR,
P.O. Box 90502, 1006 BM Amsterdam, The Netherlands

Summary

This paper reviews currently available information on corrosion and fatigue in aircraft as a background to discussing the assessment of corrosion and fatigue damage. The main topics are:

- aircraft operating environments and loads
- corrosion
- fatigue
- corrosion and fatigue
- corrosion and fatigue damage assessment.

Aircraft structures are susceptible to corrosion and fatigue damage, which concentrate at structural joints. There is a likelihood of interactions between corrosion and fatigue, especially as aircraft become older. However, it is uncertain whether in-service corrosion habitually leads to fatigue cracking, and it is also difficult to be specific about the relations between the environments and load histories that aircraft see in service. There is a need for *ad hoc* investigations to determine the in-service environmental contributions to fatigue initiation and crack growth. Structural areas removed from ageing aircraft should be invaluable sources of information for these investigations.

At present there is no established methodology for assessing the effects of corrosion on fatigue in order to estimate service lives and specify inspection intervals. This paper suggests approaches to corrosion and fatigue damage assessment that are based on current methods of fatigue analysis.

1. Introduction

Aircraft structures are susceptible to deterioration and damage by corrosion and fatigue. The type of corrosion damage depends on the materials used in construction and protection, the operating environments - both internal and

external - and the structural design details. Fatigue damage depends on the structural design details, the design stress levels and the service loads. There is also the likelihood of interactions between corrosion and fatigue, especially as aircraft become older. These interactions should be expected because both types of damage concentrate at structural joints, which have most or all of the following detrimental - but often unavoidable - features:

- (1) Stress concentrations and faying surface contacts, which crack and wear away the corrosion protection systems and also provide fatigue critical locations, notably at fastener holes and their vicinities.
- (2) Crevices for moisture entrapment.
- (3) Possible galvanic couples when steel or titanium fasteners are used.

Fleet surveys show that corrosion is a major problem and increases with aircraft age [1, 2]. Thus it is increasingly probable that corrosion will interact with fatigue and lead to an unacceptable reduction in structural integrity. Figure 1 is a schematic of the interaction of corrosion and fatigue for "short-life" and "long-life" aircraft [3]. This illustrates the increasing contribution of corrosion to the total damage of a long-life aircraft, and hence a major reduction in life owing to corrosion.

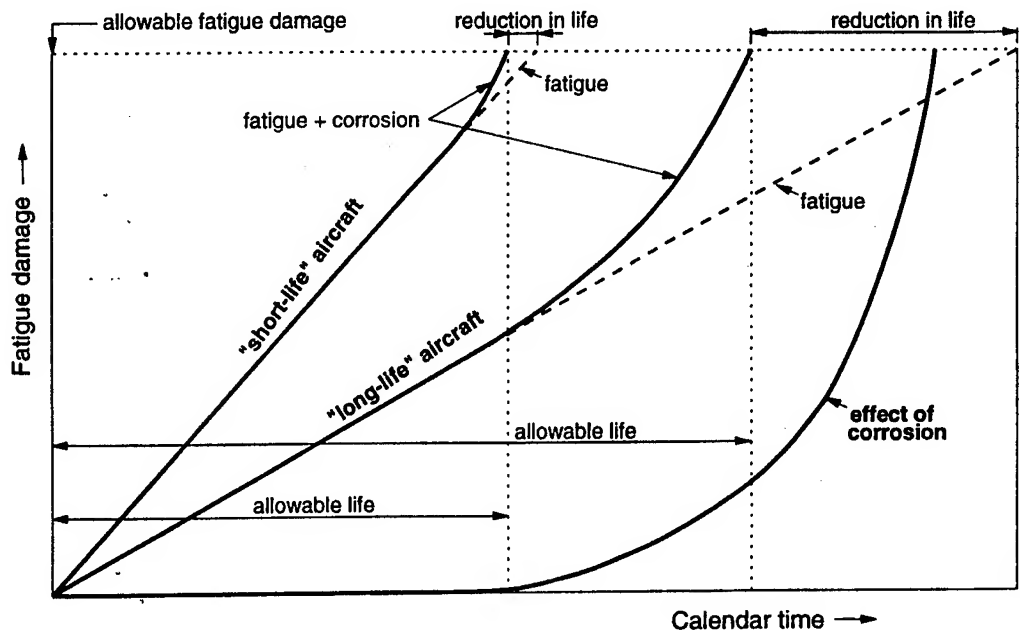


Fig. 1 Effect of corrosion on short and long fatigue life aircraft: after [3]

However, although figure 1 is informative, the designations of "short-life" and "long-life" are too straightforward. A "short" fatigue life does not necessarily mean a "short" calendar life. Some aircraft, usually military, operate only for a few hundred hours each year, resulting in long to very long calendar lives. This means that corrosion may cause much of the total damage even in so-called "short-life" aircraft.

Another important factor is the world-wide trend of extending service lives well beyond the design lives, owing mainly to budgetary constraints. Life extension requires structural auditing and reassessment with respect to fatigue. But, in addition, corrosion may be expected to become more important and require a more active programme of corrosion prevention and control [1, 2, 4, 5].

2. Aircraft Operating Environments and Loads

2.1 External Environments

Some aircraft, especially medium-to-long range civil transports, move rapidly from one climate to another and spend more than 50 % of the time in the air. Others may have a restricted area of operation and spend most of the time on the ground, either on the airfield or inside a hangar or shelter. In other words, the operating environments outside aircraft vary widely [6], and one may expect the severity of corrosion to vary also.

Tropical, coastal and industrial regions are unfavourable environments [6]. Aircraft operating in these environments and spending most of their time at low altitude and on the ground are likely to experience more corrosion, owing to consistently high humidities and moderate-to-high temperatures. Contaminants are also important. Salt is a frequent and widespread contaminant [7], and so are industrial pollutants like sulphur dioxide, ammonia and smoke particles, all of which can accelerate corrosion [6].

2.2 Internal Environments

The most important internal environment is water, which is due to condensation and occurs during flight because warm moist air on the inside - notably in pressure cabins - is in contact with structure cooled by the external environment. The water can become contaminated by leakages from galley and toilet areas, mechanical, hydraulic and electrical systems (battery acid), and also freight, including live animals.

A particular problem can occur in integral fuel tanks, namely corrosion by micro-organisms that grow in fuel-contaminating water at subtropical to tropical temperatures. This problem is controlled by removing stagnant water from the fuel supply and aircraft fuel systems, and by using biocides [7, 8].

2.3 Loads

Aircraft structures experience several types of loads, whose frequencies vary widely. Table 1 lists order-of-magnitude values of load cycle frequencies, and figure 2 illustrates some of the types of loads and their relative frequencies. Note the relatively long ground-air-ground and cabin pressurization cycles (once per flight).

Table 1 Aircraft load cycle frequencies [9]

Types of load	Cycle frequencies (Hz)
Ground-air-ground	0.00003 - 0.001
Cabin pressurization/depressurization	0.00003 - 0.0005
Manoeuvres	0.005 - 0.2
Gusts	0.1 - 10
Taxiing	0.5 - 20
Buffeting	10 - 100
Acoustic	100 - 1000

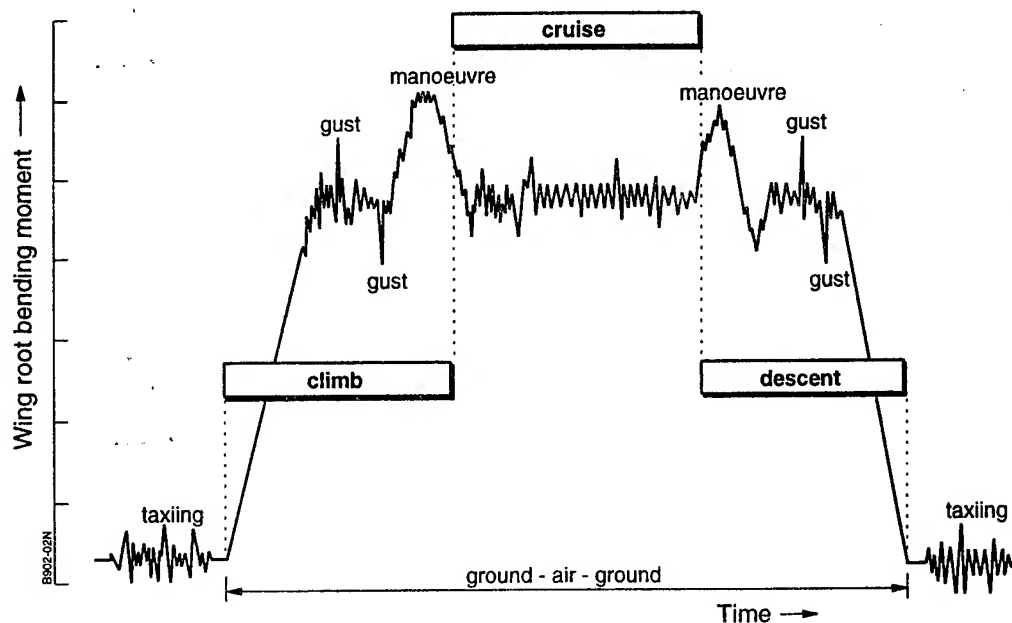


Fig. 2 Schematic of several types of aircraft loads on the wing root of a transport aircraft

2.4 Environment and Load Histories

During operation aircraft structures are subjected to a wide range of environmental conditions. These include variations in temperature and humidity, both on the ground and in the air, and changes in air pressure. Air temperature rapidly decreases to about -50°C at 10 km altitude, and flights above 3 km occur in below-freezing conditions [10]. Subsonic flight at these higher altitudes is typical for transport aircraft and "soaks" the structure at low temperatures. This results in condensation *inside* pressure cabins, as mentioned in subsection 2.2.

Air pressure decreases to about 20 kPa (0.2 atm) at 10 km altitude [11]. This means that flights with high altitude excursions result in considerable transpiration of unsealed, externally-connected joints and cavities, leading to condensation and collection of water inside the structure [12]. Pressure cabins are a special case. During climb, cruise *and* descent the overpressure with respect to the external environment forces moist air inside the aircraft to permeate the structure. Thus there is no "breathing-in" of external air during descent.

Upon landing, the aircraft may encounter freezing conditions, or wetness, or normal air, or dry air at temperatures approaching 50°C . Limited condensation on cold-soaked structure might be expected to disappear during warming to ambient conditions, but it is by no means certain that the insides of structural joints will dry out before the next flight. This will depend on the ambient conditions and the aircraft utilisation.

At present it is difficult to be more specific. However, the relation between environment and load histories will be returned to in section 5.3.2, where some evidence for alternating periods of "wetting" and "drying" inside structural joints will be given.

3. Corrosion

3.1 Costs of Corrosion

The costs of aircraft corrosion, in terms of world-wide fleets, run into hundreds of millions of dollars annually [13-15]. The grand total most probably exceeds US \$ 1000 M per annum. For military aircraft corrosion can account for up to 25-30 % of the total maintenance costs [13, 16]. For civil transport aircraft Mitchell [14] mentions a figure of 6-8 % of the direct costs of airframe maintenance.

Table 2 shows annual corrosion costs for several types of large - and ageing - USAF aircraft. In general, higher costs are associated with age and complexity [15]. However, costs may be higher than expected owing to the materials used, unfavourable operating environments (e.g. tropical and coastal regions [6]) and the structural design.

Table 2 Annual corrosion costs per aircraft for large USAF aircraft [15]: US \$ units

Aircraft type	Repair	Paint	Inspection and wash	Other costs	Material	Costs per aircraft
C-5	80,995	31,556	7274	16,159	0	135,984
C/KC-135	117,831	20,114	3796	22	6162	147,925
C-130	118,669	18,622	3820	80,148	3047	224,306
C-141	223,907	15,693	9354	0	259	249,213
B-52	288,698	45,073	4099	299	14,018	352,187

3.2 Corrosion Prevention and Control

3.2.1 Guidelines

There are many sources of guidelines for the prevention and control of corrosion in aircraft, e.g. [17-19]. The following topics are generally covered:

- (1) Selection of structural materials.
- (2) Design principles and features.
- (3) Protective treatments and surface coatings.
- (4) Supplementary protection systems (sealants, water-displacing compounds).

In fact, experience has shown that *it is impossible to prevent* corrosion: there must be corrosion control programmes during service [1, 2, 4, 5, 19, 20]. In particular, the Aloha Airlines accident [21] has stimulated the aircraft manufacturers and the USAF to develop corrosion control programmes with stringent inspection requirements for ageing aircraft.

3.2.2 Corrosion control programmes

Maintenance schedules for aircraft include several heavy maintenance visits during the service life. These heavy maintenance visits are planned on the basis

of *flight cycles* or *flight-hours*, since their main purpose is structural inspection to detect fatigue damage and repair it. However, these maintenance visits are also used for corrosion control.

The Aloha Airlines accident was soon followed by the First International Conference on Ageing Aircraft, in June 1988. The conference resulted in formation of what is now called the Airworthiness Assurance Working Group (AAWG) which established the precepts of a common approach to corrosion control programmes for civil transport aircraft. Table 3 lists these precepts.

Table 3 Precepts for industry-wide corrosion control programmes [22]

- All structural areas on aircraft will be inspected
- Programmes will be based on *calendar intervals*
- There are to be initial and repetitive inspection intervals
- Corrosion will be classified by *three levels of severity* (levels 1 - 3)
- All corrosion findings of levels 2 and 3 are to be reported to the manufacturers
- Programme implementation is to be based on the age of the aircraft
- The minimum rate of accomplishment for each operator is one aircraft per year
- Programmes will be mandated by Airworthiness Directives (ADs)
- There will be provision for alternative means of compliance
- Programmes will be reviewed annually

B9002-15N

Calendar versus flight cycle or flight-hour inspection intervals

The AAWG corrosion control programmes require the initial and repetitive inspection intervals to be based on calendar intervals, unlike the traditional fatigue-oriented maintenance. However, it is economically impractical to separate the two types of inspection and maintenance. Many civil aircraft operators have therefore elected to modify the structural fatigue inspection schedules to fit the corrosion inspection intervals. A common solution is to institute a mid-interval structural check that includes corrosion inspections of susceptible areas like the bilge, toilets and galleys [22]. This type of check has a repeat interval of about 3-5 years. A complete structural check, at twice the mid-interval, includes corrosion inspection of all areas.

The civil ADs do not apply to military aircraft. Nevertheless, the USAF - for example - is developing structural integrity programmes that include increased corrosion control for ageing aircraft [2, 4].

Structural area initial and repetitive inspection intervals

Table 4 gives examples of initial (threshold) and repetitive corrosion inspection intervals for the main structural areas in civil transport aircraft. Note that although the AAWG corrosion control programmes are specifically for ageing aircraft, the insidious nature of corrosion is recognised by early implementation. In some cases this means initial inspections as early as 5-6 years after introduction into service.

Table 4 Corrosion inspection threshold and repeat intervals (years) for Boeing civil transport aircraft [20]

General area		707/720		727		737		747	
		threshold	repeat	threshold	repeat	threshold	repeat	threshold	repeat
Wing	Outer-external	10	4	10	5	8	4	10	2
	Leading edge interior	8	2	10	5	8	4	6	1.5
	Outer-main box-interior	10	8	10	10	10	10	20	10
	Trailing edge interior	8	2	10	5	8	2	10	2
	Centre section interior	10	8	10	8	10	8	20	10
Fuselage	External (including doors and landing gear bays)	6	2	6	1.5	5	1.5	10 upper 5 lower	5 upper 2 lower
	Flightcrew compartment	Opportunity inspections and selected out-of-service/retired aircraft							
	Upper lobe interior	8	8	10	8	8	8	15	8
	Lower lobe interior (except bilge)	6	6	6	6	6	5	6	6
	Lower lobe-bilge	6	3	6	3	6	2	6	4
	Section 48 interior	10	5	10	5	8	4	10	5
V/H stabilizer	External surfaces	10	2	10	2	10	2	10	5
	Leading edges	10	8	10	8	10	8	15	8
	Main box interiors	10	8	10	8	10	5	15	8
	Trailing edges	10	8	10	4	10	5	10	5
	Centre section	10	5	10	5	10	8	10	8
	Centre engine inlet duct	-	-	10	8	-	-	-	-
Nose and main landing gear		landing gear overhaul		landing gear overhaul		landing gear overhaul		landing gear overhaul	
Powerplant and strut		4	2	5	2	engine change		7	3

Note: Some specific areas/items within the general areas have independent thresholds and repeat intervals

B902-1EN

Levels of corrosion

The AAWG precepts define three levels of corrosion severity [1, 19, 22]:

LEVEL 1

- corrosion occurring between successive inspections is local and can be reworked or blended out within the structural limits
- corrosion occurring between successive inspections exceeds the structural limits but is local and can be attributed to an unusual event
- light corrosion that *eventually* leads to cumulative reworks and blendouts exceeding the structural limits.

LEVEL 2

- corrosion occurring between successive inspections requires repair or partial replacement of a primary structural member
- corrosion occurring between successive inspections is widespread and requires reworks or blendouts approaching the structural limits.

LEVEL 3

- corrosion found during the first or subsequent inspections that is an immediate airworthiness concern.

Objective

The objective of the AAWG programmes is to control corrosion to level 1 or better. Programmes that do not control corrosion between successive inspections to level 1, or better, must be altered to meet this objective. To enable this it is essential to develop a comprehensive reporting system that includes classification of types and levels of corrosion and a data collection system that provides readily retrievable information.

A broadly similar approach is being taken by the USAF for the structural integrity corrosion control programmes mentioned previously. This approach also recognises the need to have a reporting system that enables service data analysis and feedback.

3.3 New Developments

3.3.1 In situ corrosion monitoring

Although the concept of in situ corrosion monitoring of aircraft has been around for some time, its practicality has yet to be fully demonstrated. Recent developments that could lead to workable systems include a Boeing/VPI fibre optic monitoring system, an electrical resistance method developed by Battelle, a thin film bimetallic sensor from the US Naval Air Warfare Centre (NAWC), and a range of electrochemical corrosion surveillance systems being evaluated by CAPCIS March Limited (CML):

- (1) The fibre optic system measures corrosion-induced changes in the transmission of light by aluminium-coated optical fibres. The coating can be of the same or similar chemical composition as the aluminium structure to be monitored. However, the aluminium *microstructures* will probably be quite different, leading to problems of interpretation.
- (2) The Battelle method measures changes in electrical resistance as corrosion occurs in a sensor made of the same material as the structure. In fact, electrical resistance sensors consist essentially of a thin metal wire which corrodes to form a metal oxide, thereby increasing the resistance measured across it.
- (3) The NAWC bimetallic sensor relies on environment-induced galvanic coupling to generate electrical currents, which are recorded automatically.
- (4) The corrosion surveillance systems being evaluated by CML are discussed in a recent paper [23].

3.3.2 Paint systems

There are several ongoing developments in paint systems. These include Unicoat, which is a self-priming topcoat designed to replace conventional primer + topcoat systems [24], paint systems with reduced Volatile Organic Compound (VOC) contents, and chromate-free paint systems.

The development of low VOC and chromate-free paint systems is necessary for complying with more strict legislation on environmental and health issues. The challenge is to obtain new paint systems providing similar corrosion protection to that provided by current systems.

4. Fatigue

4.1 Structural Design Philosophies

Since the 1950s there have been considerable developments in structural fatigue design philosophies, starting from the traditional safe-life approach. Basically, there are now three philosophies of designing against fatigue in aircraft structures:

SAFE-LIFE

- satisfactory life with no significant damage (i.e. cracking).

FAIL-SAFE

- satisfactory life with no significant damage (detectable cracking)
- inspectable structures
- any significant damage must be detected before safety is compromised.

DAMAGE TOLERANCE

- initial damage is assumed
- inspectable structures: fail-safe or slow crack growth
- non-inspectable structures: slow crack growth. This category is accepted as damage tolerant by the USAF but *not* by civil airworthiness authorities.

Table 5 Application of design philosophies to airframe structures [25]

Design approach		Defects assumed for new structure	Structural design category	Types of aircraft
Safe-Life	Non-inspectable or no planned inspections	No	Original Safe-Life	<ul style="list-style-type: none">• most general aviation and military aircraft• helicopters
Damage Tolerance (DT)	Planned inspections	No	Original Fail-Safe	<ul style="list-style-type: none">• pre-1980s civil transports• some helicopter components
		Yes	Fail-Safe or Slow Crack Growth	<ul style="list-style-type: none">• modern civil transport and military aircraft
	Non-inspectable or no planned inspections	Yes	Slow (Safe) Crack Growth Life	<ul style="list-style-type: none">• some areas on military aircraft

B392-16N

All these design philosophies are used, not only for different types of aircraft, but also for different categories and areas of structure in the same aircraft, for example the airframe, landing gear and engines. Table 5 gives an overview of the current situation for airframe structures.

4.2 Safety and Durability Definitions

4.2.1 Safety limit

Because aircraft structures deteriorate in service there is a safety limit. This is the time, in flight cycles or flight-hours, beyond which the risk of failure is unacceptable without *preventive action*. The preventive action depends on the structural design category, table 6.

Table 6 Preventive actions for ensuring safety

Structural design category	Preventive actions
• Safe-Life	{ • retirement from service • structural audit for life extension
• non-inspectable Slow Crack Growth	
• Fail-Safe	{ • repeated inspections: repair or replacement if required and feasible • retirement from service (often on economic grounds)
• inspectable Slow Crack Growth	

However, following the Aloha Airlines accident [21] the FAA has made a policy change with respect to preventive action for damage tolerant structures in civil transport aircraft. Plainly stated, this policy change means that one may not inspect an airframe forever [26]. More specifically, the new policy is that continued inspection for evidence of occurrence of a known problem is unacceptable for ensuring safety : structural parts must be modified or replaced to prevent the problem.

4.2.2 Durability

The necessity for an aircraft structure to be durable means primarily that the economic life, including any inspections, repairs or replacements, should equal or exceed the design life. Designing for durability concentrates on fatigue, notably the avoidance of premature and widespread fatigue cracking. However, other factors like accidental damage and environmental deterioration should also be considered, as is shown by the AAWG and USAF corrosion control programmes for ageing aircraft [1, 2, 4, 19, 22].

4.3 Fatigue Design and Analysis Methods for Damage Tolerance and Durability

4.3.1 General remarks

Table 7 summarises the fatigue analysis methods for aircraft structures. Although the manufacturers' methods may differ greatly in detail, this table shows that fatigue damage tolerance is determined basically from constant amplitude fatigue crack growth data and the use of crack growth models to predict crack growth lives under spectrum loading. Similarly, fatigue safe-life and durability are generally determined from constant amplitude S-N fatigue data and the use of cumulative damage models, for example the Palmgren-Miner rule. There are of course many detailed aspects and complications involved in fatigue analyses. Authoritative examples are given in [27, 28].

Table 7 General fatigue analysis methods for aircraft structures

	Properties	Types of data	Analysis methods and uses
Damage Tolerance	Long* fatigue crack growth	• da/dn versus ΔK	• Crack growth prediction for spectrum loading, using crack growth model(s)
		• flight simulation	• Verification of crack growth model(s) • Crack growth life estimation by interpolation of available data
Safe-Life and Durability	Fatigue life and strength	• S - N	• $\sum n/N = 1$ (Palmgren-Miner) • $\sum n/N = C$ (<i>relative</i> Palmgren-Miner)
		• flight simulation	• Determination of C • Life estimation by interpolation of available data

* The difference between *long* and *short* fatigue cracks is described briefly in subsection 4.4

4.3.2 Methods for civil transport aircraft

Table 8 is a generic survey of fatigue analysis methods for civil transport aircraft, and may be compared with tables 5 and 7. Note that both damage tolerance and safe-life/durability analysis methods are used, depending on the class of structural components. Also note that the survey in table 8 includes the ageing aircraft problem of Multiple Site Damage (MSD). This is a *safety* problem that results from the interaction of cracks at a number of adjacent locations, typically a row of fastener holes.

Table 8 Survey of fatigue analysis methods for civil transport aircraft

Classification of structural components	Analysis methods	Remarks
<u>Class I SSIs*</u> <ul style="list-style-type: none"> Single load path parts, failure potentially catastrophic (stabilizer lugs, engine mounts) Multiple load path parts with <i>poor</i> damage tolerance properties: failure potentially catastrophic Parts whose failure has very serious <i>economic</i> impact 	<u>Slow Crack Growth Life</u> <ul style="list-style-type: none"> a_i = minimum reliably detectable by <i>pre-service</i> NDI Use da/dn versus ΔK_{eff} long crack data Crack growth models for spectrum loading Scatter factors on crack growth life 	<ul style="list-style-type: none"> Damage Tolerance analysis, <i>not</i> Durability Only airframes: excludes landing gear and engines
<u>Class II SSIs*</u> <ul style="list-style-type: none"> Multiple load path parts with <i>good</i> damage tolerance properties: failure potentially catastrophic or has serious <i>economic</i> impact (pressure cabin skins, lower wing panels) 	<u>Safe-Life + Fail-Safe crack growth life</u> <ul style="list-style-type: none"> Safe-Life <ul style="list-style-type: none"> S-N curves Palmgren-Miner for spectrum loading scatter factors on life Fail-Safe crack growth <ul style="list-style-type: none"> a_i = minimum reliably detectable by <i>in-service</i> NDI use da/dn versus ΔK_{eff} long crack data crack growth models for spectrum loading scatter factors on crack growth life 	<ul style="list-style-type: none"> "Crack-free" life to be not less than half the projected economic repair life (Durability) MSD** should not occur during the economic repair life: use higher scatter factors for MSD-susceptible structures
<u>Class III: non-SSIs*</u> <ul style="list-style-type: none"> Secondary structures, failure not critical 	<u>Safe-Life</u> <ul style="list-style-type: none"> S-N curves Palmgren-Miner for spectrum loading scatter factors on life 	<ul style="list-style-type: none"> No crack growth calculations

* SSI = Structurally Significant Item

** MSD = Multiple Site Damage

B002-1 0N

4.4 New Developments

There are two recent and ongoing developments in fatigue analysis methods:

- (1) Prediction of fatigue crack growth in complex built-up structures. This development has concentrated on MSD in lap-splice riveted joints [29].
- (2) Durability and "total life" crack growth predictions based on *short-to-long** fatigue crack growth [30-33] instead of the traditional method using S-N data and cumulative damage models.

*Definition of *short* and *long* fatigue cracks is based on differences in crack growth behaviour. Short cracks are characterized by wide variations in crack growth rates, which are often much higher than those predicted by back-extrapolation of long crack growth data [34]. For most aircraft structural materials, including aluminium alloys, this apparently anomalous behaviour of short cracks ceases when the crack size reaches 0.5 mm.

Figure 3 schematically compares the current methods of fatigue life and crack growth analyses with the approaches *potentially* offered by these new developments, specifically for Class II Structurally Significant Items (SSIs). Boundaries between the methods are not exactly definable. For example, the lower diagram in figure 3 shows an overlap between durability crack growth and fail-safe crack growth. On the other hand, durability crack growth analyses should not, in principle, have to deal with MSD, which is a safety problem that should not occur during the economic repair life, see also table 8.

The caveat concerning these new developments is that they offer *potential* alternative approaches to current methods. This potential will be hard to realise for complex built-up structures. The problem of accounting for the effect of MSD on fail-safe fatigue crack growth is difficult enough, but it is probably easier to handle than durability predictions based on *short-to-long* fatigue crack growth.

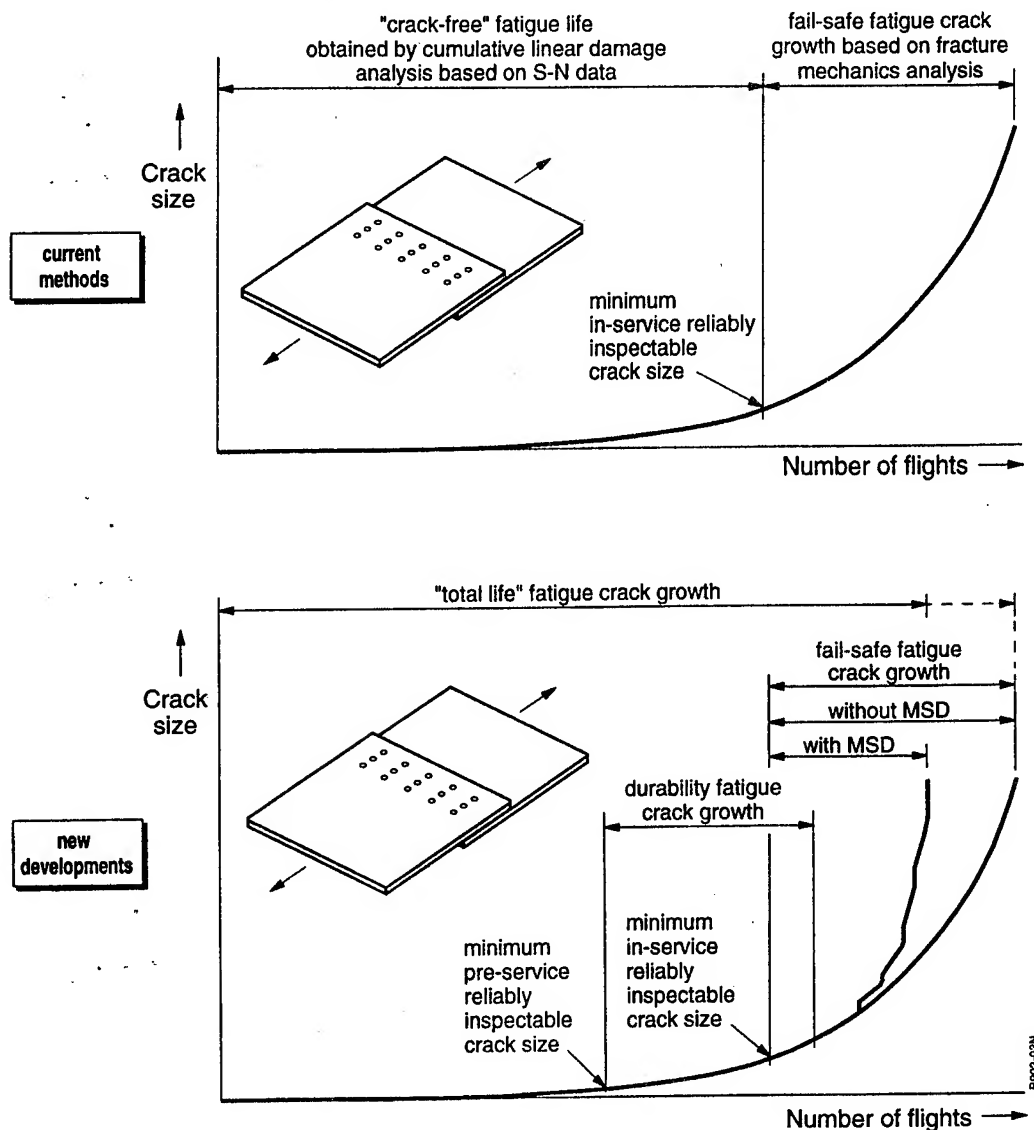


Fig. 3 Current and developing methods of fatigue life and crack growth analyses:
Class II SSIs, see table 8

5. Corrosion and Fatigue

There is a large amount of literature on the interactions of corrosion and fatigue, e.g. [35-42], including many data for aluminium alloys. Several more or less established trends may be obtained from these data and are reviewed in subsections 5.1 and 5.2. Some more recent developments are reviewed in subsection 5.3.

5.1 Corrosion Effects on Fatigue Endurance

5.1.1 Fatigue life and strength

Figure 4 is a schematic of the effects of corrosion on fatigue life and strength, as found from laboratory tests typically using salt water environments. This schematic is generally applicable to aircraft aluminium alloy coupon and structural joint specimens [35, 36, 39, 41]. There are several points to note:

- (1) At high stress levels and relatively short fatigue lives prior corrosion is more detrimental than continuous corrosion.
- (2) At lower stress levels and longer lives the concurrent action of corrosion and fatigue, i.e. continuous corrosion during fatigue cycling, is far more detrimental than the separate effects of corrosion and fatigue. In other words, the effects of corrosion and fatigue are *synergistic*.
- (3) Whether or not there is a fatigue limit in mild environments like air, there ceases to be a fatigue limit in a corrosion environment.

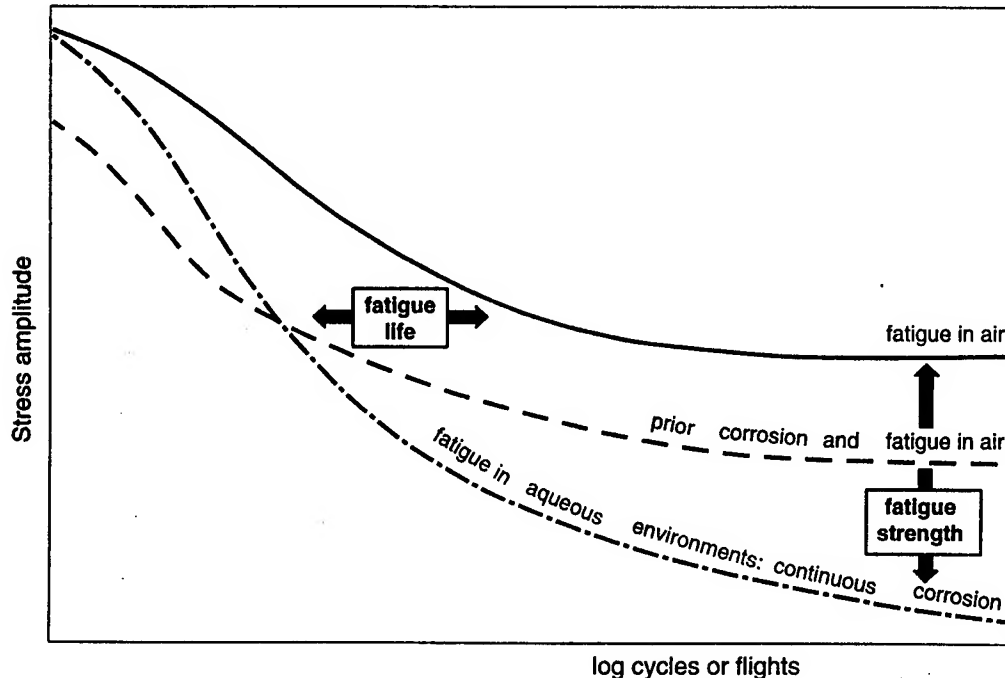


Fig. 4 Schematic of the effects of corrosion on fatigue life and strength, as found from laboratory tests

Table 9 lists specific environmental effects, including corrosion, on the long-life fatigue behaviour of aluminium alloys. These effects are of little or no practical importance compared to whether aqueous environments have access to aircraft structures, see section 2. In this respect it is remarkable that there do not appear to have been any systematic investigations of the effects of aqueous solution compositions and pH values on aircraft alloys: however see subsection 5.3.1.

Table 9 Specific effects of environmental parameters on long-life laboratory fatigue testing of aluminium alloys. After [35, 36, 41]

	Parameters	Effects
Gaseous environments	<ul style="list-style-type: none"> • Cycle frequency • Temperature • Humidity • Air pressure 	<ul style="list-style-type: none"> • Lower frequencies in the range 50 Hz - 20 kHz reduce environmental fatigue resistance • Increasing temperature decreases fatigue resistance • High humidity slightly reduces fatigue resistance • Significant life increases only at very low pressures ($< 10 \text{ Pa} = 10^{-4} \text{ atm}$)
Aqueous environments	<ul style="list-style-type: none"> • Cycle frequency • Temperature • pH • Cathodic potential 	<ul style="list-style-type: none"> • Lower frequencies reduce life for alloys susceptible to stress corrosion • Increasing temperature decreases fatigue resistance • ? (most data are for neutral aqueous NaCl solutions) • Cathodic protection can increase fatigue resistance

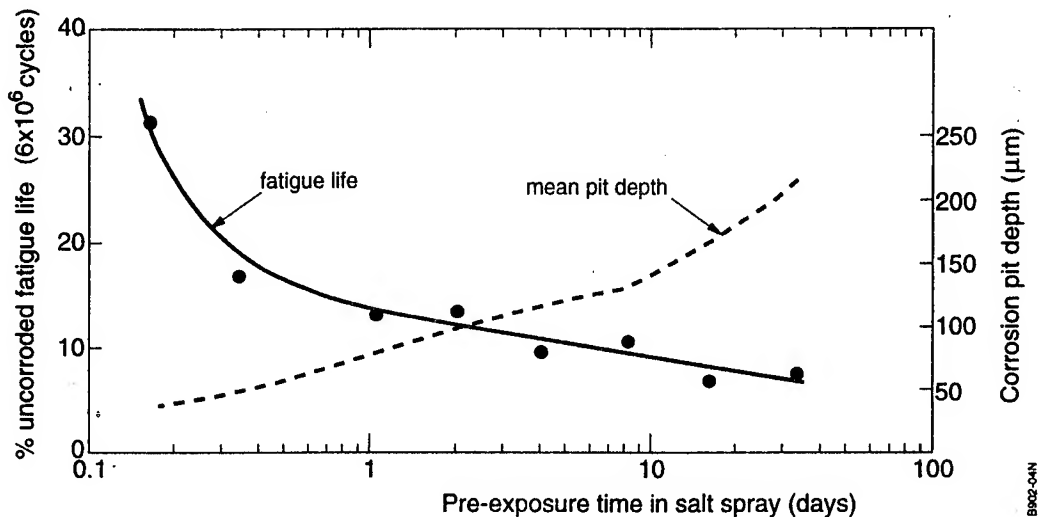


Fig. 5 Effect of corrosion pitting on long-life fatigue of the aircraft industry standard aluminium alloy 2024-T4 [43]: smooth specimen rotating bending tests, $R = -1$, in laboratory air at a cycle frequency of 60 Hz

Although figure 4 indicates that prior corrosion is less detrimental than continuous corrosion and fatigue, especially in terms of fatigue strength, it is most important to note that prior corrosion can have a very large effect on fatigue *life*. An example is given in figure 5. This figure demonstrates also that small amounts of pitting corrosion, to which all aircraft aluminium alloys are susceptible, can be highly detrimental.

5.1.2 Early stages of fatigue damage

The data in figure 5 are over 30 years old, but they have a contemporary relevance to the fatigue durability of aircraft structures, including life predictions based on short-to-long crack growth (subsection 4.4). This contemporary relevance will be illustrated with figure 6, which provides examples of short fatigue crack growth at notches representing fastener holes [34]. These data are more or less representative for cabin pressurization cycles (1 cycle equivalent to 1 flight) albeit with a maximum stress higher than would actually be used. Even so, the cracks took more than 40,000 cycles - equivalent to more than 10 years intensive usage - to grow from 50 μm to 200 μm long, which corresponds to a crack depth less than 100 μm [34].

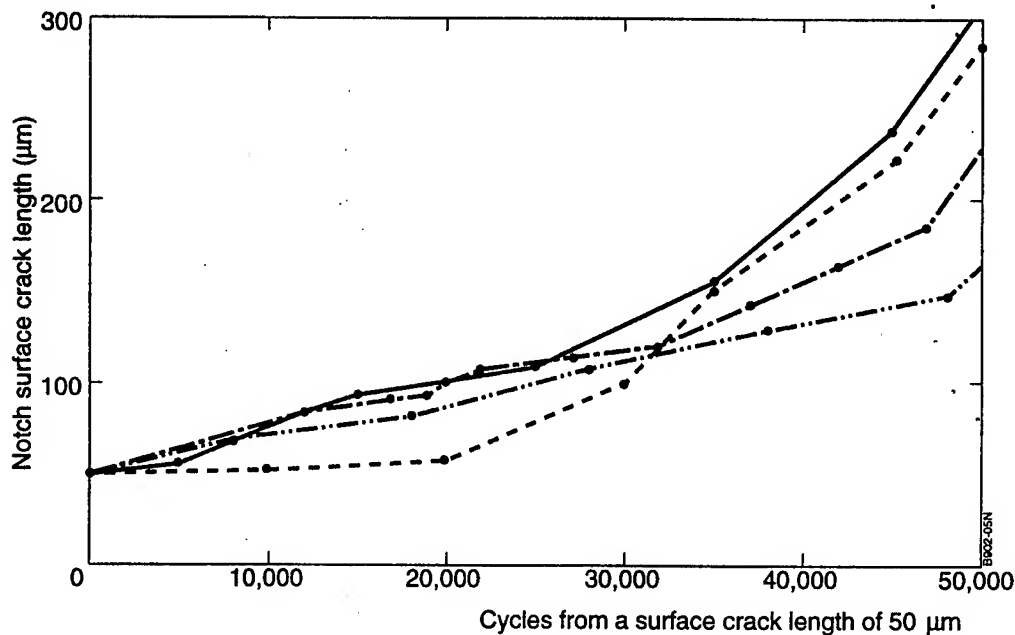


Fig. 6 Normalised short fatigue crack growth for the aircraft industry standard aluminium alloy 2024-T3 [34]: AFWAL and NASA data for Single Edge Notch Tension (SENT) specimens tested in laboratory air under constant amplitude loading, $R = 0$, with $S_{\max} = 110 \text{ MPa}$ and cycle frequencies of 5 - 20 Hz

This very slow fatigue cracking contrasts with the relative rapidity of corrosion pitting. Figure 5 shows that corrosion pits 100 μm deep are produced in less than 3 days in a salt spray environment (which, however, is exceptionally aggressive). On the other hand, the same amount of damage is obtained in only 6 months of outdoor exposure [44].

These differences in fatigue and corrosion kinetics suggest that in-service corrosion could overtake short fatigue cracks at the same location. This is also feasible even if fatigue cracks are accelerated by the corrosive environment. For example, NASA tests have shown that under severe fatigue crack accelerating conditions (a) in terms of da/dn , owing to *continuous* cycling in *salt* water, and (b) in terms of da/dt , owing *also* to a relatively high cycle frequency of 5 Hz, the short fatigue crack growth rates for 2024-T3 were, on average, 3-6 times higher than in air, figure 7. Nevertheless, the "cracking" to a depth of 100 μm was intergranular [45], which is characteristic of corrosion rather than fatigue.

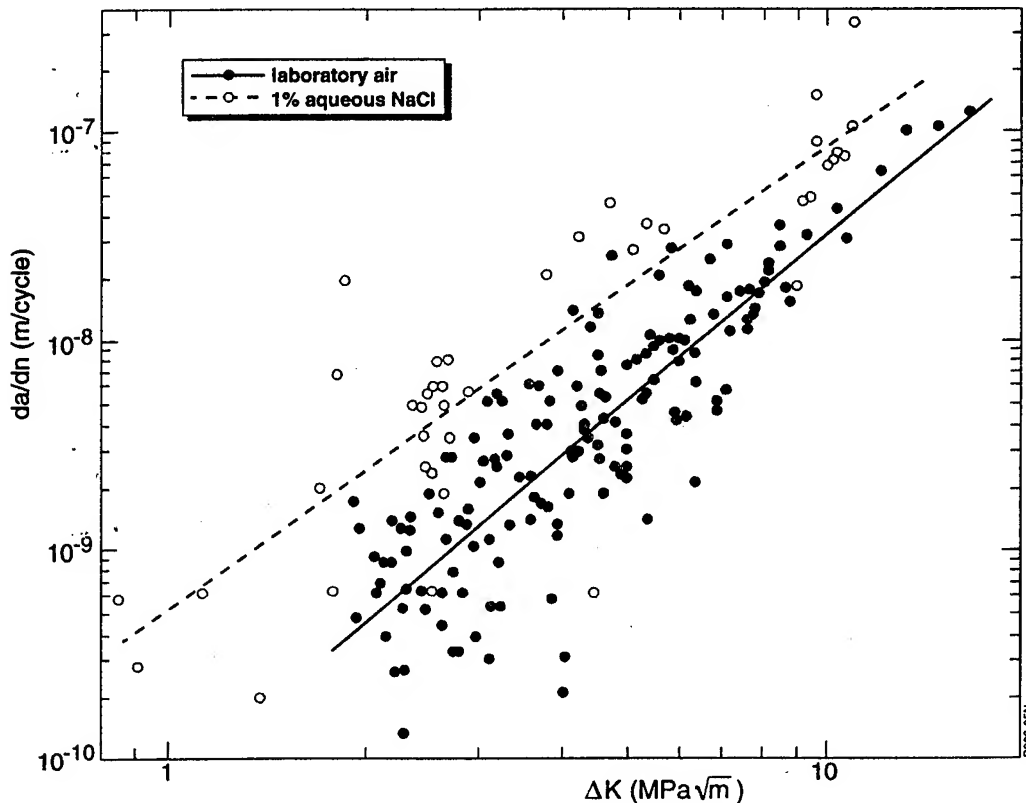


Fig. 7 Comparison of short fatigue crack growth rates in salt water and laboratory air for the aircraft industry standard aluminium alloy 2024-T3 [45]: SENT specimens tested under constant amplitude loading, $R = 0.05$, at a cycle frequency of 5 Hz

In other words, under service conditions it is possible that small amounts of localised corrosion, below the limit of in-service NDI detection [46], could go beyond pre-existing short fatigue cracks at or near fastener holes, thereby significantly reducing the fatigue durability *even though fatigue cracking had already begun*.

There are two other effects of corrosion on the early stages of fatigue damage that could be important for actual aircraft structures:

- (1) Increased numbers of fatigue cracks.
- (2) Changes in the locations of fatigue origins.

Corrosion characteristically increases the number of fatigue cracks [47-49] and might be expected to promote widespread and multiple site cracking in aircraft structures, though this is not certain and should be investigated: see also subsection 6.1.1. Widespread and multiple site cracking have implications for both safety and durability, see subsections 6.2.1 and 6.2.2.

Corrosion-induced changes in fatigue origin locations were observed in the AGARD-coordinated Fatigue in Aircraft Corrosion Testing (FACT) programme [41], which used specimens representing aircraft structural joints. These changes affected the fatigue life more than would be expected from tests on simple coupon specimens, thus demonstrating the need for realistic testing as part of life assessment.

5.2 Corrosion Effects on Fatigue Crack Growth

5.2.1 General remarks: the damage tolerance crack growth process

Fatigue crack growth in aircraft structures is best discussed in terms of the modern Damage Tolerance (DT) approach to fatigue design, mentioned in subsection 4.1. Figure 8 is a schematic of the fatigue crack growth process in terms of the DT approach. There are four regimes of crack growth.

In the first regime, fatigue crack growth begins at an initial flaw size that is either a conservative assumption or a reliable estimate derived from pre-service NDI. There is then a period of *short* crack growth up to a crack size of about 0.5 mm. As mentioned earlier, short cracks are characterized by wide variations in crack growth rates, which are often much higher than those predicted by back-extrapolation of long crack growth data. Nevertheless, the overall crack growth process in this short crack regime can be very slow, see subsection 5.1.2.

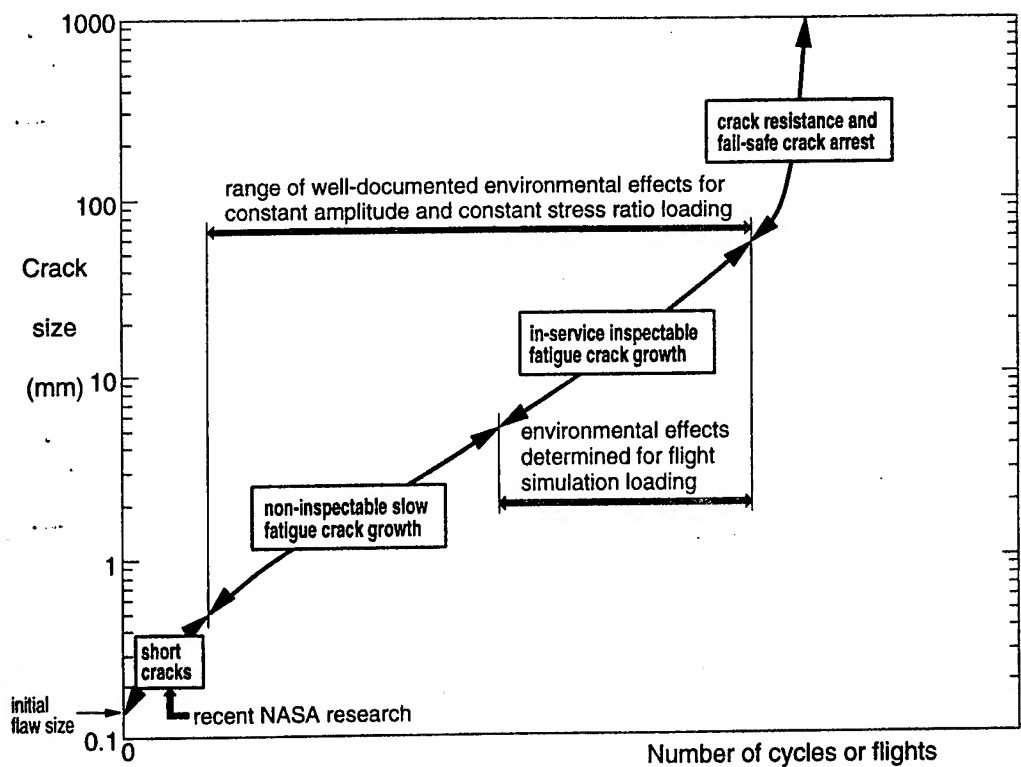


Fig. 8 Schematic fatigue crack growth curve in Damage Tolerance (DT) terms [50] showing the ranges in which environmental effects, including corrosion, have been investigated by laboratory testing

The second and third regimes pertain to *long* fatigue crack growth, i.e. crack sizes larger than 0.5 mm. The boundary between the second and third regimes is defined by in-service NDI capability which - except in special cases like the intensive inspection of lap splices in ageing aircraft - corresponds to cracks larger than about 5 mm. This boundary is also the starting-point for fail-safe crack growth analysis, see figure 3 and table 8.

The fourth regime is labelled "crack resistance and fail-safe crack arrest" in figure 8. This regime is dominated by the *monotonic* crack growth properties of crack resistance and fracture toughness. The boundary between fatigue crack growth and monotonic fracture can vary widely, since it depends on the structural configuration as well as the material properties.

5.2.2 Short crack growth

There are very few test data for the effects of corrosion on short fatigue crack growth in aluminium alloys. Figure 7 is a recent example [45], already discussed in subsection 5.1.2. This figure shows that for 2024-T3 in salt water the short fatigue crack growth rates are, on average, 3-6 times higher than in normal air.

5.2.3 Long crack growth

Constant amplitude and constant stress ratio loading

Figure 9 is a schematic of corrosion effects on constant amplitude and constant stress ratio* long fatigue crack growth in aluminium alloys. The aqueous environmental effects on crack growth rates are very significant near the threshold ΔK_{th} . However, this region of long crack growth is *not* important for the in-service inspectable fatigue crack growth regime, and is unlikely to be of interest for the non-inspectable slow crack growth regime because the design and operating stresses would have to be very low. Also, cyclic stress corrosion cracking (SCC) in aircraft structures is - or should be - a problem of the past:

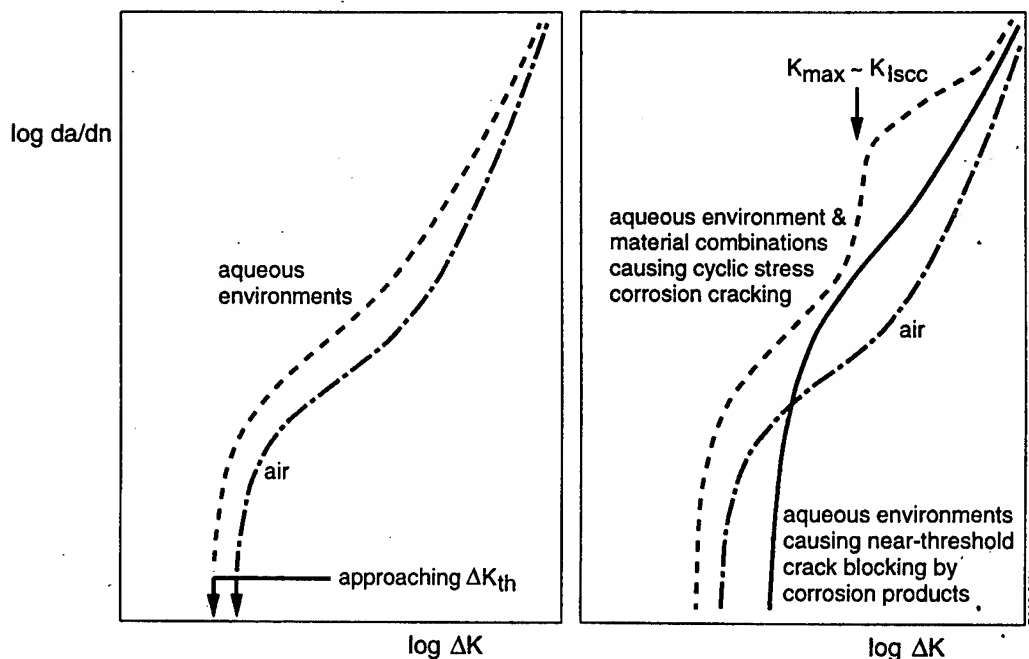


Fig. 9 Schematic of corrosion effects on constant amplitude and constant stress ratio long fatigue crack growth in aluminium alloys, as found from laboratory tests: after [51,52]

susceptible alloys and components have generally been replaced by more resistant ones. However, there are exceptions, notably in long-life military aircraft designed in the 1950s and early 1960s.

*Use of the term "constant stress ratio" as well as "constant amplitude" is strictly necessary for including results and trends from *load-shedding* tests, which are often done to obtain fatigue crack growth rates at low ΔK values. For practical purposes the load histories may be considered the same.

Excepting the near-threshold ΔK region and cyclic SCC, the following trends may be noted for the main types of aircraft aluminium alloys, the AlCuMg 2000 series and AlZnMgCu 7000 series [53]:

- (1) 7000 series alloys are more sensitive to environmental effects on long fatigue crack growth than 2000 series alloys. This includes changes in atmospheric humidity as well as changes from air to aqueous environments.
- (2) Most aqueous environment tests use neutral pH salt water. In this environment the long fatigue crack growth rates are, on average, 2-4 times higher than in normal air.

Table 10 Specific effects of environmental parameters on long fatigue crack growth during laboratory fatigue testing of aluminium alloys. After [35, 36, 62]

	Parameters	Effects
Gaseous environments	• Cycle frequency	<ul style="list-style-type: none"> Humidity and frequency effects interrelate: there is little variation in crack growth rates at low frequencies (0.02 - 100 Hz) and/or in natural air (5 - 90% R.H.) Significant decreases in crack growth rates only at partial pressures of water vapour $< 100 \text{ Pa} = 10^{-3} \text{ atm}$
	• Humidity	
Aqueous environments	• Air pressure	
	• Cycle frequency	<ul style="list-style-type: none"> Lower frequencies slightly increase crack growth rates in alloys immune to stress corrosion, but large increases in crack growth rates can occur in alloys susceptible to stress corrosion
	• Temperature	<ul style="list-style-type: none"> Increasing temperature increases crack growth rates
	• pH	<ul style="list-style-type: none"> For 7000 series alloys lowering the pH from 7 to 4 has little or no effect, or can even <i>decrease</i> crack growth rates
	• Cathodic potential	<ul style="list-style-type: none"> Crack growth rates can be reduced to levels obtained in mild environments like normal air
	• Inhibitors	

Currently there is limited information available on the environmental fatigue crack growth behaviour of modern aluminium-lithium alloys [54-59]. However, it appears that their sensitivity to environmental effects ranges from the same as that of AlCuMg 2000 series alloys to more sensitive than AlZnMgCu 7000 series alloys [60].

Table 10 lists specific environmental effects, including corrosion, on the long fatigue crack growth behaviour of aluminium alloys. As in the case of long-life fatigue behaviour, these effects are of little or no practical importance compared to whether aqueous environments have access to aircraft structures; and there is also the possibility of using specially formulated inhibitors in advanced paint systems [61], see also subsection 5.2.3.

Flight simulation variable amplitude loading

Environmental effects on flight simulation variable amplitude long fatigue crack growth have been determined only for the in-service inspectable fatigue crack growth regime, figure 8. The AlCuMg 2000 series and AlZnMgCu 7000 series aircraft aluminium alloys show a similar trend to that for constant amplitude and constant stress ratio loading, namely that 7000 series alloys are more sensitive to the change from air to aqueous environments [53, 63-66].

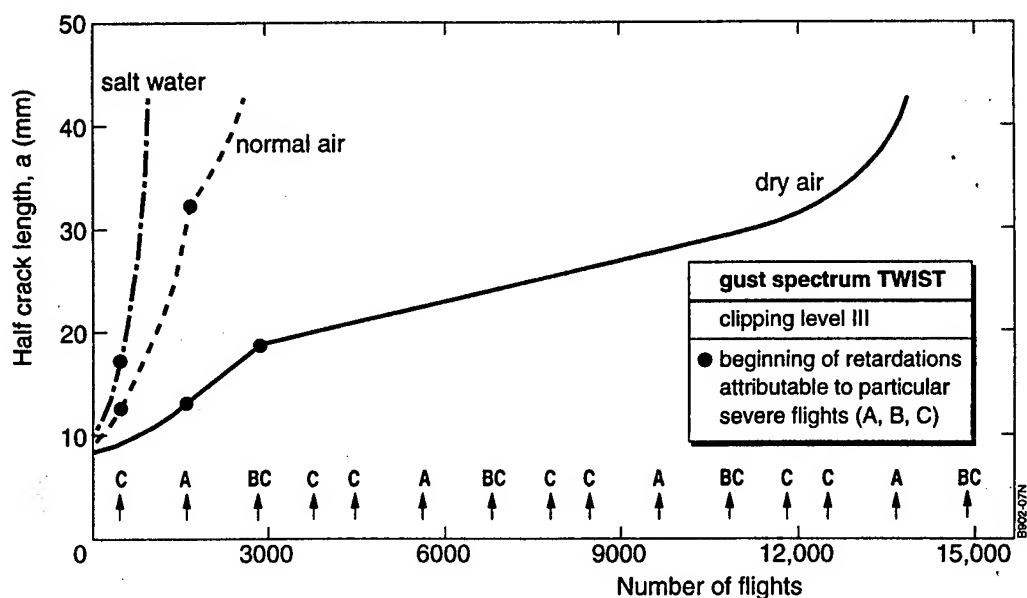


Fig. 10 Effect of environment on gust spectrum fatigue crack growth life for the aircraft industry standard aluminium alloy 7075-T6 [64]: centre-cracked tension specimens with a mean stress in flight, S_{mf} , of 70 MPa and a nominal cycle frequency of 15 Hz

However, the *degree* of environmental influence under flight simulation variable amplitude loading is sometimes much larger than would be expected from constant amplitude and constant stress ratio tests, notably for thin gauge sheet materials subjected to load histories containing peak loads that cause significant retardation of fatigue crack growth. A more aggressive environment results in basically higher fatigue crack growth rates, which not only reduce retardation after peak loads in severe (simulated) flights, but also reduce the number of severe flights encountered. Figure 10 is an example of this effect, which is best seen from a plot of crack length versus number of flights.

5.3 New Developments

5.3.1 Corrosion and fatigue life assessment

There are several recent and ongoing developments in corrosion and fatigue life assessment. The main ones will be mentioned here. These are FAA-sponsored research programmes at Lehigh University and SRI International, and a programme for the USAF C/KC-135 tanker aircraft.

The Lehigh University programme aims at a basic understanding of the processes of localised corrosion and corrosion fatigue crack initiation and growth in airframe structural aluminium alloys, specifically 2024-T3 and 7075-T651; the development of kinetic models for these processes; and integration of these models into a *probabilistic* approach to service life prediction [67]. Figure 11 is a flow diagram of the corrosion and fatigue damage processes being studied. Results so far indicate that there is indeed a competition between localised corrosion and fatigue crack initiation, and that the pit-to-crack transition size depends on cycle frequency [67]. These results are consistent with the hypothesis in subsection 5.1.2 that small amounts of localised corrosion could go beyond *pre-existing* short fatigue cracks.

The SRI International programme aims to develop a "corrosion-fatigue severity index" that could be used for aircraft inspection, and *deterministic* models for the nucleation and growth of corrosion pits and fatigue cracks from pits [68]. Advanced analysis techniques are being used to identify and characterize corrosion pits at which fatigue cracks nucleate, pit-to-crack transitions, and short-to-long fatigue crack growth. The analyses are being made on corrosion fatigue specimens from other organisations, notably Lehigh University and NASA Langley Research Centre, in-house corrosion fatigue tests on small riveted panels, and corroded skin panels removed from aircraft during maintenance.

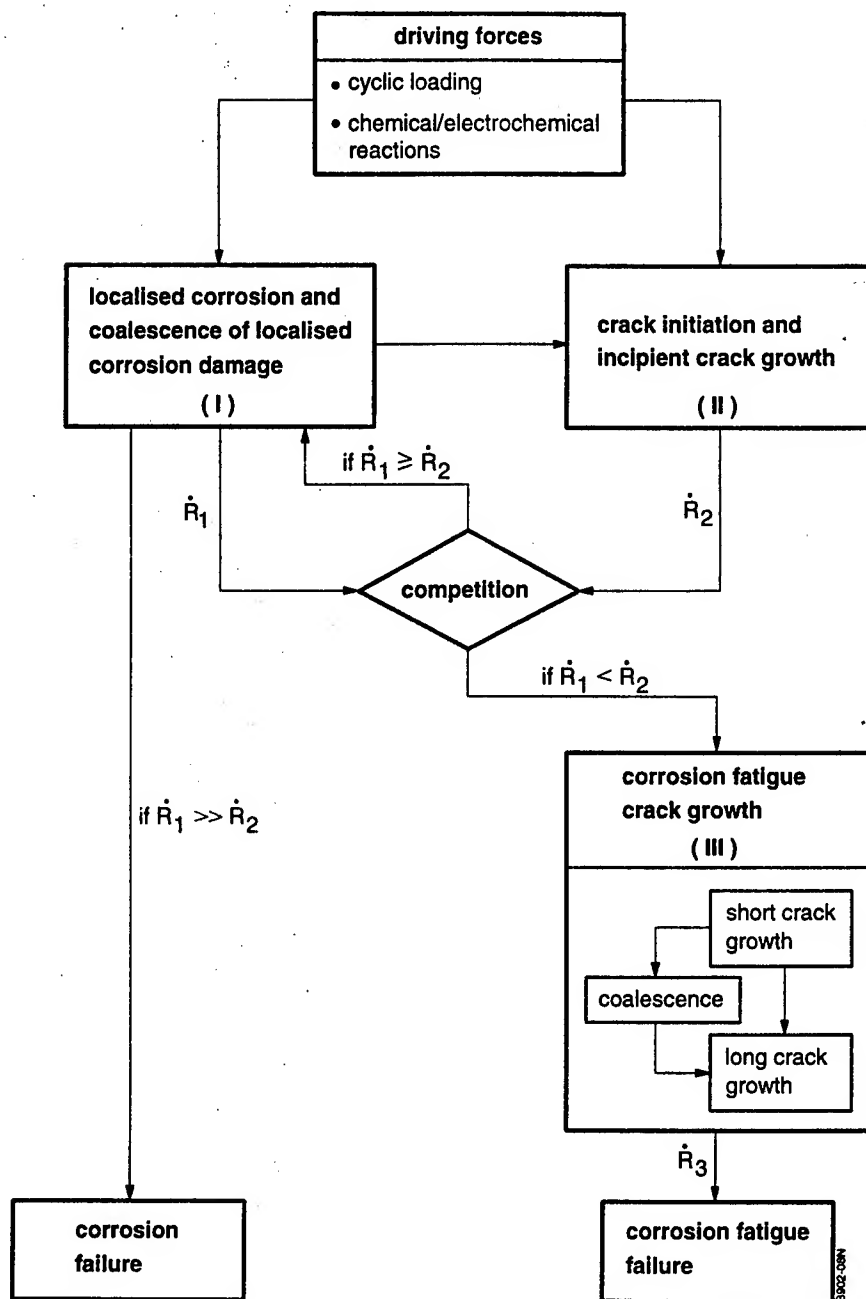
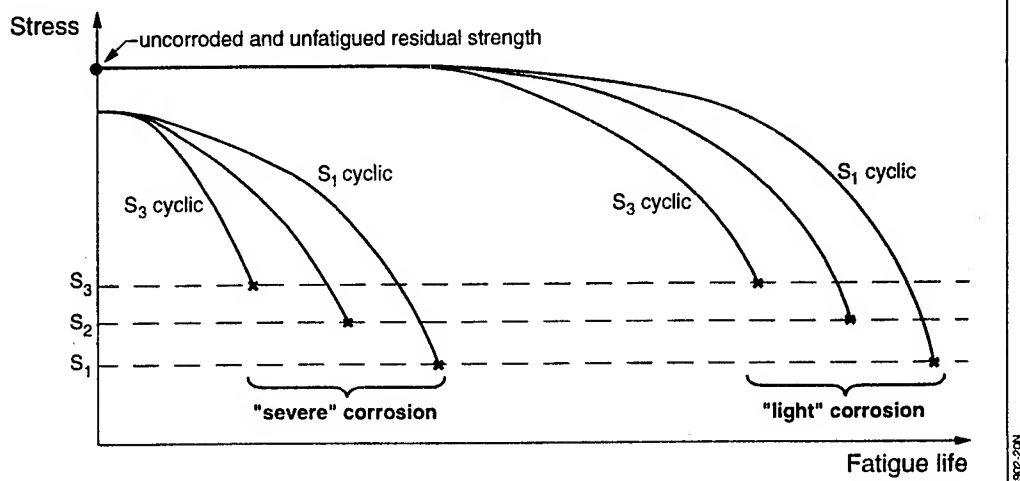


Fig. 11 Flow diagram for the corrosion and fatigue damage processes being studied in the Lehigh University programme: \dot{R}_1 , \dot{R}_2 , \dot{R}_3 are rates of accumulation of corrosion and fatigue damage

The C/KC-135 tanker aircraft date from the 1950s and are already respectably middle-aged, but it is intended to operate them until 2040 [2]. The airframe's resistance to corrosion-induced fatigue during this extremely long calendar life is of major concern. A programme combining the effects of corrosion and fatigue has been defined by the NAWC, ALCOA and the University of Utah, in consultation with the USAF. Table 11 gives an overview of this programme. The results will be used to develop life prediction models that enable corrosion effects on fatigue life to be incorporated into the Force Structural Maintenance Plan (FSMP) and Individual Aircraft Tracking Programme (IATP).

Table 11 Overview of the C/KC-135 tanker aircraft corrosion and fatigue programme

Materials	<ul style="list-style-type: none"> • 2024-T3 • 7178-T6
Specimens	<ul style="list-style-type: none"> • Fuselage lap joint, 10 types: 2024-T3 • Upper wing skin, 5 thicknesses: 7178-T6
Static pre-exposure	<ul style="list-style-type: none"> • Natural • Artificial: simulated acid rain
	} 3 degrees of corrosion: "light", "moderate", "severe"
Fatigue loading	<ul style="list-style-type: none"> • Constant amplitude, $R = 0.1$, cycle frequency 10 Hz, 3 stress levels
Fatigue environment	<ul style="list-style-type: none"> • Laboratory air, R.H. $\geq 85\%$, room temperature
Test schedules	<ul style="list-style-type: none"> • Static (monotonic) • Fatigue life: with and without corrosion • Fatigue + residual strength • Limited fatigue crack growth: 7178-T6
Analysis	<ul style="list-style-type: none"> • Corrosion - Fatigue - Residual Strength crossplot, e.g.:



5.3.2 Corrosion and fatigue crack growth

Short crack growth

As stated in subsection 5.2.2, there are very few test data for the effects of corrosion on short fatigue crack growth in aluminium alloys. However, research is in progress at the NASA Langley Research Centre [45], Lehigh University [67] and SRI International [68] as part of the US National Ageing Aircraft Research Programme (NAARP). Some of the NASA data are shown in figure 7 and are discussed in subsections 5.1.2 and 5.2.2.

Complementary to the foregoing experimental work, the NLR recently investigated MSD fatigue cracks in 2024-T3 aluminium alloy longitudinal lap splices from the lower fuselages of two commercial transport aircraft. The fatigue fracture surfaces were corroded, but only slightly, despite crack growth lives of several years. This means that the local environment must have been mild: for example, sump tank water or salt water completely destroy fatigue fracture surfaces within 2-4 weeks [69]. Two additional significant results were obtained from the MSD cracks:

- 1) Near the fatigue origins, at crack depths up to about 100 μm , the fracture surfaces were faceted, which for 2024-T3 is characteristic of crack growth rates less than 10^{-7} m/cycle [69, 70], where one cycle represents cabin pressurization during each flight. These faceted fracture surfaces showed *beach marks* consisting of light and dark bands, for example figure 12. The bands were *not* due to load variations but were most probably caused by periodic changes in the local environment during fatigue crack growth : more specifically, light-to-dark beach marks have been found on the faceted fatigue fracture surfaces of specimens tested with periodic changes in ambient humidity from "wet" to "dry" air [71, 72].
- (2) At high magnifications the light and dark bands were evidently corroded but appeared still to show successive positions of the fatigue crack front, for example figure 13. The spacings of more than six hundred of these crack fronts were measured for crack depths ranging from 30 μm to 80 μm . The average spacing was about 5×10^{-8} m, and the spacings in the light and dark bands were similar to within ± 20 %.

From these results it appears that the short fatigue cracks in the fuselage lap splices experienced varying environmental conditions, possibly limited to variations in atmospheric humidity, that were no more than mildly corrosive and whose variation did not significantly affect the fatigue crack growth rates.

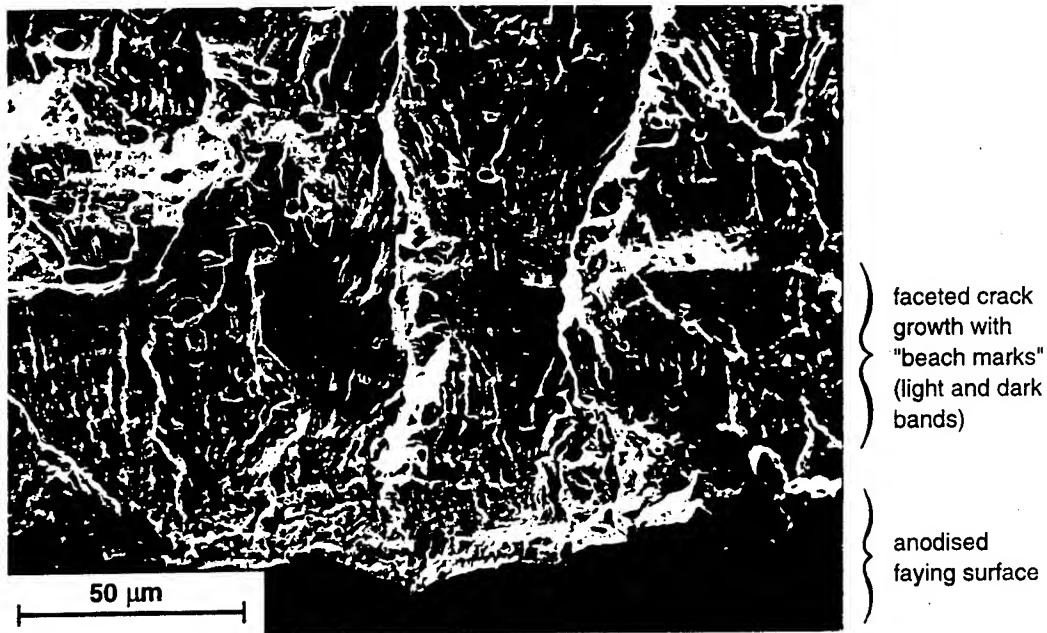


Fig 12 Multiple-origin fatigue cracking from the faying surface of a 2024-T3 aluminium alloy longitudinal lap splice in the lower fuselage of a commercial transport aircraft



Fig. 13 Successive positions of the fatigue crack front in a "beach mark". These high magnification details are partially obscured by (mild) corrosion

Long crack growth

The foregoing conclusions about in-service environmental conditions for short fatigue cracks are consistent with a statement by Chubb *et al* [73]. They refer to in-service fatigue data which suggest that crack growth rates are below those predicted by corrosion fatigue tests and closer to those obtained from tests in air. However, they also state that the processes of corrosion and fatigue tend to occur sequentially rather than concurrently, which was probably not the case for the MSD cracks investigated by the NLR.

Besides this service-related information there has been some recent long crack growth research sponsored by the UK Civil Aviation Authority (CAA) and the FAA. The CAA-sponsored work examined the effect of *prior* exfoliation corrosion on fatigue crack growth in the airframe alloys 2024-T351 and 7178-T6 [73]. For 2024-T351 there was no significant effect, but for 7178-T6 the crack growth rates in corroded areas were 2-3 times higher. This result was attributed to moisture and chemical entrapment in the corroded areas and the greater sensitivity of 7178-T6 to environmental effects. As noted in subsection 5.2.3, 7000 series alloys are more sensitive to environmental effects on long fatigue crack growth than 2000 series alloys.

The FAA-associated work concerned the influence of commercially available inhibitors on environmental fatigue crack growth in 2024 and 7075 aluminium alloys [74]. The inhibitors had little effect, which is rather surprising. On the other hand, the NAWC has shown that inhibition of crack growth depends on using specially formulated inhibitors [24, 61].

6. Discussion: Corrosion and Fatigue Damage in Aircraft

6.1 Corrosion and Fatigue Damage Occurrence

6.1.1 Fatigue crack initiation

Aircraft structures are undoubtedly damaged by corrosion and fatigue. Furthermore, the possibility of interactions between corrosion and fatigue damage - to the detriment of the structure - increases as aircraft get older. The implementation of stringent corrosion control programmes like those advocated by the AAWG and USAF will help to reduce this possibility, but it cannot be eliminated. This is because laboratory tests have demonstrated that only a minute amount of localised corrosion, virtually undetectable by in-service NDI, has a large effect on fatigue *life*.

On the other hand, the possibility of interactions between corrosion and fatigue damage is not the same as in-service occurrence. For example, although corrosion contributed to the Aloha Airlines accident [21], it was *not* implicated in the initiation of fatigue cracking. Nor was corrosion responsible for initiating the MSD cracks illustrated by figure 12, though these cracks are a special case*. At least for large transport aircraft, there is a need for definitive evidence that corrosion and fatigue habitually interact to reduce the fatigue life. In this respect it is important to note that the Institute for Aerospace Research (IAR) of the National Research Council of Canada has acquired an extensive specimen library of fuselage lap and butt joints, consisting of both corroded and uncorroded samples from transport aircraft. This specimen library should be invaluable for determining the relation, if any, between corrosion damage at and near fastener holes and the occurrence of fatigue cracks.

*The MSD cracks investigated by the NLR were in fuselage skins that had been "dimpled" around the rivet holes to avoid countersinking but still enable the rivets to be installed flush with the external surface. Unfortunately, the dimpling process resulted in internal tensile stresses and stress concentrations around the rivet holes, leading to mechanically-induced fatigue.

6.1.2 Fatigue crack growth

The local environmental conditions during fatigue crack growth in aircraft structures are poorly defined. These conditions range from moisture and chemical entrapment in severely corroded areas [73] to mild environments causing only slight corrosion over many years. Following on from this, it is largely unknown - in the absence of severe prior corrosion [73] - whether in-service fatigue crack growth rates could be significantly different from those measured during tests in laboratory air.

This problem is complicated by aircraft aluminium alloys having differing sensitivities to environmental effects on fatigue crack growth; and also, as a particular but important case, by a possible dependence of environmental effects on the very low cycle frequencies representative of cabin pressurization/depressurization. (In fact, only unloading - i.e. in this case cabin pressurization - is important for fatigue crack growth.)

As an illustration of the problem, consider the widely-used aluminium alloy 2024-T3. This material is relatively insensitive to environmental effects on fatigue crack growth, but this also means that relatively few test data are available

Table 12 Environmental effects on constant amplitude long fatigue crack growth in 2024-T3 aluminium alloy

Reference	Load cycle frequency	Baseline crack growth rate in normal or "wet" air, m/cycle	Crack growth acceleration factors relative to normal laboratory air or "wet" air		
			Dry air	Distilled water	3.5% aqueous NaCl
[75]	2 Hz	"wet" air $\left\{ \begin{array}{l} 10^{-8} \\ 5 \times 10^{-8} \\ 10^{-7} \end{array} \right.$			
			0.2	1.9	4.9
			0.8	1.2	1.8
			0.8	1.1	1.4
[52, 69]	13 Hz	normal air $\left\{ \begin{array}{l} 10^{-8} \\ 5 \times 10^{-8} \\ 10^{-7} \end{array} \right.$	Sump tank water		Synthetic seawater
			5.1 - 6.4		2.7
			2.2 - 2.3		1.5
			1.4		-

[52,53,63-66,69,73,75,76] because the alloy is less interesting from an experimental viewpoint. Table 12 provides a survey of environmental effects on constant amplitude fatigue crack growth in 2024-T3, in terms of acceleration factors relative to baseline crack growth rates in normal laboratory air or "wet" air. This survey indicates that environmental effects are important when the baseline crack growth rates are below 10^{-7} m/cycle. However, note the load cycle frequencies, which are much higher than those typical of cabin pressurization/depressurization (0.00003 - 0.0005 Hz in terms of *flights*, see table 1, and 0.001 - 0.003 Hz in terms of the climb and descent phases of a flight).

I conclude that there is not enough information available to determine the in-service environmental contribution to fatigue crack growth in aircraft structures. This situation can be remedied only by *ad hoc* research. Some significant pointers from the NLR investigation of MSD fatigue cracks in fuselage lap joints are (a) mild fracture surface corrosion, (b) *beach marks* on faceted fatigue fracture surfaces, (c) little difference in crack growth rates in the light and dark bands constituting the beach marks, and (d) crack growth rates higher than 10^{-8} m/cycle even for small cracks only 30 μ m deep. The IAR specimen library may provide much additional information helpful and necessary for defining the *ad hoc* testing conditions.

6.2 Corrosion and Fatigue Damage Assessment

At present there is no established methodology for assessing the effects of corrosion *and* fatigue in order to estimate service lives and specify inspection intervals (if any). In subsections 6.2.1 and 6.2.2 possible approaches to account

for the effects of corrosion and fatigue on safety and durability will be discussed. This will be done in the context of the DAMAGE TOLERANCE (DT) and SAFE-LIFE design philosophies, see subsection 4.1 and table 5.

6.2.1 Safety

DT structures

Damage tolerant structures are usually *inspectable* slow crack growth or fail-safe structures: non-inspectable slow crack growth structures are not accepted as damage tolerant by civil airworthiness authorities. Inspectable slow crack growth and fail-safe structures correspond respectively to Class I and Class II SSIs in transport aircraft, see table 8. This table is illustrative in that it shows that even for the most damage tolerant structures, namely Class II SSIs, a mixture of safe-life and crack growth fatigue analyses is used. Thus the initial in-service inspection is determined from a safe-life fatigue analysis, and subsequent inspection intervals are based on fatigue crack growth analysis. This is also illustrated as "current methods" in figure 3.

Figure 14 shows a possible approach to account for the influence of corrosion on the fatigue of DT structures. This is based on the assumption, mentioned in

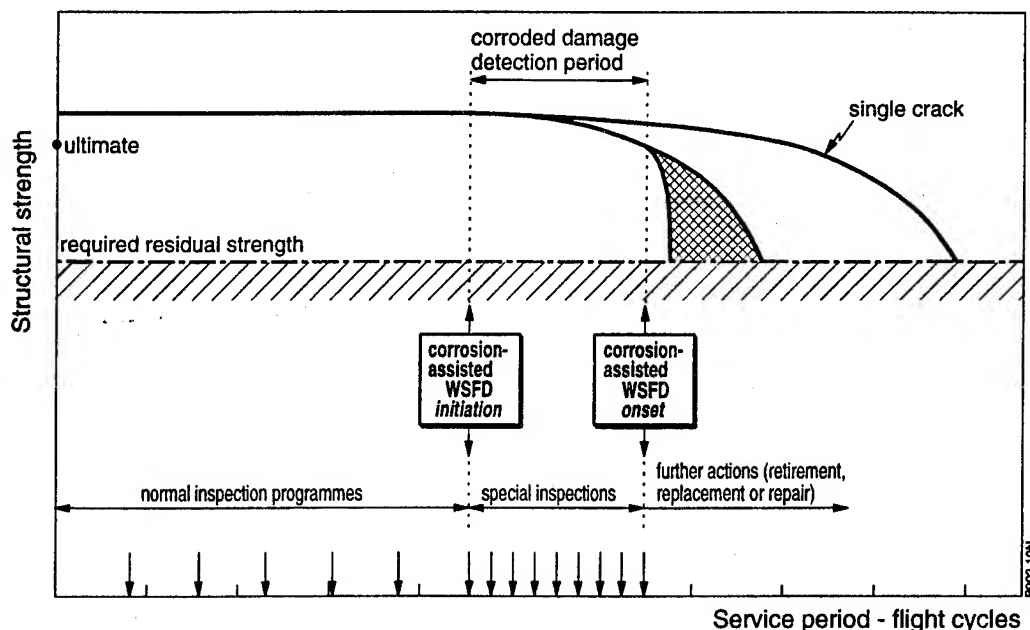


Fig. 14 Possible way of accounting for the influence of corrosion on fatigue of damage tolerant structures: WSFD = WideSpread Fatigue Damage

subsection 5.1.2, that corrosion will increase the number of fatigue cracks and might be expected to promote widespread and multiple site cracking, and on an AAWG agreement about assessing widespread fatigue damage (WSFD) [77]. *Initiation* of WSFD is the time at which the first finite crack is expected in a group of structural details where WSFD is likely: these are typically Class II SSIs like pressure cabins and wing structures. The *onset* of WSFD is the time at which crack growth rates and/or residual strength characteristics begin to diverge significantly from those attributable to isolated cracking.

The schematic in figure 14 shows an overall approach similar to that being considered in the C/KC-135 programme, see table 11. These approaches require realistic data for the effects of corrosion on fatigue crack initiation and growth in complex built-up structures. This is a formidable task which, at least in principle, could be undertaken in two ways:

- (1) Using the mixture of safe-life and crack growth fatigue analyses currently applied to Class II SSIs. This combined method could be used to determine corrosion-affected fatigue lives to a *finite crack* on the basis of S-N testing, which is discussed in subsection 6.2.3, followed by fatigue crack growth analysis that accounts for environmental effects. The finite crack size should be based on the minimum crack size reliably detectable by in-service NDI or the crack size beyond which current methods of *long* fatigue crack growth analyses are feasible, whichever is the larger. (In practice this will probably mean through-thickness cracks in complex built-up structures, i.e. cracks at least 1 mm in size).
- (2) Using "total life" predictions based on the effects of corrosion on fatigue crack initiation and *short-to-long* fatigue crack growth. This method appears to be favoured by some of the participants in the FAA-sponsored NAARP programme [67,68]. However, as mentioned in subsection 4.4, "total life" fatigue analyses will be hard to realise for complex built-up structures: on second thoughts, this statement is probably too optimistic.

Safe-life structures

Table 5 show that most general aviation and military aircraft, including helicopters, belong to this category; as also Class III SSIs in civil transport aircraft, table 8. For safe-life aircraft structures the approach to account for the influence of corrosion on fatigue is necessarily restricted to S-N testing and analysis. However, there are a number of possible testing schedules, see subsection 6.2.3.

6.2.2 Durability

With the exception of a few modern fighter aircraft, current durability methods for all categories of aircraft structures are the same as those for safe-life fatigue analysis. In other words, the approach to account for the influence of corrosion on fatigue durability currently has to be restricted to S-N testing and analysis, see subsection 6.2.3.

In future it may be possible to use durability analyses based on *short-to-long* fatigue crack growth, in which case the effects of corrosion on fatigue crack initiation and growth could be taken into account. But as mentioned earlier, this type of analysis will be hard to realise for complex built-up structures.

6.2.3 S-N testing schedules

S-N fatigue testing is of itself straightforward, but accounting for the effect of corrosion in a realistic manner is a problem. The difficulty lies in accounting for the *time* dependence of corrosion and the *cycle* -and possible *cycle frequency* -dependence of corrosion fatigue, and whether corrosion and fatigue are to be regarded as separate phenomena. For example, several types of testing schedules may be envisaged, as follows:

- prior corrosion + fatigue in air of differing humidities
- prior corrosion + corrosion fatigue
- periods of corrosion alternating with fatigue in air or aqueous environments
- corrosion fatigue *per se*.

Clearly the choice of testing schedules will depend on the type of aircraft and its actual or anticipated service usage; and also any evidence from service, for example from the IAR specimen library, on the relation between corrosion and fatigue.

As figure 1 shows, one may anticipate a greater contribution of corrosion to the total damage of aircraft with long calendar lives. Such aircraft accumulate fatigue damage relatively slowly in time. Also, it appears from laboratory tests that corrosion competes with fatigue in the early stages of damage [67], see subsections 5.1.2 and 5.3.1. Therefore it seems most reasonable to adopt the following procedure for S-N testing:

- (1) Establish from service data the types and severities of corrosion damage at and near fatigue-critical locations like fastener holes, and the relation between corrosion and the occurrence of fatigue cracks. In particular, it is important

to try and determine the time dependence of in-service corrosion damage that could lead to fatigue cracking.

- (2) Simulate service-induced corrosion damage by prior corrosion of realistic fatigue specimens. In the case of specimens representing structural joints it will probably be necessary to corrode the specimen elements before assembly.
- (3) Conduct fatigue testing on both uncorroded and pre-corroded specimens at realistic stress levels in normal air and at least one other environment. This environment should be based on service experience, for example the clues obtainable from *beach marks* and corrosion on fatigue fracture surfaces, see subsections 5.3.2 and 6.1.2. Note: if the fatigue lives to a finite crack size are required (see subsection 6.2.1) as well as the total lives, then the specimens must be monitored for cracking during testing. In fact, it is a good idea to monitor for cracking whenever feasible, with a view to better understanding the occurrence and accumulation of fatigue damage.

To estimate the corrosion-affected fatigue lives the S-N test results must first be analysed in relation to the actual or anticipated service load histories. The resulting estimates of fatigue lives must then be added to the estimated service time required for corrosion damage that could lead to fatigue cracking. (Of course the fatigue lives could be converted into service time or the corrosion-related service time could be converted into *effective* numbers of flight cycles, if wished. But in the first instance it is better to recognise - as does the AAWG - the distinction between calendar time and flight cycles or flight-hours.)

7. Conclusions

This paper reviews currently available information on corrosion and fatigue in aircraft as a background to discussing the assessment of corrosion and fatigue damage. Aircraft structures are susceptible to corrosion and fatigue damage, and both types of damage concentrate at structural joints. There is a likelihood of interactions between corrosion and fatigue, especially as aircraft become older. Neither type of damage can be fully prevented, despite stringent control programmes.

From this review and discussion the following conclusions are drawn:

- (1) Although there is a likelihood of interactions between corrosion and fatigue, it is uncertain whether corrosion damage habitually leads to fatigue initiation in service.

- (2) Although there is much apparently useful information about aircraft environments - both internal and external - and structural loads, it is difficult to be specific about the relation between service environments and load histories.
- (3) Continuing with conclusions (1) and (2) there is a need for *ad hoc* investigations to determine the in-service environmental contributions to fatigue initiation and crack growth. Structural areas removed from ageing aircraft, as in the IAR specimen library, should be invaluable sources of information for these investigations.
- (4) Laboratory tests indicate that corrosion damage competes with fatigue crack initiation, and have shown that corrosion increases the number of fatigue cracks, *can* change the locations of fatigue origins in structural joints, and greatly reduces the fatigue lives and fatigue strengths. Also, during fatigue crack growth testing the presence of an aqueous environment at the crack tip *can* significantly increase the crack growth rates.
- (5) There is no established methodology for assessing the effects of corrosion on fatigue in order to estimate service lives and specify inspection intervals. The following approaches are suggested:

SAFETY

- damage tolerant structures : an approach based on the probable occurrence of widespread fatigue damage and use of the SAFE-LIFE + FAIL-SAFE method of fatigue analysis
(typically Class II SSIs)
- safe-life structures : SAFE-LIFE fatigue analysis

DURABILITY

- all categories of structures : SAFE-LIFE/durability fatigue analysis.
- (6) Continuing with conclusion (5), S-N fatigue testing is the basis of SAFE-LIFE/durability fatigue analyses. Accounting for the effects of corrosion in a realistic manner is a problem for S-N testing. For long-life aircraft the following procedure is suggested:

- from *ad hoc* investigations, see conclusion (3), establish the types, severities and time dependence of corrosion damage in relation to fatigue cracking
- simulate service corrosion by prior corrosion of realistic fatigue specimens
- fatigue test uncorroded and pre-corroded specimens at realistic stress levels in normal air and at least one other environment based on service experience.

8. References

1. Houlihan, G.J., Corrosion control for an ageing fleet, Aerospace Corrosion Control 1992, Sawell Publications Ltd, pp. 3/1-3/13 (1992): London.
2. Nieser, D.E., OC-ALC ageing aircraft disassembly and hidden corrosion detection programme, Proceedings of the 1992 USAF Structural Integrity Programme Conference, Materials Directorate Wright Laboratory Air Force Materiel Command, Wright-Patterson AFB, pp. 624-640 (1993): Ohio.
3. Corrosion Manual, Section 1, Air Publication 119A-0200-1A, Ministry of Defence, 2nd Edition (1978): London.
4. Christian, T.F.; Hammond, D.O.; Cochran, J.B.; Morcock, D.S., Force management technology application to ageing aircraft, Proceedings of the 1989 Structural Integrity Programme Conference, Materials Laboratory Wright Research and Development Centre Air Force Systems Command, Wright-Patterson AFB, pp. 143-200 (1990): Ohio.
5. Goranson, U.G.; Miller, M., Ageing jet transport structural evaluation programmes, Structural Integrity of Ageing Airplanes, Springer-Verlag, pp. 131-140 (1991): Berlin.
6. Wallace, W.; Hoepfner, D.W.; Kandachar, P.V., AGARD Corrosion Handbook Volume 1. Aircraft Corrosion: Causes and Case Histories, AGARDograph No. 278, Advisory Group for Aerospace Research and Development, Chapter 2 (1985): Neuilly-sur-Seine.
7. Scott, J.A., Corrosion and corrosion prevention in airframes, British Corrosion Journal, Vol. 6, pp. 145-147 (1971).
8. Wallace, W.; Hoepfner, D.W.; Kandachar, P.V., AGARD Corrosion Handbook Volume 1. Aircraft Corrosion: Causes and Case Histories, AGARDograph No. 278, Advisory Group for Aerospace Research and Development, Chapter 15 (1985): Neuilly-sur-Seine.
9. Schijve, J., Fatigue of aircraft structures, Israel Journal of Technology, Vol. 8, pp. 1-20 (1970).
10. Anderson, W.E., Fatigue of aircraft structures, International Metallurgical Reviews, Vol. 17, pp. 240-263 (1972).
11. US Standard Atmosphere, US Government Printing Office (1962): Washington, D.C.

12. Hoggard, A.W., Fuselage longitudinal splice design, *Structural Integrity of Ageing Airplanes*, Springer-Verlag, pp. 167-181 (1991): Berlin.
13. Shaffer, I.S., Methodology for assessment of corrosion costs, *Workshop on Requirements for Aircraft Corrosion Control*, AGARD Report No. 714, Advisory Group for Aerospace Research and Development, pp. 9-1—9-7 (1984): Neuilly-sur-Seine.
14. Mitchell, R.G., Cost of corrosion for commercial aviation, *Workshop on Requirements for Aircraft Corrosion Control*, AGARD Report No. 714, Advisory Group for Aerospace Research and Development, p. 10-1 (1984): Neuilly-sur-Seine.
15. Kinzie, R.C., The cost of USAF corrosion maintenance, *Aerospace Corrosion Control 1992*, Sawell Publications Ltd, pp. 8/1-8/9 (1992): London.
16. Ryan, N.E., Quoted in *AGARD Corrosion Handbook Volume 1. Aircraft Corrosion: Causes and Case Histories*, AGARDograph No. 278, Advisory Group for Aerospace Research and Development, p.2 (1985): Neuilly-sur-Seine.
17. Wallace, W.; Hoepfner, D.W.; Kandachar, P.V., *AGARD Corrosion Handbook Volume 1. Aircraft Corrosion: Causes and Case Histories*, AGARDograph No. 278, Advisory Group for Aerospace Research and Development, Chapter 6 (1985): Neuilly-sur-Seine.
18. 't Hart, W.G.J., Corrosion and corrosion prevention in aircraft structures, NLR MP 85029U, National Aerospace Laboratory NLR, Amsterdam, March 1985 (in Dutch).
19. Hoggard, A.W., Control and prevention of aircraft corrosion, *Aerospace Corrosion Control 1992*, Sawell Publications Ltd, pp. 2/1-2/18 (1992): London.
20. Goranson, U.G., Continuing airworthiness of ageing jet transports, *Second Annual International Conference on Ageing Aircraft*, Atlantic Science and Technology Corporation, pp. 61-89 (1989): Cherry Hill, NJ 08003.
21. Aircraft accident report, Aloha airlines, flight 243, Boeing 737-200, N73711, Near Maui, Hawaii, April 28, 1988, NTSB Report No. NTSB/AAR-89/03, National Transportation Safety Board (1989): Washington, D.C.
22. Paone, M.L., The corrosion challenge: the impact of corrosion maintenance programmes, *Materials Evaluation*, December 1993, pp. 1373-1376.
23. Weetman, D.C.; Eden, D.A.; Cox, W.M., Health and usage monitoring systems - corrosion surveillance, *Aerospace Corrosion Control 1994*, SP Conferences, pp. 5/1 - 5/25 (1994): Gravesend, Kent.
24. Hegedus, C., Corrosion control, *Second Annual International Conference on Ageing Aircraft*, Atlantic Science and Technology Cooperation, pp. 158-165 (1989): Cherry Hill, NJ 08803.

25. Wanhill, R.J.H., Short cracks in aerospace structures, *The Behaviour of Short Fatigue Cracks*, Mechanical Engineering Publications, pp. 27-36 (1986): London.
26. Keith, L.A., Transport aircraft certification, Second Annual International Conference on Ageing Aircraft, Atlantic Science and Technology Corporation, pp. 12-18 (1989): Cherry Hill, NJ 08003.
27. Hoepfner, D.W.; Ekvall, J.; McCammond, D.; Poon, C; Venter, R., *Aircraft Structural Fatigue, Volumes I-III*, Department of Mechanical Engineering, University of Toronto: Toronto.
28. Craig, L.E.; Goranson, U.G., Airworthiness assessment of Boeing jet transport structures, Structural Fatigue as a Design Factor, Proceedings of the 10th ICAF Symposium, Aeronautics Administration, Belgium, pp. 2.2/1-2.2/62 (1979): Brussels.
29. Harris, C.E.; Heyman, J.S., Overview of NASA research related to the ageing commercial transport fleet, *Journal of Aircraft*, Vol. 30, pp. 64-68 (1993).
30. Wang, D.Y., A study of small crack growth under transport spectrum loading, *Behaviour of Short Cracks in Airframe Components*, AGARD Conference Proceedings No. 328, Advisory Group for Aerospace Research and Development, pp. 14-1-14-15 (1983): Neuilly-sur-Seine.
31. Phillips, E.P.; Newman, Jr., J.C., Impact of small-crack effects on design-life calculations, *Experimental Mechanics*, Vol. 29, pp. 221-225 (1989).
32. Wanhill, R.J.H.; Schra, L., Short and long fatigue crack growth in 2024-T3 under Fokker 100 spectrum loading, *Short-Crack Growth Behaviour in Various Aircraft Materials*, AGARD Report No. 767, Advisory Group for Aerospace Research and Development. pp. 8-1-8-26 (1990): Neuilly-sur-Seine.
33. Wanhill, R.J.H., A preliminary study of fatigue durability in terms of short and long crack growth, Proceedings of the 1992 USAF Structural Integrity Programme Conference, Materials Directorate Wright Laboratory Air Force Materiel Command, Wright-Patterson AFB, pp. 185-256 (1993): Ohio 45433-7734.
34. Newman, Jr., J.C.; Edwards, P.R., Short-crack growth behaviour in an aluminium alloy - an AGARD cooperative test programme, AGARD Report No. 732, Advisory Group for Aerospace Research and Development (1988): Neuilly-sur-Seine.
35. Various authors in *Corrosion Fatigue: Chemistry, Mechanics and Microstructure*, National Association of Corrosion Engineers (1972): Houston.
36. Various authors in *Corrosion Fatigue of Aircraft Materials*, AGARD Report No. 659, Advisory Group for Aerospace Research and Development (1977): Neuilly-sur-Seine.

37. Various authors in *The Influence of Environment on Fatigue*, The Institution of Mechanical Engineers (1977): London.
38. Various authors in *Corrosion-Fatigue Technology*, ASTM STP 642, American Society for Testing and Materials (1978): Philadelphia.
39. Various authors in *Corrosion Fatigue*, AGARD Conference Proceedings No. 316, Advisory Group for Aerospace Research and Development (1981): Neuilly-sur-Seine.
40. Various authors in *Corrosion Fatigue: Mechanics, Metallurgy, Electrochemistry, and Engineering*, ASTM STP 801, American Society for Testing and Materials (1983); Philadelphia.
41. Various authors in *The Fatigue in Aircraft Corrosion Testing (FACT) Programme*, AGARD Report No. 713, Advisory Group for Aerospace Research and Development (1989): Neuilly-sur-Seine.
42. Various authors in *Environment Assisted Fatigue*, EGF Publication 7, Mechanical Engineering Publications Limited (1990): London.
43. Harmsworth, C.L., Effect of corrosion on the fatigue behaviour of 2024-T4 aluminium alloy, ASD Technical Report 61-121, Aeronautical Systems Division Air Force Systems Command, Wright-Patterson AFB (1961): Ohio.
44. Vaessen, G.H., Investigations on aluminium-lithium alloys for damage-tolerant application. Task 2: Understanding of corrosion behaviour, BRITE/EURAM Final Report ELMT 93-005, Fokker Aircraft B.V. (1992): Schiphol.
45. Ongoing Research, NASA Langley Research Centre: Hampton.
46. Heida, J.H.; 't Hart, W.G.J., Eddy current detection of pitting corrosion around fastener holes, NLR TP 94275 L, National Aerospace Laboratory NLR, Amsterdam, June 1994.
47. Gough, H.J., Corrosion-fatigue of metals, *Journal of the Institute of Metals*, Vol. 49, pp. 17-92 (1932).
48. Daniels, R.D.; Lorkovic, W.M., Secondary damage in corrosion-fatigue of aluminium, *Metallurgical Transactions*, Vol. 2, pp. 1990-1992 (1971).
49. Kitagawa, H.; Fujita, T.; Miyazawa, K., Small randomly distributed cracks in corrosion fatigue, *Corrosion-Fatigue Technology*, ASTM STP 642, American Society for Testing and Materials, pp. 98-114 (1978): Philadelphia.
50. Wanhill, R.J.H., Status and prospects for aluminium-lithium alloys in aircraft structures, *Fatigue of Aircraft Materials*, Delft University Press, pp. 43-82 (1992): Delft.
51. McEvily, A.J.; Wei, R.P., Fracture mechanics and corrosion fatigue, *Corrosion Fatigue: Chemistry, Mechanics and Microstructure*, National Association of Corrosion Engineers, pp. 381-395 (1972): Houston.

52. Wanhill, R.J.H.; Schra, L., Corrosion fatigue crack arrest in aluminium alloys, Quantitative Methods in Fractography, ASTM STP 1085, American Society for Testing and Materials, pp. 144-165 (1990): Philadelphia.
53. Wanhill, R.J.H.; Environmental effects on fatigue of aluminium and titanium alloys, Corrosion Fatigue of Aircraft Materials, AGARD Report No. 659, Advisory Group for Aerospace Research and Development, pp. 2-1—2-37 (1977): Neuilly-sur-Seine.
54. Yoder, G.R.; Pao, P.S.; Imam, M.A.; Cooley, L.A., On corrosion-fatigue crack growth behaviour of aluminium-lithium alloy 2090 in salt water, Competitive Advances in Metals and Processes, 1st International SAMPE Metals and Metals Processing Conference, Society for the Advancement of Material and Process Engineering, Vol. 1, pp. 25-36 (1987): Covina.
55. Shin, K.S.; Lee, E.W., Effect of various environments on fatigue crack propagation of a 2090 Al-Li alloy, Light-Weight Alloys for Aerospace Applications, The Minerals, Metals and Materials Society, pp. 171-179 (1989): Warrendale.
56. Gangloff, R.P.; Piascik, R.S.; Dicus, D.L.; Newman, Jr., J.C., Fatigue crack propagation in aerospace aluminium alloys, ICAS Proceedings 1990: 17th Congress of the International Council of the Aeronautical Sciences, American Institute of Aeronautics and Astronautics, Inc. (AIAA), Vol. 1, pp. 894-908 (1990): Washington D.C.
57. Various authors in Aluminium-Lithium, DGM Informationsgesellschaft mbH (1992): Oberursel.
58. Piascik, R.S.; Gangloff, R.P., Environmental fatigue of an Al-Li-Cu alloy: Part I. Intrinsic crack propagation kinetics in hydrogenous environments, Metallurgical Transactions A, Vol. 22A, pp. 2415-2428 (1991).
59. Kemp, R.M.J.; Wilson, R.N.; Gregson, P.J., The effects of frequency and R-ratio on fatigue crack growth behaviour in Al-Li-Cu-Mg alloy (8090) plate, Fatigue and Fracture of Engineering Materials and Structures, Vol. 15, pp. 291-308 (1992).
60. Wanhill, R.J.H., Fatigue and fracture properties of aerospace aluminium alloys, NLR TP 93356 L, National Aerospace Laboratory NLR, Amsterdam, October 1993.
61. De Luccia, J.J.; Personal Communication from the Naval Air Development Centre (1980): Warminster.
62. Kemp, R.M.J., The RAE contribution to the FACT programme, The Fatigue in Aircraft Corrosion Testing (FACT) Programme, AGARD Report No. 713, Advisory Group for Aerospace Research and Development, pp. 138-161 (1989): Neuilly-sur-Seine.

63. Wanhill, R.J.H.; Jacobs, F.A.; Schijve, J., Environmental fatigue under gust spectrum loading for sheet and forging aircraft materials, *Fatigue Testing and Design*, The Society of Environmental Engineers, Vol. 1, pp. 8.1-8.33 (1976): Buntingford.
64. Schijve, J.; Jacobs, F.A.; Tromp, P.J., Environmental effects on crack growth in flight-simulation tests on 2024-T3 and 7075-T6 material, NLR TR 76104U, National Aerospace Laboratory NLR, Amsterdam, October 1976.
65. Wanhill, R.J.H., Flight simulation environmental fatigue crack propagation in 2024-T3 and 7475-T761 aluminium, *ICAS Proceedings 1980: 12th Congress of the International Council of the Aeronautical Sciences*, American Institute of Aeronautics and Astronautics, Inc. (AIAA), pp. 645-651 (1980): New York.
66. Wanhill, R.J.H.; Jacobs, F.A.; Schra, L., The effect of environment on fatigue crack propagation under gust spectrum loading in aluminium alloy sheet, and the significance for realistic testing, *The influence of Environment on Fatigue*, The Institution of Mechanical Engineers, pp. 101-109 (1977): London.
67. Wei, R.P., Semi-annual progress report for period 15 June to 14 December 1993, Lehigh University, Bethlehem, December 1993.
68. Giovanola, J.H.; Kobayashi, T.; Schmidt, C.G.; Shockey, D.A., Characterization of corrosion-fatigue in aircraft fuselages, Proposal for Research PYU 92-272, SRI International, Menlo Park, November 1992.
69. Wanhill, R.J.H.; Schra, L., Corrosion fatigue crack arrest in aluminium alloys: basic data, NLR TR 87128 U, National Aerospace Laboratory NLR, Amsterdam, July 1987.
70. Wanhill, R.J.H., Low stress intensity fatigue crack growth in 2024-T3 and T351, *Engineering Fracture Mechanics*, Vol. 30, pp. 233-260 (1988).
71. Darvish, M.; Johansson, S., Cyclic change in the humidity of the environment during fatigue crack propagation and its effect on fracture surface appearance, *Scandinavian Journal of Metallurgy*, Vol. 21, pp. 68-77 (1992).
72. Darvish, M., The cyclic change in the humidity of the environment. A new method for studying the fatigue crack at low growth rate, Dissertation No. 288, Linköping Studies in Science and Technology, Linköping University, Linköping, 1992.
73. Chubb, J.P.; Morad, T.A.; Hockenhuil, B.S.; Bristow, J.W., The effect of exfoliation corrosion on the fatigue behaviour of structural aluminium alloys, *Structural Integrity of Ageing Airplanes*, Springer-Verlag, pp. 87-97 (1991): Berlin.
74. Irving, P.E.; Hubble, M.J.; Chubb, J.P., Unpublished Research, Cranfield Institute of Technology: Cranfield.

75. Feeney, J.A.; McMillan, J.C.; Wei, R.P., Environmental fatigue crack propagation of aluminium alloys at low stress intensity levels, *Metallurgical Transactions*, Vol. 1, pp. 1741-1757 (1970).
76. Hartman, A.; Jacobs, F.A.; Nederveen, A.; de Rijk, P., Some tests on the effect of environment on the propagation of fatigue cracks in aluminium alloys, NLR Report M.2182, National Aerospace Laboratory, Amsterdam, May 1967.
77. Schmidt, H.-J.; Brandecker, B., Results of the AAWG industry committee on widespread fatigue damage, *Durability of Metal Aircraft Structures*, Atlanta Technology Publications, pp. 279-295 (1992): Atlanta.

FUSELAGE LAP SPLICE CORROSION

R. S. Piascik
Mechanics of Materials Branch
NASA Langley Research Center
Hampton, VA 23681

R.G. Kelly and M.E. Inman
Materials Science and Engineering
University of Virginia
Charlottesville, VA 22903

S.A. Willard
Lockheed Engineering & Sciences Company
NASA Langley Research Center
Hampton, VA 23681

USAF Structural Integrity Program Conference, San Antonio, TX, Nov. 28-30, 1995

OUTLINE:

- **Background**
- **Objective**
- **Proof-Of-Concept**
 - ⇒ **Destructive Examination**
 - ⇒ **Determination of Corrosion Chemistry**
 - ⇒ **Preliminary Corrosion Test Results**
- **Summary**

OBJECTIVE:

Establish a protocol for identifying aircraft structure corrosion chemistry (lap splice joint).

BACKGROUND:

Extend the service life of aging aircraft.

EXAMPLE: Extend KC-135 service to the year 2030.

BACKGROUND:

NEEDS? - Life Extension Tools for Corroded Structure

1. Analytical methods for residual strength, durability, inspection intervals, etc?

2. Qual. of repair methods?

3. Qual. of coatings, structural materials, etc?

CORROSION

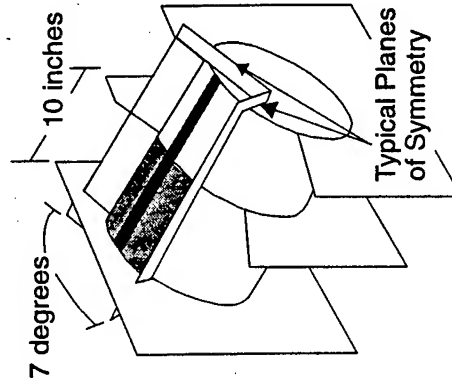
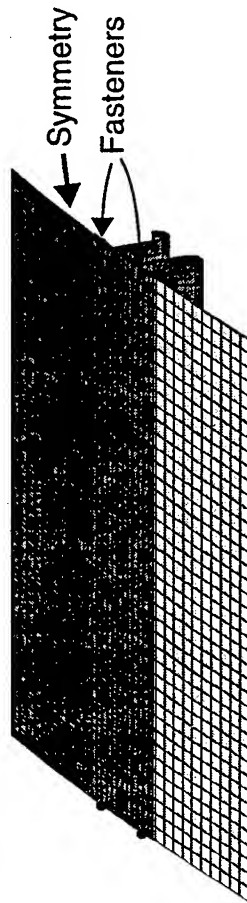
TESTING

(What Environment?)

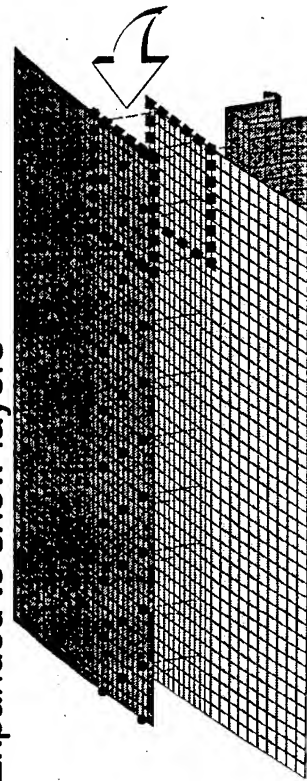
Stiffened Aluminum Lap Joint:

- Fasteners: 3 rows of 3/16 in. rivets
- Corrosion in joint: skin thinning and voluminous swelling
- Cracks: various locations in outer skin
- Loading: 8.0 psi radial pressure

Half Model



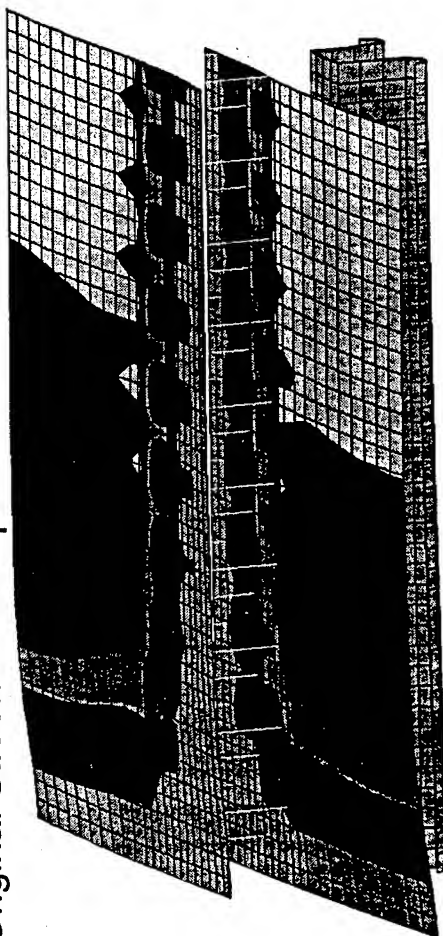
Expanded to show layers



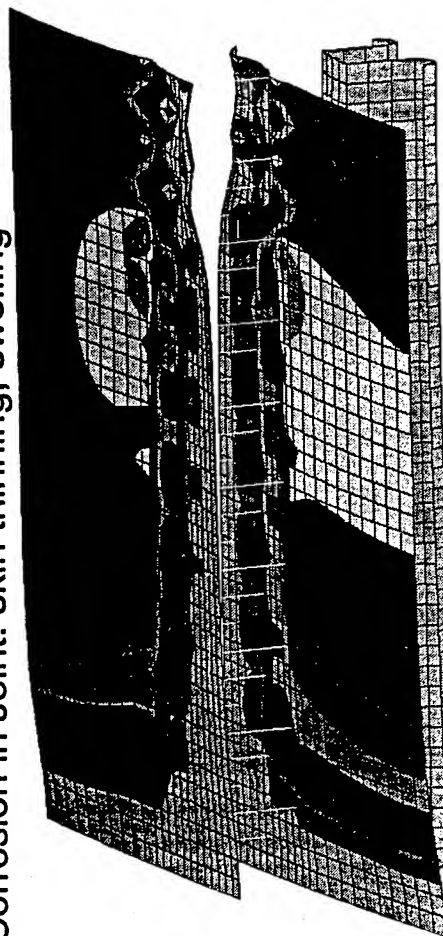
R. D. Young

Stiffened Aluminum Lap Joint: No Crack

Original Structural Components



Corrosion in Joint: skin thinning, swelling



Resultant
Hoop Stress

Max

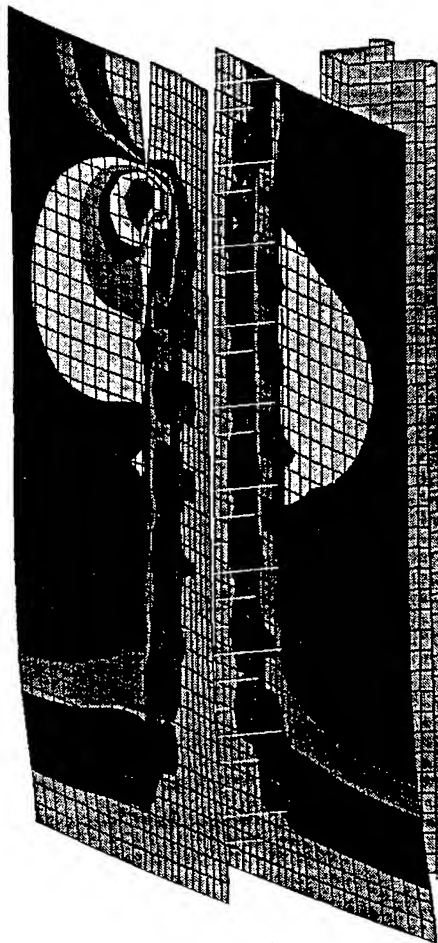


0

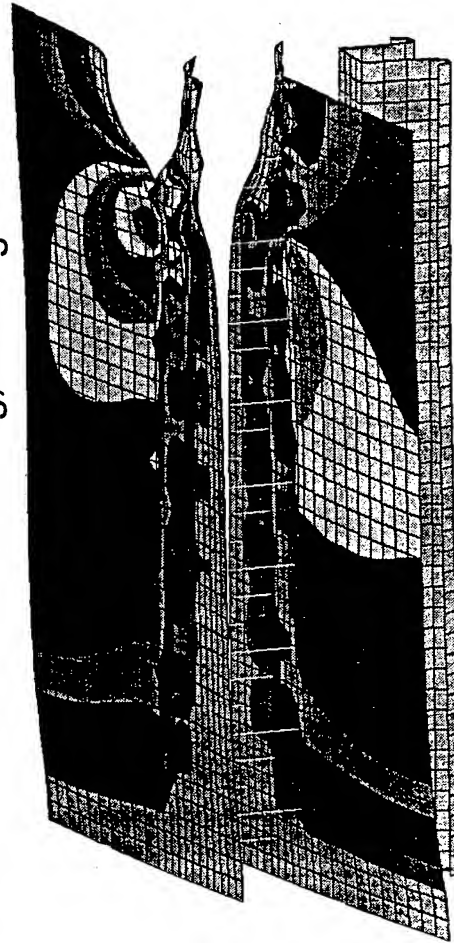
R. D. Young

Stiffened Aluminum Lap Joint: 1.5 in. half crack

Original Structural Components



Corrosion in Joint: skin thinning, swelling



Resultant
Hoop Stress

Max



0

R. D. Young

PROOF-OF-CONCEPT:

- 1. Characterize fuselage lap splice joint corrosion damage.**
- 2. Determine lap splice joint corrosion chemistry by the Capillary Electrophoresis technique.**
- 3. Simulate lap splice joint corrosion chemistry in the laboratory.**

LAP SPLICE DESTRUCTIVE EXAMINATION

Lap Splice Panel:

Aircraft History

Type: B707-320C

S/N: 20018

Delivery Date: 11/22/68

Retired Date: 8/1/87

Flight Hours: 46685

Landings: 19967

History: Unknown

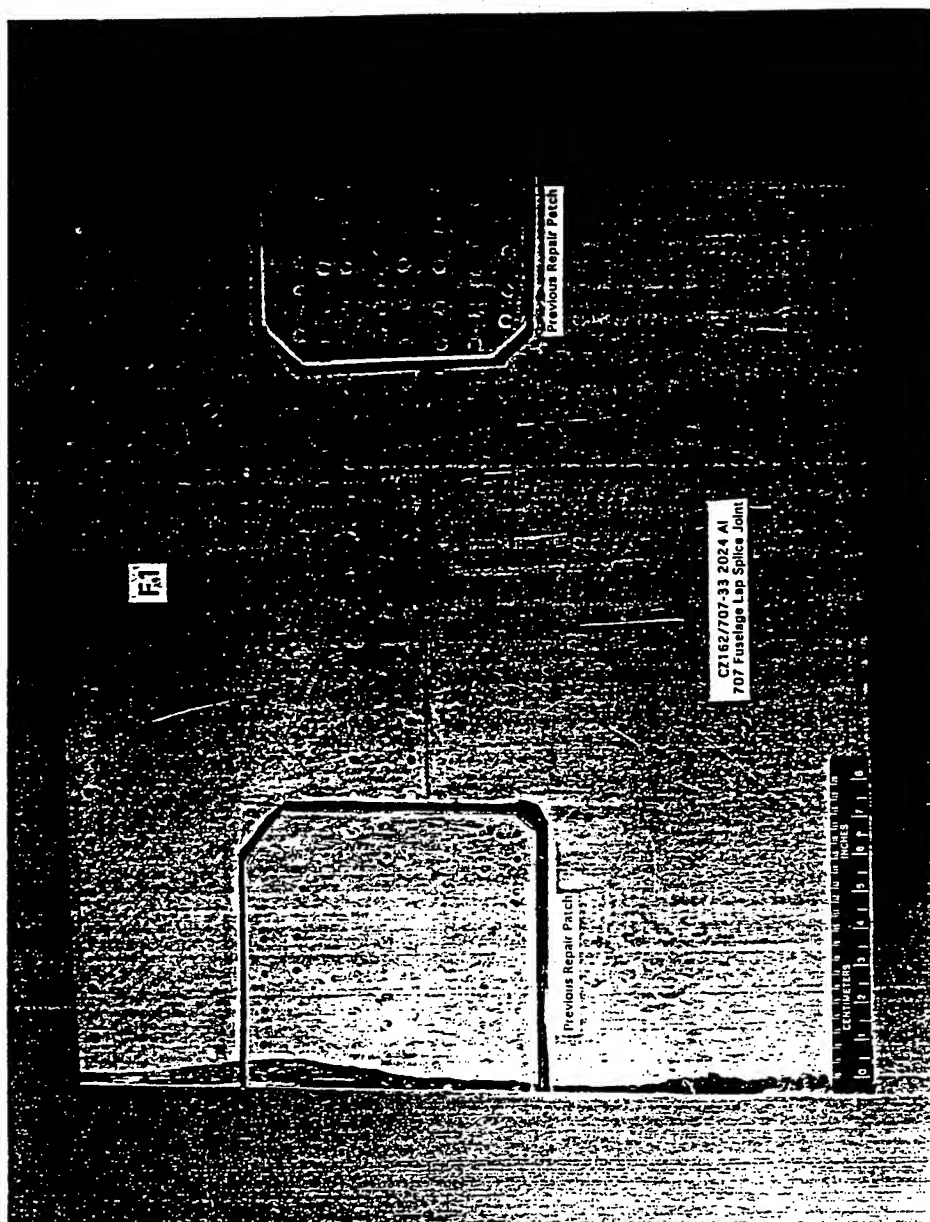
Materials of Construction

Fuselage Skin: 2024T3 clad

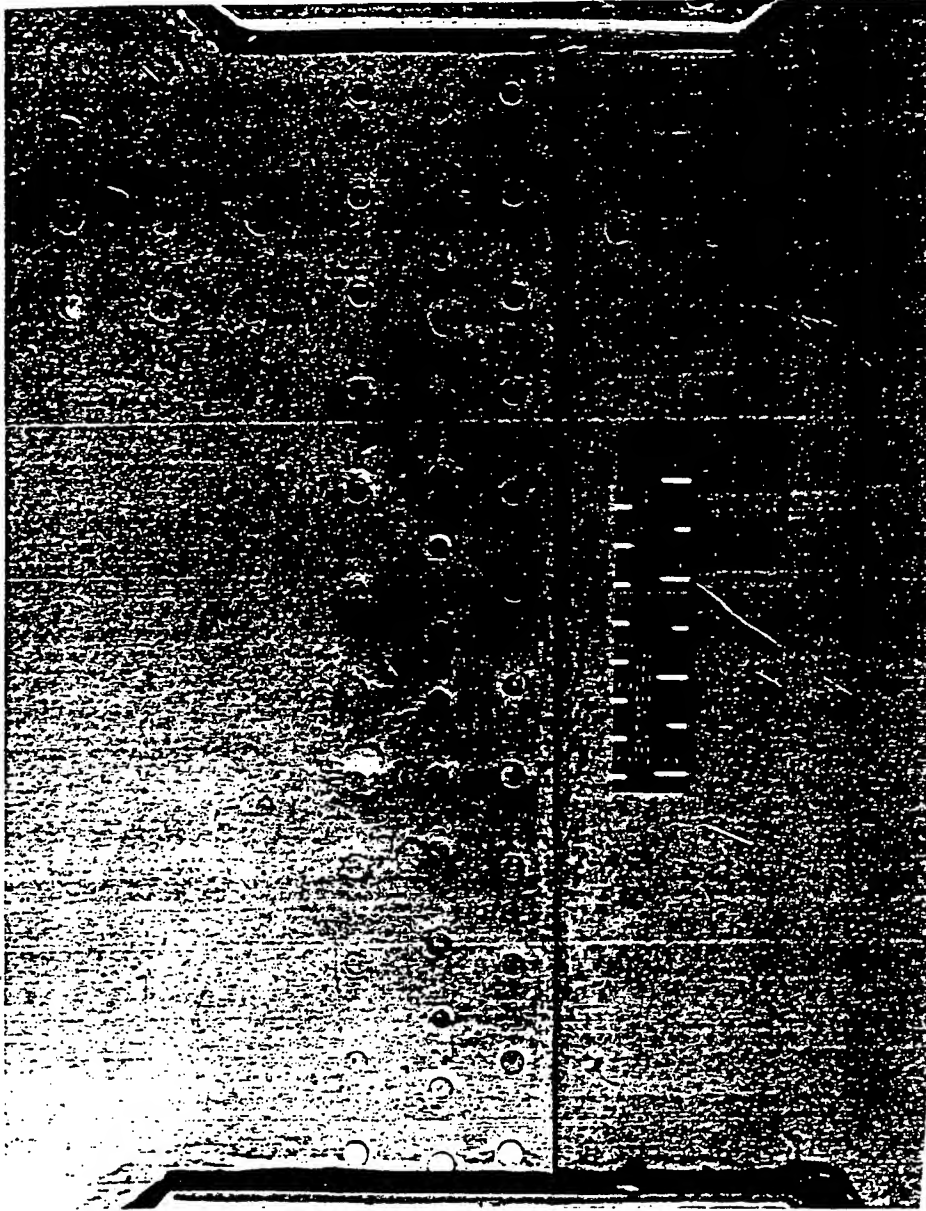
Faying Surface Painted (NO CLAD)

Rivet: 2017T4 anodized

Lap Splice Panel:



Lap Splice Panel:



Fuselage Lap Splice Corrosion



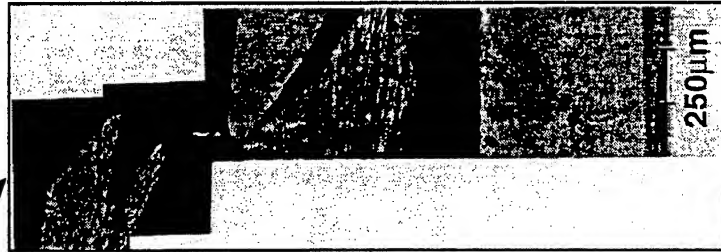
Fuselage Lap Splice Corrosion - Cut #3



(a)



(b)



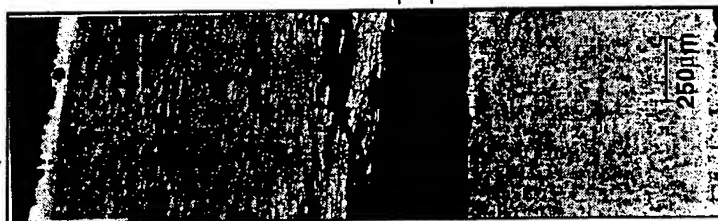
(c)

FLSC-#3

Fuselage Lap Splice Corrosion - Cut #4



(a)



(b)

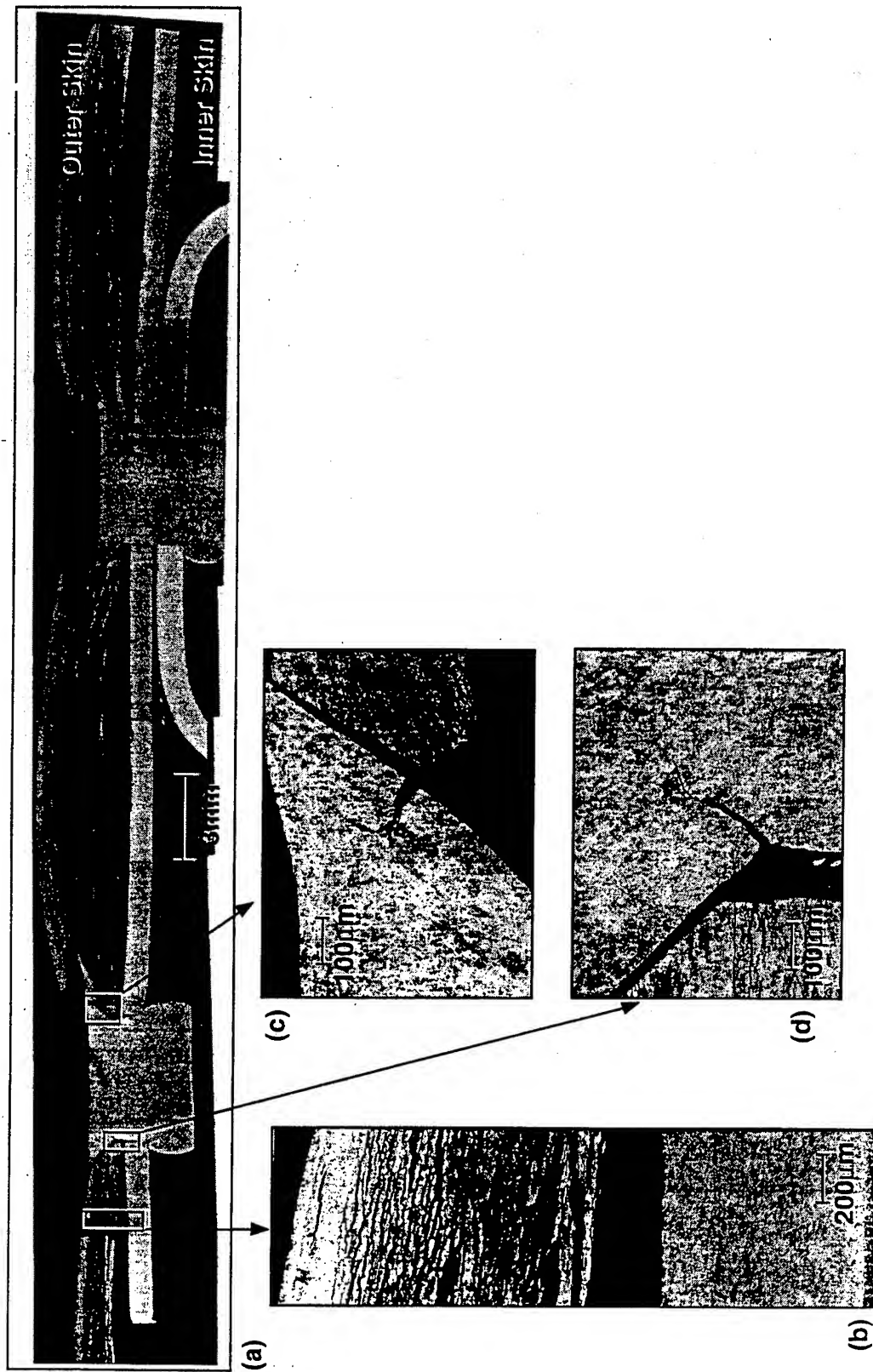


(c)

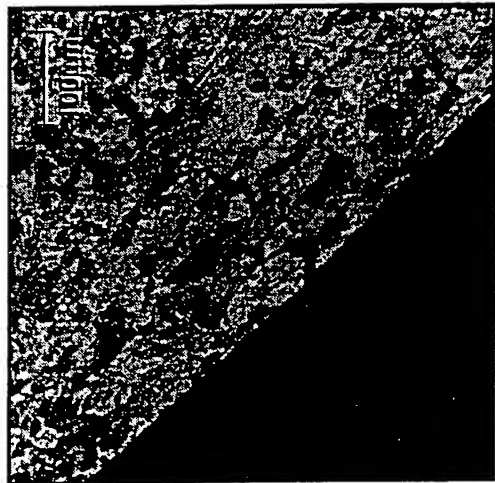
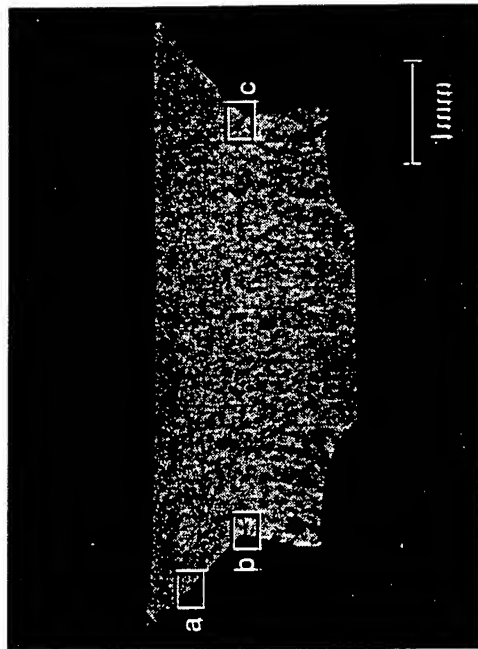


(d)

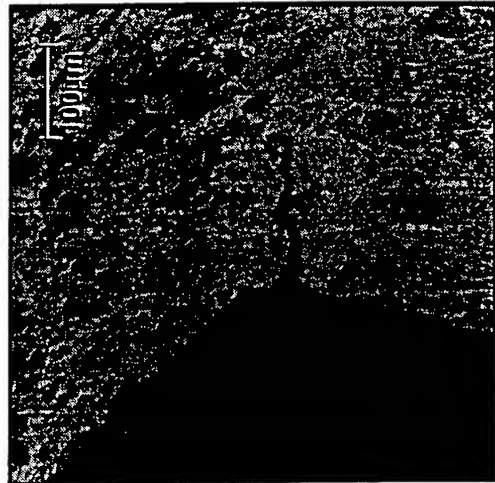
Fuselage Lap Splice Corrosion - Cut #5



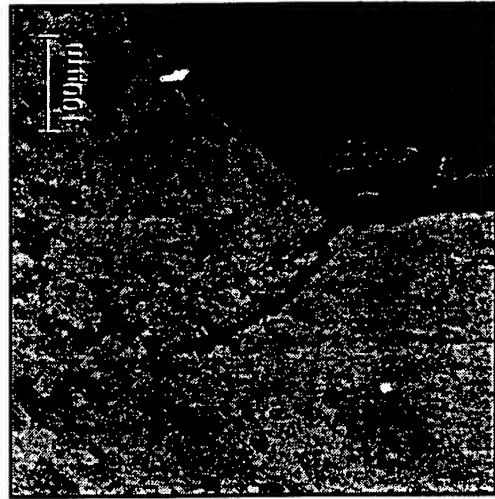
Rivet Corrosion/Cracking



a)

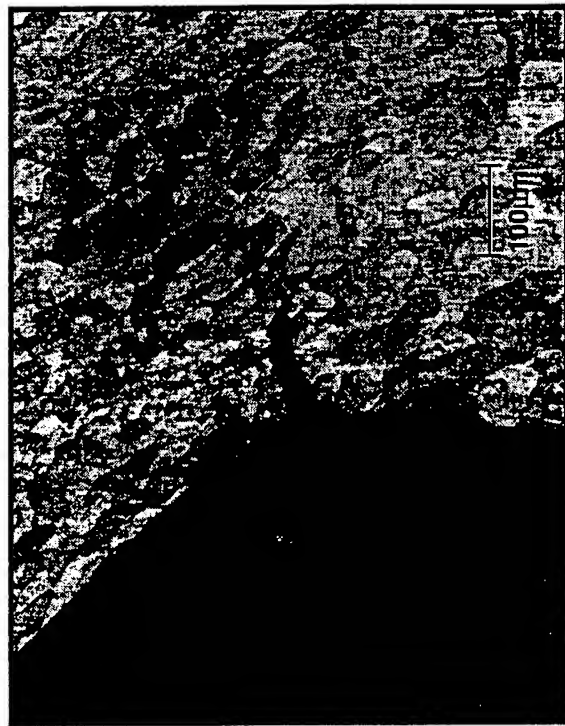
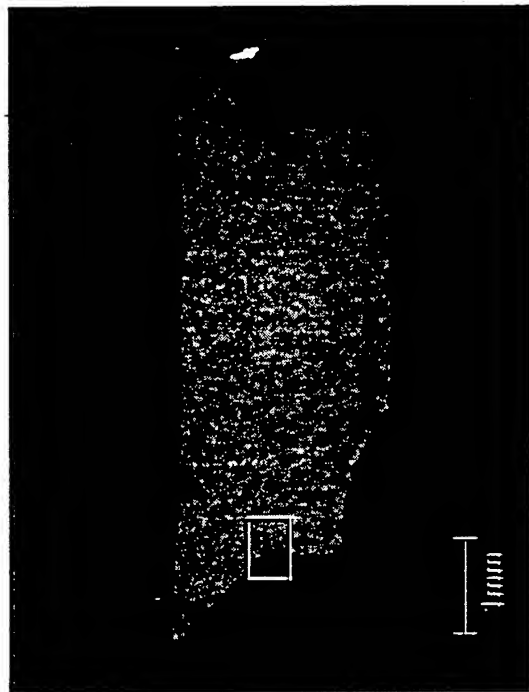


b)



c)

Rivet Corrosion/Cracking

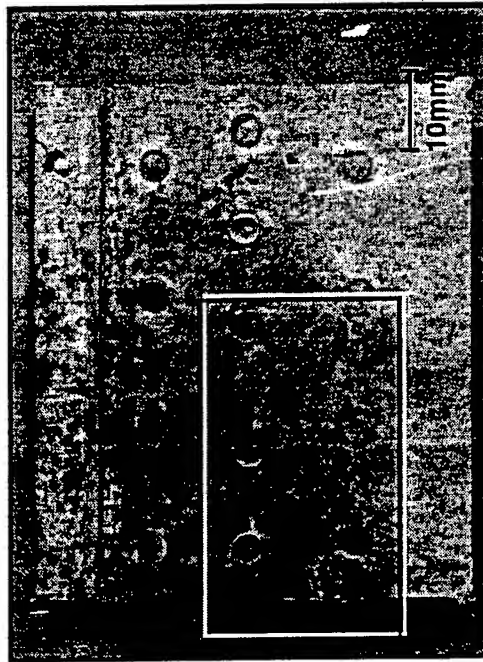
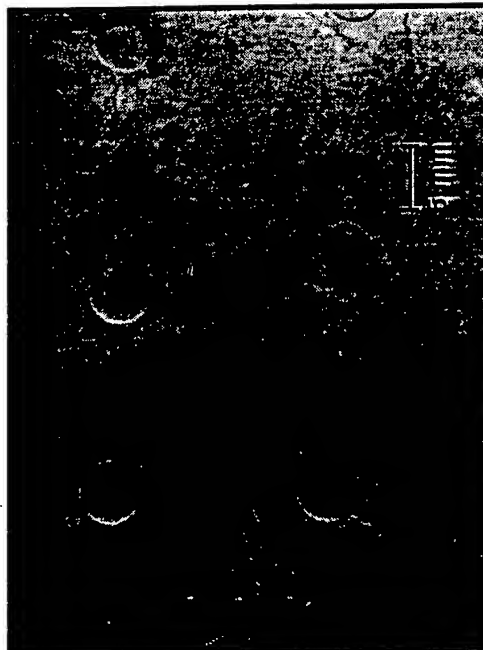


Summary (Lap Splice Examination):

- **Outer skin corrosion - Predominantly intergranular & exfoliation corrosion.**
- **Complete loss of outer skin integrity - extensive cracking (local regions exhibit little or no load carrying capability).**
- **Extensive "Pillowing" with >300% volume change due to corrosion products along faying surface.**
- **Extensive localized corrosion and intergranular cracking of rivet/shank region.**
- **High local stress (corrosion products) caused rivet head fracture due to environmental assisted cracking at rivet head/shank transition.**

LAP SPLICE CORROSION CHEMISTRY

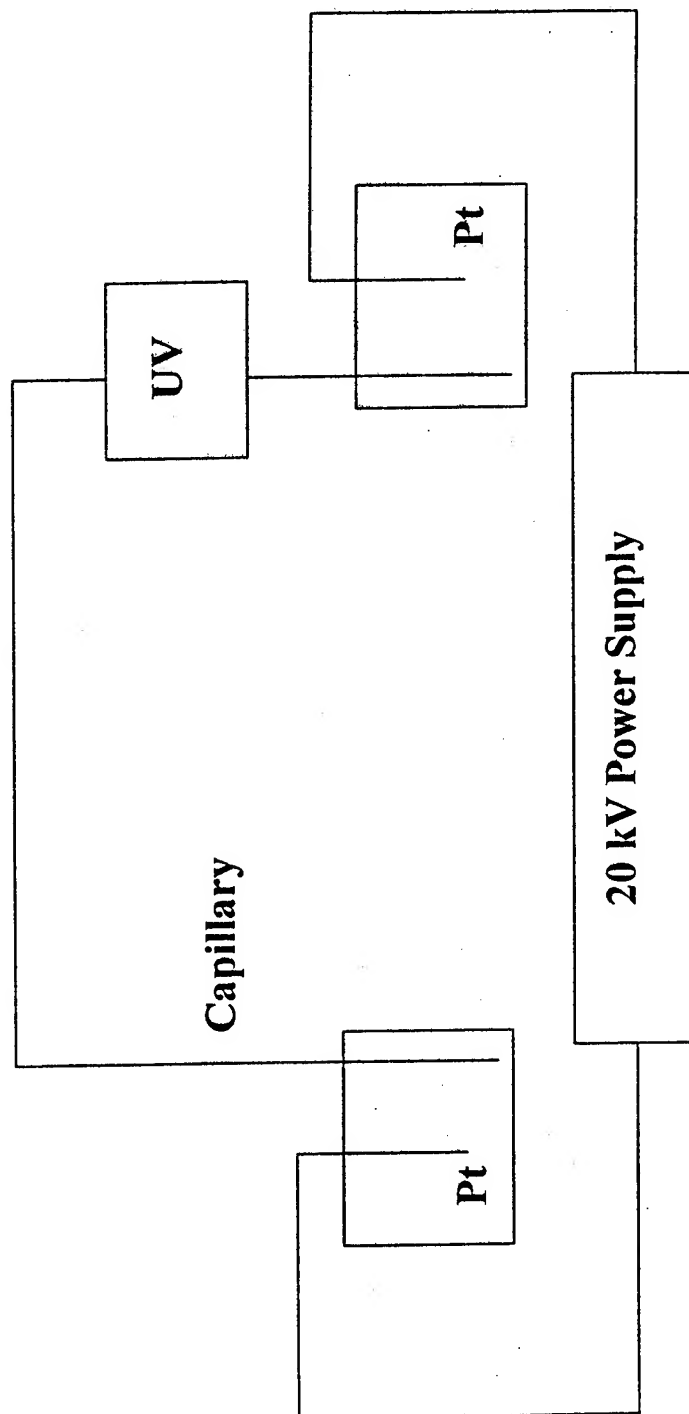
Fuselage Lap Splice Corrosion - First Cut-



CE SAMPLE COLLECTION PROCEDURE:

- Soak selected area of lap splice joint in Milli-Q water for 5 minutes.
- Collect solution samples from sites using a syringe and by rinsing surface.

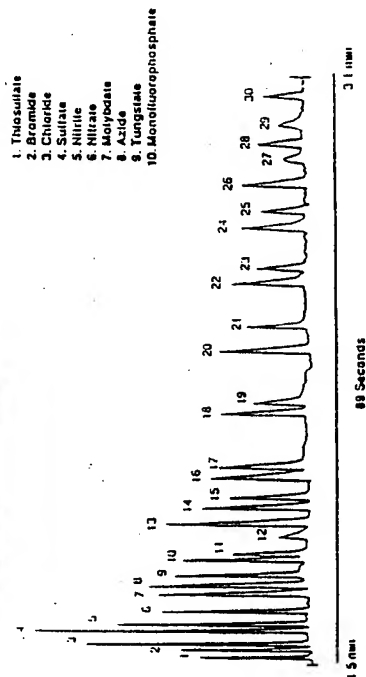
CAPILLARY ELECTROPHORESIS (CE):



CE - Detectable Species:

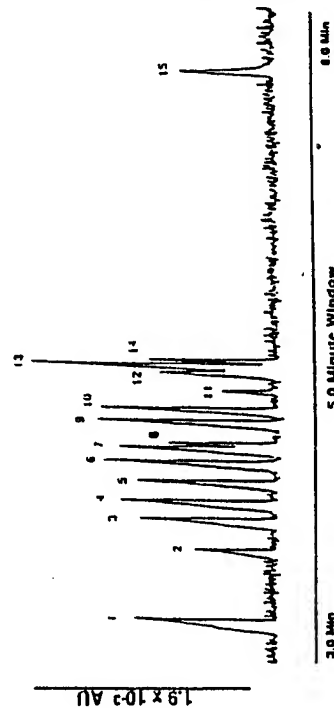
Anions & Organic Acids

- | | |
|----------------|----------------------|
| 11 Chlorate | 21. Enanesulfonate |
| 12 Chlorite | 22. Propionate |
| 13. Fluoride | 23. Propanesulfonate |
| 14. Sulfate | 24. Butyrate |
| 15. Phosphate | 25. Butanesulfonate |
| 16. Phosphate | 26. Valerate |
| 17. Chlorite | 27. Benzoate |
| 18. Glactarate | 28. Glutamate |
| 19. Carbonate | 29. Penanesulfonate |
| 20. Acetate | 30. D-Gluconate |



Cations

- | | |
|--------------|-----|
| 1. Potassium | 0.8 |
| 2. Barium | 1.5 |
| 3. Strontium | 1.5 |
| 4. Calcium | 0.7 |
| 5. Sodium | 0.6 |
| 6. Magnesium | 0.4 |
| 7. Manganese | 0.8 |
| 8. Cadmium | 0.8 |
| 9. Iron (II) | 1.0 |
| 10. Cobalt | 0.8 |
| 11. Lead | 1.0 |
| 12. Nickel | 0.6 |
| 13. Lithium | 0.2 |
| 14. Zinc | 0.4 |
| 15. Copper | 0.6 |



Note: Can also detect Al^{3+} using UV Cat-2 electrolyte

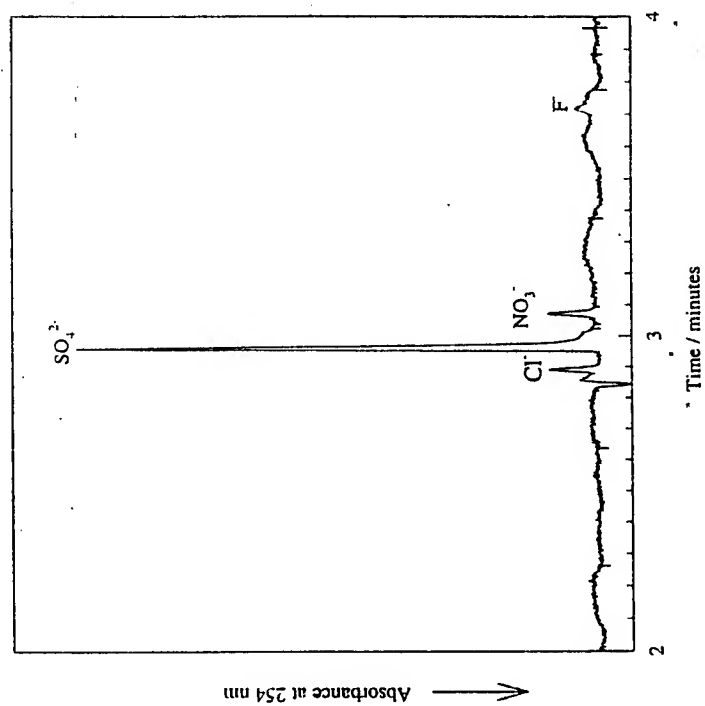
CE - List of Advantages:

- Extremely small volumes of solution analyzed:
 - 30 nL injected volume
 - better spatial resolution of site chemistry
- Mass detection limits for cations, anions and organic acids in the 10^{-11} g to 10^{-12} g range.
- Rapid analysis time - 4 to 8 min. per sample.
- Oxidation state information:
 - e.g., NO_3^- versus NO_2^-
- Robust with respect to complex matrices:
 - e.g., ppm levels of $\text{S}_2\text{O}_3^{2-}$ in 1 M Cl^-

CE Analysis Result:

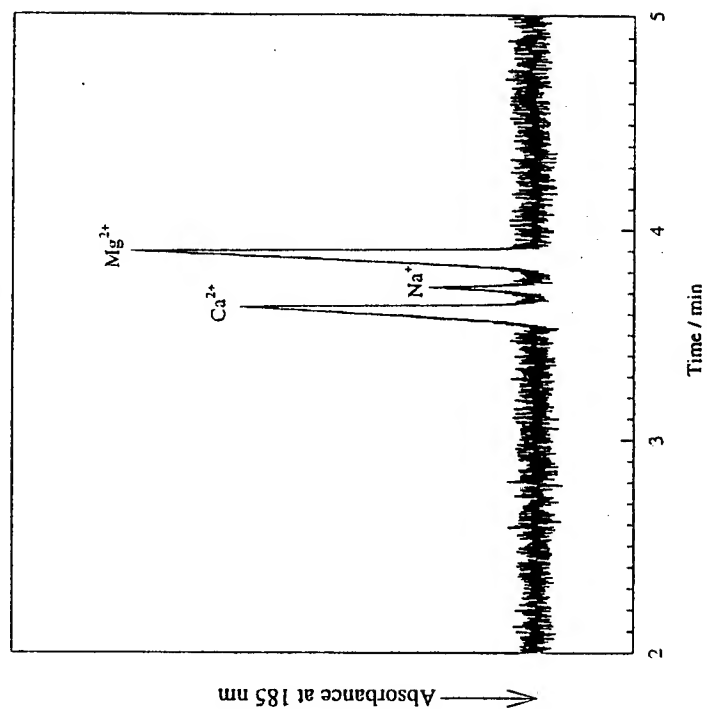
Lap Splice B2 Solution

Identification of anions using chromatate electrolyte



CE Analysis Result: Lap Splice B2 Solution

Identification of cations using UVCat1 electrolyte



Summary (Lap Splice Corrosion Chemistry):

- Identified and quantified those ions present in occluded lap-splice solution:

<u>Cations</u>	Al^{3+}	Ca^{2+}	Na^{+}	K^{+}	Ni^{2+}
<u>Anions</u>	Cl^{-}	SO_4^{2-}	NO_3^{-}		

PRELIMINARY CORROSION TEST RESULTS

Laboratory Corrosion Testing:

Purpose

- To understand lap splice corrosion kinetics using simulated site chemistry

Procedure

- Potentiodynamic testing of B2 site solution:

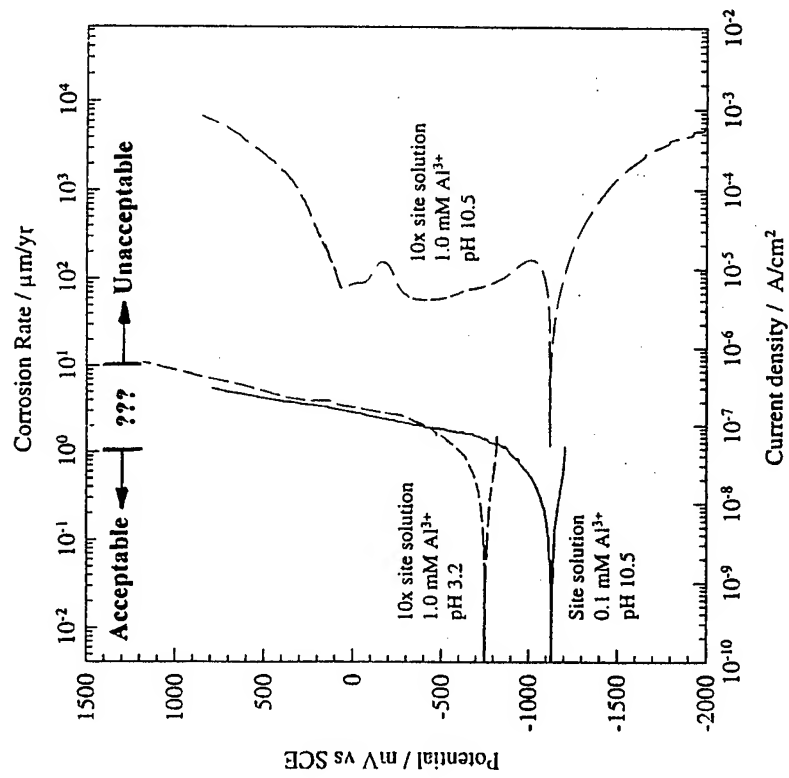
0.14 mM Al^{3+} ; 0.25 mM Mg^{2+} ; 0.20 Ca^{2+} ; 0.002 mM Na^{2+} ; 0.01 mM Cl^- ; 0.08 mM SO_4^{2-} ; 0.01 mM NO_3^- ; 0.005 mM F^-

3 variations:

<u>No.</u>	<u>Deaerated Solution</u>	<u>pH</u>
1	B2 site solution	10.5
2	10x B2 site solution	10.5
3	10x B2 site solution	3.2

Corrosion Test Result:

Electrochemical Behavior of simulated Lap-Splice solution



* 100 $\mu\text{m/yr}$ = 3.9 mpy \Rightarrow penetration of 1.2 mm skin in 12 years

Summary (Corrosion Test Results):

- Laboratory simulation of lap splice environment (potentiodynamic scans) demonstrate that dissolution rates are capable of complete penetration of fuselage outer skin during service life.



National Research
Council Canada

Conseil national
de recherche Canada

NRC-CNRC

The Effect of Corrosion on the Structural Integrity of Fuselage Lap Joints

N.C. Bellinger and J.P. Komorowski
Structures, Materials and Propulsion Laboratory
National Research Council Canada

1995 USAF Structural Integrity
Program Conference
28 - 30 November, 1995
San Antonio, Texas

Canada

2/25

Outline of Presentation

- **Background**
- **Objective**
- **Finite Element Model**
- **Results**
- **Future Work**
- **Conclusions**

NRC-CNRC

Background

- A three phase program is being carried out to apply the optical inspection technique known as D Sight to detect corrosion in fuselage joints.
- During Phase I, the level of pillowing was determined to be influenced by the corrosion product volumetric increase which was typically 6.5 times greater than the thickness loss.

AIRC-CARC

4/25

Background

- In Phase II, finite element techniques used to calibrate the D Sight images suggested that pillowing may cause high stress levels in some lap joint configurations.
- This presentation will concentrate on a specific task from Phase III of the D Sight program, particularly the stress analysis portion.

AIRC-CARC

Objectives

- To use finite element techniques to determine the effect pillowing has on the stress distribution in fuselage lap joints.
- To evaluate the effect of the stress changes on structural integrity.
- To verify the numerical analysis by carrying out accelerated corrosion tests on fuselage lap joints.

6/25

Finite Element Model

- To take into account the various loads associated with lap joints and to save computational time, a submodeling technique was used.
- Three finite element (FE) models were generated to simulate; 1) pre-stress caused by the riveting process, 2) hoop stress caused by the internal pressure and , 3) stress due to corrosion pillowing.

AIRC-CNRC

Finite Element Model

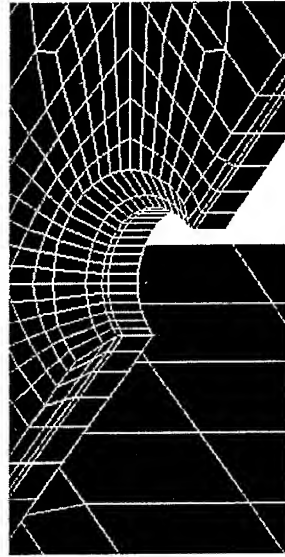
- The lap joint configuration being studied was generated using 3D, 8 node brick elements and consisted of:
 - » Two skins (outboard and inboard) of equal thickness 1.14 mm (0.045 inch), i.e. skin thickness ratio of 1.0, and one stiffener attached to the middle rivet.
 - » Three equally spaced rivets with a shank diameter of 3.96 mm (0.156 inch) and a rivet head diameter of 5.8 mm (0.23 inch).

8/25

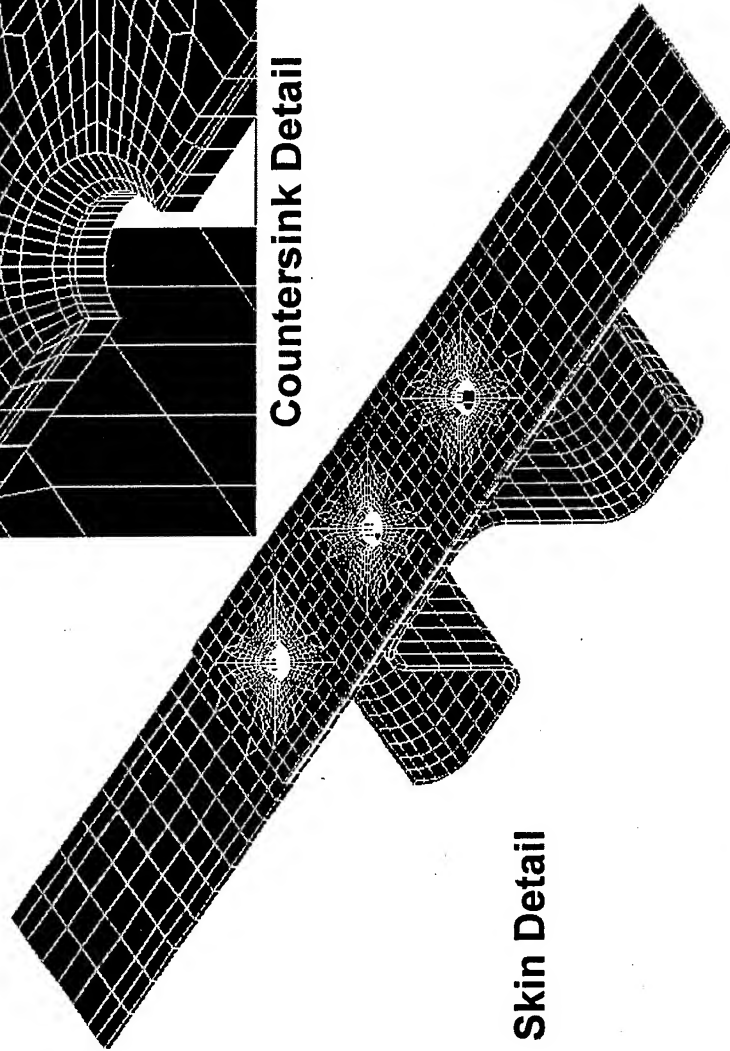
Finite Element Model



Rivet Detail



Countersink Detail



Skin Detail

NRC-CNRC

9/25

Finite Element Model

Rivet Pre-stress Model

- To simulate the pre-stress in the skins caused by the rivet clamping force, a pressure was applied to the rivet head.
- All nodes were merged to allow the surfaces to deform together.

AIRC-CARC

10/25

Finite Element Model

Hoop Stress Model

- A uniform pressure was applied along the edge of the model to simulate the hoop stress.
- Gap elements were used to simulate the rivet/skin interaction.
- It was assumed that the skins directly under the rivet heads transferred some of the load by merging the nodes in these areas.

NRC-CNRC

Finite Element Model

Corrosion Model

- To simplify the model, it was assumed that the thickness loss due to corrosion was constant throughout the entire joint.
- Given a specific thickness loss, t_{lo} , within the joint, the volume required, V_{req} , to accommodate the corrosion products was calculated using:

$$V_{req} = abt_{lo} \left[\frac{V_{mr}}{2} - 1 \right] \quad \text{where: } V_{mr} = \text{Molecular volume ratio: } \left[\frac{\text{oxide}}{\text{pure aluminum}} \right]$$

NRC · CNRC

Finite Element Model

Corrosion Model

- An initial pressure of 6.89 kPa (1 psi) was applied to the faying surfaces in the FE model and the volume under the deformed shape calculated, V_{fem} .
- The required pressure, P_{req} , which the corrosion products exert on the skins was then determined using:

$$P_{\text{req}} = \frac{V_{\text{req}}}{V_{\text{fem}}}$$

where: V_{fem} = Volume calculated at 6.89 kPa

V_{req} = Required volume given %
thickness loss

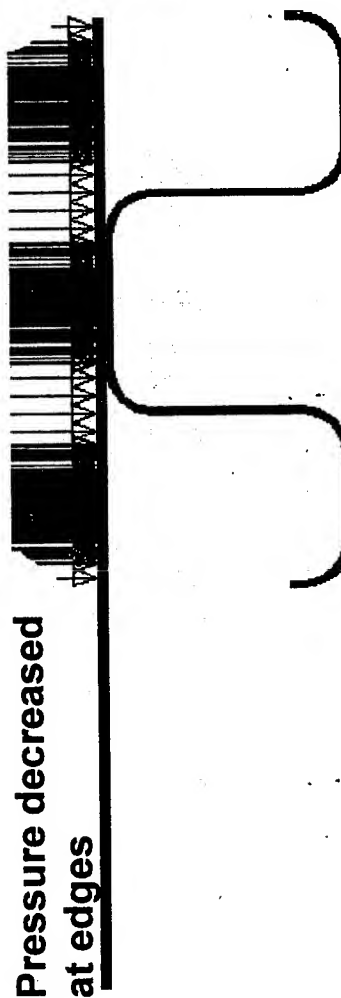
13/25

Finite Element Model

Corrosion Model



P_{req} applied to faying surfaces to
simulate the corrosion by-products.



NRC-CNRC

14/25

Results and Discussion

Finite element assumption - Rivet Pre-stress Model

- The pressure applied to the rivet heads resulted in the same level of interference in all rivet holes. The hole diameters were increased by 0.5%.
- This assumption would result in a higher pre-stress than might normally occur in an actual joint.

NRC-CNRC

Results and Discussion

Finite element assumption - Hoop Stress Model

- Merging the nodes under the rivet heads represents an ideal load transfer path (i.e., partly through the faying surfaces and partly through the rivet).
- This assumption would result in lower stress values as compared to a load transfer only through the rivet (worst case scenario).

Results and Discussion

Finite element assumption - Corrosion Model



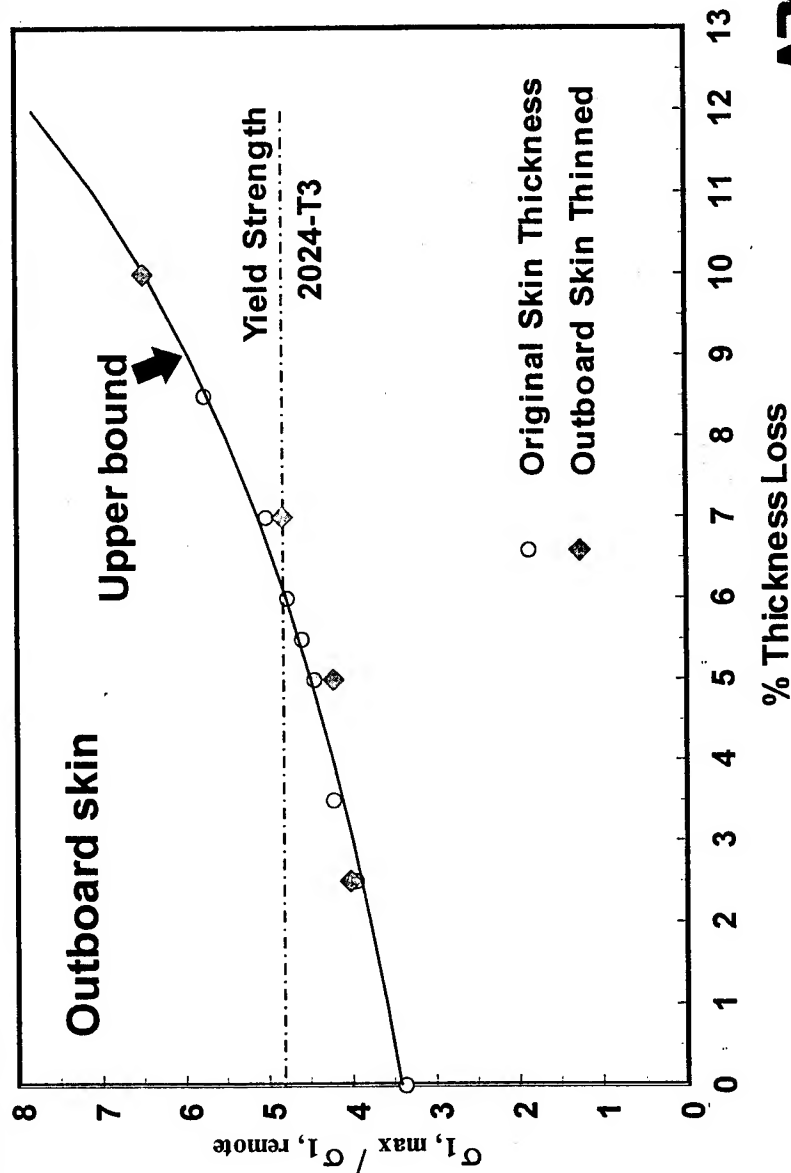
Thickness loss within a corroded lap joint

(5% to 10%)

- Assuming a constant thickness loss is unrealistic.
- Results in higher stress levels than might normally occur in a corroded lap joint.
- Can be considered an upper bound of the effect of corrosion pillowing.

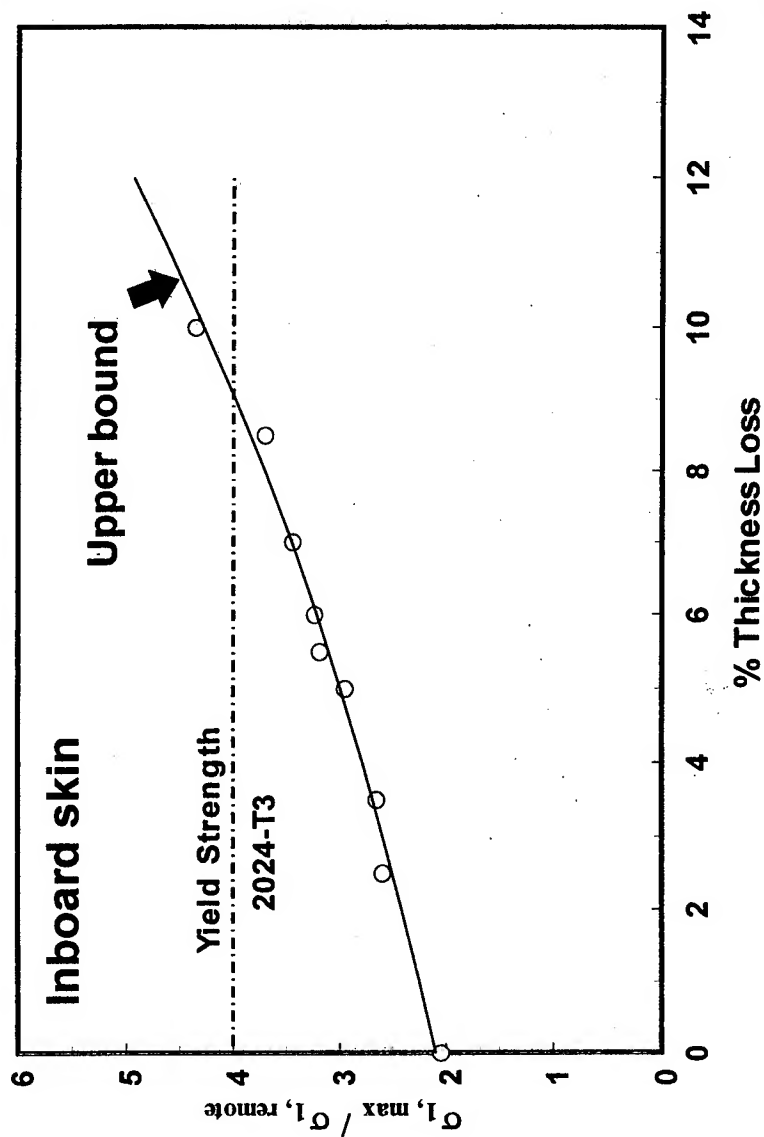
Results and Discussion

Effect of corrosion on maximum principal stress at critical rivet row



Results and Discussion

Effect of corrosion on maximum principal stress at outer rivet row



Results and Discussion

- For corrosion $\leq 5\%$ thickness loss, the maximum principal stress occurred along the inner surface of the outboard skin at the critical rivet row along a line approximately 45° to the loading direction and away from the edge of the hole.

2.5% Thickness loss



Arrows indicate location of maximum stress

NRC - CNRC

Results and Discussion

- Above 5% thickness loss, the maximum stress occurred at the outer rivet row along the inner surface of the outboard skin. This stress decreased rapidly away from the rivet hole.

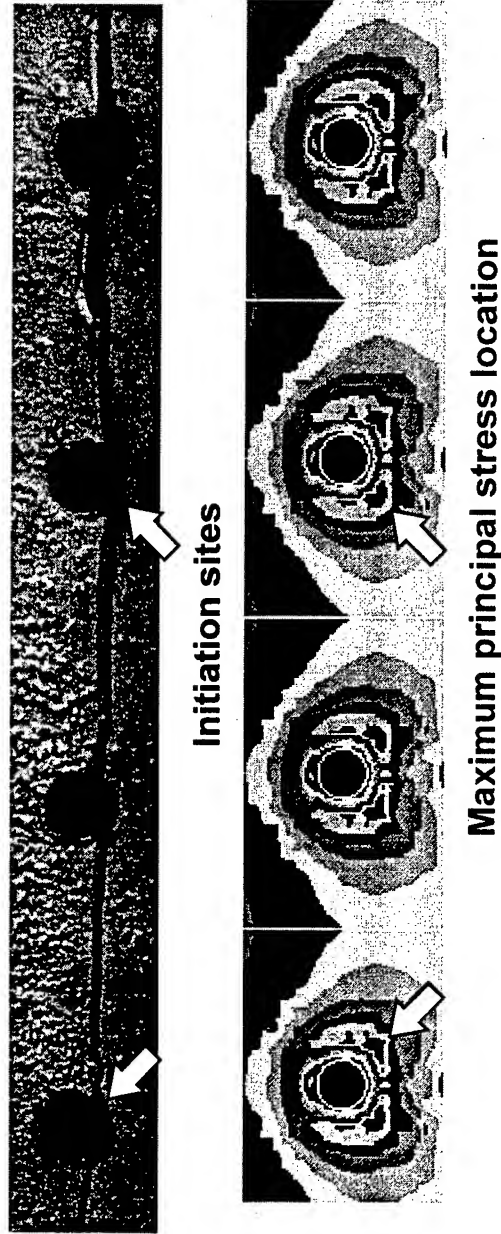
6% Thickness loss



Arrows indicate location of maximum stress

Results and Discussion

- Experimental tests carried out on accelerated corroded multi-site damage specimens indicate that cracks initiate in the area predicted by the FEM results.



Future Work

- To verify the FE results, accelerated corrosion tests will be carried out on strain gauged lap joints (same configuration as that used in the analysis) in order to periodically monitor surface strains as the corrosion develops.
- A deterministic damage tolerance study will be carried out to determine the effect that pillowing has on the life of a joint.
- Investigate the effect of skin thickness ratio on the stress distribution.

Conclusions

- Based on the assumptions made:
 - » The stress in the outboard skin at the critical rivet row can increase above yield for corrosion as low as ~ 6%.
 - » For the inboard skin, the stress at the outer rivet row (which is critical in this skin) can increase to above yield for corrosion above ~ 9%.
- Although these results represent an upper bound limit, they clearly show that the pillowing caused by the corrosion products increases the stress in the vicinity of the rivet holes in both skins.

NRC-CNRC

Conclusions

- These results also suggest that the stress changes should be taken into account when determining the minimum percentage thickness loss to be repaired.
- Even at low levels of corrosion, the life of a joint could be dramatically reduced due to the increase in stress caused by pillowling.

Acknowledgments

- This work had been funded by
 - » USAF nondevelopmental Airlift Aircraft program (NDAA), Federal Aviation Administration (FAA), Transport Canada (TC) and National Research Council Canada (NRCC)
- The work has been carried out under a collaborative agreement between:
 - » Diffracto Limited and NRCC

Effects of Cyclic Immersion in 3.5% NaCl Solution on Fatigue Crack Propagation
Rates in Aluminum 2024-T351

Ms. Julie A. Kramer*
NASA/Johnson Space Center
Houston, TX 77058-3696

Dr. David W. Hoepfner, P.E.
Professor and Director of the
Quality and Integrity Design Engineering Center
Department of Mechanical Engineering
University of Utah
Salt Lake City, UT 84112-0001

Abstract

Typical fatigue crack growth tests are conducted in a steady state environment, however, the true service conditions of most aircraft might be better simulated with a transient, or wet/dry, environmental cycle. The evaporation of the aqueous solution does not remove all of the aggressive chemical species present, and can leave deposits of these chemicals for subsequent rehydration. Future corrosion could then occur at an even stronger chemical concentration, and perhaps a higher rate. A search of technical literature has shown that virtually no testing has been done to address the effects of this wet/dry scenario.

Fatigue crack propagation studies were performed in the Quality and Integrity Design Engineering Center (QIDEC) at the University of Utah to increase the understanding of the influence of cyclic environmental exposure on crack propagation rates. Tests were conducted on aluminum 2024-T351 exposed to dry air, constant 3.5% NaCl solution and intermittent 3.5% NaCl solution environments. Results showed that the environmental cycle can have a dramatic effect on the crack propagation rate in a manner that is yet unexplained. Detailed discussions of the testing technique and crack growth rate results are presented, as well as recommendations for future research efforts.

Introduction

In this era of tenuous economics, where manufactured goods are no longer just disposed of at the end of their design life, knowledge of long-term material performance is mandatory. Nowhere is this more keenly felt than the aerospace industry, where estimated costs for the annual corrosion maintenance of world wide aging aircraft fleets are exceeding 1000 million US dollars¹. Hoepfner, et al. highlight the safety issues related to corrosion and fretting fatigue in aircraft by estimating that a minimum of 687 aviation incidents or accidents and 81 fatalities can be attributed to these phenomena in the last 20 years². Regardless of whether one wishes to examine the issue from an economic, or safety, perspective there is certainly adequate reason for concern on both fronts.

Yet, with all this having been said, corrosion fatigue is a complex phenomena, governed by multiple intrinsic and extrinsic parameters. Many of these parameters have been studied only in isolation. Some, including Schütz³, are of the opinion that full scale corrosion fatigue testing is the answer to characterizing the behavior of components in service environments. However, current aging aircraft research has done little to focus on the effects of specific service environments on fatigue, either in terms of composition or cyclic exposure intervals. Although some recent research has begun to investigate the effects of various simulated service environments⁴ on FCG, even less information is readily available on the effects of the environmental cycle on material response curves^{3,5}. Much more research must be accomplished in these areas before realistic, full-scale corrosion fatigue tests are practical.

The concern over proper chemical composition in a test environment is self-evident. The proper proportion of deleterious chemical species must be present and allowed to interact, perhaps synergistically, to obtain accurate material response. This is also true of the environmental cycle, as a cyclic wet/dry exposure to the environment more closely mimics the actual service environment of most aircraft. The evaporation of the aqueous solution does not remove all of the aggressive chemical species present, and can leave deposits of these chemicals for subsequent rehydration during condensation. This cyclic wetting is commonly seen on an

aircraft ground-air-ground cycle. Future corrosion could then occur at an even stronger chemical concentration.

The objective of these experiments was to quantify the effect of a cyclic wet/dry cycle on fatigue crack growth rate in 2024-T351 aluminum alloy. The test procedures were developed primarily from American Society for Testing and Materials (ASTM) standard E647-93 "Standard Test Method for Measurement of Fatigue Crack Growth Rates." However, this test standard specifically addresses steady-state environmental conditions and the purpose of this experiment was to evaluate dynamic environmental conditions. Therefore, deviations from E647 recommendations will be addressed specifically in the intermittent immersion testing portion of this report. Selected specimens were placed in a salt water environment for the entirety of the test, whereas others were subjected to intermittent environmental exposure over the duration of the test. These results were compared with baseline test results obtained in dry (relative humidity < 10%) air.

Test Procedures

Load Conditions

All testing was done with a sinusoidal waveform with a frequency of 1 Hz, a stress ratio (R) of 0.1 and at laboratory temperature of approximately 23°C (70°F). Specimens were precracked in fatigue with a three step procedure. Two load sheds of 10% were followed by 1.0 mm (0.040 in) of crack growth in environment at the test peak load. All precracking was done at 10 Hz. The matrix of tests conducted is provided in Table 1.

Equipment Description

Tests were conducted on an MTS closed loop electro-hydraulic servo controlled tension testing system. The system has a load capacity of 14.7 kN (3.3 kips). Testing was accomplished using Testlink™§ with an MTS 458.20 microconsole and an MTS 418.91 microprofiler. Crack growth measurements

§ Testlink™ is a software system for data acquisition and automated control of materials testing, used in conjunction with a 486 PC.

Table 1
Matrix of tests conducted

Specimen No.	Test Title	Environment	Exposure	Peak Load (kN)
1	Pilot 1	laboratory air	constant	4
2	Test 1	RH < 10%	constant	5.75
3	Test 2	RH < 10 %	constant	5
4	Test 3	3.5% NaCl	constant	5.75
5	Test 4	3.5% NaCl	constant	5.75
6	Test 5	3.5% NaCl	constant	5.75
7	Test 6	3.5% NaCl	10 min./hr.	5.75
8	Test 7	3.5% NaCl	10 min./hr.	5.75
9	Test 8	3.5% NaCl	10 min./hr.	5.75

were taken via the compliance method, utilizing an MTS model 632.03 C-21 clip-gage. Optical measurements were taken simultaneously on the front and back of the specimen with traveling optical microscopes.

Specimen Preparation

A 24 in X 24 in X 0.5 in plate of commercially available 2024-T351 aluminum was purchased for machining specimens. Figure 1 shows an optical micrograph of the material microstructure highlighting the elongated grains in the longitudinal direction. A comparison of nominal chemical composition to the test plate chemical composition is given in Table 2.

Specimens were machined by the NASA Johnson Space Center's Structures and Mechanics Division machine shop. They follow the dimensions for a standard compact tension, C(T), specimen as described in ASTM E647 with B=12.7 mm (0.50 in) and W=76.2 mm (3.00 in). Specimens were oriented so that the load was in the rolling direction and the crack growth was in the transverse direction, or L-T orientation. Starter notches were electrodischarge machined (EDM) into specimens.

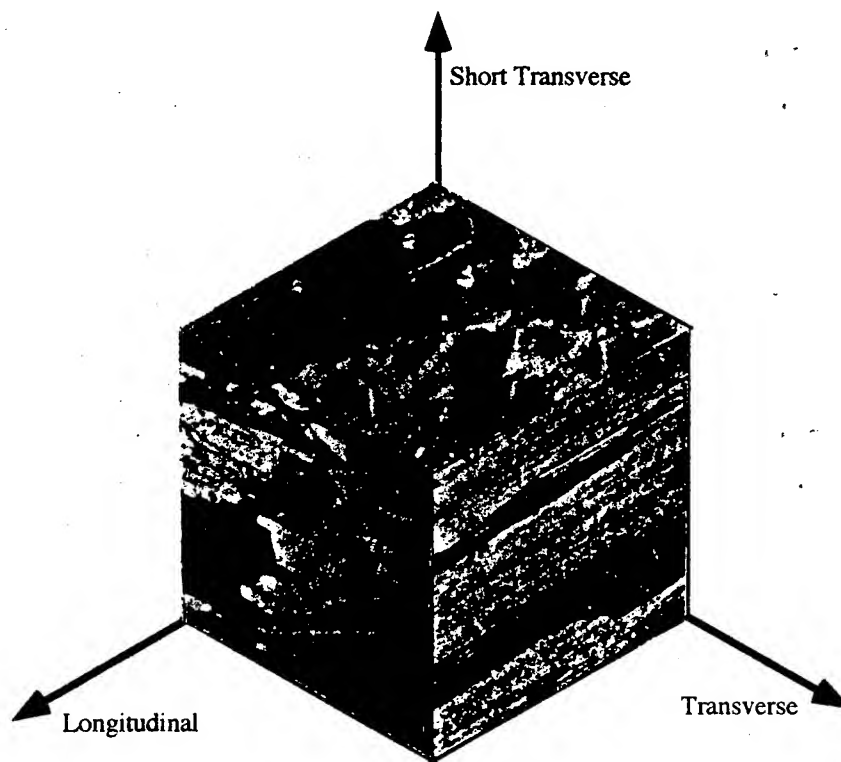


Figure 1. Representative microstructure of 2024-T351 aluminum alloy plate. Magnification 100 times.

Table 2
Chemical composition (wt%) of 2024 aluminum alloy

Element	Al	Cu	Mg	Mn	Fe	Si	Ti	Cr	Zn
Nominal Composition ^a	Bal.	3.8-4.9	1.2-1.8	0.3-0.9	< 0.50	< 0.50	< 0.15	< 0.10	< 0.25
Test Plate Composition ^b	92.74	4.74	1.56	0.62	0.19	0.04	0.03	0.01	0.05

^a Metals Handbook, 9th edition, Vol. 2, ASM International, Metals Park, OH, 1990.

^b NASA/Johnson Space Center Materials Laboratory, Houston, TX.

Specimens were prepared for testing by finishing the surfaces through a series of metallographic grade SiC papers with the final finishing direction perpendicular to the crack growth direction. Surfaces were blackened along the projected crack path to aid in optical crack length measurements.

Environment

Laboratory Air

A pilot test was performed in laboratory air to verify system performance, and to provide information on the loads for subsequent testing. Testing was done at 4 kN (0.899 kips) peak load and began with a maximum stress intensity factor range (ΔK) of approximately $5.5 \text{ MPa}\sqrt{\text{m}}$ ($5.0 \text{ ksi}\sqrt{\text{in}}$). There were no special controls placed on the environment for this test.

Dry Air

Two tests were run in a "dry air," or less than 10% relative humidity (RH), environment. For this portion of this experiment, the specimen was encased in a Plexiglas™ environmental chamber. Dehumidified air was pumped through the chamber. Relative humidity was monitored throughout the test to ensure that it did not exceed 10%.

NaCl Solution Constant Immersion

Constant immersion testing was performed by allowing gravity to draw aerated, 3.5% NaCl solution from an environmental tank, through a Plexiglas™ environmental chamber attached to the specimen and out to a waste tank (Figures 2, 3 and 4). Two manual flow restriction valves were used to regulate the fluid flow into and out of the system. Solution flow rates were between 190-350 ml/hr, while the target rate was 240 ml/hr. The chambers and lines had an approximate volume of 40 ml; therefore a 240 ml/hr flow rate would replace the fluid in the system every 10 minutes, which would be analogous to the flow rate in the intermittent immersion tests.

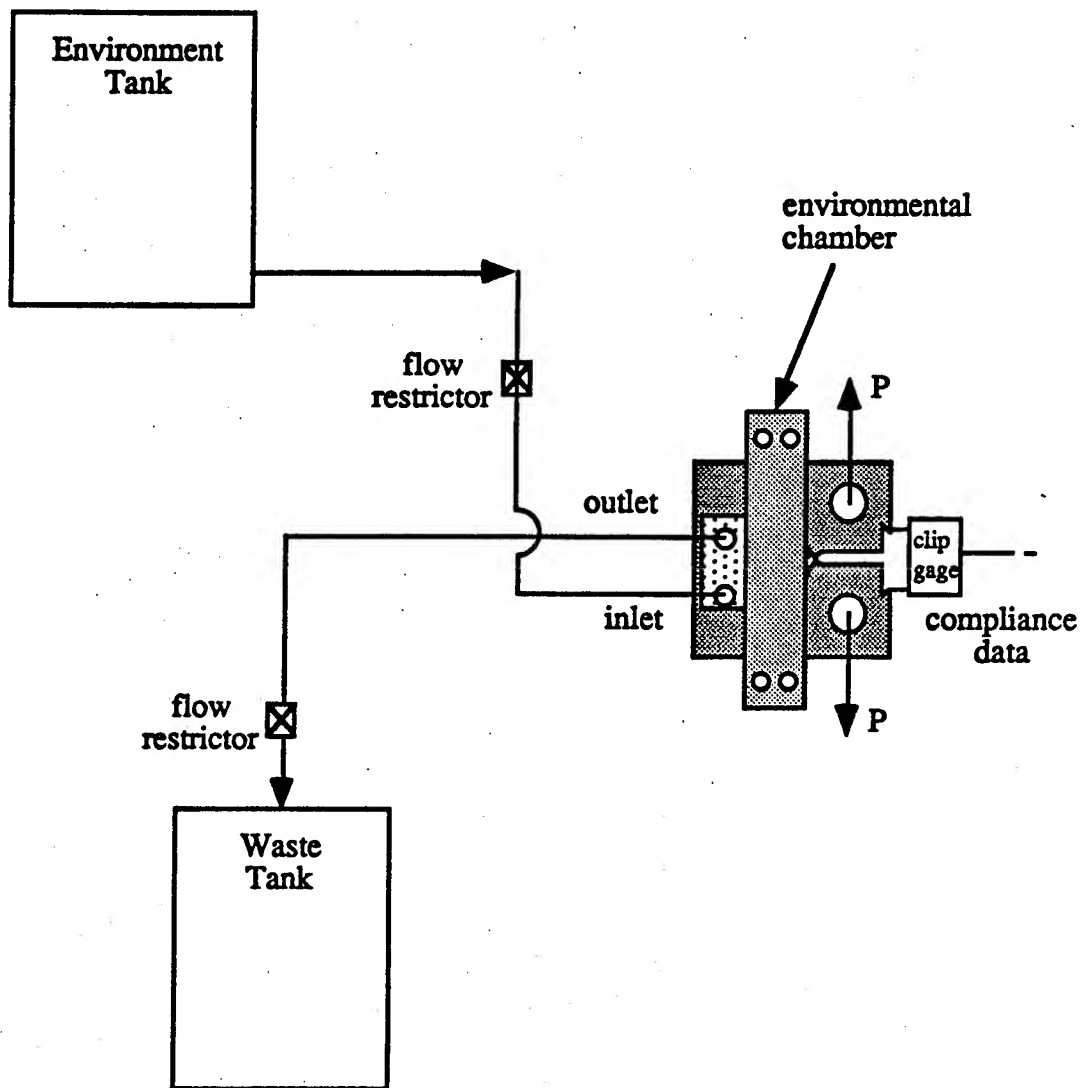


Figure 2. Schematic of the test set-up for constant immersion testing.

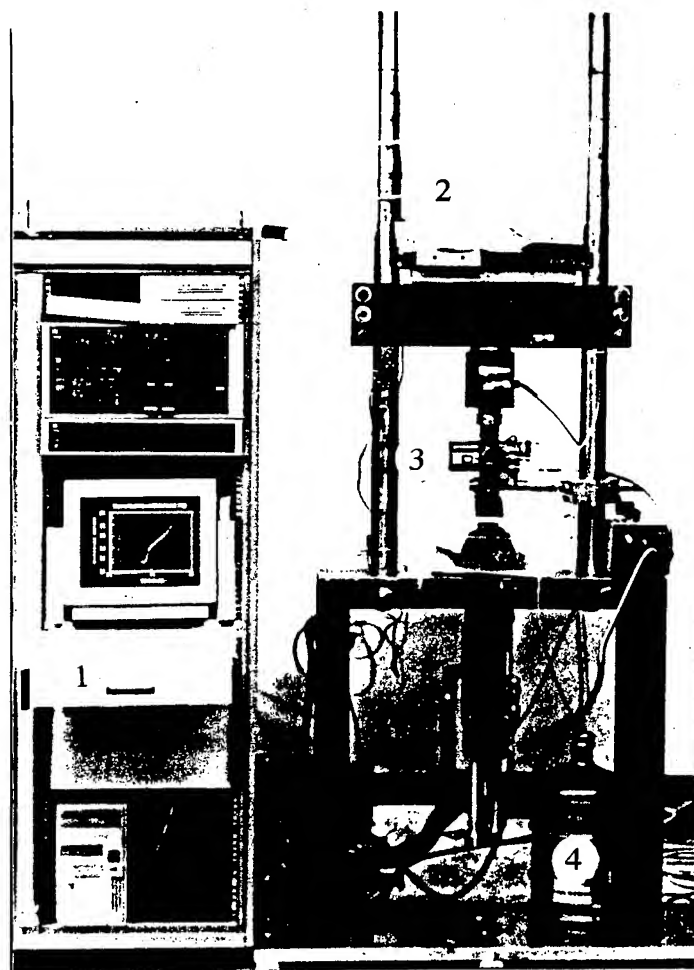


Figure 3. Photograph of the constant immersion test set-up showing, 1 the data acquisition system, 2 the environment tank, 3 the specimen and chamber, and 4 the waste tank.

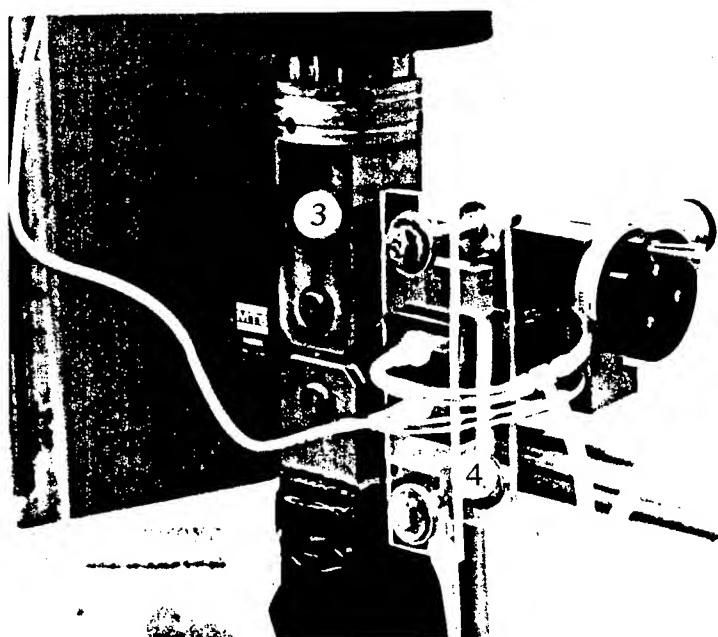
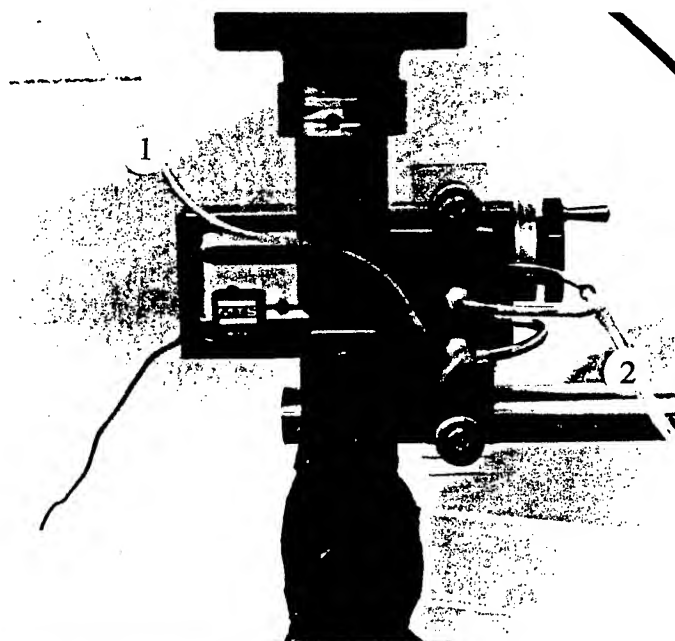


Figure 4. Close-up views of the constant immersion test set-up showing, 1 the inlet line, 2 the outlet line, 3 the grips and 4 the specimen, clamping system and environmental chamber.

NaCl Solution Intermittent Immersion

When attempting to determine the importance of various cyclic immersion parameters, ASTM G44-88 "Standard Practice for Evaluating SCC Resistance of Metals and Alloys by Alternate Immersion in 3.5% Sodium Chloride Solution" was consulted. Although G44 "does not cover tests in which specimens are placed in closed containers into which solution is periodically pumped..." (p. 168), it does provide insight into important parameters for a cyclic immersion test. Based on the recommendations of G44, tests were run with a 10-minute "wet," or on cycle followed by a 50-minute "dry," or off cycle. Also in accordance with G44, specimens were completely submerged in the NaCl solution environment in under 2 minutes, and a "mild circulation of air" (p. 170) was provided to enhance specimen drying.

Intermittent immersion testing was accomplished by utilizing a system derived from that used for constant immersion testing (Figure 5). The crack propagation path was encased in a Plexiglas™ environmental chamber (Figure 6). The flow of air or 3.5% NaCl solution was controlled by a three way solenoid valve and repeat cycle timing relay. This type of control system allowed for control of the duration of both the "wet" and "dry" portion of the environmental cycle.

As stated previously, ASTM E647 is intended for steady-state environment FCG experiments. This experiment was not steady state, and was intended to accentuate the environmental phenomena under investigation. Deviations from ASTM E647 occur because of this difference. Transient effects due to the change in environment were not avoided, but rather sought out during this test. The specimens were not immersed in environment for 24 hours preceding testing, as recommended in the standard. There were no attempts to remove corrosion products or clean the crack tip as the standard recommends. Therefore, corrosion product wedging was a factor considered in the analysis of the test results.

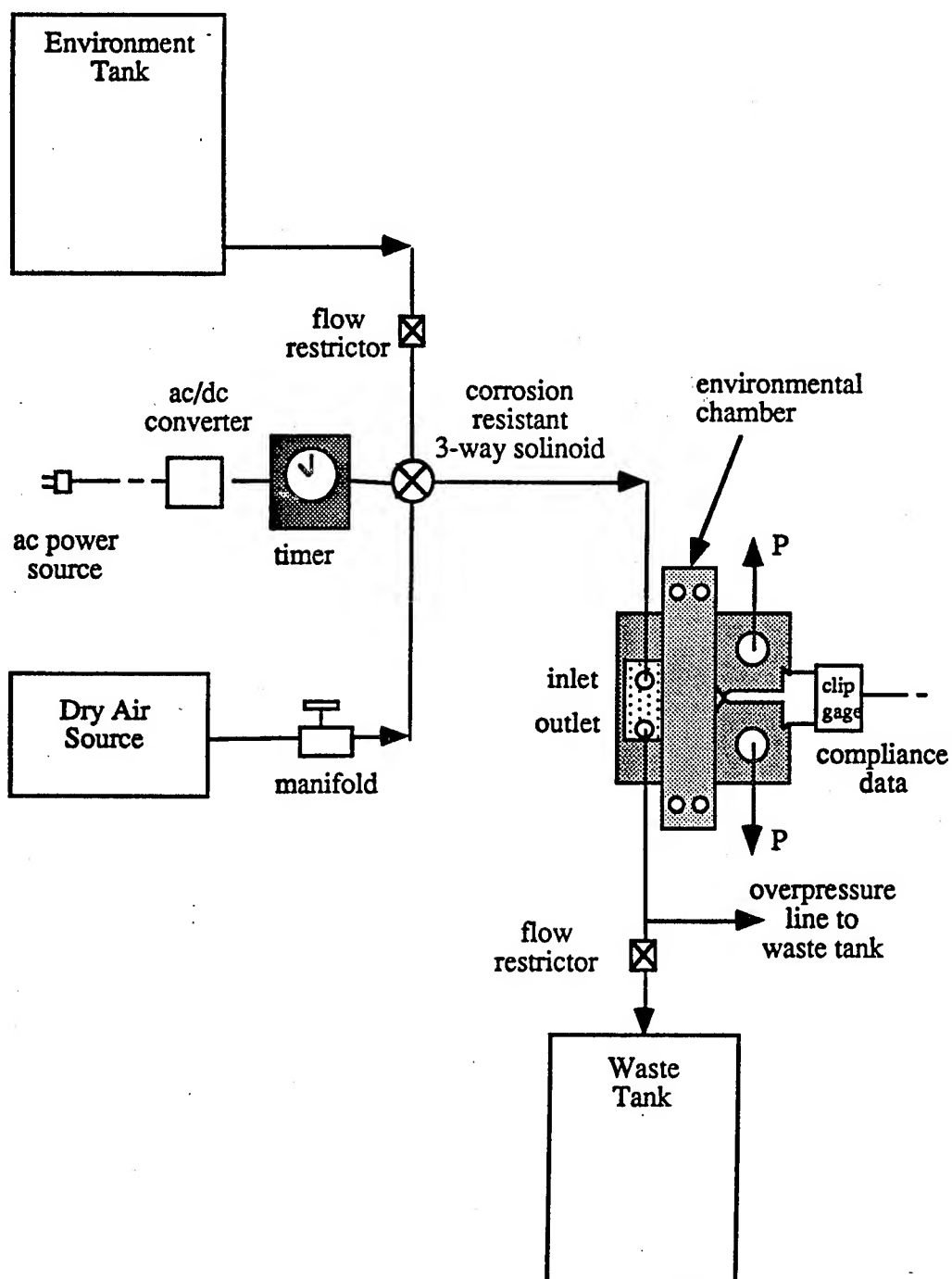


Figure 5. Schematic of the test set-up for cyclic immersion testing.

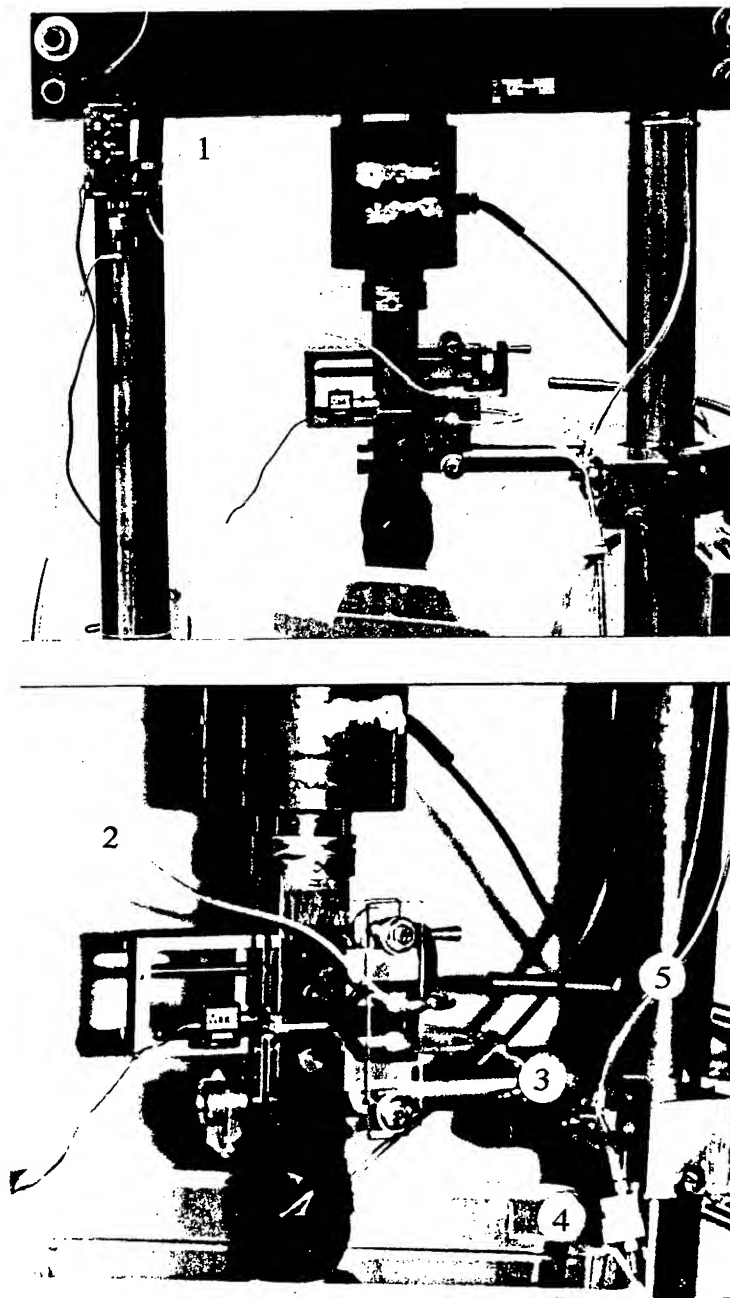


Figure 6. Photographs of the intermittent immersion test set-up showing, 1 the cycle timing device 2 the inlet line, 3 the outlet line, 4 the flow control valve and 5 the overflow line.

Results

Data Reduction Techniques

Cycle count (N) and crack length (a) data were acquired by Testlink™. Testlink™ has the capability of reducing these data to da/dN and ΔK internally, but data were imported into Excel 4.0 for reduction. For the given specimen geometry:

$$\Delta K = \frac{\Delta P}{B\sqrt{W}} \frac{(2+\alpha)}{(1-\alpha)^{3/2}} (0.886 + 4.64\alpha - 13.32\alpha^2 + 14.72\alpha^3 - 5.6\alpha^4)$$

where $\alpha = a/W$. The growth rate was determined by both the polynomial method and the secant method as described in ASTM E647.

Laboratory Air

Pilot testing was done to determine the minimum stress intensity factor required to eliminate the short crack or threshold behavior (Figure 7). It was desirable to eliminate the initial portion, region I, of the curve because of time considerations. The pilot test lasted over 18 days. Later tests ran from 24-36 hours.

Dry Air

These data were intended to be used as a baseline against which to compare further testing. It was also used to determine the peak load for further testing. Data from tests run at 5 kN (1.1 kips) and 5.75 kN (1.3 kips) peak load were compared (Figure 8). Based upon this comparison, the higher load was chosen for subsequent tests. This plot also shows how the initial portion of the curve was successfully truncated at the transition into the region II portion of the graph, which was the intent of the pilot testing.

NaCl Solution Constant Immersion

Tests results from three constant immersion tests are shown in Figure 9. When these rates were compared to the FCG rates obtained in dry air, the greatest

effect was observed in the 8-18 MPa \sqrt{m} (7.2-16.2 ksi \sqrt{in}) portion of the FCG curve (Figure 10). This effect becomes secondary to mechanical contributions to FCG rates in region III, or as the specimen approaches failure. This is consistent with other technical literature available for FCG experiments on aluminum alloys, including 2024-T351⁶⁻¹⁰. The maximum effect is an increase of FCG rate by a factor of approximately 1.6 at the lowest ΔK tested (Figure 11).

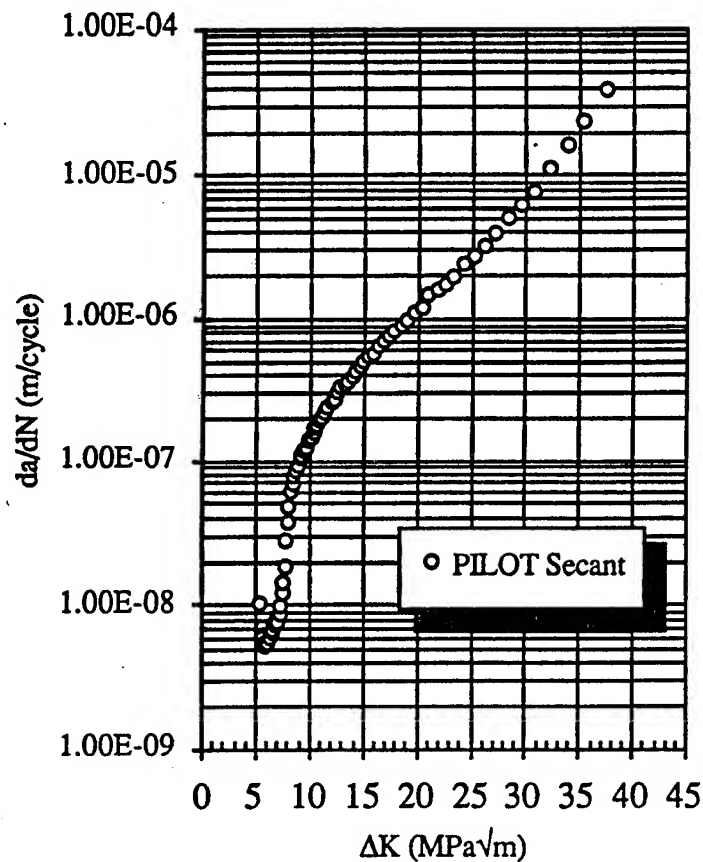


Figure 7. Results of laboratory air pilot testing showing short crack or threshold behavior at lower values of ΔK ($f=1.0$ Hz., $R=0.1$, lab air).

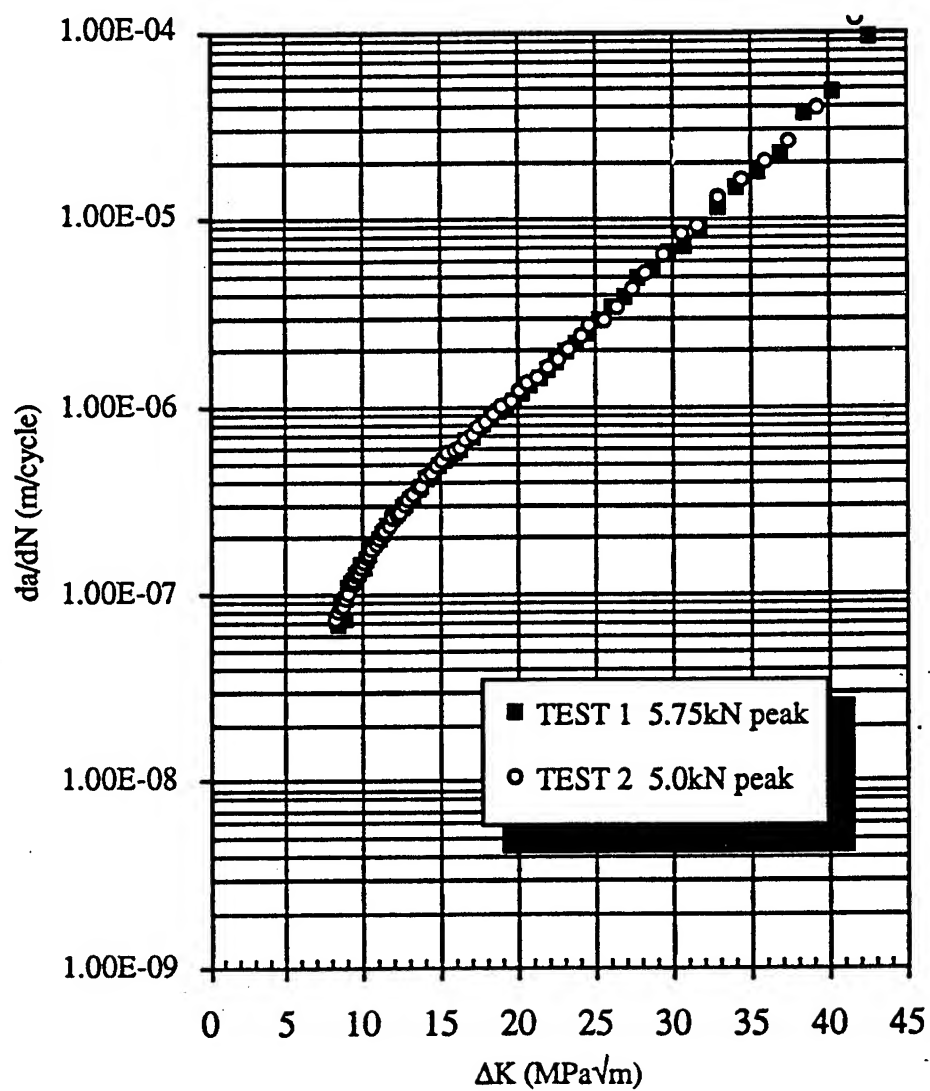


Figure 8. Comparison of crack propagation data from two different peak loads ($f=1.0$ Hz., $R=0.1$, $RH<10\%$).

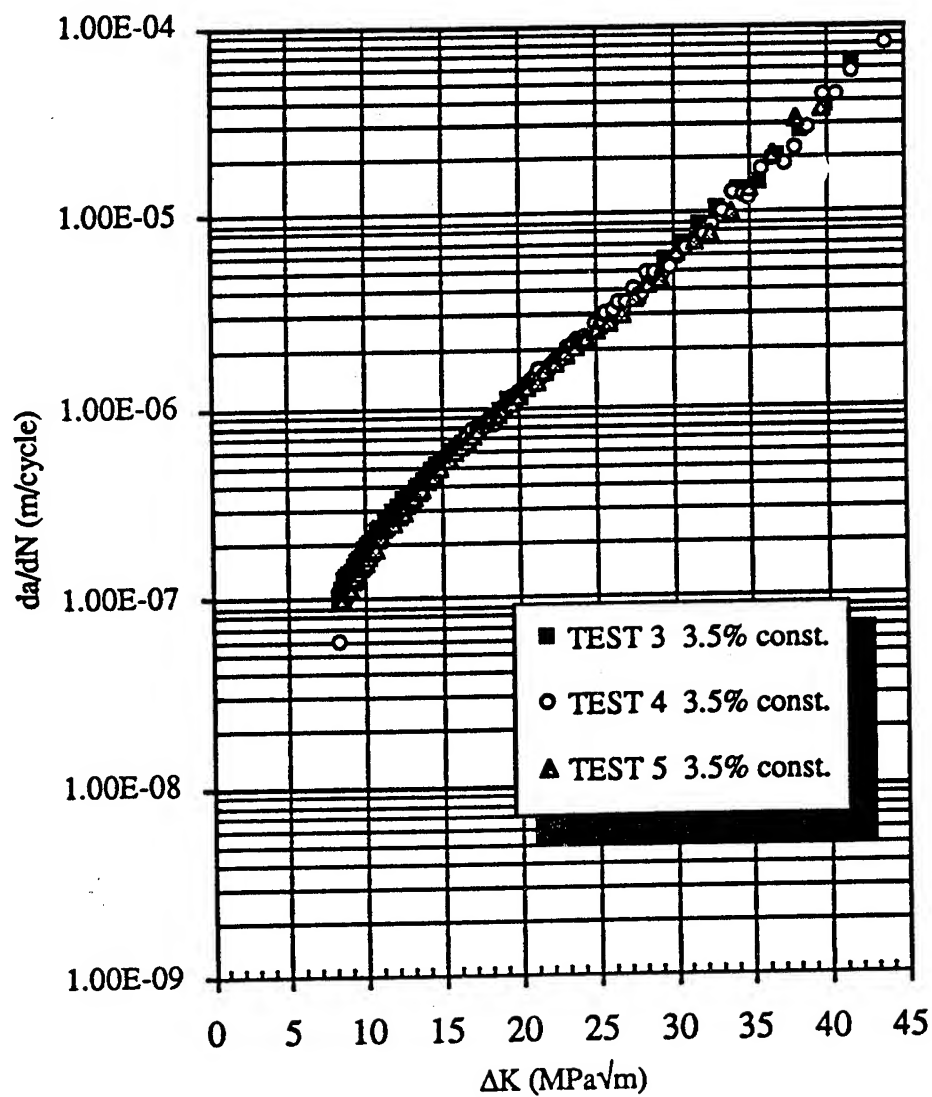


Figure 9. Comparison of three constant immersion test results ($f=1.0$ Hz., $R=0.1$, 3.5% NaCl constant immersion).

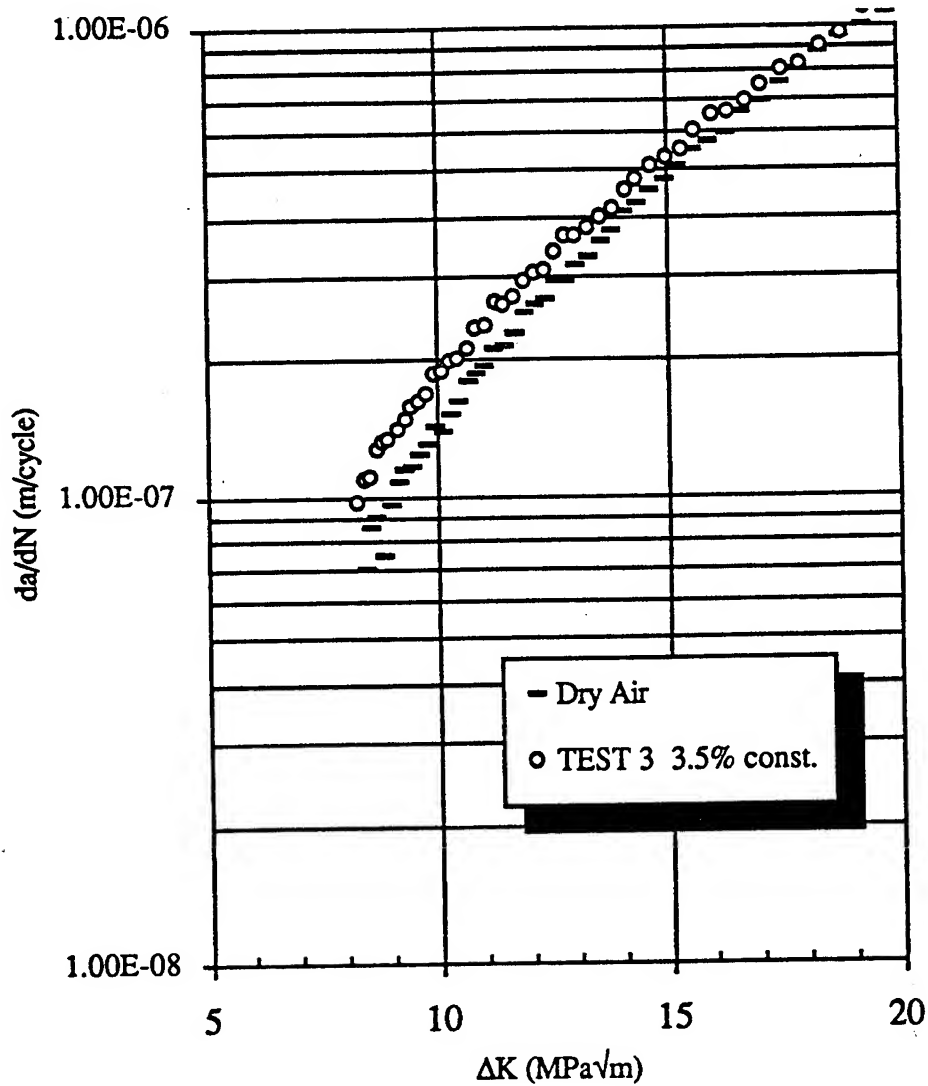


Figure 10. Comparison of dry air FCG rate and 3.5% NaCl constant immersion FCG rate in lower ΔK portion of crack propagation curve.

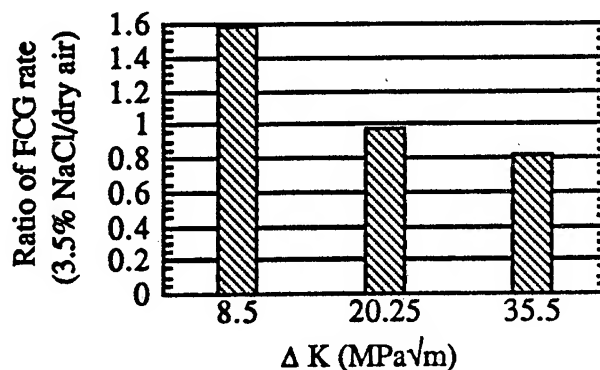


Figure 11. Comparison of fatigue crack growth rates at various ΔK for 3.5% NaCl constant immersion tests versus dry air tests.

NaCl Solution Intermittent Immersion

Intermittent immersion testing produced data with a much greater scatter, particularly in the low ΔK portion of the da/dN versus ΔK curve (Figure 12). Evaluation of the data shows "stalled" crack growth at a ΔK range of approximately 10-12 MPa \sqrt{m} (9.0-10.8 ksi \sqrt{in}). For these ΔK values the crack growth rate remains constant, or decreases, as the stress intensity factor continues to rise (Figure 13). This stalling effect actually allows the da/dN curve to drop below the curve for dry air, and give a lower crack growth rate in region II of the FCG curve and longer overall life for this test. There is also a characteristic wave associated with the intermittent immersion data in region II of the FCG curve. These ripples in the data can be seen to correspond roughly with the periods of salt solution exposure (Figure 14).

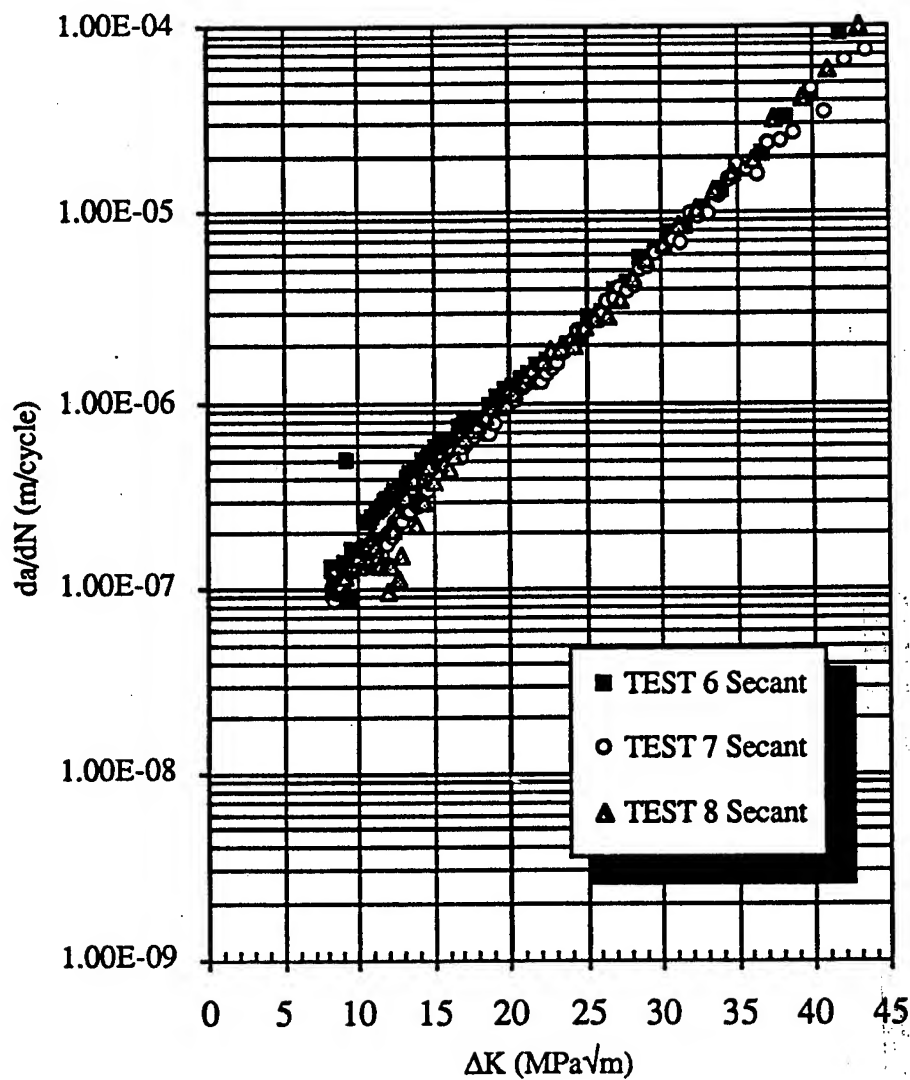


Figure 12. The greater scatter seen in the data from intermittent immersion testing as compared with the constant immersion test data seen in Figure 9, ($f=1.0$ Hz., $R=0.1$, 3.5% NaCl intermittent immersion).

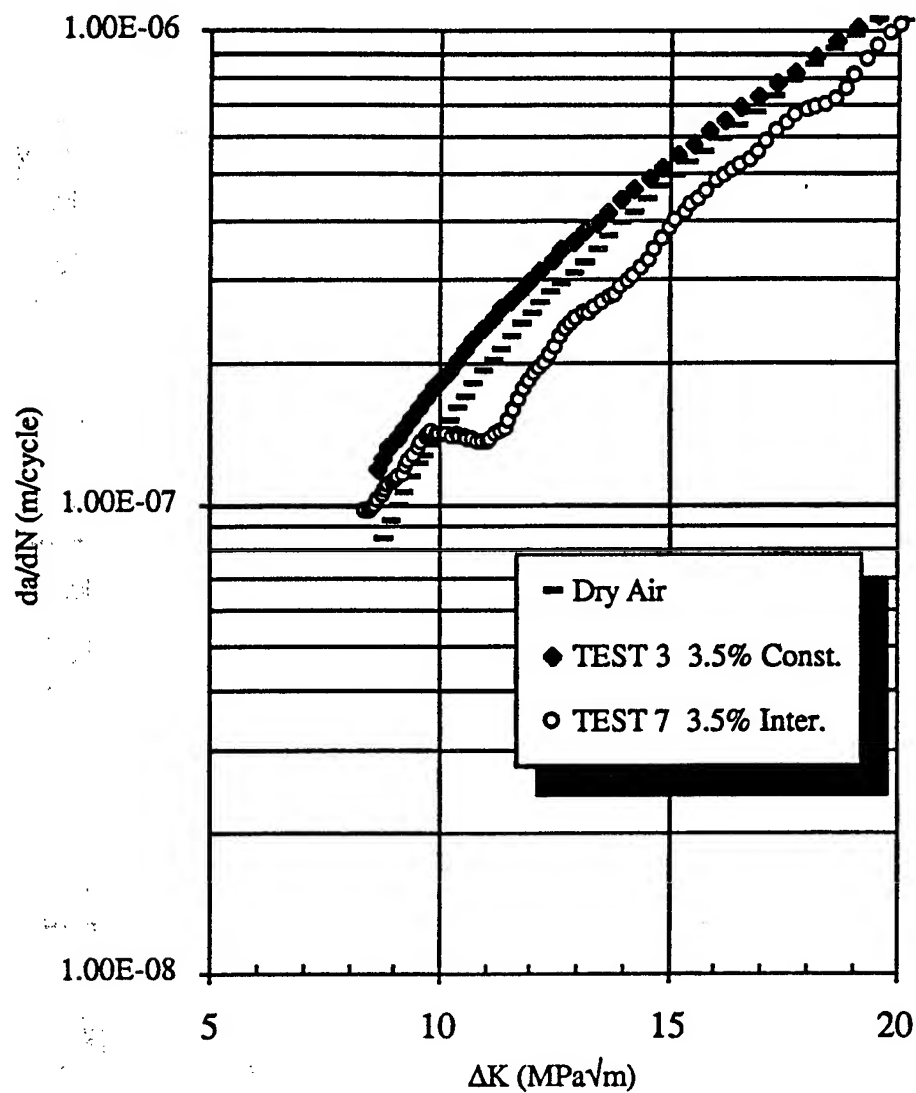


Figure 13. Effects of intermittent environmental exposure on the low ΔK portion of the crack propagation curve, ($f=1.0$ Hz., $R=0.1$, 3.5% NaCl intermittent immersion).

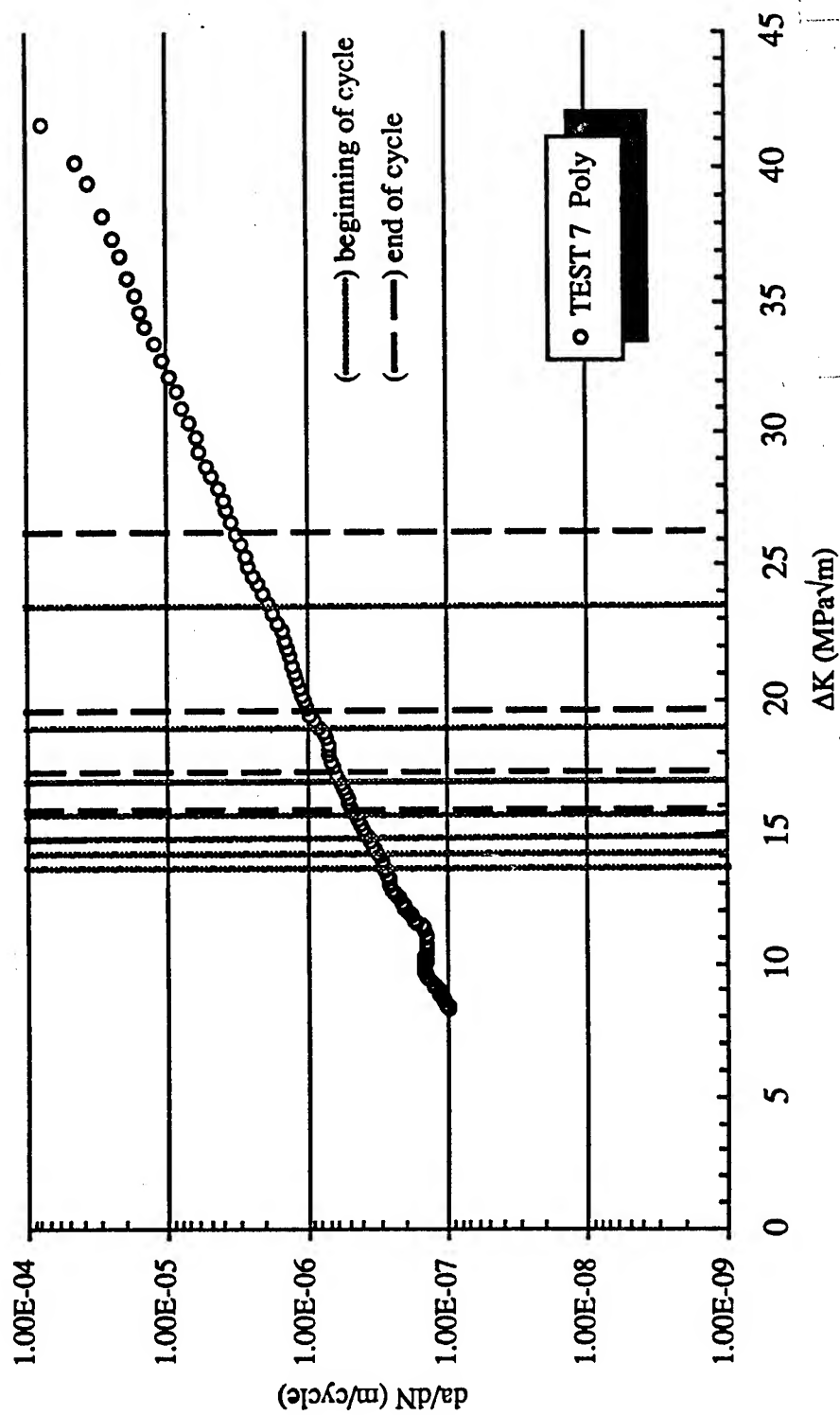


Figure 14. Overlay of the last seven alternate immersion cycles on the FCG curve.

Discussion

This investigation has produced interesting, although not entirely expected, results. The results are significant for at least two main reasons. First from an application oriented standpoint, it shows that the FCG response is affected by the environmental cycle. Although not totally understood, this effect is important to note when trying to establish realistic guidelines and requirements for corrosion fatigue testing of specimens or components. Second from a research oriented standpoint, understanding the role that these extrinsic parameters play is critical to understanding material response. A thorough understanding of this phenomenon and its mechanistic nature may ultimately lead to methods for enhancing the fatigue capabilities of many commonly utilized engineering materials.

Conclusions

Based on the conditions of this experimental program, the following conclusions are presented.

1. Fatigue crack growth rates for 2024-T351 aluminum in 3.5% NaCl solution are up to a factor of 1.6 higher than those seen in FCG in dry air. This conclusion is consistent with previously published literature on corrosion fatigue of 2024-T351.
2. An alternating environment of 3.5% NaCl solution and dry air affected the FCG of 2024-T351 in the following manner:
 - It increased the scatter seen at the lower values of ΔK tested.
 - It caused an apparent "stall" or plateau of the crack growth rate at a stress intensity factor of approximately $10\text{-}12 \text{ MPa}\sqrt{\text{m}}$ ($9.0\text{-}10.8 \text{ ksi}\sqrt{\text{in}}$).
 - A characteristic ripple in FCG curve was correlated to wet/dry cycles.
 - It increased the pitting, corrosive attack and the amount of corrosion by-products found on the fracture surface.

Further Investigations

It is suggested that a follow on experimental program be conducted with a statistically significant number of specimens. Should this produce similar results as the original investigation, the testing could be expanded to any number of commonly used materials. This would allow for an assessment of the sensitivity of various materials to the alternating environmental exposure. In depth attempts to isolate the mechanistic changes causing stalling of the fatigue crack growth rate could incorporate some of the fractographic techniques of Johansson and Darvish^{11,12}. Techniques such as altering the environmental cycle and/or the load allow them to band the fracture surface in such a manner as to make features more obvious. This would allow for a more positive correlation of events to fracture surface morphology, which is absolutely essential in any attempt to isolate mechanistic changes occurring during the test. These techniques, while currently utilized principally in the investigation of short crack phenomena, would make fractographic investigation easier and possibly more productive.

Because of the sensitivity of FCG to alternating environment at the lowest ΔK ranges tested, it would be productive to expand this investigation into even lower values of stress intensity range. Although this investigation was specifically aimed at investigating the "long" crack behavior, investigations of alternate immersion testing with decreasing ΔK tests might produce even more dramatic results than those already obtained.

References

1. Wanhill, R. 1994. Aircraft corrosion and fatigue damage assessment. National Aerospace Laboratory The Netherlands. NLR TP 94401 L. Provisional issue photocopy.
2. Hoepfner, D., L. Grimes, A. Hoepfner, J. Ledesma, T. Mills and A. Shah. 1995. Corrosion and fretting as critical aviation safety issues: Case studies, facts and figures from US aircraft accidents and incidents. In International committee on aircraft fatigue (ICAF): Proceedings of symposium in Melbourne, Australia, May 1995. To be published.
3. Schütz, W. 1995. Corrosion fatigue - The forgotten factor in assessing durability. 15th Memorial Plantema Memorial Lecture at the International committee on aircraft fatigue (ICAF): Proceedings of symposium in Melbourne, Australia, May 1995. To be published.
4. Swartz, D., M. Miller and D. Hoepfner. 1995. Chemical environments in commercial transport aircraft and their effect on corrosion fatigue crack propagation. In International committee on aircraft fatigue (ICAF): Proceedings of symposium in Melbourne, Australia, May 1995. To be published.
5. Gangloff, R. and S. Kim. 1992. Environment enhanced fatigue crack propagation in metals: Inputs to fracture mechanics life predictions. University of Virginia. SEAS Report No. UVA/528266/MSE93/111.
6. Feeney, J., J. McMillan and R. Wei. 1970. Environmental fatigue crack propagation of aluminum alloys at low stress intensity levels. Metallurgical Transactions 1 (June): 1741-1757.
7. Krupp, W., D. Hoepfner and E. Walker. 1972. Crack propagation of aluminum alloys in corrosive environments. In Corrosion fatigue: Chemistry, mechanics and microstructure, Edited by O. Devereux, A. McEvily and R. Staehle, 468-483. Houston: NACE, International.
8. McEvily, A. and R. Wei. 1972. Fracture mechanics and corrosion fatigue. In Corrosion fatigue: Chemistry, mechanics and microstructure, Edited by O. Devereux, A. McEvily and R. Staehle, 381-395. Houston: NACE, International.
9. Speidel, M. 1975. Corrosion fatigue crack growth in high strength aluminum alloys. International committee on aircraft fatigue (ICAF): Proceedings of symposium in Lausanne, Switzerland, June 1975. To be published. Preliminary photocopy.
10. Wei, R. 1970. Some aspects of environment-enhanced fatigue-crack growth. Engineering Fracture Mechanics 1: 633-651.
11. Johansson, S. 1986. Influence of cyclic condensation and cyclic immersion environment on the fatigue properties of AA 7075 clad material. In Materials Science: Proceedings of the 4th Scandinavian Symposium in Trondheim, Norway, August 1986, by The Norwegian Institute of Technology. Norway: The University of Trondheim, 123-131.
12. Darvish, M. 1992. The cyclic change in the humidity of the environment a new method for studying the fatigue crack at low growth rate. Ph.D. diss., Linköping University Sweden.

Corrosion Fatigue Interaction

*** David Y. Jeong¹, Jinmiao Zhang², Noriko Katsube²,
George W. Neat¹, Thomas H. Flournoy³, and Pin Tong⁴**

¹U.S. Department of Transportation
Volpe National Transportation Systems Center
Cambridge, MA 02142

²Ohio State University
Applied Mechanics
Columbus, OH 43210

³U.S. Department of Transportation
Federal Aviation Administration Technical Center
Atlantic City, NJ 08405

⁴Hong Kong University of Science and Technology
Clear Water Bay, Kowloon, Hong Kong

ABSTRACT

Corrosion fatigue is one of the most common failure occurrences in engineering structures. Almost all structures are exposed to environment with corrosive media at some time. What makes corrosion fatigue dangerous is that small cracks can grow rapidly to a critical size, even between scheduled inspections, leading to structural failures. Corrosion fatigue is generally caused by material degradation in the presence of micro-cracks and voids. In this paper, we limit our consideration to localized pitting produced by corrosion where the pits can act as stress raisers that affect the formation and growth of cracks. Mechanics-based models examining the effect of pitting on the local stress field are presented. The models are based on analytical and computational methods. In the computational model, the hybrid finite element method is adopted to formulate special elements that approximate the stress fields near pits and near crack tips with an adjacent pit. Specifically, the effect of pit size on stress concentration factors and stress intensity factors is examined in this paper. In order to simplify the analyses, pits are modeled as circular inclusions.

BACKGROUND

Because of the high cost of new airplanes, airlines often find it more economical to refurbish older airplanes and keep them in service beyond their original design life than to replace older airplanes with new ones. A similar situation is true for the military transport fleet. Reductions in defense spending limit replacement aircraft acquisitions. As an alternative, the military is forced to extend the service life of its existing aircraft fleet.

Aging does not pose a direct threat to the safety of the flying public or to military operations as long as the planes are well maintained. It does, however, cause reliability problems, and creates challenges for maintenance.

For airframe structures, failures associated with aging are related to metal fatigue and corrosion. Corrosion fatigue is generally caused by material degradation in the presence of micro-cracks and voids. These micro-defects are inherent in virtually all materials. Corrosive environments can promote and accelerate the growth and coalescence of these defects, especially when the material is under stress. Defect growth and coalescence represent material damage. When the structure is subjected to cyclic loading, these defects can lead to fatigue damage. Prediction of fatigue life has been studied extensively, but the details of the corrosion-damage process are not well understood. Scatter factors for corrosion can vary between 2 and 10 depending on humidity. Knowledge on the interaction between crack growth and corrosion appears to be even more primitive, although the interaction effect for 2000 and 7000 series alloys is believed to be significant. A need exists for a comprehensive study of the corrosion-damage process and the combined effect of corrosion and fatigue on structural integrity. In the present study, we focus our consideration on developing mechanics-based models to examine the effect of pitting on the local stress field which in turn affects the crack initiation and growth.

Since the Aloha accident in 1988, special emphasis has been placed on the investigation of multiple site damage (MSD) and its effect on structural integrity. Research is also required to understand the interaction between MSD and corrosion. In this paper, we will focus on the interaction between corrosion pitting and fatigue crack formation and growth. Figure 1 shows schematically various shapes of pits found in actual structures [1]. Two scenarios are considered in this paper where pits behave as stress raisers: (1) a single pit (Figure 2), and (2) a single pit near the tip of a crack (Figure 3). Stress concentration factors are determined for the former case, and stress intensity factors are calculated in the latter case. To

simplify the analyses, pits are modeled as circular inclusions¹. Figure 4 shows a schematic of the assumed pit shape and cross section. Stress concentration factors for circular pits in an infinite medium subjected to remote tension and shear are determined from analytical solutions. Stress intensity factors for a crack with a circular pit near the tip are calculated numerically from hybrid finite element formulations². For the former case, the analytical results are compared to experimental data obtained from fatigue testing of panels containing pre-existing corrosion. Pit depths were measured through metallographic and fractographic methods.

STRESS CONCENTRATION FACTORS FOR CIRCULAR PITS

We consider a thin panel with corrosion pits, and model the panel as a plane stress problem. The corrosion pits are modeled as circular inclusions and are approximated as thinner regions of the panel. Analytical solutions for the stress field in an infinite sheet with a circular pit under remote tension or shear are available in the open literature [3,4]. These solutions are typically given in terms of complex potentials. Stress concentration factors were derived from the complex variable solutions, and are shown in Figure 5. The thickness ratio is defined as (t_p/t_o) where t_o is the original or nominal sheet thickness and t_p is the remaining thickness at the pit. Thus, the pit depth is defined as $d = t_o - t_p$. The magnification in local stress due to these stress concentration factors promotes the formation, nucleation, and growth of fatigue cracking in actual structures.

In a separate research activity, flat lap-splice panels were fatigue tested by Arthur D. Little, Inc. (ADL) to examine crack growth behavior in the presence of pre-existing corrosion [5]. The panels were immersed in ASTM G44 [6] solution to replicate pitting corrosion. Metallographic and fractographic analyses were performed by the Massachusetts Institute of Technology (MIT) to determine the depth of individual pits near each rivet hole. Pit depths greater than 10 μm were measured and recorded³. The maximum and mean (average value) pit depths as well as standard deviations are listed in Table 1. In addition, the number of cycles for a crack to reach 0.1 inch is listed which is an arbitrary value used to characterize the number of cycles to crack formation. From the baseline (i.e., panels without corrosion) ADL tests [5], the average cycles to crack formation was 41,500 cycles. Most of the values for the number of cycles to reach 0.1-inch crack growth

¹ The methodology can be extended to include pits of different shapes.

² The hybrid finite element method has been applied previously in damage tolerance analysis of stiffened fuselage structures [2].

³ Unfortunately, information on the exact locations of the pits was not available.

listed in Table 1 are less than 41,500 cycles, suggesting that pits could indeed be acting as stress raisers.

Table 1. Data for Pit Depths and Corresponding Cycles to 0.1-Inch Cracks [5].

<i>Specimen ID</i>	<i>Rivet Number (L/R)</i>	<i>No. of pits</i>	<i>Max. depth (μm)</i>	<i>Mean depth (μm)</i>	<i>Standard Deviation</i>	<i>Cycles to 0.1-inch crack</i>
C3	1-6 (L)	10	61	42	13	21,626
C3	1-6 (R)	2	79	71	8	20,000
C3	1-8 (L)	5	52	45	7	27,040
C3	1-8 (R)	9	71	44	17	24,626
C3	1-9 (L)	10	73	38	19	26,864
C3	1-9 (R)	13	76	41	21	30,950
C4	1-9 (L)	5	45	28	10	28,099
C4	1-9 (R)	3	30	35	8	25,099
C5	1-8 (L)	5	45	25	12	48,049
C5	1-8 (R)	6	73	43	20	43,626
C6	1-10 (R)	3	27	19	6	33,138
C8	1-6 (L)	8	94	21	27	31,808
C8	1-6 (R)	4	32	21	9	28,300

Predictions for fatigue life for various pit depths can be estimated using the results shown in Figure 5 and the following equation:

$$N(d) = N_o \frac{1}{[scf(d)]^m} \quad (1)$$

where d is the pit depth. In addition, $scf(d)$ is the stress concentration factor as a function of the thickness ratio, $t_p/t_o = 1 - d/t_o$, shown in Figure 5 for uniaxial tension. In the case of no pitting, the stress concentration factor is equal to 1. Equation (1) assumes that the standard S-N curve obeys a power law where $1/m$ is the slope of the S-N curve. Moreover, the fatigue life for a particular pit size is assumed to be inversely proportional to the stress concentration factor for that pit size raised to the m -power. From Mil-Handbook 5 [7], the range of reported values of m for 2024-T3 aluminum varies between 3.29 and 3.97. In equation (1), N_o and m are assumed to be 41,500 cycles and 3.97, respectively. For the ADL panels, the sheet thickness, t_o , was 0.040 inch (1016 μm).

Figure 6 compares the results predicted by equation (1) with the experimental data listed in Table 1 for variations in maximum pit depths. The analysis overestimates the fatigue life by 16% to 28%. In other words, the actual stress concentration factors for the measured pits are approximately 4% to 9% higher than those predicted by modeling pits as circular inclusions. Given that the pit shape was simplified in this manner, the predictions for fatigue life of pits are encouraging.

CRACK-PIT INTERACTION

A computational model based on the hybrid finite element method was developed to examine the interaction between a crack and an adjacent pit. The term "hybrid" as used here means that one set of approximating functions are used to describe the boundary of the element, and another independent set of functions are assumed to approximate the interior of the element. For instance, in the assumed-stress hybrid method, the stress field is assumed within the element and displacements are assumed along the boundary. In this paper, the hybrid method has been adopted in the formulation of special elements. These special elements are sometimes referred to as super elements because the approximating functions for stresses and displacements are derived from analytical solutions which increases numerical accuracy. Two super elements are considered: (1) crack-tip super element, and (2) inclusion-embedded super element. The application of crack-tip super elements in the hybrid finite element method has been developed by Tong *et al.* [8], and more recently by Zhang and Katsube [9]. Also, Zhang and Katsube have developed hybrid elements for rigid [10] and elastic [11] inclusions.

Hybrid Finite Element Formulation

The formulation of hybrid elements is based on variational principles in the theory of elasticity. Generally, the principle of minimum complementary energy or the Hellinger-Reissner principle is used in hybrid formulations.

Crack-Tip Super Element

The hybrid functional for the crack tip super element is

$$\pi = \frac{1}{2} \int_{C_1} \mathbf{t}^T \mathbf{u} dS - \int_{C_1} \mathbf{t}^T \tilde{\mathbf{u}} dS \quad (2)$$

where the tractions \mathbf{t} and displacements \mathbf{u} are expressed in matrix form. Displacements are assumed to be specified along the boundary C_1 (see Figure 7).

The general form of the element stiffness matrix for the crack-tip super element is

$$\mathbf{k} = \mathbf{G}^T \mathbf{H}^{-1} \mathbf{G} \quad (3)$$

where

$$\mathbf{G} = \oint_{C_1} \mathbf{R}^T \mathbf{L} dS \quad \mathbf{H} = \oint_{C_1} (\mathbf{R}^T \mathbf{U} + \mathbf{U}^T \mathbf{R}) dS \quad (4)$$

In equation (4), \mathbf{R} relates the tractions on C_1 to β , \mathbf{U} relates the boundary displacements to the nodal displacements, and \mathbf{L} is the interpolation-function matrix defined only on the element boundary:

$$\mathbf{t} = \mathbf{R}\beta \quad \mathbf{u} = \mathbf{U}\beta \quad \tilde{\mathbf{u}} = \mathbf{L}\mathbf{q} \quad (5)$$

Inclusion-Embedded Super Element

The hybrid formulation for the a linearly elastic inclusion-embedded super element is formally described by Zhang and Katsube [11]. The most important concept in the formulation of this hybrid element is to decompose the original problem into a superposition of two boundary value problems (see Figure 8⁴). The first boundary value problem is the sheet with specified boundary displacements; the second is the inclusion with specified boundary tractions. Then, the Hellinger-Reissner variational principle can be applied to derive the following hybrid functionals:

$$\pi_s = \frac{1}{2} \left(\oint_{C_1} \mathbf{t}_s^T \mathbf{u}_s dS_1 + \oint_{C_2} \mathbf{t}_s^T \mathbf{u}_s dS_2 \right) - \oint_{C_1} \mathbf{t}_s^T \tilde{\mathbf{u}}^{(1)} dS_1 - \oint_{C_1} \mathbf{t}_s^T \tilde{\mathbf{u}}^{(2)} dS_2 \quad (6)$$

$$\pi_p = -\frac{1}{2} \oint_{C_2} \mathbf{t}_p^T \mathbf{u}_p dS_2 + \oint_{C_2} \mathbf{u}_p^T \tilde{\mathbf{t}}^{(2)} dS_2 \quad (7)$$

where the subscripts s and p refer to the sheet and inclusion, respectively.

⁴ Although the schematic illustrations of both the crack-tip and inclusion-embedded super elements shown in Figures 7 and 8 depict rectangular elements, the hybrid formulations developed by Zhang and Katsube [9-11] are fully applicable to a general polygon.

The element stiffness matrix for the inclusion-embedded super element has the following mathematical form

$$\mathbf{k} = \mathbf{G}_m^T (\mathbf{H}_m^{(1)} + \mathbf{H}_m^{(2)} + \mathbf{H}_{mp})^{-1} \mathbf{G}_m \quad (8)$$

where

$$\mathbf{G}_m = \oint_{C_1} [\mathbf{R}_m^{(1)}]^T \mathbf{L} dS_1 \quad \mathbf{G}_{mp} = \oint_{C_1} [\mathbf{R}_m^{(1)}]^T \mathbf{U}_p dS_1 \quad (9)$$

$$\mathbf{H}_m^{(1)} = \frac{1}{2} \oint_{C_1} [\mathbf{R}_m^{(1)}]^T \mathbf{U}_m + \mathbf{U}_m^T \mathbf{R}_m^{(1)} dS_1 \quad (10)$$

$$\mathbf{H}_m^{(2)} = \frac{1}{2} \oint_{C_2} [\mathbf{R}_m^{(2)}]^T \mathbf{U}_m + \mathbf{U}_m^T \mathbf{R}_m^{(2)} dS_2 \quad (11)$$

$$\mathbf{H}_{mp} = \mathbf{G}_{mp} \mathbf{H}_p^{-1} \mathbf{G}_{mp}^T \quad (12)$$

$$\mathbf{H}_p = \frac{1}{2} \oint_{C_2} [\mathbf{R}_p^{(2)}]^T \mathbf{U}_p + \mathbf{U}_p^T \mathbf{R}_p^{(2)} dS_2 \quad (13)$$

The approximating functions for stresses and displacements in the hybrid functionals must satisfy *a priori* the equilibrium equations and the constitutive relations. In the case of the crack-tip super element, an additional boundary condition must be satisfied; tractions on the crack face must be equal to zero. Approximating functions can be constructed from complex variable solutions in classical elasticity [3] to automatically satisfy these conditions. More rigorous details of the hybrid formulations can be found in Reference [9] for the crack-tip super element and Reference [11] for the inclusion-embedded super element.

Results

The finite element mesh shown in Figure 9 was used to generate stress intensity factors for a circular pit in the vicinity of a single crack. The mesh comprises 104

nodes and 66 elements⁵ including one hybrid inclusion-embedded polygonal super element [9] and one hybrid crack-tip super element [11]. Figure 10 shows results from the hybrid finite element analysis for various pit depths and distances from the crack tip. Referring to Figure 3, the geometry of the crack-pit configuration can be characterized by the following dimensions: $2a$ is the total crack length, p is the distance from the crack tip to the edge of the pit, and r is the pit radius. In the results shown in Figure 10, the pit radius is a fixed value, and is assumed to be 0.2 times the half crack length, or $r = 0.2a$. Other relevant dimensions are listed in the figure. The accuracy of this numerical procedure can be roughly estimated from Figure 10. The normalized stress intensity factors for thickness ratios equal to one should, in theory, be equal to one for an infinite medium. In the finite element discretization, a finite-width sheet is modeled. Also, linear interpolation is used between nodal values. Nevertheless, these results show that stress intensity factors increase when pits modeled as circular inclusions are present.

CONCLUDING REMARKS

Mechanics-based models have been presented to determine the effect of pits as stress raisers in sheet material. In particular, stress concentration factors for a single pit and stress intensity factors for pits interacting with a single crack were presented. In these analyses, pits were modeled as circular inclusions in order to simplify the mathematical formulations. The results give proper trends which are encouraging. The methodologies presented in this paper can be extended to include other pit shapes. In addition, the methodology can be used to examine the effect of randomly dispersed pits. These topics will be discussed in future communications.

Corrosion fatigue is a form of material degradation resulting from the growth of micro-cracks and voids under cyclic loads. For corrosion fatigue predictions, one should consider stages of the damage process that include:

- (1) material degradation or damage evolution prior to macro-crack nucleation,
- (2) macro-crack initiation, and
- (3) crack propagation.

A comprehensive theory to model corrosion and its interaction with fatigue requires

- (1) understanding corrosion mechanisms,

⁵ The number of nodes and elements would increase significantly if only conventional finite elements are used in the analysis.

- (2) determining the metallographic characteristics of corroded surfaces, especially those at the crack front, to establish corrosion effects on crack initiation and growth,
- (3) developing analysis capability to simulate and quantify damage at the microscopic level,
- (4) developing techniques to measure the mechanical properties of corrosion film, and
- (5) implementing a damage model based on finite element methods to predict corrosion fatigue.

This paper has considered only the simulation and quantification of one type of micro-damage. Extensive work is still required to fully study the problem of corrosion fatigue and its effect on structural integrity of aging aircraft.

ACKNOWLEDGMENT

The work presented in this paper was funded partially by the Research and Grant Council of Hong Kong in support of the Federal Aviation Administration Technical Center's National Aging Aircraft Research Program.

REFERENCES

- [1] ASTM G46-76, "Standard Recommended Practice for Examination and Evaluation of Pitting Corrosion," *1988 Annual Book of ASTM Standards, Volume 3.02*, American Society for Testing and Materials, Philadelphia, PA (1988).
- [2] Tong, P., "A hybrid finite element method for damage tolerance analysis," *Computers & Structures* 19, 263-269 (1984).
- [3] Muskhelishvili, N.I., *Some Basic Problems of the Mathematical Theory of Elasticity*, P. Noordhoff Ltd., Groningen, Holland (1953).
- [4] Erdogan, F., Gupta, G.D., Ratwani, M., "Interaction between a circular inclusion and an arbitrarily oriented crack," *Journal of Applied Mechanics* 41, 1007-1013 (1974).

- [5] Sigelmann, M.R., and Berry, S.R., "A Laboratory Study of the Effects of Corrosion on Fuselage Lap Splice," Volpe Center Project Memorandum, DOT-VNTSC-FA3H2-PM-93-15, July 1993.
- [6] ASTM G44-88, "Standard Practice for Evaluating Stress Corrosion Cracking Resistance of Metals and Alloys by Alternating Immersion in 3.5% Sodium Chloride Solution," *1988 Annual Book of ASTM Standards, Volume 3.02*, American Society for Testing and Materials, Philadelphia, PA (1988).
- [7] Mil-Handbook 5, U.S. Department of Defense, Washington, D.C., 1987.
- [8] Tong, P., Pian, T.H., and Lasry, S.J., "A hybrid-element approach to crack problems in plane elasticity," *International Journal of Numerical Methods in Engineering* 7, 297-308 (1973).
- [9] Zhang, J., and Katsube, N., "A hybrid finite element method for cracks," *Proceedings of the International Conference on Computational Engineering Science*, Hawaii, 2075-2080 (1995).
- [10] Zhang, J., and Katsube, N., "A hybrid finite element method for heterogeneous materials with randomly dispersed rigid inclusions," *International Journal of Numerical Methods in Engineering* 38, 1635-1653 (1995).
- [11] Zhang, J., and Katsube, N., "A hybrid finite element method for heterogeneous materials with randomly dispersed elastic inclusions," *Finite Elements in Analysis and Design* 19, 45-55 (1995).

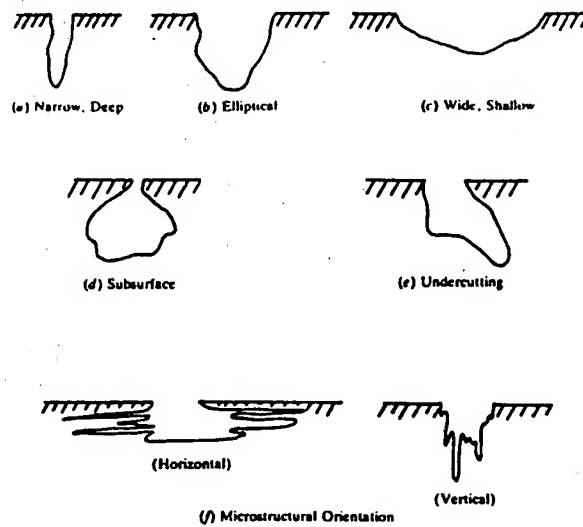


*Figure 1. Variations in shapes of pits found in actual structures
(Reproduced from Reference [1]).*

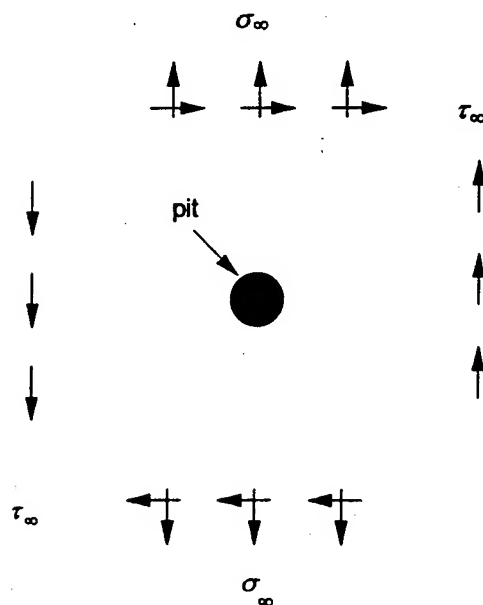


Figure 2. Circular pit in an infinite sheet subjected to remote tension and shear.

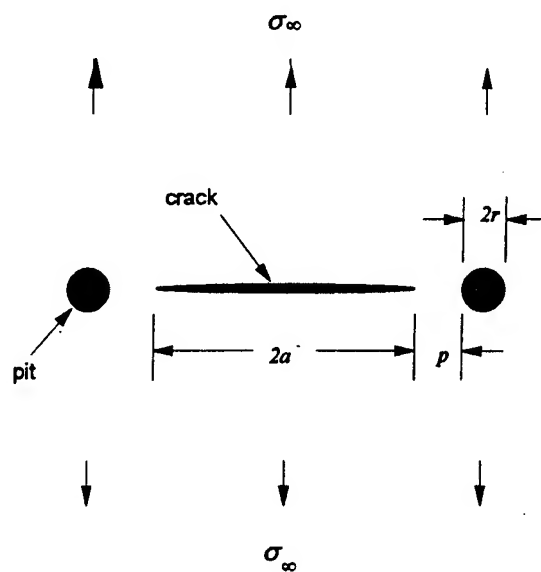


Figure 3. Interaction of a crack with circular pits.

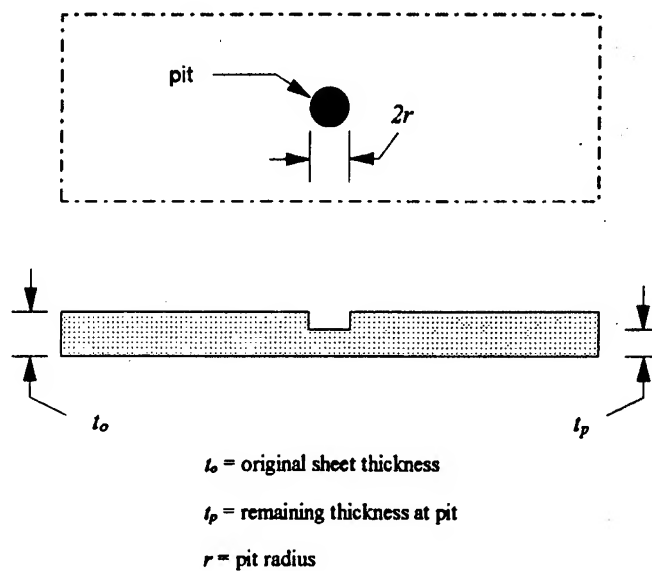


Figure 4. Schematic of the assumed pit shape and cross section.

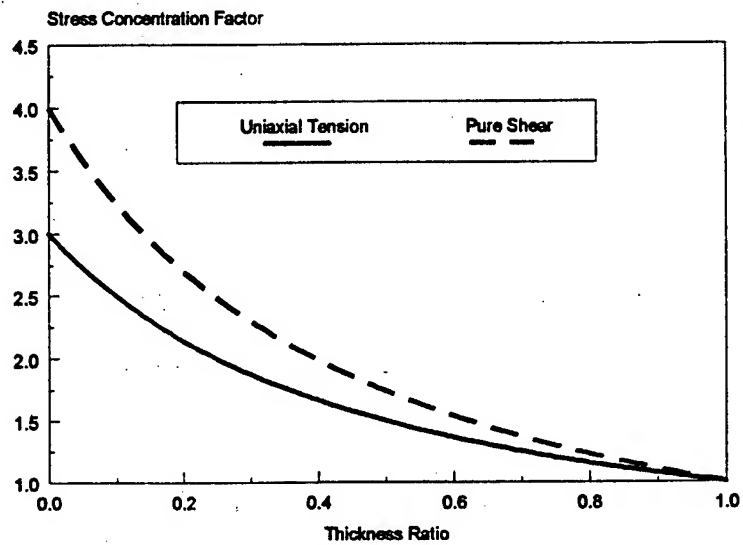


Figure 5. Stress concentration factors for various pitting depths in an infinite medium subjected to uniaxial tension or shear.

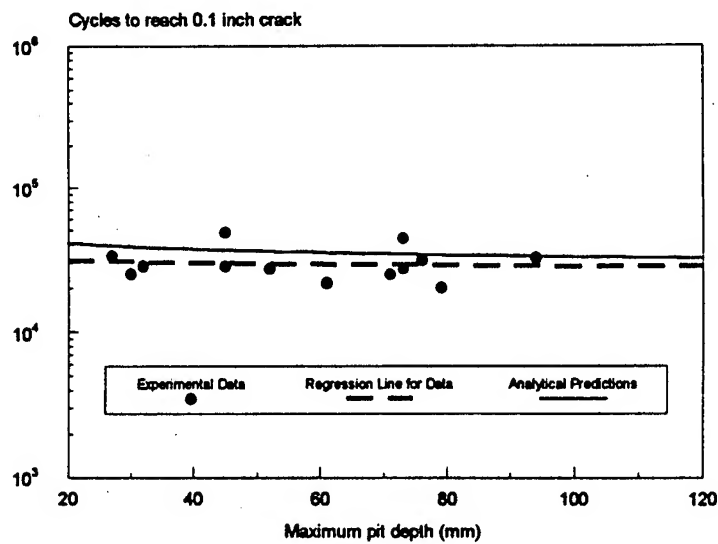


Figure 6. Comparison between analytical and experimental results for cycles to reach 0.1 inch crack growth as a function of pit depth.

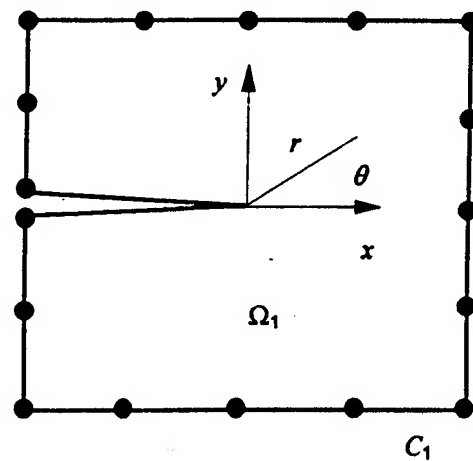


Figure 7. Schematic of hybrid crack-tip super element.

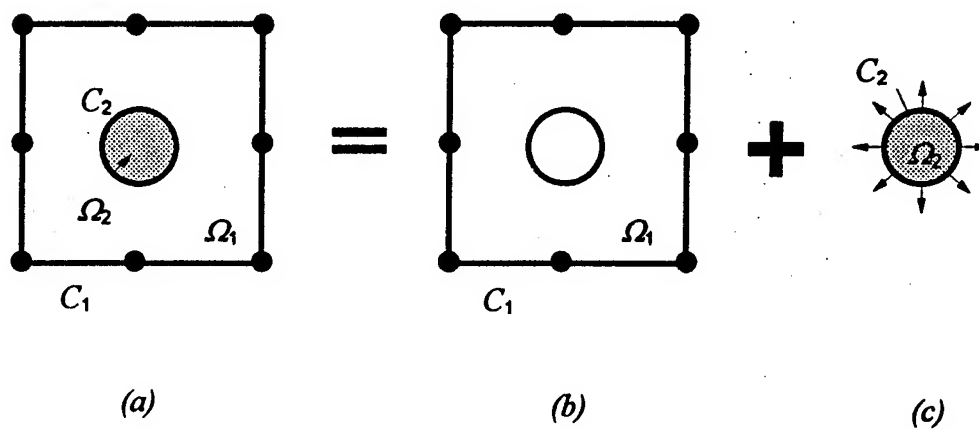


Figure 8. Element decomposition for inclusion-embedded super element.

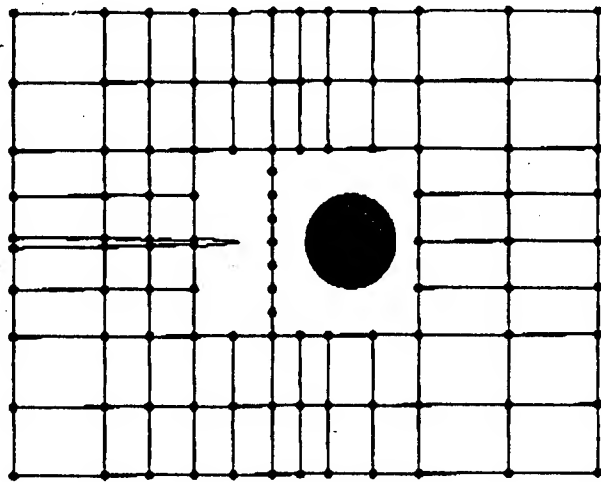


Figure 9. Finite element mesh to model interaction of a crack and an inclusion.

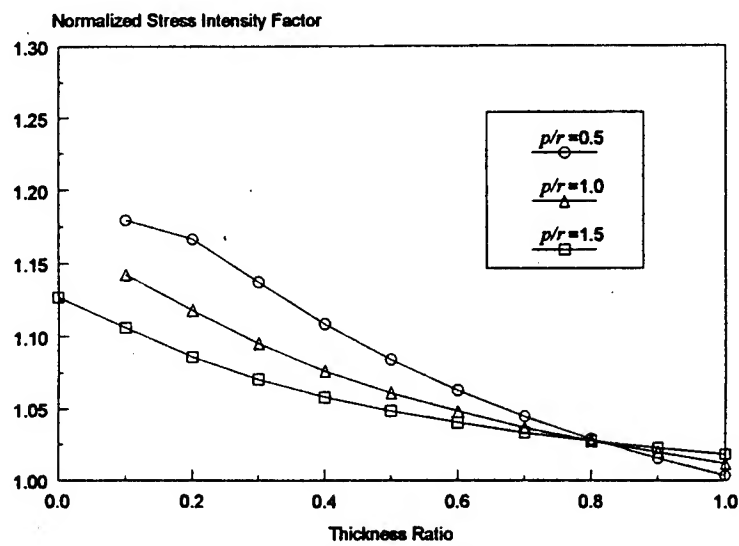


Figure 10. Effect of pits on normalized stress intensity factors ($r/a=0.2$).

SESSION XI

FORCE MANAGEMENT

Chairman: *J. Turner*, SA-ALC/LADD

Automated Readiness Integrated Engineering System (ARIES)

Presented To

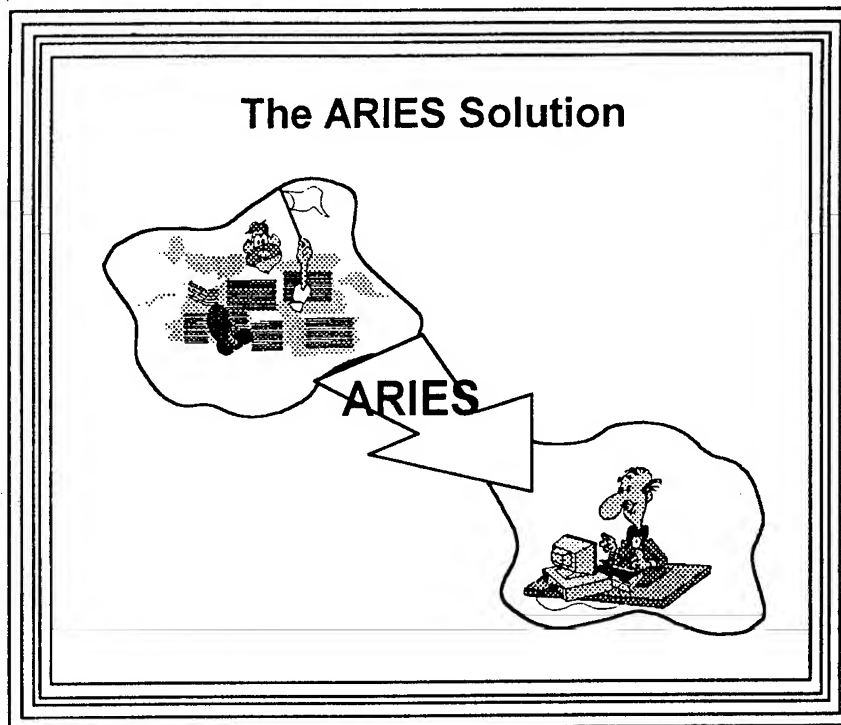
1995 USAF Aircraft Structural Integrity Program Conference

28-30 November 1995

San Antonio, Texas

Russ Alford	Carol Burke	Joe Cochran
WR-ALC/LJLEA	Lockheed Martin	Lockheed Martin
C-141 ASIP Manager	Aeronautical Systems	Aeronautical Systems

The Automated Readiness Integrated Engineering System (ARIES) is a data management program that provides the ASIP Manager and the System Program Director (SPD) with a near real time snapshot of the usage, inspections, repairs, TCTO's and mods for any given aircraft. It also provides systems health and associated trending/forecasting information. I'd like to thank Mr. Russ Alford, the C-141 ASIP Manager, and my colleague Mr. Joe Cochran for their assistance in putting together this presentation.



The C-141 Starlifter has been in service for nearly 30 years. In that time, a tremendous amount of usage and maintenance data has accumulated in various Air Force databases. All of this data is needed to effectively maintain the fleet, however it is impossible to manage manually. The ARIES program integrates the available information in a centralized, user friendly system. Information can be easily extracted and reported for an individual aircraft, all aircraft at a base, or the entire fleet.

Primary Data Sources

MORNING REPORTS (GO81)

AFTO 95 (GO81)

PDM RECORDS

DO56 AFR 66-1 MAINTENANCE DATA

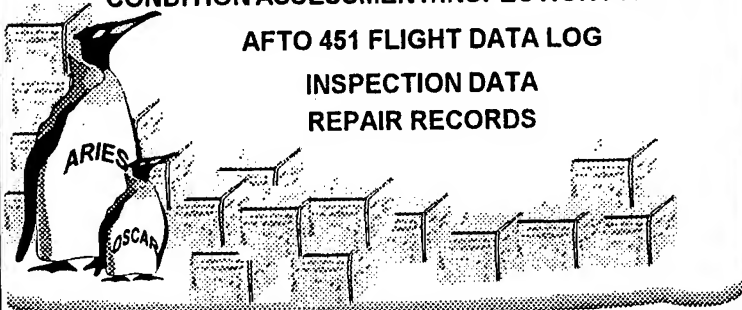
SEVERE MISSIONS LOADS RECORDING PROGRAM

CONDITION ASSESSMENT/INSPECTION PROGRAM

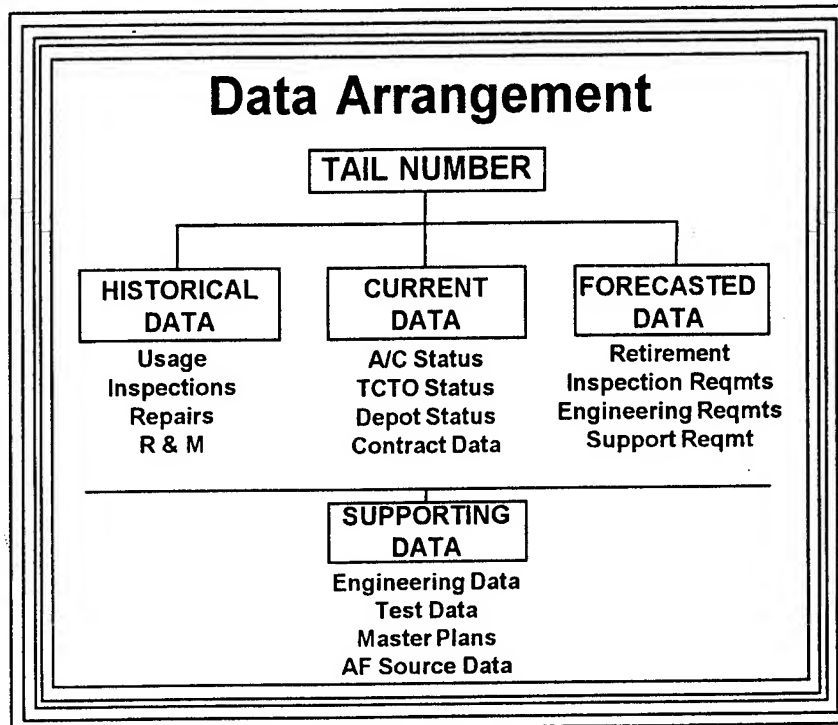
AFTO 451 FLIGHT DATA LOG

INSPECTION DATA

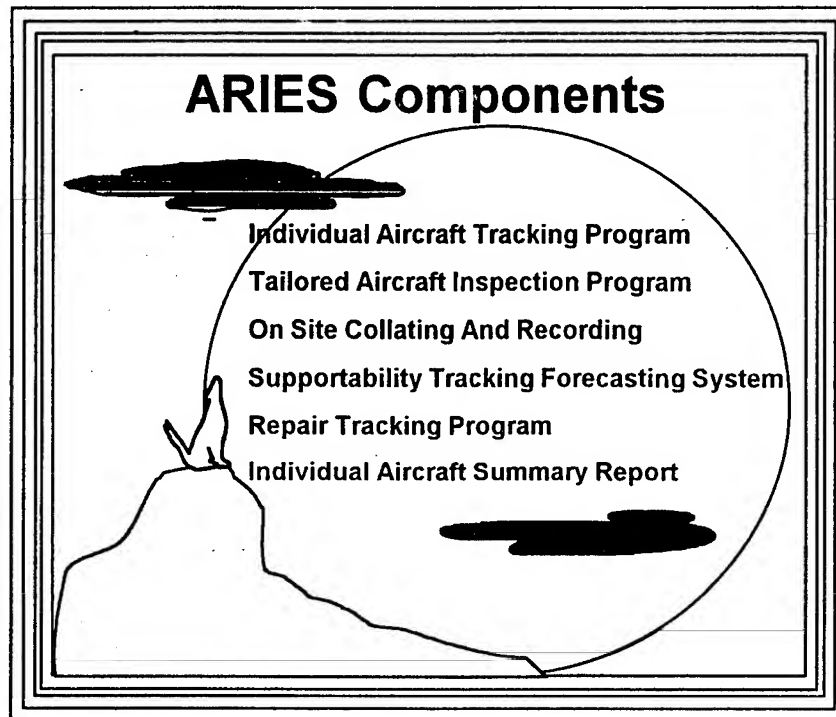
REPAIR RECORDS



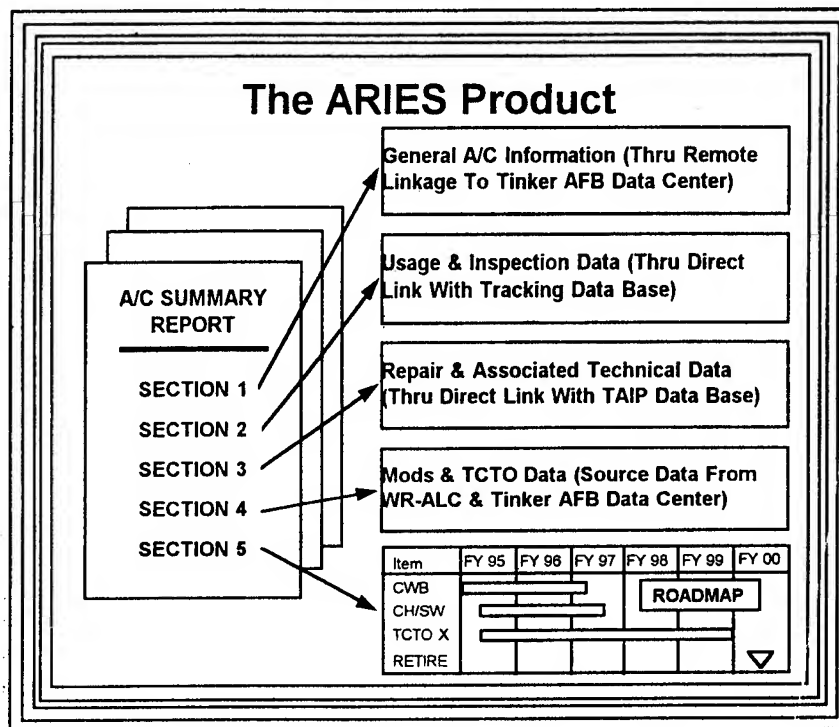
These are some of the primary data sources used by ARIES. The data comes mostly from existing databases. Also, computerized forms can be designed to replace the paper forms currently being filled out by Air Force personnel. This information could then be read directly into the ARIES system. The ARIES database provides usage, repair, inspection and systems data needed by the ASIP Manager for enhanced force management by individual tail number.



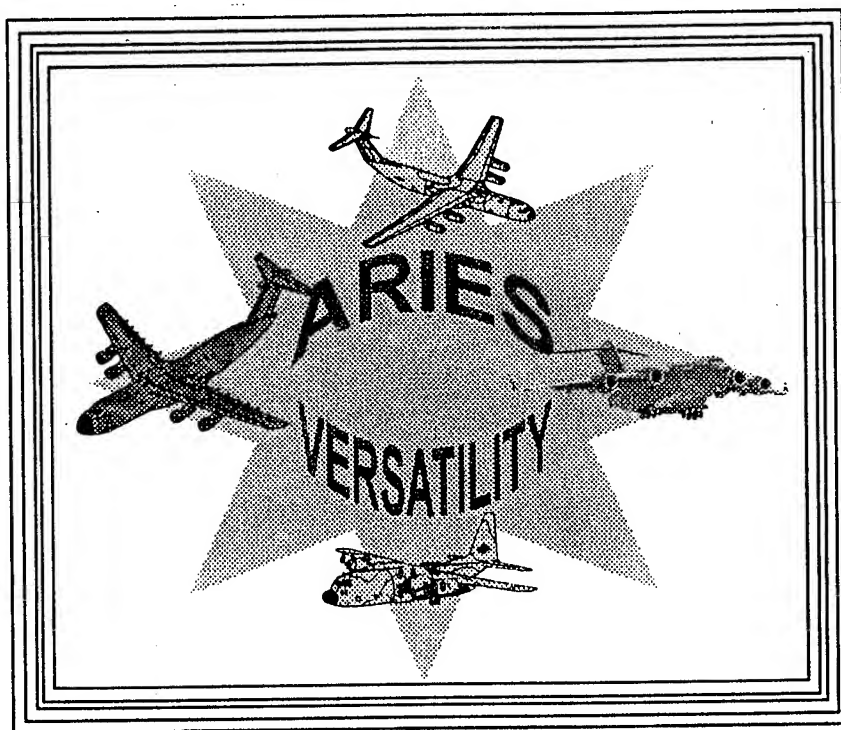
For the purpose of organization, the data has been placed into four basic categories: historical, current, forecasted and supporting. Shown here are some of the primary data that has been catalogued into each of these categories.



Although ASIP Managers may have their own versions of the various programs listed here, ARIES provides a fleet-wide, standardized reporting method. ARIES does this through several individual components. The Individual Aircraft Tracking Program (IATP) deals primarily with usage and its effect on the crack growth curves associated with each structural zone of the aircraft. The Tailored Aircraft Inspection Program (TAIP) attempts to optimize all structural and functional systems inspections with established downtimes (i.e., ISO, HSC, and PDM). On Site Collating and Recording (OSCAR) provides an electronic means of recording and reporting inspection and repair data. The Supportability program (STFS) basically tracks aircraft systems. The Repair Tracking Program tracks individual repairs in the same way the Individual Aircraft Tracking Program does for the aircraft structural zones. Finally, ARIES combines this information to generate a Summary Report for each individual tail number.



The ultimate goal of ARIES is to provide an individual aircraft summary report that can be updated at any given time. This report, which gives near real time data on aircraft, is divided into five sections. The first two sections contain general aircraft information, usage and inspection data. The third and fourth sections provide repairs, TCTOs and mods. Finally, the fifth section shows a roadmap of future activities until retirement. The accessibility of this data provides the ASIP Manager and the System Program Director a valuable force management tool.



Although ARIES was developed for the C-141, it has been designed to be exportable to other weapon systems. To give you a more descriptive overview of ARIES and how it works, Lockheed and the Air Force have produced a Video that I would like to show you now. At the end of the video, I will be happy to answer any questions you may have.

AMRL Support for RAAF F-111 ASIP

*Mr. Kevin C. Watters

Mr. Julian J. Paul

Mr. Ashley Searl

Aeronautical and Maritime Research Laboratory

506 Lorimer Street, Fishermen's Bend, 3207,

Melbourne, Victoria, Australia.

1. INTRODUCTION

The Aeronautical and Maritime Research Laboratory (AMRL), which is part of the Defence Science and Technology Organisation (DSTO) in the Australian Government Department of Defence has an ongoing program of support to the Royal Australian Air Force (RAAF) in the structural integrity management of its F-111 fleet. A current focus of this support is the analysis of in-service fatigue cracking at a location in the upper plate of the wing pivot fitting (WPF) known as fuel flow vent hole number 13 (FFVH#13).

The unusual occurrence of fatigue cracking in the upper plate of the wing, where the flight loading is compression dominated, is attributed to the presence of localised residual tensile stresses caused by cold proof load testing (CPLT). These residual stresses range up to the yield stress in magnitude. The normally compressive cyclic stresses due to in-flight manoeuvre load cycles are offset by the residual tensile stresses to become cyclic tensile stresses.

The RAAF management approach for FFVH#13 is safety by inspection, with the inspection interval derived from a durability and damage tolerance analysis (DADTA). The DADTA on which the current inspection interval is based took some account of the residual stresses by imposing a single CPLT load at the start of crack growth calculations. The inspection technique used by the RAAF for this location is magnetic rubber inspection (MRI). At each inspection when a crack is not found, the hole surface is polished by hand using abrasive paper to remove approximately 0.005 in of material. This process is known as confidence cutting and its purpose is to remove any cracks present which were below the threshold of detectability of the non-destructive inspection (NDI) method. At each inspection when a crack is found, it is removed by machining the hole to a larger shape in a generic family of rework shapes. Electro discharge machining (EDM) is used to remove the crack.

The RAAF requires a DADTA of FFVH#13 to be performed taking better account of the residual stresses. AMRL's role is to accurately determine the residual and cyclic stresses as input to this DADTA which is to be conducted by Lockheed Martin Tactical Aircraft Systems (LMTAS) under contract from the RAAF.

The AMRL approach is to: develop a substructure finite element (FE) model of the region around FFVH#13; perform an elastic/plastic analysis of the stress history of that model under CPLT cycles; use an accurate constitutive model of the D6ac steel material behaviour in the FE analysis; calibrate the model against strain data from a full-scale wing test; and provide the residual and cyclic stress distributions to LMTAS for the DADTA analysis.

Another aspect of the current AMRL F-111 structural integrity work is a detailed strain survey of the wing pivot fitting as part of a RAAF/USAF collaborative agreement. AMRL has extended the scope of its previous full-scale wing testing by modifying the test rig for variable sweep and by fitting many strain gauges to the shear ring area of the WPF and throughout the WPF in response to LMTAS requests under the RAAF/USAF agreement. Strain surveys of the WPF have been performed at a range of sweep angles and those data have been provided to LMTAS in support of their investigation of the shear ring and their development of an FE model of the whole wing pivot fitting. In return AMRL will have access to the WPF FE model developed by LMTAS.

This paper describes the current full-scale wing testing program at AMRL and the FE modelling and analysis of FFVH#13.

2. BACKGROUND

Figure 1 shows the location of FFVH#13 in the wing pivot fitting. It is in one of the integral stiffeners (number 3) in the upper plate and is closest to the wing pivot. A titanium shear web connects stiffener #3 to a corresponding stiffener on the lower plate and a substantial proportion of the wing shear loading is transmitted through it. The combined shear and bending loading and its proximity to the wing pivot make FFVH#13 the most critical of the fuel flow vent holes.

The RAAF F-111 fleet is comprised entirely of long wing models: the original F-111C's, the attrition replacement F-111A's and the recently purchased ex-USAF F-111G's. The RAAF F-111 fleet (excluding F-111G's) has experienced cracks in the majority of wings. Some wings have experienced

re-cracking after the removal of an initial crack and one wing has been reworked to the maximum allowable shape.

A previous investigation by AMRL [1] looked at optimum rework shapes for FFVH#13 when removing cracks. That investigation used an elastic FE analysis of the stresses around FFVH#13 and derived a family of rework shapes which gave a 20% reduction in the elastic stresses. The RAAF adopted that family of shapes based on this work and more recently added some extra interpolations to the family to allow progressive rework to successively larger shapes, while minimising material removal. Figure 2 shows the current RAAF rework shapes.

Cold proof load testing (CPLT) is an inspection method developed by the F-111 manufacturer to detect cracks in the high strength D6ac steel components in the aircraft. The critical crack length in D6ac steel is so small (e.g. 0.024 in for FFVH#13 at -3g) as to defy detection by the conventional NDI methods available 25 years ago, when the problem first became apparent in the early life of the aircraft type. Furthermore, access to some of the critical areas for inspection is very difficult. The principle of cold proof load testing is to cool the aircraft to -40°F so that the D6ac material becomes embrittled and the critical crack length is even smaller than at room temperature, and then apply limit loading to the aircraft. If the aircraft survives CPLT, it is cleared for a further period of safe flight before any of the very small cracks that may have been present could grow to critical length under normal operating conditions. The current CPLT interval for the RAAF F-111 fleet is 2,000 hours. The CPLT wing load cycles are:

0 → -2.4g → 0 → +7.33g → 0 at 56° wing sweep
0 → -3.0g → 0 → +7.33g → 0 at 26° wing sweep

CPLT cannot be considered as a non-destructive technique for two reasons. Firstly, and obviously, if a long enough crack is present the aircraft will be broken in CPLT. (Two RAAF F-111 wings and a stabilator spindle have failed in CPLT.) Secondly, application of limit load to the structure causes localised yielding around stress concentrators, resulting in locked-in residual stresses after CPLT. For some locations the residual stresses can be beneficial, but for others such as FFVH#13 they are detrimental.

3. FULL-SCALE WING TESTING

3.1 Description of Test Rig

The AMRL F-111 wing test rig was initially configured to test a wing and wing carry through box (WCTB) assembly at a 0° sweep angle. That rig was significantly modified for this test series to provide variable wing sweep angle capability. An overall view of the rig is shown in Figure 3 and a close view of the WCTB mount for variable sweep is shown in Figure 4. The rig allows sweep angles of 16°, 26°, 44° and 56° and provides a close simulation of the CPLT loading, with six hydraulic loading actuators configured as shown in Figure 5.

3.2 Test Wing Configurations

The AMRL test article is an ex-USAF F-111A right hand wing, whose prior history is largely unknown. At the start of the AMRL test program, FFVH#13 was essentially in its as-manufactured condition. It was tested in this baseline configuration. It was then machined to a larger size by EDM to the configuration shown as shape C in Figure 2 and tested again. The final and remaining stage is to further enlarge FFVH#13 to the configuration of shape F in Figure 2 (which represents the maximum allowable rework size) and then re-test. Only the results from the baseline configuration tests are reported here.

3.3 Instrumentation

The test instrumentation consisted of the load cells, strain gauges and displacement transducers. The loads applied by each of the six actuators were logged. Approximately 600 strain gauges were fitted to the test article and the rig. Most of them were in the shear ring area and throughout the wing pivot fitting in support of the collaboration with LMTAS. The gauges fitted at and around FFVH#13 in support of the AMRL model calibration are shown in Figure 6. The primary gauge was a five element strip gauge in the critical corner of FFVH#13 where in-service cracks have initiated (gauge 72 in Figure 6).

3.4 Load Cases

The eighteen load cases applied to the test wing are listed in Table 1. Basically, strain surveys to 60% CPLT loads in positive (upload) and negative (download) directions and for 16°, 26°, 44° and 56° wing sweeps were conducted before a set of 100% CPLT load cycles were applied. Because the data acquisition system had limited capacity, two runs of each case were required to monitor all gauges for the strain surveys. Some gauges were monitored in both runs as a consistency check and to keep a full strain history at critical locations. For the 100% CPLT cycles only a critical subset of gauges was monitored, but it included all the gauges in Figure 6.

3.5 Test Results

Figure 7 shows the deflection of the wing at maximum upload at 56° wing sweep. In this condition the strain distribution in the critical corner of FFVH#13 is shown in Figure 8 by the elements of strip gauge 72. The peak strain of 25,000 microstrain (recorded by element 3) is well beyond the yield strain of 6,750 microstrain derived from AMRL tests (see Section 4.1.3). Figure 9 shows the strain versus load history of element 3 of gauge 72 through the full CPLT cycle. The interesting feature of Figure 9 is that the plots of strain versus load¹ are not highly non-linear (as might be expected for these strain levels from the uniaxial stress-strain curve) and do not show large hysteresis even though the maximum strain is 3.3 times yield strain. This is attributed to the wing bending being mostly elastic with only very localised plastic zones. The deformation in the plastic zones is then constrained by the surrounding elastic material.

4. FFVH#13 ANALYSIS

4.1 Constitutive Modeling of D6ac Steel

4.1.1. Introduction

Under the Cold Proof Load Test (CPLT), and under flight loads, localised areas in the Wing Pivot Fitting (WPF) exceed the yield stress and experience large plastic strains. To analyse this, in particular to predict the residual stress resulting from the CPLT, a non-linear Finite Element Method (FEM) solution must be performed. This required a constitutive model which could describe the inelastic behaviour of D6ac steel under cyclic loading. Plasticity models available in existing FEM packages have proved inadequate [2].

In recent years at AMRL a state variable based constitutive model, based on the Ramaswamy-Stouffer-Bodner formulation [3,4,5], has been developed to predict the cyclic dependent, non-linear elastic-viscoplastic behaviour of D6ac steel. The model consists of a set of highly non-linear ordinary differential equations. This state variable model has subsequently been written in the form of a material module for the general purpose Finite Element Program PAFEC [6]. The implementation has been refined by using an analogue of the tangent stiffness approach (instead of initial stiffness) for

¹ Load on the wing is expressed as a percentage of the maximum upload wing root bending moment during CPLT.

iterating to the correct element stiffness matrix in plastically deformed elements. This has significantly reduced the run times for achieving structural convergence [7].

4.1.2. The Constitutive Model

The unified constitutive model developed by Ramaswamy, Stouffer and Bodner [3,4] consists of the inelastic flow equation and the rate forms of the state variables; back stress Ω_{ij} , and drag stress Z . In this formulation the inelastic flow equation is written as;

$$\dot{\epsilon}_{ij}^I = D \exp \left[-\frac{A \left(\frac{Z^2}{3K_2} \right)^n}{2} \right] \frac{(S_{ij} - \Omega_{ij})}{\sqrt{K_2}} \quad (1)$$

where $\dot{\epsilon}_{ij}^I$ is the inelastic strain rate tensor, S_{ij} is the deviatoric stress tensor and D , A and n are temperature and strain rate dependent material parameters. For D6ac, at room temperature, $D=10000$, $A=1$ and $n=3.0$. Here the second invariant of the effective deviatoric stress tensor (K_2) is defined as;

$$K_2 = \frac{1}{2} (S_{ij} - \Omega_{ij}) (S_{ij} - \Omega_{ij}) \quad (2)$$

and the evolution equation for the back stress Ω_{ij} is;

$$\dot{\Omega}_{ij} = f_2 S_{ij} + \dot{\Omega}_{ij}^I \quad (3)$$

where the inelastic back stress $\dot{\Omega}_{ij}^I$ is calculated from,

$$\dot{\Omega}_{ij}^I = f_1 \dot{\epsilon}_{ij}^I - \frac{3}{2} f_1 \frac{\Omega_{ij}}{\Omega_{\max}} \dot{\epsilon}_{\text{eff}}^I \quad (4)$$

where $\dot{\Omega}_{ij}^I$ is the inelastic back stress rate and the drag stress Z is given by,

$$Z = Z_1 + (Z_0 - Z_1) \exp(-m_0 \sigma_y \dot{\epsilon}_{\text{eff}}^I) \quad (5)$$

Details of the techniques used to evaluate the constants f_1 , f_2 , Ω_{\max} , Z_0 , Z_1 , m_0 and σ_y are given in the next section.

4.1.3. D6ac Material Constant Derivation

To develop an inelastic constitutive model, experimental data on D6ac steel are required. This section describes a series of uniaxial tension/compression tests performed on cylindrical specimens to help

understand the material behaviour under cyclic plastic loading, and to provide data for the development of the required constitutive model constants.

Several testing programs have been conducted over the past 15 years at AMRL aimed at characterising D6ac steel at strains ranging between 15,000 $\mu\epsilon$ and 20,000 $\mu\epsilon$ compression. The most recently completed test program [7] has improved the material characterisation tests by refining specimen alignment and gripping techniques in the testing machine. It was recognised that the current specimen design did exhibit slight bending at the high strain levels and this was taken into account in the development of the constants. Each test program has repeatedly demonstrated that;

1. At strain values in the order of 20,000 $\mu\epsilon$ D6ac is not fully saturated to a flat stress-strain curve in tension or compression, and
2. D6ac cyclically converges to a stable hysteresis loop within the first or second cycle whether it be a symmetric tension/compression cycle or a CPLT cycle that was applied.

The results from the current test program are being used to determine the constants required for the constitutive model. Initially first estimates of the constants are generated by rearranging the equations 1 to 5 above, [see 6]. These initial estimates are then supplied to a computer program that uses a perturbation technique to approach a set of final values which would accurately reproduce the material behaviour observed in the experimental test.

The stress vs strain produced by the current test program can be seen in Figures 10 and 11 where both tension-compression cycles and CPLT cycles of varying amplitudes were applied. Figure 10 includes a comparison between the experimental and numerical model prediction for tension and compression. Final cyclic constant determination is in progress.

4.2. F-111 FFFVH#13 Finite Element Analyses

4.2.1. Introduction

AMRL has developed FE models (FEMs) that investigate the effects of CPLT on problem areas in the F-111 WPF. The initial full wing F-111 FEM used as a starting base was obtained from General Dynamics (now LMTAS) some years ago [8]. This FEM has since been refined to represent the detail of the main titanium web and local stiffener number 3 more accurately in the vicinity of FFFVH#13. The calibration of this model and subsequent local sub-structures will be performed using data from the full-scale wing tests.

4.2.2. FE Model Description

The procedure adopted was to use the LMTAS's full wing FE model to obtain an accurate set of boundary conditions for the detailed FFVH#13 FE sub-structure model. This full wing model includes a stub-section of the wing as shown in Figure 12. AMRL incorporated the following improvements into the original full wing FE model:

1. A detailed FFVH#13 FE sub-structure model was constructed and inserted into the local region.
2. Titanium Web improvements;
 - a) A missing boss was included,
 - b) The web thickness distribution was made identical to the AMRL test wing,
 - c) The web was displaced by 5.3 mm from the plane of the stiffener.
3. Stiffener - Web links were improved to represent bolts.
4. Rotational degrees of freedom of all stiffeners were reacted at the plates.
5. Some element discontinuities found in the original model were fixed.
6. Upper plate FFVH#13 region was represented by two or more 3D elements through the thickness.

The modified full wing FE model contains 12,613 nodes, 5,994 elements and 51,273 degrees of freedom. The model consists of a combination of beam, 2D shell and 3D isoparametric elements. In addition, the inserted region contains elements with mid-side nodes.

The effect of incorporating the AMRL detailed FFVH#13 sub-structure model into the LMTAS full wing model resulted in a more accurate representation of the local region's stiffness. This one enhancement allowed the correct strain gauge calibration of the stiffener number 3 region, the results of which are shown in the following section. It should be noted that this combined model was too large to perform the required detailed plasticity analysis and therefore the AMRL sub-structure model alone was employed for that purpose.

The final FFVH#13 FE sub-structure model has 9,286 nodes, 2,564 elements and 33,882 degrees of freedom. In this model there are only 2D shell and 3D isoparametric elements which contain mid-side nodes. The region extracted consists of the section of the upper plate between stiffeners number 2 and 4 and including stiffener number 3. The titanium web was not included as all bolt loads are applied to the sub-structure by the displacement fields at the required locations. The displacement field applied to the outer boundaries of the sub-structure FEM are directly determined from the full wing model.

Figures 13 and 14 show the mesh and boundary conditions applied respectively.

4.2.3. Calibration Results

Calibration of the full wing FEM consisted of ensuring that the plate strains, web strains and stiffener number 3 strains all correlated to full scale test results previously discussed. Detailed calibration results were obtained for the inner and outer surfaces of the upper plate, stiffener # 3, and the inside surface of the lower plate. For the rosette gauges (77 to 84 in Figure 6) the principal strains were calculated and compared with those produced by the full wing FEM. The results can be seen in Table 2.

The boundary conditions from full wing calibrated model were then applied to the FFVH#13 sub-structure FE model in an elastic analysis. In addition to matching the far-field strains, this FEM was required to represent the strain distribution in the upper and lower corners of FFVH#13. It was recognised that the exact distribution of strain in this region is critically dependent upon the accuracy with which the geometry had been represented. The results of this calibration can also be seen in Table 2, and Figure 15 shows a comparison between test and FEM results for the strains around the upper and lower corners of FFVH#13. Figure 15 indicates that the local mesh density at the location of peak strain is not sufficient to represent the high variation in strain and refinement of this region is underway. This refinement should produce an increase in the predicted strains by the FEM.

The correlation between the full scale test results and the FEM elastic analysis is generally within 5% for far-field locations which indicates that the numerical predictions are in good agreement with experiment.

4.2.4. DADTA Phase

The section above has shown that the FEM analyses are representing the complex strain distributions around FFVH#13 accurately. These models can now be used to analyse the FFVH#13 re-worked geometries outlined in Ref.1 (Figure 2). The unified constitutive model will be applied to determine the associated stress states that are generated during CPLT. On completion of this work AMRL will be performing a geometric parametric study (similar to that performed on Stiffener Runout Number 2 in Ref. 2) on parameters such as local plate thickness, stiffener thickness, location of FFVH#13 from cross web along stiffener 3. Specific parameters will be determined from RAAF F-111 fleet studies currently underway. This study will indicate whether differences in

geometry between aircraft will have a significant effect on the stress and strain state at the critical FFVH#13 location. The resultant stress and residual stress analyses will be used provide an upper and lower inspection interval range.

5. CONCLUSION

AMRL has successfully developed a FE model of FFVH#13 in the F-111 wing pivot fitting. The solution process uses a sophisticated constitutive model of D6ac steel plastic behaviour through the CPLT cycles. The model has been calibrated against full-scale wing test data and has been shown to accurately predict the strain distributions in the corners of FFVH#13. However, the model has been shown to need further refinement in the critical lower inboard corner in order to accurately capture the peak strain.

References

1. Keays R. H., Molent L. and Graham A. D., 'F-111 wing pivot fitting: finite element analysis of rework of fuel flow vent hole # 13', ARL-STRUC-TM-557, Aeronautical Research Laboratory, D.S.T.O. Melbourne, Australia, July 1992.
2. Paul J., McCabe G. and Horrigan D., 'F111 Stiffener Runout #2 Parametric Study', Aeronautical and Maritime Research Laboratories, 1993.
3. Ramaswamy V.G., 'A Constitutive Model for the Inelastic Multiaxial Cyclic Response of a Nickel Base Superalloy Rene'80', A dissertation submitted to the Department of Aerospace Engineering and Engineering Mechanics College of Engineering, Division of Graduate Education and Research, University of Cincinnati, In partial fulfillment of the requirement for the degree of Doctor of Philosophy, 1985.
4. Ramaswamy V.G., Stouffer D.C. and Laflen J.H., 'A Unified Constitutive Model for the Inelastic Uniaxial Response of Rene'80 at Temperatures Between 538C and 982C', ASME Journal of Engineering Materials and Technology, Vol.112, 280-286 July, 1990.
5. Bridgford N., 'A Summary of the Bodner-Stouffer Constitutive Model', ARL-STRUC-TM-513, Aeronautical Research Laboratory, D.S.T.O. Melbourne, Australia, May 1989.

6. Paul J., Bridgford N. and Stouffer D.C., 'Progress Report on the Implementation of a Constitutive Model into the PAFEC Finite Element Package', ARL-STRUC-TM-529, AR-006-096, 1990.
7. Searl A., Trippet B., Paul J., 'Constitutive Model Development and Validation Testing for D6ac Steel', Aeronautical and Maritime Research Laboratories, 1993, (In press).
8. Molent L. and Jones R., 'Stress analysis of a boron/epoxy reinforcement for the F-111C wing pivot fitting', ARL-STRUC-REP-426, Aeronautical Research Laboratory, D.S.T.O. Melbourne, Australia, May 1987.

Table 1: F-111 Wing Test Load Cases

Case no.	Dir ^a (+ or -)	Max. Load (%CPLT)	Sweep Angle (deg.)	Maximum Load (kN)						DAS set
				E	F	G	H	I	J	
1	-	60	16	75.66	43.68		62.73			II
2	-	60	16	75.66	43.68		62.73			I
3	+	60	16	62.02	79.19	75.09	79.19	12.30	18.96	I
4	+	60	16	62.02	79.19	75.09	79.19	12.30	18.96	II
5	+	60	44	62.02	79.19	75.09	79.19	12.30	18.96	II
6	+	60	44	62.02	79.19	75.09	79.19	12.30	18.96	I
7	-	60	44	82.93			62.73			I
8	-	60	44	82.93			62.73			II
9	-	60	26	75.66	43.68		62.73			II
10	-	60	26	75.66	43.68		62.73			I
11	+	60	26	62.02	79.19	75.09	79.19	12.30	18.96	I
12	+	60	26	62.02	79.19	75.09	79.19	12.30	18.96	II
13	+	60	56	62.02	79.19	75.09	79.19	12.30	18.96	II
14	-	60	56	82.93			62.73			II
15	-	100	56	138.22			104.56			I
16	+	100	56	103.36	131.98	125.15	131.98	20.50	31.60	I
17	-	100	26	126.11	72.81		104.56			I
18	+	100	26	103.36	131.98	125.15	131.98	20.50	31.60	I

**Table 2 : COMPARISON BETWEEN FE CALIBRATION RESULTS AND
EXPERIMENTAL TEST DATA**

GAUGE No.	EXPERIMENTAL TEST DATA ($\mu\epsilon$)	LMTAS FULLWING MODEL ($\mu\epsilon$)	FFVH # 13 SUBSTRUCTURE MODEL ($\mu\epsilon$)	DESCRIPTION
38	-4765	-4474	-4500	Outer surface upper WPF, Stiffener No. 3
39	-4409	-4265	-5019	Outer surface upper WPF, Stiffener No. 3
40	-4335	-4260	-4139	Outer surface upper WPF, Stiffener No. 3
91 P1	2399	2116	2197	Mid bay inner surface upper WPF
91 P2	-4334	-4256	-4151	Mid bay inner surface upper WPF
92 P1	2269	2248	2350	Mid bay inner surface upper WPF
92 P2	-4231	-4117	-4254	Mid bay inner surface upper WPF
77/81 P1	1810	1643	1579	Inboard of and below FFVH # 13
77/81 P2	-5523	-4647	-4623	Inboard of and below FFVH # 13
78/82 P1	1768	1783	1699	Directly below FFVH # 13
78/82 P2	-4967	-4823	-4736	Directly below FFVH # 13
79/83 P1	1193	1652	1484	Outboard of and below FFVH # 13
79/83 P2	-3385	-3887	-3735	Outboard of and below FFVH # 13
80/84 P1	958	1812	1194	Directly Below FFVH # 14
80/84 P2	-3838	-4702	-3961	Directly Below FFVH # 14
72-1	-13180		-9200	FFVH # 13 Lower inboard corner
72-2	-16353		-13500	FFVH # 13 Lower inboard corner
72-3	-21549		-18000	FFVH # 13 Lower inboard corner
72-4	-17316		-13200	FFVH # 13 Lower inboard corner
72-5	-7047		-2500	FFVH # 13 Lower inboard corner
73-1	-11766		-10800	FFH # 13 Upper outboard corner
73-2	-12385		-12100	FFH # 13 Upper outboard corner
73-3	-11649		-12200	FFH # 13 Upper outboard corner
73-4	-7477		-8800	FFH # 13 Upper outboard corner
73-5	-1249		-2700	FFH # 13 Upper outboard corner

P1 : Principle Stress Direction 1
P2 : Principle Stress Direction 2

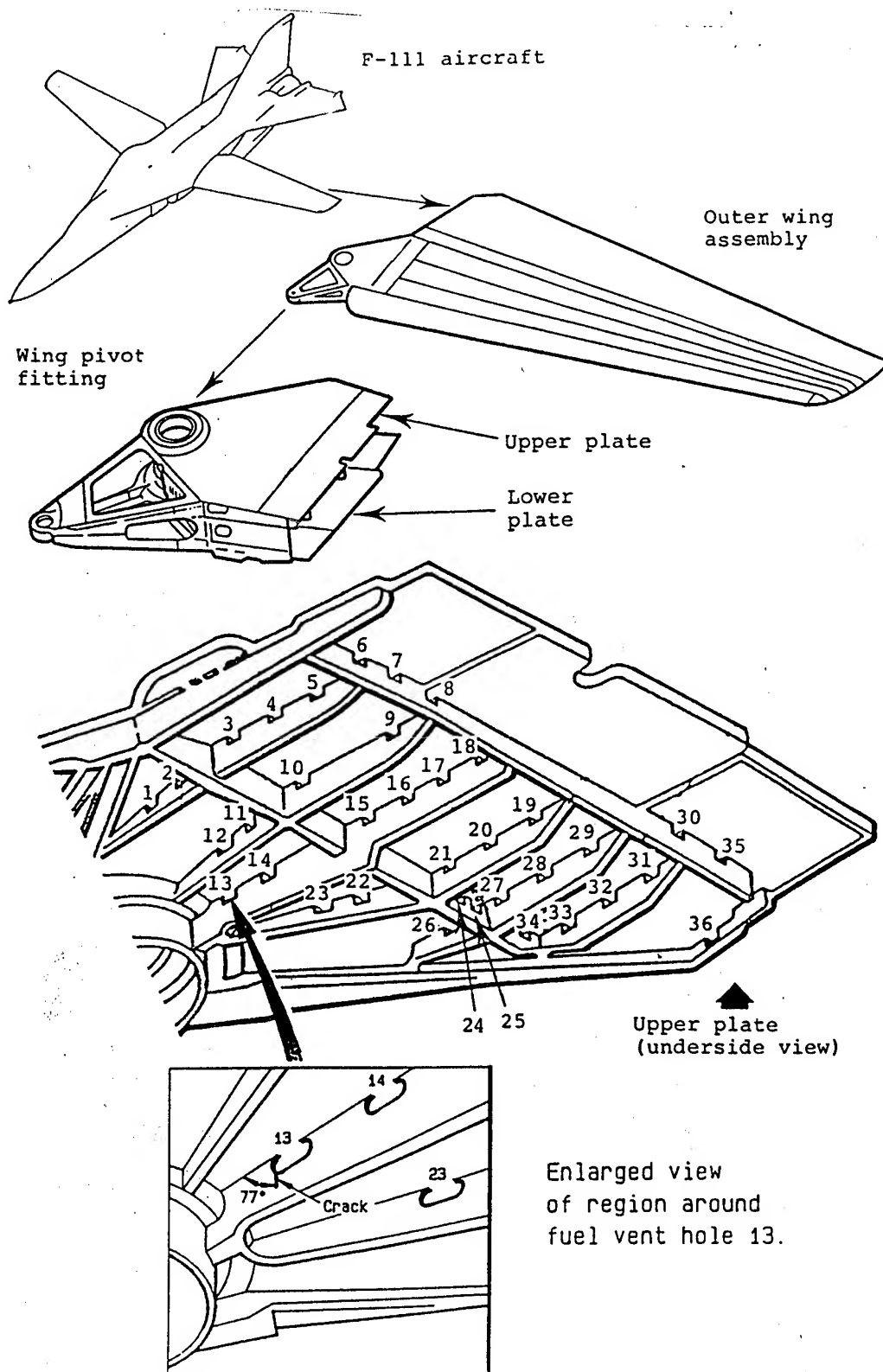


Figure 1: FFWH#13 Location

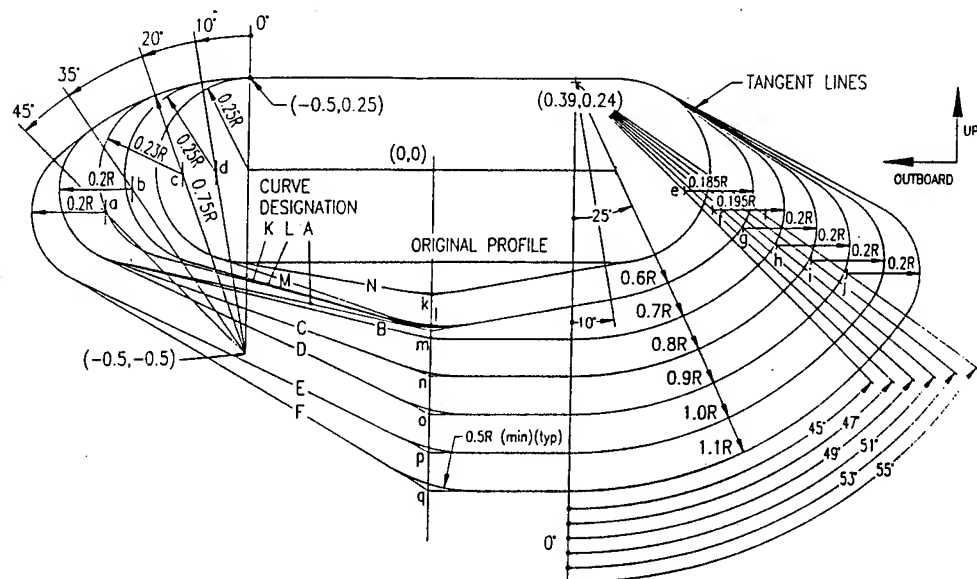


Figure 2: FFVH#13 Rework Profiles

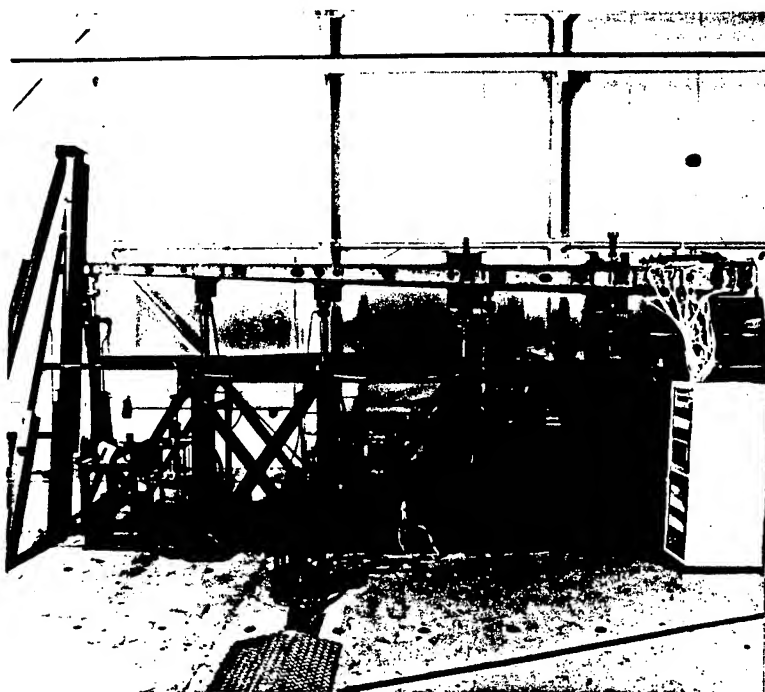


Figure 3: AMRL F-111 Wing Test Rig

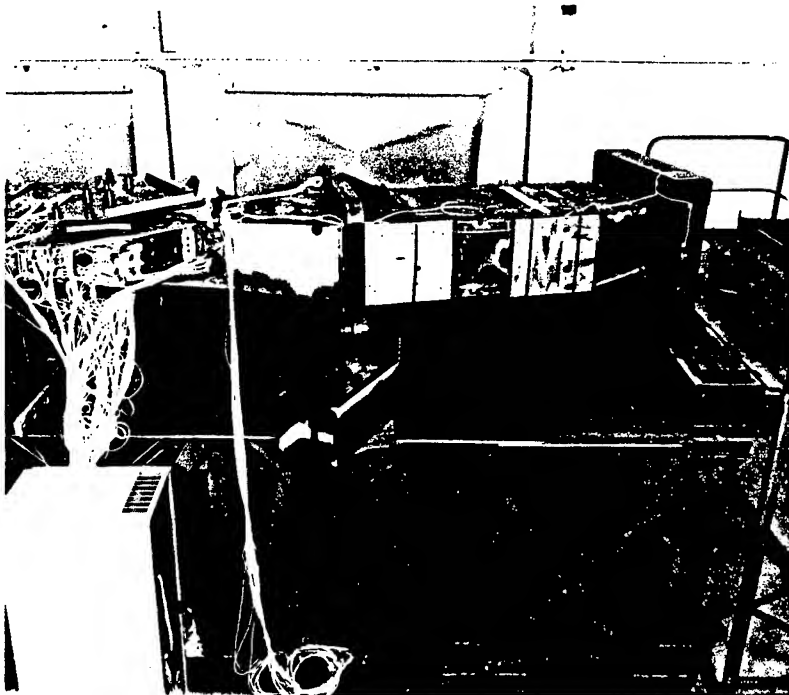


Figure 4: Variable Wing Sweep Mounting

Note: Test wing is a R11 wing

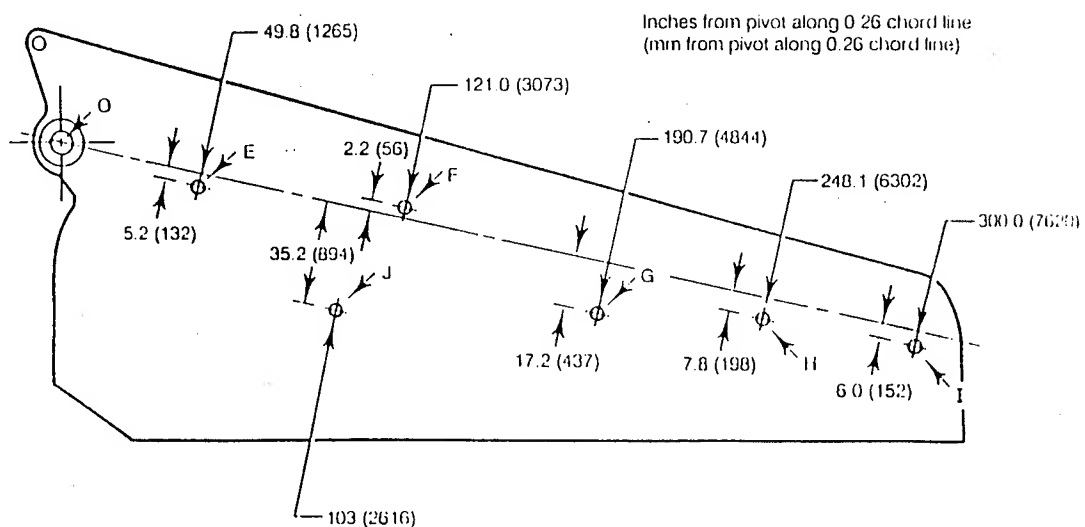


Figure 5: Location of F-111 Wing Loading Actuators

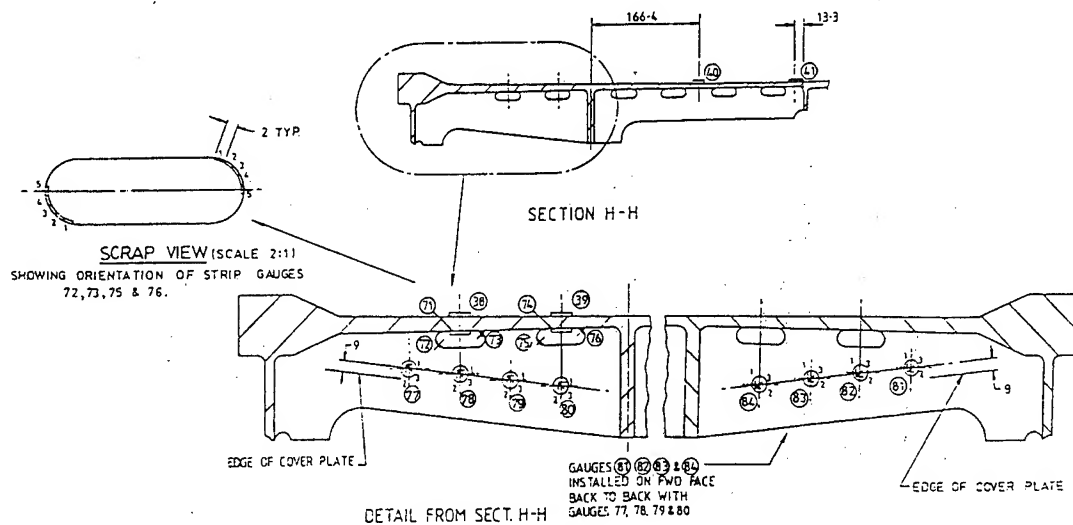


Figure 6: Strain Gauges Around FFFVH#13

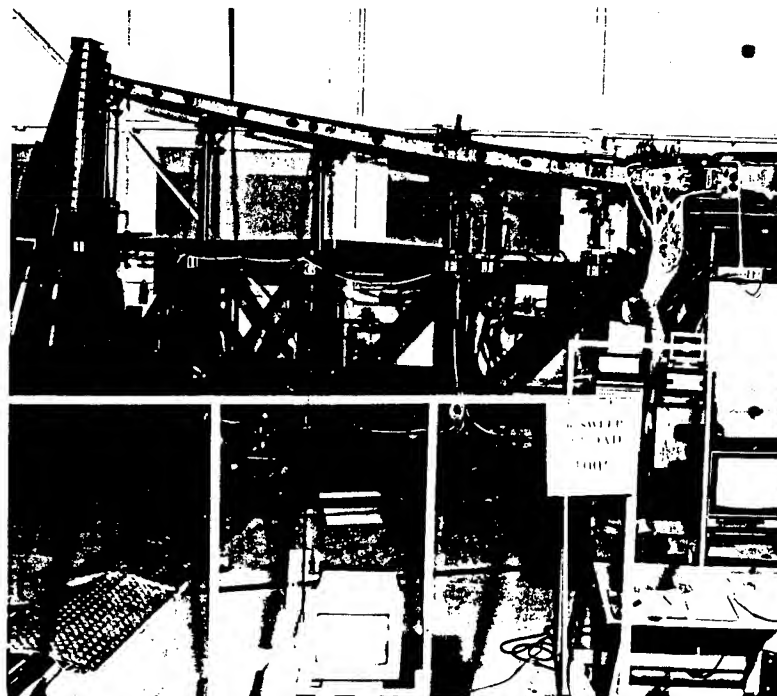


Figure 7: Wing Deflection at Maximum Upload, 56° Sweep

FUEL FLOW VENT HOLE #13 STRAIN DISTRIBUTION (100% CPLT)

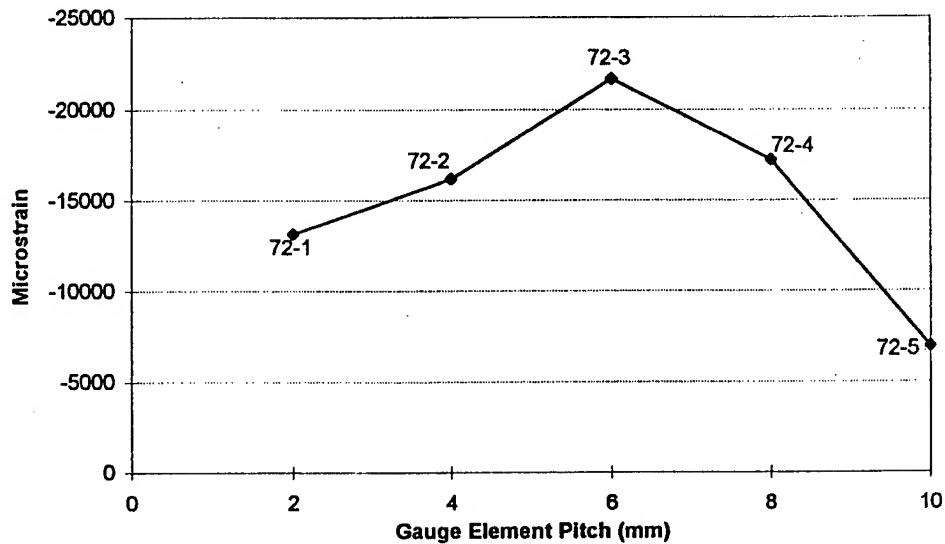


Figure 8: FFVH#13 Strain Distribution

FUEL FLOW VENT HOLE #13 PEAK STRAIN - CPLT HISTORY

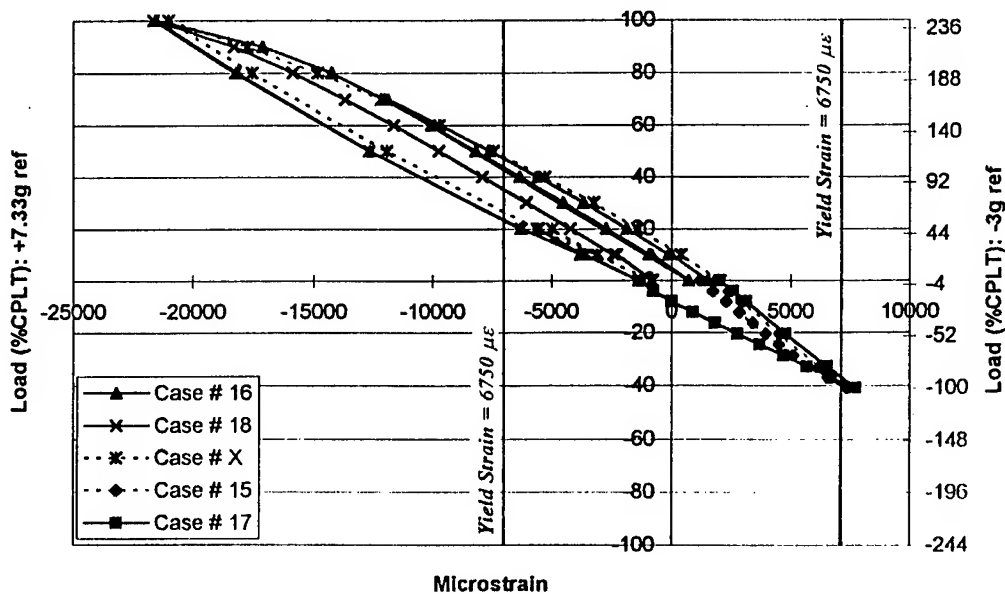


Figure 9: FFVH#13 Peak Strain History Through CPLT

FIGURE 10 : COMPARISON OF CALCULATED AND EXPERIMENTAL
MONOTONIC TENSION/COMPRESSION RESPONSE FOR D6AC STEEL

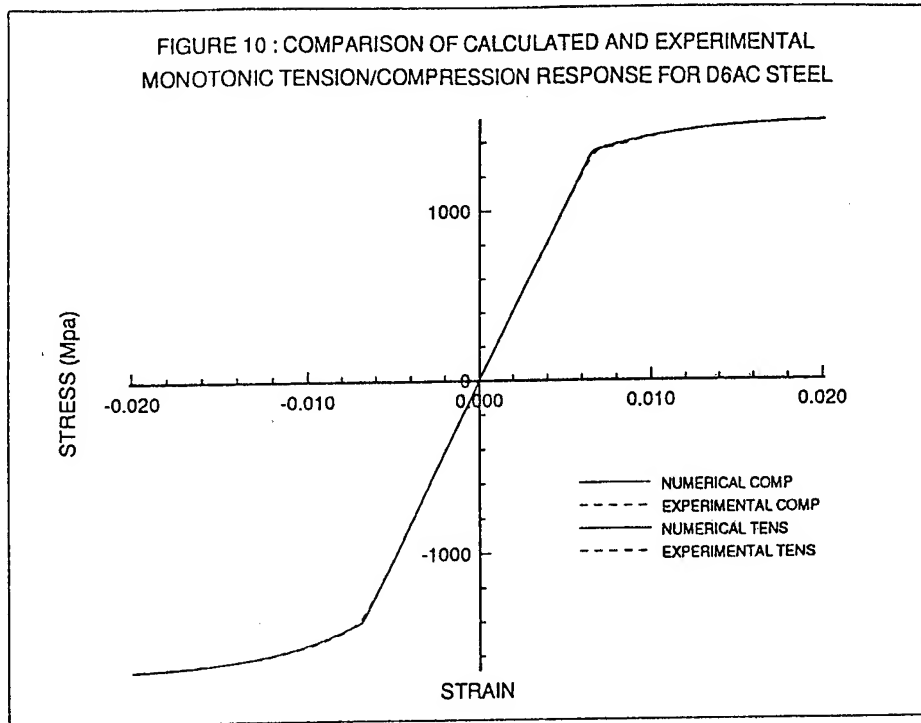


FIGURE 11 : VARIOUS CPLT CYCLE TEST
TEST D6AC STEEL

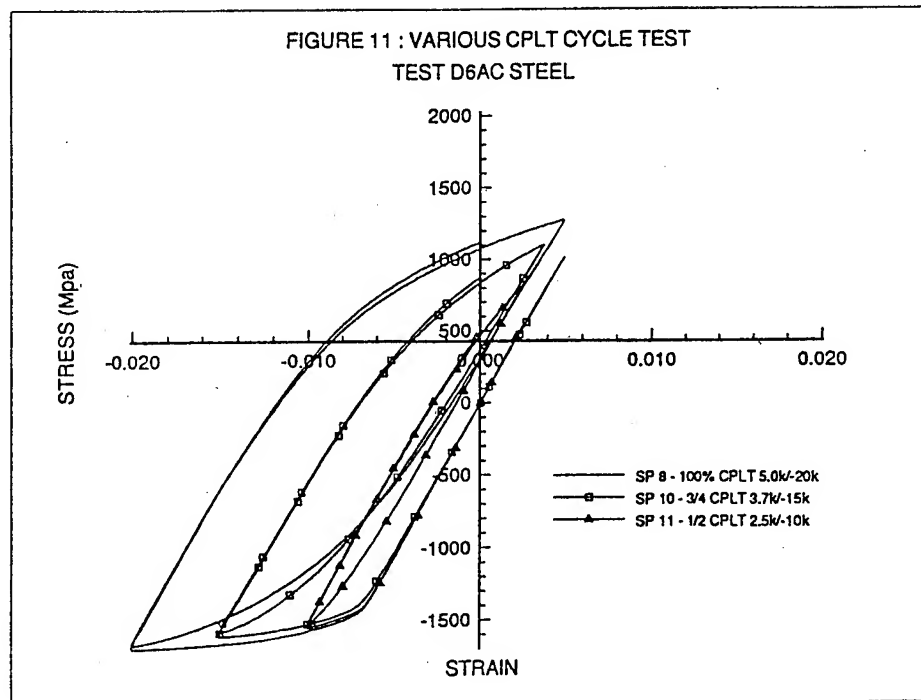
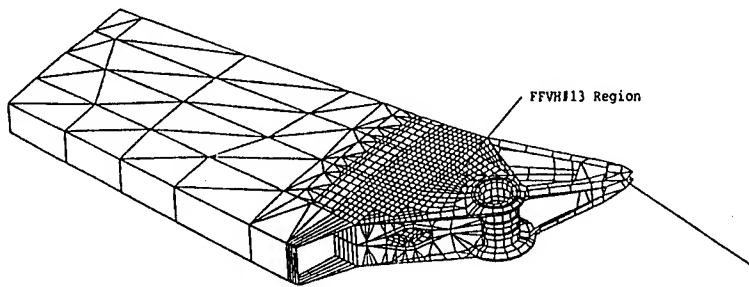
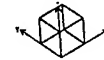


Figure 12: F-111 Full Wing FEM



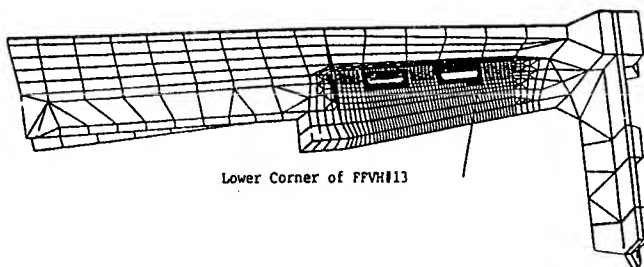
LINEAR
STATICS

ROTATION
X = 315
Y = 30
Z = 30



TITLE

Figure 13: FFVH#13 Sub-Structure FEM

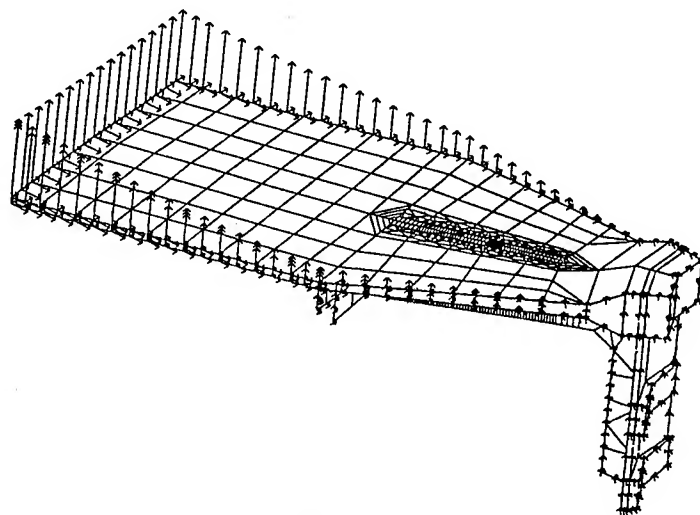


LINEAR
STATICS

ROTATION
X = 345
Y = 6
Z = 4



TITLE



LINEAR
STATICS

ROTATION
X = 30
Y = 345
Z = 345

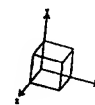
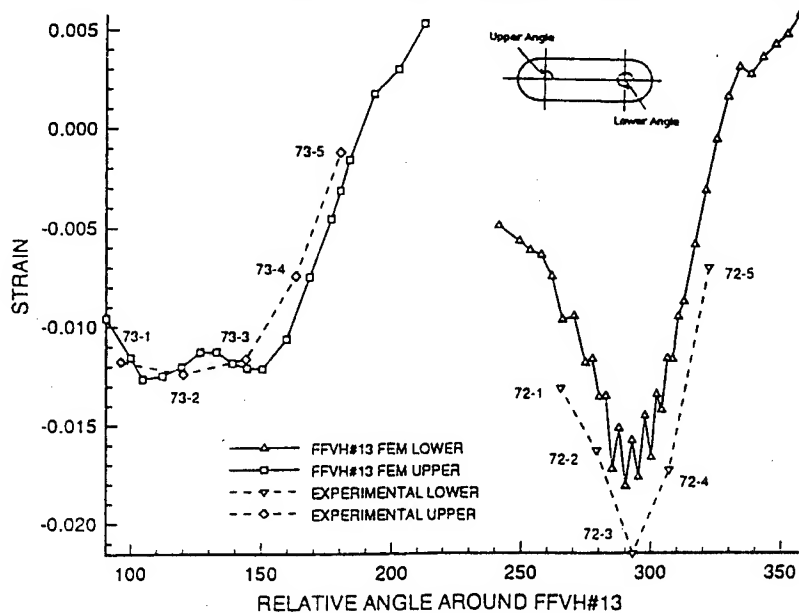


Figure 14: FFVH#13 Sub-Structure

Boundary Conditions Applied
Bolt Displacements not displayed

TITLE

FIGURE 15 : Comparison between Experimental Data and FEM for FFVH#13



RNZAF Project KESTREL

Wing Commander M.G. Pobog Jaworowski

***Squadron Leader J.L.P. ten Have**

Air Staff

HQ NZ Defence Force

Private Bag

Wellington, 6000

New Zealand

jtenhave@canard.central.co.nz

Project Kestrel is the P-3 structural component replacement and Refurbishment Program which the Royal New Zealand Air Force (RNZAF) have begun to implement across their fleet.

Project Kestrel was conceived in 1989 during a review of the structural life of the RNZAF P-3 fleet. The RNZAF had developed the ability to automatically process the raw exceedance data obtained from the fatigue meters fitted to each RNZAF P-3 aircraft. About 12 000 hours of raw fatigue meter data, which represented about 20 percent of all RNZAF P-3 flights was analysed and the results were plotted against the known exceedance spectra of the USN and RAAF fleets.

As expected, but previously unproven, RNZAF P-3 exceedance usage in the Nz (normal axis) was found to be as severe as that of the RAAF, and twice as severe than that of the USN. That is, a USN P-3 which has flown 15 000 airframe hours would be only half as fatigue damaged as a RNZAF P-3 which had flown the equivalent number of airframe hours. This finding meant the RNZAF suddenly discovered that it was operating the worlds most fatigue damaged P-3s. In 1989 the estimated RNZAF P-3s Fatigue Life Index was greater than 110.

A further 8 000 hours of raw fatigue meter data have been processed, increasing our useful usage database to about 20 000 hours. This additional

analysis confirmed our original finding and the RNZAF remained world leaders in terms of P-3 fatigue damage accrual. The concern raised by the awareness of advanced airframe life was compounded by the recent completion of an extensive and successful avionic upgrade across the fleet.

A detailed discussion of the high rate of "g" accrual is beyond the scope of this paper and the mechanisms are not fully understood. Likely contributing factors are:

- a. a small P-3 fleet;
- b. full fleet utilisation; and
- c. operation from a remote land-mass in the South Pacific.

Significantly, the high rate of fatigue damage in our P-3 fleet mirrors the experience with other RNZAF aircraft types.

A brief outline of RNZAF funding is required to understand the logic used to proceed with Project Kestrel. New Zealand is not a rich nation in monetary terms. Our annual Defence vote in all activities is just over one billion New Zealand dollars or, less than the capital cost of one B2 bomber. It follows that all procurement action associated with New Zealand Defence equipment is ruthlessly scrutinised by Defence, Treasury and others. Projects which can not be shown to have the lowest life cycle cost or are not related to the production of Defence outputs are usually deferred for further study or eliminated.

Project Definition

This climate of financial constraint prevailed when the RNZAF considered its options with the P-3K in 1989. We had the oldest, predominantly lightweight, most fatigue damaged P-3s in the world. There was little available money for capital procurement and, according to the latest Government review of New Zealand's Defence needs, the provision of Maritime surveillance remained high on the list of Government priorities.

A complete, full scale fatigue test to a representative service spectrum has never been conducted on a P-3 but concerns for the safety of RNZAF P-3 aircraft were not immediate. The RNZAF conducted its own Depot level maintenance of its P-3 aircraft. The aircraft were serviced to a high standard and the structural

condition of each airframe was well known. Additionally, RNZAF has remained abreast of the technology associated with P-3 Service Life Extension Programs, (SLEPs). The RNZAF has yet to observe significant fatigue damage in the known fatigue sensitive areas.

Significant caution was appropriate as the RNZAF had embodied numerous repairs to ameliorate the effects of corrosion, particularly in the outer wings, horizontal stabilisers and engine nacelles. The number and complexity of these repairs has been steadily increasing and continued, long term structural integrity was less certain.

Age and fatigue damage accrual continued to increase. The attendant structural change, due to repair, diminished confidence that the available SLEP technology remaining a valid means of determining where fatigue cracks might develop. In spite of the uncertainty, a new aircraft was and is beyond New Zealand's means. For this reason, alternative means of restoring the structural integrity, for ten to fifteen years, were examined.

Three options for maintaining the long term structural airworthiness of the RNZAF P-3K fleet seemed available:

- a. Option 1: Keep the current airframes and invest heavily in a P-3 structural analysis capability so as to accomplish a Durability and Damage Tolerance type analysis on each individual airframe structural configuration;
- b. Option 2: Buy a completely new P-3 aircraft shell and reuse the Avionics and Engines from the existing aircraft; or
- c. Option 3: Replace the fatigue critical major structural components of the existing airframes so as to eliminate any long term fatigue risk.

Option 1 was financially attractive compared to the other two options. However, the following disadvantages outweighed the apparent savings:

- a. The risk of a significant fatigue related structural defect was not eliminated, particularly as repairs are embodied upon repairs;
- b. The manhour content of the existing P-3K depot level maintenance activity would continue to rise; and

c. Aircraft availability was expected to decrease over the 10 to 15 year period as the effects of corrosion demanded more analytical effort and repair time.

Option 2 eliminated the disadvantages of Option 1 but, considering the unique RNZAF P-3K aircraft configuration, this option proved relatively expensive for six aircraft over a 20 year life. This option was rejected because of cost.

Option 3 was eventually considered viable if, as a minimum, the outer wings and horizontal stabilisers were replaced and the reworked aircraft was left in RNZAF service for a further 20 years. This option was financially and technically unattractive if the wing center section needed to be replaced. Fortunately, the wing center section and the fuselage were not considered fatigue critical.

Phase 1 Technical Feasibility study

RNZAF Project Kestrel gathered real momentum in 1992. A contract was signed with Lockheed to determine the technical feasibility of fitting new P-3C outer wings and horizontal stabilisers to our existing five P-3B lightweight and one P-3B heavyweight aircraft. A team of RNZAF Engineers assisted Lockheed with the study, which was conducted at the Marietta plant over the period 21 January to 3 March 1993. The findings of the Phase 1 study have been published under Lockheed Report LG93ER0026 of 30 April 1993. This report contains information which is the joint property of the New Zealand Government and Lockheed. The Phase 1 study was based on the following assumptions:

- a. The study must assume a further 20 year aircraft life;
- b. As a minimum, the outer wings and horizontal stabilisers will be replaced;
- c. The original aircraft landing gear was retained;
- d. The current operational weight limits for the P-3K lightweight aircraft were retained;
- e. A fuel dump capacity will be added to the No 5 tank (five P-3B lightweight aircraft only);
- f. The new outer wing must be capable of accepting a wing tip fitted with an ESM antenna;

- g. The production P-3C fuselage to outer wing fillet panel upper surface dome nut installation must be replaced with a modified installation to completely eliminate the dome nuts;
- h. Current RNZAF P-3K usage would remain indicative of the next 20 years usage; and
- i. The wiring of the wings and horizontal stabiliser will be replaced.

Wing Center Section and Outer Wing

The importance of the wing center section became obvious from the beginning of the study. The retention of the complete light weight wing center section posed a problem which was not fully appreciated during the initial RNZAF study of option 3. An additional risk emerged because there was no hard service history nor fatigue test data which could be used to prove that the existing wing center section could last for a further 20 years. This risk could be significantly reduced by the replacement of the center section lower plank assembly in conjunction with the outer wing. The decision to change the wing center section lower plank assembly achieved the following advantages:

- a. Concern with the wing center section fatigue is almost completely eliminated. The lower surface is the tension member;
- b. Production P-3C BL 65 straps can be utilised on the lower tension surface, thereby obviating the need for an expensive, RNZAF unique, lower strap design, and
- c. A P-3C production outer wing BL 65 bulkhead can also be utilised.

Stress levels in the wing center section rear spar, upper plank assembly and rib/truss assemblies are low and are considered unlikely to cause a fatigue problem in the next 20 years. The same degree of assurance was not obvious for the center section front spar. Although the RNZAF believed that the front spar is unlikely to require rework for a further 20 year service life, a full fatigue analysis of this structure has been carried out to quantify the risk. This analysis was conducted as part of the Phase two study effort.

Three minor modifications are required to install a production P-3C lower plank assembly to a P-3B lightweight wing center section. These modifications are :

- a. The BL 65 upper straps require a new profile to account for the increased end tab thickness of the P3C planks. A proposed configuration was determined such that the reprofiled straps are symmetrical and do not alter the existing load path across the BL 65 joint. Lockheed and the RNZAF agreed that this new strap did not need structural testing
- b. The interface of the P3C No 9 planks with the rear spar must be milled down to a P-3B lightweight thickness so that the new lower plank assembly can be accommodated within the existing P-3B lightweight wing center section contour. Once again, Lockheed and the RNZAF agree that this modification does not need structural testing.
- c. Subsequent analysis has resulted in the replacement of the front center spar lower boom. By reinstalling this member slightly higher than the original, the No 1 Plank could be fitted without modification.

Given a new P-3C wing center section lower plank assembly with the three minor modifications, the installation of a new P-3C outer wing onto an existing P-3B lightweight fuselage is relatively straight forward. With the exception of the upper surface dome nuts, a standard P-3C outer wing will be utilised for the project.

There was one further complication with outer wings. New nacelles were not currently being manufactured. The Phase I study confirmed that the existing P-3B lightweight nacelles could be installed onto the new P-3C outer wings. To this end, the appropriate tooling has been developed to remove and install the nacelles. The nacelles are being structurally refurbished during the outer wing replacement effort.

Horizontal stabiliser

The Phase 1 study concluded that the installation of a P-3C horizontal stabiliser onto a P-3B lightweight fuselage could be effected without any modifications. Tooling to accomplish the replacement of the stabiliser in one piece has been identified. As with the wing center section components, Lockheed

and the RNZAF agreed that the new horizontal stabiliser installation does not need structural testing.

The Fuselage

The empennage has been assessed as being capable of achieving the desired life extension. However, as with the wing center section, very little hard service facts or fatigue test data exists to prove beyond doubt that the remainder of the fuselage could, in fact, last a further 20 years. Accordingly, a fatigue analysis of a point in the fuselage believed to experience the highest stress was undertaken as part of the Phase 2 study effort. This point is the fuselage crown just aft of the wing and loading in the form of both pressurisation and aircraft manoeuvre is being considered. Interestingly enough, previous P-3 SLEP analyses have not included manoeuvre loads during fuselage fatigue calculations (fatigue was based on pressurisation loading alone). No fatigue problem was indicated by the analysis.

Phase 2 Technical Feasibility study

Although the Phase 1 study determined that the replacement of the outer wings, horizontal stabiliser and wing center lower plank assembly could be accomplished with little technical risk and without undue expense, a Phase 2 study effort was embarked upon and was completed in December of 1993. The aim of the Phase 2 study, which was conducted jointly by Lockheed and the RNZAF, was to determine:

- a. what components, if any, of the wing center section front spar and crown of the fuselage (just aft of the wing) need to be replaced in order to achieve a 20 year life extension of the RNZAF P-3K aircraft;
- b. the best installation approach for the wing center section lower surface and the horizontal stabiliser;
- c. the spares required to effect a limited structural (non-cosmetic) refurbishment of the nacelles;
- d. a modular work-task based project plan for the overall work activity;
- e. the identification of the long lead-time materials in the new outer wings, horizontal stabilisers, wing center section lower plank assembly, No 5 Fuel Dump modification kit and a host of miscellaneous support parts; and

- f. a budgetary cost for the project.

The engineering design activity will be completed in May 1996 and fabrication of hardware has begun. The fatigue analyses are very conservative and are indicative of the expected service life of our P-3K aircraft. The cost of the entire project and the detail of where the project might be accomplished has yet to be finalised.

Summary

RNZAF Project Kestrel had the aim of extending the service life of the RNZAF P-3K in an environment where New Zealand's Defence expenditure is limited.

As at November 1995 :

- a. the Interim Engineering Design Technical Review has been completed;
- b. the Engineering Design is due to be complete in May 1996;
- c. hardware production has been initiated;
- d. the hardware integration contractor selection process has begun
- e. the nacelle refurbishment tooling contract is underway.

The replacement of the existing outer wings, horizontal stabilisers and wing center section lower plank assemblies as well as the refurbishment of the nacelles appears a low risk and relatively inexpensive means of achieving that aim.

Application of Object Technology to an Aircraft Structural Integrity Program
FAA Flight Inspection Learjet Model 60
and Canadair Challenger CL601-3R aircraft

Tim Kelley
E-Systems
Greenville Division
P.O. Box 6056
Greenville, TX 75403-6056

Abstract

E-Systems is currently under contract with the FAA to develop and implement an Aircraft Structural Integrity Program (ASIP) for the Learjet Model 60 (Figure 1) and the Canadair Challenger CL601-3R (Figure 2) aircraft being acquired for the FAA Flight Inspection Fleet. The program for each aircraft type is based on damage tolerance/ fracture mechanics methodology and consists primarily of a Durability and Damage Tolerance Assessment (DADTA), an Individual Aircraft Tracking Program (IATP), a Loads/Environmental Spectra Survey (L/ESS), and a Fleet Structural Maintenance Plan (FSMP). An ASIP Master Plan integrates all of the above elements into a cohesive structural integrity program..

Learjet and Canadair, as subcontractors to E-Systems, are performing the DADTA and submitting data packages to E-Systems in support the IATP, L/ESS, FSMP and ASIP Master Plan tasks. E-Systems is concentrating on the IATP and L/ESS tasks while integrating the subcontractor input for the FSMP and ASIP Master Plans.

The IATP will be automated largely in software by the application of Object Technology to the IATP and L/ESS tasks. The final software set is required to read, store and process flight recorder data from all Learjet Model 60 and Canadair Challenger CL601-3R aircraft in the FAA Flight Inspection Fleet. All aircraft will be equipped with Flight Data Recorders and a full complement of instrumentation including strain sensors. The locations of the MSR and LSR strain

sensors are shown in Figures 3 and 4. Processing the data will consist of transforming the flight recorder data into analytical fatigue crack predictions at each aircraft's control points. The control points will be modeled using crack growth algorithms and material properties from the DADTA reports and are shown in Figures 5 and 6.

Applying Object Technology to the IATP and L/ESS produces a software set that can accommodate both the Learjet Model 60 and Canadair Challenger CL601-3R aircraft, and is optimized for flexibility and reuse. The final IATP system is intended to be easily modified to incorporate additional control points, or even aircraft types.

Introduction

The purpose of the FAA Flight Inspection ASIP is to assure continuing long-term structural integrity and airworthiness for the FAA Flight Inspection fleet. The flight inspection usage differs from the basic Learjet Model 60 and Canadair Challenger CL601-3R design usage. The flight inspection mission profiles are characterized by extensive operation below 2,000 feet mean sea level (MSL) which contrasts dramatically with a typical corporate jet operational scenario.

This paper focuses on technology transfer between software engineering and aircraft structural analysis. Historically it can be shown that the art of software development suffers in comparison to the more established engineering disciplines. In fact, some software experts have declared that software development is more a craft than an engineering discipline [1]. It's now a rare development project that comes in anywhere near on time, much less under budget [2].

E-Systems is applying modern software engineering practices in the form of Object Technology to the domain of fracture mechanics and individual aircraft tracking programs. The goal is an IATP system that is adaptable to the addition of multiple aircraft types with maximum reuse of the basic software system parts.

Current Aircraft in the IATP System

The IATP system is being designed to track both the Medium Size/ Medium Range (MSR) Learjet Model 60 and the Large Size/ Long Range (LSR) Canadair Challenger CL601-3R. These aircraft differ in size, manufacturer, fracture analysis methodology, flight recorder parameters and original certification basis. The IATP system is still flexible enough to share the majority of the software being written between both aircraft types.

The Learjet Model 60 has a maximum gross takeoff weight of 23,500 pounds with a maximum operating altitude of 51,000 feet. The Model 60 is certified under Amendment 23 of FAR Part 25.571 and was evaluated using fatigue and static fail safe methodologies. Learjet performed a fracture mechanics based damage tolerance analysis of the modified Model 60 Flight Inspection aircraft as part of this program [3].

The Canadair Challenger CL601-3R has a maximum gross takeoff weight of 45,100 pounds with a maximum operating altitude of 41,000 feet. The Challenger is certified to Amendment 45 of FAR 25.571 as a "damage tolerant" aircraft. However, to account for the unique FAA usage, Canadair developed new loads and stress spectra and reassessed the aircraft structural integrity [4].

IATP Software System Requirements

The IATP System will read, store and process flight recorder data collected from each of the FAA Flight Inspection MSR and LSR aircraft. The raw data will be stored in a database to facilitate the processing and reporting of the final tracking results to the FAA. Processing the raw data is defined as the conversion of flight recorder data into fatigue crack predictions for the MSR and LSR aircraft, and to provide maintenance and inspection recommendations to the FAA.

The IATP fatigue crack growth system is based on the Learjet Model 60 MSR Service Life Analysis and the Canadair Challenger Model CL601-3R LSR DADTA.

Fatigue crack growth requirements involve the growth of cracks at each control point resulting from an applied stress spectrum. The control point analysis includes the effects of material properties, geometry of the structure and crack growth retardation.

Crack growth analysis involves growth in both the depth and length directions as applicable. A crack which has grown through the material thickness in the depth direction continues to grow in the length direction until failure.

Material properties include critical stress intensity factor (K_{Ic}), yield stress (F_{ty}) and crack growth rate data (da/dn) which are based on constant amplitude crack growth per stress cycle (σ_{max} , σ_{min}) as a function of stress ratio R ($\sigma_{min} / \sigma_{max}$) and stress intensity factor (K). The material properties are supplied by the aircraft manufacturer. The data is stored as look-up tables or Walker equation coefficients.

Stress intensity factors are a function of the applied stress and structural geometry. Geometry factors are often normalized to the known solution for a center crack in

an infinite plate. This factor scales the center crack solution and is denoted as a beta (β) factor. In the case of the Learjet Model 60, beta factors vary by crack length and depth and are stored in tables and accessed by look-up routines. The Challenger Model CL601-3R approach involves both β tables and complete K solutions using Canadair supplied equations.

The growth of a crack can be retarded by the formation of an enlarged plastic zone at the tip of the crack. The IATP software uses the same Generalized Willenborg Retardation Model as did Learjet and Canadair.

The control points identified by Learjet and Canadair will be modeled in the IATP System for each aircraft to be tracked. The IATP System control points will simulate the analysis performed by Learjet and Canadair and will be tested against the MSR and LSR DADTA results.

Object Technology

Software Crisis

"Of all the monsters who fill the nightmares of our folklore, none terrify more than werewolves, because they transform unexpectedly from the familiar into horrors. For these, we seek bullets of silver that can magically lay them to rest. The familiar software project has something of this character, usually innocent and straightforward, but capable of becoming a monster of missed schedules, blown budgets, and flawed products. So we hear desperate cries for a silver bullet, something to make software costs drop as rapidly as computer hardware costs do". [5]

The IATP System is sufficiently complex that constructing it poses a risk. Software systems are prone to defects, and can be so rigid that it's nearly impossible to make major changes without total redesign. E-Systems goal is to create an automated IATP system that is still flexible enough to handle the addition of different aircraft types with varying structural integrity analysis styles.

History of Software Development

To place Object Technology in perspective one must first look at the evolution of software engineering from the days of the first computer. The following overview of software engineering history is paraphrased from reference [2].

Single Procedure

The first programs were single inline procedures that flowed linearly from begin to end. This worked fine for smaller programs but became unwieldy with size

increases. The single procedure also suffered if more than one person was required to work on the effort.

Modular Programming

The solution to the Single Procedure limitations was to break large scale programs down into smaller components that can be constructed independently, then combined to form the complete system. This strategy is called Modular Programming. The first form of Modular Programming came with the invention of the subroutine in the early 1950s. A subroutine is created by pulling a sequence of instructions out of the main routine and giving it a separate name. The subroutine can then be executed by the main program by simply calling the subroutine by name whenever it is required. Subroutines provided a natural division of labor. The problem was that subroutines did not automatically provide well designed (modular) programs.

Structured Programming

In the late 1960s computer science refined Modular Programming into Structured Programming. Structured Programming is founded on functional decomposition, a top-down approach to system design where a program is systematically broken down into smaller and smaller components until a level of individual subroutines is reached. Separate teams of programmers work on the various components and assemble them into the final program.

Structured Programming significantly improved software development but its limitations are now painfully apparent. The primary problem is that the method assumes total understanding of the system at the beginning of design. Once the development is underway, new knowledge of the system will be gained, and possible changes in original requirements can be imposed resulting in redesign of the functional decomposition. Every project reaches a point where it cannot stand another redesign and the programming staff tries to just make it work.

Object-Oriented Approach

The Object-Oriented approach to software engineering originated in the late 1960s in a computer language called 'Simula' developed in Norway. Simula was an acronym for 'simulation language' and was created to support computer simulations of real-world processes. The authors wanted to build working models of complex physical systems that could contain thousands of components. This led to a new paradigm in programming where the modules are based on the physical objects being modeled in the simulation. This was a natural evolution of

the standard Modular Programming approach of the day. The simulation objects already had behavior defined, and each object also had to maintain information about its own status. It was not necessary to look for another way to package procedures (subroutines) and data when the problem already was organized.

An object is a 'software package' that contains a collection of related procedures and data. In an object-oriented approach, procedures or subroutines are called methods, and the data is referred to as variables.

One of the barriers to understanding object-technology is the specialized vocabulary that has grown up around it. However, it is possible to boil Object-Speak down to ten basic terms: object, method, message, class, subclass, instance, inheritance, encapsulation, abstraction, and polymorphism.

Objects communicate to each other through messages. A message has three parts, a receiver object, a method name and any required parameters. An object-oriented program is a collection of objects sending messages to each other. Again, the simulation heritage of Object Technology is apparent.

There may be many objects of any given type. A Class is a template that defines the methods and variables to be included in a particular type of object. Objects are then 'instances' of a Class. A software engineer 'writes' classes, and a program will then instantiate objects from those classes and message passing begins between objects.

Encapsulation is a mechanism to promote information hiding by packaging data and procedures together. In the object-oriented approach, the data inside an object can only be accessed by the objects methods.

Inheritance is a mechanism whereby one class can be defined as a special case of a more general class, automatically including the methods and variable definitions of the general class. The specialized class is said to be a subclass of the general class.

Data abstraction is the ability to define problem unique data types and treat them as if they were a part of the computer language you are using. Object-oriented languages provide this ability through the Class.

Hiding alternative procedures behind a common interface is called polymorphism, a Greek term meaning "many forms". This allows objects such as a square, a circle and a triangle to all have a method called 'draw'. The system need only tell the

object to 'draw' itself without regard for the details of how drawing varies between object types.

Potential Benefits

The attraction of companies to migrate to Object Technology is the lure of trying to solve the software crisis. The following benefits are possible with the proper application of Object technology.

Faster Development

Structured Programming shared data between all subroutines. This meant that any subroutine could damage the data and thereby cause any other subroutine to fail. By creating independent objects that are based on the problem being solved, teams of software engineers can develop complex systems that do not fail due to internal inconsistencies. Objects protect their data through encapsulation and communication between objects is tightly confined to the methods defined for that object. Also, proper use of inheritance allows classes to reuse class definitions for purposes of specialization.

Higher Quality

Again, due to encapsulation, object-oriented systems are less fragile than their structured counterparts. Also, the majority of object-oriented systems are created with a high level of reuse of existing classes, either from the language vendor itself, or from previous company projects. This reuse of already proven code directly contributes to software quality.

Easier Maintenance

All software behavior is contained within objects. Software errors are traced to the offending object and corrected. This contrasts significantly from conventional programming where subroutine behavior is dependent on the call sequence and the data passed. Reproducing error conditions can be labor intensive and tracing the source of the error is sometimes difficult.

Reduced Cost

Systems are created by reusing existing components (classes). In the case of the IATP System, once the MSR is modeled and developed, the basic software components provide the basis of the LSR software.

Increased Scalability

As Object Technology provides improved modularization, object-oriented programming is particularly well suited to developing large-scale systems. Large

systems are easier to build and maintain when built out of subsystems that can be developed and tested independently.

Better Information Structures

Through the use of composite objects, class hierarchies and other structures, object technology can effectively represent the complex information that an aircraft tracking program represents.

Increased Adaptability

The biggest payoff for this system will be its adaptability. Specifically this will be the ability to add new aircraft types that were never part of the original design, and the existing parts of the system will treat the new aircraft as if they were there from the beginning. This adaptability comes with the added advantage that the existing system requires no modifications to accept the new aircraft type.

IATP Design

Classes in an object design should represent 'things' in the problem domain. As such, the IATP System has classes such as LearjetFleet, LearjetM60, ControlPoint, Crack, Material and WillenborgRetardationModel. Each class has data attributes, such as a LearjetM60 'knows' its serial number, total flight hours and time to next inspection.

IATP Design Example

To illustrate some differences between Object Technology and conventional software practices, consider the basic problem of calculating crack growth. This example begins with some 'main' program requesting a control point to 'grow' its crack. The simplified abstraction of this function is to have the control point perform the following steps:

1. Calculate the stress intensity factor for the applied stress cycle.
2. Reduce the stress intensity factor for any crack tip plastic zone effects.
3. Compute the incremental growth from the applied stress cycle.

Figure 7 shows a functional approach to this problem. With only one control point in the picture at this time, and it having only one phase, the diagram does not look too bad at first. But upon further inspection it is seen that all data is accessed by multiple functions. This coupling of the functions through shared data violates the modular programming concept. This results in each function relying on the behavior of any other function sharing the data. As more control points are added, with each having multiple phases, many more functions must be added as any two

functions may not have the same name. This large collection of functions will be intricately tied through common data accesses, and as the complexity increases, the usual result is mysterious errors and unpredictable behavior.

The Object approach is represented by Figure 8. In this design, the objects Control Point, K Solution, Material and Retardation Model are identified. The key distinction is that the data is encapsulated within each of the objects. Communication between objects is restricted to methods defined for each object. As this design is scaled up to include multiple control points, multiple aircraft and multiple phases at a control point, the basic design is intact. Each control point may require unique K Solution objects, but all stress intensity solution objects will respond to the 'calculateK' method in their own way. Some will invoke equations, others will use look-up tables, but the adjacent objects in the system are unaffected provided a calculation for K is returned from the 'calculateK' message. The collection of methods that an object will respond to is referred to as the objects public interface.

The object design also allows for greater flexibility. The final system will require many unique 'types' of control points, materials, and stress intensity solutions. But the basic design is able to provide a 'plug and play' capability where the pieces of each control point solution can be created independently and dropped into the system without fear of system collapse. Another example of this design flexibility is the Retardation Model. Initially it was anticipated that all control points would only need one retardation object. However, a coupon test will be used to determine spectral retardation effects for the Learjet MSR control points. The final MSR DADTA will be updated to incorporate the coupon test results by adjusting the shut-off overload ratio factor in the retardation model. The object design shown here can easily adapt to this new requirement by simply providing custom retardation model objects to the control points of interest. The basic system still operates the same.

Object Modeling Technique

In order to communicate a design more descriptively, a graphical annotation convention is used. The Object Modeling Technique (OMT) also known as the Rumbaugh method is used for the IATP software development [6]. This design method is centered on an Object Model of the system being created.

The Object Model represents the static, structural, "data" aspects of a system. It provides the essential framework into which the dynamic and functional models can be placed. Objects are the units into which the system can be divided. The model is represented graphically with object diagrams containing object classes.

Classes are arranged into hierarchies sharing common structure and behavior and are associated with other classes. Classes define the attribute values carried by each object instance and the operations which each object performs or undergoes.

There are basically two components associated with the object diagram, classes and associations. Classes in the object diagrams are represented as a rectangular box subdivided into three sections. The top section of the class box is the class name. The middle section lists all of the instance variables that describe the attributes of the class. The bottom section lists all of the methods that describe the behavior of the class. Links and associations are the means for establishing relationships among the classes. A link is a physical or conceptual connection between object instances. An association describes a group of links with common structure and common semantics. An association describes a set of potential links in the same way that a class describes a set of potential objects.

For the diagrams that define the IATP system, classes are rectangular subdivided into thirds with class name, instance/class variables, and instance/class methods. Associations found in the object diagrams include: aggregation, inheritance, ordering, qualifiers, and multiplicity.

Aggregation denotes a "HAS A" relationship between classes, i.e., class A contains class B if a diamond connects class A to an association with class B.

Inheritance denotes an "IS A" relationship between classes, i.e., class B is a type of class A if the triangle that connects classes A and B points to class A.

Ordering appears as the word ordered enclosed by braces, {ordered}, over the end of the association denoting the class whose instances must be ordered.

Qualifiers reduce the effective multiplicity of an association. One-to-many and many-to-many associations may be qualified. The qualifier distinguishes among the set of objects at the many end of an association. For example, a Learjet fleet has many aircraft, but a Learjet fleet qualified by a serial number identifies one unique aircraft. So the serial number qualifier on the fleet reduces the one-to-many multiplicity of the aircraft.

Multiplicity specifies how many instances of one class may relate to a single instance of an associated class. A solid ball is the OMT symbol for "many," meaning zero or more. A hollow ball indicates "optional," meaning zero or one. A line without multiplicity symbols indicates a one-to-one association.

The system design begins with a root that serves as the starting point for the entire project. It also gives the database an object from which to begin a tree hierarchy. The root contains fleets and fleets contain aircraft. The following three figures graphically describe part of the prototype design of the IATP System.

IATP Preliminary Design

A prototype IATP system was developed and tested. A portion of the prototype design is presented here to provide an example of an object oriented design at a sufficiently detailed level of abstraction to actually represent a simple working system.

The first Object Model (Figure 9) shows the top level design depicting aircraft being organized into fleets under a common root class. Individual aircraft are identified within a fleet by serial number. All aircraft can print a report about themselves, and all aircraft can 'grow cracks'.

The second Object Model (Figure 10) reveals that each LearjetM60 contains a collection of ControlPoints and a collection of LJFlightDataDownload objects. This shows that the LearjetM60 does not care how many or what kind of control points it has as each control point object will respond to defined methods such as 'grow crack' in its own way.

The last Object Model (Figure 11) shows that a ControlPoint associates with a Crack object that in turn associates with Material and Stress Intensity Solution objects. This shows how the LearjetM60, ControlPoint and Crack objects do not care what kind of Stress Intensity Solution object is connected as long as the public interface is consistent.

Sample IATP Prototype Operation

The following figures show some screen displays from the IATP prototype. The basic system begins by displaying an opening screen as shown in Figure 12. The operator selects the aircraft of interest from the list of aircraft presented in the left hand scroll box. After an aircraft is selected, the screen displayed in Figure 13 presents the data for the selected aircraft. Notice that the variables displayed (serial number, total flights, landings, etc.) are instance variables in the object diagram shown in Figure 7). The lower right hand screen now contains two small scroll boxes. The left one contains the flight recorder data that has been stored but not yet used to grow cracks for this aircraft. The right small window contains the control points for this aircraft. If a control point is selected, it can be displayed as shown in Figure 14. Similarly the flight recorder data can be displayed as shown in Figure 15.

As cracks are grown, the current flight recorder data window is emptied. If the operator wishes to 'ungrow' cracks, a screen will show the previous crack states of the aircraft for every time that the 'grow cracks' command was issued. The operator may select a previous state and the aircraft will be 'restored' to the flight

hours and crack lengths at that time, with all subsequent flight recorder data restored to the flight recorder data window ready for further crack growth.

Program Schedule and Status

The current FAA ASIP MSR and LSR ASIP program calls for IATP startup on 22 August 1996. The IATP prototype is complete and work is in progress on the deliverable system. The FAA FIA MSR Learjet Model 60 control points have been developed and tested. They will be modified as needed pending the results of the coupon test program. The FAA FIA LSR Canadair Challenger CL601-3R control points are under development and will be completed by February 1996.

Summary

The MSR and LSR ASIP programs are on schedule and will be activated in August of 1996. The IATP program is being developed now and will support the August 1996 startup requirement. The IATP software system is object-oriented and promises an large improvement in system quality, flexibility and sophistication over conventionally constructed tracking systems.

As the FAA Flight Inspection MSR and LSR aircraft accumulate flight hours in a hostile low level environment, the IATP system will provide detailed maintenance and inspection recommendations to the FAA. At the same time, the L/ESS data contained in the IATP system will further define the low level operational environment unique to flight inspection aircraft.

List of References

1. Love, Tom, Object Lessons, SIGS Books, 1993.
2. Taylor, David A. ,Object-Oriented Technology: A Managers Guide. Addison-Wesley Publishing, 1990.
3. 50 SN85-6, Model 60 FIAS Service Life Analysis, 19 June 1995.
4. RAS 601-916, DADT Analysis for Inspection Aircraft, 15 September 1995.
5. Brooks, Frederick P., The Mythical Man-Month (20th Anniversary Edition). Addison-Wesley Publishing, 1995.
6. Rumbaugh, J., Blaha, M., Premerlani, W., Eddy, F., Lorensen, W. Object-Oriented Modeling And Design, Prentice Hall, 1991.

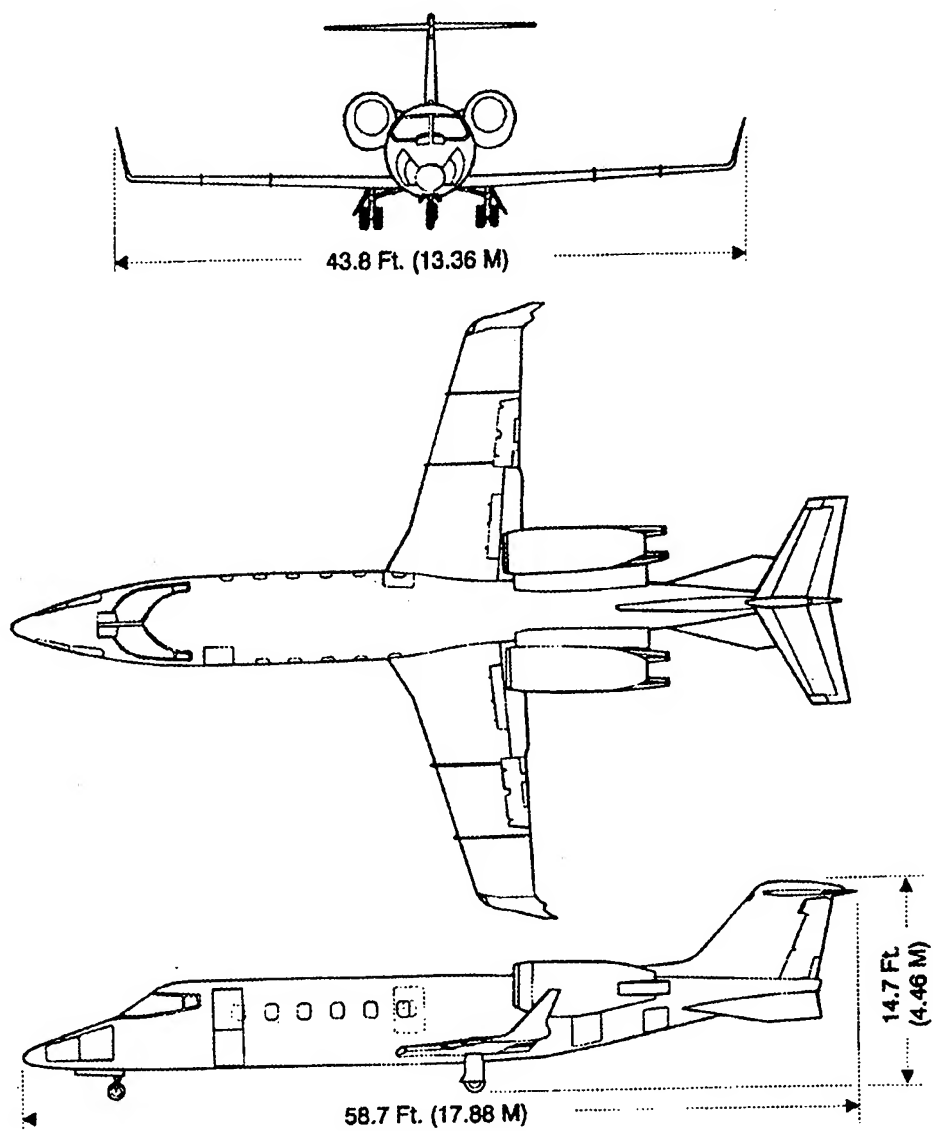


Figure 1 Learjet Model 60 MSR Flight Inspection Aircraft

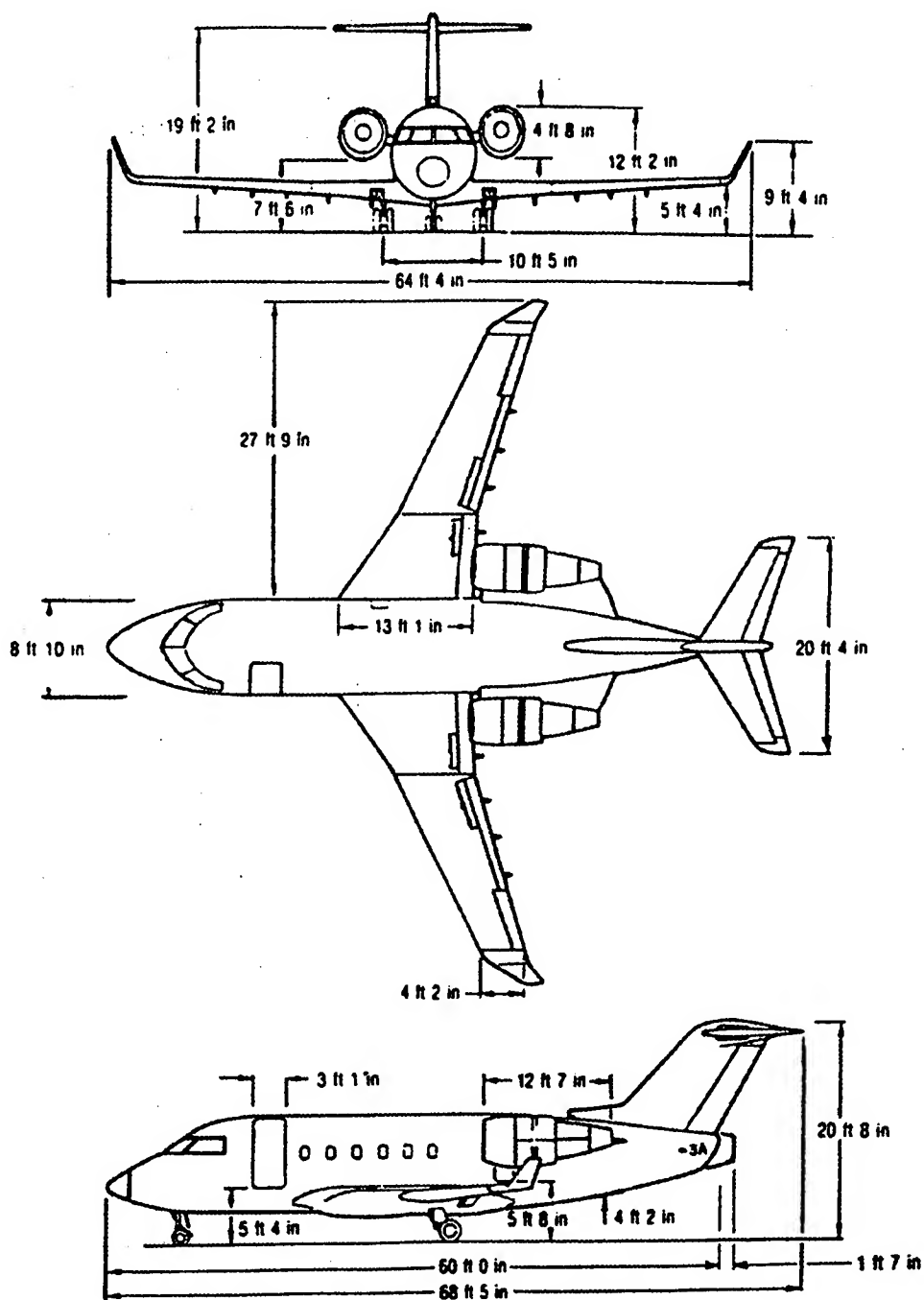
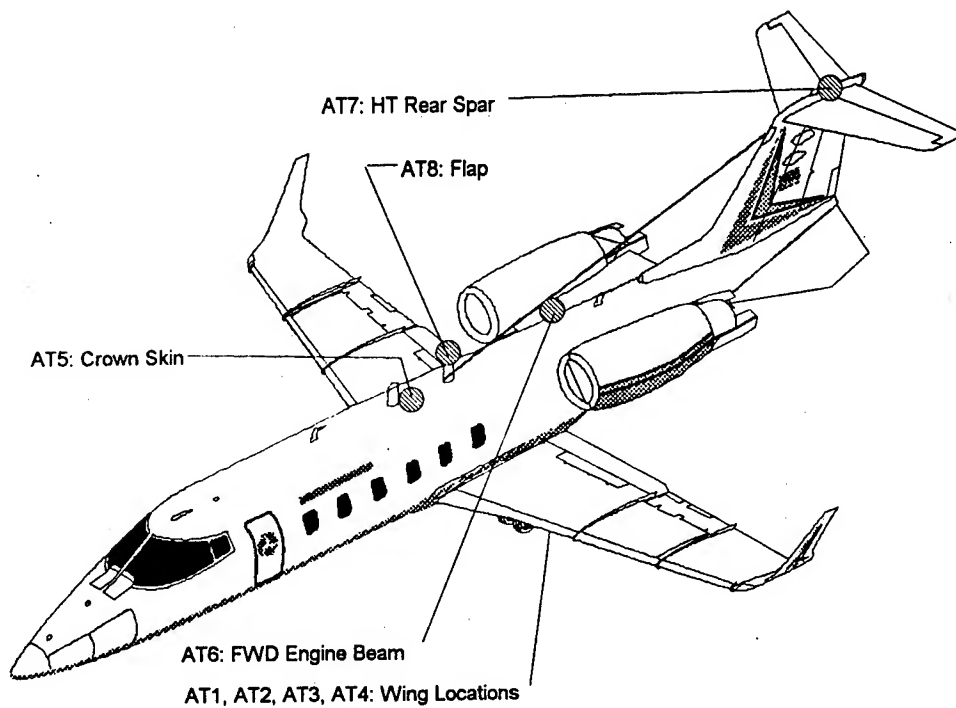
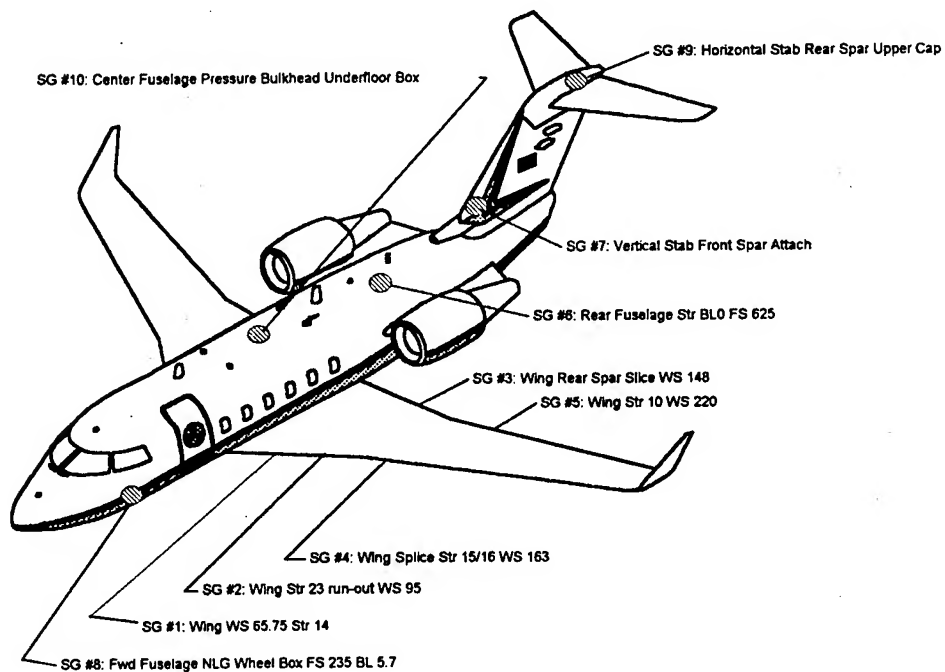


Figure 2 Canadair Challenger CL601-3R LSR Flight Inspection Aircraft



**Figure 3 FAA Flight Inspection (MSR) Learjet Model 60
Flight Data Recorder Strain Sensor Locations**



**Figure 4 FAA Flight Inspection (LSR) Challenger CL601-3R
Flight Data Recorder Strain Sensor Locations**

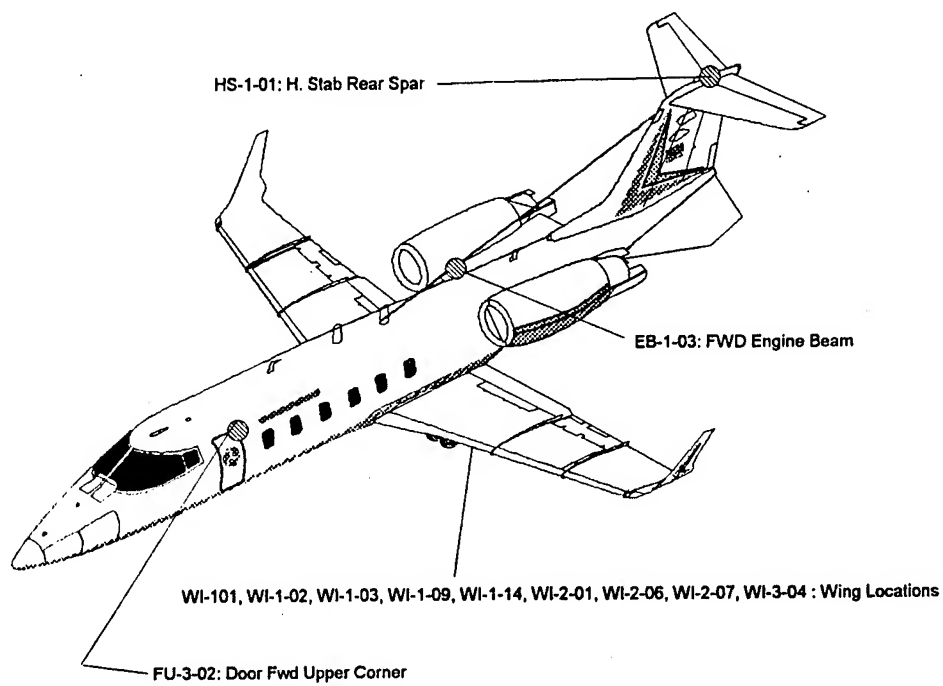


**Figure 5 FAA Flight Inspection (MSR) Learjet Model 60
DADTA Control Point Locations**

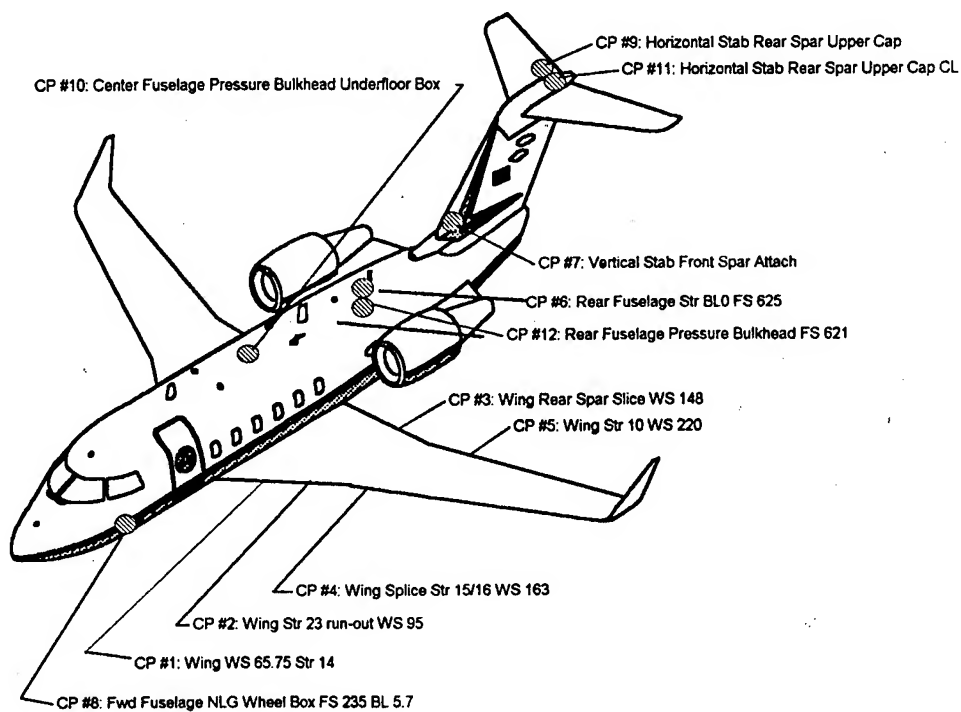


**Figure 6 FAA Flight Inspection (LSR) Challenger CL601-3R
DADTA Control Point Locations**

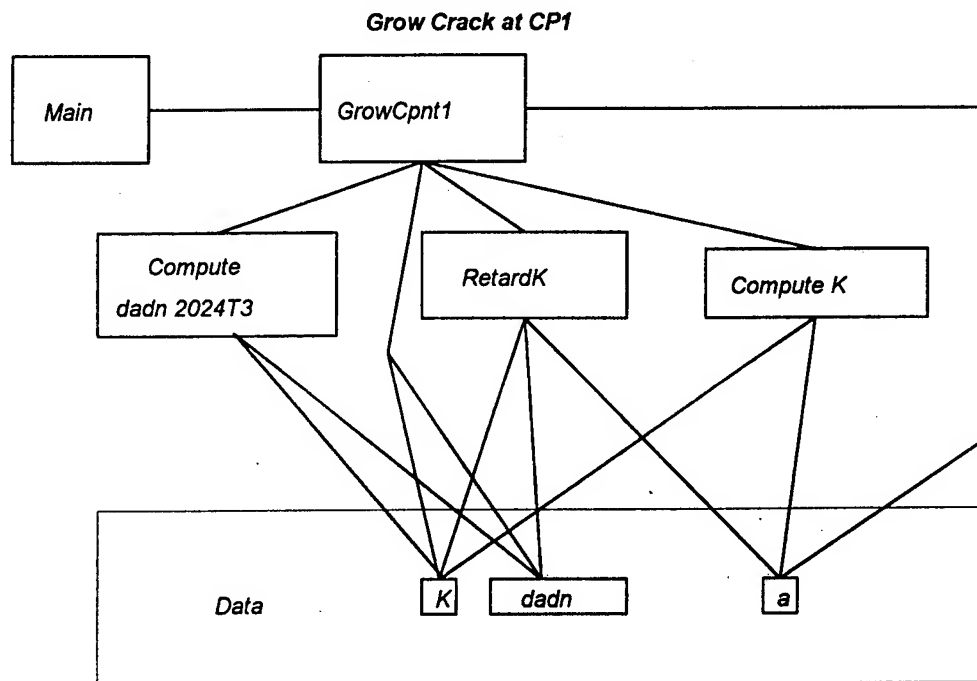


Figure 7 Example of Structured Design

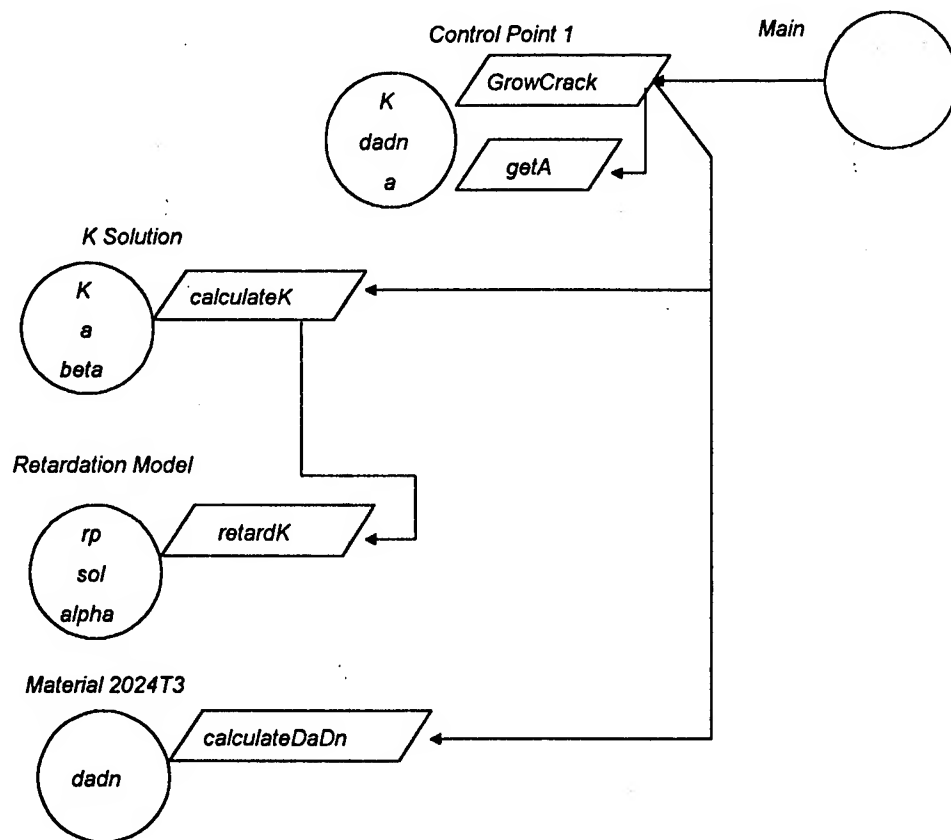


Figure 8 Example of Object-Oriented Design

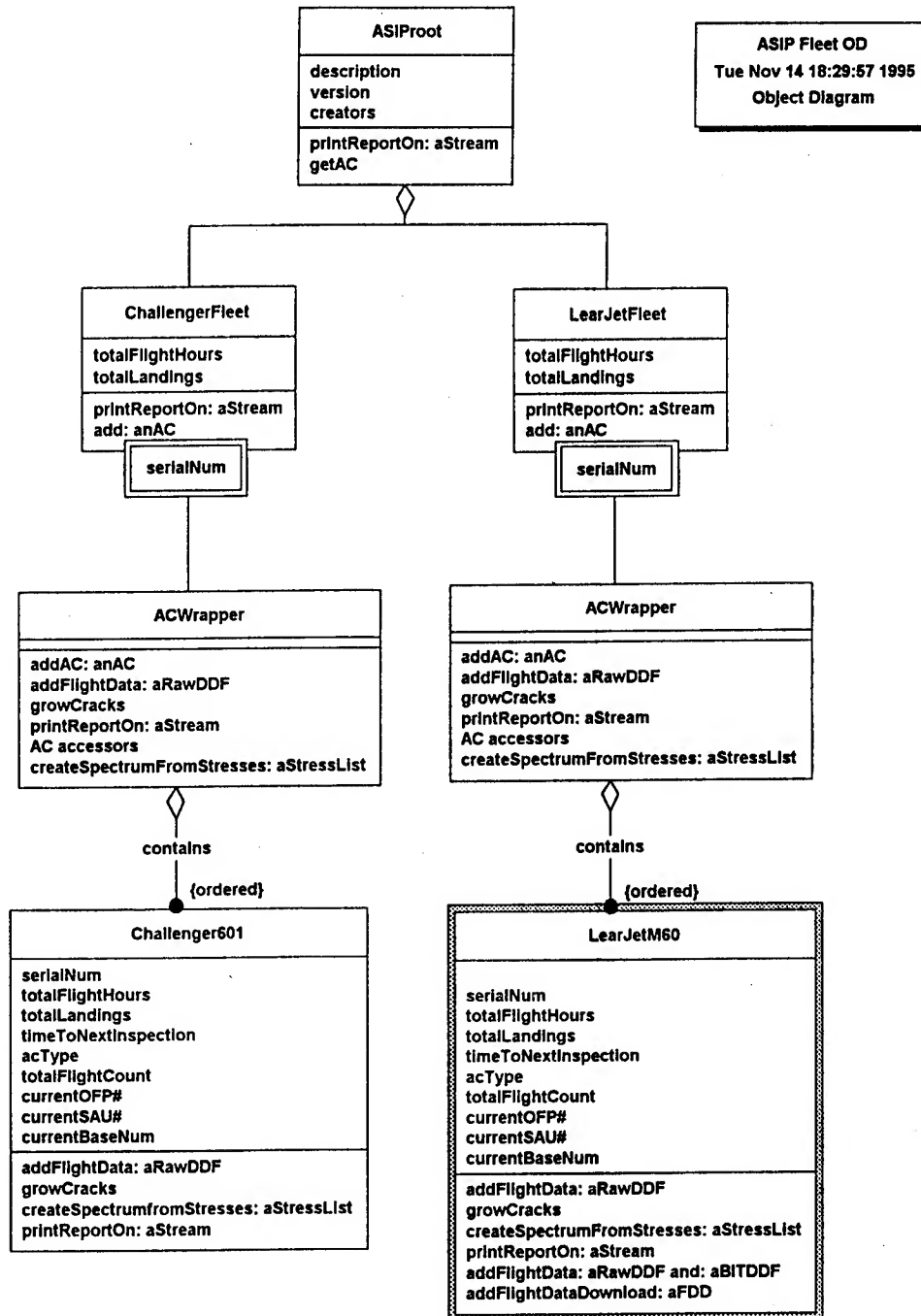


Figure 9 Top Level IATP Object Diagram

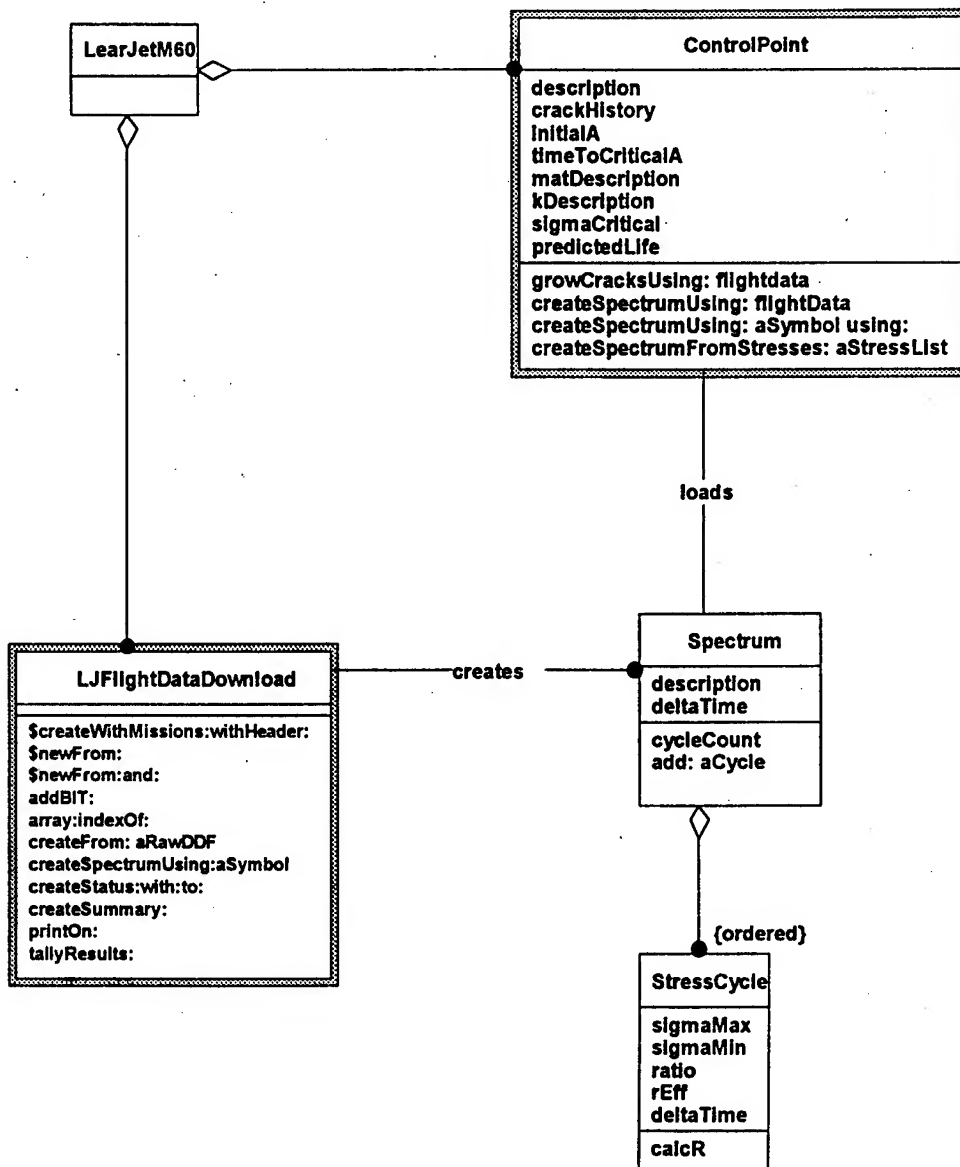


Figure 10 Aircraft-Control Point-Flight Data Object Diagram

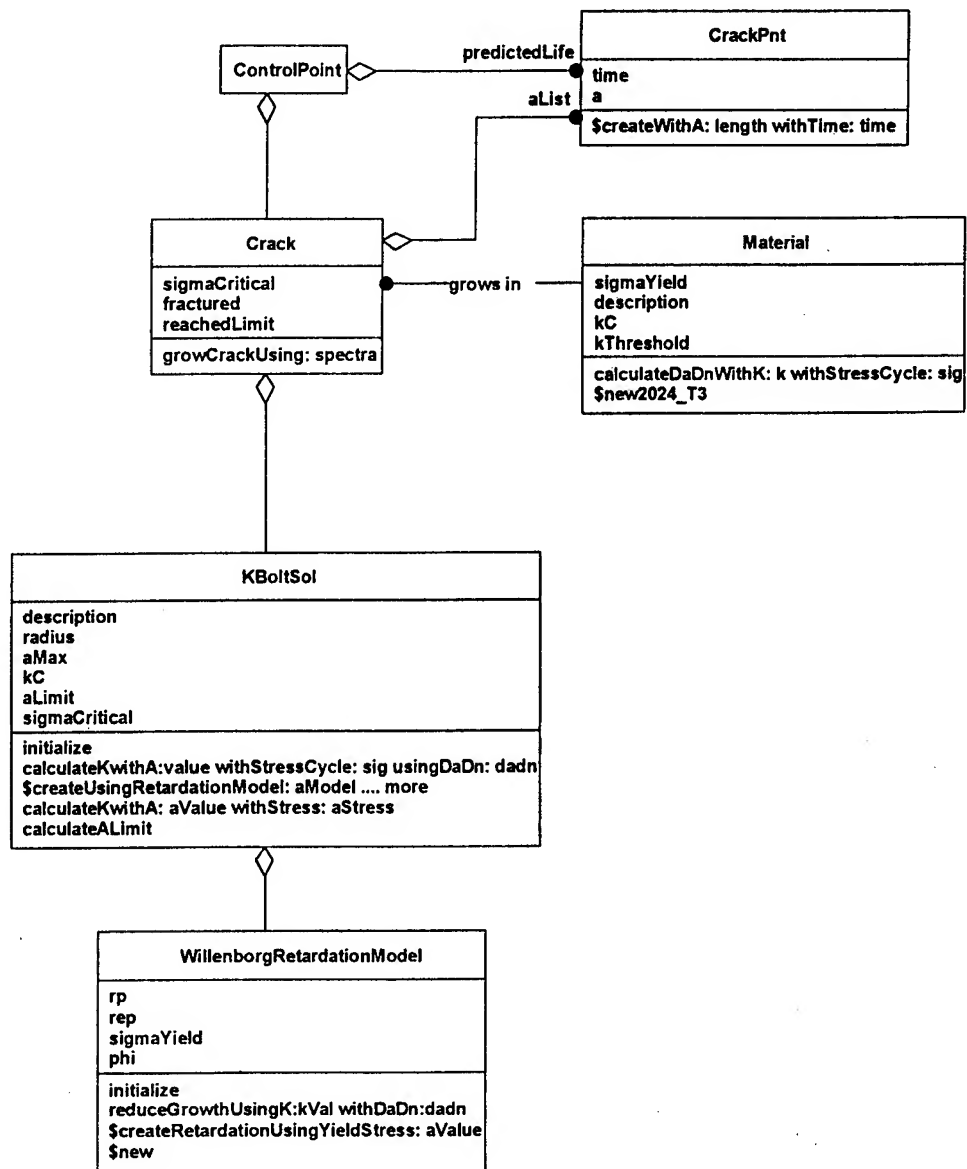


Figure 11 Crack Growth Object Diagram

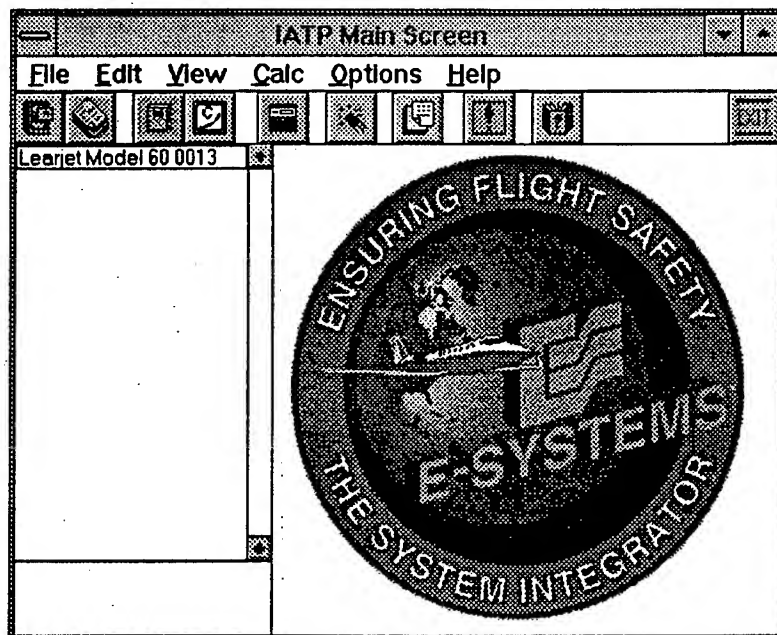


Figure 12 IATP System Opening Screen

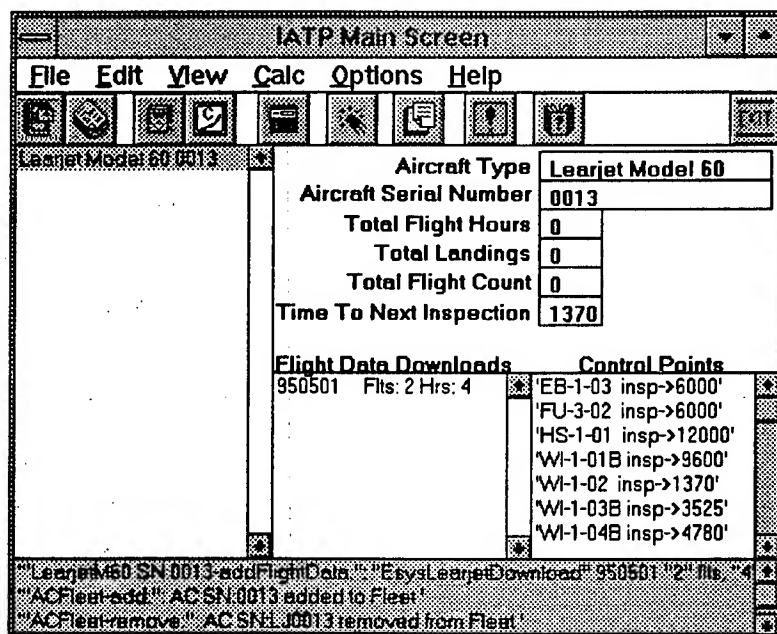


Figure 13 IATP System Aircraft t Screen

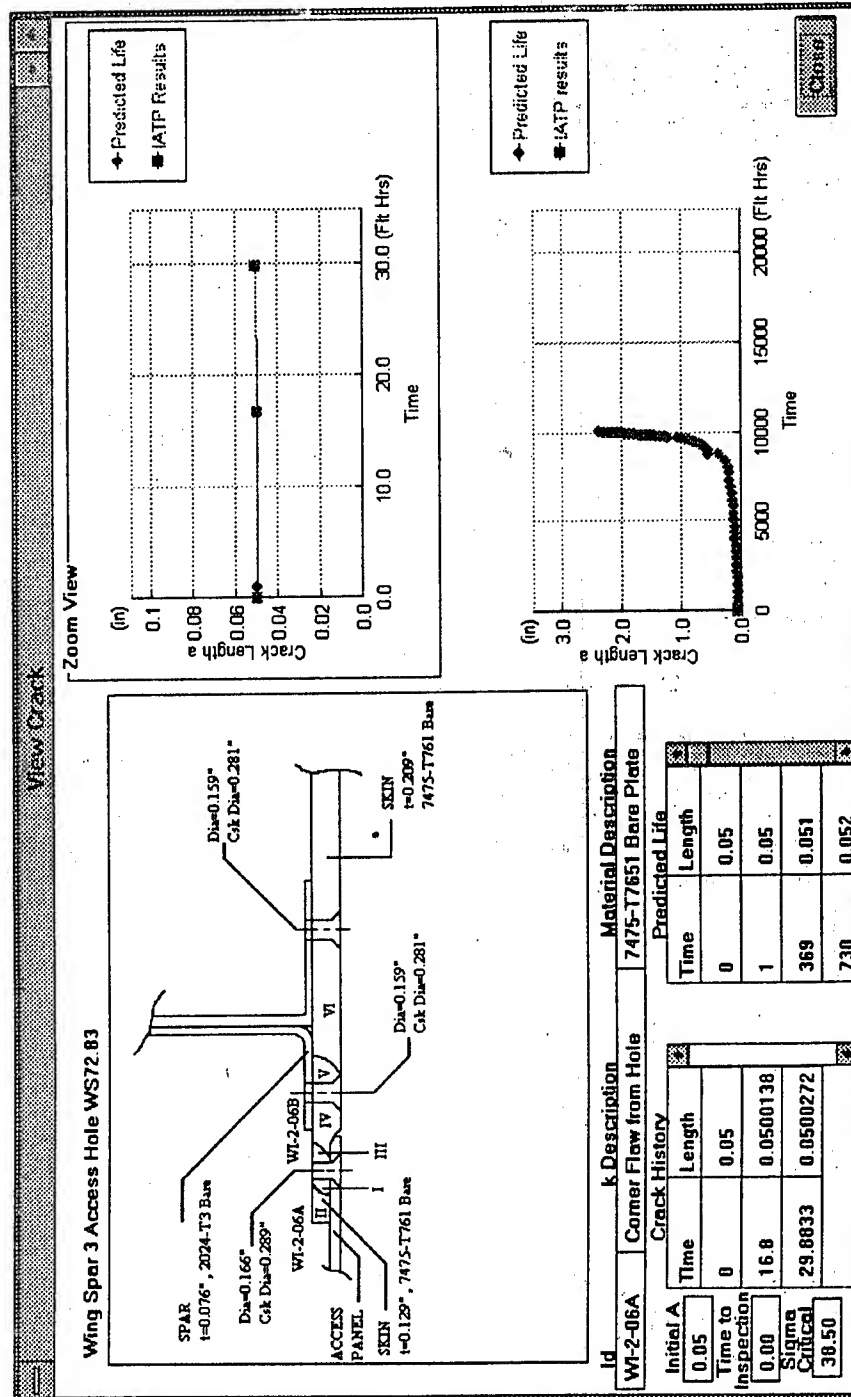


Figure 14 Control Point Screen

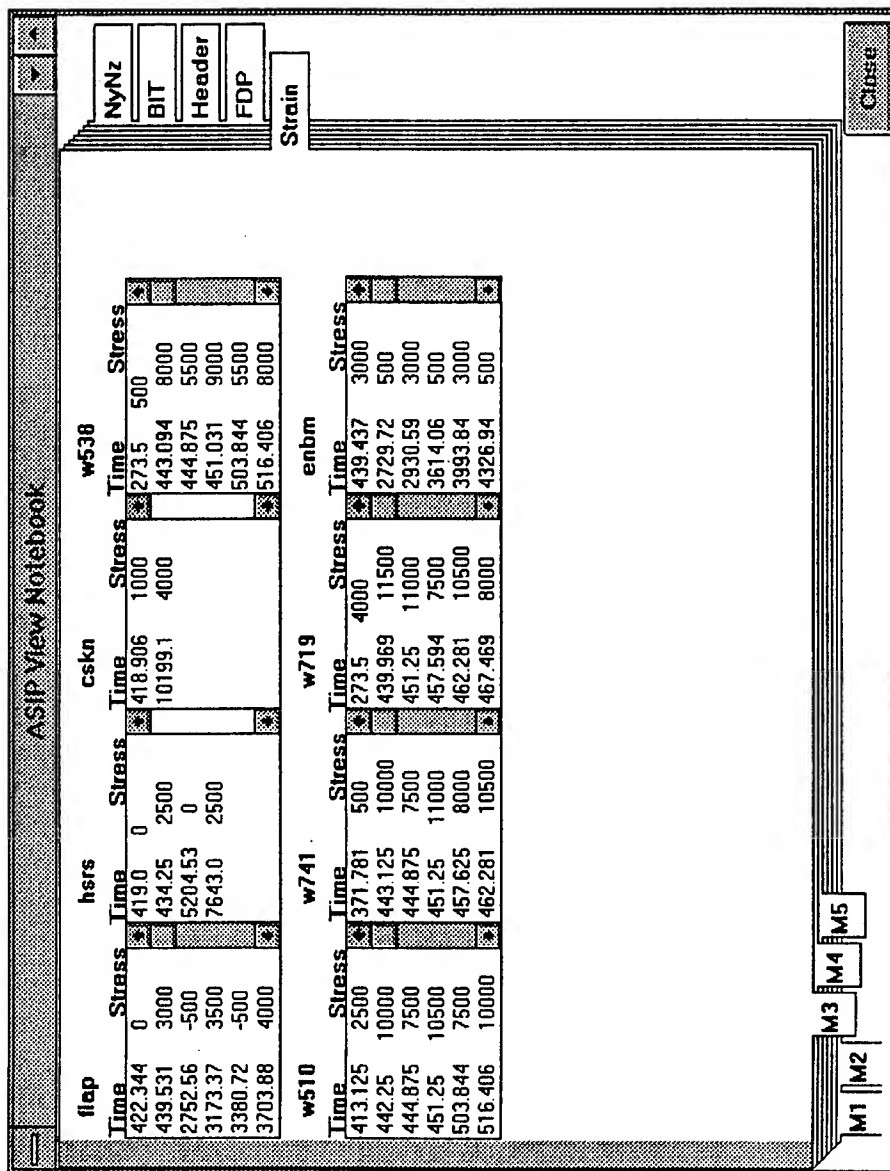


Figure 15 Flight Recorder Data Screen

ATTENDEES LIST

MR KAZUHIKO ABE
STRUCTURAL DESIGN ENG
MITSUBISHI HEAVY IND LTD
10 OYE-CHO MINATO-KU
NAGOYA-SHI AICHI-KEN JA 455-0001
(052)-611-8022
FAX: (052)-613-0752

MR JAMES J ABEL
FLIGHT SCIENCES DEPT
CHRYSLER TECH AIRBORNE SYS
7500 MAEHR M/S 1135
PO BOX 154580
WACO TX 76715-4580
(817)-867-4116
FAX: (817)-867-4597

MR RUSSELL E ALFORD
C-141 ASIP MGR
US AIR FORCE
WR-ALC/LJLEA
270 OCMULGEE CT
ROBINS AFB GA 31098-1646
(912)-926-9146
FAX: (912)-926-9142

MR ROBERT D ALLEN JR
MGR STRUC TEST LAB
LOCKHEED AERO SYS CO
M/S 0484 DEPT 73-51
86 S COBB DR
MARIETTA GA 30063-0484
(770)-494-3972
FAX: (770)-494-2028

MR ROBERT ALLERSTON
ROYAL AIR FORCE
NON DESTRUCTIVE TEST SQUAD
RAF ST ATHANMORLEY
BARRY S GLASMORGAN S WALES UK-0001

MR JAMES M ALPER
NAVAL AIR WARFARE CTR
MS 08 CODE 4331R
JACKSONVILLE & STREET RD
WARMINSTER PA 18974-0001
(215)-441-1137
FAX: (215)-441-2790

MR HANS R ANSELL
SAAB MILITARY AIRCRAFT
SAAB SCANIA AB
MS TUDLB
LINKOPING SWEDEN S 58188-0001
(461)-318-1698
FAX: (461)-318-3363

MR KAZUNOBU AOYAMA
RES ENGR
MITSUBISHI HEAVY IND LTD
MATLS RES SECTION
10 OYE-CHO
MINATO-KU
NAGOYA JAPAN 455

MR ALBERT J ARRIETA
AERO ENGR
US AIR FORCE
OC-ALC/TIESM
4750 STAFF DR
TINKER AFB OK 73145-3317
(405)-736-5008
FAX: (405)-736-3992

MR JOHN E ARSTINGSTALL
PROG MNG
GONZALEZ DESIGN ENG
104 MID AMERICA BLVD
MIDWEST CITY OK 73110-6009
(405)-732-6632

MR CHARLES A BABISH
AEROSPACE ENGR
US AIR FORCE
ASC/YCEF/C17 SPO
2600 PARAMOUNT PL
WRIGHT-PATTERSON AFB OH 45440-0001
(513)-255-5427
FAX: (513)-255-3207

MR ROBERT M BADER
CONSULTANT
1613 KINGSWAY DR
XENIA OH 45385-9589
(513)-426-4871

MR JOHN T BAILEY
BAILEY ENGR SERVICES
RT 1 BOX 100D
JUSTIN TX 76247-0001
(817)-935-3680

DR MEHMET I BASCI
DIRECTOR
SWALES & ASSOC INC
5050 POWDERMILL RD
BELTSVILLE MD 20705-0001
(301)-572-1445
FAX: (301)-595-5518

MR PRESTON R BATES
RES ENGR
GEORGIA TECH RES INST
AERO LAB CCRF 2-111
225 N AVE NW
ATLANTA GA 30332-0844
(404)-528-7887
FAX: (404)-528-3271

MR KENNETH R BEAHAN
STRUC ENGR MGR
THE BOEING CO
3801 S OLIVER
M/S K83-14
WICHITA KS 67210-0001
(316)-526-2341
FAX: (316)-526-4214

MR JON L BEARD
US AIR FORCE
OC-ALC/LACRA
STE 2AC489
TINKER AFB OK 73145-3019
(405)-736-3834
FAX: (405)-736-5604

MR YVES BEAUVAIS
ENGR
BOMBARDIER INC
MONTREAL INTL AIRPORT
CARGO RD A-4
MIRABEL QUEBEC CANADA J7N-1C7
(514)-476-4414

DR THEODOR H BEIER
BRANCH CHIEF TECH
MCDONNELL DOUGLAS AERO
MS 1022147
PO BOX 516
ST LOUIS MO 63166-0516
(314)-232-0634
FAX: (314)-234-8915

DAVID R BEIL
AERO ENG
DEPT OF THE AIR FORCE
LAFME
5020 DUDLEY BLVD
MCCLELLAN AFB CA 95652-0001
(916)-643-0253
FAX: (916)-643-1405

MR NICK BELLINGER
NATL RES COUNCIL
INST FOR AERO RES
BLDG M14 MONTREAL RD
OTTAWA ONTARIO CANADA K1A-0R6
(613)-993-2410
FAX: (613)-952-7136

DR ALAN P BERENS
UNIV OF DAYTON RES INST
300 COLLEGE PARK DR
DAYTON OH 45469-0120
(513)-229-4475
FAX: (513)-229-3712

MR ROBERT L BERGER
US AIR FORCE
ASC/ENFA BLDG 125
2335 SEVENTH ST STE 6
WRIGHT-PATTERSON AFB OH 45433-7809
(513)-255-2030
FAX: (513)-255-5677

LTC KARL-ROMAN BERLINGHOF
NATO LIAISON
NATO EARLY WARNING FORCE CMD
OC-ALC/LAKI-NATO
3001 STAFF DR STE 2AH110
TINKER AFB OK 73145-3022
(405)-736-3108
FAX: (405)-736-4360

MR HENRY K BERRY
PRESIDENT
ENGINEERING INC
41 RESEARCH DR
HAMPTON VA 23666-1394
(804)-865-0100
FAX: (804)-766-2437

MR RONALD J BIRDSEYE
LOCKHEED AERO SYS CO
M/S 0160 DEPT 73-78
2792 CANDLELIGHT CT
MARIETTA GA 30067-0001
(404)-973-7969
FAX: (404)-494-9617

MR MELVIN E BISHOP
MATLS ENGR
US AIR FORCE
WL/MLS-OL BLDG 165
BYRON & SECOND STS
ROBINS AFB GA 31098-1640
(912)-926-3284
FAX: (912)-926-6619

MR RAY BISHOP
US AIR FORCE
ASC/YTE BLDG 56
2100 MONAHAN WAY
WRIGHT-PATTERSON AFB OH 45433-0001
(513)-255-9306
FAX: (513)-255-8516

MR ROBERT L BISHOP JR
E-SYSTEMS GREENVILLE DIV
CBN 151
POB BOX 6056
GREENVILLE TX 75403-6056
(903)-457-7364
FAX: (903)-457-5611

MR EDWARD BITTEL
SQUADRON LEADER
ROYAL AIR FORCE
ENG 17A RAF
RM 421/LACON HOUSE
LONDON UK WCIX 8RY-0001
(071)-305-6688
FAX: (071)-305-6653

MR FRANZ BLAHA
CANADIAN MARCONI CO
600 FREDERIK PHILIPS BLVD
SAINT-LAURENT PQ
QUEBEC MONTREAL CANADA H4M-2S9
(514)-748-3075
FAX: (514)-748-3136

MR NEIL W BLAYLOCK
PRINCIPAL ANALYST
SW RESEARCH INSTITUTE
BLDG 53
6220 CULEBRA RD
SAN ANTONIO TX 78238-0001
(210)-522-3238
FAX: (210)-522-5606

MR SCOTT C BLEDSOE
AERO ENG
AV8 ISST
AIR VEHICLE
500 A HWY 70 W
HAVELOCK NC 28532-0001
(919)-466-8517
FAX: (919)-466-8502

DR ANDERS F BLOM
ANDERS BLOM
FFA
PO BOX 11021
BROMMA SWEDEN S-161 11-0001

CAPT DIMITRIOS BORNOS
HELLENIC AIR FORCE
IOANNOU FOKA 125
11146 GALATSI
ATHENS GREECE 19200-0001

MR KEVIN L BOYD
SR RES SCIENTIST
US AIR FORCE
WL/FIBEC FRACTURE TEST FAC
2130 EIGHTH ST/STE 1
WRIGHT-PATTERSON AFB OH 45433-7542
(513)-255-0434
FAX: (513)-476-7379

MR LARRY BRATCHER
LOGISTICS MNG
US AIR FORCE
OO ALC LAKIT
3001 STAFF DR/STE 2AH110
TINKER AFB OK 23145-3022
(405)-736-2195
FAX: (405)-736-4360

MR BRADLEY J BRAUN
PROD DEV
SYS & ELECTRONICS INC
190 GORDON ST
ELK GROVE VILLAGE IL 60007-0001
(847)-228-0985
FAX: (847)-228-1164

MR CRAIG L BROOKS
MCDONNELL AIRCRAFT CO
FATIGUE & FRACTURES METHODS
M/C 0012741
PO BOX 516
ST LOUIS MO 63166-0516
(314)-232-9391
FAX: (314)-232-7809

MR ALBERT G BRUETSCH
AERO ENGR
US AIR FORCE
SM-ALC
5020 DUDLEY BLVD
MCCLELLAN AFB CA 95652-1391
(916)-643-5300
FAX: (916)-643-1405

AXEL R BRUHN
LTC
GAF AMO
POSTFACH 902500 KOLN
III B1B
COLOGNE GERMANY 51140-0001

DR THOMAS R BRUSSAT
SENIOR STAFF ENGINEER
LOCKHEED MARTIN AERO SYS
ZONE 0987 DEPT 73-HE
86 S COBB DR
MARIETTA GA 30063-0987
(404)-793-0132
FAX: (404)-793-0149

DR ROBERT J BUCCI
SR TECH CONSULTANT
ALCOA TECH CTR
100 TECHNICAL DR
ALCOA CTR PA 15069-0001
(412)-337-2671
FAX: (412)-337-5436

MR WILLIAM F BUCKEY
PROJ ENGR
US AIR FORCE
ASC/ENFSL
812G 56 2100 MONAHAN WY
WRIGHT-PATTERSON AFB OH 45433-6533
(513)-255-9306
FAX: (513)-255-8516

LT GREG BUCKNER
US AIR FORCE
ASC/YSDF
2275 D STREET STE 4
WRIGHT-PATTERSON AFB OH 45433-0001
(513)-255-9518
FAX: (513)-476-4276

MR JAMES S BURD
STRUCTURAL ANALYST
CHRYSLER TECH AIRBORNE SYS
HO8 223
PO BOX 9650
MELBOURNE FL 32902-9650
(407)-951-6203
FAX: (407)-951-6115

MS CAROL A BURKE
ENGINEER
LOCKHEED MARTIN AERO
MS 0160 7325
86 S COBB DR
MARIETTA GA 30063-0001
(770)-494-7693
FAX: (770)-494-9610

DR O HAL BURNSIDE
DIRECTOR
SOUTHWEST RES INST
6220 CULEBRA RD
PO DRAWER 28510
SAN ANTONIO TX 78228-0510
(210)-522-2332
FAX: (210)-522-3042

CAPT LAWRENCE M BUTKUS
AFIT & GEORGIA TECH
MECH ENGRG
GRADUATE BOX 71
ATLANTA GA 30332-0405
(404)-894-2853
FAX: (404)-853-9140

MR CHARLES F BUYNAC
MATLS ENGR
US AIR FORCE WL/MLLP
BLDG 655 RM 173
2230 TENTH ST STE 1
WRIGHT-PATTERSON AFB OH 45433-7817
(513)-255-9807
FAX: (513)-255-9804

MR DAVID J CALLIGAN
MENASCO AEROSYSTEMS INC
PO BOX 500
4000 S HWY 157
EULESS TX 76040-0500
(817)-685-3574
FAX: (817)-283-4591

MR DAVID D CAMPBELL
SPEC ENG
LOCKHEED MARTIN AERO CO
MS 0160
86 S COBB DR
MARIETTA GA 30063-0001
(770)-494-6990
FAX: (770)-494-9610

MR T VAL CANNON
CUSTOMER TECH SUPPORT ENGR
BOEING DEF & SPACE GRP
M/S 3E-JC
PO BOX 3999
SEATTLE WA 98124-2499
(206)-657-3586
FAX: (206)-657-3736

MR GEORGE CARDEA
ARINC
STE 210
4335 PIEDRAS DR W
SAN ANTONIO TX 78228-1210
(210)-733-7559
FAX: (210)-733-9406

MR JOE CARDINAL
ENGR
SOUTHWEST RES INST
6220 CULEBRA RD
PO DRAWER 28510
SAN ANTONIO TX 78238-5166
(210)-522-2687
FAX: (210)-522-3486

MR DONALD W CHAFFEE
LOCKHEED AERO SYS
M/S 0199 D/73-05 CC34
86 S COBB DR
MARIETTA GA 30063-0199
(770)-494-3074
FAX: (770)-494-5207

MR GARY CHAMBERLAIN
AERO ENGR
US AIR FORCE
WR-ALC/TIEDD
420 SECOND ST/STE 100
ROBINS AFB GA 31098-1640
(912)-926-4228
FAX: (912)-926-1743

DR CHRISTOS C CHAMIS
AEROSPACE ENGR
NASA LEWIS RES CTR
MS 49-6
21000 BROOKPARK RD
CLEVELAND OH 44135-3191
(216)-433-3252
FAX: (216)-433-5649

DR JAYCEE H CHUNG
SEC MGR
E-SYS INC
CBN 204
PO BOX 6056
GREENVILLE TX 75403-6056
(903)-457-5096
FAX: (903)-408-8793

MR GREG CLEVELAND
SMITHS INDUSTRIES
4141 EASTMAN AVE SE
GRAND RAPIDS MI 49518-8727
(616)-241-8522
FAX: (616)-241-7965

MR JOSEPH B COCHRAN
STAFF ENGR
LOCKHEED AERO SYS CO
DEPT 73-25 ZONE 0160
86 S COBB DR
MARIETTA GA 30063-0160
(770)-494-2166
FAX: (770)-494-9610

MR HAIM COHEN
ISRAELI AIR FORCE
7 BARAK ST
HERZELIA ISRAEL

CMD DOUG CONNOR
US COAST GUARD
CMDT (G-EAE-3)
2100 SECOND ST SW
WASHINGTON DC 20593-0001
(202)-267-0204
FAX: (202)-267-4135

MR BRITT COVINGTON
AIR FORCE SAFETY AGENCY
HQ AFSA/SESE
9700 AVENUE G
KIRTLAND AFB NM 87117-5670
(505)-846-0990
FAX: (505)-846-6826

MR BRADFORD A COWLES
MGR MECH & MATLS STRUCT
PRATT & WHITNEY
MS 707-20
PO BOX 109600
WEST PALM BEACH FL 33410-9600
(407)-796-6554
FAX: (407)-796-6443

DR MATTHEW CREAGER
CONSULTANT
STRUCTURAL INTEGRITY ENGRG
STE 200
9560 TOPANGA CANYON BLVD
CHATSWORTH CA 91311-0001
(817)-718-2195
FAX: (818)-718-2212

MR DAVID J CODDINGTON
TECH PROG MGR
FATIGUE TECH INC
100 ANDOVER PARK W
SEATTLE WA 98188-2868
(206)-246-2010
FAX: (206)-244-9886

2D LT DAVID S CONLEY
AERO ENGR
US AIR FORCE
WL/FIBEC
BLDG 45 2130 EIGHTH ST
WRIGHT-PATTERSON AFB OH 45433-0001
(513)-255-6104
FAX: (513)-476-4999

MR THOMAS D COOPER
UNIVERSAL TECHNOLOGY CORP
4031 COLONEL GLENN HWY
DAYTON OH 45431-0001
(513)-426-8530
FAX: (513)-426-8755

MR WILLIAM D COWIE
STRUC INTEGRITY INTEGRATION ENGR
GE AIRCRAFT ENGINES
M/S H315
ONE NEUMANN WAY
CINCINNATI OH 45215-6301
(513)-552-4908
FAX: (513)-552-4921

MR DAVID M CRAIG
PRATT & WHITNEY
M/S 01 MA3
1000 MARIE VICTORIN
LONGUEIL MONTREAL CANADA J4G-1A1
(514)-647-3736
FAX: (514)-647-2319

MR JEAN-MARCEL DAUPHANT
MINISTRY OF DEFENSE
STPA
4 AVE DE LA PORTE D'ISSY
75015 PARIS FRANCE-0001

T J DE VRIES
DELFT UNIV OF TECH
DELFT NETHERLANDS

MR ANDREW R DEAN
US AIR FORCE
SA-ALC/LADD
514 SHOP LN/STE 2
KELLY AFB TX 78241-6434
(210)-925-4525

MR MARK S DEFAZIO
AERO ENGR
US AIR FORCE
ASC/YPVF
WRIGHT-PATTERSON AFB OH 45433-7205
(513)-255-4236
FAX: (513)-476-4896

MR ANTHONY G DENYER
TECH STAFF
ROCKWELL INTL
2600 WESTMINSTER BLVD
PO BOX 3644/MS SL-15
SEAL BEACH CA 90740-7644
(310)-797-2825
FAX: (310)-797-3756

MR BORO DJORDJEVIC
THE JOHNS HOPKINS UNIV
CTR NDE
MARYLAND HALL 102
3400 N CHARLES ST
BALTIMORE MD 21218-0001
(410)-516-5215
FAX: (410)-516-5293

MR DAVID E DOUGLAS
C-130 PROJ ENGR
ARINC
USN (USMC)
2551 RIVA RD
ANNAPOLIS MD 21403-0001
(410)-266-4432

MR JOHN P DOWSON
CHIEF TECH
ROYAL AF
E3D ENGINEERING
RAF WADONETON
LINCOLN UK LN59NB-0001

MIKE J DUBBERLY
CONSULTANT
FATIGUE TECH INC
6250 TERRAPIN DR
MANASSAS VA 22111-3807
(703)-791-3634
FAX: (703)-791-5467

MR ERIC T EASTERBROOK
ENGRG MGR
FATIGUE TECH INC
100 ANDOVER PARK W
SEATTLE WA 98188-2868
(206)-246-2010
FAX: (206)-244-9886

MR ROBERT G EASTIN
BR MGR
MCDONNELL DOUGLAS AERO
M/S TA-EEO 159-59
1510 HUGHES WAY
LONG BEACH CA 90810-1870
(310)-982-5423
FAX: (310)-982-2179

MR C B EATON
CHRYSLER TECH AIRBORNE SYS
M/S 1135
7500 MAEHR
WACO TX 76715-4580
(817)-867-4285
FAX: (817)-867-4597

DR CHARLES ELLIOTT III
RES ASST PROF
UNIV OF UTAH
MECH ENGR
MEB ROOM 3209
SALT LAKE CITY UT 84112-0001
(801)-585-6429
FAX: (801)-581-8692

MR JOHN H ELSNER
RES ENGR
ANALYTICAL SERVICES & MATLS INC
FATIGUE & FRAC TEST FAC
BLDG 65 AREA B
WRIGHT-PATTERSON AFB OH 45433-0001
(513)-255-0434
FAX: (513)-476-7379

MR PAUL ELWELL
MOOG ESPRIT
SENECA & JAMISON RDS
E AURORA NY 14052-0018
(716)-687-4478
FAX: (716)-652-0633

MS ANN M EMBREY
FEDERAL AVIATION ADMIN
AVIATION SYS STDS
M/S AVN-347
6500 S MCARTHUR
OKLAHOMA CITY OK 73125-4932
(405)-954-8713
FAX: (405)-954-9532

MR JOSEPH W EVANCHO
PRESIDENT
STRUCTURAL LAMINATES CO
510 CONSTITUTION BLVD
NEW KENSINGTON PA 15068-0001
(412)-339-6888
FAX: (412)-339-6978

FLT LT MICHAEL P EVANS
RAF ST ATHAN
ROYAL AIR FORCE
RAT ST ATHAN
NDT SQUADRON
BARRY S GLAMORGAN CF62 4LB-UK

MR ROBERT G EVANS
STRUCTURAL ENGR
US AIR FORCE
OC-ALC/LABEF
PO 621
CHOCTAW OK 73020-0001
(405)-736-5194
FAX: (405)-736-5598

MR RICHARD A EVERETT JR
US ARMY VEHICLE STRUCTURES DIR
NASA LANGLEY RES CTR
M/S 188E
ANSRL-VS-S
HAMPTON VA 23681-0001
(804)-864-3459
FAX: (804)-864-8911

MR JOAO FI FALCAO
STRUC SCIENCES GRP LDR
NORTHROP GRUMMAN CORP
MO9-223
PO BOX 9650
MELBOURNE FL 32904-9650
(407)-951-6467
FAX: (407)-951-6115

CAPT SCOTT FAWAZ
US AIR FORCE
TECHNICAL UNIVERSITY DELFT
KLUYVERWEG 1
2629 HS DELFT
NETHERLANDS

UDO G FICHTLER
CAPT
GAF AMO
POSTFACH 902500 KOLN
COLOGNE GERMANY 51140-0001

MR SCOTT S FIELDS
PROJ ENGR
MCDONNELL DOUGLAS AERO
M/S 1022147
PO BOX 516
ST LOUIS MO 63166-0001
(314)-234-0032
FAX: (314)-234-8915

MS GUADALUPE FLORES
AERO ENGR TECH
US AIR FORCE
SA-ALC/LADD
514 SHOP LN BLDG 323 STE 2
KELLY AFB TX 78241-6434
(210)-925-4525

DR THOMAS H FLOURNOY
CORROSION TECH MGR
FEDERAL AVIATION ADMIN
FAA TECHNICAL CTR
AGING AIRCRAFT AAR 430
ATLANTIC CITY NJ 08405-0001
(609)-485-5327
FAX: (609)-485-4569

MR ROYCE G FORMAN
SR SCIENTIST
NASA JOHNSON SPACE CTR
MATERIALS BRANCH (EM2)
HOUSTON TX 77058-0001
(713)-483-8926
FAX: (713)-244-2319

MAJ ROBERT S FREDELL
MTLS DIV CHF
US AIR FORCE
2354 FAIRCHILD DR
HQ USAFA/DFEN STE 6112
USAF ACADEMY CO 80840-6240
(719)-472-2196
FAX: (719)-472-2944

MR JOCHEN P FUHR
DIPLOMA ENGINEER
LUITWAIENWERFT 13
CORROSION CONTROL QA
LANDSHUTER STR 70
ERDING GERMANY 85435-0001

DR JOSEPH P GALLAGHER
HEAD STRUC INTEG
UNIV OF DAYTON RES INST
300 COLLEGE PARK DR
DAYTON OH 45469-0120
(513)-229-4417
FAX: (513)-229-3712

MR DEWAYNE J GARRETT
STRESS SECTION HEA
CHRYSLER TECH INC
DEPT FLIGHT SCIENCES
7500 MAEHR RD MS 1135
WACO TX 76715-0001
(817)-867-4267
FAX: (817)-867-4597

SYLVAIN FORGUES
BOMBARDIER CANADAIR DSD
10000 CARGO A-4 STREET
MONTREAL INTL AIRPORT
MIRABEL QUEBEC CANADA J7N-1H3
(514)-476-4000
FAX: (514)-476-4416

MR JOBST F FRANK
GERMAN MOD
AMC PO BOX 33668
WRIGHT-PATTERSON AFB OH 45433-0668
(513)-255-6660
FAX: (513)-255-1970

MR CARL A FRENCH
PRINCIPAL ENGR
BOEING DEF & SPC GRP
2601 LIBERTY PKWY
MIDWEST CITY OK 73110-0001
(405)-739-1410
FAX: (405)-739-1416

MR RICHARD GAGNON
CANADIAN ARMED FORCES
AERO EQUIP PROG MGMT
GEORGE A PARKS BLDG
OTTAWA ONTARIO CANADA K1A-0K2
(613)-491-9573
FAX: (613)-943-2765

MR HARISH GANAPATHY
RES ASSIS
PURDUE UNIV
SCHOOL OF AERO & ASTRO
1282 GRISSOM HALL #350
W LAFAYETTE IN 47907-1282
(317)-496-1990
FAX: (317)-496-0307

MR PHIL K GATLIN
ASSO FELLOW
PRATT & WHITNEY
PO BOX 109600
M/S 731-82
W PALM BEACH FL 33410-9600
(407)-796-3492
FAX: (407)-796-5362

MR WILLIAM L GEESE
US AIR FORCE
ASC/YTJ BLDG 56
2100 MONOHAN WAY
WRIGHT-PATTERSON AFB OH 45433-7014
(513)-255-9306
FAX: (513)-255-8516

MR ROBERT D GIESE
AEROSPACE ENGR
SCIENTECK/LACM
447N 3500W
WEST POINT UT 84015-0001
(801)-392-6980
FAX: (801)-392-6996

DR BRUCE R GIRDWOOD
DR
MTLS SCIENCE & TECH
PO BOX 395
PRETORIA S AFRICA 0001-0001
(012)-841-2226
FAX: (012)-841-3378

LT DAVE A GOLDSTEIN
AERO ENGR
US AIR FORCE OC-ALC/TILOF
2017 DOWNING ST
TINKER AFB OK 73120-0001
(405)-736-5306
FAX: (405)-736-3086

DR MATTHEW J GOLIS
PRES
ADVANCED QUALITY CONCEPTS
264 FAIRLAWN
PO BOX 141388
COLUMBUS OH 43214-0001
(614)-268-0518
FAX: (614)-267-6288

HUMBERTO N GONCALO
LT COL
PORTUGUESE AF
CLAFA
AMADORA PORTUGAL 2730 AL-0001
(351)-471-3549
FAX: (351)-471-6361

MR DAVID GRAHAM
CHIEF ENG
DSTO AERO LAB
506 GRIMER ST
FISHERMENS BEND
MELBOURNE VC 3207-0001

DR ALTEN F GRANDT JR
PURDUE UNIV
AERO & ASTRO
1282 GRISSOM HALL
W LAFAYETTE IN 47907-1282
(317)-494-5141
FAX: (317)-494-0307

MR BILLY J GREGG
PRATT & WHITNEY
PO BOX 2691
W PALM BEACH FL 33402-0001

MR LOUIS L GRENIER
CANADIAN FORCES
DEPT OF NATIONAL DEFENCE
MGEM G R PEARKES BLDG
OTTAWA ONTARIO CANADA K1A-OK2
(613)-991-9541
FAX: (613)-998-6922

MR STEPHEN C GRESLEY
PROG MGR
SMITHS INDUSTRIES
M/S 231
4141 EASTERN SE
GRAND RAPIDS MI 49505-8727
(616)-241-8643
FAX: (616)-241-7318

MR RICHARD L GROVER
NORTHROP GRUMMAN CORP
M/S T245/GK
8900 E WASHINGTON BLVD
PICO RIVERA CA 90660-0001
(310)-948-8944
FAX: (310)-948-8068

MR CORNELIS B GUIJT
RES ENGR
US AIR FORCE ACADEMY
DFEM
2354 FAIRCHILD DR/MS 6H2
COLORADO SPRINGS CO 80840-6240
(219)-472-3043
FAX: (219)-472-2944

JAN WILLEM GUNNINK
VP TECH & DESIGN
STRUCTURAL LAMINATES CO
KLUYVERWEG 1
2629 HS DELFT
THE NETHERLANDS

MR GEORG GUNTHER
G GUNTHER
DEUTSCHE AERO AG
LME222
PO 801160
MUNCHEN GERMANY 81663-0001

MR RATKO H GVOZDIC
AEROSPACE ENGINEER
MARTEC LIMITED
AEROSPACE
1888 BRUNSWICK ST
SUITE 400
HALIFAX CANADA B37 3J8-0001
(902)-425-5101
FAX: (902)-421-1923

MR FRED HAAKE
MANAGER EXP MECH
PRATT & WHITNEY
MS 706-06
PO BOX 109600
WEST PALM BEACH FL 33410-9600
(407)-796-6579
FAX: (407)-796-6443

PROF GEORGE T HAHN
MATLS SCI & ENGRG
VANDERBILT UNIV
STATION B
PO BOX 1592
NASHVILLE TN 37235-0001

MR KEVIN B HALL
ACS ENG
LOCKHEED
DEPT 73-25/ZONE 0160
1433 LIVINGSTON DR
MARIETTA GA 30064-0001
(404)-494-4712
FAX: (404)-494-9610

MR STEPHEN R HALL
CELERIS AERO CANADA INC
PO BOX 51001
ORLEANS
ONTARIO CANADA K1E-3W4
(613)-837-1161
FAX: (613)-834-6420

MR DAVID W HARPER
CHIEF ENGINEER
US AIR FORCE
HQ AFSA/SES
9700 AVE G SE
KIRTLAND AFB NM 87117-5670
(505)-846-0996
FAX: (505)-846-2721

DR CHARLES E HARRIS
NASA LANGLEY RES CTR
M/S 188E
HAMPTON VA 23681-0001
(804)-864-3492
FAX: (804)-864-7729

MR JIM HARRISON
METAL IMPROVEMENT CO INC
1618 S IDA
WICHITA KS 67211-0001
(316)-267-8201
FAX: (316)-267-5735

MR JAMES A HARTER
US AIR FORCE
WL/FIBEC BLDG 45
2130 EIGHTH STREET STE 1
WRIGHT-PATTERSON AFB OH 45433-7542
(513)-255-6104
FAX: (513)-476-4999

MR ROBERT LEE HARTLEY
AERO ENGR
US AIR FORCE

MR SCOT HARVEY
B-1B STRUC ENGR TEAM COORD
US AIR FORCE
OC-ALC/LABEF
BIB SSM
TINKER AFB OK 73020-0001
(405)-736-2749
FAX: (405)-736-5598

MR JUERGEN HEILIG
HQ NAEWFC
FCLE
HQ NAENFC
B 7010 SHAPE
BELGIUM

MR MICHAEL HEINER
US AIR FORCE
OO-ALC/LFIT
6089 WARDLEIGH RD
HILL AFB UT 84056-5838
(801)-777-9318
FAX: (801)-773-9782

GEORGE H HEINTZ
LCDR
US COAST GUARD
AIRCRAFT REPAIR & SUPPLY CENTER
ELIZABETH CITY NC 27909-0001
(919)-335-6631
FAX: (919)-335-6463

MR GRANT D HERRING
AEROSPACE ENGR
OGDEN ALC/LACM
F4 STRUCTURES
7278 4TH ST
HILL AFB UT 84056-5205
(801)-777-0535
FAX: (801)-777-5374

MS PAMELA HERZOG
AERO ENGR
US AIR FORCE
OC-ALC/LAKRA
3001 STAFF DR/STE 2AH110
TINKER AFB OK 73145-3022
(405)-736-3343
FAX: (405)-736-5412

MR THOMAS E HESS
NAVAL AIR WARFARE CTR
CODE 4.3.3
PO BOX 5152/MS08
WARMINSTER PA 18974-0591
(215)-441-1463
FAX: (215)-956-4005

DR PAUL HEULER
INDUST-BETRIEBSGESELLSCHAFT
TAB
EINSTEINSTRASSE 20
OTTOBRUNN GERMANY

MR JAMES M HILL
US AIR FORCE
OC-ALC/TILO
TINKER AFB OK 73145-0001
(405)-736-2663
FAX: (405)-736-3086

PROF BEN M HILLBERRY
MECH ENGRG
PURDUE UNIV
BLDG 1288
1282 GRISSOM HALL
W LAFAYETTE IN 47907-1282
(317)-494-5721
FAX: (317)-494-0539

MR CARL K HINGER
VICE PRES
AEROSTRUCTURES INC
1725 JEFFERSON DAVIS HWY
SUITE 701
ARLINGTON VA 22203-0001
(703)-413-1600
FAX: (703)-413-1611

DR MARGERY E HOFFMAN
AEROSPACE ENGR
NAVAL AIR WARFARE CTR
CODE 4333
PO BOX 5152/M/S 08
WARMINSTER PA 18974-0591
(215)-441-1695
FAX: (215)-956-4005

DR MASAMICHI HONGO
FRACTURE MECH SPEC
PRATT & WHITNEY CANADA
1000 MARIE-VICTORIN
LONGUEUIL QUEBEC CANADA J4G-1A1
(514)-677-9411
FAX: (514)-647-2553

MR CHRISTOPHER HOYLE
HEAD FATIGUE/FRACTURE
BAE AEROSTRUCTURES
MILITARY BUSINESS UNIT
GREENGATE; MIDDLETON
MANCHESTER UK M241SA-0001

MR TROY S HULLANDER
ASIP MNG
NAVAL AVIATION DEPOT
500A HWY 70 W
HAVELOCK NC 28532-0001
(919)-466-8519
FAX: (919)-466-8502

MR LEX C HUTCHESON
PROG MGR
SVERDRUP TECH INC
ADV SYS GROUP
4538 CENTERVIEW DR
SUITE 130
SAN ANTONIO TX 78228-0001
(210)-733-3383
FAX: (210)-733-3389

MAJ YASUHIRO ISAKARI
JAPAN DEFENCE AGENCY
1-2-24 IKEJIRI
SETAGAYA-KU
TOKYO JAPAN 154-0001

MR JOSEPH R HOLTON
DESIGN & STRUCT MGMT
LOCKHEED MARTIN AERONAUTICAL SYS CO
M/S 0199 D/73-24
86 S COBB DR
MARIETTA GA 30063-0160
(404)-494-2885
FAX: (404)-494-9617

MR WALLY C HOPPE
PHYSICIST
SYSTEMS RES LABS
2800 INDIAN RIPPLE RD
DAYTON OH 45440-3696
(513)-427-7761
FAX: (513)-427-7745

CAPT NEIL F HUBER
TEAM LEAD
US AIR FORCE WL/POTC
1950 FIFTH ST
WRIGHT-PATTERSON AFB OH 45433-0001
(513)-255-2734
FAX: (513)-255-2660

MR NOEL M HUPP
GONZALEZ ENG
6633 E STATE BLVD
FT WAYNE IN 46815-0001
(219)-486-6226
FAX: (219)-485-2918

MR NICHOL HUYNH
ENGINEER
US AIR FORCE
ENGR & TECH SERV
C/KC-135 MANAGMENT DIR
3001 STAFF DR STE 2AC489
TINKER AFB OK 73145-0001
(405)-736-3832
FAX: (405)-736-5604

MR DANIEL A JANSEN
AS&M
FATIGUE & FRACTURE TEST FAC
BLDG 65/AREA B
WRIGHT-PATTERSON AFB OH 45433-0001
(513)-255-0434
FAX: (513)-476-7379

MR RANDY L JANSEN
AERO ENGR
US AIR FORCE
WR-ALC/TIEDD
420 2ND ST/STE 100
ROBINS AFB GA 31098-1640
(912)-926-4228
FAX: (912)-926-1743

MS MALDWYN JENKINS
BOMBARDIER INC
10000 CARGO RD A-4
MONTREAL INTL AIRPORT
MIRABEL QUEBEC CANADA J7N-1H3
(514)-476-4201
FAX: (514)-476-4207

MR FRANK R JOHNSON JR
LEAD STRUC ANALYST
E SYSTEMS
MS CBN 204
MAJORS FIELD
GREENVILLE TX 75403-0001
(903)-457-3278
FAX: (903)-457-7871

LT COL CRAIG R JONES
WR-ALC/LJEA
PO BOX 11424
ALBUQUERQUE NM 87192-0424
(505)-845-9063
FAX: (505)-844-8711

LTCOL JOHN R JOOSTEN
LT COL
ROYAL NETHERLANDS AF
MOD FIGHTER DIV
BINCKHORSTLAAN 135
PO BOX 20703
THE HAGUE NETHERLAND 2500ES-0001

MR OO-CHUL JUN
ADD
3-HWANG-2GLE TEAM
PO BOX 35
YUSEONG TAEJON S KOREA-0001

MR MARK JARVIS
S3 PROG ENG
LMAS GA
70 E1
8305 CHAISTAIN
ATLANTA GA 30342-0001
(770)-494-3643
FAX: (770)-494-8478

DR DAVID Y JEONG
MECH ENG
US DEPT OF TRANS
M/S DTS-76
KENDALL SQ
CAMBRIDGE MA 02142-1093
(617)-494-3654
FAX: (617)-494-3066

MR HERMAN E JOHNSON
FRACTURE MECHANICS
PRATT & WHITNEY
M/S 714-03
PO BOX 109600
W PALM BEACH FL 33418-9600
(407)-796-5151
FAX: (407)-796-8993

MR YOUNG S JOO
AGENCY FOR DEF DEV
BLDG 3-1-1
YUSONG PO BOX 35-3
TAEJON KOREA
(042)-821-3349
FAX: (042)-823-3400

MR VICTOR JUAREZ
SR ENGRG SPEC
LOCKHEED MARTIN TAC AIR SYS
M/Z 2846
PO BOX 748
FT WORTH TX 76101-0001
(817)-763-2926
FAX: (817)-762-2634

MR MASAMI KAGEYAMA
JAPAN DEFENSE AGY
3RD RESEARCH CTR
1-2-10 SAKAE-CHO
TACHIKANA TOKYO JAPAN-190

HARUHIRO KANEKO
MITSUBISHI HEAVY IND LTD
NAGOYA AEROSPACE SYS
10 OYE-CHO MINATO-KU
NAGOYA
455 JAPAN-0001
(052)-611-8027
FAX: (052)-611-8125

MR MITCHELL KAPLAN
ENGR
WILLIS & KAPLAN
720 ARMSTRONG DR
BUFFALO GROVE IL 60089-0001
(708)-215-7757

MR TIMOTHY C KELLEY
E-SYSTEMS
CBN 101
PO BOX 6056
GREENVILLE TX 75403-6056
(903)-457-4719
FAX: (903)-457-4413

MR ALAN P KERR
CHIEF DESIGN ENGINEER
ARTI/DYNCORP
1 RIDGMAR CENTRE
6500 W FREEWAY
FT WORTH TX 76116-2187
(817)-737-1656
FAX: (817)-737-1605

MR PAUL J KLOSE
ASI ID LSA
ROYAL AUSTRALIAN AF
RAAF WILLIAMS
LAVERTON BASE
LAVERTON VIC 3027-0001

LT SHANE A KNIGHTON
C-5 STRUC ENGR
US AIR FORCE
SA-ALC/LADS
14001 OAK MEADOWS #1612
UNIVERSAL CITY TX 78148-0001
(210)-925-6852
FAX: (210)-925-2087

MR SAM KANTIMATHI
PRESIDENT
FATIGUE CONCEPTS
300 SALAMON FALLS RD
EL DORADO HILLS CA 95762-9734
(916)-933-3360
FAX: (916)-933-3361

LTC ROLF KEIMER
LIAISON OFFICER
GERMAN AIR FORCE
AIR LOGISTICS CNTR OGDEN
OO-ALC / LAI-GY
6089 WARDLEIGH RD
HILL AFB UT 84056-5838
(801)-777-5743
FAX: (801)-773-7620

MR DAVE F KELLY
US AIR FORCE
SA-ALC/LADD
514 SHOP LN/STE 2
KELLY AFB TX 78241-6420
(210)-925-4525
FAX: (210)-925-9940

MR PHILLIP C KLOOS
MTS SYSTEMS CORP
AERO STRUCT & MATLS GRP
M/S MTD-3
14000 TECHNOLOGY DR
EDEN PRARIE MN 55344-2290
(612)-937-4854
FAX: (612)-937-4515

MR ANDREW J KNIGHT
FLIGHT LEIUTENANT
ROYAL AIRFORCE
LSS2 FLME1
BLK L PO BOX 70
HUNTINGDON ENGLAND PE172P4-0001

MR JAMES KOKORIS
NORTHROP GRUMMAN CORP
M/S B13-025
S OYSTER BAY RD
BETHPAGE NY 11714-0001
(516)-346-8814
FAX: (516)-346-3290

DR H J KONISH
TECH SPECIALIST
ALCOA TECH CTR
100 TECHNICAL DR
BLDG D-PDM
ALCOA CTR PA 15069-0001
(412)-337-2736
FAX: (412)-337-5436

MS JULIE KRAMER
NASA JOHNSON SPACE CTR
MC ES23
2101 NASA RD
HOUSTON TX 77058-0001
(713)-483-8866
FAX: (713)-483-3789

MR SRINIVAS KRISHNAN
RES SCIENTIST
AS&M
FATIGUE & FRAC TEST FAC
BLDG 65 AREA B
WRIGHT-PATTERSON AFB OH 45433-0001
(513)-255-0434
FAX: (513)-476-7379

MR MARCEL JBM LAMBRICHS
MAJOR
ROYAL NETHERLANDS AF
BINCHORSTLAAN 135
PO BOX 20703
THE HAGUE NETHERLAND 2516 BA-0001

MR RICHARD R LAURIDIA
TECH PROJ MGR
NORTHROP GRUMMAN
M/S 49L-66
PO BOX 655907
DALLAS TX 75265-5907
(214)-266-4267
FAX: (214)-266-2407

MR EUN U LEE
MTL ENG
NAVAL AIR WARFARE CTR
MS 03 4342
22541 MILLSTONE RD
PATUXENT RIVER MD 20670-5304
(301)-342-8069
FAX: (301)-342-8062

MR ROBERT KRAFT
TECH TEAM LEADER
PRATT & WHITNEY
M/S 715-97
PO BOX 109600
W PALM BEACH FL 33410-9600
(407)-796-2414
FAX: (407)-796-9001

DR BOGDAN R KRASNOWSKI
SR ENG SPEC
BELL HELICOPTER
600 E HURST BLVD
HURST TX 76053-0001
(817)-280-2127
FAX: (817)-280-8772

MR JOSEPH S KUZNIAR
DEP PROG MGR LOG
US AIR FORCE
WL/CCI BLDG 45
2130 EIGHTH ST/STE 1
WRIGHT-PATTERSON AFB OH 45433-7542
(513)-255-5430
FAX: (513)-476-4572

CAPT NORMAND LANDRY
NATIONAL DEFENCE HDQUARTERS
MAJ GEN GEO PEARKES BLDG
DTA 3-3-8
OTTAWA ONTARIO CANADA K1A-0K2
(613)-993-2320
FAX: (613)-613-9986

CAPT SERGE A LE GUELLEC
CANADIAN FORCES
DIR OF TECH AIRWORTHINESS
DTA 3-3-8
MAJ GEN GEO PEARKES BLDG
OTTAWA ONTARIO CANADA K1A-0K2
(613)-993-2320
FAX: (613)-998-6922

MR JEONG S LEE
AGENCY FOR DEF DEV
BLDG 3-1-1
YUSONG PO BOX 35-3
TAEJON KOREA
(042)-821-3349
FAX: (042)-823-3400

MR BENOIT JJB LEFEBURE
CANADIAN FORCES (DEPT OF NATL DEF)
AIRCRAFT ENGRG ORG
BLDG 155 ROCKCLIFF
OTTAWA ONTARIO CANADA K11-0K2
(613)-991-9571
FAX: (613)-993-2765

MR KEVIN LEWIS
MEASUREMENT SYS INC
STE B
2262 NORTHWEST PKWY
MARIETTA GA 30067-0001
(770)-951-0878
FAX: (770)-951-8920

MR EUI I LIM
DURABILITY & DAMAGE TOLERANCE
MCDONNELL DOUGLAS CORP
MC 801-45
3855 LAKEWOOD BLVD
LONG BEACH CA 90846-0001
(310)-593-6730
FAX: (310)-982-7755

DR JOHN W LINCOLN
TECH EXPERT
US AIR FORCE ASC/ENFS
BLDG 125
2335 SEVENTH ST STE 6
WRIGHT-PATTERSON AFB OH 45433-7809
(513)-255-6879
FAX: (513)-255-4789

MR KO-WEI LIU
MCDONNELL DOUGLAS AERO
M/S TA-EEX 159-59
1510 HUGHES WAY
LONG BEACH CA 90810-1864
(310)-982-5422
FAX: (310)-982-5164

DR TAI-SHENG LIU
STRUC MECH GRP DTA SPEC
CHRYSLER TECHNOLOGIES
M/S 1135
PO BOX 154580
WACO TX 76715-4580
(817)-867-7408
FAX: (817)-867-4597

MR MORGAN A LOWE
LOCKHEED MARTIN
5600 SAND LAKE RD
MP-708
ORLANDO FL 32819-8907
(407)-356-9973
FAX: (407)-356-6725

MR AUDGEIR LUNDE
ROYAL NORWEGIAN AF MATL CMD
M/S DFIS
PO BOX 10
N2007 KJELLER NORWAY

MR PANAGIOTIS MAHERAS
HELLENIC AIR FORCE
RESEARCH CENTRE (KETA)
16501 GLYFADA
ATHENS GREECE 19200-0001

MR CHRIS MANDERS
CHRYSLER TECH AIRBORNE SYS
M/S 1135
7500 MAEHR
WACO TX 76705-0001
(817)-867-4051
FAX: (817)-867-4597

DR SHERRELL D MANNING
LOCKHEED MARTIN TACT AIR SYS
M/Z 4267
PO BOX 748
FT WORTH TX 76101-0001
(817)-935-2913
FAX: (817)-935-3800

MR NORMAN MARCHAND
AMRA TECHNOLOGIES
STE 300
4700 DE LA SAVANE
MONTREAL CANADA H4P-1T7
(514)-344-2252
FAX: (514)-344-1866

DR GEORGE A MATZKANIN
DIR
NTIAC TRI
415 CRYSTAL CREEK DR
AUSTIN TX 78746-4725
(512)-263-2106
FAX: (512)-263-3530

MR JAMES J MAZZA
MTLS ENGR
US AIR FORCE WL/MLSE
2179 TWELFTH ST STE 1
WRIGHT-PATTERSON AFB OH 45433-7718
(513)-255-7484
FAX: (513)-476-4419

MR ALLAN MCCRAY
CAE AVIATION LTD
PO BOX 9864
EDMONTON INTL AIRPORT
EDMONTON ALBERTA CANADA T5J-2T2
(403)-890-6623
FAX: (403)-890-6543

DR PETER C MCKEIGHAN
SR RESEARCH ENGR
SOUTHWEST RESEARCH INST
6220 CULEBRA RD
PO DRAWER 28510
SAN ANTONIO TX 78228-0510
(210)-522-3617
FAX: (210)-522-5122

MR MIKE MCMAHON
NAVAL AIR SYS CMD
1421 JEFFERSON DAVIS HWY
WASHINGTON DC 22243-5120
(703)-604-3400
FAX: (703)-604-4396

MR ROBERT D MEADOWS
FEDERAL AVIATION ADMIN
14312 SE 111TH ST
OKLAHOMA CITY OK 73165-0001
(405)-794-1318

MR WILLIAM B MAYS
SYSTEMS RESEARCH IND
AUTOMATED INSPECTION SYS
2800 INDIAN RIPPLE RD
DAYTON OH 45440-3696
(513)-427-7776
FAX: (513)-427-7745

MR JOHN MCCOURY
CHRYSLER TECH AIRBORNE SYS
M/S 1135
7500 MAEHR
WACO TX 76715-4580
(817)-867-4254
FAX: (817)-867-4597

MR SIDNEY MCKEEL
AERO ENGR
US AIR FORCE
SA-ALC/LPFE B171
303 WILSON BLVD/STE 3
KELLY AFB TX 78241-5443
(210)-925-6474
FAX: (210)-925-0095

MR ROBERT L MCKINLEY
LEAD STRUC ENGR
US AIR FORCE
ASC/YTJ/BLDG 56
2100 MONAHAN WAY
WRIGHT-PATTERSON AFB OH 45433-7014
(513)-255-7076
FAX: (513)-255-8516

MR LEONARD J MEADOWS
RAAF TLO FOSTP
ROYAL AUSTRALIAN AIR FORCE
NRC/IAR
BLDG M14/MONTREAL RD
OTTAWA ONTARIO K1A OR6-0001
(613)-993-4817
FAX: (613)-952-7136

DR CHRIS C MGRER
FAA TECH CTR
AIRCRAFT SAFETY DIRECTORATE
AAR 430
ATLANTIC CITY NJ 08405-0001
(609)-485-4284
FAX: (609)-485-4569

MR RICHARD P MICKLOS
NAVAL AIR WARFARE CENTER
CODE 4333
MS 08
WARMINSTER PA 18974-0591
(215)-441-2893
FAX: (215)-956-4005

LCDR JOSEPH E MIHELIC
US COAST GUARD
ARSC ENGINEERING
ELIZABETH CITY NC 27909-0001
(919)-335-6837
FAX: (919)-335-6463

MR GERALD H MINTZ
TECH STAFF
ROCKWELL INTL
VEHICLE & SYS ANALYSIS
M/S AD46
12214 LAKEWOOD BLVD
DOWNEY CA 90241-0001
(310)-922-3358
FAX: (310)-922-3532

MR GEOFFREY O MITCHELL
ARINC RES CORP
STE 500 A
5600 LIBERTY PKWY
MIDWEST CITY OK 73110-2835
(405)-739-0939
FAX: (405)-739-0003

MR W CRAIG MITCHELL
US AIR FORCE
OO-ALC/LAIA F-4 TCG
6089 WARDLEIGH RD
HILL AFB UT 84056-5838
(801)-777-5891
FAX: (801)-773-7620

MR CALVIN MOORE
MTLS ENGR
US AIR FORCE
OC-ALC/TIESM
4750 STAFF DR
TINKER AFB OK 73145-3317
(405)-736-5008
FAX: (405)-736-3992

MR STEVEN MOORE
CHIEF TECH
ROYAL AIR FORCE
STRUCTURES FLIGHT
HQ LOGISTICS CMDT
WYTON HUNTINGDON
CAMBERIDGESHIRE ENGLAND-0001

MR MARK K MORRELL
SYSTEMS ENG
PRATT & WHITNEY
MS 713 55
PO BOX 109600
W PALM BEACH FL 33410-9600
(407)-796-3693
FAX: (407)-796-3637

MS SARAH MORROW
DEFENSE RES AGENCY MOD UK
MSI P69 BLD
DRA FARNBOROUGH
HANTS ENGLAND

MR EDWIN G MULLIN
NAVAL AVIATION DEPOT NI
ISST-R&M CODE 41600
PO BOX 357058
SAN DIEGO CA 92135-7058
(619)-545-0745
FAX: (619)-545-0763

MR FRED D MULLINS
US AIR FORCE
2230 TENTH ST STE 1
WRIGHT-PATTERSON AFB OH 45433-0001
(513)-255-9795
FAX: (513)-255-9804

MR TOMMY MULLIS
NDI ENGR
US AIR FORCE
WR-ALC/TIEDM
420 2ND ST STE 100
ROBINS AFB GA 31098-0001
(912)-926-4489
FAX: (912)-926-1743

MR GEORGE W NEAT
US DOT/VOLPE CTR
KENDALL SQUARE
M/S DTS-74
CAMBRIDGE MA 02142-1093
(617)-494-2679
FAX: (617)-494-3096

MR' ROGER NESJE
ROYAL NORWEGIAN AF
MATERIAL COMMAND
PO BOX 10
KJELLER NORWAY N2007-0001

MS HOANG NGUYEN
US AIR FORCE
OC-ALC/LAKRA
3001 STAFF DR/STE 2AH110
TINKER AFB OK 73145-3022
(405)-736-2748
FAX: (405)-736-5412

MR TOM V NGUYEN
FATIGUE ENGR
LEARJET INC
PO BOX 7707
MS 29
WICHITA KS 67277-7707-0001
(316)-946-6367

MS CATHY NGUYEN-QUOC
STRESS CHALLENGER
CANADAIIR/BOMBARDIER
DEPT 771
400 COTE VERTE WEST
DORVAL QUEBEC CANADA H4S-1Y9
(514)-855-7548
FAX: (514)-855-8201

MR JANGWHAN O
ADD
PN 305-600
3-HWANG-2
PO BOX 35
YUSEONG TAEJON TX S KOREA-0001

MR THOMAS R O'CONNOR
DYNCORP/ARTI
1 RIDGMAR CTR
6500 W FREEWAY
FT WORTH TX 76116-0001
(817)-737-1656
FAX: (817)-737-1605

MR ROBERT K ODIAN
PRINCIPAL ENG
STRUCTURAL INTEGRITY ENGRG
9560 TOPANGA CYN
M/S 200
CHATSWORTH CA 91311-0001
(818)-718-2195
FAX: (818)-718-2212

MR MITSUGI OHKI
MGR
MITSUBISHI HEAVY IND LTD
1 TOYOKA TOYOYAMA-CHO
NISHIKASUGAI-GUN
AICHI-KEN 480-02
JAPAN

MR MATS-OLOF OLSSON
DEFENCE MATL ADM
S-115 88
STOCKHOLM SWEDEN

DR IREWOLE R ORISAMOLU
MGR PROG MECH & REL GRP
MARTEC LIMITED
STE 400
1888 BRUNSWICK ST
HALIFAX NOVA SCOTIA
(902)-425-5101
FAX: (902)-421-1923

CAPT YASUO OTANI
JAPAN DEFENSE AGY
3RD RESEARCH CTR
1-2-10 SAKAE-CHO, TACHIKAWA
TOKYO JAPAN-190

MR TIM PADFIELD
CAE AVIATION LTD
PO BOX 9864
EDMONTON INTL AIRPORT
EDMONTON ALBERTA CANADA T5J-2T2
(403)-890-6498

MR RALPH F PAGLIA
USAF WL/MLS-OL
485 QUENTIN ROOSEVELT RD
STE 7
KELLY AFB TX 78441-6426
(210)-925-6408
FAX: (210)-925-2021

MR CARLOS PAIRAZAMAN
RES PHYSICIST
SYSTEM RESEARCH LABS
SYS RES LABS
2800 INDIAN RIPPLE
DAYTON OH 45440-3696
(513)-427-7850
FAX: (513)-427-7745

S PATEL
PRATT & WHITNEY
E HARTFORD CT

DR DONALD B PAUL
CHF STRUC DIV
US AIR FORCE WL/FIB
BLDG 45
2130 EIGHTH ST STE 1
WRIGHT-PATTERSON AFB OH 45433-7542
(513)-255-3031
FAX: (513)-255-3740

MR SIMON PELLETIER
PROJ ENGR
AMRA TECHNOLOGIES
4700 DE LA SAVANE
STE 300
MONTREAL CANADA H4P-1T7
(514)-344-2252
FAX: (514)-344-1866

MR JORGE D PEREZ
AEROSPACE ENGR
US AIR FORCE
SA-ALC/LADD
514 SHOP LN/STE 2
KELLY AFB TX 78241-6434
(210)-925-4525
FAX: (210)-925-3854

DR RIGO PEREZ
MCDONNELL DOUGLAS AERO
M/S 1022147
PO BOX 516
ST LOUIS MO 63166-0516
(314)-234-0656
FAX: (314)-234-8915

MR JOHN R PHILLIPS
MTLS ENG
US COAST GUARD
TAMSCO
USCG ARSC ENG
ELIZABETH CITY NC 27-0001
(919)-335-6710
FAX: (919)-335-6463

DR ROBERT PIASCIK
NASA LANGLEY RES CTR
M/S 188E
HAMPTON VA 26381-0001
(804)-864-3483

DR ANDREW C PICKARD
MGR DIVIL ENG COMP MGMT
ALLISON ENGINE CO
SPEED CODE 1-15
PO BOX 420
INDIANAPOLIS IN 46206-0420
(317)-230-3646
FAX: (317)-230-2816

MR STEPHEN W PICKENS
GRP ENGR
LEARJET CORP
M/S 29
ONE LEARJET WAY
WICHITA KS 67209-0001
(316)-946-2423
FAX: (316)-946-2809

DR DANIEL S PIPKINS
PROJ ENGR
KNOWLEDGE SYS INC
81 EAST MAIN ST
FORSYTH GA 31029-0001
(912)-994-4051
FAX: (912)-994-4051

MR CHRISTOPHER J POMFRET
ABDA
STE 201
3040 PRESIDENTIAL DR
FAIRBORN OH 45324-0001
(513)-427-2229

MR ROBERT E PRICE
LOGISTIC DATA MGR
CASC US AIR FORCE (LGHD)
74 N WASHINGTON AVE
BATTLE CREEK MI 49017-0001
(616)-961-5442

MR ADARSH K PUN
NORTHROP GRUMMAN
M/S 3852/63
ONE NORTHROP AVE
HAWTHORNE CA 90250-0001
(310)-332-4200
FAX: (310)-332-0583

CHRIS T RATCLIFFE
DIR OF MKTG
MEASUREMENT SYS INC
STE B
2262 NORTHWEST PKWY
MARIETTA GA 30067-0001
(770)-951-0878
FAX: (770)-951-8920

MR DAVID L RATZER
AEROSPACE ENGR
US AIR FORCE
SA-ALC/LADD
514 SHOP LN/STE 2
KELLY AFB TX 78241-6434
(210)-925-4525
FAX: (210)-925-3854

MR DANIEL C REGISTER
US AIR FORCE
WR-ALC/TIEDD
420 2ND ST STE 100
ROBINS AFB GA 31098-1640
(912)-926-4228
FAX: (912)-926-1743

MR LEONARD F REID
VP ENGRG PROG
FATIGUE TECH INC
100 ANDOVER PARK W
SEATTLE WA 98188-2868
(206)-246-2010
FAX: (206)-244-9886

MR EUGENE R REINHART
PRESIDENT
REINHART & ASSO INC
PO BOX 9802
NO 303
AUSTIN TX 78766-0001
(512)-834-8911
FAX: (512)-834-1266

MR KARI J RENKO
FINNISH AIR FORCE
HQ TECH SECTION
PO BOX 30
TIKKAKOSKI FINLAND FIN 41161-0001

MR ROBERT R RENNELL
ARINC
STE 500A
5600 LIBERTY PKWY
MIDWEST CITY OK 73110-2835
(405)-739-0939
FAX: (405)-739-0003

DR PIERRE R ROBERGE
ROYAL MILITARY COLLEGE
CHEMISTRY & CHEM ENGR
KINGSTON ONTARIO CANADA K7K-520
(613)-541-6000
FAX: (613)-542-9489

MR THOMAS A ROBERTS
PRIN STAFF ENGR
LOCKHEED AIRCRAFT
1800 E AIRPORT DR
PO BOX 33
ONTARIO CA 91761-8033
(909)-395-6690
FAX: (909)-395-6500

MR DENNIS ROMANO
ADVERSARY STRUCTURES MGR
NAVAL AVIATION DEPOT NI
CODE 433C R&E
302 DIABLE CREEK CT
CLAYTON CA 94517-0001
(619)-545-0956
FAX: (619)-545-0763

MR JAMES L RUDD
CHF STRUC INTEGRITY BR
US AIR FORCE
2130 EIGHTH ST/STE 1
WL/FIB/BLDG 45 RM 203A
WRIGHT-PATTERSON AFB OH 45433-6553
(513)-255-4269
FAX: (513)-255-3740

MR TIMOTHY K RYAN
PRIN ENGR
ARINC INC
AQUISITION SYSTEMS
2551 RIVA RD
M/S 1-203
ANNAPOLIS MD 21401-7465
(410)-266-4856
FAX: (410)-573-3171

MR JOHN M SAENZ
US AIR FORCE
OC-ALC/LIINT
TINKER AFB OK 73145-0001
(405)-736-2509
FAX: (405)-736-7262

CAPT FELIX SCHAFBERG
GAF
PO BOX 902500/502/09
COLOGNE GERMANY 51140-0001

COL JOHN R ROGACKI
DEPUTY DIR
US AIR FORCE WL/FI-1
2130 EIGHTH ST STE 1
WRIGHT PATTERSON AFB OH 45433-7542
(513)-255-4012
FAX: (513)-255-3438

MR KAJ A ROSANDER
CHIEF ENG TECH
SAAB MILITARY AIRCRAFT
STRUCTURAL TECH
LINKOPING SWEDEN 58188-0001

MR WARD D RUMMEL
D & W ENTERPRISES LTD
8776 W MOUNTAIN VIEW LN
LITTLETON CO 80125-9406
(303)-977-1751
FAX: (303)-977-1145

MR JAMES F SADLER
STRUC INTEGRITY MGR
CURTISS-WRIGHT FLIGHT SYS
DEPT 500
300 FAIRFIELD RD
FAIRFIELD NJ 07004-0001
(201)-575-2267
FAX: (201)-575-2591

MR GILLES SARRAZIN
BOMBARDIER CANADAIR DSD
10000 CARGO A-4 ST
MONTEAL INTL AIRPORT(MIRABEL)
MIRABEL QUEBEC CANADA J7N-1H3
(514)-476-4655
FAX: (514)-476-4451

MS MARY W SCHLEIDER
SECTION LDR
MERCER ENGR RES OFFICE
ENGR ANALYSIS & DESIGN
1861 WATSON BLVD
WARNER ROBINS GA 31093-0001
(912)-929-6400
FAX: (912)-929-6406

MR KURT H SCHRADER
SR RES ENGR
SOUTHWEST RES INST
6220 CULEBRA RD
PO DRAWER 28510
SAN ANTONIO TX 78228-0510
(210)-522-3322
FAX: (210)-522-3042

DR CHRIS C SEHER
MGR AIRWORTHINESS ASSUR R&d BRCH
FED AVIATION ADMIN
AAR-430
ATLANTIC CITY INTL NJ 08405-0001
(609)-485-4284
FAX: (609)-485-4569

MR JEFF SERMERSHEIM
SR PROJ ENGR
MCDONNELL DOUGLAS AERO
MC 0013390
PO BOX 516
ST LOUIS MO 63166-0516
(314)-234-1690
FAX: (314)-777-1045

MR LEONARD L SHAW
AEROSPACE ENGR
US AIR FORCE WL/FIBG
STE 2
2145 FIFTH ST
WRIGHT-PATTERSON AFB OH 45433-7006
(513)-255-5200
FAX: (513)-255-6684

MR WILLIAM R SHEPPARD
SR TECH SPEC
NORTHROP GRUMMAN CORP
AGING AIRCRAFT PROJ
ONE NORTHROP AVE
MS 3852/63
HAWTHORNE CA 90250-0001
(310)-332-9635
FAX: (310)-332-0583

DR DONALD A SHOCKEY
ASSOC DIR
SRI INTL
333 RAVENSWOOD AVE
MENLO PARK CA 94025-0001
(415)-859-2587
FAX: (415)-859-2260

MR DONALD R SHRADER
PRES
TECHNIREP INC
76 LAKENGREN DR
EATON OH 45320-2680
(513)-623-9966
FAX: (513)-456-9944

MR JOHN M SLYE
US AIR FORCE
ASC/YTJVA
BLDG 56 2100 MONAHAN WAY
WRIGHT-PATTERSON AFB OH 45433-7014
(513)-255-9306
FAX: (513)-255-8516

MR JOHNNY R SMITH
GRP ENGR
RAYTHEON AIRCRAFT CO
9709 E CENTRAL
PO BOX 85/DEPT 918
WICHITA KS 67201-0085
(316)-676-7719
FAX: (316)-676-8556

MS MARTHA A SMITH
ADV REPAIR TECH INTL
6500 WEST FREEWAY
FT WORTH TX 76116-2187
(817)-737-1655
FAX: (817)-737-1605

MS MARTY SMITH
SENIOR DESIGN ENGR
DYNCORP/ARTI
ONE RIDGMAR CENTRE
6500 W FREEWAY
FT WORTH TX 76116-0001
(817)-737-1655
FAX: (817)-737-1605

MR NEIL D SMITH
BRISTOL AEROSPACE LTD
LIFE CYCLE SUPPORT
660 BERRY ST
PO BOX 874
WINNIPEG MANITOBA CANADA R3C-2S4
(204)-775-8331
FAX: (204)-783-2168

MR JAMES Y SONG
STRUC ENGR
US AIR FORCE
WL/MLS-OL
5225 BAILEY LP/BLDG 243E
MCCLELLAN AFB CA 95652-2510
(916)-643-3810
FAX: (916)-643-0487

MR TIMOTHY J SORENSEN
AERO ENGR
US AIR FORCE
OO-ALC/LFAS
6080 GUM LANE
HILL AFB UT 84056-5825
(801)-777-9601
FAX: (801)-777-3928

MR VINCENT S SPANEL
CHF ENGR
US AIR FORCE
ASC/LPGH
BLDG 57
WRIGHT-PATTERSON AFB OH 45433-7200
(513)-255-3773

MR DIRK-JAN SPIEKHOUT
NATL AEROSPACE LAB
LOADS DEPT
SALLAND 13 EMMELOORD
THE NETHERLANDS

MR WILLIAM H SPROAT
PROJ ENGR
CUSTOM LIVING CONCEPTS
192 RIDGEVIEW TR SE
CARTERSVILLE GA 30120-0001
(770)-975-0927

MR BRIAN J STELLY
ENG MGR
E SYSTEMS GREENVILLE DIV
FM 1570 MAJORS FIELD
MS CBN 192
GREENVILLE TX 75403-0001
(903)-457-7345
FAX: (903)-457-5605

MR HALLOCK F SWIFT
SR RES SCIENTIST
UNIV OF DAYTON RES INST
SHROYER PARK CENTER RM1930
300 COLLEGE PARK
DAYTON OH 45469-0182
(513)-229-3860
FAX: (513)-229-3869

MR RALPH E SYKES
SPEC ENG
LOCKHEED MARTIN AERO
DEPT 73-25 MS 0160
86 S COBB DR
MARIETTA GA 30063-0001
(770)-494-4302
FAX: (770)-494-9610

MR MATTHEW P SZOLWINSKI
NOSEG FELLOW/ RES ASSIS
PURDUE UNIV
SCHOOL OF AERO & ASTO
1282 GRISSOM HALL #315
W LAFAYETTE IN 47907-1282
(317)-496-1990
FAX: (317)-494-0307

DR REDA TADROS
BMW ROLLS RR
ESCHWENWEG 11
DAHLEWITS GERMANY D-15827-0001

CAPT GRANT L TAKAHASHI
TEAM LEAD
HQ AFMC ENPS
4375 CHIDLAW RD
STE 6
WPAFB OH 45433-5006
(513)-257-1656
FAX: (513)-257-0841

MR LARRY E TARRANT
AEROSPACE ENGR
US AIR FORCE
OC-ALC/TILOF
7851 2ND ST/RM 107
TINKER AFB OK 73145-9145
(405)-736-5424
FAX: (405)-736-3086

MR JOHN L TEN HAVE
ENG
ROYAL NEW ZEALAND AF
PRIVATE BAG
AIRSTAFF FREY BRG BLDG
WELLINGTON NZ

MR MARK A THOMAS
AERO ENG
NAVAL AIR WARFARE CTR
MS 08 CODE 4333
PO BOX 5152
WARMINSTER PA 18974-0591
(215)-441-3971
FAX: (215)-441-2797

DR SANJAY TIKU
RES ASSO
ECOLE POLYTECHNIQUE
MATEIAL SCIENCE & METALLURGY
PO BOX 6079 STATION CENTRE-VILLE
MONTREAL CANADA H3C-3A7
(514)-344-2252
FAX: (514)-344-1866

MR DANIEL O TIPPS
GRP LEADER
UNIV DAYTON RES INST
STRUCTURAL INTEGRITY
300 COLLEGE PK
DAYTON OH 45469-0120
(513)-229-4417
FAX: (513)-229-3712

MR PAUL R TOIVONEN
SR PROJ ENGR
MCDONNELL DOUGLAS
M/C 102 2091
PO BOX 516
ST LOUIS MO 63166-0516
(314)-234-4912
FAX: (314)-232-1394

MR PETER N TOIVONEN
MCDONNELL DOUGLAS
M/C 102-2091
PO BOX 516
ST LOUIS MO 63166-0516
(314)-234-4912
FAX: (314)-232-1394

MR PAUL F TRESE
ENGINEER
MCDONNELL DOUGLAS C-17
5442 CARITA
LONG BEACH CA 90808-0001
(310)-982-5285
FAX: (310)-982-5164

MR DOUGLAS E TRITSCH
GRP LEADER
UNIV DAYTON RES INST
STRUCTURAL INTEGRITY
300 COLLEGE PK
DAYTON OH 45469-0120

MR BILLY R TRUSSELL
F-15 ASIP MGR
US AIR FORCE
WR-ALC/LFEFS
296 COCHRAN ST
ROBINS AFB GA 31098-1622
(912)-926-5482
FAX: (912)-926-5463

MR JIMMY A TURNER
BR CHF
US AIR FORCE
SA-ALC/LADD
514 SHOP LN/STE 2
KELLY AFB TX 78241-6434
(210)-925-4525

MR MIKE TYSON
LOCKHEED-GEORGIA COMPANY
D/73-76 ZONE 0160
86 S COBB DR
MARIETTA GA 30068-0160
(770)-494-1869
FAX: (770)-494-9610

MR NORIO UEHARA
SYS ENGR
MITSUBISHI HEAVY IND LTD
COMP & ENGR MGMT DEPT
10 OYE CHO MINATO-KU
NAGOYA JAPAN

MR DAVID A ULMAN
ENGR SPEC SR
LOCKHEED MARTIN TACTICAL AIR SYS
SSTRUCTURES & DESIGN
MS 4272
FT WORTH TX 76101-0001
(817)-935-3559
FAX: (817)-935-3800

MR BRADLEY D VAN PEURSEM
VICE PRES
WEST COAST INDUSTRIES
14900 WHITMAN AVE N
SEATTLE WA 98133-0001
(206)-365-7513
FAX: (206)-365-7483

DR A K VASUDEVAN
PROG MGR
OFF OF NAVAL RES
CODE 332
800 N QUINCY ST
ARLINGTON VA 22217-5660
(703)-696-8181
FAX: (703)-696-0934

MR MARK VREEKE
SR SCIENTIST
ELTRON RESEARCH INC
STE E
2830 WILDERNESS
BOULDER CO 80301-0001
(303)-440-8008
FAX: (303)-440-8007

MR TOM WADE
US COAST GUARD HQ
2100 2ND ST SW
WASHINGTON DC 20593-0001
(202)-267-2816
FAX: (202)-267-4135

MR RAY A WALDBUSSER
C-130 ASIP MGR
US AIR FORCE
WR-ALC/LBLRS
265 OCMULGEE CT
ROBINS AFB GA 31098-1647
(912)-926-6012
FAX: (912)-926-0970

MR ROB VAN OOST
STRUCTURAL LAMINATES CO
KLUYVERWEG #1
2629 HT
DELFT NETHERLANDS 262985-0001

MR CRAIG B VAN WAY
NORTHROP CORP
M/S 3852/63
ONE NORTHROP AVE
HAWTHORNE CA 90250-3277
(310)-332-9639
FAX: (310)-332-0583

LT COL MARINUS C VOS
ROYAL NETHERLANDS AIR FORCE
OO-ALC/LFA-NE
6061 GUM LN
HILL AFB UT 84056-0001
(801)-777-7741
FAX: (801)-773-7250

CHUONG VU NGOC
BOMBARDIER CANADAIN INC
10000 CARGO RD A4
MIRABEZ QUEBEC J7N 1H3-0001
(514)-476-4354
FAX: (514)-476-4207

MR GARY K WAGGONER
CHF
US AIR FORCE WL/MLS
BLDG 652
2179 TWELFTH ST STE 1
WRIGHT-PATTERSON AFB OH 45433-7718
(513)-255-2282
FAX: (513)-476-4419

DR RUSSELL J H WANHILL
NATL AEROSPACE LAB
PO BOX 153
EMMELOORD
THE NETHERLANDS

MR KEVIN C WATTERS
F-111 TASK MGR
AERO & MARITIME RES LAB
506 LORIMER ST
PO BOX 4331
MELBOURNE VICTORIA AUSTRALIA-3207

MR ANTHONY WAYNE
KC-130 PROJ ENGR
PROGRAM MANAGER AIR
USN(USMC)
PSC BOX 8026
CHERRY POINT NC 28533-0026
(919)-466-8091
FAX: (919)-466-5360

MR DONALD A WELLMANN
MGR BUSINESS DEVP
NAVAL AIR WARFARE CTR
6000 E 21ST ST
MS-16
INDIANAPOLIS IN 46219-0001
(317)-306-4465
FAX: (317)-306-4480

MR MICHAEL J WHISNANT
MKT MGR
MOOG ESPRIT
140 MAYHEW WAY
PHEASANT HILL CA 94523-0001
(510)-947-0400
FAX: (510)-947-0900

MR DAVID J WHITE
CONSULTANT
AEROSTRUCTURES
1725 JEFF DAVIS HWY
ARLINGTON VA 22202-0001
(703)-413-1600
FAX: (703)-413-1611

DR WILLIAM WHITE
US AIR FORCE
WR-ALC/TIE
255 2ND ST STE 122
ROBINS AFB GA 31098-1637
(912)-926-0540
FAX: (912)-926-7420

MR DAVID H WIELAND
RES ENGR
SOUTHWEST RES INST
6220 CULEBRA RD
SAN ANTONIO TX 78228-0510
(210)-522-3864
FAX: (210)-522-3042

MR ROBERT I WILKINS
MANAGER
ROCKWELL INTL SPACE SYS
MC AC04 DEPT 287
12214 LAKEWOOD BLVD
DOWNEY CA 90241-7009
(310)-922-3609
FAX: (310)-922-3728

MR BILL WILKINSON
SR PROJ ENGR
PRATT & WHITNEY CANADA
1000 MARIE VICTORIA
M/S OILE4
LONGUEUIL QUEBEC CANADA J4G-1A1
(514)-647-2241
FAX: (514)-647-7461

MR MARK K WILSON
LEAD ENGR
US AIR FORCE
ASC/ENFS
2335 7TH ST/STE 6
WRIGHT-PATTERSON AFB OH 45433-7809
(513)-255-5485
FAX: (513)-476-4546

MR WILLIAM W WILSON
MANAGER DURABILITY
LOCKHEED MARTIN AERO CO
D 73-25 MS 0199
86 S COBB DR
MARIETTA GA 30063-0001
(770)-494-3093
FAX: (770)-494-9617

DR BARRIE D WRIGHT
CHIEF
BRITISH AEROSPACE (MAD)
STRUCTURES W310C
WARTON AERODROME
PRESTON LANCASHIRE ENG PR41AX-0001

MR RICHARD WURM
EQPM SPECIALIST
US AIR FORCE
OO-ALC/LACI F-4 TCG
6089 WARDLEIGH RD
HILL AFB UT 84056-5838
(801)-777-6886
FAX: (801)-773-7620

DR HSING C YEH
PROJ ENGR
US AIR FORCE
ASC/ENFS BLDG 125
2335 SEVENTH ST STE 6
WRIGHT-PATTERSON AFB OH 45433-7809
(513)-255-3330
FAX: (513)-476-4546

MS JUDY YEUNG
BOMBARDIER CANDAIR DSD
10000 CARGO A-4 STREET
MONTREAL INTL AIRPORT
MIRABEL QUEBEC CANADA J7N-1H3
(514)-476-4000
FAX: (514)-476-4416

MR JAMES D YOST
DPRO-BHT
PO BOX 1605
FT WORTH TX 76101-1605
(817)-280-7609
FAX: (817)-280-7061

MR JESS W YOUNG
F-4 CHIEF
OGDEN ALC/LACM
7278 4TH ST
HILL AFB UT 84056-5205
(801)-777-5291
FAX: (801)-777-5374

DR MASOOD A ZAIDI
SR PRINCIPAL ANALYST
MCDONNELL DOUGLAS AERO
2401 E WARDLOW RD
MS 71-11
LONG BEACH CA 90807-4418
(310)-593-9569
FAX: (310)-593-0648

MR MICHAEL L ZEIGLER
US AIR FORCE
WL/FIBEC
2130 EIGHTH ST/STE 1
WRIGHT-PATTERSON AFB OH 45433-7542
(513)-255-6104
FAX: (513)-476-4999